Transactions of the ASME®

HEAT TRANSFER DIVISION
Chairman, J. M. CHENOWETH
Secretary, J. B. KITTO, JR.
Technical Editor, G. M. FAETH
Associate Technical Editors
J. V. BECK
R. O. BUCKIUS
I. CATTON
R. GREIF
F. P. INCROPERA
H. R. JACOBS
A. D. KRAUS
P. J. MARTO
D. M. McELIGOT
W. A. SIRIGNANO

BOARD ON COMMUNICATIONS
Chairman and Vice President
R. NICKELL

Members-at-Large
J. LLOYD
R. REDER
F. SCHMIDT
M. FRANKE
M. KUTZ
T. MIN
F. LANDIS
R. ROCKE
W. WINER
R. GENTILE
B. ZIELS
R. MATES

President, E. L. DAMAN
Executive Director,
D. L. BELDEN
Treasurer,
ROBERT A. BENNETT

PUBLISHING STAFF
Mng. Dir., Publ., JOS. SANSONE
Managing Editor,
CORNELIA MONAHAN
Sr. Production Editor,
VALERIE WINTERS
Editorial Prod. Asst.,
MARISOL ANDINO

**Transactions of the ASME, Journal of Heat Transfer** (ISSN 0022-1481) is published quarterly (Feb., May, Aug., Nov.) for $155 per year by The American Society of Mechanical Engineers, 345 East 47th Street, New York, NY 10017. Second class postage paid at New York, NY and additional mailing offices. POSTMASTER: Send address changes to The Journal of Heat Transfer, c/o THE AMERICAN SOCIETY OF MECHANICAL ENGINEERS, 22 Law Drive, Box 2300, Fairfield, NJ 07007-2300.
**CHANGES OF ADDRESS** must be received at Society headquarters seven weeks before they are to be effective. Please send old label and new address.
**PRICES:** To members, $29.00, annually; to nonmembers, $155.00.
Add $15.00 for postage to countries outside the United States and Canada.
**STATEMENT from By-Laws.** The Society shall not be responsible for statements or opinions advanced in papers or . . . printed in its publications (B7.1, para. 3).

**INDEXED** by Applied Mechanics Reviews and Engineering Information, Inc.

# Journal of Heat Transfer

Published Quarterly by The American Society of Mechanical Engineers

VOLUME 111 • NUMBER 1 • FEBRUARY 1989

## ANNOUNCEMENTS



## TECHNICAL PAPERS

(Contents continued)



## TECHNICAL NOTES

J. E. Seem

S. A. Klein

W. A. Beckman

J. W. Mitchell

Solar Energy Laboratory,
University of Wisconsin—Madison,
Madison, WI 53706

# Transfer Functions for Efficient Calculation of Multidimensional Transient Heat Transfer

*Finite difference or finite element methods reduce transient multidimensional heat transfer problems into a set of first-order differential equations when thermal physical properties are time invariant and the heat transfer processes are linear. This paper presents a method for determining the exact solution to a set of first-order differential equations when the inputs are modeled by a continuous, piecewise linear curve. For long-time solutions, the method presented is more efficient than Euler, Crank–Nicolson, or other classical techniques.*

## Introduction

Transfer function and response factor methods are used in building simulation programs to compute long-time solutions of transient heat transfer problems in which the system properties are linear and time invariant. Response factors relate the output of a system to a time series of current and past inputs. Transfer functions additionally relate the current output to past outputs, significantly reducing computational effort. In both cases, the inputs or driving functions are modeled by a continuous, piecewise linear curve or equivalently, a series of triangular pulses. Transfer function and response factor methods are more efficient for solving long-time heat transfer problems than Euler, Crank–Nicolson, or other classical techniques because there is no critical time step and the internal temperature distribution is not calculated.

The definition of transfer function used in the field of heat transfer in buildings is different from that used in the field of automatic controls. In automatic controls, a transfer function is the Laplace or $z$ transform of the output divided by the Laplace or $z$ transform of the input. In heat transfer, a transfer function is a difference equation that relates the outputs of a linear, time-invariant system to a time series of current and past inputs, and a time series of past outputs. In this paper, the latter definition will be used.

For one-dimensional problems, Stephenson and Mitalas (1967) determine the "exact" set of transfer functions and/or response factors by solving the conduction equation by Laplace and/or $z$ transforms. To develop response factors or transfer functions for multidimensional heat transfer, it is necessary to discretize the problem spatially by use of finite difference or finite element techniques. Spatial discretization results in a set of first-order differential equations.

Ceylan and Myers (1980) present a method for calculating transfer functions for multidimensional heat transfer from a set of first-order differential equations, which requires the calculation of eigenvalues and eigenvectors of a matrix. Their method involves first calculating response factor coefficients and then converting the response factor coefficients into transfer function coefficients.

This paper presents a method for calculating transfer functions for multidimensional heat transfer that results in fewer coefficients than the method of Ceylan and Myers. In addition, the intermediate step of calculating response factor coefficients is eliminated and it is not necessary to calculate the eigenvalues and eigenvectors of a matrix. The necessary equations and algorithms for computing transfer functions for multidimensional heat transfer are included in this paper. These transfer functions allow computationally simple and accurate two or three-dimensional heat transfer calculations. The method is useful for calculating heat transfer in buildings.

Contributed by the Heat Transfer Division and presented at the ASME/AIChE National Heat Transfer Conference, Pittsburgh, Pennsylvania, August 9–12, 1987. Manuscript received by the Heat Transfer Division November 20, 1987. Keywords: Building Heat Transfer, Numerical Methods.

## Analytical Solution

A state space formulation has traditionally been used to analyze linear systems that may have many inputs and outputs. A heat transfer problem may be formulated in a state space representation by using finite-difference or finite-element methods (Myers, 1971) to discretize the problem spatially. A state space representation for a continuous, linear, time-invariant system is

$$\frac{d\mathbf{x}}{d\tau} = \mathbf{A}\mathbf{x} + \mathbf{B}\mathbf{u} \tag{1}$$

$$\mathbf{y} = \mathbf{C}\mathbf{x} + \mathbf{D}\mathbf{u} \tag{2}$$

Equation (1) is called the state equation and equation (2) is called the output equation in a state space formulation.

In a number of textbooks (Brogan, 1985; Bronson, 1973; Chen, 1984) the solution to a system of first-order differential equations with constant coefficients is given by

$$\mathbf{x}_{t+\delta} = e^{\mathbf{A}\delta}\mathbf{x}_t + \int_t^{t+\delta} e^{\mathbf{A}(t+\delta-\tau)}\mathbf{B}\mathbf{u}(\tau)d\tau \tag{3}$$

The exponential matrix is defined by the power series

$$e^{\mathbf{A}\delta} = \mathbf{I} + \mathbf{A}\delta + \frac{\mathbf{A}^2\delta^2}{2!} + \frac{\mathbf{A}^3\delta^3}{3!} + \ldots + \frac{\mathbf{A}^n\delta^n}{n!} + \ldots \tag{4}$$

Appendix A describes a numerically efficient method for computing the exponential matrix.

The first term on the right-hand side of equation (3) is called the complementary function, force-free response, or zero-input response, and the second term on the right-hand side of equation (3) is called the particular integral, forced response, or zero-state response. The zero-input response of a system involves the response of the state variables to the conditions at time $t$ and the zero-state response is the convolution integral, which integrates the response of the state variables to the inputs between times $t$ and $t+\delta$. Inputs between times $t$ and $t+\delta$ are modeled by a continuous, piecewise linear function and are calculated by

$$\mathbf{u}(\tau) = \mathbf{u}_t + \frac{(\tau - t)}{\delta}(\mathbf{u}_{t+\delta} - \mathbf{u}_t) \tag{5}$$

At this point, the solution of the state equation for heat transfer applications differs from the solution of the state

equations in digital control systems because inputs for digital control systems are not continuous, piecewise linear functions. Åström and Wittenmark (1984) discuss input construction for digital control systems. Substituting equation (5) into equation (3) results in

$$\mathbf{x}_{t+\delta} = e^{\mathbf{A}\delta}\mathbf{x}_t + \int_t^{t+\delta} e^{\mathbf{A}(t+\delta-\tau)}\mathbf{B}\left[\mathbf{u}_t + \frac{(\tau-t)}{\delta}(\mathbf{u}_{t+\delta}-\mathbf{u}_t)\right]d\tau \tag{6}$$

By making the change of variables $\alpha = \tau - t$, equation (6) can be rewritten as

$$\mathbf{x}_{t+\delta} = e^{\mathbf{A}\delta}\mathbf{x}_t + \left[\int_0^{\delta} e^{\mathbf{A}(\delta-\alpha)}d\alpha\right]\mathbf{B}\mathbf{u}_t + \left[\int_0^{\delta} \alpha e^{\mathbf{A}(\delta-\alpha)}d\alpha\right]\left[\frac{\mathbf{B}}{\delta}(\mathbf{u}_{t+\delta}-\mathbf{u}_t)\right] \tag{7}$$

Appendix B describes the steps for integrating the two integrals in equation (7). The solution to the first integral is

$$\int_0^{\delta} e^{\mathbf{A}(\delta-\alpha)}d\alpha = \mathbf{A}^{-1}(e^{\mathbf{A}\delta}-\mathbf{I}) \tag{8}$$

and the solution to the second integral is

$$\int_0^{\delta} \alpha e^{\mathbf{A}(\delta-\alpha)}d\alpha = \mathbf{A}^{-1}\mathbf{A}^{-1}(e^{\mathbf{A}\delta}-\mathbf{I}) - \mathbf{A}^{-1}\delta \tag{9}$$

Substituting the solution of the two integrals, equations (8) and (9), into equation (7) yields

$$\mathbf{x}_{t+\delta} = \Phi\mathbf{x}_t + (\Gamma_1 - \Gamma_2)\mathbf{u}_t + \Gamma_2\mathbf{u}_{t+\delta} \tag{10}$$

where

$$\Phi = e^{\mathbf{A}\delta}$$

$$\Gamma_1 = \mathbf{A}^{-1}(e^{\mathbf{A}\delta}-\mathbf{I})\mathbf{B} = \mathbf{A}^{-1}(\Phi-\mathbf{I})\mathbf{B}$$

$$\Gamma_2 = \left[\mathbf{A}^{-1}\mathbf{A}^{-1}(e^{\mathbf{A}\delta}-\mathbf{I}) - \mathbf{A}^{-1}\delta\right]\frac{\mathbf{B}}{\delta} = \mathbf{A}^{-1}\left[\frac{\Gamma_1}{\delta} - \mathbf{B}\right]$$

Equation (10) relates the states at time $t+\delta$ to the states at time $t$ and the inputs at the times $t$ and $t+\delta$.

The forward shift operator $F$ (Box and Jenkins, 1976) defined by

$$Fz_t = z_{t+\delta} \tag{11}$$

will be now be used to relate the states to previous inputs. Using the forward shift operator, equation (10) can be written as

$$(F\mathbf{I} - \Phi)\mathbf{x}_t = (F\Gamma_2 + \Gamma_1 - \Gamma_2)\mathbf{u}_t \tag{12}$$

Multiplying equation (12) by the inverse of the $(F\mathbf{I} - \Phi)$ matrix gives

$$\mathbf{x}_t = (F\mathbf{I} - \Phi)^{-1}(F\Gamma_2 + \Gamma_1 - \Gamma_2)\mathbf{u}_t \tag{13}$$

Substituting equation (13) into equation (2) yields

$$\mathbf{y}_t = \left[\mathbf{C}(F\mathbf{I} - \Phi)^{-1}(F\Gamma_2 + \Gamma_1 - \Gamma_2) + \mathbf{D}\right]\mathbf{u}_t \tag{14}$$

Equation (14) relates the outputs from the system to the inputs.

The inverse of the $(F\mathbf{I} - \Phi)$ matrix is equal to the adjoint of $(F\mathbf{I} - \Phi)$ divided by the determinant of $(F\mathbf{I} - \Phi)$ (Wiberg, 1971). The degree of $F$ for the determinant of the $(F\mathbf{I} - \Phi)$ matrix is at most $n$ and the degree of $F$ for the adjoint of $(F\mathbf{I} - \Phi)$ is at most $n-1$. Thus, the $(F\mathbf{I} - \Phi)$ matrix can be written as

$$(F\mathbf{I} - \Phi)^{-1} = \frac{\mathbf{R}_0F^{n-1} + \mathbf{R}_1F^{n-2} + \ldots + \mathbf{R}_{n-2}F + \mathbf{R}_{n-1}}{F^n + e_1F^{n-1} + \ldots + e_{n-1}F + e_n} \tag{15}$$

The $\mathbf{R}$ matrices and the $e$ scalar constants can be determined by computing the adjoint of the $(F\mathbf{I} - \Phi)$ matrix and dividing by the determinant of the $(F\mathbf{I} - \Phi)$ matrix or by using Leverrier's algorithm (Wiberg, 1971) described in Appendix C. Substituting equation (15) into (14) results in

$$(F^n + e_1F^{n-1} + \ldots + e_n)\mathbf{y}_t = \Big[\mathbf{C}(\mathbf{R}_0F^{n-1} + \mathbf{R}_1F^{n-2} + \ldots + \mathbf{R}_{n-2}F + \mathbf{R}_{n-1})(F\Gamma_2 + \Gamma_1 - \Gamma_2) + \mathbf{D}(F^n + e_1F^{n-1} + \ldots + e_n)\Big]\mathbf{u}_t \tag{16}$$

Multiplying the matrices on the right side of equation (16) and combining common terms of the forward shift operator gives

$$(F^n + e_1F^{n-1} + \ldots + e_n)\mathbf{y}_t = \Big\{(\mathbf{C}\mathbf{R}_0\Gamma_2 + \mathbf{D})F^n + \Big[\mathbf{C}(\mathbf{R}_1\Gamma_1 - \mathbf{R}_1\Gamma_2 + \mathbf{R}_2\Gamma_2) + e_2\mathbf{D}\Big]F^{n-2} + \ldots + \Big[\mathbf{C}(\mathbf{R}_{n-2}\Gamma_1 - \mathbf{R}_{n-2}\Gamma_2 + \mathbf{R}_{n-1}\Gamma_2) + e_{n-1}\mathbf{D}\Big]F + \Big[\mathbf{C}(\mathbf{R}_{n-1}\Gamma_1 - \mathbf{R}_{n-1}\Gamma_2) + e_n\mathbf{D}\Big]\Big\}\mathbf{u}_t \tag{17}$$

## Nomenclature

$a_{ij}$ = entry in row $i$ and column $j$ of the $\mathbf{A}$ matrix
$A$ = area
$\mathbf{A}$ = $(n \times n)$ constant coefficient matrix
$\mathbf{B}$ = $(n \times p)$ constant coefficient matrix
$\mathbf{C}$ = $(m \times n)$ constant coefficient matrix
$C$ = thermal capacitance
$c$ = specific heat
$\mathbf{D}$ = $(m \times p)$ constant coefficient matrix
$e$ = transfer function coefficients for previous outputs
$F$ = forward shift operator
$h$ = convection coefficient
$\mathbf{I}$ = identity matrix
$k$ = integer used in algorithm for calculating exponential matrix
$L$ = number of terms in truncated power series of exponential matrix
$m$ = number of outputs
$n$ = number of state variables
$p$ = number of inputs
$q''$ = heat flux
$R$ = thermal resistance
$\mathbf{R}$ = $(n \times n)$ constant coefficient matrix
$\mathbf{S}$ = $(m \times p)$ matrix of transfer function coefficients for inputs
$t$ = discrete point in time
$T$ = temperature
$\mathbf{u}$ = vector of $p$ inputs
$\mathbf{x}$ = vector of $n$ state variables
$\mathbf{y}$ = vector of $m$ outputs
$z$ = value of a state or signal
$\alpha$ = dummy variable
$\Gamma_1$ = $(n \times p)$ matrix
$\Gamma_2$ = $(n \times p)$ matrix
$\delta$ = time step
$\tau$ = time
$\Phi$ = $(n \times n)$ exponential matrix

**Subscripts**

$in$ = inside temperature
$out$ = outside temperature
$t$ = state or signal at time $t$
$t + n\delta$ = state or signal $n$ time steps ahead of time $t$

Using the definition of the forward shift operator, equation (17) can be rewritten as

$$\mathbf{y}_{t+n\delta} + e_1\mathbf{y}_{t+(n-1)\delta} + \ldots + e_n\mathbf{y}_t = (\mathbf{C}\mathbf{R}_0\Gamma_2 + \mathbf{D})\mathbf{u}_{t+n\delta}$$
$$+ \left\{\mathbf{C}\left[\mathbf{R}_0(\Gamma_1 - \Gamma_2) + \mathbf{R}_1\Gamma_2\right] + e_1\mathbf{D}\right\}\mathbf{u}_{t+(n-1)\delta}$$
$$+ \left\{\mathbf{C}\left[\mathbf{R}_1(\Gamma_1 - \Gamma_2) + \mathbf{R}_2\Gamma_2\right] + e_2\mathbf{D}\right\}\mathbf{u}_{t+(n-2)\delta} + \ldots$$
$$+ \left\{\mathbf{C}\left[\mathbf{R}_{n-2}(\Gamma_1 - \Gamma_2) + \mathbf{R}_{n-1}\Gamma_2\right] + e_{n-1}\mathbf{D}\right\}\mathbf{u}_{t+\delta}$$
$$+ \left[\mathbf{C}\mathbf{R}_{n-1}(\Gamma_1 - \Gamma_2) + e_n\mathbf{D}\right]\mathbf{u}_t \tag{18}$$

Shifting the inputs and outputs in equation (18) $n$ time steps back gives

$$\mathbf{y}_t + e_1\mathbf{y}_{t-\delta} + \ldots + e_n\mathbf{y}_{t-n\delta} = (\mathbf{C}\mathbf{R}_0\Gamma_2 + \mathbf{D})\mathbf{u}_t$$
$$+ \left\{\mathbf{C}\left[\mathbf{R}_0(\Gamma_1 - \Gamma_2) + \mathbf{R}_1\Gamma_2\right] + e_1\mathbf{D}\right\}\mathbf{u}_{t-\delta}$$
$$+ \left\{\mathbf{C}\left[\mathbf{R}_1(\Gamma_1 - \Gamma_2) + \mathbf{R}_2\Gamma_2\right] + e_2\mathbf{D}\right\}\mathbf{u}_{t-2\delta} + \ldots$$
$$+ \left\{\mathbf{C}\left[\mathbf{R}_{n-2}(\Gamma_1 - \Gamma_2) + \mathbf{R}_{n-1}\Gamma_2\right] + e_{n-1}\mathbf{D}\right\}\mathbf{u}_{t-(n-1)\delta}$$
$$+ \left[\mathbf{C}\mathbf{R}_{n-1}(\Gamma_1 - \Gamma_2) + e_n\mathbf{D}\right]\mathbf{u}_{t-n\delta} \tag{19}$$

Equation (19) can be written more compactly as

$$\mathbf{y}_t = \sum_{j=0}^{n} (\mathbf{S}_j\mathbf{u}_{t-j\delta}) - \sum_{j=1}^{n} (e_j\mathbf{y}_{t-j\delta}) \tag{20}$$

where

$$\mathbf{S}_0 = \mathbf{C}\mathbf{R}_0\Gamma_2 + \mathbf{D}$$

$$\mathbf{S}_j = \mathbf{C}\left[\mathbf{R}_{j-1}(\Gamma_1 - \Gamma_2) + \mathbf{R}_j\Gamma_2\right] + e_j\mathbf{D} \quad \text{for} 1 \le j \le n-1$$

$$\mathbf{S}_n = \mathbf{C}\mathbf{R}_{n-1}(\Gamma_1 - \Gamma_2) + e_n\mathbf{D}$$

Equation (20) is a transfer function equation that relates current outputs to time series of current and past inputs and time series of past outputs. Ceylan and Myers' derivation results in one additional **S** coefficient. The additional **S** coefficient is usually not significant.

The transfer function coefficients in equation (20) may become numerically insignificant as $j$ increases. Thus, the effort of calculating transfer function coefficients can be reduced if only numerically significant coefficients are calculated. A large amount of computer memory would be required to store the $n$ $n \times n$ **R** matrices if equation (20) was used to calculate transfer functions. Fortunately, the storage requirement for the **R** matrices can be reduced to 2 $n \times n$ matrices if Leverrier's algorithm is combined with equation (20). Appendix D contains the steps for computing numerically significant transfer function coefficients with a minimum amount of storage for the **R** matrices.

## Results

The equations and algorithms presented in this paper were used to write a 150 line FORTRAN program for calculating transfer functions from a state space formulation. (The program used a library routine in LINPACK (1979) for calculating the inverse of a matrix.) The program was used to compute sets of transfer function coefficients for 2 through 50 node finite-difference models of a 0.3 m homogeneous concrete wall with a density of 2200 kg/m$^3$, specific heat of 0.84 kJ/kg-°C, thermal conductivity of 1.7 W/m-°C, and convection coefficients at both sides of the wall of 8.3 W/m$^2$-°C. Inside and outside air temperatures were the inputs to the transfer function equation and the heat flux at the interior surface of the wall was the output. Appendix E contains the steps required to calculate transfer function coefficients for a two-node finite-difference model. (When the number of nodes in the finite-difference or finite-element model is small, an interactive matrix package such as Matlab (1982) can be used to compute transfer function coefficients.) Mitalas and Arsenalt's program (1971), which is based upon the solution of a system of partial differential equations, was also used to compute transfer function coefficients. Transfer function coefficients for a 2, 5, and 20 node finite-difference models and the Mitalas and Arsenalt program are compared in Table 1. As the number of nodes in the finite-difference model increase, the transfer function coefficients from the state space formulations approach those of Mitalas and Arsenalt, which are based upon the solution of the partial differential equation (i.e., the continuous model).

**Table 1 Transfer function coefficients for a 0.3 m concrete wall and two, five, and twenty-node finite-difference models of the concrete wall**

| Transfer Function Coefficient | Partial Differential Equation | 2 node | 5 node | 20 node |
|---|---|---|---|---|
| $S_0$ Out. Temp.W/m$^2$-°C | 0 | 0.0094 | 0.0006 | 0 |
| $S_1$ Out. Temp. W/m$^2$-°C | 0.0057 | 0.0346 | 0.0108 | 0.0057 |
| $S_2$ Out. Temp. W/m$^2$-°C | 0.0301 | 0.0079 | 0.02450 | 0.0301 |
| $S_3$ Out. Temp. W/m$^2$-°C | 0.0227 | 0 | 0.0097 | 0.0221 |
| $S_4$ Out. Temp. W/m$^2$-°C | 0.0028 | 0 | 0.0006 | 0.0028 |
| $S_0$ Ins. Temp. W/m$^2$-°C | -6.8395 | -7.8820 | -7.1530 | -6.8554 |
| $S_1$ Ins. Temp. W/m$^2$-°C | 12.8767 | 13.9866 | 15.3087 | 12.9579 |
| $S_2$ Ins. Temp. W/m$^2$-°C | -7.3415 | -6.1566 | -11.1153 | -7.4482 |
| $S_3$ Ins. Temp. W/m$^2$-°C | 1.2935 | 0 | 3.2980 | 1.3406 |
| $S_4$ Ins. Temp.W/m$^2$-°C | -0.0500 | 0 | -0.4015 | -0.0551 |
| $S_5$ Ins. Temp.W/m$^2$-°C | 0.0006 | 0 | 0.0165 | 0.0006 |
| $e_1$ | -1.7442 | -1.6820 | -1.9782 | -1.7502 |
| $e_2$ | 0.9050 | 0.7037 | 1.3116 | 0.9147 |
| $e_3$ | -0.1395 | | -0.3509 | -0.1437 |
| $e_4$ | 0.0041 | | 0.0383 | 0.0045 |
| $e_5$ | 0.0000 | | -0.0014 | 0.0000 |

To compare the transfer functions, heat fluxes were computed when the air temperature on one side of the wall varied with the periodic temperature profile

$$T = -15°\text{C} + 2.8°\text{C}\sin[(\tau\pi)/24\text{ h}]$$

and the air temperature on the other side of the wall was −17.7°C. Figure 1 (outside air temperature varying) and Fig. 2 (inside air temperature varying) contain a graph of the heat flux at the interior surface of the wall for transfer functions based upon two and five-node finite-difference models and the continuous model. Table 2 contains the sum of squares of the residuals (SSQ) between the calculated heat flux for the finite-difference models and the continuous model for a 24 hour period. As the number of nodes in the finite-difference model increases the SSQ decreases.

Table 3 contains the central processing unit (CPU) time of a Micro Vax computer to compute all transfer function coefficients, numerically significant coefficients, and the exponential matrix for different numbers of nodes. (The tolerance limit in Appendix D for the calculation of numerically signifi-

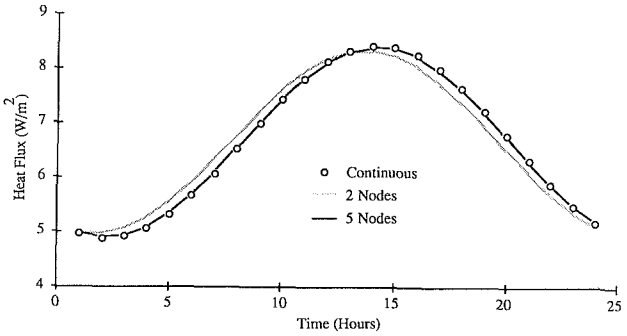


**Fig. 1 Heat flux at interior surface of concrete wall with outside air temperature varying**

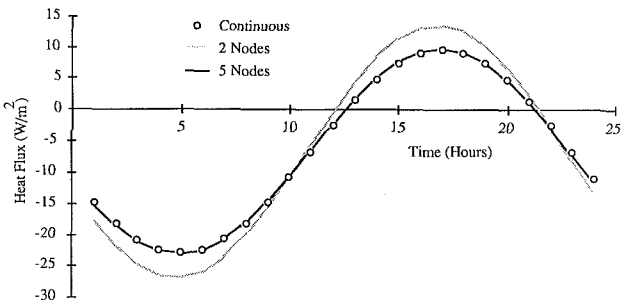


**Fig. 2 Heat flux at interior surface of concrete wall with inside air temperature varying**

cant coefficient was 0.000001.) Table 3 demonstrates the importance of computing only numerically significant coefficients. Also, a majority of the effort in calculating numerical significant coefficients involves the calculation of the exponential matrix.

## Application

Building simulation programs such as DOE-2, TRNSYS, and TARP (1980, 1983, 1983) currently use transfer functions or response factors to model one-dimensional heat transfer through walls, roofs, and floors. Many walls of common construction cannot be accurately modeled with one-dimensional heat transfer. The equations and algorithms described in this paper can be used to calculate transfer functions for walls that require two-dimensional models, e.g., walls that contain metal tee-bars or tie rods. Simulation programs could use these transfer functions to model multidmensional heat transfer in building elements. The ASHRAE handbook of fundamentals (1977, 1981, 1985) lists tables of transfer functions for one-dimensional heat transfer through multilayered slabs. These tables could be updated to include walls that have multidimensional heat transfer. An example demonstrating the importance of properly modeling a roof deck section with steel bulb tees follows.

Transfer function coefficients were generated for one-dimensional and two-dimensional models of a roof deck section taken from an example in ASHRAE (1977, 1981, 1985). Figures 3 shows the inputs ($T_{in}$, $T_{out}$) and output ($q''$) for the transfer functions. The transfer functions were determined for the section of the roof deck shown in Fig. 4. Transfer function coefficients for the one-dimensional model were determined for a multilayered roof with the same area-weighted thermal physical properties as the roof deck section. The steady-state response for the one-dimensional model is equal to the steady-state response in the ASHRAE example. Figure 5 shows the nodal spacing for the two-dimensional finite difference model. Table 4 contains the thermal physical properties of the materials in the roof. The outside convection coefficient is 34 W/m²-°C and the inside convection coefficient is 9.3

**Table 2 Sum of squares of the residuals between continuous model and finite-difference model for a 24 hour period**

| | Sum of Square of Residuals $W^2/m^4$ | |
|---|---|---|
| Number of Nodes | Outside Temp. Varying | Inside Temp. Varying |
| 2 | 1.0 | 200.0 |
| 5 | 0.017 | 1.6 |
| 10 | 0.00070 | 0.060 |
| 15 | 0.00012 | 0.010 |
| 20 | 0.000035 | 0.0030 |

**Table 3 CPU time to compute the exponential matrix, all transfer function coefficients, and all numerically significant transfer function coefficients**

| | Central Processing Unit Time in Seconds | | |
|---|---|---|---|
| Number of Nodes | Exponential Matrix | All Coefficients | Numerically Significant Coefficients |
| *10* | *0.25* | *0.54* | *0.32* |
| 20 | 1.8 | 4.7 | 2.1 |
| 30 | 6.1 | 19.1 | 6.8 |
| 40 | 15.0 | 54.5 | 16.3 |
| 50 | 30.6 | 123.2 | 32.9 |

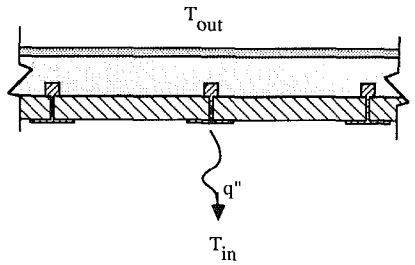


**Fig. 3 Roof deck with bulb tees 0.6 m on center**

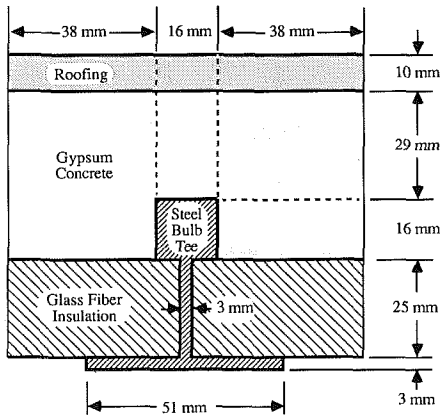


***Fig. 4 Section of the roof deck***

W/m²-°C. Table 5 contains the transfer function coefficients for the one-dimensional and two-dimensional models of the roof deck section.

A graph of a 0.56°C (1°F) step change in outdoor temperature with an indoor temperature equal to zero for one and two-dimensional models can be seen in Fig. 6. The steady-state and transient response for the two models is significantly different. This graph demonstrates the importance of properly modeling the steel bulb tees in the roof deck section.

The equations presented in this paper could be used to compute a comprehensive room transfer function (CRTF) for a room. A CRTF is a single transfer function that relates the loads for a room, zone, or building to the inputs, e.g., solar

**Table 4 Thermal properties of the materials in the roof deck**

| Material | Thermal Conductivity (W/m-°C) | Density (kg/m$^3$) | Specific Heat (kJ/kg-°C) |
|---|---|---|---|
| Roofing | 0.16 | 110.0 | 1.5 |
| Gypsum Concrete | 0.24 | 82.0 | 0.88 |
| Steel | 45.0 | 7800.0 | 0.50 |
| Glass Fiber | 0.036 | 8.0 | 0.96 |

**Table 5 Transfer function coefficients for one-dimensional and two-dimensional models of roof deck section**

| | ONE-DIMENSIONAL | | | TWO-DIMENSIONAL | | |
|---|---|---|---|---|---|---|
| i | Outside Temp. $S_i$ (W/m$^2$-°C) | Inside Temp. $S_i$ (W/m$^2$-°C) | $e_i$ | Outside Temp. $S_i$ (W/m$^2$-°C) | Inside Temp. $S_i$ (W/m$^2$-°C) | $e_i$ |
| 0 | 0.508 | -6.280 | | 0.304 | -4.567 | |
| 1 | 1.172 | 4.571 | -0.406 | 0.857 | 3.536 | -0.469 |
| 2 | 0.115 | -0.085 | 0.004 | 0.125 | -0.257 | 0.019 |
| 3 | 0.000 | 0.000 | 0.000 | 0.000 | 0.002 | -0.000 |

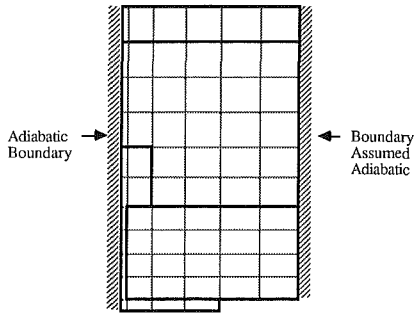


**Fig. 5 Nodal spacing of two-dimensional finite-difference model**

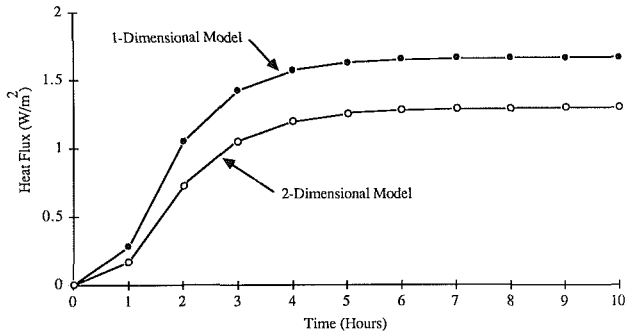


**Fig. 6 Response to 0.56°C (1°F) step change in outdoor temperature for a section of the roof deck**

gains outdoor temperature, indoor temperature. Seem et al. (1987) have reported on the computational savings of using a CRTF over the heat balance method discussed in ASHRAE (1977, 1981, 1985).

## Conclusion

There are a number of areas of application, besides walls, where transfer functions for multidimensional heat transfer could be used. Transfer functions could be developed to model multidimensional heat transfer processes in an attic, a basement, or earth-contact structure, or a room or building. These transfer functions could be used to improve the speed and accuracy of building simulation programs. Transfer functions for all these applications can be efficiently calculated by using the algorithms presented in this paper.

## Acknowledgments

Financial support for this work has been provided by Lawrence Berkeley Laboratory, University of California and the Solar Heating & Cooling Research Development Branch, Office of Conservation and Solar Applications, U. S. Department of Energy.

## References

*ASHRAE Handbook of Fundamentals*, 1977, 1981, 1985, American Society of Heating, Refrigeration, and Air Conditioning Engineers, Atlanta, GA.

Åström, K. A., and Wittenmark, B., 1984, *Computer-Controlled Systems Theory and Design*, Prentice-Hall, Inc., Englewood Cliffs, NJ, pp. 20-32.

Atkinson, K. E., 1978, *An Introduction to Numerical Analysis*, Wiley, New York, pp. 415-421.

Box, G. E. P., and Jenkins, G. M., 1976, *Time Series Analysis Forecasting and Control*, Holden Day, San Francisco, CA, p. 8.

Brogan, W. L., 1985, *Modern Control Theory*, 2nd ed., Prentice Hall, Inc., Englewood Cliffs, NJ.

Bronson, R., 1973, *Modern Introductory Differential Equations*, McGraw-Hill, New York.

Cadzow, J. A., and Martens, H. R., 1970, *Discrete-Time and Computer Control Systems*, Prentice-Hall, Inc., Englewood Cliffs, NJ, pp. 389-390.

Ceylan, H. T., and Myers, G. E., 1980, "Long-Time Solutions to Heat Conduction Transients With Time-Dependent Inputs," ASME JOURNAL OF HEAT TRANSFER, Vol. 102, No. 1, pp. 115-120.

Chen, C.-T., 1984, *Linear System Theory and Design*, Holt, Rinehart and Winston, New York.

DOE-2, 1980, "DOE-2 Reference Manual, Version 2.1," Report LBL-8706, Revision 1, Lawrence Berkeley Laboratory, CA.

Klein, S. A., et al., 1983, "TRNSYS A Transient System Simulation Program," Solar Energy Laboratory, University of Wisconsin—Madison, Engineering Experiment Station Report 38-12, Dec.

*Linpack User's Guide*, 1979, Society for Industrial and Applied Mathematics, Philadelphia, PA.

*Matlab*, 1982, Interactive Matrix Language, University of Wisconsin—Madison, MACC Academic Computing Center, Revision 1.

Mitalas, G. P., and Arseneault, J. G., 1971, "Fortran IV Program to Calculate z-Transfer Functions for the Calculation of Transient Heat Transfer Through Walls and Roofs," *Proceedings of the Conference on Use of Computers for Environmental Engineering Related to Buildings*, Gaithersburg, MD, NBS Building Science Series 39, Oct.

Moler, C., and Van Loan, 1978, "Nineteen Dubious Ways to Compute the Exponential of a Matrix," *Society for Industrial and Applied Mathematics Review*, Vol. 20, No. 4, pp. 801-836.

Myers, G. E., 1971, *Analytical Methods in Conduction Heat Transfer*, McGraw-Hill, New York.

Seem, J. E., Klein, S. A., Beckman W. A., and Mitchell, J. W., 1987, "Comprehensive Room Transfer Functions for Efficient Calculation of the Transient Heat Transfer Processes in Buildings," presented at the 1987 ASME/AIChE National Heat Transfer Conference, Technical Session on Heat Transfer in Buildings, Pittsburgh, PA, Aug.

Stephenson, D. G., and Mitalas, G. P., 1967, "Cooling Load Calculations by Thermal Response Factor Method," *ASHRAE Transactions*, Vol. 73, Part I, pp. III.1.1.-III.1.7.

Stephenson, D. G., and Mitalas, G. P., 1971, "Calculation of Heat Conduction Transfer Functions for Multi-layer Slabs," *ASHRAE Transactions*, Vol. 77, Part II, pp. 117-126.

Walton, G. N., 1983, "Thermal Analysis Research Program Reference Manual (TARP)," National Bureau of Standards, NBSIR 83-2655.

Wiberg, D. M., 1971, *State Space and Linear Systems*, McGraw-Hill, New York, pp. 117-118.

# APPENDIX A

## Calculation of the Exponential Matrix

The calculation of the exponential matrix is an important step in the calculation of transfer functions from a system of first-order differential equations with constant coefficients. There are a number of different methods available for calculating the exponential of a matrix. Moler and Van Loan (1978) have compared 19 different algorithms for calculating the exponential of a matrix and have concluded that the power series expansion with scaling and squaring is one of the most effective methods. This method is described below.

The approximation

$$e^{\mathbf{A}\delta} \approx \mathbf{I} + \mathbf{A}\delta + \frac{\mathbf{A}^2\delta^2}{2!} + \frac{\mathbf{A}^2\delta^3}{3!} + \ldots + \frac{\mathbf{A}^L\delta^L}{L!} \qquad (21)$$

for the exponential matrix is obtained by truncating the power series expansion for the exponential matrix, equation (4), after $L$ terms. A criterion is required for determining the number of

terms to keep. Cadzow and Martens (1970) give the following relation for calculating $L$:

$$L = \text{minimum of } \{3\|\mathbf{A}\delta\|_\infty + 6\} \text{ or } 100 \tag{22}$$

$\|\mathbf{A}\delta\|_\infty$ is a matrix row norm (Atkinson, 1978). The matrix row norm is calculated by

$$\|\mathbf{A}\delta\|_\infty = \underset{1\le i\le n}{\text{Maximum}} \sum_{j=1}^{n} |a_{ij}\delta| \tag{23}$$

Equations (21) and (22) can be used to calculate the exponential of a matrix with at least six digits of accuracy. From equation (22) it can be seen that the number of terms in the truncated power series expansion increases and thus the computational effort increases as the matrix norm of $\mathbf{A}\delta$ increases. Scaling and squaring can be used to reduce the computational effort when the matrix norm of $\mathbf{A}\delta$ is large.

The following steps can be used to calculate the exponential matrix by a truncated power series expansion with scaling and squaring:

1 Use equation (23) to calculate $\|\mathbf{A}\delta\|_\infty$
2 Find the smallest integer $k$ such that $2^k \ge \|\mathbf{A}\delta\|_\infty$
3 Divide all entries in the matrix $\mathbf{A}\delta$ by $2^k$
4 Determine $L$ from equation (22) for $[\mathbf{A}\delta/2^k]$
5 Calculate $e^{[\mathbf{A}\delta/2^k]}$ from equation (21)
6 Square $e^{[\mathbf{A}\delta/2^k]}$ $k$ times to obtain $e^{\mathbf{A}\delta}$

## APPENDIX B

### Integration of Integrals in Equation (7)

This appendix contains the steps for evaluating the two integrals in equation (7). Substituting the power series expansion for $e^{-\mathbf{A}\alpha}$, equation (4), into the first integral in equation (7) results in

$$\int_0^\delta e^{\mathbf{A}(\delta-\alpha)}d\alpha = e^{\mathbf{A}\delta}\left[\int_0^\delta \left(\mathbf{I} - \mathbf{A}\alpha + \frac{\mathbf{A}^2\alpha^2}{2!} + \ldots\right)d\alpha\right] \tag{24}$$

Integrating the power series expansion for $e^{-\mathbf{A}\alpha}$ term by term and substituting in the limits of integration gives

$$\int_0^\delta e^{\mathbf{A}(\delta-\alpha)}d\alpha = \left(\mathbf{I} + \mathbf{A}\delta + \frac{\mathbf{A}^2\delta^2}{2!} + \ldots\right)\left(\mathbf{I}\delta - \frac{\mathbf{A}\delta^2}{2} + \frac{\mathbf{A}^2\delta^3}{3!} - \ldots\right) \tag{25}$$

Multiplying the two power series in equation (25) and combining common terms results in

$$\int_0^\delta e^{\mathbf{A}(\delta-\alpha)}d\alpha = \mathbf{I}\delta + \frac{\mathbf{A}\delta^2}{2!} + \frac{\mathbf{A}^2\delta^3}{3!} + \frac{\mathbf{A}^3\delta^4}{4!} + \ldots \tag{26}$$

Equation (26) can be rewritten as

$$\int_0^\delta e^{\mathbf{A}(\delta-\alpha)}d\alpha = \mathbf{A}^{-1}\left(\mathbf{I} + \mathbf{A}\delta + \frac{\mathbf{A}^2\delta^2}{2!} + \frac{\mathbf{A}^3\delta^3}{3!} + \ldots\right) - \mathbf{A}^{-1}$$

$$= \mathbf{A}^{-1}(e^{\mathbf{A}\delta} - \mathbf{I}) \tag{27}$$

Next, the second integral in equation (7) will be determined by following a similar procedure.

$$\int_0^\delta \alpha e^{\mathbf{A}(\delta-\alpha)}d\alpha = e^{\mathbf{A}\delta}\left[\int_0^\delta \left(\mathbf{I}\alpha - \mathbf{A}\alpha^2 + \frac{\mathbf{A}^2\alpha^3}{2!} - \ldots\right)d\alpha\right]$$

$$= \left(\mathbf{I} + \mathbf{A}\delta + \frac{\mathbf{A}^2\delta^2}{2!} + \ldots\right)\left(\frac{\mathbf{I}\delta^2}{2} - \frac{\mathbf{A}\delta^3}{3} + \frac{\mathbf{A}^2\delta^4}{8} - \ldots\right)$$

$$= \frac{\mathbf{I}\delta^2}{2!} + \frac{\mathbf{A}\delta^3}{3!} + \frac{\mathbf{A}^2\delta^4}{4!} + \frac{\mathbf{A}^3\delta^5}{5!} + \ldots$$

$$= \mathbf{A}^{-1}\mathbf{A}^{-1}\left(\mathbf{I} + \mathbf{A}\delta + \frac{\mathbf{A}^2\delta^2}{2!} + \ldots\right) - \mathbf{A}^{-1}\mathbf{A}^{-1} - \mathbf{A}^{-1}\delta$$

$$= \mathbf{A}^{-1}\mathbf{A}^{-1}\left(e^{\mathbf{A}\delta} - \mathbf{I}\right) - \mathbf{A}^{-1}\delta \tag{28}$$

## APPENDIX C

### Leverrier's Algorithm

Wilberg (1971) presents a proof of Leverrier's algorithm for calculating the inverse of the $(F\mathbf{I} - \Phi)$ matrix. Leverrier's algorithm for calculating the $e$ scaler constants and $\mathbf{R}$ matrices in equation (15) consists of the following sequential relationships:

$$\mathbf{R}_0 = \mathbf{I} \qquad e_1 = \frac{\text{Tr}(\Phi\mathbf{R}_0)}{1}$$

$$\mathbf{R}_1 = \Phi\mathbf{R}_0 + e_1\mathbf{I} \qquad e_2 = -\frac{\text{Tr}(\Phi\mathbf{R}_1)}{2}$$

$$\mathbf{R}_2 = \Phi\mathbf{R}_1 + e_2\mathbf{I} \qquad e_3 = -\frac{\text{Tr}(\Phi\mathbf{R}_2)}{3}$$

$$\vdots \qquad\qquad \vdots$$

$$\mathbf{R}_{n-1} = \Phi\mathbf{R}_{n-2} + e_{n-1}\mathbf{I} \qquad e_n = -\frac{\text{Tr}(\Phi\mathbf{R}_{n-1})}{n}$$

where Tr $(\mathbf{G})$ is the trace of the matrix $\mathbf{G}$. The trace of a matrix is equal to the sum of the diagonal elements of the matrix.

## APPENDIX D

### Efficient Calculation of Transfer Functions

A large amount of computer memory would be required to store the $n$ $n\times n$ $\mathbf{R}$ matrices if Leverrier's algorithm were used to compute transfer function coefficients. Fortunately, the storage requirement can be reduced to two $n\times n$ matrices if Leverrier's algorithm is combined with the analytical solution. Also, it may not be necessary to calculate all transfer function coefficients because the coefficients may become numerically insignificant as $j$ increases. The absolute values of the $e_j$ coefficients decrease as $j$ increases. This fact can be used as a criterion to stop calculating transfer function coefficients. The following steps can be used to compute numerically significant coefficients with a minimum amount of computer storage for the $\mathbf{R}$ matrices (only two $n\times n$ $\mathbf{R}$ matrices need to be stored):

1 Compute the exponential matrix $\Phi = e^{\mathbf{A}\delta}$
2 Use equation (10) to compute $\Gamma_1$ and $\Gamma_2$
3 Use equation (20) to compute $\mathbf{S}_0$
4 $\mathbf{R}_{\text{new}} = \mathbf{I}$
5 For $j = 1$ to $n-1$ with a step size of 1

$$\mathbf{R}_{\text{old}} = \mathbf{R}_{\text{new}}$$

$$e_j = -\frac{\text{Tr}(\Phi\mathbf{R}_{\text{old}})}{j}$$

$$\mathbf{R}_{\text{new}} = \Phi\mathbf{R}_{\text{old}} + e_j\mathbf{I}$$

$$\mathbf{S}_j = \mathbf{C}[\mathbf{R}_{\text{old}}(\Gamma_1 - \Gamma_2) + \mathbf{R}_{\text{new}}\Gamma_2] + e_j\mathbf{D}$$

Stop if the absolute value of $e_j$ is less than a tolerance limit

6 $e_n = -\dfrac{\text{Tr}(\Phi\mathbf{R}_{\text{new}})}{n}$

7 $\mathbf{S}_n = \mathbf{C}\mathbf{R}_{\text{new}}(\Gamma_1 - \Gamma_2) + e_n\mathbf{D}$

## APPENDIX E

### Two-Node Example

This appendix demonstrates the calculation of a transfer function equation for a homogeneous plane wall with constant thermal properties. Heat transfer through the wall is assumed to be one dimensional. Inputs are inside and outside air temperatures. The heat flux at the interior surface of the wall is the output of interest. The first step in calculating a transfer function equation is to use finite-difference methods to discretize the problem spatially. A two-node finite-difference model can be seen in Fig. 7.

Energy balances performed at the two nodes result in the set of first-order differential equations

$$C\frac{dT_1}{d\tau}=hA(T_{out}-T_1)+\frac{T_2-T_1}{R} \tag{29}$$

$$C\frac{dT_2}{d\tau}=hA(T_{in}-T_2)+\frac{T_1-T_2}{R} \tag{30}$$

The resistance between the nodes can be calculated from the following equation:

$$R=\frac{L}{kA} \tag{31}$$

The thermal capacitance of a node can be calculated by

$$C=\frac{\rho cLA}{2} \tag{32}$$

The heat flux across the interior surface of the wall can be calculated by

$$q''=h(T_2-T_{in}) \tag{33}$$

Equations (29) through (33) can be formulated in the following state space representation by letting the temperatures of the nodes be the two states:

$$\begin{bmatrix}\frac{dT_1}{d\tau}\\ \frac{dT_2}{d\tau}\end{bmatrix}=\begin{bmatrix}-\frac{1}{RC}-\frac{hA}{C} & \frac{1}{RC}\\ \frac{1}{RC} & -\frac{1}{RC}-\frac{hA}{C}\end{bmatrix}\begin{bmatrix}T_1\\ T_2\end{bmatrix}$$

$$+\begin{bmatrix}\frac{hA}{C} & 0\\ 0 & \frac{hA}{C}\end{bmatrix}\begin{bmatrix}T_{out}\\ T_{in}\end{bmatrix}$$

$$[q'']=[0 \quad h]\begin{bmatrix}T_1\\ T_2\end{bmatrix}+[0 \quad -h]\begin{bmatrix}T_{out}\\ T_{in}\end{bmatrix}$$

For a 0.3 m concrete wall with a density of 2200 kg/m$^3$, specific heat of 0.84 kJ/kg-°C, thermal conductivity of 1.7 W/m-°C, and convection coefficients of 8.3 W/m$^2$-°C, the matrices in the state space formulation become

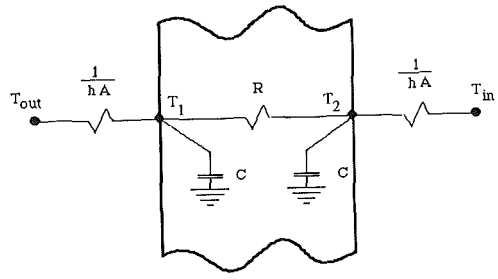


Fig. 7 Two-node model of plane wall

$$\mathbf{A}=\begin{bmatrix}-0.1757 & 0.0714\\ 0.0714 & -0.1757\end{bmatrix}\text{h}^{-1} \quad \mathbf{B}=\begin{bmatrix}0.1043 & 0.0\\ 0.0 & 0.1043\end{bmatrix}\text{h}^{-1}$$

$$\mathbf{C}=[0.0 \quad 8.3]\,\text{W/m}^2\text{-°C} \quad \mathbf{D}=[0.0 \quad -8.3]\,\text{W/m}^2\text{-°C}$$

The exponential matrix $\Phi$ can be calculated by the algorithm described in Appendix A or by the techniques demonstrated by Brogan (1985) or Chen (1984). The Brogan and Chen methods are easier to use when making hand calculations of an exponential matrix. For this example, the exponential matrix with a 1 hour time step is

$$\Phi=e^{\mathbf{A}\delta}=\begin{bmatrix}0.8410 & 0.0600\\ 0.0600 & 0.8410\end{bmatrix}$$

Carrying out the matrix manipulations described by equation (10) results in

$$\Gamma_1=\mathbf{A}^{-1}(\Phi-\mathbf{I})\mathbf{B}=\begin{bmatrix}0.0957 & 0.0033\\ 0.0033 & 0.0957\end{bmatrix}$$

$$\Gamma_2=\mathbf{A}^{-1}\left[\frac{\Gamma_1}{\delta}-\mathbf{B}\right]=\begin{bmatrix}0.0492 & 0.0011\\ 0.0011 & 0.0492\end{bmatrix}$$

The inverse of the $(F\mathbf{I}-\Phi)$ matrix is computed by dividing the adjoint of the $(F\mathbf{I}-\Phi)$ matrix by the determinant of the $(F\mathbf{I}-\Phi)$ matrix.

$$(F\mathbf{I}-\Phi)^{-1}=\begin{bmatrix}F-0.8410 & -0.0600\\ -0.0600 & F-0.8410\end{bmatrix}^{-1}$$

$$=\frac{\begin{bmatrix}F-0.8410 & 0.0600\\ 0.0600 & F-0.8410\end{bmatrix}}{(F-0.8410)(F-0.8410)-0.0600^2}$$

$$=\frac{\begin{bmatrix}1 & 0\\ 0 & 1\end{bmatrix}F+\begin{bmatrix}-0.8410 & 0.0600\\ 0.0600 & -0.8410\end{bmatrix}}{F^2-1.6820\,F+0.7037}$$

The constant coefficient matrices and scaler constants in equation (15) are

$$e_1 = -1.6820$$
$$e_2 = 0.7037$$

$$\mathbf{R}_0 = \mathbf{I}$$

$$\mathbf{R}_1 = \begin{bmatrix} -0.8410 & 0.0600 \\ 0.0600 & -0.8410 \end{bmatrix}$$

Equation (20) can be used to compute the S matrices.

$$\mathbf{S}_0 = \mathbf{C}\mathbf{R}_0\Gamma_2 + \mathbf{D} = [0.0094 \quad -7.8820]\ \mathrm{W/m^2\text{-}^\circ C}$$

$$\mathbf{S}_1 = \mathbf{C}[\mathbf{R}_0(\Gamma_1 - \Gamma_2) + \mathbf{R}_1\Gamma_2] + e_1\mathbf{D}$$
$$= [0.0346 \quad 13.9866]\ \mathrm{W/m^2\text{-}^\circ C}$$

$$\mathbf{S}_2 = \mathbf{C}\mathbf{R}_1(\Gamma_1 - \Gamma_2) + e_2\mathbf{D} = [0.0079 \quad -6.1566]\ \mathrm{W/m^2\text{-}^\circ C}$$

The transfer function equation for this two-node example is

$$q''_t = \mathbf{S}_0\mathbf{u}_t + \mathbf{S}_1\mathbf{u}_{t-\delta} + \mathbf{S}_2\mathbf{u}_{t-2\delta} - e_1 q''_{t-\delta} - e_2 q''_{t-2\delta}$$
$$= 0.0094T_{t,out} + 0.0346T_{t-\delta,out} + 0.0079T_{t-2\delta,out}$$
$$- 7.8820T_{t,in} + 13.9866T_{t-\delta,in}$$
$$- 6.1566T_{t-2\delta,in} + 1.682q''_{t-\delta} - 0.7037q''_{t-2\delta}$$

# ERRATA

Errata for "Natural Convection Heat Transfer From a Discrete Thermal Source on a Vertical Surface" by T. L. Ravine and D. E. Richards, published in the November 1988 issue of the ASME JOURNAL OF HEAT TRANSFER, Vol. 110, pp. 1007–1009:

Figure 2 was printed upside down. The correct orientation of the figure is shown below.

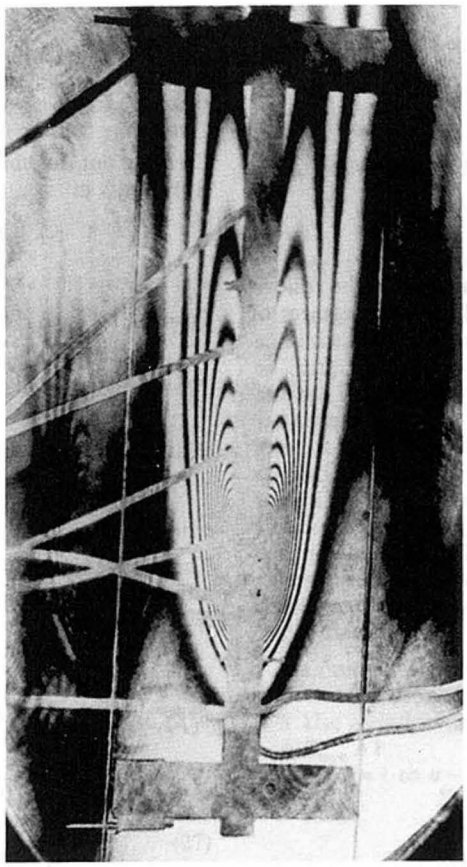

**Fig. 2 Interferograms of a vertical flat plate with a discrete thermal source ($Ra_l = 5774$, $d/l = 2.00$, and $L/l = 9.00$)**

# The Fundamentals of Sliding Contact Melting and Friction

**A. Bejan**
Department of Mechanical Engineering and Materials Science, Duke University, Durham, NC 27706
Fellow ASME

*This paper focuses on the phenomenon of melting and lubrication by the sliding contact between a phase-change material and a smooth flat slider. The first part of the study considers the limit in which the melting is due primarily to "direct heating," that is, to the temperature difference between the solid slider and the melting point of the phase-change material. It is shown that in this limit the relative motion gap has a uniform thickness and that the friction factor decreases as both the normal force and the temperature difference increase. The second part considers the limit where the melting is caused mainly by the frictional heating of the liquid formed in the relative motion gap. This gap turns out to have a converging-diverging shape that varies with the parameters of the problem. As the normal force increases, a larger fraction of the melt is pushed out through the upstream opening of the relative motion gap. Means for calculating the melting speed, the friction factor, and the temperature rise along the slider surface are developed.*

## 1 Introduction

The subject of this paper is a most basic phenomenon of combined melting and lubrication that can occur at the interface between two solid parts, one of which is at its melting point. One way to visualize this phenomenon rapidly is to think of the kitchen experiment in which a stick of butter is rubbed against a metallic plate, or against a well-polished wooded block. These two situations are, more or less, covered by the isothermal-base and adiabatic-base models presented in sections 3 and 4, respectively.

The melting and lubrication phenomenon addressed here has both classical and modern applications. The classical application is the explanation it provides for the relatively low coefficient of sliding friction on ice and snow. The original explanation offered for this observation is due to Osborne Reynolds (1901), who suggested that the liquid film formed between skate and ice is due to "pressure melting," that is, to the fact that the melting point of ice decreases as the pressure increases (Cravalho and Smith, 1981). Careful studies conducted over the past five decades have shown that the liquid film is created in fact by the viscous friction in the liquid film itself (see, for example, Bowden and Hughes, 1939; Bowden, 1953; Evans et al., 1976; Oksanen and Keinonen, 1981; Akkok et al., 1987). The theoretical work that has been done on this problem is concerned primarily with the heat transfer processes external to the relative motion gap, namely, the heat transfer into the ice and into the skate. The analytical models described in this literature are one-dimensional, in the sense that they neglect the spatial (longitudinal and sideway) variations of the heat and fluid flow characteristics over the sliding-contact area. In the two problems considered in this paper, the focus is on the variation of the temperature and velocity fields over the area wetted by the melt.

Among the more modern applications of the phenomenon worth noting is the coating of a metallic part with another metal whose melting point is considerably lower. The function of the latter is to melt and serve as lubricant in the manufacturing process to which the former may be subjected. Another application is in the field of interior ballistics, where a projectile (e.g., brass bullet) melts superficially as it travels along the gun barrel (Aung, 1986). A third application—the one that first drew my attention to this phenomenon—is to the subject of "close-contact" melting, which now is receiving increased attention (see, for example, Moallemi and Viskanta, 1986a, 1986b; Prasad and Sengupta, 1987; Bahrami and Wang, 1987). In the close-contact melting problem the relative motion and the associated frictional heating of the liquid film are not important; however, the fluid mechanics (lubrication) part of the problem is similar to the fluid mechanics component of the present study.

Contributed by the Heat Transfer Division for publication in the JOURNAL OF HEAT TRANSFER. Manuscript received by the Heat Transfer Division October 9, 1987. Keywords: Conduction, Phase-Change Phenomena.

## 2 Physical Model

There are two basic configurations that suggest the simplified model on which the present theory is based, namely, the case of a block of phase-change material pressed against a moving solid surface (Fig. 1*a*) and the case of a solid block pressed against the moving surface of a semi-infinite phase-change material (Fig. 1*b*). In both configurations the function of the solid is to "melt" the phase-change material, either by means of direct heat transfer (section 3) or by virtue of the heat generated by friction in the relative motion gap (section 4).

In the configuration of Fig. 1(*a*) the melting of the phase-change material produces a steady (constant thickness) liquid film covering the swept portion of the moving solid surface. Relative to a stationary observer, the block of phase-change material travels downward with the velocity $V$. We shall refer to $V$ as the "melting" speed (rate) of the phase-change material. In the second configuration (Fig. 1*b*), the solid block is stationary along the vertical. However, the sliding-contact melting process eats into the phase-change material the same way as in Fig. 1(*a*). Note the slight tilt of the sliding contact interface in Fig. 1(*b*), which means that the solid block is indeed moving into the phase-change material: This movement is in the direction normal to the sliding contact interface.

For the sake of simplicity we key the analytical model on the configuration shown in Fig. 1(*a*), because in that case the flat solid surface (the "slider") travels in a direction parallel to itself. The main features of the model are identified in Fig. 1(*c*). The coordinate system $(x, y, z)$ is attached to the frontal plane of the phase-change material and to the horizontal plane formed by the surface of the moving solid. Projected on the horizontal plane, the sliding contact area is the rectangle $L \times B$, where $L$ is the dimension measured in the direction of relative motion. The block of phase-change material is being pushed vertically downward with a known normal force $F_n$. The melting rate (or the vertical velocity $V$) is one of the unknowns of the problem. The semi-infinite solid moves to the right with the known velocity $U$. The net tangential force $F_t$ experienced by it and, reciprocally, by the melting block, is another important unknown of the problem. This second unknown is represented alternatively by the friction coefficient defined as $\mu_f = F_t/F_n$.

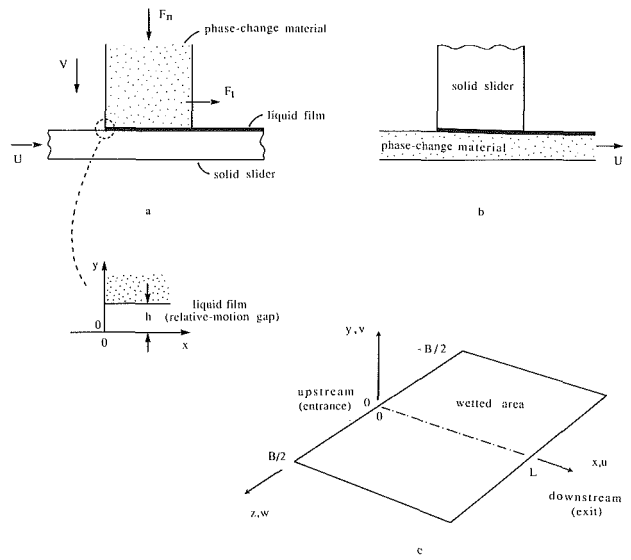


**Fig. 1 (*a*) Block of phase-change material pressed against a solid slider; (*b*) solid block pressed against a moving bed of phase-change material, and (c) the shape and dimensions of the sliding-contact area**

## 3 Direct Heating

**3.1 Temperature Distribution.** In order to isolate the melting by sliding contact phenomenon from other heat transfer processes that might compete in the configurations of Figs. 1(*a*) and 1(*b*), we model the block of phase-change material as isothermal at the melting temperature $T_m$. In this section we are concerned with the melting caused by direct heating across the sliding contact area; therefore, we model the moving solid as isothermal ($T_s$) and assume that the temperature difference $\Delta T = T_s - T_m$ is a known constant.

The focus is on the thin liquid film that fills the sliding-contact gap. The vertical dimension of this gap $h$ is in general a function of both $x$ and $z$. Neglecting the effect of thermal diffusion in the $x$ and $z$ directions, we recognize the energy conservation equation

$$u\frac{\partial T}{\partial x}+v\frac{\partial T}{\partial y}+w\frac{\partial T}{\partial z}=\alpha\frac{\partial^2 T}{\partial y^2}+\frac{\mu}{\rho c}\Phi \tag{1}$$

in which the last term represents the effect of internal heat generation by fluid friction. Collected on the left side of equation (1) are the convection terms, whose representative scale is $U\Delta T/L$. The scale of the vertical diffusion effect (the first term on the right side of the equation) is $\alpha\Delta T/h^2$, while the scale of the volumetric heating effect is $(\mu/\rho c)(U/h)^2$. Comparing these scales we see that the effects of convection and frictional heating can be neglected if, simultaneously, $Uh^2/(\alpha L)<1$ and $\mu U^2/(k\Delta T)<1$. If these inequalities are true in an order of magnitude sense, we may retain only the vertical thermal diffusion term in the energy equation (1) in order to deduce the temperature distribution in the liquid layer

$$T=\Delta T\left(1-\frac{y}{h}\right) \tag{2}$$

The unknown gap thickness $h$ follows from the melting condition that controls the position of the upper surface of the liquid gap

$$-k\left(\frac{\partial T}{\partial y}\right)_{y=h}=\rho h_{sf}V \tag{3}$$

in which $h_{sf}$ is the usual thermodynamics notation for the latent heat of fusion ($h_{sf}$ should not be confused with the gap height $h$). Combining equations (2) and (3) we find that the height $h$ varies inversely with the normal speed $V$

$$h=\frac{k\Delta T}{\rho h_{sf}V} \tag{4}$$

The important conclusion to draw at this stage is that the liquid gap thickness $h$ is a constant. This constant is still unknown, because the melting speed $V$ is not specified. Intuitively we expect a relationship between $V$ and the normal force applied on the block of phase-change material ($F_n$); therefore, we now turn our attention to the fluid mechanics part of the thin liquid film problem.

**3.2 Pressure Distribution.** The treatment of the fluid mechanics part is a two-dimensional extension of Osborne Reynolds' classical theory of lubrication (Batchelor, 1967), according to which the liquid inertia and the pressure variations in the transverse direction ($y$) are negligible. We are interested in determining the pressure field $P(x, z)$ in order to connect it eventually to the applied normal force

## Nomenclature

$B$ = width of sliding-contact area, Fig. 1
$c$ = specific heat of liquid
$c_s$ = specific heat of slider material
$F_n$ = normal force, Fig. 1
$F_t$ = tangential force, Fig. 1
$G$ = negative of the pressure gradient $= -dP/dx$
$h$ = vertical dimension of the relative motion gap
$h_{sf}$ = latent heat of fusion
$H$ = dimensionless vertical dimension of the relative motion gap $= hU/(LV)$
$I_n$ = total pressure (normal force) integral, equation (37)
$I_p$ = pressure distribution integral, equation (34)
$I_t$ = tangential force integral, equation (45)
$k$ = thermal conductivity of liquid
$k_s$ = thermal conductivity of slider material
$K_n$ = coefficients, equation (16)
$L$ = longitudinal dimension of sliding-contact area
$m$ = dimensionless parameter proportional to the viscosity, equation (39)
$M$ = dimensionless group, equation (31)
$P$ = difference between the pressure in the liquid film (gap) and the ambient pressure
$P_n$ = average pressure $= F_n/(LB)$
$\tilde{P}_n$ = dimensionless average pressure $= P_n/(\alpha\mu/L^2)$
Pe = Peclet number $= UL/\alpha$
$q$ = scale of heat transfer per unit area of slider surface
$Q_x$ = height-integrated flow rate in the longitudinal direction, equation (10)
$Q_z$ = height-integrated flow rate in the sideways direction, equation (11)
$Q_0$ = flow rate through the upstream opening ($x=0$), leaving the relative motion gap, equation (28)

$$F_n = \int_{x=0}^{L} \int_{z=-B/2}^{B/2} P(x, z)\, dz dx \tag{5}$$

The longitudinal and sideways momentum equations are

$$\frac{\partial P}{\partial x} = \mu \frac{\partial^2 u}{\partial y^2} \quad \text{and} \quad \frac{\partial P}{\partial z} = \mu \frac{\partial^2 w}{\partial y^2} \tag{6}$$

Integrated twice in the vertical direction and subjected to the velocity boundary conditions $u = w = 0$ at $y = h$, and $u = U$ and $w = 0$ at $y = 0$, equations (6) read

$$u(x, y, z) = \frac{1}{2\mu}\left(\frac{\partial P}{\partial x}\right) y(y-h) + U\left(1 - \frac{y}{h}\right) \tag{7}$$

$$w(x, y, z) = \frac{1}{2\mu}\left(\frac{\partial P}{\partial z}\right) y(y-h) \tag{8}$$

Defining next the height-integrated flow rates

$$Q_x(x, z) = \int_0^h u dy \quad \text{and} \quad Q_z(x, z) = \int_0^h w dy \tag{9}$$

we learn from equations (7) and (8)

$$Q_x = \frac{1}{12\mu}\left(-\frac{\partial P}{\partial x}\right) h^3 + \frac{1}{2} Uh \tag{10}$$

$$Q_z = \frac{1}{12\mu}\left(-\frac{\partial P}{\partial z}\right) h^3 \tag{11}$$

Considering now the conservation of mass in the liquid-filled gap

$$\frac{\partial u}{\partial x} + \frac{\partial v}{\partial y} + \frac{\partial w}{\partial z} = 0 \tag{12}$$

and the fact that "melting" at the upper interface is written as a "blowing" condition, $v = -V$ at $y = h$, we integrate equation (12) from $y = 0$ to $y = h$ and obtain

$$\frac{\partial Q_x}{\partial x} - V + \frac{\partial Q_z}{\partial z} = 0 \tag{13}$$

Note that in deriving equation (13) we invoked also the impermeable bottom wall condition $v = 0$. It is now a simple matter to differentiate equations (10) and (11) and combine them with equation (13) for the purpose of eliminating $Q_x$ and $Q_z$. The result is a single equation for $P(x, z)$

$$\frac{\partial^2 P}{\partial x^2} + \frac{\partial^2 P}{\partial z^2} = -12 \frac{\mu V}{h^3}, \text{ (const)} \tag{14}$$

The boundary conditions on $P(x, z)$ are homogeneous along the entire perimeter of the sliding contact area, namely, $P = 0$ at $x = 0$ and $x = L$, and $P = 0$ at $z = -B/2$ and $z = B/2$. Under different notations, the Poisson-type problem (14) occurs frequently in the field of heat transfer (e.g., Hagen-Poiseuille flow through a duct of rectangular cross-section, Bejan, 1984); therefore, its solution can be written down immediately

$$P = \frac{6\mu V}{h^3} x(L-x) + \sum_{n=0}^{\infty} K_n \cos\left[(2n+1)\pi\left(\frac{x}{L} - \frac{1}{2}\right)\right] \cosh\left[(2n+1)\pi \frac{z}{L}\right] \tag{15}$$

where

$$K_n = \frac{48(-1)^{n+1}\mu V L^2}{(2n+1)^3 \pi^3 h^3 \cosh\left[(2n+1)\dfrac{\pi B}{2L}\right]} \tag{16}$$

Integrated over the sliding-contact area, in accordance with equation (5), this pressure distribution yields

$$F_n = \frac{\mu V L^3 B}{h^3} \phi \tag{17}$$

in which $\phi$ is a dimensionless coefficient that depends only on the geometric aspect ratio $B/L$

$$\phi\left(\frac{B}{L}\right) = 1 - \frac{192L}{\pi^5 B} \sum_{n=0}^{\infty} \frac{\tanh\left[(2n+1)\dfrac{\pi}{2}\dfrac{B}{L}\right]}{(2n+1)^5} \tag{18}$$

The function $\phi(B/L)$ has been calculated and plotted in Fig. 2. Of particular interest is the behavior of this function in the "wide" contact area limit

$$\phi \cong 1, \text{ when } \frac{B}{L} \gg 1 \tag{19}$$

and in the "slender" contact area limit

## Nomenclature (cont.)

$\tilde{Q}_0$ = dimensionless upstream opening flow rate $= Q_0/(VL)$
Ste = Stefan number $= c\Delta T/h_{sf}$
$T$ = temperature difference above the melting point $T_m$
$T_m$ = melting point and temperature of phase-change material
$T_s$ = temperature of the solid slider (section 3)
$\Delta T$ = temperature difference between the solid slider and the phase-change interface
$\Delta T_f$ = scale of $\Delta T$ in the limit where the heating is due entirely to friction $= (\mu/k)U^2$
$\tilde{T}$ = dimensionless excess temperature function, equation (47)
$\tilde{T}_{\text{avg}}$ = $L$-averaged temperature of the surface of the solid slider
$u, v, w$ = velocity components, Fig. 1
$U$ = tangential velocity, Fig. 1
$V$ = vertical velocity, or melting speed, Fig. 1
$\tilde{V}$ = dimensionless factor $= I_n^{1/2}$
$x, y, z$ = Cartesian coordinates, Fig. 1
$\alpha$ = thermal diffusivity of the liquid
$\beta$ = dimensionless parameter proportional to the normal force, equation (41)
$\eta$ = dimensionless vertical position $= y/h$
$\mu$ = viscosity
$\mu_f$ = friction coefficient $= F_t/F_n$
$\tilde{\mu}_f$ = dimensionless factor $= I_t/I_n^{1/2}$
$\xi$ = dimensionless longitudinal position $= x/L$
$\rho$ = density of liquid
$\rho_s$ = density of slider material
$\phi$ = dimensionless function of the geometric aspect ratio $B/L$, equation (18)
$\Phi$ = viscous dissipation function, equation (1)

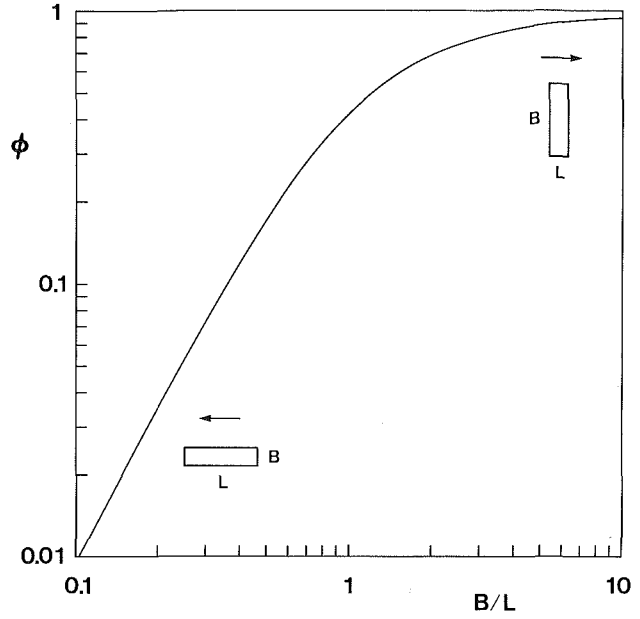


**Fig. 2 Effect of aspect ratio on the total normal force, equations (17) and (18)**

$$\phi \cong \left(\frac{B}{L}\right)^2, \text{ when } \frac{B}{L} \ll 1 \tag{20}$$

**3.3 Results.** Equation (17) is the relation needed for calculating the melting speed $V$. Instead of $F_n$ we may use the averaged applied pressure $P_n = F_n/(LB)$, in order to rewrite equation (17) as $V = P_n h^3/\mu L^2 \phi$. Combining this result with equation (4) we deduce the geometric slenderness ratio of the relative motion gap

$$\frac{h}{L} = \left(\frac{\text{Ste}}{\tilde{P}_n}\phi\right)^{1/4} \tag{21}$$

in which the Stefan nunmber (Ste) and $\tilde{P}_n$ are dimensionless notations for the imposed temperature difference and average pressure (see the Nomenclature). Combining equations (17) and (21) we can show that $V$ is proportional to $F_n^{1/4}$.

The tangential friction force $F_t$ is obtained finally by combining its definition with equation (7) and (15)

$$F_t = -\int_{x=0}^{L}\int_{z=-B/2}^{B/2} \mu\left(\frac{\partial u}{\partial y}\right)_{y=0} dz dx = \mu \frac{U}{h} LB \tag{22}$$

for which the gap spacing $h$ is given by equation (21). The corresponding friction coefficent is

$$\mu_f = \text{Pe}\, \tilde{P}_n^{-3/4} (\text{Ste}\,\phi)^{-1/4} \tag{23}$$

where Pe is the Peclet number $UL/\alpha$. In conclusion, the friction coefficient increases linearly with the tangential velocity $U$. It decreases monotonically as the imposed normal pressure and temperature difference increase.

The results developed in this section hold in those situations in which the inequalities discussed under equation (1) are satisfied. We can show that the condition for a negligible convection effect is the same as the "small Peclet number" requirement

$$Pe < \left(\frac{\tilde{P}_n}{\text{Ste}\,\phi}\right)^{1/2} \tag{24}$$

The negligible frictional heating effect condition is best left in the form of the inequality $\mu U^2/(k\Delta T) < 1$. Since in the present problem both $\Delta T$ and $U$ are specified, this condition identifies the ceiling order of magnitude of the property ratio $\mu/k$ that marks the breakdown of the assumption of negligible frictional heating.

## 4 Frictional Heating

**4.1 Formulation of the Problem.** Consider next the reverse of the $\mu/k$ assumption employed in the preceding section, namely, a relative motion gap in which the melt is generated solely by the frictional heating effect. Again, in order to isolate this particular phenomenon from potentially competing heat transfer processes, we model the block of phase-change material as isothermal at the fusion temperature $T_m$. At the same time we assume that the bottom surface of the relative motion gap (the moving surface) is adiabatic. In this problem, then, all the heat that is being generated through friction is sunk eventually into the liquid-solid interface, in accordance with equation (3).

It pays to take an early look at the energy equation (1) and to recognize that in the present problem the scale of the temperature difference measured vertically across the liquid film is not an externally imposed parameter (i.e., not a degree of freedom). Let $\Delta T_f$ be this unknown scale. The energy equation (1) describes the competition between three scales, $U\Delta T_f/L$, $\alpha\Delta T_f/h^2$, and $(\mu/\rho c)/(U/h)^2$, representing in order the effects of convection, transverse conduction, and frictional heat generation. In what follows we assume that the convection effect is again negligible, i.e., that the energy balance is between frictional heating and vertical thermal diffusion. It is out of this balance that we deduce the transversal temperature difference scale, $\Delta T_f \sim (\mu/k)U^2$, or the temperature scale of the solid slider ($T_m + \Delta T_f$). The "negligible convection" assumption on which this conclusion rests is simply $U\Delta T_f/L < \alpha\Delta T_f/h^2$.

The engineering quantities of interest in this problem are the gap thickness $h$, the melting speed $V$, and the friction coefficent $\mu_f$. These quantities were investigated also in the "direct heating" regime analyzed in the preceding section. An additional unknown in the present problem is the temperature distribution along the solid (bottom) surface of the relative motion gap. It turns out that unlike in the preceding section the gap thickness ($h$) and the temperature of the liquid film are functions of position ($x$, $z$). This analytical complication can be moderated somewhat by making the additional assumption that the sliding-contact area is sufficiently wide, $B \gg L$, so that the only meaningful spatial variation of $h$ and the bottom wall temperature is in the longitudinal direction ($x$).

**4.2 Parametric Solution.** The temperature distribution in the liquid film is obtained by solving the simplified energy equation

$$\frac{\partial^2 T}{\partial y^2} = -\frac{\mu}{k}\left(\frac{\partial u}{\partial y}\right)^2 \tag{25}$$

in which $T$ and $u$ are functions of $x$ and $y$. Combining this equation with the longitudinal velocity distribution (7), integrating twice, and applying the boundary conditions $T = 0$ at $y = h(x)$, and $\partial T/\partial y = 0$ at $y = 0$, we obtain

$$T = \frac{\mu}{k}\left[\frac{G^2h^4}{24\mu^2}(1-\eta)(2\eta^3 - 2\eta^2 + \eta + 1) - \frac{Gh^2U}{6\mu}(1-\eta)^2(2\eta+1) + \frac{U^2}{2}(1-\eta^2)\right] \tag{26}$$

where $G(x) = -dP/dx$ and $\eta = y/h$.

Note, however, that in the wide contact area limit equations (10) and (13) read

$$Q_x = \frac{1}{12\mu}\left(-\frac{dP}{dx}\right)h^3 + \frac{1}{2}Uh, \quad \text{and} \quad \frac{dQ_x}{dx} = V \tag{27}$$

Integrating the second equation starting from the entrance of the relative motion gap ($x = 0$), we find that $Q_x$ increases linearly in the longitudinal direction

$$Q_x = -Q_0 + Vx \tag{28}$$

where $Q_0$ is the net liquid flow rate squirting out to the left, through the entrance to the gap (Fig. 1). We see shortly that under a sufficiently high normal force $F_n$ some of the total liquid flow rate generated by melting ($VL$) escapes to the left ($Q_0$), while the remainder ($VL - Q_0$) is swept to the right through the downstream opening. The net contribution of these last observations is that the group ($Gh^2$) appearing on the right side of equation (26) is a relatively simple function of longitudinal position ($x$) and gap height ($h$)

$$-\frac{Gh^2}{6\mu U} = 1 - \frac{2}{H}(\xi - \tilde{Q}_0) \tag{29}$$

where the dimensionless variables $H$, $\xi$, and $\tilde{Q}_0$ are defined in the Nomenclature.

The solution hinges on being able to determine the gap profile $h(x)$, now represented by the dimensionless $H(\xi)$. For this we invoke one more time the melting interface condition (3), which in view of equations (26) and (29) becomes

$$H = 3M\left[1 - \frac{2}{H}(\xi - \tilde{Q}_0)\right]^2 + M \tag{30}$$

In this equation $M$ is a temporarily convenient dimensionless group whose noteworthy property is that it decreases when $V$ and, presumably, $F_n$ increase

$$M = \frac{\mu U^3}{\rho h_{sf} L V^2} \tag{31}$$

Equation (30) is a cubic in $H(\xi)$; its numerical solution would be straightforward if $\tilde{Q}_0$ and $M$ could be specified independently. In reality, these two parameters are related through the condition that the excess pressure $P$ must be zero not only at the gap entrance ($x = 0$) but also at the exit ($x = L$). In the present problem this condition amounts to writing

$$\int_0^L \left(\frac{dP}{dx}\right) dx = 0 \tag{32}$$

which according to equation (29), means

$$\int_0^1 \left[\frac{1}{H^2} - \frac{2}{H^3}(\xi - \tilde{Q}_0)\right] d\xi = 0 \tag{33}$$

The solution for $H(\xi)$ and the other quantities of interest is "parametric," in the sense that the numerical procedure begins with choosing a value of $\tilde{Q}_0$, which plays the role of "parameter." Note that the proper domain of $\tilde{Q}_0$ is [0, 1] and that the $\tilde{Q}_0 = 1$ extremity represents the case where the liquid film becomes strangled at this downstream end. In this limit the melt (total flowrate $VL$) has no choice but to escape through the upstream opening. This limit corresponds to an infinite normal force, as can be seen by examining the behavior of the normal force integral $I_n$ defined later in equation (37) and plotted in Fig 3.

The opposite limit, $\tilde{Q}_0 = 0$, is simply a limitation of the present theory, which beginning with Fig. 1 is based on the idea that the melt fills the relative motion gap over its entire length. Note that negative $\tilde{Q}_0$ values indicate a net flow of liquid through the $x = 0$ entrance *into* the relative motion gap, which implies that existence of a film of molten phase-change material upstream of $x = 0$ along the solid slider. Despite this limitation the numerical solution was extended also into the domain of negative (and not too large) $\tilde{Q}_0$ values, with the understanding that in this region the results are qualitative.

Figures 3 and 4 show the heart of the solution, namely, the one-to-one relationship between $M$ and $\tilde{Q}_0$, and the gap shape $H(\xi)$. The $M$ versus $\tilde{Q}_0$ curve was obtained by first fixing $\tilde{Q}_0$, and then guessing an $M$ value in order to solve equation (30) for $H(\xi)$. Finally, the calculated gap profile $H(\xi)$ was tested against the integral condition (33). In case of failure the procedure was repeated using an improved guess for the value of parameter $M$. Figure 3 shows that $M$ decreases monotonically with $\tilde{Q}_0$ [note also the use of $(1 - \tilde{Q}_0)$ on the abscissa], which means that an increasing fraction of the melt flow rate is squeezed out through the upstream opening as the normal (advancement) velocity $V$ increases.

In Fig. 4 we see the peculiar shape of the relative motion gap. It is a converging-diverging shape whose smallest cross section (neck) occurs in the downstream half of the gap. The section of the gap situated upstream of the neck is two to three times thicker (taller) than the downstream section. The transition between the two sections is smooth: The function $H(\xi)$ is single-valued over the $\xi$ domain [0, 1]; in other words, the cubic equation (30) has only one real root.

Hand in hand with the characteristic shape of the relative motion gap goes the pressure distribution, which is illustrated in Fig. 5. Plotted on the ordinate is the dimensionless integral

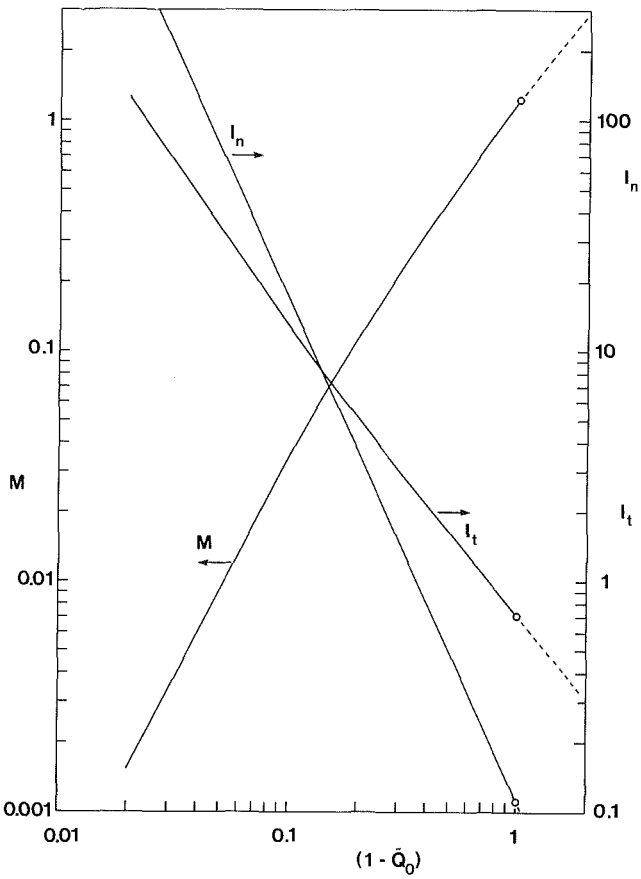


**Fig. 3 Key features of the parametric solution for melting caused by frictional heating**

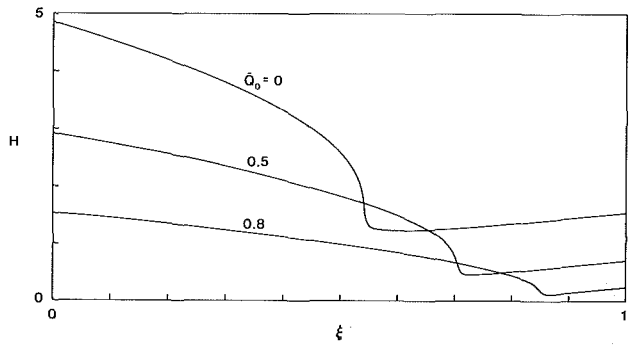


**Fig. 4 Shape of the relative motion gap, and the effect of increasing $\tilde{Q}_0$**

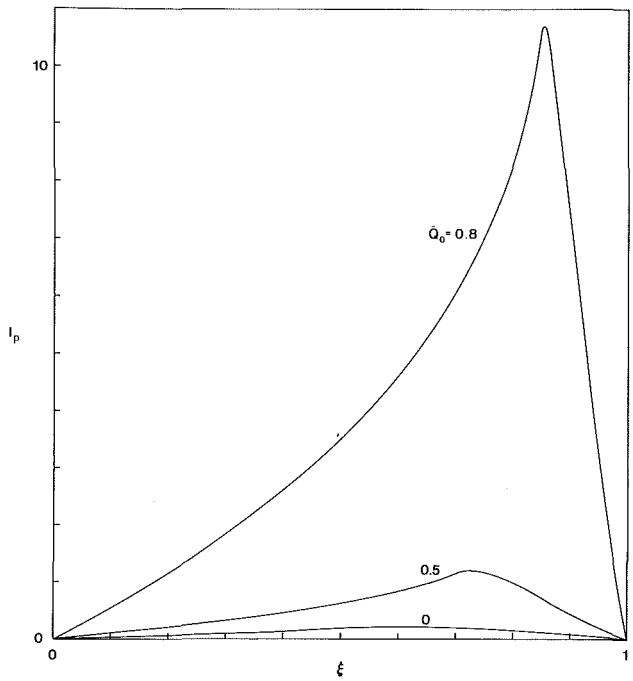


**Fig. 5 Pressure distribution in the relative motion gap, and its response to changes in $\tilde{Q}_0$**

$$I_p(\xi)=\int_0^{\xi} 6\left[\frac{1}{H^2}-\frac{2}{H^3}\,(\xi'-\tilde{Q}_0)\right]d\xi' \tag{34}$$

which (one can show) is proportional to the excess pressure built in the melt layer

$$P=\frac{\mu U^3}{LV^2}\,I_p(\xi) \tag{35}$$

Note that the pressure integral condition used earlier, equation (33), is the same as claiming zero excess pressure at the downstream opening, $I_p(1)=0$. In Fig. 5 we see that the pressure peaks immediately downstream of the cross-sectional change discovered in Fig. 4. The necking of the cross section and the pressure maximum migrate toward the downstream end as $\tilde{Q}_0$ increases, or as $V$ and the applied normal force increase. The necking becomes also less abrupt. At the same time, the average thickness of the gap decreases and the excess pressure increases.

**4.3 Melting Speed.** The gap shape (Fig. 4) and the pressure distribution (Fig. 5) are interesting; however, the user of the sliding-contact melting process is more interested in overall quantities such as the melting speed $V$, the needed normal force $F_n$, the friction factor, and the potential overheating of the solid surface that rubs against the phase-change material. All these quantities can be reconstructed based on the solution reported in Figs. 3 and 4. To begin with, the total normal force per unit length in the $z$ direction is

$$\frac{F_n}{B}=\int_0^L P dx=\frac{\mu U^3}{V^2}\,I_n \tag{36}$$

where $I_n$ is another dimensionless integral defined by

$$I_n=\int_0^1 I_p(\xi)d\xi \tag{37}$$

This integral has been plotted in Fig. 3, which shows that $I_n$ is a single-valued function of the parameter of the solution ($\tilde{Q}_0$).

Our immediate task is to replace the parameter $\tilde{Q}_0$ with one that can be calculated immediately based on the data (e.g., dimensions, properties) specified in the problem statement.

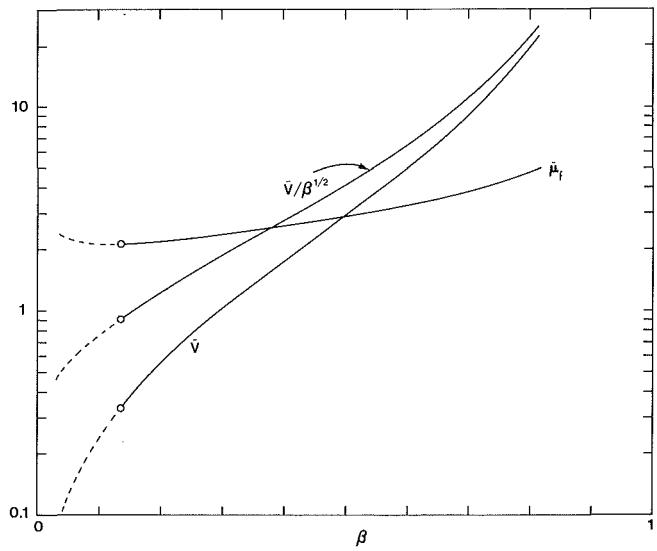


**Fig. 6 Chart for calculating the melting speed and friction factor in the melting regime dominated by frictional heating**

Note first that instead of $F_n$ we may use the average pressure $P_n=F_n/(BL)$; combining equation (36) with the $\tilde{P}_n$ definition given in the Nomenclature, we obtain

$$\tilde{P}_n=\left(\frac{U}{V}\right)^2 \mathrm{Pe}\, I_n \tag{38}$$

Given the one-to-one relationship between $M$ and $\tilde{Q}_0$ (Fig. 3), we may regard $I_n$ as a function of the parameter $M$, equation (31). The $M$ parameter can now be abandoned by recognizing that $M=(U/V)^2 m$, in which the new group

$$m=\frac{\mu U}{\rho h_{sf} L} \tag{39}$$

is known as soon as the relative speed, the swept length, and the properties of the phase-change material are known. Eliminating $(U/V)^2$ between equation (38) and $M=(U/V)^2 m$ yields

$$m\,\frac{\tilde{P}_n}{\mathrm{Pe}}=I_n M \tag{40}$$

where the right side of the equation is a function of only $\tilde{Q}_0$ (Fig. 3).

In conclusion, by combining equation (40) with Fig. 3 we have the opportunity to replace $\tilde{Q}_0$ with a new "parameter" for the same problem, namely, the group

$$\beta=m\,\frac{\tilde{P}_n}{\mathrm{Pe}} \tag{41}$$

This new group is readily accessible, as $m$, $\tilde{P}_n$, and Pe are dimensionless counterparts of the data supplied in the problem statement.

The melting speed $V$ can now be calculated using equation (38)

$$V=U\left(\frac{\mathrm{Pe}}{\tilde{P}_n}\right)^{1/2}\tilde{V}(\beta) \tag{42}$$

for which the function $\tilde{V}(\beta)=[I_n(\beta)]^{1/2}$ has been plotted in Fig 6. This function increases appreciably as the new abscissa parameter $\beta$ increases. The point that separates the solid line from the dashed-line portion of the curve corresponds to the case of zero flow through the upstream opening ($\tilde{Q}_0=0$), for which $\beta=0.135$ and $\tilde{V}(0.135)=0.333$.

The question of whether $V$ increases with the applied pressure $\tilde{P}_n$ is answered by examining the makeup of equation (42) and the shape of the function $\tilde{V}(\beta)$ (Fig. 6). Since $\beta$ is pro-

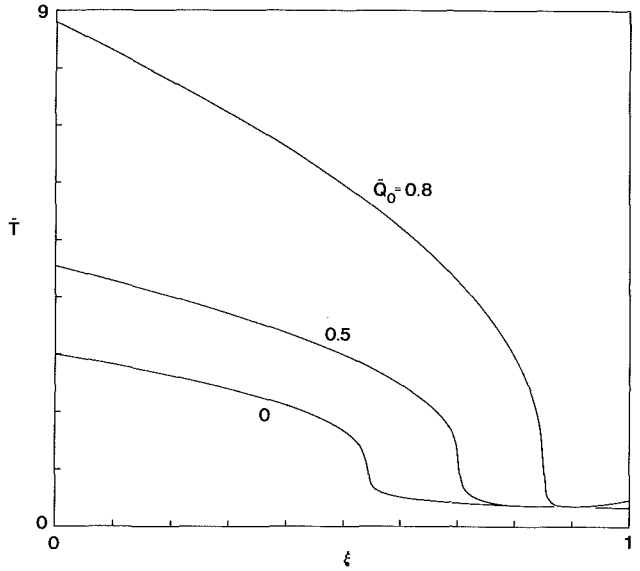


Fig. 7 Temperature distribution along the solid slider

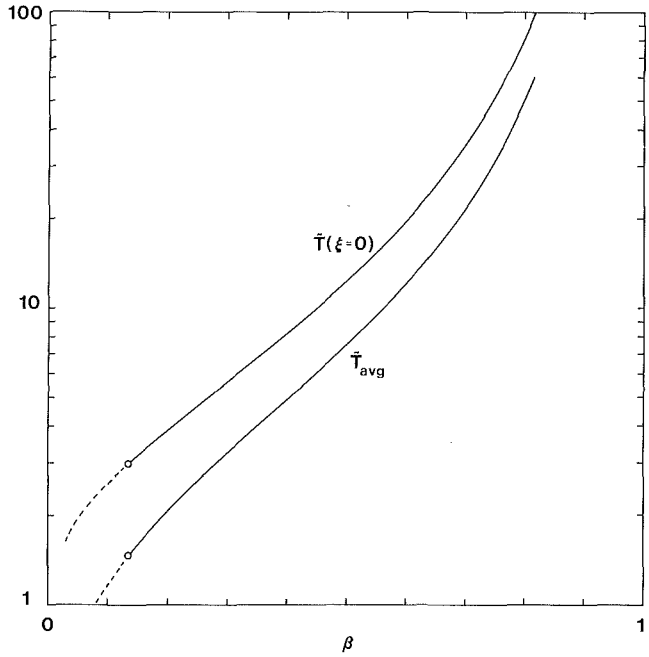


Fig. 8 Highest temperature ($\tilde{T}$ at $\xi=0$) and $L$-averaged temperature of the solid slider

portional to the pressure "number" $\tilde{P}_n$, equation (41), and since $\tilde{V}$ increases faster than $\beta^{1/2}$, the net effect of $\tilde{P}_n^{-1/2}\tilde{V}$ on the right side of equation (42) is a function that increases monotonically as $\tilde{P}_n$ increases. This can be seen by rewriting equation (42) as

$$V = Um^{1/2}\frac{\tilde{V}(\beta)}{\beta^{1/2}} \tag{43}$$

and by examining the curve labeled $\tilde{V}/\beta^{1/2}$ in Fig. 6. Equations (42) and (43) are two alternative routes to the same unknown of the problem $V$.

**4.4 Friction Factor.** According to the definition (22), the total tangential force per unit length in the $z$ direction is

$$\frac{F_t}{B} = \mu\frac{U^2}{V}I_t \tag{44}$$

where $I_t$ stands for the integral

$$I_t = \int_0^1 \left(\frac{1}{H} + \frac{H}{2}\frac{dI_p}{d\xi}\right)d\xi \tag{45}$$

As shown in Fig. 3 this integral is a function of $\tilde{Q}_0$ or, via equations (40) and (41), a function of $\beta$. The friction factor is obtained by dividing equation (44) by equation (36) and using the result developed already for $V$. An efficient way to catalog this result is to write it as

$$\mu_f = \left(\frac{\mathrm{Pe}}{\tilde{P}_n}\right)^{1/2}\tilde{\mu}_f \tag{46}$$

where $\tilde{\mu}_f = I_t/I_n^{1/2}$ is a dimensionless correction coefficient that depends only on $\beta$. The $\tilde{\mu}_f(B)$ function has been plotted in Fig. 6; it increases slowly as $\beta$ increases (or as $\tilde{P}_n$ increases).

**4.5 Temperature of the Solid Surface.** The remaining question is how much hotter than the phase-change material must the slider surface become in order to sustain the steady-state frictional melting analyzed in this section. The answer follows from setting $\eta=0$ in equation (26) and using equation (29)

$$T = \frac{\mu}{k}U^2\tilde{T} \tag{47}$$

where $\tilde{T}(\xi, \tilde{Q}_0)$ [or $\tilde{T}(\xi, \beta)$] is the dimensionless excess temperature function

$$\tilde{T} = \frac{3}{2}\left[1-\frac{2}{H}(\xi-\tilde{Q}_0)\right]^2 + \frac{3}{2} - \frac{2}{H}(\xi-\tilde{Q}_0) \tag{48}$$

This function is displayed in Fig. 7, which shows that the "hot spot" always occurs at the upstream opening of the relative motion gap. For a given value of the parameter $\tilde{Q}_0$ (or $\beta$) the slider surface excess temperature is significantly higher in the upstream (taller) section of the relative motion gap than in the downstream section. As the applied pressure increases, $\tilde{Q}_0$ and $\beta$ increase, and so does the temperature of the upstream section of the slider surface. The surface temperature in the downstream section is practically insensitive to changes in the applied normal force, even though the cross section in this region decreases as $\tilde{Q}_0$ increases (Fig. 4). The surface temperature distribution $\tilde{T}$ resembles in shape the profile of the relative motion gap $H$. In both cases the "neck" migrates toward the downstream opening.

The effect of the normal force on the excess temperature of the slider surface is summarized in Fig. 8. Both the highest temperature ($\tilde{T}$ at $\xi=0$) and the $L$-averaged temperature ($\tilde{T}_{avg}$) increase as $\beta$ increases. The average temperature is defined as

$$\tilde{T}_{avg}(\beta) = \int_0^1 \tilde{T}(\xi, \beta)d\xi \tag{49}$$

Finally, it is instructive to look at the temperature field that bridges the gap between the slider surface temperature calculated above and the temperature of the phase-change surface. The latter is represented by $\tilde{T}=0$ over the entire length of the relative motion gap. Figure 9 shows the temperature profiles in a sequence of three cross sections ($\xi=0$, 0.5, and 1) along the gap. The gap shape pictured in the figure corresponds to the case of zero flow through the upstream opening, $\tilde{Q}_0=0$ (or $\beta=0.135$).

The common feature of these cross-sectional temperature profiles is the temperature gradient at the upper surface; this gradient must be the same at any $\xi$, because the melting speed $V$ is independent of longitudinal position, equation (3). It is because of the constancy of this temperature gradient that the slider surface excess temperature $\tilde{T}(\eta=0)$ must vary, more or less, as $H(\xi)$. However, it is worth noting that the cross-sectional temperature profiles are not "similar"; for example, the temperature profile across the downstream opening ($\xi=1$, Fig. 9) is considerably flatter than the profile across the upstream opening ($\xi=0$, Fig. 9).

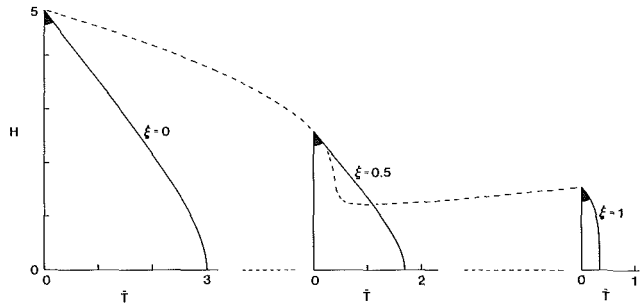


**Fig. 9 Three profiles showing the temperature distribution in the liquid film ($\tilde{Q}_0 = 0$)**

## 5 Observations Concerning the Slider Surface Model

The study of the two distinct limits of the melting by sliding contact phenomenon (sections 3 and 4) was made possible by two important assumptions regarding the heat transfer behavior of the solid substrate (the slider). These assumptions effectively decoupled the liquid film heat transfer process from the transient conduction that always takes place in the slider. Now, when we have the analytical conclusions of sections 3 and 4 in hand, it is necessary to establish the parametric domain in which these conclusions are valid.

**5.1 Isothermal Slider Assumption.** In the case where the melting is dominated by direct heating from the relatively warmer slider, section 3, the key assumption is that the slider temperature $T_s$ (or $\Delta T$) is constant and known. This is true only if the heat transfer sucked out of the slider does not depress the slider surface temperature by an amount $\Delta T_s$ that is comparable with or greater than $\Delta T$. It can be shown that the $\Delta T_s \ll \Delta T$ condition is equivalent to

$$\frac{k_s \rho_s c_s}{k \rho c} > \mathrm{Pe}^{-1} \left( \frac{\mathrm{Ste}}{\tilde{P}_n} \phi \right)^{-1/2} \tag{50}$$

Note that according to equation (24) the right side of the above inequality is a number greater than one. This means that the $(k_s \rho_s c_s)$ group of the solid slider must exceed the equivalent product of melt properties $(k \rho c)$ by a certain factor, which, in an order of magnitude sense, is greater than one.

**5.2 Adiabatic Slider Assumption.** In the limit of friction-dominated melting, section 4, we assumed that the slider surface is adiabatic. This model holds only if the actual heat transfer proceeding downward into the slider $q_s$ is negligible relative to the heat transfer landing at the same time at the two-phase interface $q_m$. It is not difficult to show that the $q_s < q_m$ requirement is the same as writing

$$\frac{k_s \rho_s c_s}{k \rho c} < \tilde{P}_n \left( \frac{I_t}{\mathrm{Pe} \tilde{V}} \right)^2 \tag{51}$$

In conclusion, the slider material must have a sufficiently low $(k_s \rho_s c_s)$ value in order for the adiabatic slider surface assumption to be valid. Recall that the same property group must exceed a certain order of magnitude in order to justify the isothermal slider surface assumption, equation (50).


## Acknowledgments

The support received from the National Science Foundation through Grant No. CBT-8711369 is gratefully acknowledged.


## References


Akkok, M., Ettles, C. M., McC., and Calabrese, S. J., 1987, "Parameters Affecting the Kinematic Friction of Ice," ASME *Journal of Tribology*, Vol. 109, pp. 552–561.

Aung, W., 1986, "Heat Transfer in Interior Ballistics," presented at the *Korea-U.S.A. Heat Transfer Seminar*, Seoul National University, Oct. 21.

Bahrami, P. A., and Wang, T. G., 1987, "Analysis of Gravity and Conduction-Driven Melting in a Sphere," ASME JOURNAL OF HEAT TRANSFER, Vol. 109, pp. 806–809.

Batchelor, G. K., 1967, *An Introduction to Fluid Dynamics*, Cambridge University Press, Cambridge, United Kingdom, pp. 219–222.

Bejan, A., 1984, *Convection Heat Transfer*, Wiley, New York, p. 105.

Bowden, F. P., 1953, "Friction on Snow and Ice," *Proc. Roy. Soc.*, Vol. A 217, pp. 462–478.

Bowden, F. P., and Hughes, T. P., 1939, "The Mechanism of Sliding on Ice and Snow," *Proc. Roy. Soc.*, Vol. A 172, pp. 280–298.

Cravalho, E. G., and Smith, J. L., Jr., 1981, *Engineering Thermodynamics*, Pitman, Boston, p. 341.

Evans, D. C. B., Nye, J. F., and Cheeseman, K. J., 1976, "The Kinetic Friction of Ice," *Proc. Roy. Soc.*, Vol. A 347, pp. 493–512.

Moallemi, M. K., and Viskanta, R., 1986a, "Analysis of Close-Contact Melting Heat Transfer," *Int. J. Heat Mass Transfer*, Vol. 29, pp. 855–867.

Moallemi, M. K., and Viskanta, R., 1986b, "Analysis of Melting Around a Moving Heat Source," *Int. J. Heat Mass Transfer*, Vol. 29, pp. 1271–1282.

Oksanen, P., and Keinonen, J., 1982, "The Mechanism of Friction of Ice," *Wear*, Vol. 78, pp. 315–324.

Prasad, A., and Sengupta, S., 1987, "Numerical Investigation of Melting Inside a Horizontal Cylinder Including the Efffects of Natural Convection," ASME JOURNAL OF HEAT TRANSFER, Vol. 109, pp. 803–806.

Reynolds, O., 1901, *Papers on Mechanical and Physical Subjects II*, Cambridge University Press, Cambridge, United Kingdom, p. 737.

J. D. Maltson
Research Student.

D. Wilcock

Department of Mechanical Engineering,
Coventry Polytechnic,
West Midlands, United Kingdom

C. J. Davenport[1]
Covrad Heat Transfer,
Canley, Coventry,
West Midlands, United Kingdom

# Comparative Performance of Rippled Fin Plate Fin and Tube Heat Exchangers

*Continuous rippled fins are preferred to interrupted fins in applications where fouling by fibrous matter or insects is a problem. The performance characteristics of three rippled fin heat exchangers have been measured in a thermal wind tunnel. The results of these measurements are reported and comparisons are made with published data on similar surfaces. The performance evaluation criteria used as the basis for the comparisons were those recommended by Shah (1978). The tested rippled fin surfaces were found to have a higher performance than a similar surface reported in Kays and London (1984). The heat transfer enhancement was found to be dependent upon the profile of the fin.*

## Introduction

Plate fin and tube heat exchangers are widely used throughout industry in a variety of applications. This type of heat exchanger is used particularly for the cooling of water or oil flows of vehicular or stationary internal combustion engines. The usual arrangement is that water or oil flows in the tubes, while air flows across the fins. However, while there is little evidence to suggest that interrupted fins are more prone to fouling, many users prefer continuous fins in situations where fouling by fibrous matter is a serious consideration. Data on continuous fins have been available for many years from Kays and London (1984). New data are presented here for two new types of rippled fin, which show considerable advantages over the data of Kays and London. Tests have been conducted in a small thermal wind tunnel on three heat exchangers. The two new fin geometries are compared against the data of Kays and London by the methods suggested by Shah (1978). The comparisons are made using the $j/f$ ratio against the Reynolds number, heat transfer coefficient against the pumping power per unit surface area, heat transfer rate per unit volume against the pumping power per unit volume, and heat transfer rate against the fan power required. The usefulness of the various comparative methods, as the basis for decisions, is dicussed as to the choice of heat exchanger for a particular application.

## Experimental Investigation, Procedure, and Results

**Heat Exchanger Geometry.** The heat exchangers consisted of thin, flat-sided tubes, which were arranged such that the stagger repeated on the fourth tube row. However, heat exchangers having only three tube rows were tested. This type of tube arrangement is known as "echelon," as shown in Fig. 1. Three heat exchangers were used in the investigation, two exchangers having the same fin profile but different fin pitches, and one exchanger having a different ripple shape at a single fin pitch (see Figs. 2 and 3 and Table 1). The two profiles are each characterized by three parameters, the ripple pitch, the large ripple radius, and either the ripple double amplitude or the smaller radius of curvature. The fins were made of copper having a thickness of 0.076 mm. The water tubes were made of brass and coated with a thin layer of solder. All three heat exchangers had the same tube arrangement of 196 tubes per meter width of heat exchanger. The heat exchangers were compared with the data of Kays and London, the geometric details of which are also given in Table 1.

**Procedure and Data Reduction.** The performance of the heat exchanger samples was measured in a thermal wind tunnel. This thermal wind tunnel has been used extensively in previous investigations and is described by Davenport (1983a, 1983b). The tube-side liquid used was water, temperature controlled at approximately 80°C; the gas-side fluid was air drawn in at the ambient laboratory condition, through wire mesh damping screens, a smooth contraction section, and a flow straightener. The inlet air temperature was measured by a mercury-in-glass thermometer and the air temperature difference was measured by an array of nine chromel-alumel thermocouples, which had been mounted on copper wire grids. The thermocouples were arranged on a square uniform mesh having a mesh side length of 0.038 m. The inlet water temperature was measured by a single chromel-alumel thermocouple, referred to the inlet air temperature, and the water temperature difference was measured by an array of four chromel-alumel thermocouples. Typical temperature rises for the air were between 20° and 45°, corresponding to water temperature decreases of 1.4° and 0.1°, respectively. The air

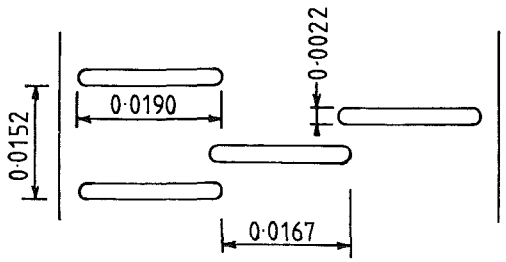


Fig. 1 Diagram showing the tube layout in the heat exchangers

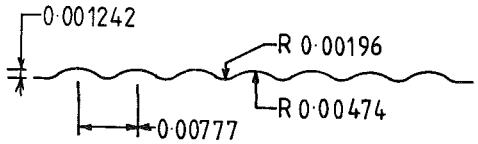


Fig. 2 Profile of fin A (surface 1)

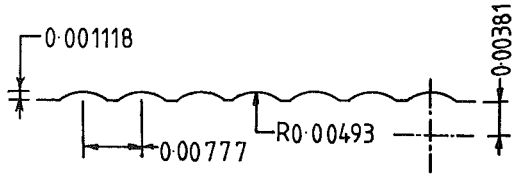


Fig. 3 Profile of fin B (surfaces 2 and 3)

[1]Present address: Alcan International Ltd., Banbury Laboratories, Banbury, Oxfordshire, United Kingdom.

Contributed by the Heat Transfer Division for publication in the JOURNAL OF HEAT TRANSFER. Manuscript received by the Heat Transfer Division May 21, 1987. Keywords: Enclosure Flows, Forced Convections, Heat Exchangers.

**Table 1 Geometry details**

| Surface | 1 | 2* | 3 | plain† | ruffled† |
|---|---|---|---|---|---|
| Geometry | | | | | |
| Fins/m | 353 | 354 | 282 | 358 | 366 |
| Hydraulic diameter, mm | 4.53 | 4.52 | 5.54 | 4.206 | 4.12 |
| $\sigma$ | 0.828 | 0.810 | 0.833 | 0.788 | 0.788 |
| $\beta$, $m^2/m^3$ | 760 | 764 | 643 | 735 | 748 |
| Fin area/total | 0.825 | 0.830 | 0.792 | 0.813 | 0.814 |
| Profile | A | B | B | plain | ruffle |
| Tubes/m | 196 | 196 | 196 | 214 | 214 |
| $L_f$, mm | 60.1 | 61.0 | 61.0 | 60.2 | 60.2 |
| Depth, mm | 58.4 | 58.4 | 58.4 | 60.2 | 60.2 |

*Surface 2 had been solder dipped.
†Kays and London geometry data.

velocity in the tunnel, upstream of the heat exchanger, was measured by a rotating vane anemometer, which had been calibrated by performing a 36 point pitot probe traverse across the working section over the full range of velocities. Each traverse was then integrated and a mean velocity calculated. The tunnel working section was 0.15 m by 0.15 m. The volumetric flow rate of water was measured by one of two calibrated rotameters. The air pressure drop was measured by an inclined manometer. The pressure drop through the heat exchanger was large, thus forcing air through the fin channels adjacent to the side walls. Full account of the ambient atmospheric pressure and the relative humidity of the air were taken.

The heat transferred through the heat exchanger was based on air-side measurements. The upstream air temperature was uniform after passing through the wire screens. The water temperature difference was very small and the uncertainty in the measurement became relatively large, but this had the effect of producing a highly uniform air exit temperature. Thus the heat transferred $Q_a$ was calculated as follows:

$$Q_a = m_a \cdot Cp_{a,m} \cdot (T_{a,o} - T_{a,i})$$

where

$$m_a = V_{tun} \cdot \rho_{a,i} \cdot A_{tun}$$

and $V_{tun}$ is the measured air velocity in the wind tunnel.

The overall heat transfer coefficient was defined from the following equation:

$$Q_a = U \cdot A_{ht} \cdot T_{md}$$

where $T_{md}$ is the mean temperature difference between the two fluids, evaluated for the heat exchanger in cross flow. Hence

$$T_{md} = T_{lmdt} \cdot F_{md}$$

The logarithmic mean temperature difference was defined in the usual way for counterflow as

$$T_{lmtd} = \frac{(T_{w,i} - T_{a,o}) - (T_{w,o} - T_{a,i})}{\ln [(T_{w,i} - T_{a,o})/(T_{w,o} - T_{a,i})]}$$

The mean temperature difference factor for crossflow was evaluated by the method of Roetzel and Nicole (1975). This was initially done to investigate the accuracy of the logarithmic mean temperature difference for counterflow applied to a heat exchanger in cross flow. The range of the crossflow factor calculated for these test results was 0.995 to 1.00.

The air-side resistance was calculcated from the overall heat transfer coefficient equation, having a knowledge of all the other values. The overall coefficient incorporates all of the thermal resistances acting between the two fluids.

$$\frac{1}{U} = \frac{1}{\eta_o \cdot h_a} + \frac{A_{ht}}{h_w \cdot A_{wh}} + \left[\frac{A_{ht}}{A_{wh}} \cdot \left(\frac{t_t}{k_t} + \frac{t_s}{k_s}\right)\right]$$

The water-side heat transfer coefficient was calculated from the equations of Kern and Kraus (1972) for transitional and turbulent flow in circular tubes. These equations are also applicable to noncircular channels where the hydraulic diameter of the tube is used in nondimensional numbers.

The fin effectiveness, heat transfer coefficient, and fin efficiency were calculated together by an iterative procedure. The fin effectiveness and the fin efficiency were calculated assuming a rectangular fin of constant thickness. Although the geometry of the fin is not quite rectangular, due to the layout of the tubes, this solution is thought to be a good approximation. The equations used were as follows:

## Nomenclature

$A_c$ = minimum flow cross-sectional area
$A_{fc}$ = area of copper in fin for heat conduction
$A_{fi}$ = fin area for heat transfer
$A_{fr}$ = frontal area of heat exchanger
$A_{fs}$ = area of solder film on fin for heat conduction
$A_{ht}$ = total heat transfer surface area
$A_{tun}$ = tunnel flow area
$A_{wh}$ = area of heat transfer water side
$b$ = half the spanwise length of fin between tubes
$Cp$ = specific heat capacity at constant pressure
$D_h$ = hydraulic diameter
$E$ = pumping power per unit surface area
$f$ = friction factor
$F_{md}$ = crossflow correction factor
$Fd$ = ducting power loss
$Fp$ = fan power
$G_c$ = mass flux at the minimum flow area $= m_a/A_c$
$h$ = heat transfer coefficient
$j$ = Colburn $j$ factor
$k$ = thermal conductivity
$k_f$ = thermal conductivity of copper fin
$L_f$ = streamwise length of fin
$m$ = mass flow rate
$P_{dc}$ = pressure drop across the heat exchanger core
$Pp$ = pumping power
Pr = Prandtl number
$P_{fa}$ = perimeter of fin
$Q$ = heat transfer rate
Re = Reynolds number
St = Stanton number
$t$ = thickness
$T$ = temperature
$T_{lmtd}$ = log mean temperature difference
$T_{md}$ = mean temperature difference
$U$ = overall heat transfer coefficient
$V$ = velocity
$z$ = fin efficiency parameter
$\beta$ = air-side heat transfer surface area per unit volume of heat exchanger
$\eta_f$ = fin efficiency
$\eta_o$ = fin effectiveness
$\mu$ = dynamic viscosity
$\rho$ = density
$\sigma$ = ratio of minimum flow to frontal flow cross-sectional area $= A_c/A_{fr}$

**Subscripts**

$a$ = air
$i$ = inlet
$m$ = mean temperature
$o$ = outlet
$s$ = solder layer
$t$ = brass water tubes
$tun$ = wind tunnel
$std$ = standard temperature and pressure
$w$ = water

$$\eta_o = 1 - \left[\left(\frac{A_{fi}}{A_{ht}}\right) \cdot (1 - \eta_f)\right]$$

$$\eta_f = \frac{\tanh\,(z \cdot b)}{(z \cdot b)}$$

where

$$z = \left[\frac{h_a \cdot p_{fa}}{(A_{fc} \cdot k_f) + (A_{fs} \cdot k_s)}\right]^{0.5}$$

The conductive term in the fin efficiency equation allowed for the fin having a film of solder on its surfaces. This arose when a sample core had been "dipped" in solder to improve the fin-to-tube contact. Only one of the heat exchangers (surface 2) had been dipped in solder; the others were baked. From past practical experience a solder film thickness of 0.03 mm was used to calculate the cross-sectional area of the solder layer. The fin efficiency equation assumes that the direction of heat conduction within the fin is parallel in the copper and solder regions.

The Colburn $j$ factor was calculated from

$$j = \mathrm{St}_{a,\,m} \cdot (\mathrm{Pr}_{a,\,m})^{2/3}$$

where the Stanton number

$$\mathrm{St}_{a,\,m} = \frac{h_a \cdot A_c}{m_a \cdot Cp_{a,\,m}}$$

The air-side Reynolds number was based on the mass velocity flux at the minimum flow cross-sectional area and the hydraulic diameter defined by Kays and London (1984) for a finned tube bank

$$\mathrm{Re}_a = \frac{m_a \cdot D_{h,\,a}}{A_c \cdot \mu_{a,\,m}}$$

$$D_{h,\,a} = \frac{4 \cdot A_c \cdot L_f}{A_{ht}}$$

The friction factor was calculated from the equation given by Kays and London (1984), (equation (2-26$b$))

$$P_{dc} = \frac{G_c}{2 \cdot \rho_{a,\,i}} \left[(1 + \sigma^2) \cdot \left(\left(\frac{\rho_{a,\,i}}{\rho_{a,\,o}}\right) - 1\right) + f \cdot \frac{A_{ht} \cdot \rho_{a,\,i}}{A_c \cdot \rho_{a,\,m}}\right]$$

The form drag in the heat exchanger is accounted for in the friction factor and calculated as an equivalent shear stress.

**Experimental Results.** The basic results of the heat transfer and flow friction tests are given graphically in Figs. 4 and 5. Smooth lines were drawn through the data points on large-scale versions of these graphs. The data read directly from the smooth lines are presented in Table 2 and were used for the comparison of the new heat exchangers with data previously published.

## Uncertainty Estimation of the Experimental Data

The Monte Carlo Simulation Method was used to estimate the uncertainties associated with the calculated nondimensional numbers. This uncertainty analysis method has previously been used to estimate the uncertainties associated with a finned tube bank by Obray et al. (1986). The 95 percent certainty intervals were obtained from the 2.5 and 97.5 percent points in the ordered generated distributions of 1000 values. These distributions were generated by random sampling from

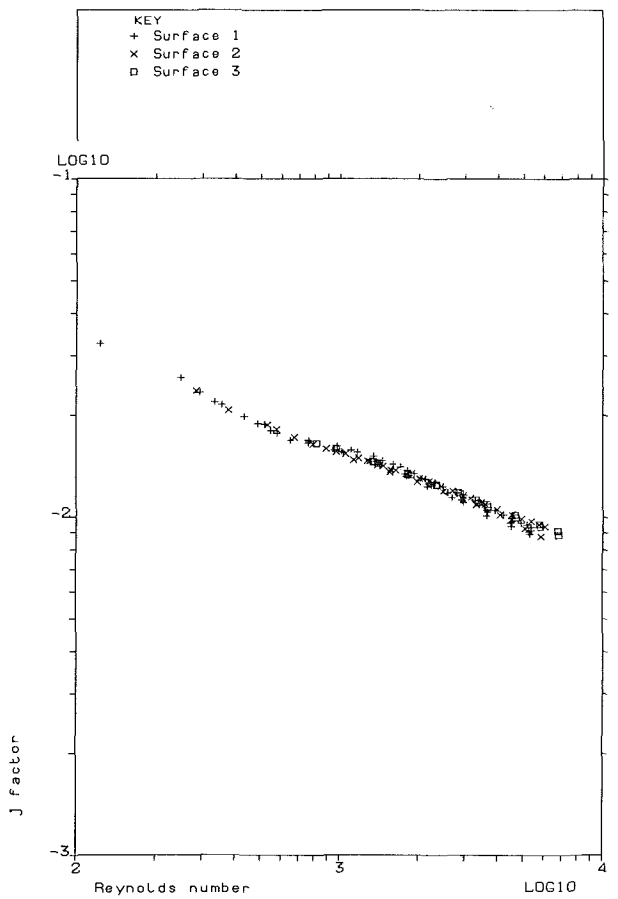


Fig. 4 Graph of the measured $j$ factor against the Reynolds number

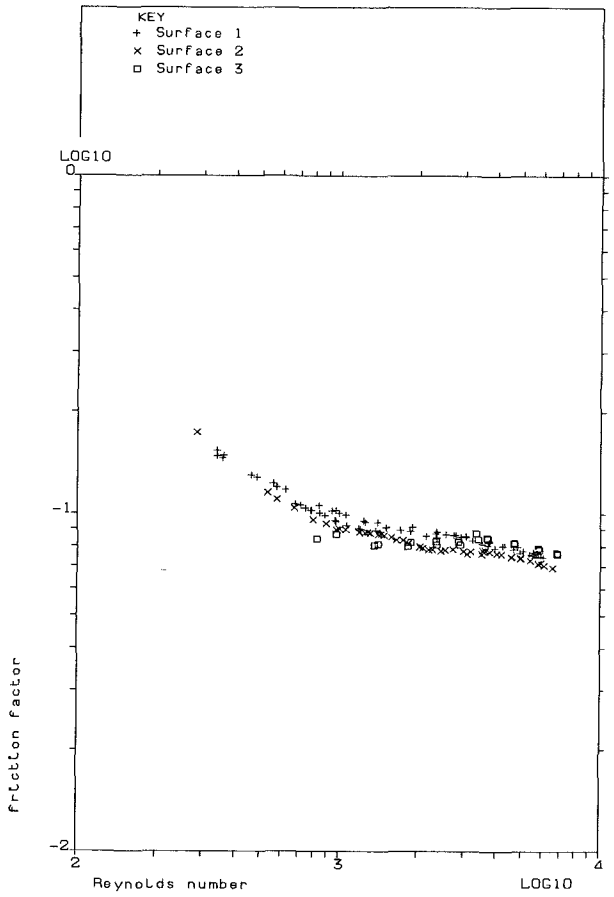


Fig. 5 Graph of the measured friction factors against the Reynolds number

**Table 2 Performance data**

| Surface 1 | | | Surface 2 | | | Surface 3 | | |
|---|---|---|---|---|---|---|---|---|
| Re | $j$ | $f$ | Re | $j$ | $f$ | Re | $j$ | $f$ |
| 500 | 0.0190 | 0.128 | 500 | 0.0190 | 0.117 | 1000 | 0.01595 | 0.085 |
| 750 | 0.0167 | 0.107 | 750 | 0.0166 | 0.099 | 1250 | 0.0149 | 0.083 |
| 1000 | 0.0159 | 0.097 | 1000 | 0.0154 | 0.090 | 1500 | 0.01415 | 0.082 |
| 1250 | 0.0151 | 0.093 | 1250 | 0.0146 | 0.088 | 2000 | 0.01310 | 0.082 |
| 1500 | 0.0145 | 0.091 | 1500 | 0.0140 | 0.087 | 2500 | 0.0123 | 0.0818 |
| 2000 | 0.0131 | 0.088 | 2000 | 0.0129 | 0.081 | 3000 | 0.0116 | 0.0822 |
| 2500 | 0.0121 | 0.087 | 2500 | 0.0121 | 0.078 | 3500 | 0.0110 | 0.0856 |
| 3000 | 0.0114 | 0.086 | 3000 | 0.0114 | 0.0775 | 4000 | 0.0105 | 0.0842 |
| 3500 | 0.0108 | 0.083 | 3500 | 0.0109 | 0.077 | 5000 | 0.00990 | 0.081 |
| 4000 | 0.0101 | 0.082 | 4000 | 0.0104 | 0.077 | 6000 | 0.00935 | 0.078 |
| 5000 | 0.0094 | 0.078 | 5000 | 0.0097 | 0.074 | 7000 | 0.00895 | 0.076 |
| 5500 | 0.0091 | 0.077 | 6000 | 0.0090 | 0.072 | | | |

uniform distributions, for measured variables and performing the data reduction 1000 times. The experimental tolerances used in the simulation were the discrimination of each measurement and are given in Table 3. The certainty intervals calculated are given in Fig. 6, for a typical data set. These results represent a certainty estimate on data points in a single sample experiment. At least two separate tests were carried out for each heat exchanger, and the data presented here are those that were read from the smooth lines drawn through many data points. Therefore the certainty interval estimates presented here are an overestimate of the actual interval of the calculated nondimensional numbers.

## Performance Evaluation Criteria Used for the Comparison

The performance evaluation criteria used in the comparison were those recommended by Shah (1978). These criteria all required the $j$ factor, friction factor, and Reynolds number, together with the geometry specification. Where the gas-side properties were required at a standard temperature and pressure, these were taken to be for dry air at 25°C and 1.01325 bar, respectively. The four methods are as follows:

1 *The ratio of j factor to the friction factor, against Reynolds number*, generally known as the "flow area goodness factor," suggested by London (1964).

2 *The standardized heat transfer coefficient against the pumping power per unit of heat transfer surface area* suggested by London and Ferguson (1949), where

$$h_{std} = \frac{j \cdot \mathrm{Re} \cdot \mu_{std} \cdot Cp_{std}}{D_{h,a} \cdot \mathrm{Pr}_{\mathrm{std}}^{2/3}}$$

and

$$E_{std} = \frac{f \cdot \mathrm{Re}^3 \cdot \mu_{std}{}^3}{2 \cdot \rho_{std}{}^2 \cdot D_{h,a}{}^3}$$

3 *The performance of the heat exchanger per unit volume*, the criterion suggested by Shah (1978). This method includes the effect of the fin effectiveness, which is an important factor in heat exchanger evaluation. A good performance using this criterion gives the best heat exchanger to use where the size of the unit is an important consideration.

$$\eta_o \cdot h_{std} \cdot \beta = \frac{j \cdot \mathrm{Re} \cdot 4 \cdot \sigma \cdot \eta_o \cdot Cp_{std} \cdot \mu_{std}}{\mathrm{Pr}_{\mathrm{std}}^{2/3} \cdot D_{h,a}^2}$$

and

$$E_{std} \cdot \beta = \frac{f \cdot \mathrm{Re}^3 \cdot 4 \cdot \sigma \cdot \mu_{std}^3}{2 \cdot \rho_{std}^2 \cdot D_{h,a}^4}$$

4 *The actual heat transfer rate performance against the gas-side fan power.* This is the heat exchanger design process described by Bergles et al. (1975). It involves the setting up of a system, the heat exchanger being only a part of the system. The engineer can then use the performance characteristics for various heat exchangers within the system and calculate the required performance evaluation criteria. For the purposes of comparison, the fluid flow rates and temperatures used were those of a typical application for this type of heat exchanger, which was that of engine water cooling of an agricultural tractor.

**Table 3 Discrimination tolerances for the measured variables**

| | |
|---|---|
| Anemometer constant | ±1. percent |
| Anemometer counts* | ±1.0 percent, ±last digit |
| Barometer, mercury height | ±0.00005 m |
| Barometer temperature | ±0.5°C |
| Heat exchanger (flow) length | ±1. percent |
| Heat exchanger (tube) length | ±1.3 percent |
| Heat exchanger width | ±1.3 percent |
| Inlet air temperature | ±0.5°C |
| Pressure drop, 0–5 kN/m² | ±10. N/m² |
| 0–1 kN/m² | ±2. N/m² |
| 0–500 N/m² | ±1. N/m² |
| Relative humidity | ±25. percent |
| Temperature differences* | |
| thermocouple output (mV) | ±0.1 percent, ±last digit |
| Thickness of copper fin | ±6. percent |
| Thickness of solder on fins | ±33. percent |
| Thickness of solder on tubes | ±33. percent |
| Tube breadth | ±5. percent |
| Tube pitch | ±1.6 percent |
| Tube wall thickness | ±14. percent |
| Tube width | ±4. percent |
| Tunnel flow area | ±1.5 percent |
| Water flow rate | ±10 percent |

*The tolerances on these variables also included the maximum and minimum readings of three measurements at one flow setting.

The system considered consisted of a water cooler where the inlet temperatures of the fluids were specified as 80.0°C for the water and 20.0°C for the air. The frontal area of the heat exchangers was 1 m by 1 m. For this comparison all the heat exchangers had three tube rows and the depths (air flow lengths) were very similar. The fin thickness was set to 0.076 mm for all compared surfaces. The mass flow rate of water in the tubes was 5.47 kg/s, which is typical of units for agricultural vehicles. The mass flow rate of air was found from the Reynolds number of the test data and the heat transfer coefficient from the associated $j$ factor, and calculated using fluid properties evaluated at the mean temperatures of the last iteration, until convergence.

The fan power was analyzed in three components, the pumping power for the heat exchanger alone, the ducting power loss, and the power necessary to accelerate the air flow from rest to the inlet velocity of the heat exchanger, i.e.,

$$Fp = Pp + Fd + \left(m_a \cdot \frac{V_{a,i}^2}{2}\right)$$

where

$$Pp = V_{ai} \cdot A_{fr} \cdot p_{dc}$$

For heat exchangers that operate at high velocities, the power to accelerate the flow and to drive it through the ducting can be a significant proportion of the total fan power, and needs to be evaluated. The flow acceleration through the heat

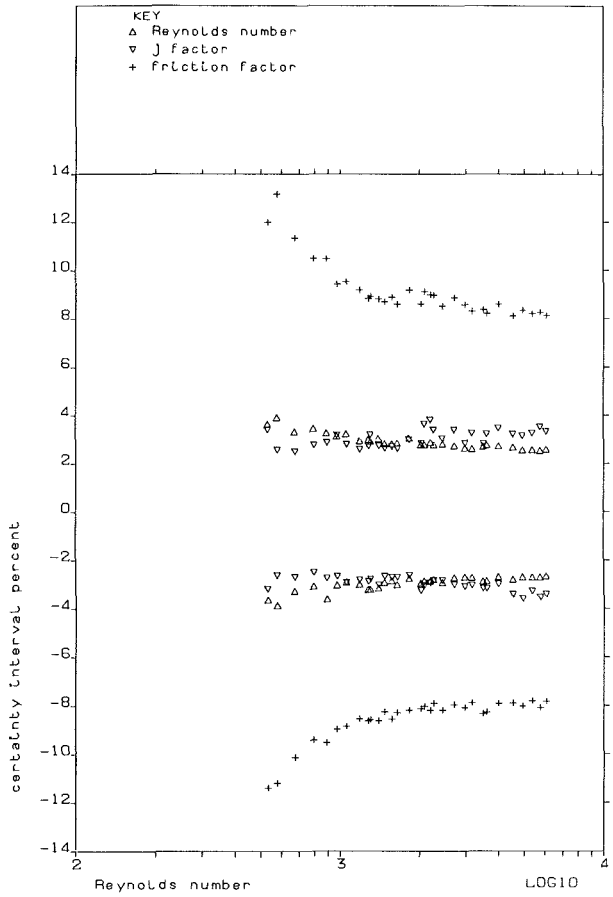


Fig. 6 Typical graph of the 95 percent certainty interval for the non-dimensional numbers

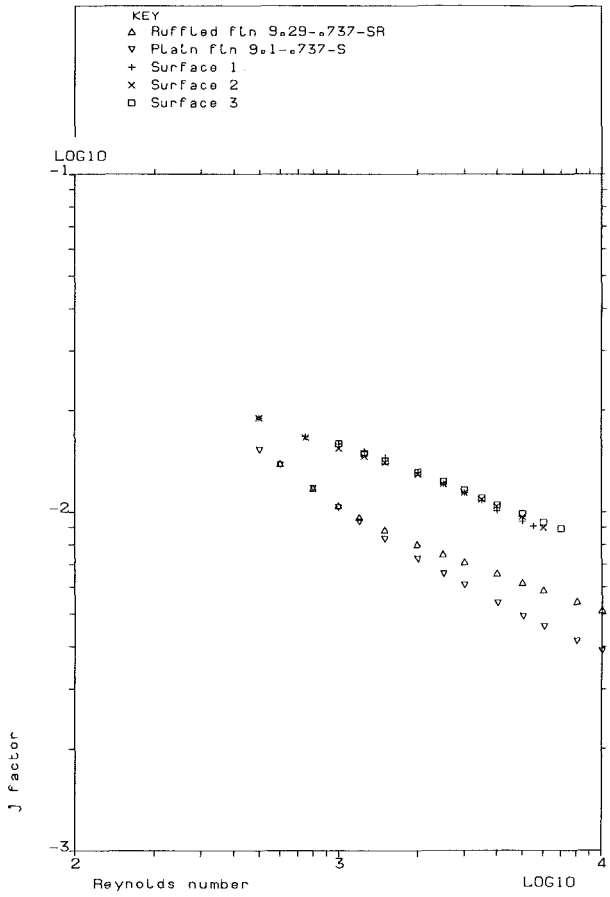


Fig. 7 Comparison of the *j* factor against the Reynolds number

exchanger due to the increase in the specific volume of the gas is taken into account in the pressure drop calculation. In the present comparison the ducting loss *Fd* was assumed negligible, but for real systems this should be included in the calculation of the fan power.

To quantify easily the relative performance of the heat exchangers, a performance ratio has been used. This ratio was defined as the ratio of the heat transfer rate for the heat exchanger relative to that of the reference surface against the fan power. This ratio is a modification to the ratio R3c of Bergles et al. (1975).

## Comparison of Heat Exchanger Surfaces

Comparisons are made against two similar finned tube heat exchangers reported by Kays and London (1984). The two surfaces used as the basis of the comparison with the new data were the plain fin 9.1-0.737-S and the 9.29-0.737-SR ruffled fin. These two surfaces will subsequently be referred to as plain and ruffled surfaces.

**Geometry Comparison.** The differences between the Kays and London fins and those of the present investigation are:

1 The plain surface is a straight flat fin.

2 The double amplitude of the ruffled surface was 0.635 mm (0.025 in.) compared with 1.242 mm for surface 1 (Fig. 2) and 1.118 mm for surfaces 2 and 3 (Fig. 3).

3 The wave pitch of the ruffled surface was 6.35 mm (0.25 in.) compared with 7.77 mm for all the surfaces 1-3.

4 There are small differences in the tube sizes and layout.

5 The Kays and London fin pitches were 358 (plain) and 366 (ruffled) fins per meter compared with 353 and 351 for surfaces 1 and 2. Surface 3 had 282 fins per meter.

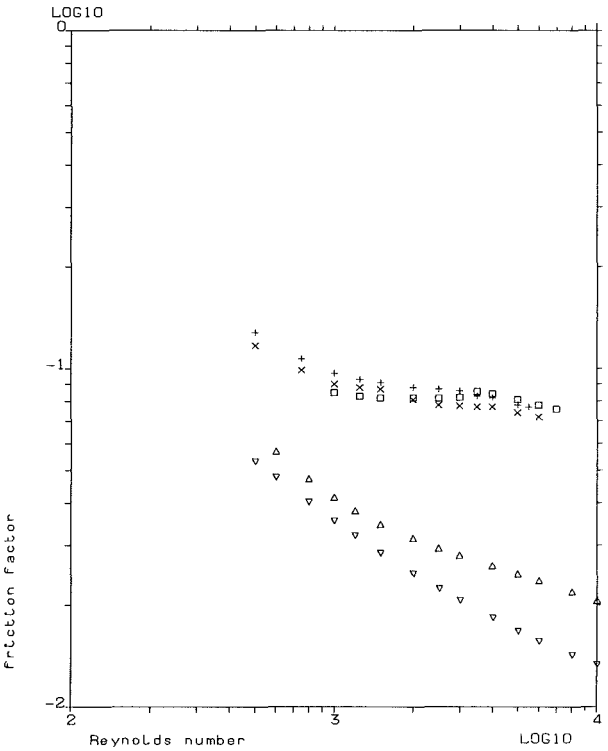


Fig. 8 Comparison of the friction factor against the Reynolds number

**Heat Transfer and Flow Friction Comparisons.** Preliminary comparisons of the *j* factor and friction factor against the Reynolds number showing the individual characteristics of

heat transfer ($j$ factor) and pressure drop (friction factor) against the Reynolds number are important. The comparisons are shown in Figs. 7 and 8, respectively. For heat exchangers of similar hydraulic diameter, these comparisons against the Reynolds number may be considered as being at common gas-side mass flow rate. These graphs show that all the surfaces 1–3 have higher $j$ and friction factors than the data of Kays and London. The plain fin has the lowest $j$ and friction factors. At the higher Reynolds numbers the $j$ factors for all surfaces are higher than that of the plain surface. This is due to the turbulence that is generated by the wavy surface (acting as a turbulence promoter), increasing the heat transfer coefficient. The complex flow associated with the wavy nature of the fin profile generates a form drag that increases the pressure drop, seen as increased friction factors in Fig. 8.

The comparisons of the new rippled fins by the four recommended criteria are now presented. The plotting symbols used in Figs. 7–13 (see Fig. 7) represent the same surface on each of the performance graphs. The $j$ factor to friction factor ratios against the Reynolds number are compared in Fig. 9. The London and Ferguson (1949) and Shah (1978) performance comparisons are plotted in Figs. 10 and 11, respectively. Lastly the Bergles et al. performance evaluation criteria are plotted in Fig. 12 and the associated performance ratio is shown in Fig. 13. For this last performance graph the Kays and London plain fin surface was designated as the reference surface. The heat transfer rates for all the surfaces relative to the reference surface did not lie on the same fan power values and interpolation of these data was necessary to produce the ratio. To overcome the problem of interpolation an equaton was fitted to the data set (of the Bergles et al. criteria) of the reference surface. Using the regression equation, the heat transfer rates for the reference surface were calculated at the same fan power values of the rippled surfaces. As the regression was not a perfect fit, the reference surface data are also plotted in Fig. 13.

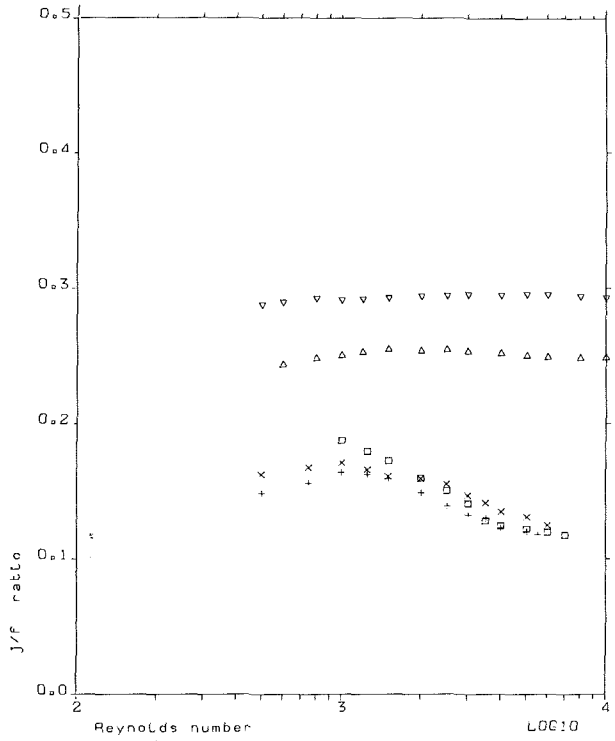


**Fig. 9 Comparison of the *j/f* ratio against the Reynolds number**

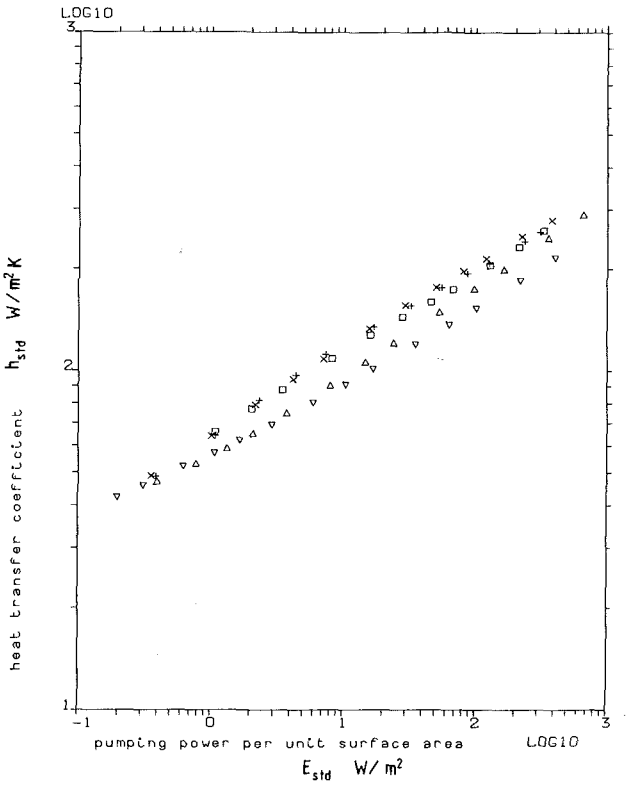


**Fig. 10 Comparison of the heat exchanger performance based on the criteria of London and Ferguson**

## Discussion

Comparison of heat exchanger surfaces has been studied by many authors; however, information regarding the validity of the various performance evaluation criteria is very limited.

On the basis of the $j/f$ ratio (Fig. 9) the new rippled surfaces are inferior to the plain and ruffled fins. However, there are disadvantages in using the $j/f$ ratio. Firstly a problem encountered in this study was the choice of the plane at which the minimum flow cross-sectional area and hence the core mass flux calculated. The flow passes through a short constriction where the second tube row interferes with the flow in the first row (see Fig. 1). It was felt that the representative velocity occurred on a plane between one tube row only. However, had the other plane been chosen, the Reynolds number, $j$ factor, and friction factor would have been different due to the different area used in the data reduction, without affecting the actual performance characteristics of mass flow rate, heat transfer coefficient, and pressure drop. Consider the following cases where the different surfaces have a similar hydraulic diameter. Where the two surfaces have the same $j$ factor against Reynolds number values, they both have the same heat transfer coefficient performance against the Reynolds number. If one of the surfaces has higher friction factors, then the surface with the lower friction factors has the best performance. The same argument applies to the case where the friction factor performance against the Reynolds number is the same for the two surfaces. The surface having the highest $j$ factors clearly has the better performance. Now consider the case where one surface has a higher $j$ factor and a higher friction factor relationship against Reynolds number than another. The heat transfer performance and the friction power expenditure are both different, between surfaces at the same Reynolds number. The $j/f$ ratio gives no indication as to the real performance of the heat exchangers, as it is limited to common mass flow rates. However the performance of the surface with the higher $j$ factors may have a better performance when operating at a lower mass flow rate and the friction power expenditures for the two surfaces are equal. In this case the $j$ factor to friction factor ratio is not a good indicator of

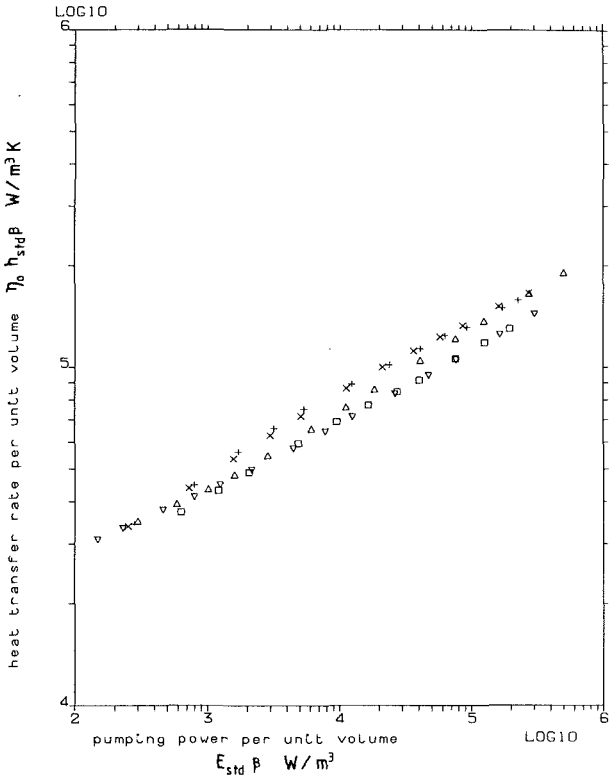


**Fig. 11 Comparison of the heat exchanger performance based on the criteria of Shah**

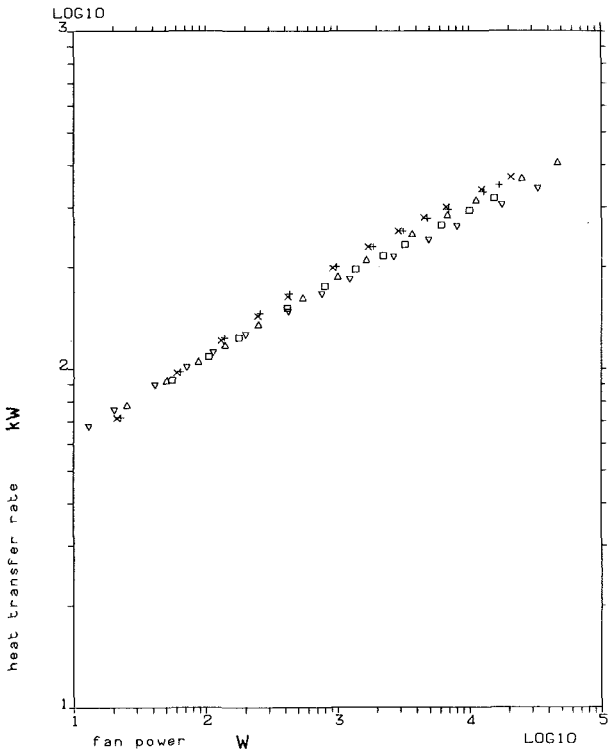


**Fig. 12 Comparison of the heat exchanger performance based on the criteria of Bergles et al.**

performance when plotted against the Reynolds number and a more powerful comparative method is required.

When compared with the criteria of London and Ferguson (1949) and Shah (1978) (Figs. 10 and 11) rippled surfaces 1 and 2 are superior to the plain and ruffled fins. Surface 3 appears

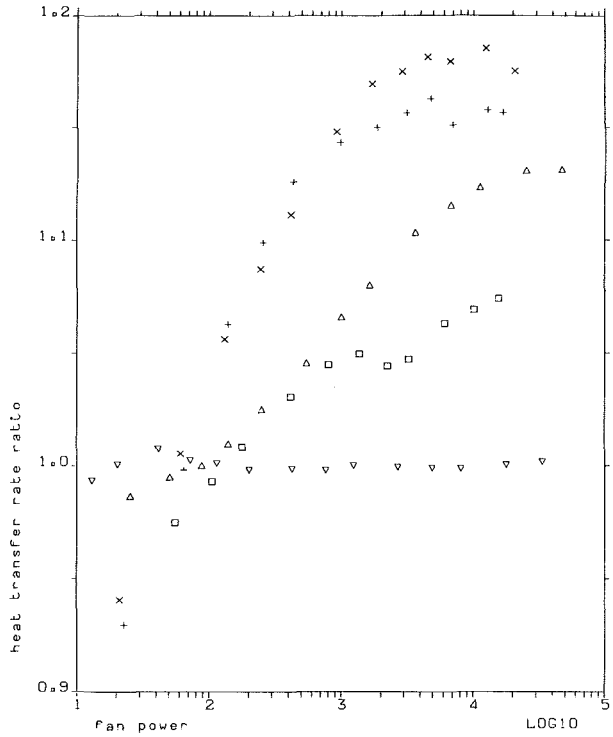


**Fig. 13 Comparison of the heat exchanger performance by the heat transfer rate ratio; criteria of Bergles et al. plain surface used as reference**

superior to the ruffled surface in the case of Fig. 10 and generally inferior in the case of Fig. 11.

The criteria of Bergles et al. (1975) take full account of the relevant flow and geometric factors and actually compare the surfaces in a particular application. It is felt that this is by far the most useful method. Due to the logarithmic scales of Fig. 12, the advantages or otherwise of one surface against another are hard to discern. As a result Fig. 13 is presented as a performance ratio with the plain fins taken as the basis of comparison. The result of the comparison of heat exchanger surfaces using the performance ratio in Fig. 13 is discussed below. At very low fan powers the plain surface has the highest performance, and the rippled surfaces have the lowest performance. However at intermediate and high fan powers, there is a significant increase in the performance of the rippled fin surfaces. The enhancement of the rippled surfaces relative to the ruffled surface is fan power dependent, but varies from 5 percent at fan powers greater than 100 W to a maximum of 7 percent for a fan power of 1 kW. At higher fan powers the performance of the rippled surfaces 1 and 2 are different. Surface 2 has a slightly better performance. At a fan power of 10 kW the increases in heat transfer of surfaces 1 and 2 relative to the ruffled surface are 2.5 and 5 percent, respectively. These differences are statistically significant. The actual heat transfer rates at these fan powers for the compared surfaces are given in Fig. 12. Surface 3 is seen to be inferior to all but the plain fins. This is due to the low number of fins per meter for this arrangement.

Although the London–Ferguson and Shah performance criteria have predicted the best surface, based on the results of the Bergles et al. design process, these criteria are very superficial. The heat transfer characteristics of these two criteria are calculated per unit temperature difference, giving the same mean (log mean) temperature difference for the heat exchangers under comparison, which may not be the case in practice. The fluid property variations are not taken into consideration, as constant values are used and the tube-side resistance is also not accounted for in the comparison.

The enhanced performance of the rippled fins when compared with the ruffled fins is due to the nature of the flow. Flow visualization studies have shown complex fluid flow patterns. These flow studies were limited to Reynolds numbers less than 2500 and were representative of the flow in ripple fin channels without tubes. At low velocities the flow separates from the ripple peaks allowing large areas of slowly recirculating vortices to exist, inhibiting heat transfer. As the velocity increased, the recirculation regions in the grooves three to four ripples downstream of a laminar inlet became unstable and vortices were shed, thus generating turbulence. The position of flow instability moved closer to the inlet with increasing velocity. A tentative explanation of the flow at higher velocities is that the turbulent flow causes delayed separation from the ripples in the turbulent flow region. The turbulence generated was seen to enhance the heat transfer.

## Conclusion

1 The performance characteristics of rippled fin heat exchangers have been measured and the results of this investigation have been presented. When compared on a performance ratio basis the rippled fins have advantages of up to 7 percent over previously published data for ruffled fins (Kays and London, 1984). This is attributed to the ripple geometry used. The heat transfer enhancement of the wavy fin is dependent upon the shape and dimensions of the ripple profile.

2 Comparisons have been made using several performance evaluation criteria. The $j$ factor to friction factor ratio was found to be an unsatisfactory method of comparing heat transfer surfaces. It is important to realize the limitations of a particular criterion used in an evaluation process. An engineer selecting a heat transfer surface would benefit from using the more powerful performance evaluation criteria of Bergles et al. (1975), which can be modified to suit his particular application. The effect of the fin density becomes easy to visualize using the performance ratio (Fig. 13).

## Acknowledgments

The authors wish to thank the Department of Mechanical Engineering at Coventry Polytechnic, and Covrad Heat Transfer, for making available the experimental facilities.

The authors acknowledge the assistance of C. D. Obray and C. C. Wright of the Department of Statistics and Operational Research with the statistical analysis.

The support of Mr. J. D. Maltson as a research student by the Science and Engineering Research Council and Covrad Heat Transfer is also acknowledged.

## References

Bergles, A. E., Junkhan, G. H., and Bunn, R. L., 1975, "Performance Criteria for Cooling Systems on Agricultural and Industrial Machines," SAE Paper No. 751187.

Davenport, C. J., 1983a, "Heat Transfer and Flow Friction Characteristics of Louvred Heat Exhanger Surfaces," *Heat Exchangers: Theory and Practice*, J. Taborek, G. F. Hewitt, and N. Afgan, eds., pp. 397–412.

Davenport, C. J., 1983b, "Correlations for Heat Transfer and Flow Friction Characteristics of Louvred Fins," *AIChE Symposium Series 225*, Vol. 79, pp. 19–27.

Kays, W. M., and London, A. L., 1984, *Compact Heat Exchangers*, 3rd ed., McGraw-Hill, New York.

Kern, D. Q., and Kraus, A. D., 1972, *Extended Surface Heat Transfer*, McGraw-Hill, New York, pp. 26–29.

London, A. L., 1964, "Compact Heat Exchangers, Part 2. Surface Geometry," *Mechanical Engineering*, Vol. 86, pp. 31–34.

London, A. L., and Ferguson, C. K., 1949, "Test Results of High-Performance Heat Exchanger Surfaces Used in Aircraft Intercoolers and Their Significance for Gas-Turbine Regenerator Design," *Trans. ASME*, Vol. 71, pp. 17–26.

Obray, C. D., Wright, C. C., and Baldwin, S. J., 1986, "A Comparative Study of Monte-Carlo Simulation and Taylor Series Approaches to the Derivation of Uncertainty Estimates. A Case Study on Compact Heat Exchangers," *Proc. 1st Int. Conference Modelling Under Uncertainty*, Institute of Physics Conference No. 80, I.O.P. Publishing Ltd., pp. 243–254.

Roetzel, W., and Nicole, F. J. L., 1975, "Mean Temperature Difference for Heat Exchanger Design – A General Approximate Explicit Equation," ASME JOURNAL OF HEAT TRANSFER, Vol. 97, pp. 5–8.

Shah, R. K., 1978, "Compact Heat Exchanger Surface Selection Methods," *Sixth International Heat Transfer Conference*, Toronto, Vol. 4, pp. 193–199.

# An Extension to the Irreversibility Minimization Analysis Applied to Heat Exchangers

**S. Aceves-Saborio**
Research Assistant.

**J. Ranasinghe**
Research Assistant.

**G. M. Reistad**
Professor and Head.

Department of Mechanical Engineering,
Oregon State University,
Corvallis, OR 97331

*The irreversibility minimization method of heat exchanger optimization is extended to include a term to account for the exergy of the material of construction of the heat exchanger. The method permits physically realistic optimization to be conducted with the resulting optimum designs providing conceptually beneficial guideposts, which do not change with time or location. Such optima are in contrast to the optima obtained by presently advocated methods, which on one hand indicate unrealistic infinite area heat exchangers, and on the other hand point to optima that may change dramatically with location and time. Although the analysis presented here does not represent a "cure-all" for heat exchanger analysis (economic optimization is still recommended), it does provide valuable conceptual insights and nonchanging guideposts for optimal design. Accompanying exergetic efficiency expressions using the same type of material exergy term show physically more realistic values than the usual expressions.*

## Introduction

One of the useful aspects of the exergy concept in thermodynamics is that it allows performance limits to be evaluated. As problems are formulated such that all factors that cannot be changed are represented, the importance of the limits increases. The method presented in this paper represents an approach to make the performance limits more realistic for heat exchangers.

The irreversibility minimization method was first applied to heat exchangers by McClintock (1951). Various authors have since used this technique for heat exchanger analysis, particularly since the work of Bejan (1977, 1980) where results regarding basic design variables were developed in a generalized, nondimensional manner. The work in this area has been reviewed by Bejan (1987) and Ranasinghe et al. (1987). The irreversibility minimization method is quite useful for evaluating design parameters at fixed total heat exchanger area. However, the method only considers the exergy losses associated with the heat exchanger operation, and does not consider the exergy or economic cost of the heat exchanger itself. As a result of this, the global optimum usually results in a heat exchanger with infinite area: an unacceptable result from an engineering design viewpoint.

Thermoeconomics, developed by Tribus and Evans (1962) and Obert and Gaggioli (1963), has been applied to heat exchangers by various authors, including London and Shah (1983) and Tapia and Moran (1986). A recent review of thermoeconomics has been presented by Gaggioli and El-Sayed (1987). Thermoeconomic analyses can take into account all the costs associated with building and operating a heat exchanger, and global optimization yields the realistic result of a finite area heat exchanger. Thermoeconomics also gives the designer the ability to decompose a global system into individual isolated components in a way such that optimizing the individual components yields a good approximation to the optimum design of the global system (Evans et al., 1983). The thermoeconomically optimum heat exchanger design must change as the costs vary with location and time. Thus, the thermoeconomic optimum design for one location and time does not serve as a good guidepost for the optimal design in another location and time.

This paper presents an extension of the minimum irreversibility generation analysis wherein the irreversibility generation equation includes a term that takes into account the exergy value of the heat exchanger materials and the application life of the heat exchanger.[1] This method yields optimal designs that do not change with time or location and that represent the desired optimal design in the limit of exergy costs being dominant relative to labor and profits. The resulting optimal designs are physically more realistic than those obtained from the usual irreversibility minimization methods, and although the designs do not represent the optimal design from a thermoeconomic viewpoint, they represent limits that may serve as guideposts for design. Such guideposts are quite useful conceptually and particularly important in times of rapidly changing and unpredictable economic parameters.

In addition to the basic method presented, this paper presents (*i*) the application of the method to counterflow heat exchangers, (*ii*) a modification to adjust the optimal technical design to reflect limits imposed by the present state of the technology, (*iii*) an evaluation of exergetic efficiencies of heat exchangers including the principle of the inclusion of the exergy of the material, (*iv*) an analysis to show the relationship of the thermoeconomic optimum relative to the optimum of the present method, and (*v*) several specific applications.

## Basic Method

The objective function for the basic irreversibility minimization analysis for a heat exchanger in a nondimensional form is (Bejan, 1977)

$$Ns = \frac{\dot{I}}{T_o\, C_{\max}} \tag{1}$$

In this equation $\dot{I}$ represents the irreversibilities occurring within the heat exchanger. The irreversibilities have been

Contributed by the Heat Transfer Division for publication in the JOURNAL OF HEAT TRANSFER. Manuscript received by the Heat Transfer Division October 26, 1987. Keywords: Heat Exchangers, Thermodynamics and Second Law.

[1] The concept of charging a device for an energy (or exergy) term that considers the materials of the device is not new. It has been considered in various manners, principally as "net energy analyses." The focus of this paper is to develop a more general, thermodynamically rigorous evaluation that can be widely accepted. Some discussion of methods closely related to net energy analysis is presented later in this paper in the section "Modification of Basic Method."

shown to consist mainly of those due to heat transfer and pressure drop. Thus, $Ns$ can be expressed as

$$Ns = Ns_{\Delta T} + Ns_{\Delta p} \tag{2}$$

The heat transfer term has been further divided into terms that can be reduced by additional surface area and those that result from the capacity mismatch ($Ns_{\text{imbalance}}$) of the heat exchanger streams (Bejan, 1987). These irreversibility terms are illustrated qualitatively in Fig. 1. This figure shows that $Ns_{\Delta T}$ and $Ns_{\Delta p}$ have a local optimum, but the global optimum corresponds to the infinite area heat exchanger limit.

This paper proposes that the irreversibility term in equation (1) include a term to account for the exergy of the materials of the heat exchanger, and that equation (2) would then become

$$Ns = Ns_{\Delta T} + Ns_{\Delta p} + Ns_m \tag{3}$$

The logic of this is that a minimum exergy expenditure equal to the exergy of the materials is required to make the heat exchanger from the dead state. This is an exergy expenditure that is effective for the "application life" of the heat exchanger.

Thus, the equivalent irreversibility rate assignable to the materials of the heat exchanger is the exergy of the materials $\mathcal{E}_m$ divided by the application life[2] of the heat exchanger

$$\dot{I}_m = \frac{\mathcal{E}_m}{t_{ap}} \tag{4}$$

and in nondimesionalized form:

$$Ns_m = \frac{\dot{I}_m}{T_o\, C_{\max}} \tag{5}$$

To illustrate the method, $\mathcal{E}_m$ needs to be determined. The exergy of heat exchanger materials can be divided into chemical and thermomechanical exergies. Materials acquire chemical exergies when they are transformed from the dead state into their final form. Materials also have thermomechanical exergy if they operate at temperatures or pressures different from that of the dead state or if they store elastic exergy as a result of deformations during the manufacture of the heat exchanger. Hence, the exergy of a heat exchanger material can be written as

$$\mathcal{E}_m = \mathcal{E}_{m,ch} + \mathcal{E}_{m,ph} \tag{6}$$

where $\mathcal{E}_{m,ch}$ is the chemical exergy and $\mathcal{E}_{m,ph}$ is the thermomechanical exergy of the heat exchanger material.

The chemical exergy is found by calculating the maximum work that can be obtained when the material under consideration is brought to chemical equilibrium with the components of the dead state. The method is illustrated by Moran (1982) and Kotas (1985), where a table of chemical exergy values for common materials with respect to a standard dead state is included.

Heat exchangers operate at pressures and temperatures different from those of the dead state. Heat exchanger materials then have a thermomechanical exergy different from zero.

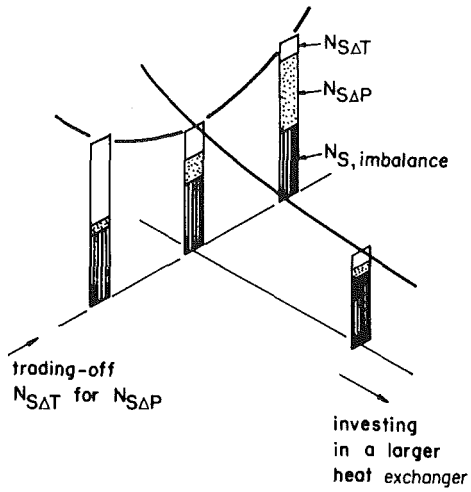


**Fig. 1 The structure of the total irreversibility generation in a heat exchanger (after Bejan, 1987)**

[2]The application life is a crucial parameter in the overall analysis presented here. Some people may, in fact, argue that because of this term, the analysis here no longer is just thermodynamic in nature. The authors respect this position, but also feel that as soon as it is indicated that an optimum engineering design is desired, we must pass the fence from pure science to the design process. We feel that the use of an application life is realistic for analyzing designs. Depending on the specific application, the actual life of a heat exchanger in the specified application may be very short or quite long. There are many instances where the application life is as short as one year and many others where it may be as long as 15 to 20 years. If the designer wants to be as close to pure science as possible, he/she take the application life as the actual physical life of the heat exchanger operating with the given media (i.e., the time before the unit would be physically destroyed by corrosion, etc.). If, on the other hand, the designer wants the optima to reflect the economic application life, he/she should use a time period that reflects the minimum acceptable payback period as the application life.

## Nomenclature

$A$ = area
$C$ = cost
$C_{\min}$, $C_{\max}$ = capacity rate
$E$ = elasticity modulus
$\mathcal{E}$ = exergy
$\dot{I}$ = irreversibility rate
$l$ = length
$Nc$ = economic objective function (equation (28))
$Ns$ = irreversibility generation number
NTU = number of transfer units
$p$ = width
$t$ = thickness
$T$ = temperature
$t_{ap}$ = application life
$U$ = overall heat transfer coefficient
$V$ = volume
$\gamma$ = material exergy parameter (equation (10))
$\epsilon$ = heat exchanger effectiveness (and strain in Appendix)
$\sigma$ = stress
$\tau$ = inlet temperature ratio
$\psi$ = exergetic efficiency
$\omega$ = capacity rate ratio = $C_{\min}/C_{\max}$

**Subscripts**

0 = dead state
1 = cold stream
2 = hot stream
$c$ = thermoeconomic value
$cf$ = counterflow
$ch$ = chemical
$e$ = exit
$f$ = fuel
$I$ = value at current state of technology
imbalance = quantity due to capacity rate imbalance
$m$ = material
$p$ = product
$pf$ = parallel flow
$ph$ = thermomechanical
$\Delta p$ = pressure drop
$\Delta T$ = heat transfer
$y$ = yield point

**Superscripts**

$*$ = optimum value
$'$ = conventional values (not including material exergy)

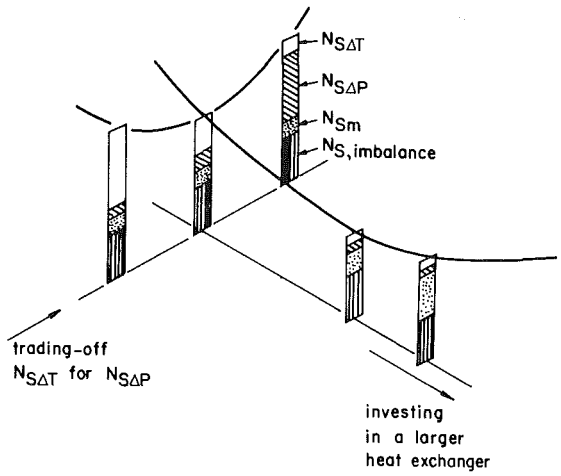


**Fig. 2 The structure of the total irreversibility generation in a heat exchanger including the material irreversibility**

However, these exergy values are small relative to the chemical exergy of the material, and can be neglected in the analysis. The elastic exergy resulting from deforming a material into a heat exchanger pipe is estimated here by following a simplified procedure, as shown in the appendix. The result for the thermomechanical component of the material exergy is

$$\mathcal{E}_{m,ph} = \frac{t\,\sigma_y^2\,A}{2\,E} \tag{7}$$

where $t$ is the thickness, $\sigma_y$ is the yield stress, $E$ is the elasiticity modululs, and $A$ is the lateral area of pipe.

Figure 2 is a modification of Fig. 1 that includes the material irreversibility contribution. The material irreversibility increases as the area is increased, yielding optimum designs with a finite area. For a fixed area, the material irreversibility is approximately constant, and the inclusion of the material irreversibility term does not affect the optimum design.

## Application

The following sections present the objective function developed previously (equation (3)) for a case when $Ns_{\Delta p}$ is negligible and ideal gas behavior can be assumed for the heat exchanger streams. The analysis also neglects heat losses to the surroundings. The method developed is applied to counterflow heat exchangers.

**Objective Function.** Consider the case of a heat exchanger with negligible pressure drop irreversibility. Equation (3) then becomes

$$Ns = Ns_{\Delta T} + Ns_m \tag{8}$$

As previously discussed, the heat exchanger material has an exergy value at the moment of installation. The exergy value of the heat exchanger can be viewed as being used up after a time equal to the application life $t_{ap}$. The decrease in the exergy of the material can be considered as an irreversibility generation rate given by

$$Ns_m = \frac{A\,\dot{I}_A}{T_0\,C_{\max}} = \gamma\,\omega\,\mathrm{NTU} \tag{9}$$

where $\dot{I}_A = \dot{I}_m/A$ is the irreversibility rate per unit area of the heat exchanger, $\omega$ is the capacity rate ratio $C_{\min}/C_{\max}$, and $\gamma$ is the material exergy parameter defined as

$$\gamma = \frac{\dot{I}_A}{T_0\,U} \tag{10}$$

When ideal gas behavior is assumed for the flowing fluid, and there are no heat losses to the surroundings, the heat transfer irreversibility generation number is

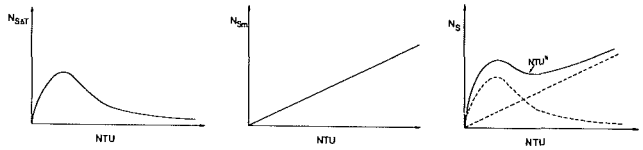


**Fig. 3 The nondimensional irreversibility generation number (objective function) as a function of NTU, showing: (a) contribution from $Ns_{\Delta T}$, (b) contribution from $Ns_m$, and (c) total ($Ns_{\Delta T} + Ns_m$)**

$$Ns_{\Delta T} = \omega\,\ln\left[1 + \frac{\epsilon}{\tau}\,(1-\tau)\right] + \ln[1 + \omega\epsilon(\tau - 1)] \tag{11}$$

where $\epsilon$ is the effectiveness of the heat exchanger and $\tau$ is the inlet temperature ratio.

Substitution of (9) and (11) into (8) yields the final form of the objective function

$$Ns = \omega\,\ln\left[1 + \frac{\epsilon}{\tau}\,(1-\tau)\right] + \ln[1 + \omega\epsilon(\tau - 1)] + \gamma\,\omega\,\mathrm{NTU} \tag{12}$$

This objective function can be used to optimize any heat exchanger if the $\epsilon$-NTU relationship is known and the assumptions made during the development of this equation are satisfied. The $\epsilon$-NTU relationships for many heat exchanger configurations are given in Kays and London (1984). Objective function (12) is used next for the design optimization of a counterflow heat exchanger.

**Optimization of Counterflow Heat Exchangers.** The variation of $Ns_{\Delta T}$ with NTU for a counterflow heat exchanger is shown in Fig. 3(*a*). When the material irreversibility is not included in the analysis, $Ns_{\Delta T}$ is equal to $Ns$. As illustrated in Fig. 3(*a*), the value of $Ns_{\Delta T}$ increases from zero with increasing NTU, reaches a maximum, and then decreases to a minimum at infinity. This minimum $Ns_{\Delta T}$ has a value of zero for a balanced heat exchanger. The decrease in irreversibility on the left side of the maximum was shown by Bejan (1980) to be due to insufficient heat transfer across a temperature difference of order $T_2 - T_1$. Bejan (1987) also showed that designing a heat exchanger in this region would violate the principle of thermodynamic "isolation" of the component being optimized. This region was also identified by Sekulic and Baclic (1987) as unsuitable for operating a counterflow heat exchanger.

The value of $Ns_m$ increases linearly with NTU as illustrated in Fig. 3(*b*). The objective function $Ns$ is the sum of $NS_{\Delta T}$ and $Ns_m$, and is shown in Fig. 3(*c*). This figure shows that the irreversibility due to adding more heat exchanger area balances with the reduction in heat transfer irreversibility, and hence the total irreversibility of the heat exchanger has a minimum. Here the optimum NTU is designated NTU*. Designing a heat exchanger to operate at this optimum point ensures the minimum destruction of exergy. Therefore, increasing the area to the limit of an infinitely large heat exchanger does not decrease the irreversibility but increases it, because an infinite amount of exergy would be used in building such a heat exchanger.

Since the value of $\gamma$ is a function of the overall heat transfer coefficient $U$, the point of minimum irreversibility generation rate corresponds to a given $U$. In the present analysis the value of $U$ has to be known to calculate $\gamma$ and NTU*. This additional degree of freedom is due to the assumption of negligible pressure drop. Therefore, $U$ should be in a range where this assumption is not violated. However, when the pressure drop is considered, an optimum value of $U$ for a given surface area can be obtained from the best balance between $Ns_{\Delta T}$ and $Ns_{\Delta p}$ (see Fig. 2).

Three extreme cases that can be encountered in designing a counterflow heat exchanger are shown in Figs. 4(*a*) through 4(*c*). The case corresponding to a small capacity rate ratio is

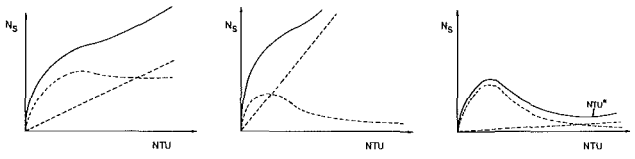


**Fig. 4 Nondimensional irreversibility generation number as a function of NTU showing three limiting cases: (a) small capacity rate ratio $\omega$, (b) large material exergy parameter $\gamma$, and (c) small material exergy parameter $\gamma$**

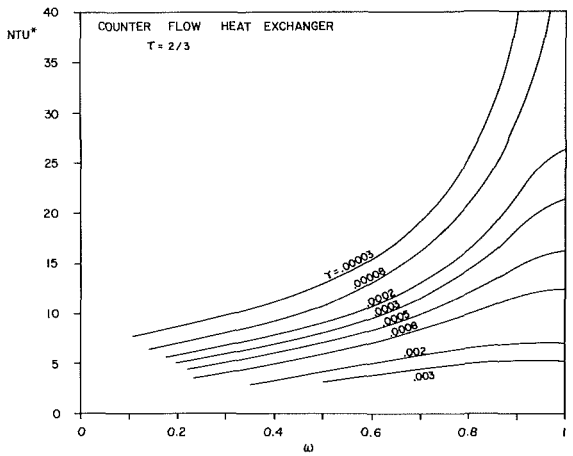


**Fig. 5 Optimum NTU as a function of the balance ratio and the material exergy parameter $\gamma$ for a counterflow heat exchanger with $\tau = 2/3$**

shown in Fig. 4(*a*). The irreversibility due to the capacity rate imbalance dominates in this case and the decrease in heat transfer irreversibility with increase in area is negligible. There is no minimum in this case, and the heat exchanger size has to be determined by the required duty or economic limitations. Large values of $\gamma$ result in there being no optimum value of *Ns*, as shown in Fig. 4(*b*). This is due to having a short application life for the heat exchanger or a very small value of *U*. These conditions result in the irreversibility due to added area being much more than the reduction in heat transfer irreversibility. The case of a very large application life for the heat exchanger is shown in Fig. 4(*c*). A point of minimum exergy destruction exists in this case, but NTU* is very large.

The variation of NTU* with the capacity rate ratio $\omega$ for various values of $\gamma$ is shown in Fig. 5. This figure does not show a value of NTU* for small values of $\omega$ since, as stated before, there is no optimum design for small capacity rate ratios. Figure 5 corresponds to an inlet temperature ratio $\tau$ of 2/3 (Witte, 1983, reports that this value of $\tau$ pertains to most liquid–liquid, liquid–air, and gas–air heat exchangers). Reducing $\tau$ increases the irreversibility due to heat transfer at a given NTU and hence increases the NTU*, and vice versa. The use of Fig. 5 to obtain NTU* for a counterflow heat exchanger is illustrated by an example in a later section.

## Modification of Basic Method

Current processes to produce materials have low efficiencies, and the actual exergy expenditure for a given heat exchanger is much greater than just the exergy of the material. The objective function for irreversibility minimization analysis can be formulated to take into account all the exergy expenses associated with the fabrication of the material. This method was used in a specific case by Boyd et al. (1981) to analyze a simplified heat exchanger model. They considered a material contribution to the irreversibility generation equation. This contribution was calculated as the exergy[3] spent in mining, smelting, refining, milling, and transporting the heat exchanger material. The analysis was based on average values for exergy expenses and transporting distances. Le Goff and Giulietti (1982) also included a material energy term in the global energy consumption equation. The material energy was estimated from the component dimensions by using empirical equations. The authors applied these estimates to find optimum heat exchanger designs for different objective functions based on energy, economics, and combinations of the two.

Another way of including the irreversibilities generated in the process of building a heat exchanger is to divide the material irreversibility rate by an adequate efficiency for the overall construction process. Chapman and Roberts (1985) list overall efficiencies for manufacture of some important materials. The objective function expressing the global irreversibility generation at the current state of technology is

$$Ns_I = Ns_{\Delta T} + Ns_{\Delta p} + Ns_{mI} \tag{13}$$

where

$$Ns_{mI} = \frac{Ns_m}{\psi_m} \tag{14}$$

and $\psi_m$ is the exergetic efficiency[4] for the overall manufacturing process.

When ideal gas behavior is assumed for the flowing fluids and the pressure drop irreversibility is small, the objective function reduces to

$$Ns_I = \omega \ln\left[1 + \frac{\epsilon}{\tau}(1-\tau)\right] + \ln[1 + \omega\epsilon(\tau-1)] + \gamma_I \omega \text{ NTU} \tag{15}$$

with the nondimensional parameter $\gamma_I$ defined as

$$\gamma_I = \frac{\gamma}{\psi_m} \tag{16}$$

Both objective functions given by equations (12) and (15) have the same functional form, and are identical when the exergetic efficiency of the manufacturing process is unity. The same optimization procedure used for equation (12) is then applicable for (15), and an optimum $\text{NTU}_I$ for a counterflow heat exchanger can also be obtained from Fig. 5 for a given value of $\gamma_I$. The optimum value of $\text{NTU}_I$ is designated by $\text{NTU}_I^*$ (i.e., NTU* is the optimum when $\gamma$ is used in Fig. 5, and $\text{NTU}_I^*$ is the optimum when $\gamma_I$ is used in the same figure).

## Exergetic Efficiency

The exergetic efficiency of a plant component is defined in a variety of ways in the literature. The following expression is selected for this work (Tsatsaronis and Winhold, 1985):

$$\psi_{hx} = \frac{\mathcal{E}_p}{\mathcal{E}_f} \tag{17}$$

where $\mathcal{E}_p$ is the rate of exergy gained by the product, and $\mathcal{E}_f$ is the rate of exergy loss by the fuel. When the component is a heat exchanger designed for heating, the rate of exergy gained by the cold stream is equal to $\mathcal{E}_p$, and the rate of exergy loss by the hot stream plus the rate of exergy loss due to the heat exchanger material is equal to $\mathcal{E}_f$. When the irreversibility con-

[3] The analysis presented was based on energy consumption rather than exergy consumption. However, all the energy sources considered are either electricity or high-grade fuels, so that the exergy and energy consumption are approximately equal.

[4] One of the present authors (Reistad) has in the past advocated the term "effectiveness" to denote second law efficiencies. In light of the acceptance of the term exergy, the expression "exergetic efficiency" is preferred.

tribution from the material is not included in the analysis, the rate of exergy loss by the fuel is the rate of exergy loss by the hot stream, and is designated as $\mathcal{E}_f'$. The exergetic efficiencies for a heat exchanger with and without the irreversibility contributions from the material are developed next.

The exergy gained by the product is

$$\mathcal{E}_p = \mathcal{E}_{1e} - \mathcal{E}_1 \tag{18}$$

When the material irreversibility rate is not included, the exergy loss by the fuel is

$$\mathcal{E}_f' = \mathcal{E}_2 - \mathcal{E}_{2e} \tag{19}$$

When the material irreversibility rate is included, the exergy loss by the fuel is given by

$$\mathcal{E}_f = \mathcal{E}_2 - \mathcal{E}_{2e} + \dot{I}_A A \tag{20}$$

For an ideal gas, when pressure drop irreversibility and heat losses to the surroundings are negligible, the above equations can be written as

$$\mathcal{E}_p = C_{\min} T_1 \epsilon \left[\frac{1}{\tau} - 1\right] - T_0 C_{\min} \ln\left[1 + \epsilon\left(\frac{1}{\mathcal{E}} - 1\right)\right] \tag{21}$$

$$\mathcal{E}_f' = C_{\max} T_1 \omega \epsilon \left[\frac{1}{\tau} - 1\right] + T_0\ C_{\max} \ln[1 - \omega\epsilon(1-\tau)] \tag{22}$$

$$\mathcal{E}_f = C_{\max} T_1 \omega \epsilon \left[\frac{1}{\tau} - 1\right] + T_0\ C_{\max} \ln[1 - \omega\epsilon(1-\tau)] + \gamma\ T_0 C_{\min} \mathrm{NTU} \tag{23}$$

where $T_1$ is the inlet temperature of the cold stream. The value of $\gamma$ is replaced by $\gamma_I$ to take into account all the irreversibilities associated with the manufacturing process, at the current state of technology. The exergetic efficiencies with and without the material irreversibility rate, $\psi_{hx}$ and $\psi_{hx}'$, respectively, can now be written as

$$\psi_{hx} = \omega \left\{ \frac{\left(\frac{T_1}{T_0}\right)\epsilon(\tau^{-1} - 1) - \ln[1 + \epsilon(\tau^{-1} - 1)]}{\left(\frac{T_1}{T_0}\right)\omega\epsilon(\tau^{-1} - 1) + \ln[1 - \omega\epsilon(1-\tau)] + \gamma\ \omega\ \mathrm{NTU}} \right\} \tag{24}$$

$$\psi_{hx}' = \omega \left\{ \frac{\left(\frac{T_1}{T_0}\right)\epsilon(\tau^{-1} - 1) - \ln[1 + \epsilon(\tau^{-1} - 1)]}{\left(\frac{T_1}{T_0}\right)\omega\epsilon(\tau^{-1} - 1) + \ln[1 - \omega\epsilon(1-\tau)]} \right\} \tag{25}$$

The equations developed above for the exergetic efficiency are now applied to both counterflow and parallel flow heat exchangers.

The variations of the exergetic efficiencies $\psi_{hx}$ and $\psi_{hx}'$ with effectiveness for counterflow and parallel flow heat exchangers with the same $\gamma$ ($\gamma = 0.01$), are shown in Fig. 6. This figure is for a balanced capacity rate with the cold stream inlet temperature equal to the dead state temperature. The exergetic efficiency $\psi_{hx}$ is always less than $\psi_{hx}'$. At the infinite heat exchanger limit ($\epsilon = 0.5$ for parallel flow heat exchanger, $\epsilon = 1.0$ for the counterflow heat exchanger) $\psi_{hx}$ tends to zero while $\psi_{hx}'$ is a maximum. The exergetic efficiency $\psi_{hx,pf}$ for the parallel flow heat exchanger at a given $\epsilon$ is always lower than $\psi_{hx,cf}$ for a counterflow heat exchanger, and this difference can be clearly seen at values of the effectiveness close to 0.5. The exergetic efficiencies $\psi_{hx}'$ for the parallel and counterflow heat exchangers are the same. However, for a given duty (a given effectiveness in Fig. 6) a counterflow heat exchanger is known to be more attractive than a parallel flow unit, because

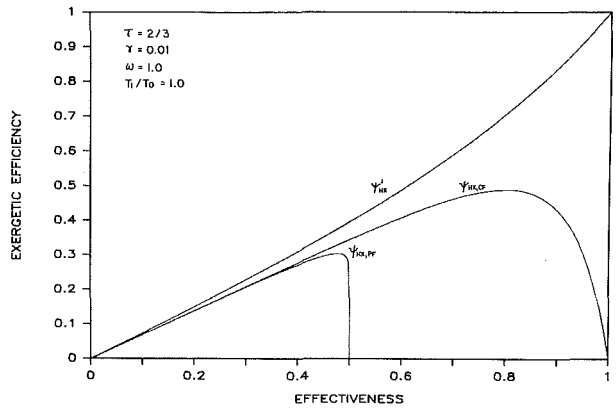


**Fig. 6 Exergetic efficiencies for counterflow and parallel flow heat exchangers with ($\psi_{hx}$) and without ($\psi_{hx}'$) the effect of the material irreversibility, for a balanced capacity ratio $\omega$ of 1, an inlet temperature ratio $\tau$ of 2/3, and a material exergy parameter $\gamma$ equal to 0.01**

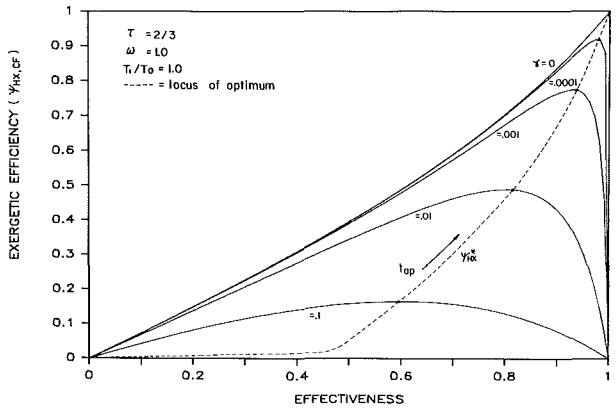


**Fig. 7 Exergetic efficiency of a counterflow heat exchanger as a function of heat exchanger effectiveness for different values of the material exergy parameter $\gamma$**

of the reduced area; this is properly shown in the exergetic efficiency if the material irreversibility is included as illustrated in Fig. 6. The irreversibility rate in building and operating an infinite area heat exchanger makes the exergetic efficiency in the large heat exchanger area limit tend to zero, when the application life is finite. Hence, including the material irreversibility results in physically realistic values for the exergetic efficiency.

The parameter $\gamma$ is inversely proportional to the application life of the heat exchanger, $t_{ap}$. When the application life approaches zero, $\gamma$ tends to infinity and the exergetic efficiency $\psi_{hx}$ is equal to zero in the limit. However, if the heat exchanger has an infinite application life, then $\gamma$ is equal to zero, and the exergetic efficiency $\psi_{hx}$ is equal to $\psi_{hx}'$. The variation of the exergetic efficiency $\psi_{hx}$ with effectiveness for a balanced counterflow heat exchanger is shown in Fig. 7, for different values of $\gamma$. This figure is for a heat exchanger inlet temperature ratio of 2/3 and the cold stream inlet temperature equal to the dead state temperature. Figure 7 shows that $\psi_{hx,cf}$ increases with decreasing $\gamma$ (increasing application life $t_{ap}$), for a given value of $\epsilon$, and has a maximum for any value of $\gamma$. The dotted line on Fig. 7 shows the locus of the maximum exergetic efficiency $\psi_{hx}^*$, with the arrow indicating the direction of increasing application life. When the heat exchanger is reversible ($\psi_{hx} = 1$), then $\gamma = 0$ and $\epsilon = 1$. This shows that an infinite area balanced counterflow heat exchanger with an infinite application life is reversible. Hence, including the material irreversibility term results in adding a time constraint in the reversible heat exchanger limit.

## Thermoeconomic Analysis

In thermoeconomics, the objective function becomes the total cost of operation. This includes capital costs and irreversibility penalty costs. Assuming that the capital costs are proportional to the area, the objective function becomes

$$C_T = C_A\ A + C_{\Delta T}\ \dot{I}_{\Delta T} + C_{\Delta p}\ \dot{I}_{\Delta p} \tag{26}$$

where $C_A$ is the capital cost per unit area of the heat exchanger and $C_{\Delta T}$ and $C_{\Delta p}$ are the cost associated with heat transfer and pressure drop irreversibilities, respectively. The various methods of calculating $C_{\Delta T}$ and $C_{\Delta p}$ are reviewed by Ranasinghe et al. (1987).

The objective function can be nondimensionalized as follows:

$$Nc = \frac{C_T}{C_{\Delta T} T_0\ C_{\max}\ t_{ap}} \tag{27}$$

Under the assumptions of ideal gas behavior and negligible pressure drop irreversibility, the objective function becomes

$$Nc = \omega\ \ln\left[1 + \frac{\epsilon}{\tau}(1-\tau)\right] + \ln[1 + \omega\epsilon(\tau - 1)] + \gamma_c\ \omega\ \text{NTU} \tag{28}$$

where the nondimensional parameter $\gamma_c$ is defined as

$$\gamma_c = \frac{C_A}{C_{\Delta T}\ T_0\ U\ t_{ap}} \tag{29}$$

Note that the thermoeconomic objective function given by equation (28) has the same functional form as the two previously derived irreversibility rate based objective functions given by equations (12) and (15). The only difference is that the value of $\gamma_c$ has to be used instead of $\gamma$ or $\gamma_I$. This property simplifies the optimization procedure, since Fig. 5 can be used to obtain the optimum NTU, when the heat exchanger being optimized is a counterflow unit. The optimum NTU obtained from thermoeconomic analysis is designated $\text{NTU}_c^*$. The next section shows the relationship of NTU*, $\text{NTU}_I^*$, and $\text{NTU}_c^*$ for a specific case.

## Specific Applications

The evaluation of the optimum value of NTU for a counterflow heat exchanger based on minimum irreversibility or minimum cost of irreversibility is illustrated by the following example. This section also includes a discussion on the significance of the results.

**Example.** Determine NTU*, $\text{NTU}_I^*$, and $\text{NTU}_c^*$ for a counterflow heat exchanger for values of the application life of 5 and 10 years, and for $U = 40$ and 70 W/m$^2$-K. The capacity rate ratio and the inlet temperature ratio are $\omega = 0.7$ and $\tau = 2/3$, respectively. The heat exchanger shell and tubes are made of carbon steel, and some data for the steel tubes are given in Table 1. The cost of heat exchanger area is approximately 72 \$/m$^2$ (from Matley, 1983), an estimate for the cost of heat transfer irreversibility is 0.056 \$/kW-hr, and the gross energy requirement to produce steel tubes is $35.7 \times 10^3$ J/kg (from Chapman and Roberts, 1985). The temperatures $T_0 = 298$ K and $T_1 = 298$ K.

**Solution.** The thermomechanical exergy of the material can be calculated from equation (7) as

$$\mathcal{E}_{m,ph} = \frac{t\ \sigma_y^2\ A}{2\ E} = 649\ A\ \text{(J)}$$

The chemical exergy of the heat exchanger material is

$$\mathcal{E}_{m,ch} = (6764 \times 10^3)(7770)(3.2 \times 10^{-3})\ A\ \text{(J)}$$
$$= 1.6818 \times 10^8\ A\ \text{(J)}$$

The thermomechanical exergy of the material is much smaller than the chemical exergy. The total material exergy $\mathcal{E}_m$ is then approximately equal to the chemical exergy $\mathcal{E}_{m,ch}$.

**Table 1 Data for carbon steel tubes**

| | |
|---|---|
| Density | 7770 kg/m$^3$ |
| Thickness | 3.2 mm |
| Chemical exergy | 6764 kJ/kg |
| Yield stress | $2.896 \times 10^8$ Pa |
| Young's modulus | $2.068 \times 10^{11}$ Pa |

**Table 2 Values of $\gamma$, $\gamma_I$, and $\gamma_c$ for heat exchanger in example**

| U (W/m$^2$°K) \ $t_{ap}$ (years) | 5 | | | 10 | | |
|---|---|---|---|---|---|---|
| | $\gamma$ | $\gamma_I$ | $\gamma_c$ | $\gamma$ | $\gamma_I$ | $\gamma_c$ |
| 40 | $8.942 \times 10^{-5}$ | $4.709 \times 10^{-4}$ | $2.462 \times 10^{-3}$ | $4.471 \times 10^{-5}$ | $2.355 \times 10^{-4}$ | $1.231 \times 10^{-3}$ |
| 70 | $5.1098 \times 10^{-5}$ | $2.6908 \times 10^{-4}$ | $1.407 \times 10^{-3}$ | $2.555 \times 10^{-5}$ | $1.345 \times 10^{-4}$ | $7.035 \times 10^{-4}$ |

**Table 3 Values of NTU* for heat exchanger in example**

| U (W/m$^2$°K) \ $t_{ap}$ (years) | 5 | | | 10 | | |
|---|---|---|---|---|---|---|
| | NTU* | $\text{NTU}_I^*$ | $\text{NTU}_c^*$ | NTU* | $\text{NTU}_I^*$ | $\text{NTU}_c^*$ |
| 40 | 15.5 | 10 | 5 | 18 | 12 | 7 |
| 70 | 17.5 | 12 | 6.5 | 19.5 | 14 | 8.5 |

The effectiveness of the manufacturing process for carbon steel tubes can be calculated as

$$\psi_m = \frac{6764}{35.7 \times 10^3} = 0.19$$

The cost of heat transfer irreversibility is

$$C_{\Delta T} = \frac{0.056}{3600 \times 1000} = 1.556 \times 10^{-8}\ (\$/\text{J})$$

The values of $\gamma$, $\gamma_I$, and $\gamma_c$ can now be calculated by using equations (10), (16), and (19), respectively, as

$$\gamma = \frac{1.6818 \times 10^8}{298\ U\ t_{ap}} = \frac{564 \times 10^3}{U\ t_{ap}}$$

$$\gamma_I = \frac{\gamma}{0.19} = \frac{2970 \times 10^3}{U\ t_{ap}}$$

$$\gamma_c = \frac{72}{(1.556 \times 10^{-8})(298) U\ t_{ap}} = \frac{15527 \times 10^3}{U\ t_{ap}}$$

The results are summarized in Table 2.

Finally, the NTU* values can be obtained from Fig. 5, or by solving the objective functions as shown in Fig. 8. The results are summarized in Table 3.

**Comments on Results.** The variation of *Ns* with NTU for the three objective functions considered, when the overall heat transfer coefficient is 40 W/m$^2$ K and the application life is 5 years, is shown in Fig. 8. The magnitudes of the optimum NTU are in the order $\text{NTU}^* > \text{NTU}_I^* > \text{NTU}_c^*$. The value of NTU* and the corresponding irreversibilities are constant, independent of time and location. The irreversibility corresponding to this optimum is the absolute minimum and corresponds to the case when all the manufacturing processes of the heat exchanger are ideal. As discussed previously, $\text{NTU}_c^*$ is time and location dependent due to the costs $C_A$ and $C_{\Delta T}$. The value of $\text{NTU}_I^*$ is a weaker function of time and location than $\text{NTU}_c$. This is because $\text{NTU}_I^*$ is only a function of the exergetic efficiencies of the heat exchanger manufacturing processes, which only varies with an improvement in the technology and

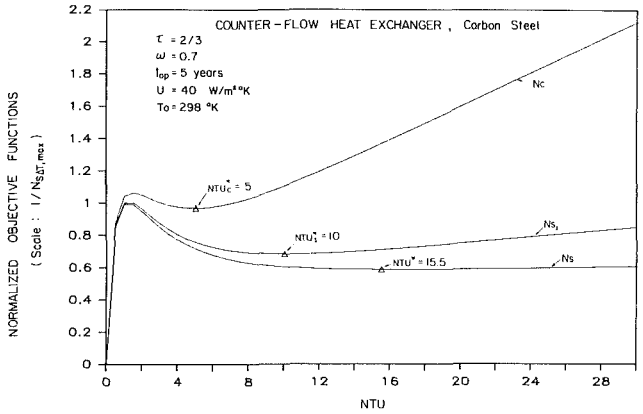


**Fig. 8 Values of NTU for minimum irreversibility generation (equation (12)), minimum irreversibility generation at present state of technology (equation (15)), and minimum thermoeconomic cost (equation (28))**

is relatively insensitive to the political environment, location, etc. In a world of diminishing fuel resources we can expect $NTU_c^*$ to move toward $NTU_I^*$ with time. However, the cost of material might increase with increasing fuel cost. The collection and analysis of heat exchanger data over a period of time should be undertaken to establish this relationship. This would allow the heat exchanger design engineers to decide on the best possible NTU* value for the heat exchanger for the most efficient operation during its application life period.

## Conclusions

The method presented in this paper, which adds an irreversibility term due to the material of construction of the heat exchanger in the overall irreversibility minimization equation for heat exchanger optimization, allows physically realistic optimization to be conducted. The resulting optimum designs provide conceptually beneficial guideposts that do not change with time or location. Such optima are in contrast to the optima obtained by presently advocated methods, which on one hand indicate unrealistic infinite area heat exchangers and on the other hand point to optima that may change dramatically with location and time.

The optima obtained by the method indicated here are conceptually similar to the economic optimization, and, in fact the same nondimensionalized curves may be used, in some instances, for both optimizations. The optima obtained from the basic method delineated here specify heat exchanger areas that are significantly larger than those corresponding to an economic optimization, and their use is restricted; their primary value lies in their representing nonchanging upper limits. With modifications to represent the current state of technology, the method delineates optima that are substantially closer to those specified by current thermoeconomic optimizations.

Exergetic efficiency expressions that similarly include an irreversibility term due to the material of construction of the heat exchanger show physically more realistic values than the usual expressions that do not include such a term. Such exergetic efficiencies clearly show the thermodynamic advantage of counterflow as compared to parallel flow arrangements, and they show a value of zero for all infinite area heat exchangers except those with infinite application lives. This is in contrast to some other usual exergetic expressions that show counterflow and parallel flow units having equal efficiencies and that can yield values of 100 percent for infinite area heat exchangers.

Although the analysis presented here does not represent the "cure-all" for heat exchanger analysis, it does provide conceptually valuable analysis methods and nonchanging guideposts for optimal design.

## Acknowledgments

The authors wish to acknowledge partial support of this project by the USDA.

## References

Bejan, A., 1977, "The Concept of Irreversibility in Heat Exchanger Design: Counterflow Heat Exchangers for Gas-to-Gas Applications," ASME JOURNAL OF HEAT TRANSFER, Vol. 99, pp. 374–380.

Bejan, A., 1980, "Second Law Analysis in Heat Transfer," *Energy*, Vol. 5, pp. 721–732.

Bejan, A., 1987, "Thermodynamics of Heat Transfer Devices," *Second Law Analysis of Thermal Systems*, Proc. IVth Intl. Symp. on 2nd Law Analysis of Thermal Systems, M. J. Moran and E. Sciubba, eds., ASME, New York, pp. 1–15.

Boyd, J. M., Bluemel, V., Keil, T. H., Kucinkas, G. R., and Molinari, S., 1981, "The Second Law of Thermodynamics as a Criterion for Heat Exchanger Design," *Energy*, Vol. 6, pp. 603–609.

Chapman, P. F., and Roberts, F., 1983, *Metal Resources and Energy*, Butterworths, London.

Evans, R. B., Kadaba, P. V., and Hendrix, W. A., 1983, "Essergetic Functional Analysis for Process Design and Synthesis," *Efficiency and Costing*, ACS Symposium Series, pp. 239–261.

Gaggioli, R. A., and El-Sayed, Y. M., 1987, "A Critical Review of Second Law Costing Methods," *Second Law Analysis of Thermal Systems*, Proc. IVth Intl. Symp. on 2nd Law Analysis of Thermal Systems, M. J. Moran and Sciubba, eds., ASME, New York, pp. 59–73.

Kays, W. M., and London, A. L., 1984, *Compact Heat Exchangers*, McGraw-Hill, New York.

Kotas, T. J., 1985, *The Exergy Method of Thermal Plant Analysis*, Butterworths, London.

LeGoff, P., and Giulietti, M., 1982, "Comparison of Economic and Energy Optimizations for a Heat Exchanger," *International Chemical Engineering*, Vol. 22, No. 2, pp. 252–268.

London, A. L., and Shah, R. K., 1983, "Costs of Irreversibilities in Heat Exchanger Design," *Heat Transfer Engineering*, Vol. 4, No. 2, pp. 59–73.

Matley, J., 1984, *Modern Cost Engineering: Methods and Data*, Vol. II, McGraw-Hill, New York.

McClintock, F. A., 1951, "The Design of Heat Exchangers for Minimum Irreversibility," presented at the ASME Annual Meeting, Paper No. 51-A-108.

Moran, M. J., 1982, *Availability Analysis: A Guide to Efficient Energy Use*, Prentice-Hall, New York.

Obert, E. F., and Gaggioli, R. A., 1963, *Thermodynamics*, 2nd ed., McGraw-Hill, New York.

Ranasinghe, J., Aceves-Saborio, S., and Reistad, G. M., 1987, "Optimization of Heat Exchangers in Energy Conversion Systems," *Second Law Analysis of Thermal Systems*, Proc. IVth Intl. Symp. on 2nd Law Analysis of Thermal Systems, M. J. Moran and E. Sciubba, eds., ASME, New York, pp. 29–38.

Sekulic, D. P., and Baclic, B. S., 1987, "The Four "E"s of a Heat Exchanger," *Second Law Analysis of Thermal Systems*, Proc. IVth Intl. Symp. on 2nd Law Analysis of Thermal Systems, M. J. Moran and E. Sciubba, eds., ASME, New York, pp. 39–42.

Tapia, C. F., and Moran, M. J., 1986, "Computer-Aided Design and Optimization of Heat Exchangers," *Computer-Aided Engineering of Energy Systems Optimization*, ASME, Vol. AES 2-1, pp. 93–104.

Tribus, M., and Evans, R., 1962, "Thermoeconomics," UCLA Report N. 62-63.

Tsatsaronis, G., and Winhold, M., 1985, "Exergoeconomic Analysis and Evaluation of Energy-Conversion Plants—1. A New General Methodology," *Energy*, Vol. 10, pp. 69–80.

Witte, L. C., and Shamsundar, N., 1983, "A Thermodynamic Efficiency Concept for Heat Exchange Devices," ASME *Journal of Engineering for Power*, Vol. 105, pp. 199–203.

# APPENDIX

## Elastic Exergy of a Material Due to Deformation

The material in this appendix shows the evaluation of elastic exergy of a material due to deformation, which is one component of the overall exergy of the heat exchanger material. The case of heat exchanger tubes is considered.

Assume that the material used to manufacture the heat exchanger tubes is initially in the form of a flat plate with no elastic exergy stored. The plate has a thickness $t$, length $l$, and width $p$. The plate material is assumed to have a simplified stress–strain diagram as indicated in Fig. A1. A tube manufac-

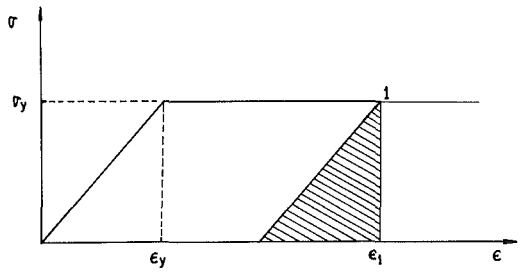


Fig. A1 Simplified stress-strain diagram for the material in the sample calculation

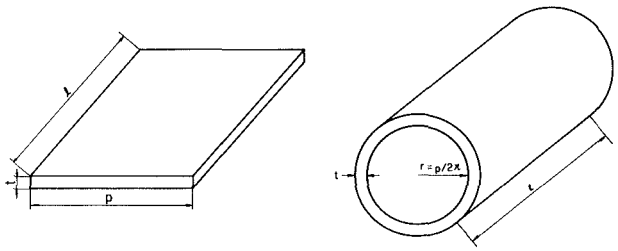


Fig. A2 Initial and final shape of the material, (a) before deformation, and (b) after deformation

tured from this plate has a form as shown in Fig. A2. The elastic theory predicts the following functional form for the stress distribution in the tube:

$$\sigma = E\,\epsilon = \frac{E\,y}{r} \tag{A1}$$

where $y$ is the radial coordinate measured from the center of the tube. The stress at the tube wall ($y = t/2$) from equation (A1) is:

$$\sigma_\omega = \frac{E\,t}{2\,r} \tag{A2}$$

This value is much larger than the yield stress for practical applications in most materials. The high value of the stress causes the pipe region near the wall to deform plastically, while the material behaves elastically in a small region near the center. The stress distribution in the tube wall is indicated in

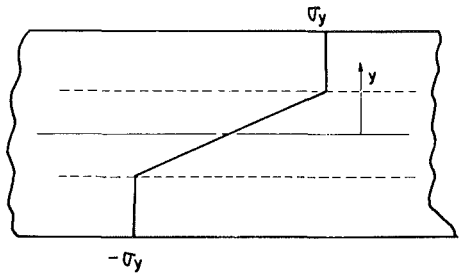


Fig. A3 Stress distribution along the pipe wall

Fig. A3. The stress varies linearly with $y$ in the elastic region and has a constant value $\sigma_y$ in the plastic region, according to the assumed $\sigma$–$\epsilon$ behavior of the material. In most practical cases the wall is thick enough so that the elastic zone is small relative to the total volume. Under this assumption, the total exergy in the material is

$$\mathcal{E}_{m,ph} = \int_v \frac{1}{2}\,\sigma\,\epsilon\,dv$$

$$= \frac{1}{2}\,\sigma_y\,\frac{\sigma_y}{E}\,V = \frac{plt\,\sigma_y^2}{2\,E} \tag{A3}$$

and the elastic exergy of the material per unit area is

$$\frac{\mathcal{E}_{m,ph}}{A} = \frac{t\,\sigma_y^2}{2\,E} \tag{A4}$$

The work necessary to produce the deformation in the material is greater than the value of the elastic exergy (equation (A4)). This is because part of the work has to be spent in deforming the material plastically, and this part of the work is not recoverable. Figure 1 shows a comparison between the exergy and work input. Point 1 corresponds to a point near the wall, in the plastic zone. The work investment in deforming this element of material corresponds to the area under the curve from $\epsilon = 0$ to $\epsilon = \epsilon_1$. Since the exergy spent in deforming the material plastically is not recoverable, the only contribution to the exergy is the elastic part of the work, which corresponds to the shaded area. The exergy can then be only a small fraction of the work input, with a major part of the work being dissipated.

# An Inverse Convection Problem

**A. Moutsoglou**
Mechanical Engineering Department,
South Dakota State University,
Brookings, SD 57007

*The nature of inverse problems in convective environments is investigated. The ill-posed quality inherent in inverse problems is verified for free convection laminar flow in a vertical channel. A sequential function specification algorithm is adapted for the semiparabolic system of equations that governs the flow and heat transfer in the channel. The procedure works very well in alleviating the ill-posed symptoms of inverse problems. The performance of a simple smoothing routine is also tested for the prescribed conditions.*

## Introduction

The inverse heat conduction problem is formally defined as the estimation of the surface heat flux history from measured temperature histories inside a heat-conducting body. The inverse heat conduction problem has received much attention in the past two decades. The recent book by Beck et al. (1985) gives an excellent comprehensive review of the literature, and summarizes the various approaches and significant contributions made in the study of inverse conduction heat transfer problems.

Despite the relatively large interest expressed in inverse conduction problems, inverse convection problems have not attracted much attention. Inverse problems for steady, two-dimensional boundary layer flows were discussed by Keller and Cebeci (1972), Cebeci et al. (1975), and Cebeci (1976). For instance, the inverse problem studied by Cebeci (1976) was concerned with the determination of the spatial free-stream velocity variation for a prescribed local skin-friction coefficient or a prescribed displacement thickness in compressible boundary layer flows. In all of these studies however, the ill-posed nature of the problem was not fully disclosed as the calculated local skin-friction coefficients and displacement thicknesses from the solution of the direct problem were utilized as an input to the inverse problem for the test cases considered. According to Cebeci (1976) "such a procedure is necessary because a slight error in the experimental skin-friction coefficient will severely affect the computed velocity distribution." Of course the very procedure adopted reduces the solution of the pseudo-inverse problem to a simple modification of the algorithm used for the direct problem, but fails to address the intricate nature of the truly inverse problems. Radwan and Lekoudis (1984), in an inverse mode calculation for incompressible flow over infinite swept wings, experienced oscillations in the calculated skin-friction coefficients. They were able to suppress them by employing a weighted upwind modification in their finite difference scheme.

In view of the fact that no study seems to exist addressing the intriguing nature of inverse problems in convective heat transfer, such an investigation is presented herein. The present work is a study of a computational scheme that might become an essential part of an experimental procedure for determining surface temperature and heat flux variations in convective environments. The methodology has applications in various external and internal convective flows as well as flows in enclosures.

In illustrating the methodology, this study is concerned with the task of having to estimate the arbitrary steady-state wall temperature and surface heat flux variation on the left plate of a channel, with fluid flowing as shown in Fig. 1, without having access to the left plate itself. If estimates for the right plate ($y=H$) surface temperature $T_R(x)$ and heat flux variations $q_R(x)$ exist, and furthermore the inlet ($x=0$) velocity and temperature profiles $u_i(y)$ and $T_i(y)$ are known or can be measured, then one can predict the unknown surface temperature $T_L(x)$ and heat flux variation $q_L(x)$ of the left plate ($y=0$) from the consideration of the inverse convection problem. In determining the surface temperature and heat flux variation of the right plate, which is accessible to instrumentation, one can either attempt to measure the quantities directly (for instance using thermocouples and appropriately designed heat flux gages), or attempt to estimate them from internal temperature measurements by solving an improperly posed Cauchy problem. In either case, the inherent fluctuations of the measured or predicted data for the right plate may result, unless special care is taken, in unacceptable and/or unstable predictions for the left plate wall temperature and heat flux distributions. All of the characteristics that make the inverse conduction problem so challenging are inherent in the inverse convection problem for the simple channel flow problem discussed above. This can be attested by the fact that one can recognize that the governing steady-state energy equation for the limiting hydrodynamically fully developed flow in a two-dimensional channel is analogous to the one-dimensional transient diffusion equation in a finite slab with spatially dependent thermal diffusivity.

In this study, a sequential function specification method appropriate for parabolic and semi-parabolic flows is utilized for the inverse problem considered. A whole domain regularization technique best suited for elliptic flows, on the other hand, is adapted for an inverse elliptic internal flow problem in a follow-up paper (Moutsoglou, 1988).

## I Direct Heat Transfer Problem

**Analysis.** In order to provide a means for evaluating the performance of the inverse methodology considered, a computational algorithm that provides solution to the direct heat transfer problem is first devised. The direct heat transfer problem is defined as one where thermal boundary conditions are prescribed for both the left and right walls of the channel. For the test case considered a triangular heat flux is prescribed at the left wall ($y=0$), while the right wall ($y=H$) is insulated.

To parabolize the system of equations that governs free convection flow in a channel, it was necessary first to neglect the axial diffusion of momentum and heat, and second to decouple the longitudinal and lateral pressure gradients. The latter is achieved by representing the local pressure $p(x, y)$ as the sum of a cross-sectional mean pressure $\bar{p}(x)$, which drives the main flow, and a perturbation about the mean $\hat{p}(x, y)$, which drives the cross-stream flow. The decoupling further requires that $d\bar{p}/dx \gg \partial\hat{p}/\partial x$.

To nondimensionalize the governing system of equations, the following dimensionless parameters are defined:

$$X=\frac{x}{H\mathrm{Gr}_H},\quad Y=\frac{y}{H},\quad U=\frac{uH}{\nu\,\mathrm{Gr}_H},\quad V=\frac{vH}{\nu}$$
$$\theta=k\frac{T-T_\infty}{q_{\mathrm{ref}}H},\quad \bar{P}=\frac{\bar{p}-p_\infty}{\rho\nu^2}\frac{H^2}{\mathrm{Gr}_H^2},\quad \hat{P}=\frac{\hat{p}}{\rho\nu^2}H^2 \tag{1}$$

Contributed by the Heat Transfer Division for publication in the JOURNAL OF HEAT TRANSFER. Manuscript received by the Heat Transfer Division March 18, 1987. Keywords: Conduction, Conjugate Heat Transfer.

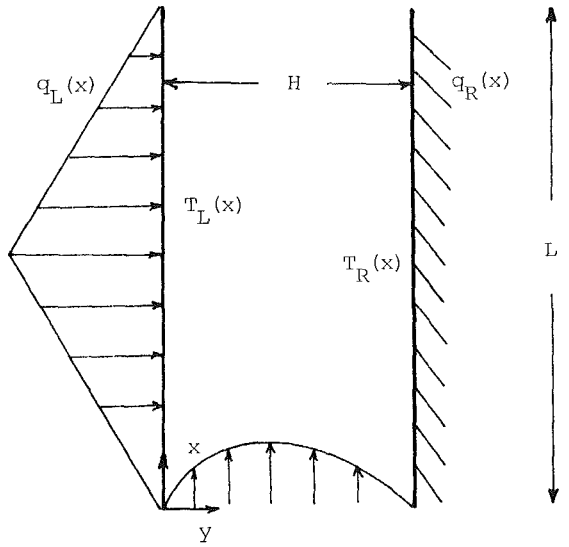


**Fig. 1 Flow schematic and coordinate system**

where $T_\infty$ and $p_\infty$ are the surrounding ambient temperature and pressure, $H$ is the channel width, and $\mathrm{Gr}_H$ is a modified Grashof number based on some reference heat flux, $q_{\mathrm{ref}}$.

$$\mathrm{Gr}_H = \frac{g\beta\, q_{\mathrm{ref}}\, H^4}{\nu^2\, k} \tag{2}$$

Noting that $dp_\infty/dx = -\rho_\infty g$, the Boussinesq approximation is invoked to approximate the buoyancy term as $g(\rho_\infty - \rho) = \rho g\beta(T - T_\infty)$. The dimensionless form of the governing system of equations for steady, two-dimensional laminar free convection flow in a vertical channel can thus be expressed as

$$\frac{\partial U}{\partial X} + \frac{\partial V}{\partial Y} = 0 \tag{3a}$$

$$U\frac{\partial U}{\partial X} + V\frac{\partial U}{\partial Y} = -\frac{d\bar{P}}{dX} + \frac{\partial^2 U}{\partial Y^2} + \theta \tag{3b}$$

$$U\frac{\partial V}{\partial X} + V\frac{\partial V}{\partial Y} = -\frac{\partial \hat{P}}{\partial Y} + \frac{\partial^2 V}{\partial Y^2} \tag{3c}$$

$$U\frac{\partial \theta}{\partial X} + V\frac{\partial \theta}{\partial Y} = \frac{1}{\mathrm{Pr}}\frac{\partial^2 \theta}{\partial Y^2} \tag{3d}$$

The corresponding boundary conditions are written as

$$U = U_i,\ V = 0,\ \bar{P} = 0,\ \theta = 0 \text{ at } X = 0 \tag{4a}$$

$$U = 0,\ V = 0 \text{ at } Y = 0 \text{ and } 1 \tag{4b}$$

$$\frac{\partial \theta}{\partial Y} = -\frac{q_L(X)}{q_{\mathrm{ref}}} \text{ at } Y = 0;\ \frac{\partial \theta}{\partial Y} = 0 \text{ at } Y = 1 \tag{4c}$$

$$\bar{P} = 0 \text{ at } X = X_L \tag{4d}$$

**Computational Procedure.** The semiparabolic nature of the equations stems from the form of the boundary conditions, namely that the velocity profile $U_i$ at the inlet ($X = 0$) is unknown, while the pressure imbalance $\bar{P}$ has to vanish also at the exit of the channel, $x = L$ or $X = X_L$. Thus, even though downstream events cannot influence upstream conditions, a marching procedure may only be used iteratively. To circumvent this difficulty, a constant value for $U_i = 0.15$ was fixed for all calculations performed for the test case. Thus, the length of the channel $X_L$ was determined as the length where the pressure imbalance $\bar{P}$ acquired the value of zero (equation (4*d*)), and the computations were terminated. This procedure alleviated any iterations required under standard conditions, where the length of the channel is known, and the initial velocity has to be found from iteration.

The nonlinear momentum and energy equations (3) and (4) were solved by a marching finite difference method. The computational scheme utilized the control volume suggested by Patankar and Spalding (1972), while adopting the finite difference procedure of Patankar (1980) that employs the power law scheme for treating the convection-diffusion terms. A Newton-Raphson iterative method suggested by Raithby and Schneider (1979) was utilized in computing the axial mean pressure gradient from the requirement of overall mass conservation. The elliptic problem that arises at each cross-stream plane was solved by the SIMPLER algorithm of Patankar (1980). Thus the cross-stream velocities were computed by imposing the continuity constraint. The Tridiagonal Matrix Algorithm of Thomas was employed in solving the resultant system of algebraic equations.

**Results.** The direct heat transfer problem described by equations (3) and (4) was solved for a prescribed triangular heat flux, $q_L(X)/q_{\mathrm{ref}}$ (equation (4*c*)), on the left wall of the channel ($Y = 0$), for air with a Prandtl number of 0.7

$$\frac{q_L(X)}{q_{\mathrm{ref}}} = \begin{cases} X & \text{for } X \le 0.6 \\ 1.2 - X & \text{for } X \ge 0.6 \end{cases} \tag{5}$$

Forty-three grid points were deployed at every cross section,

## Nomenclature

$C$ = dimensionless standard deviation of the right wall temperature, equation (7)
$e$ = Gaussian random error
$\mathrm{Gr}_H$ = modified Grashof number $= g\,\beta\, q_{\mathrm{ref}}\, H^4/\nu^2 k$
$g$ = gravitational acceleration
$H$ = channel width
$k$ = thermal conductivity
$L$ = length of channel
$P$ = dimensionless pressure
$p$ = pressure
$\mathrm{Pr}$ = Prandtl number
$q$ = local heat flux
$S$ = least-squares sum, equation (9)
$T$ = temperature
$U, V$ = dimensionless axial and transverse velocity components
$u, v$ = axial and transverse velocity components
$X, Y$ = dimensionless axial and transverse coordinates
$x, y$ = axial and transverse coordinates
$Z$ = sensitivity coefficient, equation (11)
$\beta$ = coefficient of thermal expansion
$\Delta X$ = dimensionless axial step size
$\epsilon$ = additive error, equation (7)
$\theta$ = dimensionless temperature
$\nu$ = kinematic viscosity
$\rho$ = density
$\sigma$ = dimensionless standard deviation of the estimated heat flux, equation (17)

**Subscripts**

$c$ = computed
$d$ = direct
$L$ = left wall
$M$ = representative axial location
$m$ = measured
$R$ = right wall

**Superscripts**

$\bar{}$ = mean
$\hat{}$ = perturbation
$*$ = guessed

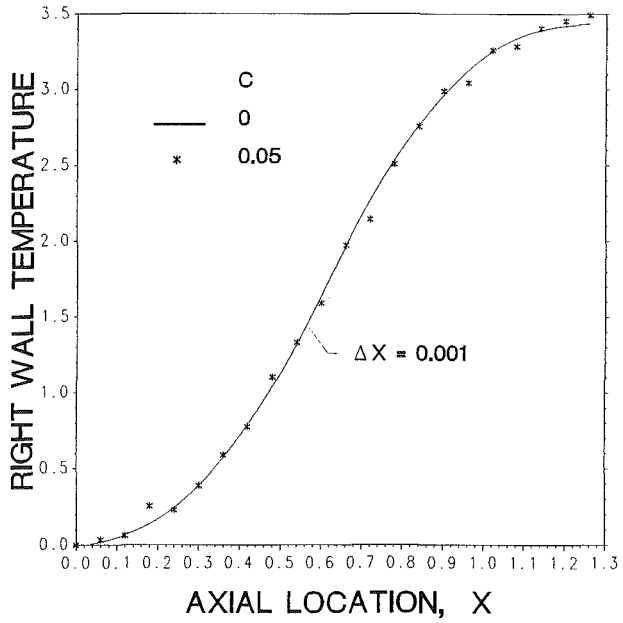


Fig. 2 "Exact" right wall temperature with and without superposed random errors

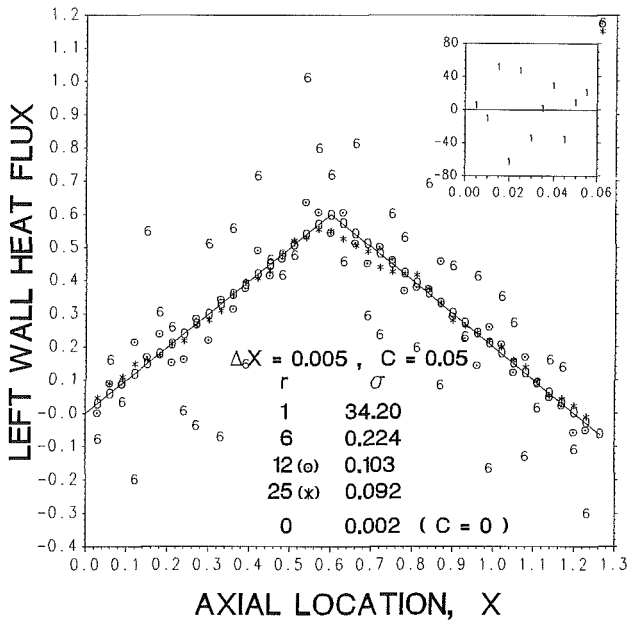


Fig. 3 Estimation of left wall heat flux from solution of the inverse problem, $\Delta X = 0.005$, $C = 0.05$

and results matched with those of 23 cross-stream grid points to within $10^{-4}$. Results for the dimensionless temperature variation of the right insulated wall $\theta_{Rd}(X)$ are plotted in Fig. 2 for the grid independent results ("exact" solution), a priori, obtained with $\Delta X = 0.001$. The subscript $d$ in $\theta_{Rd}$ denotes the solution of the direct heat transfer problem.

## II Inverse Heat Transfer Problem

The inverse convection problem is defined as one where the temperature variation $T_R(x)$ of the insulated *right* wall is now provided as an additional input, but no information regarding the heat flux or temperature variation of the left wall is given. Estimates for those quantities, namely $q_L(x)$ and $T_L(x)$, are actually the desired output of the inverse methodology. Thus, the thermal boundary conditions, equation (4*c*), appropriate for the direct problem are now replaced by

$$\theta = \theta_R(X) \text{ at } Y = 1; \quad \frac{\partial \theta}{\partial Y} = 0 \text{ at } Y = 1 \qquad (4c')$$

where $\theta_R(X)$ is the prescribed temperature variation of the right wall.

Contrary to the direct problem where a thermal boundary condition is prescribed for each surface (boundary value problem), the inverse problem involves the prescription of both boundary conditions on one surface (initial value problem). Thus, a slight modification of the solution algorithm utilized for the direct problem should alleviate this inconvenience. This was achieved by two separate procedures: (*i*) A noniterative procedure that solves for the temperature of element $j$, $\theta_j$, from the tridiagonal form of the discretized energy balance for element $j+1$, starting from the outmost right element where both temperature and right heat flux are known; and (*ii*) an iterative Newton–Raphson scheme.

Since for inverse problems the longitudinal steps will depend on the position where the sensors are located, several arbitrary constant streamwise step sizes were chosen in the inversion schemes. With the right wall temperature variation obtained from the solution of the direct problem, $\theta_{Rd}(X)$, the straightforward inversion was tested using various stepsizes. With the same step size used for the direct problem, $\Delta X = 0.001$, the two procedures mentioned in the paragraph above produced the same triangular heat flux of the left wall, assigned by equation (5), to an accuracy of $10^{-5}$. As larger step sizes were implemented in the inversion scheme, the numerical bias introduced by the larger step sizes resulted in a relative shift of the predicted left wall heat flux. Such results are illustrated with the symbol 0 in Figs. 3, 4, and 5, which are for inversion stepsizes of $\Delta X = 0.005$, 0.03, and 0.12, respectively. As can be observed from the figures, the stepsize bias does not incur any ill-posed effects on the solution. The predicted left wall heat flux does not possess any oscillations, is triangular in shape, and is shifted rightward by an amount of about half of the difference between the corresponding and "exact" axial stepsizes, $(\Delta X - 0.001)/2$. This apparent success of the straightforward inversion algorithm is superficial. In a realistic case the right wall temperature variation is not prescribed from the solution of the direct problem but rather is obtained from local measurements or from a computational procedure that might involve a direct or inverse heat conduction problem on the right wall itself. Either way, the axial variation of the right wall temperature $\theta_{Rm}(X)$, where the subscript $m$ denotes measured profile, will be slightly different than that of $\theta_{Rd}(X)$. To account for this unavoidable discrepancy, the measured right wall temperature $\theta_{Rm}(X)$ is simulated by superposing small random errors inherent in any measurement to the right wall temperature $\theta_{Rd}(X)$ obtained from the solution of the direct problem

$$\theta_{Rm}(X_i) = \theta_{Rd}(X_i) + \epsilon_i \qquad (6)$$

The additive errors $\epsilon_i$ are written as

$$\epsilon_i = Ce_i \qquad (7)$$

where $e_i$ are the Gaussian random errors of zero mean and standard deviation of unity, and the constant $C$ is chosen to make the standard deviation of $\epsilon_i$ equal to the desired value. It is noted that additive errors, which have a constant variance with $i$, better simulate errors associated with measuring sensors, as the same magnitude of error occurs for low as well as high temperatures.

Additive errors inherent in measuring devices were employed in the test cases considered. To illustrate the magnitude of the random noise, the measured right wall temperature profile $\theta_{Rm}(X)$, according to equation (6) with standard deviation of $C = 0.05$, is depicted with the symbol * in Fig. 2.

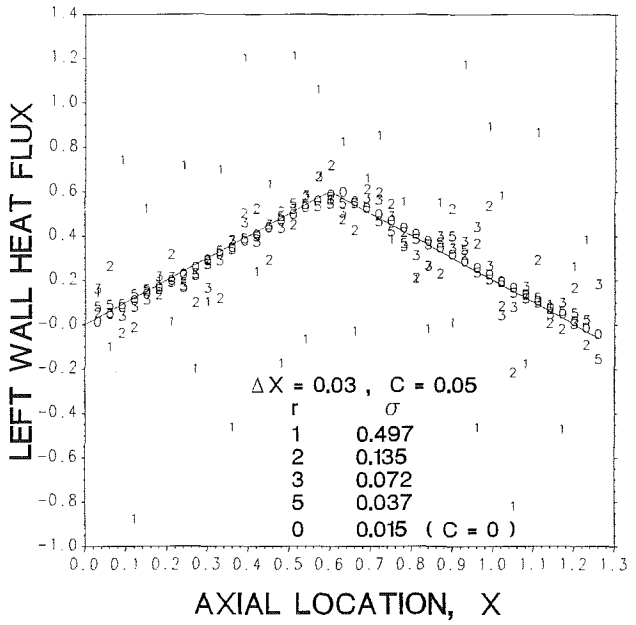


Fig. 4 Estimation of left wall heat flux from solution of the inverse problem, $\Delta X = 0.03$, $C = 0.05$

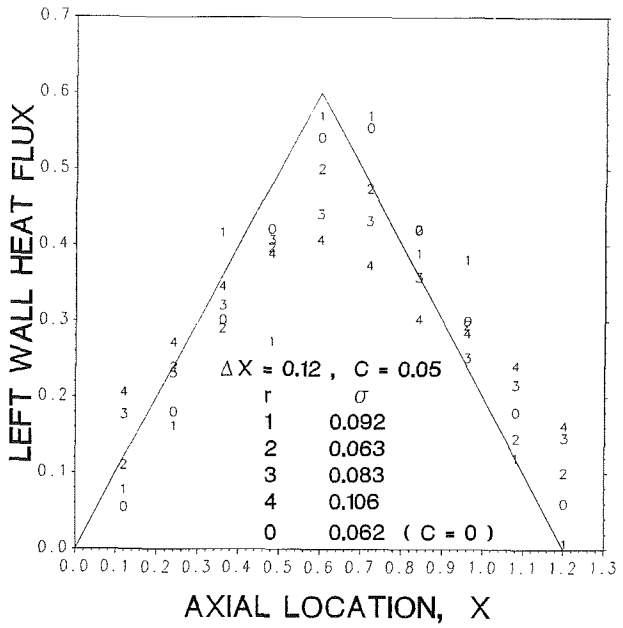


Fig. 5 Estimation of left wall heat flux from solution of the inverse problem, $\Delta X = 0.12$, $C = 0.05$

The straightforward inversion algorithm was first tested with Gaussian random errors with standard deviation of $C = 0.05$ superposed, as implied from equations (6) and (7), on the right wall temperature obtained from the direct solution $\theta_{Rd}(X_i)$. Results for the axial variation of the dimensionless heat flux of the left wall $q_L(X)/q_{\text{ref}}$, for three streamwise step sizes of $\Delta X = 0.005$, 0.03, and 0.12, are illustrated in Figs. 3, 4, and 5, respectively. In the figures, the solid line represents the exact triangular heat flux prescribed by equation (5). Results for the noisy data with standard deviation 0.05, obtained with the straightforward inversion algorithm, are indicated with the symbol 1 in the three figures. No convergence was attainable for axial locations beyond 0.06 for the step size of $\Delta X = 0.005$. The predicted heat flux data in all three figures possess the characteristics of ill-posed problems, highly oscillatory results that tend to become unstable as the axial stepsize decreases. The amplitude of oscillations decreases as the stepsize increases. However, the obvious disadvantage of large step sizes is their inability to yield pertinent information with regards to abruptly changing left wall heat flux.

To correct the ill-posed nature of inverse problems with poisoned data, the sequential function specification technique devised by Beck (1970) for inverse conduction problems is adapted for the present convection problem. The method most appropriate for parabolic (or semiparabolic) systems of equations is described in considerable detail in Beck et al. (1985), and only the highlights of the procedure are discussed herein. Accordingly, in order to add stability in estimating the dimensionless heat flux of the left wall $q_{L,M}$ at axial location $X_M$, use is made of the solution in $r-1$ downstream axial locations. A value $q^*_{L,M}$ is initially guessed for the left wall heat flux $q_{L,M}$. The same guessed value is temporarily assigned for the left wall heat fluxes in the $r-1$ downstream axial locations $X_{M+1}$, $X_{M+2}, \ldots, X_{M+r-1}$

$$q_{L,M} = q_{L,M+1} = q_{L,M+2} = \ldots = q_{L,M+r-1} = q^*_{L,M} \tag{8}$$

With the left wall heat flux guessed from equation (8), and the right wall insulated, the direct problem is solved to obtain estimates for the right wall temperatures $\theta^*_{Rc}$ at axial locations, $X_M, X_{M+1}, \ldots, X_{M+r-1}$, without the use of the measured right wall temperatures $\theta_{Rm}$. A least-squares sum is then formed between the computed and measured right wall temperatures

$$S = \sum_{i=1}^{r} (\theta_{Rm_{M+i-1}} - \theta_{Rc_{M+i-1}})^2 \tag{9}$$

The sum is then minimized with respect to the sought flux component $q_{L,M}$

$$\frac{\partial S}{\partial q_{L,M}} = 0 = \sum_{i=1}^{r} (\theta_{Rm_{M+i-1}} - \theta_{Rc_{M+i-1}}) Z_{R_{M+i-1}} \tag{10}$$

where $Z_{R_{M+i-1}}$ are the sensitivity coefficients defined by

$$Z_{R_{M+i-1}} \equiv \frac{\partial \theta_{Rc_{M+i-1}}}{\partial q_{L,M}} \quad \text{for } i = 1, \ldots, r \tag{11}$$

Next, the computed temperature at the right wall is expanded in a Taylor series about the guessed value of the left wall heat flux $q^*_{L,M}$ as

$$\theta_{Rc_{M+i-1}} = \theta^*_{Rc_{M+i-1}} + Z_{R_{M+i-1}} \Delta q_{L,M} \quad \text{for } i = 1, \ldots, r \tag{12}$$

Combining equations (10) and (12), one can solve for $\Delta q_{L,M}$ from

$$\Delta q_{L,M} = \frac{\sum_{i=1}^{r} (\theta_{Rm_{M+i-1}} - \theta^*_{Rc_{M+i-1}}) Z_{R_{M+i-1}}}{\sum_{i=1}^{r} Z^2_{R_{M+i-1}}} \tag{13}$$

where $\theta^*_{RC}$ are the computed right wall temperatures based on the guessed left wall heat flux $q^*_{L,M}$. Thus, once the sensitivity coefficients $Z_R$ are computed, a better guess for the left wall heat flux at the axial location $X_M$ is obtained from

$$q_{L,M} = q^*_{L,M} + \Delta q_{L,M} \tag{14}$$

This new estimate is then again assigned to the $r-1$ downstream axial locations as indicated by equation (8), and the procedure is reiterated until the magnitude of $q_{L,M}$ is smaller than a set convergence criterion, $5 \times 10^{-5}$. The value of $q_{L,M}$ is then retained only for the axial location $X_M$, and the procedure is repeated for the next axial location $X_{M+1}$ as the solution is marched downstream.

The computational scheme described above requires the estimation of the sensitivity coefficients defined from equation (11). Even though the sensitivity coefficients may be evaluated from differences of the temperatures formed from

two values of the left wall heat flux $q^*_{L,M}$ that differ by a small value, it is computationally more efficient to evaluate them directly from their own differential equation. This is achieved by differentiating the energy equation and associated boundary conditions, equations (3*d*), (4*a*), and (4*c*), with respect to the unknown dimensionless left wall heat flux $q_L$. With $Z_{M+i-1} = \partial\theta_{M+i-1}/\partial q_{L,M}$, one obtains at each axial location $X_M$, for $i = 1, \ldots, r$

$$U_{M+i-1}\frac{\partial Z_{M+i-1}}{\partial X} + V_{M+i-1}\frac{\partial Z_{M+i-1}}{\partial Y} = \frac{1}{\mathrm{Pr}}\frac{\partial^2 Z_{M+i-1}}{\partial Y^2} \tag{15}$$

$$Z_M = 0 \text{ at } X = X_{M-1}; \quad \frac{\partial Z_{M+i-1}}{\partial Y} = -1 \text{ at } Y = 0;$$

$$\frac{\partial Z_{M+i-1}}{\partial Y} = 0 \text{ at } Y = 1 \tag{16}$$

It is noted here that in writing equation (15) the implicit dependence of the velocity field on temperature through the buoyancy force was not accounted for as $U$ and $V$ were considered independent of $q_L$. This is only an approximation made to simplify the iteration procedure, and bears no influence on the temperature and velocity profiles once the iteration procedure has converged. Equations (15) and (16) were solved by the same finite difference algorithm described earlier in the computational procedure section, once the velocity profile was determined. The computed values of the sensitivity coefficients at the right wall ($Y = 1$), where the sensors are located, then provide the required values $Z_{R_{M+i-1}}$ in equation (13).

In the corrective iterative scheme just described, if $r = 1$, no downstream axial points are involved in the determination of the left wall heat flux $q_{L,M}$ at $X_M$. Subsequently, the procedure reduces to the straightforward inversion of the direct problem that utilizes a Newton–Raphson scheme as described earlier. Thus with no downstream points ($r = 1$) to add stability to the inversion process, the scheme reproduced the highly oscillatory results for the left wall heat flux, indicated by the symbol 1 in Figs. 3, 4, and 5, when the noisy data of standard deviation of $C = 0.05$ was prescribed for the right wall temperature (equations (6) and (7)). However, when one or more downstream axial locations are included in the iteration scheme, considerable improvement in general is achieved in predicting the left wall heat flux.

Inasmuch as the visual inspection of the figures is valuable in assessing the performance of the inverse methodology, a quantitative criterion can also be established by defining a dimensionless standard deviation of the estimated left wall heat flux $\sigma$ as

$$\sigma = \left[\frac{1}{n}\sum_{i=1}^{n}(q_{L_i} - q_{Lc_i})^2\right]^{1/2} \tag{17}$$

In the above equation, $q_L$ and $q_{Lc}$ are, respectively, the exact and computed values of the dimensionless left wall heat flux, and $n$ is the number of the streamwise axial locations used in the inversion scheme. The standard deviation of the estimated left wall heat flux $\sigma$, calculated from equation (17), is listed in each of the following figures for all cases considered.

In Figs. 3, 4, and 5 the symbol $r$ corresponds to the inclusion of $r-1$ downstream axial locations in the sequential function specification scheme. As evidenced by the magnitude of the standard deviation $\sigma$, as the step size increases fewer downstream points in the corrective procedure fare better overall. When $C = 0.05$, for a given axial stepsize $\Delta X$, in general it is found that roughly $0.12/\Delta X$ downstream points in the function specification scheme provide the smallest standard deviation between the predicted and exact left wall heat flux. Thus, 24 downstream axial locations ($r = 25$, symbol *) is the best overall choice when $\Delta X = 0.005$ (Fig. 3), while four ($r = 5$) and one ($r = 2$) downstream points provide, respectively, the best estimates for axial step sizes of $\Delta X = 0.03$ (Fig. 4) and $\Delta X = 0.12$ (Fig. 5).

The largest local deviations of the left wall heat flux estimates occur at the last axial location, as no downstream axial points are available to add stability to the inversion scheme. This is particularly conspicuous at low axial step sizes when the inversion is extremely sensitive to random errors. For instance, for $\Delta X = 0.005$ in Fig. 3, if one excludes the last point from estimating the standard deviation for $r = 25$ (symbol *), $\sigma$ is reduced by 44 percent to a value of 0.051, whereas the exclusion of the last two points diminishes the standard deviation to a value of 0.029, a 69 percent decrease from that of 0.092 indicated in the figure. At larger step sizes these effects are not pronounced.

The visual observations noted earlier with regards to the performance of the straight inversion scheme in Figs. 3, 4, and 5 are qualified by noting the corresponding standard deviations. When random errors are superposed on the exact right wall temperature, the standard deviation of the left wall heat flux, $\sigma$, predicted from the straight inversion scheme ($r = 1$), decreases by two orders as the step size increases from 0.005 to 0.12. When no random errors are superposed, $C = 0$, the straight inversion scheme (symbol 0 in the three figures) is well posed, and the standard deviation is indicative of the bias introduced by the use of larger than 0.001 axial step sizes. The magnitude of the standard deviation is thus approximately of the order $(\Delta X - 0.001)/2$. This confirms that the ill-posed behavior of the inverse problem is due to the randomness of the fluctuations superimposed on the right wall temperature rather than a shift (bias with no random errors) of the input data for the right wall temperature, caused by the use of different step sizes in the inversion scheme.

The effect of the magnitude of the standard deviation $C$ of the superposed random errors on the performance of the inversion scheme is illustrated in Table 1. Calculated standard deviations of the left wall heat flux $\sigma$ are depicted for three different random error standard deviations of $C = 0.025$, 0.05, and 0.1 for a fixed axial step size of $\Delta X = 0.06$. As expected the ill-posed behavior of the inverse problem subsides as the standard deviation $C$ shrinks. As manifested by the magnitude of the standard deviation of the estimated heat flux $\sigma$ in the table, in general fewer downstream axial points in the sequential function specification scheme seem to be needed as the standard deviation of the random errors $C$ decreases: three downstream points ($r = 4$) for standard deviation of $C = 0.1$, two ($r = 3$) for $C = 0.05$, and one ($r = 2$) for $C = 0.025$.

The standard deviations indicated for $C = 0$ in Table 1 denote the bias introduced due to the stepsize $\Delta X$. When the bias is subtracted from the corresponding standard deviation at any $C$, the resultant $\sigma$ is a measure of the deviation due to the random errors superposed alone. These resultant deviations are found to be almost directly proportional to the standard deviation $C$, verifying the quasi-linearity of the governing equations.

In predicting the sensitivity of the inversion scheme to the sensor interspace and consequently the number of sensors employed, a study of the sensitivity coefficients is of para-

**Table 1 Effect of random error standard deviation $C$ on $\sigma$, $\Delta X = 0.06$**

| | $\sigma$ | | | |
|---|---|---|---|---|
| $r$ | $C = 0$ | $C = 0.025$ | $C = 0.05$ | $C = 0.1$ |
| 1 | 0.031 | 0.098 | 0.185 | 0.363 |
| 2 | 0.032 | 0.046 | 0.067 | 0.113 |
| 3 | 0.039 | 0.051 | 0.066 | 0.095 |
| 4 | 0.051 | 0.061 | 0.071 | 0.093 |

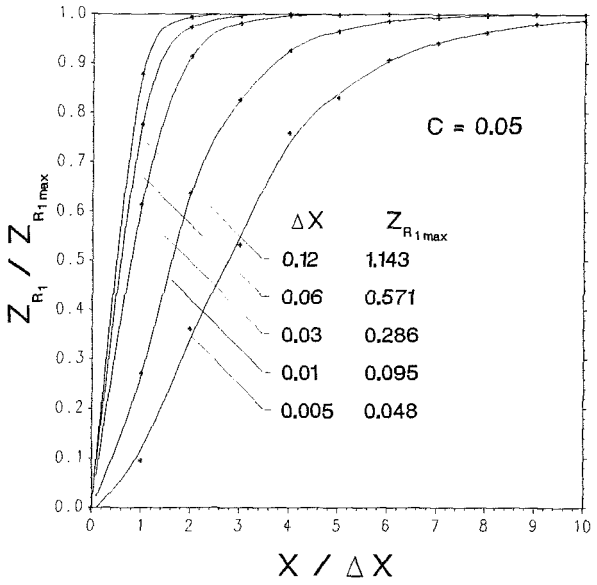


Fig. 6 Heat flux sensitivity coefficients of the right wall for the first sensor, $C = 0.05$

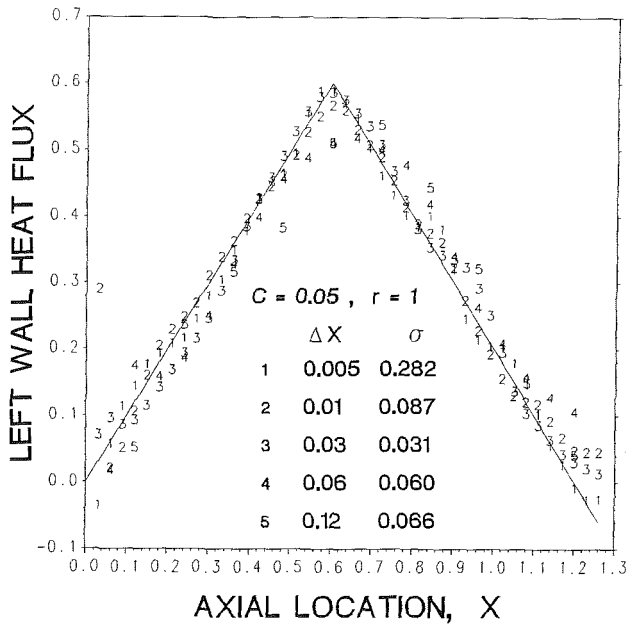


Fig. 7 Estimation of left wall heat flux from solution of the straight inversion scheme with initial smoothing of the noisy data, $C = 0.05$

mount importance (see Beck et al., 1985). For a given interspace $\Delta X$, the axial variation of the right wall sensitivity $Z_{R_j}$ for any sensor located at $X_j = j\Delta X$ can be determined from

$$U\frac{\partial Z_j}{\partial X} + V\frac{\partial Z_j}{\partial Y} = \frac{1}{\Pr}\frac{\partial^2 Z_j}{\partial Y^2} \tag{18}$$

$$Z_j = 0 \text{ for } X < X_j \tag{19}$$

$$\frac{\partial Z_j}{\partial Y} = \begin{cases} -1 \text{ for } X = X_j \\ 0 \text{ for } X \neq X_j \end{cases} \text{ at } Y = 0; \quad \frac{\partial Z_j}{\partial Y} = 0 \text{ at } Y = 1 \tag{20}$$

In writing equation (18), the implicit dependence of the velocities $U$ and $V$ on the heat flux $q_j$ at $X_j$ was neglected. This allows the predetermination of the sensitivity coefficients that provide valuable information in the design and estimation of the inverse problem.

The axial variation of the right wall sensitivity coefficient for the first sensor $Z_{R_1}$, located at $X_1 = \Delta X$, is plotted for several sensor intervals $\Delta X$ in Fig. 6. The velocities $U$ and $V$, needed for the solution of equations (18)-(20), are obtained from the straight inversion of equations (3)-(4) using the measured right wall temperature with random errors of standard deviation $C = 0.05$. Since the governing equations for the velocities are well posed, the effect of the erratic left wall heat flux oscillations due to straight inversion on the sensitivity coefficients is marginal. For instance, for $\Delta X = 0.005$, which represents the most severe case, the sensitivity coefficients shown in Fig. 6 differ by less than 6 percent from those obtained using the velocity profiles corresponding to $C = 0$. This verifies the assumption in deriving equation (18).

In Fig. 6, small sensitivity coefficients are associated with small $\Delta X$, which signify areas of difficulty with large susceptibility to measurement errors. The length ratio $X/\Delta X$ required for the sensitivity ratio $Z_{R_1}/Z_{R_{1,\max}}$ to approach unity is also an indication of the severity of the ill-posed quality of the inversion scheme, as is the magnitude of $Z_{R_1}/Z_{R_{1,\max}}$ when the ratio $X/\Delta X$ is unity. High length ratios for $Z_{R_1}/Z_{R_{1,\max}} \to 1$, and low sensitivity ratios when $X/\Delta X = 1$, suggest large sensitivities of the inversion solution to measurement errors. Both ratios may be used as criteria for predicting the required number of downstream axial locations, $r - 1$, to be utilized in the sequential function specification algorithm. The right wall sensitivity coefficients for $j = 2, \ldots n$, display similar behavior to those for $j = 1$ illustrated in Fig. 6, with the exception that they are displaced $\Delta X$ apart.

A more direct approach to handle the ill-posed nature of inverse problems may seem to be the initial smoothing of noisy data for the right wall temperature, and the direct inversion without any special treatment. To test the degree of success of such a straightforward procedure, the "exact" right wall temperature data obtained from the direct solution with an axial stepsize of $\Delta X = 0.001$ were first corrupted with random fluctuating errors of standard deviation of 0.05. Then, the noisy data for axial points corresponding to step sizes of $\Delta X = 0.005$, 0.01, 0.03, 0.06, and 0.12 were each smoothed using a cubic spline algorithm (IMSL subroutine DCSSCV) that required no special information with regards to the input data. The DCSSCV routine calculates a cubic spline curve, which smooths a given set of data points, using statistical considerations to determine the amount of smoothing required (Craven and Wahba, 1979). The smoothed data were then supplied to the straightforward inversion scheme as the right wall temperature data.

The predictions of the straightforward inversion algorithm ($r = 1$) for the left wall heat flux using each corresponding axial step size $\Delta X$ are illustrated in Fig. 7, where the solid line represents the exact prescribed variation of the heat flux. It is found that the performance of such a procedure, for the step sizes considered, is comparable to that of the sequential function specification algorithm. This can be attested by comparing the standard deviation of the results of the straight inversion in Fig. 7, to those of the sequential function specification algorithm in Figs. 3, 4, and 5. The largest local deviations of the left wall heat flux estimates occur at the initial axial locations. For instance, for $\Delta X = 0.005$, if one omits the first three axial points in estimating the standard deviation, $\sigma$ is reduced to a value of 0.068, a 75 percent decrease from 0.282, depicted in Fig. 7. At larger step sizes these effects subside.

The commendable performance of the smoothing procedure is only conditional and warrants further clarification. Smoothing routines by themselves in general have been found not to be reliable inversion schemes. For instance, when the same smoothing procedure was tested for the elliptic inverse convection problem considered by Moutsoglou (1988), it failed to alleviate the unsteady oscillations associated with

direct inversion schemes. The criterion of the performance of the smoothing procedure lies in the severity of the ill-posed quality of the problem under consideration. The severity of the inverse problem, in turn, is best depicted via the sensitivity coefficients. The sensitivity coefficients plotted in Fig. 6 do not display any lag for all stepsizes considered, in contrast to those shown for the inverse heat conduction problem for a plate insulated on one side (p. 31, Beck et al., 1985). Thus, even for $\Delta X = 0.005$ the magnitude of the sensitivity coefficient is large enough for the sensor at $X = 0.005$ to yield considerable information that enables the smoothing routine to perform satisfactorily. With the severity of the ill-posed quality intensifying as the axial stepsize decreases, it is expected that at smaller $\Delta X$ the magnitude of the sensitivity coefficients will not become appreciable until $X/\Delta X$ exceeds unity. With no or little information available with regards to the heat flux at $X_M$ from the sensor located at that point and possibly neighboring downstream sensors, the performance of the smoothing routine should deteriorate significantly. It is noted that the physical parameters affecting the magnitude of the step size are the length and width of the channel, as well as the reference heat flux and fluid properties.

The smoothing procedure employed can be easily incorporated into the sequential function specification scheme to improve the performance of the latter. Combinations of various inverse algorithms with smoothing filters have been investigated and found to perform superbly (Raynaud, 1986).

## Conclusions

The ill-posed nature of inverse problems in convective heat transfer environments is revealed for free convection laminar flow in a channel. It is demonstrated that the ill-posed behavior of the inverse problem stems primarily from the randomness of the fluctuations rather than a shift (a bias with no superposed errors) of the input data. A sequential function specification algorithm best suited for parabolic equations was successfully adopted in alleviating the ill-posed symptoms of the inverse problem. The apparent success of a smoothing procedure coupled with a straightforward inversion algorithm is directly related to the largeness of the step sizes utilized in this study.

## Acknowledgments

The valuable suggestions provided by Professor J. V. Beck during the review of the manuscript are gratefully acknowledged.

## References

Beck, J. V., 1970, "Nonlinear Estimation Applied to the Nonlinear Heat Conduction Problem," *International Journal of Heat and Mass Transfer*, Vol. 13, pp. 703–716.

Beck, J. V., Blackwell, B., and St. Clair, C. R., Jr.,1985, *Inverse Heat Conduction, Ill-Posed Problems*, Wiley-Interscience, New York.

Cebeci, T., Berkant, N., Silivri, I., and Keller, H. B., 1975, "Turbulent Boundary Layers With Assigned Wall Shear," *Computers and Fluids*, Vol. 3, pp. 37–49.

Cebeci, T., 1976, "An Inverse Boundary-Layer Method for Compressible Laminar and Turbulent Boundary Layers," *Journal of Aircraft*, Vol. 13, No. 9, pp. 709–717.

Craven, P., and Wahba, G., 1979, "Smoothing Noisy Data With Spline Functions," *Numerische Mathematik*, Vol. 31, pp. 377–403.

Keller, H. B., and Cebeci, T., 1972, "An Inverse Problem in Boundary-Layer Flows: Numerical Determination of Pressure Gradient for a Given Wall Shear," *Journal of Computational Physics*, Vol. 10, pp. 151–161.

Moutsoglou, A., 1988, "Solution to an Inverse Convection Problem Using the Whole Domain Regularization Technique," submitted to the *Journal of Thermophysics and Heat Transfer*.

Patankar, S. V., and Spalding, D. B., 1972, "A Calculation Procedure for Heat, Mass, and Momentum Transfer in Three-Dimensional Parabolic Flows," *International Journal of Heat and Mass Transfer*, Vol. 15, pp. 1787–1806.

Patankar, S. V., 1980, *Numerical Heat Transfer and Fluid Flow*, Hemisphere Publishing Corporation, Washington, D.C.

Radwan, S. F., and Lekoudis, S. G., 1984, "Boundary-Layer Calculations in the Inverse Mode for Incompressible Flows Over Infinite Swept Wings," *AIAA Journal*, Vol. 22, pp. 737–743.

Raithby, G. D., and Schneider, G. E., 1979, "Numerical Solution of Problems in Incompressible Fluid Flow: Treatment of the Velocity-Pressure Coupling," *Numerical Heat Transfer*, Vol. 2, pp. 417–440.

Raynaud, M., 1986, "Combination of Methods for the Inverse Heat Conduction Problem With Smoothing Filters," AIAA Paper No. 86-1243.

# Heat Transfer and Pressure Drop Characteristics of an Assembly of Partially Segmented Plates

**Y. N. Lee**[1]
Borg-Warner Research Center,
Des Plaines, IL 60018

*The heat transfer and pressure drop characteristics of an assembly of plates in a rectangular duct, with part of each plate segmented transversely and the segments inclined at 25 deg to the flow, have been investigated experimentally in the range of Reynolds numbers between 900 and 4000. The segmented-to-total width ratios $\beta$ were 0.81 and 0.61. Mass transfer measurements of naphthalene were made to obtain the heat transfer coefficient. A new spray technique is described for preparing the mass transfer models, which are so complex that previously reported techniques cannot be applied. The mass transfer models simulate louvered fin surfaces used currently in industries. The heat transfer coefficient is found to be a strong function of the segmented-to-total plate width ratio $\beta$, and it decreases as $\beta$ decreases. The heat transfer coefficient of an existing louver fin heat exchanger whose geometries are in close proximity to one of the model configurations was compared with that of the model, and good agreement was obtained between the two. The pressure drop (through the plate assembly) measurements showed that the pressure drop is mainly due to inertia loss in the experimental range of the present work, and that the streamwise, per-row pressure drop coefficient $K_p$ is a function of only $\beta$ and independent of the Reynolds number $N_{Re,Dh}$. It was found, for a fixed blower power, that there exists an optimum Reynolds number $(N_{Re,Dh})_{opt}$ for maximum Nusselt number at a given segmented-to-total width ratio $\beta$. A similar trend is also found for a fixed pressure drop.*

## Introduction

Flow interruption created in flow passages at periodic intervals is a popular means for heat transfer enhancement in compact heat exchangers. Slit fins used for various industrial compact heat exchangers and louvered fins for automotive radiators are examples. The slit fin provides a means of boundary layer control; namely, new velocity and thermal boundary layers develop over each fin segment created by the slit. Since the developing boundary layer flow is characterized by higher heat transfer coefficients than a fully developed flow, performance enhancement is obtained. The louvered fin attempts further enhancement by inclining the segments against the fluid flow to create turbulence and vorticity. Since, however, any thermal improvement is normally accompanied by a pressure drop penalty, an optimum balance between the two must be sought.

There are numerous publications in which the effectiveness of the aforementioned augmentation was investigated. In most cases, however, measurements were made of the average heat transfer coefficient through wind tunnel tests of actual heat exchangers (Kay and London, 1964; Shah, 1975; Wietig, 1975; Beauvais, 1962; Smith, 1972). Although useful, this approach does not provide detailed information on the fundamental processes occurring within the heat exchanger. In a previous paper (Lee, 1986), the heat transfer and pressure drop characteristics of an array of short plates aligned at angles to the flow in a rectangular duct were investigated, where the plates span the entire duct width. The objective of the work was to look into the role of the plate angle to the flow between 20 and 35 deg. It was found that an increase of the plate angle increased heat transfer with a pressure drop penalty as expected. However, the heat transfer coefficient of the experimental model was significantly higher than that of a comparable louvered fin heat exchanger.

One objective of the present paper is to investigate the role of the segmented-to-total plate width $\beta$ ($= W_s/W$) to resolve this discrepancy; the previous work amounts to the limiting case of $\beta = 1.0$. To this end, the heat transfer and pressure drop characteristics of an assembly of three plates in a straight rectangular duct ($W = 156.5$ mm $\times H = 62.5$ mm), which are partially segmented ($\beta = 0.81$ and 0.61) in the traverse direction to the flow, were investigated. Each plate has eight segments whose angle to the flow was 25 deg. As will be shown in the main body of the present paper, $\beta$ plays an important role, and good agreement was obtained between the heat transfer coefficient of the model and that of the comparable louvered fin heat exchanger discussed in a previous work (Lee, 1986).

The experimental technique for determining the heat transfer characteristics is the naphthalene sublimation technique used in prior investigations (Lee, 1986; Cur and Sparrow, 1978; Sparrow and Hajiloo, 1980), and mass transfer measurements of naphthalene were made to obtain the heat transfer coefficient. Due to the complexity of the model geometry in the present work, however, the previous method of preparing mass transfer models cannot be applied. Thus, a second objective of the present paper is to present a new spray coating technique to prepare the models. While the previously reported techniques are suitable for simple surface geometries such as flat plates (Cur and Sparrow, 1978; Sparrow and Hajiloo, 1980), and also for complex but continuous surface geometries such as canted-ribe plates (Lee, 1980), the present method can be applied to any complex surfaces regardless of whether it is continuous or not. As mentioned above, there are a total of three partially segmented plates used for the experiments (plate pitch $H_p = 20.83$ mm), among which the test plate is located in the middle between the two other "dummy plates." The dummy plates are there simply to satisfy the fluid dynamic boundary conditions. The test plate is made of metal

[1] *Present address:* Heat Transfer Research & Development, Ltd., 1010 West Lonnquist Boulevard, Mt. Prospect, IL 60056.

Contributed by the Heat Transfer Division and presented at the ASME Winter Annual Meeting, Anaheim, California, December 7-12, 1986. Manuscript received by the Heat Transfer Division December 22, 1986. Keywords: Forced Convection, Heat Exchangers.

substrate (aluminum, 0.406 mm thick), both sides of which are coated with a layer of naphthalene 0.115 mm thick; the overall thickness $t$ of the test plate (metal substrate and naphthalene coating) is 0.635 mm. On the other hand, the dummy plates are made of aluminum, 0.635 mm thick. The flow length of all segments is fixed at $L_p = 14.94$ mm; thus the thickness to flow length ratio is $t/L_p = 0.0425$, and the aspect ratio $\alpha(= W/(H_p - t))$ is fixed at 7.748. The hydraulic diameter is fixed at $Dh = 35.78$ mm; thus $L_p/Dh = 0.418$.

In addition to the heat transfer studies, pressure drop through the plate assembly was measured to determine the net and the overall pressure drop with the identical values of $t/L_p$ and $H_p/L_p$ to those of the heat transfer assembly but in a scaled-down duct (2.5:1).

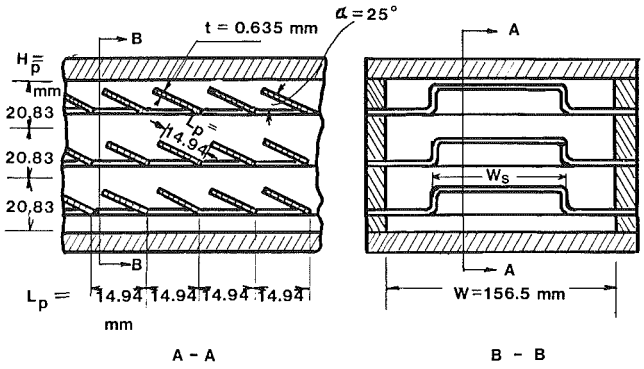


Fig. 1 Test section for mass transfer tests

## Experiments

**Test Section for Mass Transfer Tests.** The principal dimensions of the test section for mass transfer tests are shown in Fig. 1. As shown it consists of an assembly of three plates housed in a duct of 156.5 mm × 62.5 mm. The plates are partially segmented and the segments (eight in number in each plate) are canted at 25 deg to the flow. The two outer "dummy" plates are part of the upper and lower portions of the duct, and the test plate is sandwiched between the two portions of the duct. As indicated earlier, the thickness of the dummy plate is 0.635 mm while that of the metal substrate is 0.406 mm. The difference between the two thicknesses amounts to the additional thickness due to naphthalene coating. Details of the coating technique, as well as a technique of constructing the partially segmented plates, will be described later.

The test section equipped with the test plate coated with naphthalene is stored in a constant temperature room at 25°C until it reaches an equilibrium condition and is ready for tests.

**Test Section for Pressure Drop Tests.** The construction of the test section for pressure drop studies is identical to that for mass transfer tests, except that the dimensions are scaled down to 2.5:1 and all plates have identical thickness. The test section has an upstream duct and a downstream duct whose flow cross section is identical to that of the test duct with no plates.

**Partially Segmented Plate.** Construction of a partially segmented plate model from a continuous plate (length $L = 119.52$ mm) is difficult due to the fact that the material (aluminum sheet) is torn during the forming process. Even

## Nomenclature

$A_c$ = minimum cross-sectional flow area, $m^2$
$A_m$ = total active mass (heat) transfer area, $m^2$
$C_p$ = specific heat capacity at constant pressure, kJ/kg K
$Dh$ = hydraulic diameter of plate assembly $= 4A_c/(A_m/L)$, m
$D$ = diffusion coefficient, $m^2/h$
$e$ = roughness height, m
$f$ = coefficient of friction $= \Delta P_f/\{(0.5\rho V^2_{max})(L_p/D_h)N\}$
$H$ = duct height, m
$H_p$ = distance between plates, m
$h$ = heat transfer coefficient, $kW/m^2K$
$h_m$ = mass transfer coefficient, m/h
$k$ = thermal conductivity, kW/mK
$k_e$ = exit pressure loss coefficient $= \Delta P_e/(0.5\rho V^2_{max})$
$(Ke)_{max}$ = maximum $K_e$
$K_p$ = pressure coefficient/row $= \Delta P_p/(0.5\rho V^2_{max} K_p N)$
$L$ = total length of plate, m
$L_p$ = segment length in flow direction, m
$M$ = total mass sublimated during a time period, kg
$n$ = power to Prandtl number and Schmidt number
$N$ = number of segments per plate
$N_{Nu,Dh}$ = Nusselt number based on $D_h = hDh/k$
$(N_{Nu,Dh})_{00}$ = Nusselt number of continuous duct
Pr = Prandtl number of air $= C_p\mu/k$
$N_{Re,Dh}$ = Reynolds number $= V_{max}Dh/\nu$
$(N_{Re,Dh})_{opt}$ = optimum $N_{Re,Dh}$
Sc = Schmidt number $= \nu/D$
$N_{Sh,Dh}$ = Sherwood number $= h_mDh/D$
$P$ = pressure, mm Hg
$P_{Baro}$ = barometric pressure, mm Hg
$\Delta P_N$ = net pressure drop of plate assembly, $N/m^2$
$\Delta P_T$ = total pressure drop of assembly, $N/m^2$
$\Delta P_f$ = pressure drop due to friction, $N/m^2$
$\Delta P_p$ = pressure drop due to plate assembly, $N/m^2$
$\Delta P_e$ = entrance/exit losses, $N/m^2$
$t$ = plate thickness, m
$V_{max}$ = average flow velocity through $Ac$, m/h
$W$ = duct width, m
$W_s$ = segmented width, m
$X$ = distance from #1 pressure tap, m
$\alpha$ = aspect ratio $(= W/(H_p - t))$ for plate assembly or continuous duct
$\beta$ = segmented-to-total plate width ratio $= W_s/W$
$\delta$ = thickness of laminar sublayer, m
$\epsilon$ = surface roughness $= e/Dh$
$\theta$ = angle of attack of segment with respect to flow, deg
$\rho$ = density of air, $kg/m^2$
$\Delta\rho_m$ = log mean density difference, $kg/m^3$
$\rho_{nw}$ = naphthalene vapor density at the plate surface, $kg/m^3$
$\mu$ = absolute viscosity of air, kg/hm
$\nu$ = kinematic viscosity of air, $m^2/h$
$\tau$ = time, s

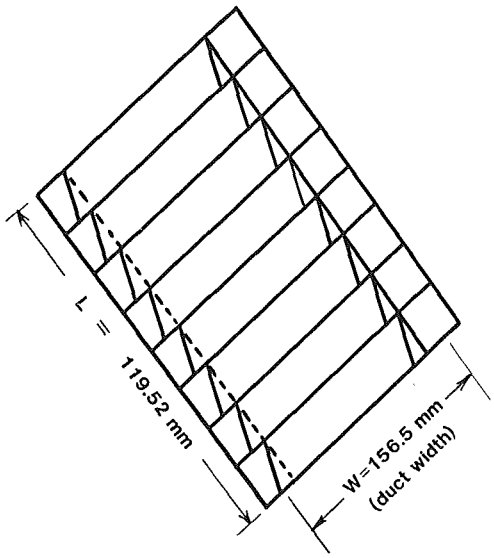


Fig. 2 Assembly of miniplates

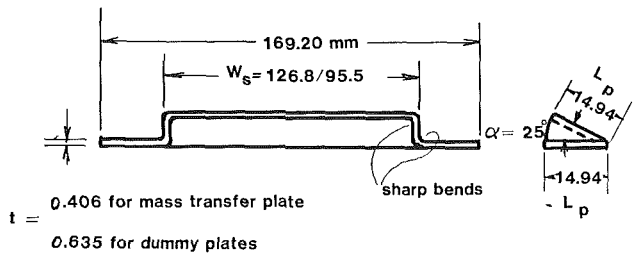


Fig. 3 Miniplates

when the material is not torn, preservation of the geometry so as to conform to the desired contour of the entire length of the plate presents problems since it requires expensive equipment. A simple method of preparing the test plate, which circumvents these difficulties, has been worked out using a multiple-miniplate concept. In this method we arrange consecutively eight identical miniplates (length $L_p = 14.94$ mm) such that an aggregate of the miniplates will simulate the desired plate contour. The configuration of the simulated test plate for mass transfer tests is shown in Fig. 2. The individual miniplates (Fig. 3) are made using specially prepared dies.

An identical method is used for preparing miniplates for pressure drop tests except that the dimensions shown in Figs. 2 and 3 are scaled down to 2.5:1.0 and the thickness of all plates is identical. Burrs created during the process of slitting are carefully removed from the miniplates.

**Preparation of Mass Transfer Model.** As indicated in the Introduction, prior techniques of preparing mass transfer models (Lee, 1986; Cur and Sparrow, 1978; Sparrow and Hajiloo, 1980), which require machining of naphthalene slabs or thickly coated surfaces to produce a flat surface, cannot be applied, since the heat transfer surfaces under consideration in the present work are highly complex so that no machining is applicable.

A new spray technique is used in the present work. A sketch of the spray technique apparatus is shown in Fig. 4. Compressed air is supplied from a high-pressure air source "1," and splits into primary and secondary circuits. The primary air flow is regulated with primary control valve "2," which controls air flow and pressure depression at air nozzle "4." The primary air is heated at primary heater "3." Molten naphthalene in reservoir "5" is discharged through liquid nozzle "6." The secondary air after being heated at secondary heater "7" is mixed with cool air around the primary jet stream, thus controlling the temperature of the mixture of hot primary air and relatively cool air being entrained.

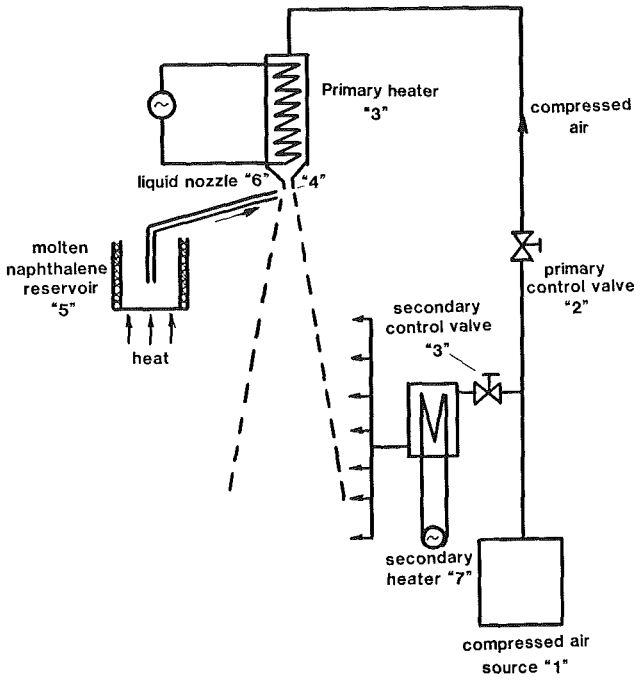


Fig. 4 Naphthalene spray system

The procedure of coating naphthalene on the miniplates is now discussed. A set of miniplates is arranged consecutively as shown in Fig. 2. Two end portions, which do not participate in the mass transfer, are covered with tape. When the miniplate set is placed under the active primary air jet, naphthalene liquid discharged from the liquid nozzle will change to droplets and solidfy upon impact on the miniplates, which are at a lower temperature than the temperature of liquid naphthalene. Similarly, naphthalene spray is applied on the other side of the miniplate set. The thickness of the coated layer is controlled to be 0.115 mm. A check of the overall thickness of the plates showed that the thickness is uniform within ± 5 percent. The surface roughness condition can also be controlled with the control of external conditions such as position of the liquid nozzle with respect to the primary jet nozzle, primary jet velocity, temperatures of air being entrained and the metal substrate, etc. Under appropriate conditions, the roughness height of the surface $e$ can be held within 0.050 mm.

**Experimental Apparatus and Procedure.** The main features of the test rig are given in detail by Lee (1986, 1980). In brief, a number of mass transfer models prepared as per the technique described in the preceding subsection are stored in a constant temperature chamber until they reach the equilibrium temperature (25°C). The experimental setup is contained in this chamber. The chamber itself is housed in a larger, well-insulated room. The room temperature is also controlled to maintain a temperature of 25 ± 1°C. Further details of the experimental setup and procedure are available from Lee (1986, 1980).

The primary quantity required for the evaluation of the mass transfer coefficient is the change of mass during a data run. This quantity is obtained from weighing the mass transfer model immediately before and after the run. The mass transfer measurements are made with a precision balance (Mettler H315). The resolution of the balance is $10^{-6}$ g. The

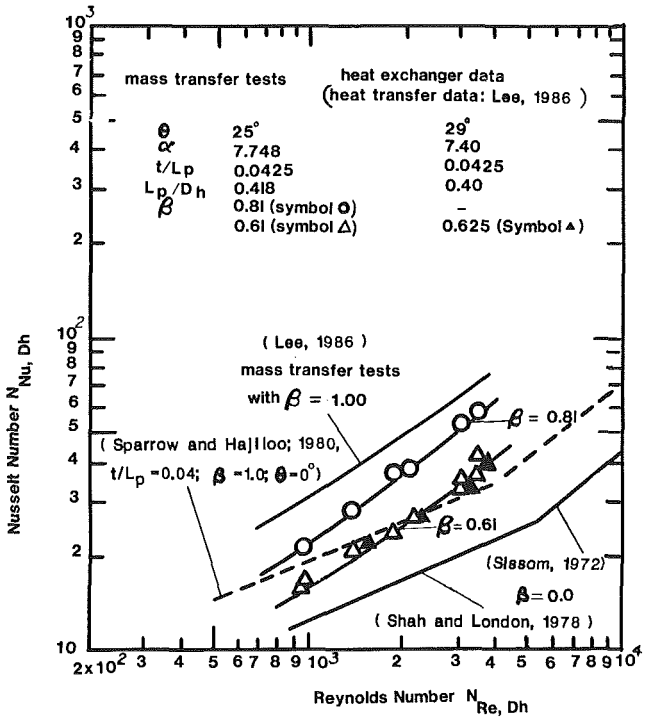


Fig. 5 Heat transfer results

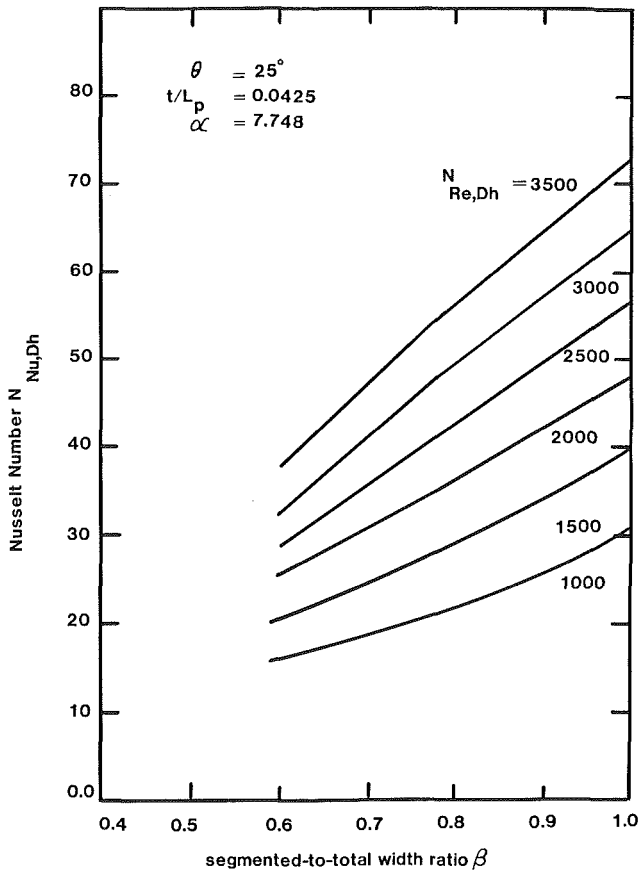


Fig. 6 Effect of $\beta$ on heat transfer

measured loss of mass is controlled to be approximately 0.150 g. Another quantity needed in the data reduction is the naphthalene vapor density at the mass transfer surface, which is determined from a vapor pressure-temperature relation (Sogin, 1958).

The run times are adjusted so that the mass loss is sufficient to the required accuracy of data; however the change in the thickness of the naphthalene coating during a data run is small (less than $1.4\times10^{-4}$ cm). Pressure drop measurements along the inlet duct (38.1 cm long) and the outlet duct (20.5 cm) are made via an MKS transducer having a resolution of 0.0001 mm Hg.

## Data Reduction of Heat Transfer Results

The mass transfer coefficient $h_m$ of the mass transfer model can be expressed as

$$h_m = M/(A_m \tau \Delta\rho_m) \tag{1}$$

where $M$ is the overall mass transfer obtained from weighing mass loss of a mass transfer model during a test run. $A_m$ is the mass transfer area, and $\rho_m$ is the log mean density difference (Lee, 1986). The log mean density can be determined with $M$ measured and naphthalene vapor density at the mass transfer surface as determined from the vapor pressure-temperature relation as noted earlier.

Once the mass transfer coefficient has been determined, it may be expressed in nondimensional form in terms of the Sherwood number $N_{Sh,Dh}$ defined as

$$N_{Sh,Dh} = h_m Dh/D \tag{2}$$

The experimental results expressed by the Sherwood numbers will be presented as a function of the Reynolds number defined by

$$N_{Re,Dh} = \rho V_{max} Dh/\mu \tag{3}$$

From the analogy of heat and mass transfer, the Nusselt number $N_{Nu,Dh}$ is

$$N_{Nu,Dh} = N_{Sh,Dh}(Pr/Sc)^n \tag{4}$$

Pr is the Prandtl number of the heat transfer fluid and $n$ is 0.4 or 1/3. If the ratio (Pr/Sc) is small as with air, the two Nusselt numbers obtained from using the two values of $n$ differ by about 8 percent. In the present work, $n$ is taken to be 0.4.

Since, however, the mass transfer surface area in the present model test section is much less than the total surface area for the flow, questions arise as to whether the normal definition of the mass transfer coefficient $h_m$ based on the log mean density above is valid. In order to examine this, the mass transfer coefficient was calculated based on three density differences separately: the log mean, the average, and the inlet. The coefficients obtained using the three methods were, however, identical in the present range of experiments. Therefore, the heat transfer coefficient derived from the mass transfer coefficient obtained in the present work is considered to be identical to the heat transfer coefficient based on the log mean temperature. Also, in the previous paper (Lee, 1986), a selected number of tests confirmed that the average heat transfer coefficient is identical even if all plates in the entire assembly participate in heat transfer.

## Heat Transfer Results

The heat transfer results obtained as per the preceding section are shown in Fig. 5 in terms of the Nusselt number $N_{Nu,Dh}$ and the Reynolds number $N_{Re,Dh}$ with segmented-to-total plate width ratios $\beta=0.61$ and 0.81. Superimposed are also the results with $\beta=1.0$ reproduced from the previous work (Lee, 1986). To compare with the limiting case of $\beta=0$, the Nusselt number of a developing flow in a rectangular duct ($\alpha=7.748$, $L/Dh=3.344$) formed with two adjacent plates, which are assumed to be continuous without segments (Shah and London, 1978; Mercer et al., 1967), are also included. From Fig. 5, it is seen that the Nusselt number $N_{Nu,Dh}$ is a strong function of $\beta$, and that the former increases with an increase in the lat-

ter. For instance, the Nusselt number $N_{Nu,Dh}$ at $N_{Re,Dh}=2000$ increases over the unsegmented duct by factors of 2.18, 3.22, and 4.17, with $\beta=0.61$, 0.81, and 1.0, respectively. To see the effect of $\beta$ on $N_{Nu,Dh}$ more clearly, the results of Fig. 5 are transposed to Fig. 6 in terms of $N_{Nu,Dh}$ and $\beta$ with $N_{Re,Dh}$ as the parameter. It is seen that heat transfer enhancement due to an increase in $\beta$ is more pronounced at high $N_{Re,Dh}$.

At this juncture, it may be appropriate to review the work of other investigators on a case of $\beta=1.0$ and $\theta=0$ deg (Sparrow and Hajiloo, 1980). Their results with $t/L_p=0.04$ are superimposed in Fig. 5. It is seen that inclining the segments of $\beta=1.0$ at $\theta=25$ deg to the flow not only improves the Nusselt number $N_{Nu,Dh}$ significantly but also makes the slope of the Nusselt number increase over that with $\theta=0$ deg.

The surface condition of the naphthalene-coated surface is not perfectly smooth as discussed earlier. Therefore it may be appropriate at this juncture to examine the effect of the surface roughness $e$ of the coated surface on the heat transfer results. While in the laminar flow region there is practically no effect, the effect in the turbulent region is worth examination. An estimation of the laminar sublayer thickness at $N_{Re,Dh}=4000$, however, shows that the sublayer thickness $\delta$ is significantly higher than the roughness height of the surface $e$. Therefore, the heat transfer results presented here require no corrections.

In order to take into account a possible error due to any extraneous mass transfer occurring during the installation of the test section in the test setup and its removal, the test section was installed and removed repeatedly at different waiting times without air flow through the test section. Data so obtained were used to correct the experimental results. Other sources of error exist. One is due to temperature difference between the mass transfer model and air flow; another is due to their temperature fluctuation. In both cases, the deviation was kept within $\pm 0.2°$ F. Since a deviation of one degree in Fahrenheit is estimated to cause an error of 8 percent in data reduction, to be discussed later, the error due to temperature deviation is within $\pm 5$ percent.

**Comparison With Data of Louvered Fin Heat Exchanger.** An objective of the present work is to establish a building block toward the global heat transfer correlations characterizing any louvered fins. As indicated earlier, initial work has been conducted toward this on an idealized heat exchanger where the louvered-to-total width ratio $\beta$ is equal to unity (Lee, 1986). In the actual heat exchangers, however, $\beta$ is always less than unity. The results with $\beta=1.0$ showed a significant deviation from data of a louvered fin automotive radiator ($\alpha=7.4$, $L_p/Dh=0.4$, $\beta=0.625$, and $\theta=29$ deg) (Lee, 1986). For this reason, it is interesting to compare the preceding results ($\beta<1$) with the same data. These are superimposed in Fig. 5. A comment is in order at this time. The heat transfer coefficient of the heat exchanger above is determined on the basis of the entire heat exchanger surface area including that of the tube wall, while the results of the model ($\alpha=7.748$, $L_p/Dh=0.418$, $\beta=0.61$, and $\theta=25$ deg) are on fins only. Therefore a somewhat lower heat transfer coefficient is expected from the heat exchanger. On the other hand, since $\theta$ of the heat exchanger is higher ($\theta=29$ deg) than that of the model ($\theta=25$ deg), a slightly higher coefficient is expected from the former than from the latter. Considering that the two effects may cancel out, it is remarkable to see that the heat exchanger data are close to those of the present work.

## Pressure Drop Results

The total pressure drop $\Delta P_T$ through the duct having the plate assembly can be broken down into three components, which are the pressure drop due to friction $\Delta P_f$, the pressure drop due to inertia losses through the plate assembly $\Delta P_p$, and the entrance/exit losses $\Delta P_e$, respectively (Lee, 1986).

$$\Delta P_T=(\Delta P_f+\Delta P_p)+\Delta P_e \tag{5}$$

where the quantity in the bracket is the net pressure drop through the plate assembly

$$\Delta P_N=\Delta P_f+\Delta P_p \tag{6}$$

Figure 7 is a typical pressure drop pattern along the duct ($\beta=0.81$, average velocity = 9620 m/h) when the segments are oriented against the air flow. The abscissa shows the distances of pressure taps from pressure tap #1, which is located at 25.4 mm away from the duct inlet. Pressure drop #1 is installed away from the duct inlet to eliminate the entrance effect. It is seen that the pressure drop data fall on a straight line in the upstream section, and that near the trailing edge, there is substantial pressure depression. However, the pressure depression is recovered along the downstream duct and data fall on a straight line again. Without the plate assembly, the two straight lines would be colinear. Thus, the net pressure drop $\Delta P_N$ of the assembly is the difference offset by the two lines.

However, the total pressure drop $\Delta P_T$ varies depending on where the duct exit ends in Fig. 7. For instance, if the duct terminates at the end of the assembly, $\Delta P_e$ and hence $\Delta P_T$ become its maxima.

The pressure drop measured with the segments oriented at a positive angle to the air flow showed that the net pressure drop $\Delta P_N$ is identical regardless of whether the segments are oriented at a positive or negative angle to the air flow.

Each of the above pressure drop compoenents can be expressed by

$$\Delta P_f=0.5\rho V_{max}^2 f L_p N/Dh \tag{7}$$

$$\Delta P_p=0.5\rho V_{max}^2 K_p N \tag{8}$$

$$\Delta P_e=0.5\rho V_{max}^2 K_e \tag{9}$$

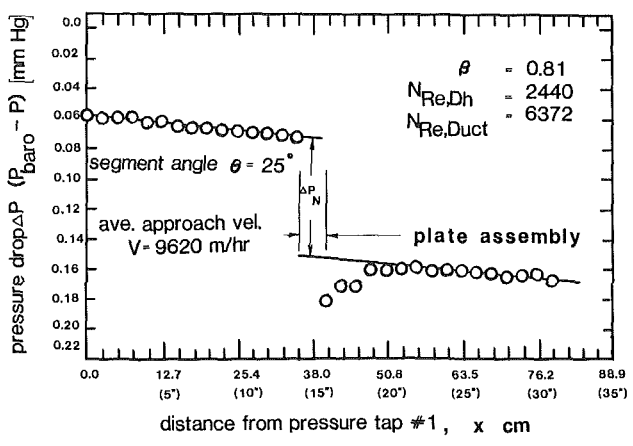


Fig. 7 Pressure drop distribution in duct

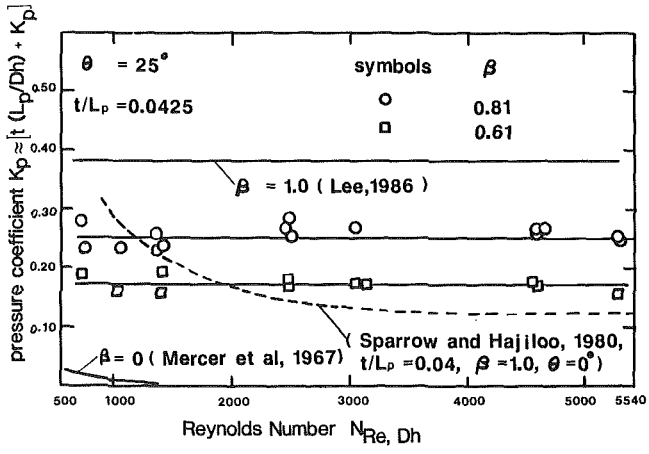


Fig. 8 Pressure coefficient versus Reynolds number

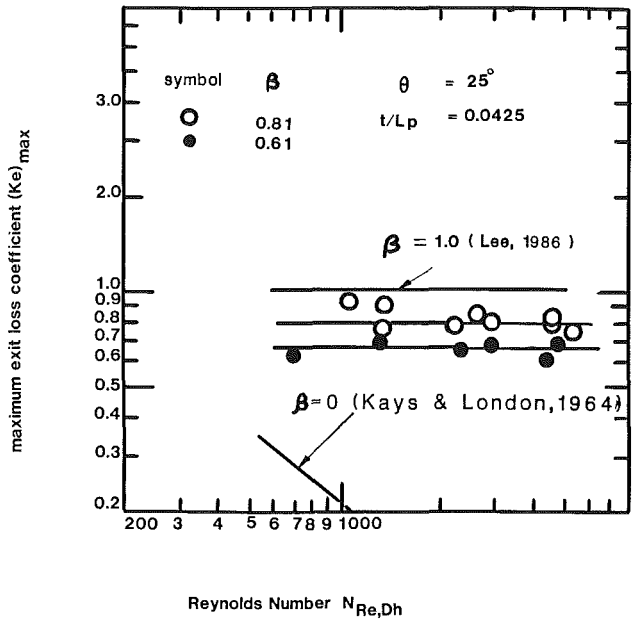


Fig. 9 Maximum exit loss coefficient

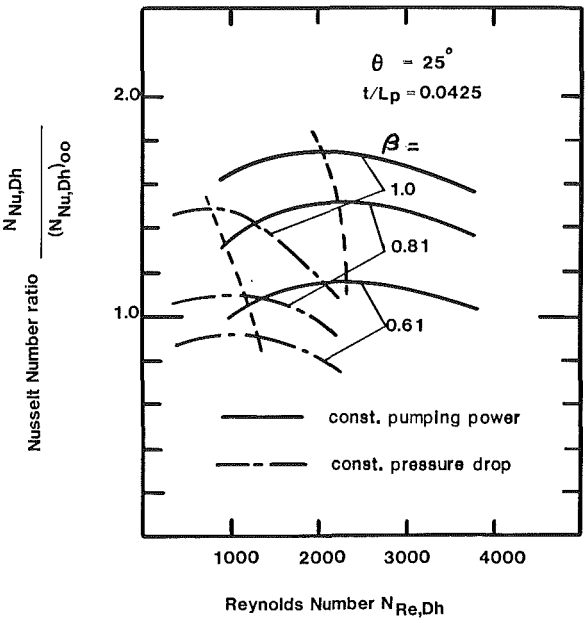


Fig. 10 Optimum conditions

Hence

$$\Delta P_N = 0.5\rho V_{\max}^2 N\{f(L_p/Dh) + K_p\} \quad (10)$$

The pressure coefficients $K_p$ (and also $K_e$) are due to inertia losses and independent of the Reynolds number $N_{Re,Dh}$ for a given $\beta$; however, $f(L_p/Dh)$ is a function of both $N_{Re,Dh}$ and $L_p/Dh$.

**Pressure Coefficient per Row $K_p$.** Pressure drop data obtained as per the procedure outlined in Fig. 7 are plotted ($\theta = 25$ deg) in terms of the bracketed value of equation (10) $\{f(L_p/D_h) + K_p\}$ versus the Reynolds number $N_{Re,Dh}$ with $\beta$ as the parameter in Fig. 8. It is seen that $\{f(L_p/Dh) + K_p\}$ is constant for a given $\beta$. This suggests that $f(L_p/Dh) << K_p$ as expected (Lee, 1986). To compare with the limiting case of $\beta = 0$, the pressure coefficient of a developing flow in a rectangular duct (Mercer et al., 1967) is also included.

Now, it may be appropriate to review the work of other investigators in the case of $\beta = 1.0$ and $\theta = 0$ deg (Sparrow and Hajiloo, 1980). Their results with $t/L_p = 0.04$ are superimposed in Fig. 8. They show that the pressure coefficient is significantly lower than that of $\theta = 25$ deg for $N_{Re,Dh} \geq 3000$. However as $N_{Re,Dh}$ decreases, the pressure coefficient increases due to skin friction and, for $N_{Re,Dh} \leq 500$, it appears to be approaching that of the case of $\beta = 1$ and $\theta = 25$ deg. This finding along with that of Fig. 5 on heat transfer suggests that there is a definite advantage in inclining the segments for $N_{Re,Dh} \leq 500$.

**Exit Loss Coefficient $K_e$.** As indicated earlier the exit loss, which is due to inertia loss, varies with the degree of pressure recovery in the downstream. To estimate the upper limit of its impact, the maximum exit loss coefficient $(K_e)_{\max}$ is plotted in Fig. 9. As expected, $(k_e)_{\max}$ is independent of $N_{Re,Dh}$, and it increases with $\beta$; the limiting case of $\beta = 1$ (Lee, 1986) is also shown.

## Performance Evaluation

The preceding sections of the paper demonstrated that an assembly of partially segmented plates with the segments aligned at angles to the flow direction has an advantage over a long plate duct in heat transfer but is accompanied by a pressure drop increase. Now the two systems are evaluated with a constraint common to both. One convenient constraint is the fixed pumping power to operate them. The Nusselt number ratio $N_{Nu,Dh}/(N_{Nu,Dh})_{00}$ will be used as the criterion for the heat transfer performance where $(N_{Nu,Dh})_{00}$ is the Nusselt number for the long continuous plate duct.

For equal pumping power, it can be shown readily that the following condition must be met:

$$N_{Re,Dh}^3 K_p = (N_{Re,Dh})_{00}^3 f L_p/Dh \quad (11)$$

Let us assume that $f$ follows the Blasius correlation as per the results of Lee (1986). For a given Reynolds number $N_{Re,Dh}$, the Reynolds number of the long duct $(N_{Re,Dh})_{00}$ that satisfied equation (11) can be computed. The Nusselt number ratio is then obtained from Fig. 5. The computed results are plotted in Fig. 10. It is seen that the improvement in the $N_{Nu,Dh}$ of the segmented plate assembly is more pronounced at high $\beta$. It is also seen that an optimum Reynolds number $(N_{Re,Dh})_{opt}$ exists that will produce the maximum Nusselt number for a given segmented-to-total width $\beta$.

A similar analysis can also be made on the constraint of constant pressure drop. The results are superimposed in Fig. 10. It is seen that the effect of $\beta$ on the Nusselt number is similar to that of the case of constant pumping power. However, the Nusselt number ratios are lower and peak Nusselt number ratios occur at lower $N_{Re,Dh}$ than with the constraint of constant pumping power. An interesting observation is also the fact that, with $\beta = 0.61$, which is a typical value for many louvered fin heat exchangers, the Nusselt number ratios are less than unity. In other words, when pressure drop itself is more important than the economy of heat exchanger maintenance, a heat exchanger having louvered fins ($t/L_p = 0.0425$, $\theta = 25$ deg) will have an advantage, only if $\beta \geq 0.81$, over identical heat exchangers with the louvered fins replaced by flat continuous fins.

## Concluding Remarks

The present work has demonstrated that the segmented-to-total plate width ratio $\beta$ is a most significant parameter, which influences the performance of louvered fins, and that there exists an optimum Reynolds number $(N_{Re,Dh})_{opt}$ for a given segmented-to-total width ratio $\beta$.

The present work provides an incentive for future investiga-

tion of the heat transfer and pressure drop characteristics of partially segmented plates having segment angles other than the present 25 deg.

## References


Beauvais, F. N., 1962, "An Aerodynamic Look at Automotive Radiators," Mid-Year SAE Meeting.

Cur, N., and Sparrow, E. M., 1978, "Experiments on Heat Transfer and Pressure Drop for a Pair of Colinear, Interrupted Plates Aligned With the Flow," *Int. J. Heat Mass Transfer*, Vol. 21, pp. 1069–1080.

Kays, W. M., and London, A. L., 1964, *Compact Heat Exchangers*, 2nd ed., McGraw-Hill, New York.

Lee, Y. N., 1986, "Heat Transfer and Pressure Drop Characteristics of an Array of Plates Aligned at Angles to the Flow in a Rectangular Duct," *J. Heat Mass Transfer*, Vol. 29, pp. 1553–1563.

Lee, Y. N., 1986, "Heat Transfer Characteristics of Canted-Rib Plate Heat Exchanger," presented at the ASME 1986 Winter Annual Meeting, Anaheim, CA.

Lee, Y. N., 1980, "Technological Advancement in All Aluminum Plate-Type Oil Coolers," *Compact Heat Exchangers*, ASME HTD-Vol. 10, pp. 145–152.

Mercer, W. E., et al., 1967, "Laminar Forced Convection in the Entrance Region Between Parallel Flat Plates," ASME JOURNAL OF HEAT TRANSFER, p. 251.

Shah, R. K., 1975, "Perforated Heat Exchanger Surfaces. Part 2—Heat Transfer and Flow Friction Characteristics," ASME Paper No. 75-WA/HT-9.

Shah, R. K., and London, A. L., 1968, "Offset Rectangular Plate-Fin Surface—Heat Transfer and Flow Friction Characteristics," ASME *Journal of Engineering for Power*, Vol. 90, pp. 218–228.

Shah, R. K., and London, A. L., 1978, "Laminar Flow Forced Convection in Ducts," *Advances in Heat Transfer Supplement 1*, Academic Press, New York.

Sissom, L. E., and Pitts, D. R., 1972, *Elements of Transport Phenomena*, McGraw-Hill, New York.

Smith, M. C., 1972, "Performance Analysis and Model Experiments for Louvered Fin Evaporator Core Developments," SAE Paper No. 720078.

Sogin, H. H., 1958, "Sublimation From Disks to Air Streams Flowing Normal to Their Surfaces," *Trans. ASME*, Vol. 80, pp. 66–71.

Sparrow, E. M., and Hajiloo, A., 1980, "Measurements of Heat Transfer and Pressure Drop for an Array of Staggered Plates Aligned Parallel to an Air Flow," ASME JOURNAL OF HEAT TRANSFER, Vol. 102, pp. 427–432.

Wieting, A. R., 1975, "Empirical Correlation for Heat Transfer and Flow Friction Characteristics of Rectangular Offset-Fin Plate-Fin Heat Exchangers," ASME JOURNAL OF HEAT TRANSFER, Vol. 97, pp. 488–490.

# Turbulent Heat Transfer and Friction in Pin Fin Channels With Lateral Flow Ejection

**S. C. Lau**
Associate Professor.
Mem. ASME

**J. C. Han**
Associate Professor.
Mem. ASME

**Y. S. Kim**
Graduate Assistant.

Department of Mechanical Engineering,
Texas A&M University,
College Station, TX 77843-3123

*Experiments were conducted to study the effects of lateral flow ejection on the overall heat transfer and pressure drops for turbulent flow through pin fin channels. The two test sections of the investigation were rectangular channels with staggered arrays of six and eight streamwise rows of pins, respectively. The pin length-to-diameter ratio was one and both the streamwise and spanwise pin spacings were 2.5 times the pin diameter. Heat transfer and friction data were obtained for various ejection exit geometries, for ejection ratios between 0 and 1, and for Reynolds numbers between 6000 and 60,000. The results of the study show that, for any given ejection ratio, the overall Nusselt number increases with increasing Reynolds number. However, the overall Nusselt number is reduced by as much as 25 percent as the ejection ratio is increased from 0 to 1 over the range of Reynolds number studied. The Nu-Re-$\epsilon$ relationship, which is insensitive to varying the ejection exit geometry, can be correlated by the equation $(Nu/Nu_0) = (Nu_1/Nu_0)^{\epsilon}$, where $Nu_0 = c_0 Re^m$ and $Nu_1 = c_1 Re^n$ are the overall Nusselt numbers in the 0 and 100 percent lateral flow ejection cases, respectively. The results also show that the overall friction factor is independent of the flow Reynolds number over the range of Reynolds number studied. However, the friction factor is strongly dependent on the ejection ratio as well as the geometries of the straight flow exit and lateral ejection flow exit.*

## Introduction

Pin fins have been used in the internal cooling channels near the trailing edges of gas turbine blades to enhance the heat transfer to the cooling air. The cutaway view of a typical modern gas turbine blade is shown in Fig. 1. The cooling air enters the pin fin channel at the base of the blade and exits through ejection holes at the tip of the blade and through ejection slots along the trailing edge of the blade. The lateral air ejection cools the blade trailing edge where the small blade thickness prevents the extension of the pin fin channel to the trailing edge. In the present investigation, the effect of lateral flow ejection on the turbulent heat transfer characteristics in pin fin channels has been studied systematically. The results of the study are applicable to the design of effectively cooled turbine blades that are not susceptible to failure due to thermal stresses.

Due to manufacturing constraints of internally cooled turbine blades, the pin length-to-diameter ratio ($L/D$) of the turbine blade pin fin channels is on the order of one. The heat transfer characteristics of the flow through these channels are very different from those of flows through channels with very long pin fins (with large $L/D$, as in crossflow heat exchangers) and channels with very short pin fins (with small $L/D$, as in plate-fin-and-tube heat exchangers). VanFossen (1982) and Brigham and VanFossen (1984) studied the heat transfer in channels with staggered arrays (4 and 8 rows) of pin fins with $S/D = 2$ and 4, $X/D = 1.73$ and 3.46, and $L/D = 0.5$, 2, and 4. Their major findings were that the overall heat transfer coefficients for channels with short pin fins were lower than those for channels with longer pin fins but were much higher than those for plain channels with no pins, and that, for long pin fins with $L/D > 2$, the heat transfer depended on both the pin length-to-diameter ratio and the Reynolds number while, for short pin fins with $L/D < 2$, the heat transfer depended on the Reynolds number only.

Metzger et al. (1982a, 1982b, 1984) investigated the overall and row-averaged heat transfer in large-aspect-ratio rectangular channels with staggered short pin fin arrays ($L/D = 1$). In Metzger et al. (1982a), the test channel was made of ten copper segments. Each of the segments was individually heated, contained one spanwise row of pins, and was insulated from adjacent segments with plastic spacers. Results included the streamwise development of the row-averaged Nusselt number for $S/D = 2.5$, $X/D = 1.5$ and 2.5, and for the Reynolds number up to $10^5$. Correlations were provided for the overall Nusselt numbers for the two pin configurations as functions of the Reynolds number.

Metzger and Haley (1982b) conducted experiments with the apparatus used in Metzger et al. (1982a) by replacing the copper (conducting) pins with wooden (nonconducting) pins. The streamwise development of the row-averaged Nusselt number in the copper pin and wooden pin cases showed the same rapidly increasing then gradually decreasing trend. The overall heat transfer in the wooden pin case was lower than that in the copper pin case at high Reynolds numbers and was higher at low Reynolds numbers.

Metzger et al. (1984) also studied the effects of using flattened pins and of varying the orientation of the pin fin array with respect to the main flow direction on the heat transfer and pressure losses in pin fin channels. They observed that, by varying the orientation of the pin fin array, it was possible to increase the heat transfer and, at the same time, reduce the pressure loss. They also found that the use of flattened pins increased the heat transfer slightly but doubled the pressure loss.

Lau et al. (1985, 1987) conducted naphthalene sublimation experiments to study the distributions of the local endwall heat transfer coefficient in channels with aligned and staggered pin fin arrays ($L/D = 1$, $S/D = 2.5$, $X/D = 1.25$, 2.5). The effects of varying the Reynolds number, the pin configuration, and the entrance length on the local endwall heat transfer coefficient distribution were examined. Overall and row-averaged Nusselt numbers were found to be in good agreement with those presented in Metzger et al. (1982a, 1982b).

All of the aforementioned studies are for the flow of cooling

Contributed by the Heat Transfer Division and presented at the 24th National Heat Transfer Conference, Pittsburgh, Pennsylvania, August 9-12, 1987. Manuscript received by the Heat Transfer Division September 3, 1987. Keywords: Finned Surfaces, Forced Convection, Turbulence.

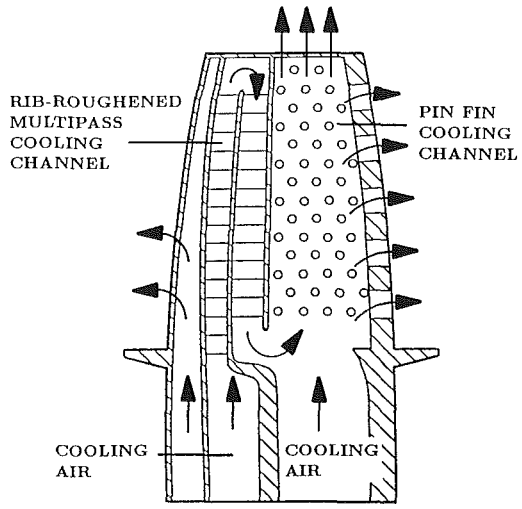


**Fig. 1 Cutaway view of a typical modern internally cooled turbine blade**

air straight through rectangular channels with short pin fins. In the internal pin fin cooling channel in a typical turbine blade, air enters at the base of the blade. Some of the cooling air exits through ejection holes at the tip of the blade while the rest of the air is ejected through slots along the trailing edge of the blade. The gradually decreasing mass flow in the main flow direction due to the lateral ejection of the cooling air and the turning of the ejection air stream should affect the heat transfer to the cooling air. Studies on pin fin channel heat transfer so far have not taken into consideration such effects.

In the present investigation, heat transfer experiments were performed with two pin fin channels – one with six rows of pins in the straight flow direction and the other with eight rows of pins. The pin length-to-diameter ratio ($L/D$), the streamwise spacing ($X/D$), and the spanwise spacing ($S/D$) of the pins were 1.0, 2.5, and 2.5, respectively. Results were obtained for various ejection hole and slot geometries, for ejection ratios ($\epsilon$, defined as the ratio of the ejection flow rate to the total mass flow rate) between 0 and 1.0, and for Reynolds numbers (based on the pin diameter and the maximum flow velocity) between 6000 and 60,000. The heat transfer experiments were complimented by pressure measurement experiments, which were conducted with one of the aforementioned test channels with six rows of pins in the straight flow direction.

## Experimental Apparatus

A schematic of the test apparatus for the present investigation is shown in Fig. 2. The main components of the air flow loop were a flow development channel, the test section, two downstream channels, two settling chambers, two calibrated orifice flow meters, and control valves.

Two test sections were constructed for the present investigation. The first test section was a 15:1 rectangular channel with an inlet flow cross section of 6.4 mm (0.25 in.) by 95.3 mm (3.75 in.). A staggered array of six rows of pin fins was installed in the test section, as shown in Fig. 3(*a*). The length-to-diameter ratio of the pins was one, that is, the diameter of the pins was the same as the height of the test channel. The streamwise spacing and the spanwise spacing of the pins were both 2.5 times the pin diameter.

The first test section was constructed entirely of copper. The top, bottom, and side walls of the test section were all 6.4 mm (0.25 in.) thick. The pins were cut from slightly oversized circular copper rods and were machined on a lathe to attain a diameter of 6.4 mm (0.25 in.) ± 0.025 mm (0.001 in.). The assembly of the copper test section was a very complicated task. Firstly, a staggered array of holes ($X/D=S/D=2.5$) of diameter 6.3 mm (0.247 in.) ± 0.025 mm (0.001 in.) was machined on the top and bottom walls. The pins, whose ends were rounded slightly, were inserted with a hydraulic press simultaneously through the holes on one of the two walls. After that, the protruded ends of the pins were inserted, with the hydraulic press, through the holes on the other wall. During the process, square space bars were used to ensure that the distance between the two walls was 6.4 mm (0.25 in.).

After the top and bottom walls and the pins were in place, the left side wall and flanges were soldered onto the test section. The flanges were made of copper for the attachment of the upstream and downstream channels. Solder was also used to seal the gap between the holes and the pin to prevent air leakage during experiments.

The exit blockages were also made of copper and were 6.4 mm (0.25 in.) thick. The various configurations of the blockages are shown in Fig. 3(*a*). These blockages were not attached permanently to the test section. Rather, they were held in place by the flanges.

## Nomenclature

$A$ = total channel surface area exposed to air flow
$c_0$ = coefficient, equation (6)
$c_1$ = coefficient, equation (7)
$c_p$ = specific heat of air at $\bar{T}_b$
$D$ = pin diameter
$f$ = friction factor, equation (5)
$k$ = thermal conductivity of air at $\bar{T}_b$
$L$ = pin length
$\dot{m}$ = mass flow rate of air
$m$ = exponent, equation (6)
$n$ = exponent, equation (7)
$N$ = number of pin rows along the straight flow direction
Nu = overall Nusselt number, equation (1)
$\mathrm{Nu}_0$ = overall Nusselt number, $\epsilon=0$, equation (6)
$\mathrm{Nu}_1$ = overall Nusselt number, $\epsilon=1$, equation (7)
$\dot{q}_{in}$ = power input
$\dot{q}_{loss}$ = rate of heat loss through insulation
Re = Reynolds number based on pin diameter and maximum flow velocity, equation (3)
$S$ = spanwise pin spacing
$\bar{T}_b$ = average bulk temperature
$T_{bi}$ = inlet bulk temperature
$T_{bo}$ = outlet bulk temperature, equation (2)
$\bar{T}_w$ = average wall temperature
$u_{max}$ = maximum air velocity in test section
$\dot{V}$ = rate of total volumetric flow through test channel
$\dot{V}_1$ = rate of volumetric flow through straight flow exit
$\dot{V}_2$ = rate of volumetric flow through lateral flow exit
$X$ = streamwise pin spacing
$\Delta p$ = overall pressure drop
$\Delta p_1$ = pressure drop for flow through straight flow exit
$\Delta p_2$ = pressure drop for flow through lateral flow exit
$\Delta T_{lm}$ = log mean temperature difference
$\epsilon$ = ejection ratio, ratio of ejection flow rate to total mass flow rate
$\nu$ = kinematic viscosity of air at $\bar{T}_b$

The outer surfaces of the top and bottom walls were machined to a smooth and flat finish on a mill for the installation of two 400-W strip heaters. The construction of the test section was carried out to ensure that the dimensions of the test section were within a tolerance of ± 0.025 mm (0.001 in.), and that there was good physical contact between the walls and the pins as well as between the heaters and the outer surfaces of the test channel.

Thirteen holes (nine in the top wall and four in the bottom wall) and shallow grooves were machined on the top and bottom walls for the installation of thermocouples. The holes, which were 1.6 mm (0.063 in.) in diameter, were only slightly less than 6.4 mm (0.25 in.) deep and were distributed over the top and bottom walls. The placement of the thermocouple is indicated in Fig. 3(*a*). Small 36-gauge copper-constantan thermocouples with Teflon insulation were employed.

Before the insertion of a thermocouple junction into a hole, a drop of Silver Print conductive paint (which is made of pure silver and is commonly used by electricians to repair damaged circuit boards) was allowed to drip down to the bottom of the hole. The thermocouple junction was then inserted such that the junction touched the bottom of the hole. Masking tape was used to hold the thermocouple in place temporarily until the conductive paint dried. Epoxy was then used over the hole and in the shallow groove to hold the thermocouple in place.

Silver Print conductive paint was also applied to the outer surfaces of the test channel before the installation of the two strip heaters. The relatively small size of the test section, the use of the copper for the entire test section, and of the highly conductive silver paint resulted in a maximum spatial variation of the wall temperatures of less than 1.1°C (2°F) in all the tests.

The second test section, which was constructed of aluminum, had an entrance flow cross section of 12.7 mm (0.50 in.) by 142.9 mm (5.63 in.) (that is, an aspect ratio of 11.25). It had a staggered array of eight rows of four pin fins 12.7 mm (0.50 in.) in diameter with both the streamwise spacing and the spanwise spacing of 2.5 times the diameter (Fig. 3*b*). The top and bottom walls were 19.1 mm (0.75 in.) thick. As shown in Fig. 3(*b*), the downstream and lateral exit cross sections were eight evenly distributed holes of 1.27 mm (0.5 in.) in diameter and four 12.7 mm (0.5 in.) by 31.8 mm (1.25 in.) rectangular slots, respectively.

The major difference between the construction of the aluminum test section and that of the copper test section was the attachment of the pins onto the test section walls. The aluminum pins were machined to 12.7 mm (0.5 in.) long and were bonded to the test section walls with Permabond ESP 110 epoxy adhesive. The procedure consisted of the preparation of a template with a staggered array of holes slightly larger than 12.7 mm (0.5 in.) in diameter, the careful placement and attachment of the pins onto one of the walls, the installation of the other wall on the top of the pins, and the baking of the test section in a furnace at 204°C (400°F) for about two hours.

The installation of the thermocouples and of the heaters on the aluminum test section was similar to that in the copper test section case except that 25 thermocouples (15 in the top wall and 10 in the bottom wall) were used to measure the wall temperatures. Two identical 500-W strip heaters connected in series were used to provide heat to each of the two primary walls. For test runs using the aluminum test section, the maximum spatial variation of the measured wall temperatures was found to be up to 5.6°C (10°F).

For each of the two test sections, the entrance section was a rectangular duct with a flow cross section identical to that at the entrance of the test section and with a length equivalent to 12 times the hydraulic diameter of the test section. The exit sections were short rectangular channels to duct the air to the settling chambers and the orifice flow meters. The test section, the entrance, and downstream ducts were heavily insulated.

A centrifugal blower was used to draw air through the test flow loop in the copper-test-channel runs. Dry compressed air was used in the aluminum-test-channel experiments. Silicon

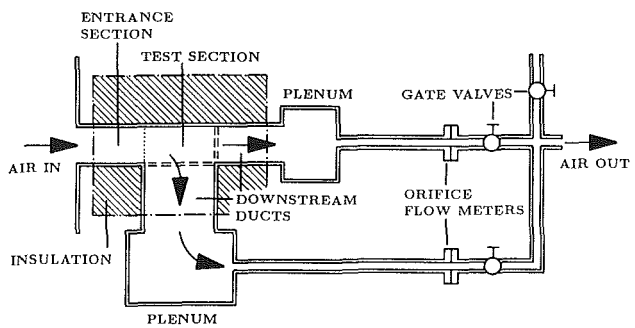


Fig. 2 Schematic of test flow loop

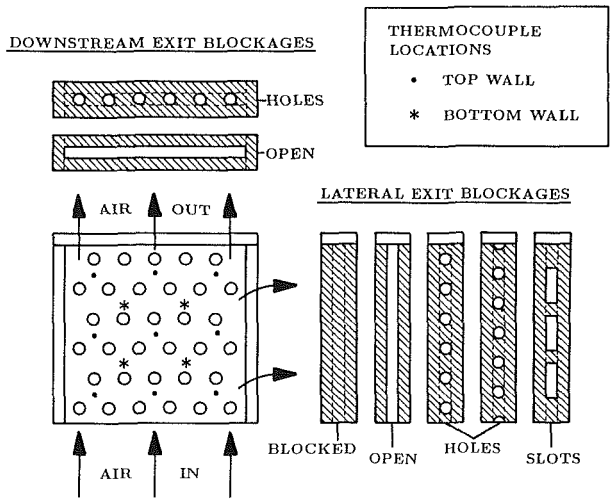


Fig. 3(*a*) First test section with exit blockages and thermocouple locations shown

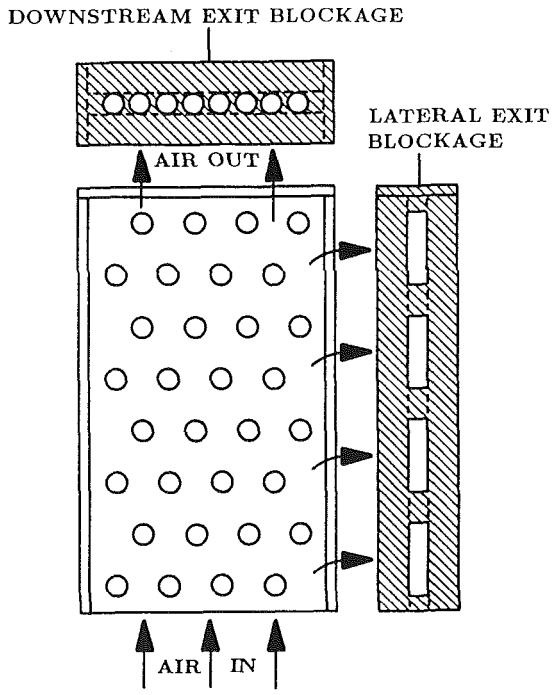


Fig. 3(*b*) Second test section with exit blockages shown

Table 1 Test section configurations

| Configuration | Test section material | Downstream exit | Lateral exit | Pin rows in main flow direction | Total number of pins |
|---|---|---|---|---|---|
| A | Copper | Open | Blocked | 6 | 33 |
| B | Copper | Open | Open | 6 | 33 |
| C | Copper | Open | 6 holes, aligned | 6 | 33 |
| D | Copper | Open | 6 holes, shifted | 6 | 33 |
| E | Copper | Open | 3 slots | 6 | 33 |
| F | Copper | 6 holes | 3 slots | 6 | 33 |
| G | Aluminum | 8 holes | 4 slots | 6 | 32 |

rubber sealant was applied to all joints along the flow loop to prevent air leakage during experiments.

Seven thermocouples were used to measure the temperatures at the inlet and at the two exit cross sections. Four thermocouples monitored the temperatures on the strip heaters. Thermocouple outputs were recorded with a data logger. The total power input to the strip heaters was controlled with a variable transformer and measured with two 5 1/2-digit true rms multimeters (the two meters were used to measure the current through the heaters and the voltage drop across the heaters, respectively.)

The rates of air flow through the downstream and the lateral cross sections of the test section were controlled with three gate valves and measured with the two calibrated orifice flow meters along with a number of oil (specific gravity = 0.826) manometers, including an inclined manometer.

The test apparatus for the pressure measurement experiments was the flow loop for the heat transfer experiments with the copper test section. Four static pressure taps were installed on the top wall of each of the two exit ducts – three taps at 57.2 mm (2.25 in.) and one at 158.8 mm (6.25 in.) downstream of the exit slots/holes. Two static pressure taps located at a distance of 57.2 mm (2.25 in.) from the test section entrance were used to measure the pressure upstream of the test section.

During any pressure measurement experiment, the downstream pressures at the two flow exits were measured with respect to the upstream pressure with U-tube and inclined oil manometers. Although other pressure indicators with high resolution, such as electronic pressure gages and micromanometers, were available for the present investigation, they were not needed since the pressure drops across the orifice flow meters and across the test section were generally quite large.

## Experimental Procedure

Preliminary experiments were performed to determine the relationship between the pressure drop across each of the orifice flow meters and the corresponding mass flow rate. A computer program, which could be run on a microcomputer situated near the test apparatus, was then prepared. The program enabled the accurate setting of the mass flow rates at the beginning of a test run based on the desired Reynolds number and ejection ratio of the run.

To prepare for a test run, the appropriate exit blockage plates were installed. After the exit ducts were attached to the test section and all the joints were sealed with silicon rubber sealant, the flow loop was tested for possible air leakage.

To initiate a test run, air was allowed to flow through the test section. The ejection ratio and the flow Reynolds number were set by adjusting the two downstream gate valves and by monitoring the pressure drops across the orifices. Power input to the heaters was adjusted so that the wall temperatures were approximately 19.4°C (35°F) above the inlet air temperature. The system was then left to attain steady state. At the end of about one hour, all the thermocouple readings were recorded every ten minutes. Steady state was assumed when all the thermocouple readings did not change by more than ± 0.06°C (± 0.1°F) over a period of 30 minutes. A typical test run lasted about two hours. During the second hour of the test run, the atmospheric pressure, the pressure drops across the orifice flow meters, and the static pressures (gage) upstream of the orifices were recorded periodically.

In a pressure measurement experiment, the static pressures at the taps upstream of the test section with respect to the atmospheric pressure and the pressure drops across the test section (the pressures at the taps downstream of the two flow exits with respect to the pressures at the taps upstream of the test section entrance) were measured and recorded. As in a typical heat transfer experiment, the flow rate and the ejection ratio in a pressure experiment were determined by measuring the pressure drops across the orifice flow meters.

A total of more than 160 heat transfer experiments and 130 pressure experiments was made. The various configurations of the test section for the runs are summarized in Table 1. Data were obtained for Reynolds numbers between 6000 and 60,000, and for ejection ratios between 0 and 1.0. The raw data of all the test runs can be found in a dissertation by Kim (1987).

Supplementary tests were conducted to determine the heat losses through the insulation during heat transfer test runs. With no flow through the test flow loop, heat was supplied to the strip heaters. The total heat input (which, at steady state, was equal to the heat loss through the insulation) and the steady-state temperatures in the test section walls and on the heaters were recorded. A relationship between the heat loss to the surrounding air and the average wall-to-ambient temperature difference [for $\Delta T$ between 11°C (20°F) and 50°C (90°F)] was established. When the copper test section was tested, steady-state wall temperatures were observed in less than 24 hours. However, for the larger aluminum test section, it took as long as two days for the wall temperatures to reach their steady-state values.

## Data Reduction and Error Analysis

The power input to the test section is the total power input to the strip heaters minus the heat loss through the insulation. The heat loss is estimated based on the area-weighted average of the wall temperatures and the heater temperatures, the room temperature during the test, and the relationship between the steady-state heat loss and the wall-to-ambient temperature difference obtained in supplementary tests described in the last section.

The overall Nusselt number is calculated as follows:

$$\mathrm{Nu} = \{[(\dot{q}_{\mathrm{in}} - \dot{q}_{\mathrm{loss}})/A]/\Delta T_{lm}\}(D/k) \tag{1}$$

where $A$ is the total channel surface area exposed to the air flow including the areas of the top and bottom walls, the pins, the sidewall, and of the downstream blockages. The log mean temperature difference, $\Delta T_{lm}$, is in terms of $\bar{T}_w$, $T_{bi}$, and $T_{bo}$. The outlet air temperature $T_{bo}$ is evaluated as

$$T_{bo} = T_{bi} + (\dot{q}_{in} - \dot{q}_{\mathrm{loss}})/(\dot{m}c_p) \tag{2}$$

The flow Reynolds number is based on the pin diameter and the air velocity at the minimum flow cross section in the test section.

$$\mathrm{Re} = u_{\max} D/\nu \tag{3}$$

The total required pumping power can be written as

$$\Delta p \dot{V} = \Delta p_1 \dot{V}_1 + \Delta p_2 \dot{V}_2 \tag{4}$$

where $\dot{V}_1$, $\dot{V}_2$, $\Delta p_1$, and $\Delta p_2$ are the volumetric flow rates and the measured pressure drops for flow through the straight exit and the lateral exit, respectively. If the density of the flowing

air does not vary significantly in the test channel, an overall friction factor can be defined as

$$f = [\Delta p_1(1-\epsilon) + \Delta p_2 \epsilon]/[(1/2)\rho u_{\max}^2 N] \quad (5)$$

where $N$ is the number of rows of pins in the straight flow direction.

The tolerance of all the dimensions of the two test sections is ± 0.001 in. (±0.025 mm). Therefore, it is estimated that the uncertainties of A and D are both ± 0.4 percent. Using the estimated uncertainties of ± 2.5 percent and ± 6 percent for the actual power input to the test section and for the log mean temperature difference, respectively, and the uncertainty estimation method of Kline and McClintock (1953), the maximum uncertainty in the calculated Nusselt number is ± 6.5 percent. Similarly, the maximum uncertainties in the calculated Reynolds number and friction factor are estimated to be ± 5.0 percent and ± 8.0 percent, respectively.

## Results and Discussion

In the present investigation, the overall heat transfer coefficients for pin fin channels with six and eight streamwise rows of pins were determined for various flow outlet geometries (as shown in Figs. 3*a* and 3*b*) and ejection ratios. Experimental results are presented in this section in separate plots of the overall Nusselt numbers as functions of the Reynolds number for ejection ratios of 0, 0.25, 0.5, 0.75, and 1.0.

In Fig. 4, the overall Nusselt number for flow through the copper test section with the downstream exit cross section wide open and the ejection exit cross section blocked (configuration A) is plotted versus the Reynolds number. In the figure, experimental results from Metzger et al. (1982a) and VanFossen (1982) are also shown. The results of Metzger et al. (1982a) are from their correlation given in equation (6) of their paper for flow through a 25:1 channel with ten streamwise rows of ten pins. The pins and the top and bottom walls of their test channel were made of copper while the side walls were insulated. The heat transfer data by VanFossen (1982) are based on the correlation given in equation (16) of his paper, which was from a least-squares curve fit of four sets of data obtained using a test section with four rows of copper or wooden pins. In using equation (16) of VanFossen (1982) to calculate the Nusselt number, the Reynolds number is based on the dimensions of the present copper test section. Thus, the equation becomes $Nu = 0.103\ Re^{0.685}$. It should also be noted that the side walls of the test section used in VanFossen (1982) were made of a phenolic plastic.

Figure 4 shows that the present data fall on a straight line and compared very well with the published correlations of Metzger et al. (1982a) and VanFossen (1982). The maximum deviations of the present data from those based on the two published correlations are 5 percent and 3 percent, respectively.

In Fig. 4, the Dittus–Boelter correlation for turbulent flow in a plain rectangular channel is also shown for comparison. Based on the present data, the addition of the pin fins increases the overall Nusselt number (based on the total wall and pin surface area) by about 64 and 40 percent at Re = 10,000 and 30,000, respectively.

In case B, the downstream exit cross section as well as the ejection exit cross section are both wide open. Experimental data for ejection ratios of 0, 0.25, 0.5, 0.75, and 1.0 are shown in Fig. 5. In general, the overall Nusselt number increases with increasing Reynolds number. Also, at a given Reynolds number, the Nusselt number decreases with increasing ejection ratio. It can also be seen that, for each ejection ratio, the data fall approximately on a straight line. Two least-squares curve fit straight lines are drawn through the data for ejection ratios of 0 and 1.0, as represented by the two solid lines. The two lines are almost parallel except that they converge slightly as the Reynolds number increases.

In order to facilitate the correlation of all the data, evenly distributed straight dotted lines are constructed between the two least-squares curve fit lines through the data for ejection ratios of 0.25, 0.5, and 0.75. These dotted lines, although not least-squares curve fit lines, pass through most of the data points for the respective ejection ratios. As a result, it becomes evident that the overall Nusselt number as a function of the Reynolds number and the ejection ratio may be correlated with a very simple equation. The correlation of all the data obtained in the present investigation will be presented and discussed at the end of this section.

From Fig. 5, it can be seen that the overall Nusselt number decreases with increasing ejection ratio. At Re = 20,000, the overall Nusselt number for $\epsilon = 0$ (no ejection) is reduced by 21.1 percent when $\epsilon = 1$ (100 percent of flow through ejection exit). The corresponding reduction is slightly higher at lower Reynolds numbers and lower at higher Reynods numbers.

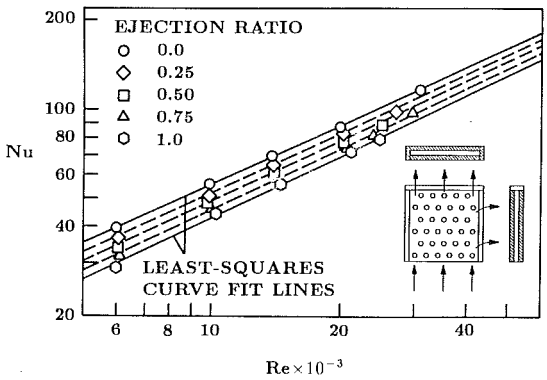


Fig. 5 Nu as a function of Re and $\epsilon$, Case B

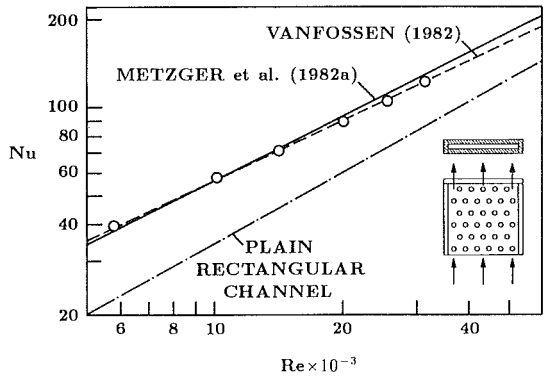


Fig. 4 Comparison of present data with those from references

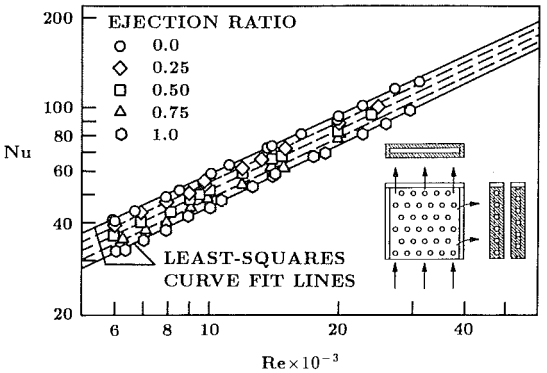


Fig. 6 Nu as a function of Re and $\epsilon$, Cases C and D

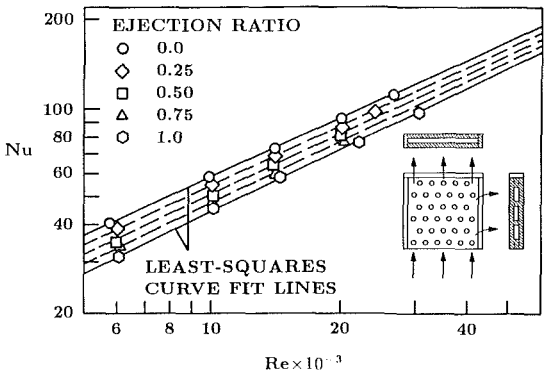


Fig. 7 Nu as a function of a Re and $\epsilon$, Case E

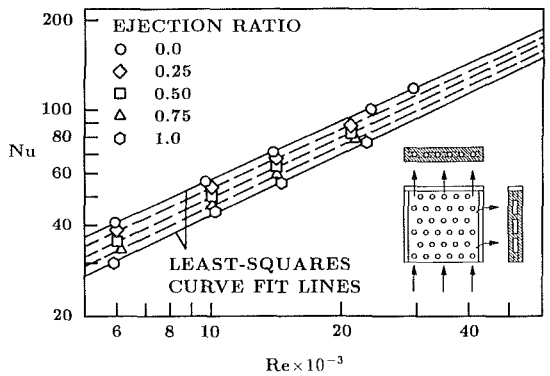


Fig. 8 Nu as a function of Re and $\epsilon$, Case F

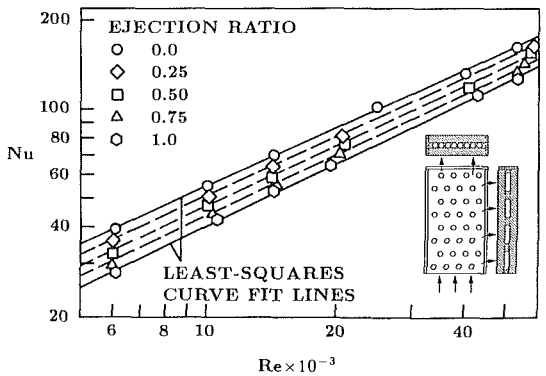


Fig. 9 Nu as a function of Re and $\epsilon$, Case G

In Fig. 6, the data for cases C and D are presented. In both of these two cases, the downstream exit cross section is wide open, while the ejection exit cross section consists of six evenly distributed holes whose diameter is equal to the channel height. The ejection holes in case C are aligned with the pin rows while those in case D are shifted by half the distance between pin rows. Since it was found that there was no significant difference between the Nu–Re–$\epsilon$ relationships in the two cases, the two sets of data are plotted in Fig. 6 using one set of symbols. As in Fig. 5, two least-squares curve fit lines for $\epsilon$ = 0 and $\epsilon$ = 1 as well as three evenly spaced dotted lines between the two least-squares curve fit lines for $\epsilon$ = 0.25, 0.50, and 0.75 are plotted through the data points. It can be seen that, for a given ejection ratio, the Nusselt number increases with respect to the Reynolds number according to an equation of the form $Nu = aRe^b$, where $a$ and $b$ are constants. At Re = 10,000 and 30,000, the overall Nusselt numbers for $\epsilon$ = 1 are 21.4 and 19.1 percent lower than those for $\epsilon$ = 0, respectively.

The arrangement of the ejection holes, aligned or shifted, with respect to the pin rows, does not appear to affect the Nu–Re–$\epsilon$ relationship. The reduction in the overall heat transfer in a pin fin channel with increasing lateral ejection may be due to the decrease in the mass flow in the straight through direction. The blockage at the lateral exit cross section and the turning of the ejection portion of the flow may also contribute to the overall heat transfer decrease.

For flow through the test pin fin channel with a wide open downstream exit cross section and with three 3:1 slots at the lateral exit cross section (case E), the experimental data are presented in Fig. 7. The similarity between the data given in Fig. 7 and those shown in Fig. 6 earlier suggests that the overall heat transfer in a pin fin channel with lateral flow ejection is affected only mildly by changing the ejection exit cross section geometry.

The final two sets of data – those for cases with holes at the downstream exit cross section and slots at the ejection exit cross section (cases F and G) – are shown in Figs. 8 and 9. The copper test section of case F, which is the same one used in all the earlier cases, has six staggered rows of five and six pins while the aluminum test section of case G is a larger test section with eight staggered rows of four pins, whose diameter is two times that of the pins in the copper test sectioin. In the latter case, data are obtained for Reynolds numbers up to 60,000.

In comparing Figs. 8 and 9, the two least-squares curve fit lines for $\epsilon$ = 0 are parallel with the one in case G slightly lower (by about 4 percent) than that in case F. The small difference may be due to the difference in the geometries of the two test sections, which are made of different materials, and the conductance resistance between the pins and the endwalls in the aluminum test section as a result of the use of epoxy for the installation of the pins.

As in the earlier cases, the two least-squares curve fit lines for $\epsilon$ = 0 and $\epsilon$ = 1 in cases F and G converge slightly with increasing Reynolds number. At Re = 10,000, 20,000, and 30,000, there are decreases in the overall Nusselt number in case F of 24.1, 22.3, and 21.2 percent, respectively, when the ejection ratio is increased from 0 to 100 percent. The corresponding values in case G are 26.4, 24.0, and 22.5 percent, which are slightly larger than the previous values. Therefore, the use of the aluminum test section with a slightly different length-to-width ratio and with two more streamwise pin rows as compared to the copper test section does not change the general trends of Nu–Re–$\epsilon$ relationship.

For all the cases studied, the coefficients and the exponents of the equations for the least-squares curve fit lines

$$Nu_0 = c_0\ Re^m, \quad \text{when } \epsilon = 0 \tag{6}$$

and

$$Nu_1 = c_1 Re^n, \quad \text{when } \epsilon = 1 \tag{7}$$

are listed in Table 2. Since, in each of the cases studied, most of the present data for $\epsilon$ = 0.25, 0.50, and 0.75 fall on straight lines, which are evenly spaced between the two least-squares curve fit lines for $\epsilon$ = 0 and $\epsilon$ = 1, all the data can be correlated by the following equation:

$$Nu = c_0^{(1-\epsilon)} \cdot c_1^{\epsilon} \cdot Re^{[m(1-\epsilon)+n\epsilon]} \tag{8}$$

When equation (8) is divided by $Nu_0$, the equation becomes

$$(Nu/Nu_0) = (Nu_1/Nu_0)^{\epsilon} \tag{9}$$

If all of the data in cases A through F are plotted on a single graph, the coefficients $c_0$, $c_1$, and the exponents $m$, $n$, in the equations for $Nu_0$ and $Nu_1$ can be determined to be 0.1274, 0.0794, 0.6638, and 0.6875, respectively. Equation (9) can then be rewritten as

$$(Nu/Nu_0) = (0.6232\ Re^{0.0237})^{\epsilon} \tag{10}$$

Equation (9) and (10) can be used to predict the overall heat

Table 2 Values of coefficients and exponents for equations (6) and (7)

| Case | $\epsilon=0$ | | $\epsilon=1$ | |
|---|---|---|---|---|
| | $Nu_0=c_0Re^m$ | | $Nu_1=c_1Re^n$ | |
| | $c_0$ | $m$ | $c_1$ | $n$ |
| A | 0.1329 | 0.6580 | – | – |
| B | 0.1275 | 0.6606 | 0.0632 | 0.7075 |
| C | 0.1199 | 0.6707 | 0.0700 | 0.7026 |
| D | 0.1171 | 0.6746 | 0.0764 | 0.6953 |
| E | 0.1354 | 0.6590 | 0.0756 | 0.6932 |
| F | 0.1366 | 0.6562 | 0.0764 | 0.6894 |
| G | 0.1305 | 0.6561 | 0.0617 | 0.7041 |

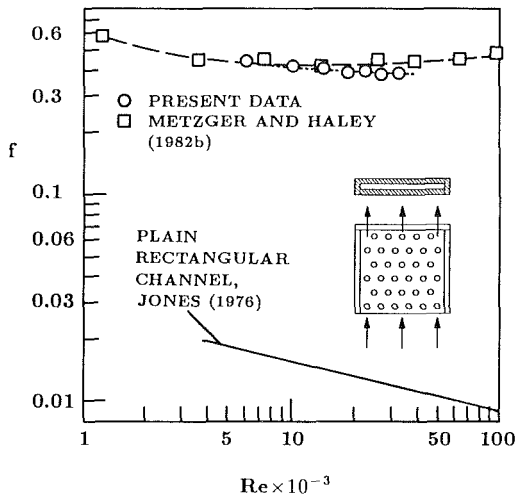


Fig. 10 Comparison of present data with those from Metzger and Haley (1982b) and Jones (1976)

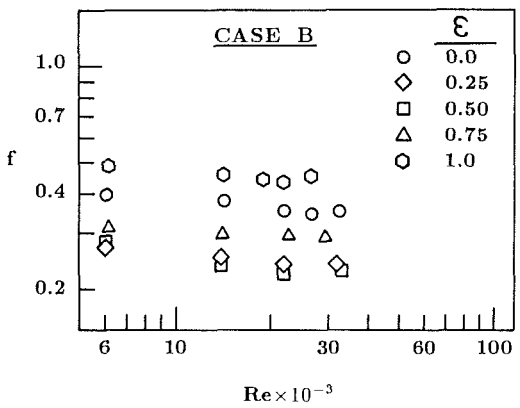


Fig. 11 $f$ as a function of Re and $\epsilon$, Case B

transfer for turbulent flow in pin fin channels with lateral flow ejection.

The results of the pressure experiments are presented in Figs. 10 through 13. In each of the figures, the overall friction factor, defined in equation (5) in the Data Reduction section, is plotted as a function of the flow Reynolds number for various ejection ratios.

Firstly, in Fig. 10, the present pressure drop results for straight flow through the test channel with an open straight-flow exit cross section and a blocked lateral exit (configuration A, $\epsilon=0$) are compared with the pressure data of Metzger and Haley (1982b) and the pressure drop for the flow through a straight, rectangular channel with no pin fins (Jones, 1976). The present data compare well with those of Metzger and

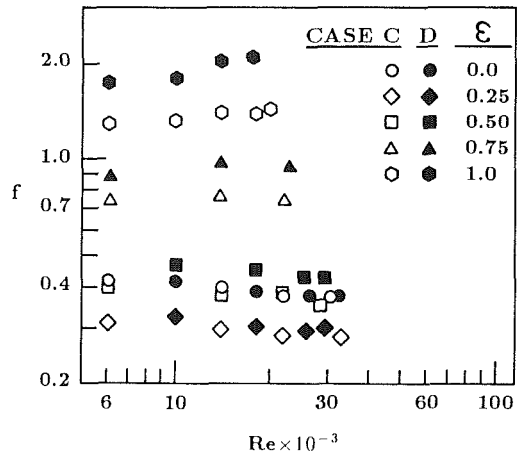


Fig. 12 $f$ as a function of Re and $\epsilon$, Cases C and D

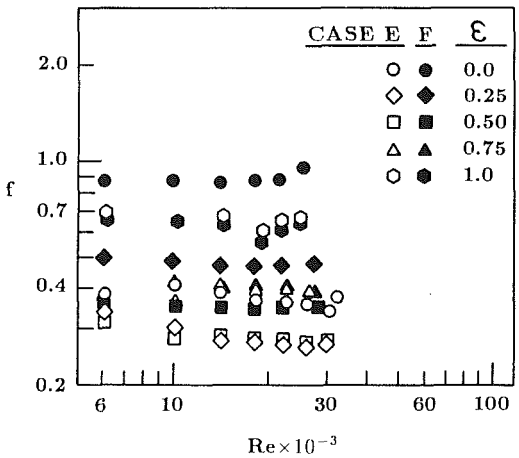


Fig. 13 $f$ as a function of Re and $\epsilon$, Cases E and F

Haley (1982b) which are for the flow through a channel with 10 rows of pin fins, with the present results slightly lower than the published data. The channel pressure drops measured in the two studies are both dependent only mildly on the flow Reynolds number. As expected, the pressure drops across pin fin channels are much higher than that across a smooth channel with no pin for the same mass flow rate.

In Fig. 11, pressure results are presented for configuration B, with both the straight flow exit and the lateral flow exit wide open (that is, no blockage). For all ejection ratios, the overall friction factor depends only mildly on the flow Reynolds number over the range of Reynolds number studied. For straight flow through the pin fin channel, the values of the overall friction factor are about the same as those in the case of open straight flow exit and blocked lateral exit (configuration A).

When $\epsilon = 1.0$, the overall friction factors are about 20 to 25 percent higher than those in the case of no lateral ejection flow ($\epsilon = 0$). The turning of the flow through a 90 deg angle and the recirculation of trapped air at the corner between the solid side wall and the straight flow exit in the $\epsilon = 1$ case may have caused the additional pressure drop in the pin fin channel. The overall friction factors for the other three ejection ratios are generally lower than those in the previous two cases. The low values of the overall friction factor for the partial lateral ejection cases may be due to the turning of the main flow toward the lateral flow exit in such a way that the pin array appears to be an in-line array to the flow.

The overall friction factors for configurations C through F are presented in Figs. 12 and 13. The additional pressure drops

across the exit blockages significantly affect the overall friction factor, which no longer depends on the ejection ratio only. However, in all cases, the overall friction factor is not dependent on the Reynolds number over the range of Reynolds number studied.

The pressure drop across a given exit blockage depends on the configuration of the flow cross section of the blockage. When the flow cross section of an exit blockage is small, it can be expected that the pressure drop across the exit blockage will be large. Comparing the pressure drops for the flow of air straight through the pin fin channel with a wide open exit flow cross section (configuration E) and with six evenly distributed holes of 6.4 mm (0.25 in.) in diameter (configuration F) at the exit, the additional pressure drop caused by the partially blocked exit is evident in Fig. 13.

## Concluding Remarks

Experiments have been conducted to study the effects of lateral flow ejection on the overall heat transfer and pressure drops for turbulent flow through pin fin channels with pin length-to-diameter ratio of one and with streamwise and spanwise pin spacings of 2.5 times the pin diameter. The Reynolds number ranges from 6000 to 60,000. The results of the study, which are applicable to gas turbine blade design, show that, for any given ejection ratio (the ratio of the rate of ejection to the total flow rate), the overall Nusselt number increases with increasing Reynolds number according to an equation of the form $Nu = aRe^b$, where $a$ and $b$ are constants. The overall Nusselt number is reduced by as much as 25 percent as the ejection ratio is increased from 0 to 1. The Nu–Re–$\epsilon$ relationship is insensitive to varying the ejection exit cross section geometry. The variation of the overall Nusselt number with respect to the ejection ratio is given by the equation $(Nu/Nu_0) = (Nu_1/Nu_0)^\epsilon$, where $Nu_0$ and $Nu_1$ are the overall Nusselt numbers in the zero and 100 percent lateral flow ejection cases, respectively.

The results also show that the overall friction factor is independent of the flow Reynolds number over the range of Reynolds number studied. However, the friction factor is strongly dependent on the ejection ratio as well as the straight flow exit and lateral ejection flow exit geometries.

## Acknowledgments

This research was supported in part by the National Science Foundation (Grant No. MEA 83-00722).

## References

Brigham, B. A., and VanFossen, G. J., 1984, "Length to Diameter Ratio and Row Number Effects in Short Pin Fin Heat Transfer," ASME *Journal of Engineering for Gas Turbines and Power*, Vol. 106, pp. 241–245.

Jones, O. C., Jr., 1976, "An Improvement in the Calculation of Turbulent Friction in Rectangular Ducts," ASME *Journal of Fluids Engineering*, Vol. 98, pp. 173–181.

Kim, Y. S., 1987, "Turbulent Heat Transfer in Short Pin Fin Channels," Ph.D. Thesis, Texas A&M University, College Station, TX.

Kline, S. J., and McClintock, F. A., 1953, "Describing Uncertainties in Single-Sample Experiments," *Mechanical Engineering*, Vol. 75, pp. 3–8.

Lau, S. C., Kim, Y. S., and Han, J. C., 1987, "Local Endwall Heat/Mass Transfer in a Pin Fin Channel," *Heat Transfer and Fluid Flow in Rotating Machinery*, Hemisphere, Washington, DC, pp. 64–75.

Lau, S. C., Kim, Y. S., and Han, J. C., 1985, "Effects of Fin Configuration and Entrance Length on Local Endwall Heat/Mass Transfer in a Pin Fin Channel," ASME Paper No. 85-WA/HT-62.

Metzger, D. E., Berry, R. A., and Bronson, J. P., 1982a, "Developing Heat Transfer in Rectangular Ducts With Staggered Arrays of Short Pin Fins," ASME JOURNAL OF HEAT TRANSFER, Vol. 104, pp. 700–706.

Metzger, D. E., and Haley, S. W., 1982b, "Heat Transfer Experiments and Flow Visualization for Arrays of Short Pin Fins," ASME Paper No. 82-GT-138.

Metzger, D. E., Fan, C. S., and Haley, S. W., 1984, "Effects of Pin Shape and Array Orientation on Heat Transfer and Pressure Loss in Pin Fin Arrays," ASME JOURNAL OF HEAT TRANSFER, Vol. 106, pp. 252–257.

VanFossen, G. J., 1982, "Heat-Transfer Coefficients for Staggered Arrays of Short Pin Fins," ASME *Journal of Engineering for Power*, Vol. 104, pp. 268–274.

# Experiments on Forced Convection From a Horizontal Heated Plate in a Packed Bed of Glass Spheres

**K. J. Renken**

Department of Mechanical Engineering,
University of Wisconsin—Milwaukee,
Milwaukee, WI 53201

**D. Poulikakos**

Department of Mechanical Engineering,
University of Illinois at Chicago,
Chicago, IL 60680

*This paper presents an experimental investigation of boundary-layer forced convective heat transfer from a flat isothermal plate in a packed bed of spheres. Extensive experimental results are reported for the thermal boundary-layer thickness, the temperature field, and the local wall heat flux (represented by the local Nusselt number). Theoretical findings of previous investigations using the Darcy flow model as well as a general model for the momentum equation accounting for flow inertia and macroscopic shear with and without variable porosity are used to evaluate the theoretical models. Several trends are revealed regarding the conditions of validity of these flow models. Overall, the general flow model including variable porosity appears to perform better, even though the need for serious improvements in modeling becomes apparent.*

## Introduction

The number of investigations on convective heat transfer through a fluid-saturated porous medium has been on the rise during the past decade. Many thermal engineering systems are in need of a better understanding of forced convection through porous materials. Such applications include building thermal insulations, grain storage, heat exchangers, geothermal systems, oil extraction, filtering devices, and catalytic reactors. These diverse applications have made it essential that the thermal engineering community focus its research interest on the fundamentals of porous media transport processes.

Most of the existing engineering studies interested in fluid flow and heat transfer phenomena in porous media are based on the Darcy flow model, which states that the volumetrically averaged velocity is proportional to the pressure gradient. This simplified linear mathematical model performs well within a limited range of "slow" flows, but it neglects several important physical effects. These effects include the boundary, the inertia, and the variable porosity effects that predominate in many thermal engineering applications. The boundary effect accounted for by the Brinkman friction term in the momentum equation makes it possible to satisfy the no-slip condition on a solid boundary. The Forchheimer inertia term represents the inertial forces, which are significant for "fast" flows. Finally, the spatial variation of the matrix porosity is responsible for flow channeling, which yields high velocity near a solid boundary.

The boundary and inertia effects in porous media forced convective heat transfer from a flat plate were first analyzed by Vafai and Tien (1981) for a constant porosity medium. These effects were shown to play a significant role in highly permeable media, high Prandtl number fluids, and fast flows. A similar study was reported recently by Beckermann and Viskanta (1987) and Vafai and Thiyagaraja (1987). For the case of a fully developed momentum boundary layer, a closed-form analytical solution for the velocity profile and an approximate solution for the thermal boundary-layer thickness and the local Nusselt number were obtained by the former. The investigations note that porosity variations near the wall, for example, in packed beds of spheres, will alter the results considerably due to the channeling of the flow near the wall. This variable porosity effect has been observed and studied by several researchers (Schwartz and Smith, 1958; Schertz and Bischoff, 1969; Benenati and Brosilow, 1962; Chandrasekhara and Vortmeyer, 1979) interested in velocity distributions in packed beds.

The works of Vafai (1984) and Vafai et al. (1985) document theoretically the effect of flow channeling on flat plate forced convection while Poulikakos and Renken (1987) and Renken and Poulikakos (1988) thoroughly investigate this phenomenon for forced convection at the thermal entry and fully developed regions in a channel filled with a porous medium. In all of these investigations, significant differences when compared to the Darcy model were found in the flow field, the temperature field, and in heat transfer.

Very few studies on forced convection through a porous medium are experimental. Even fewer studies have compared modeling and experiments. The works reported by Vafai et al. (1985) and Renken and Poulikakos (1988) exemplify the few exceptions. More relevant to the present study is the work of Vafai et al. (1985). Their investigation focused on porous media flat plate boundary-layer forced convection for a matrix consisting of 5 and 8-mm-dia. packed spheres. Comparisons of experimental and numerical results were presented for the average Nusselt number as a function of the Reynolds number based on pore diameter and the two types of beads used. Numerical results for the temperature distribution and local Nusselt number are also presented. No local experimental heat transfer results (temperature profiles or Nusselt numbers) were reported.

This paper presents an experimental study of forced convection from an isothermal horizontal flat plate in a bed of glass spheres. The experiments are performed in the regime of parameters where most of the above-mentioned effects are important. The experimental setup measures the solid boundary and the fluid/porous matrix composite temperatures as well as the local heat flux at the solid boundary. An experimental approximation for the growth of the developing thermal boundary-layer thickness is also reported. The experimental findings are then compared to closed-form, approximate, and numerical solutions of previous investigations (Vafai and Tien, 1981; Beckermann and Viskanta, 1987; Vafai et al., 1985; Cheng, 1977; Bejan, 1985).

Based on the agreement of theory and the present experiments, certain conclusions are drawn regarding the range of validity and the accuracy of the theoretical models.

Contributed by the Heat Transfer Division for publication in the JOURNAL OF HEAT TRANSFER. Manuscript received by the Heat Transfer Division March 3, 1988. Keywords: Forced Convection, Packed and Fluidized Beds, Porous Media.

## Experimental Apparatus and Procedures

The experimental apparatus employed in this investigation is shown schematically in Fig. 1. The system provided a means of accurately measuring the fluid flow and heat flux for an experiment whose main purpose was to obtain forced convection results for a horizontal flat plate inside a liquid-saturated porous medium.

The experimental apparatus (Fig. 1) is a horizontal isothermal surface constructed of a sheet of 7750 alloy aluminum. This surface constitutes the top wall of a rectangular channel filled with glass beads and has dimensions of 1.91 × 19.0 × 152 cm (height × width × length). The metal surface is attached to acrylic side walls (7.62 × 15.2 × 152 cm), which are fastened to a bottom plate with dimensions identical to those of the upper surface. Attached to the heated test section is an entrance section, which is constructed entirely of acrylic plastic and has dimensions of 7.62 × 15.2 × 91.4 cm. In this section the flow becomes uniform before it enters the heated section. The upper portion of each section is removable so that the porous medium can be packed easily into the system. The porous medium consisted of uniform 3-mm-dia. soda lime glass spheres, which were carefully placed into the test section to ensure uniformity in the structure of the porous matrix. The same packing was used in all experiments. The measured core porosity of the liquid-saturated packed spheres is 0.369. The spheres are held in place at both ends of the test section by rigid meshed screens.

Temperatures along the plate surface and throughout the packed bed of spheres are monitored with 132 copper-constantan thermocouples of approximately 0.5 mm o.d. Sixteen thermocouples are embedded into the plate surface to measure the constant boundary temperature while 116 thermocouples are positioned vertically within the porous matrix along the horizontal centerline of the test section. These thermocouples are attached to 11 different porous vertical screens by being copper-oxidized into specially designed thermocouple nylon screen holders. The experimental accuracy of the thermocouples is ±0.15°C.

Upstream of the test section is a water reservoir that stored degassed tap water. To ensure particle-free water, a 5 μm polypropylene water filter is inserted into the flow system. Three air relief valves located in the entrance section allowed the removal of gas bubbles that may have passed through the water filter. A submersible pump and two globe valves controlled the steady-state flow conditions, which are reached within a relatively short period of time. Two pressure taps inserted from the side walls into the bed of packed spheres are connected to a U-tube mercury manometer, which measures the differential pressure across the porous medium heated test section. The precision of the manometer is dependent upon the liquid used and is approximately 12.4 Pa for mercury filled manometers. The accuracy of the pressure measurement was 1 percent. An industrial rotameter measures the flow rates, which have a range of 0.757–9.46 ℓ/min with a factory calibrated accuracy of ±2 percent full scale. An additional experimental check on the flow-rate calibration produced negligible variation in measured values.

The heating of the top wall is performed with the help of ten mica strip heaters, which are clamped along the length of the top aluminum plate 5.08 cm apart. Each strip heater could provide 500 W and a maximum sheath temperature of 900°F. For efficient operation, a thin layer of silicone heat sink compound was applied to the bottom of each heater, which is then fastened firmly to the aluminum plate by 6.35-cm-wide clamping bars. The entire heated test section is insulated with a high-

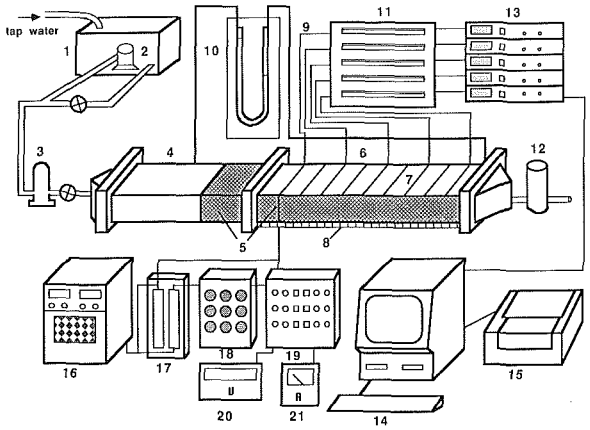


1. Water Tank 2. Submersible Pump 3. Water Filter 4. Entrance Section 5. Fluid Saturated Packed Sphere Bed 6. Heated Section 7. Strip Heaters 8. Insulation 9. Thermocouples 10. U-tube Mercury Manometer 11. Thermocouples Board 12. Rotameter 13. Data Acquisition Units 14. Personal Computer 15. Printer 16. Power Supplies 17. Copper Strip Board 18. Rheostat Board 19. Circuit Board 20. Voltmeter 21. Ammeter

**Fig. 1 Experimental setup**

## Nomenclature

$C$ = inertia coefficient (0.55 for a matrix of spherical beads)
$d_p$ = sphere diameter
$K$ = permeability, equation (3)
$K_\infty$ = free-stream permeability
$k_b$ = thermal conductivity of glass spheres
$k_e$ = effective thermal conductivity of porous medium, equations (1) and (2)
$k_f$ = fluid thermal conductivity
$L$ = horizontal extent of flat plate
$\mathrm{Nu}_X$ = local Nusselt number
$P$ = pressure
$\mathrm{Pe}_X$ = local Peclet number, equation (9)
$\mathrm{Pr}_e$ = effective Prandtl number, equation (17)
$\mathrm{Pr}_m$ = modified Prandtl number, equation (12)
Re = convective Reynolds number, equation (11)
$\mathrm{Re}_m$ = modified Reynolds number, equation (15)
$\mathrm{Re}_p$ = Reynolds number based on pore diameter $= \dfrac{K_\infty d_p}{\rho\nu^2}\dfrac{dP}{dX}$
$T$ = temperature
$T_w$ = wall temperature
$T_\infty$ = free-stream temperature
$U_c$ = characteristic velocity, equation (16)
$U_\infty$ = free-stream velocity
$u$ = $x$-component velocity
$u_\infty$ = dimensionless free-stream velocity, equation (18)
$X$ = horizontal Cartesian coordinate, Fig. 2
$x$ = dimensionless horizontal coordinate = $X/\sqrt{K_\infty}$
$Y$ = vertical Cartesian coordinate, Fig. 2
$y$ = dimensionless vertical coordinate = $Y/\sqrt{K_\infty}$
$\alpha_e$ = effective thermal diffusivity of porous medium
$\Delta_T$ = thermal boundary-layer thickness
$\delta_T$ = dimensionless thermal boundary-layer thickness = $\Delta_T/\sqrt{K_\infty}$
$\eta$ = dimensionless similarity variable, equation (8)
$\theta$ = dimensionless temperature, equation (7)
$\mu$ = fluid dynamic viscosity
$\nu$ = fluid kinematic viscosity
$\rho$ = fluid density
$\tau_W$ = dimensionless wall shear stress, equation (20)
$\phi$ = porosity
$\phi_\infty$ = core porosity

temperature board, which is 2.54 cm thick and provides high thermal resistance. The estimated heat loss was approximately 2 percent. Two d-c power supplies are employed to power the strip heaters; ten rheostats control the flow of current, and hence the temperature of the heated surface. An ammeter and a logging multimeter are used to measure current and voltage, respectively. A modern data acquisition system is employed to record accurately and swiftly the temperatures from the many thermocouples that were embedded in the porous medium and positioned in the heated plate. The data acquisition units contained thermocouple compensation and built-in Type T thermocouple linearization.

Measurements were carried out on a consistent basis once steady-state hydrodynamic and thermal conditions were reached. Temperatures, flow rates, total currents, and total voltages, as well as currents and voltages for each strip heater, were recorded when a complete set of temperature data showed no difference to within the experimental accuracy of $\pm 1°C$. The experiments were run within the calibrated range of flow rates and the plate temperatures were varied between 10°C and 40°C. The inlet water temperatures varied between 6°C and 12°C. After each test run the heated test section was emptied, thoroughly flushed, and filled with water.

The fluid properties (e.g., density, specific heat, viscosity, and thermal conductivity) were based on the inlet temperature and were calculated using regression curve fits. The standard error of the fluid property estimates was negligible. The experimental effective thermal conductivity was computed from empirical formulas supplied by the literature (Weaver and Viskanta, 1986; Combarnous and Bories, 1975; Veinberg, 1967; Chellaiah and Viskanta, 1988). For a randomly packed spherical bed, the equations for the parallel and the Veinberg models that were used in the experimental calculations are, respectively:

$$k_e = \phi_\infty\, k_f + (1-\phi_\infty)\, k_b \tag{1}$$

$$k_e + \phi_\infty \left(\frac{k_e}{k_f}\right)^{1/3} (k_b - k_f) - k_b = 0 \tag{2}$$

where $\phi_\infty$ is the experimental value of porosity at the core, $k_f$ is the thermal conductivity of the fluid, and $k_b$ is the thermal conductivity of the glass spheres. Since the experimental value of $k_e$ differed by less than 1 percent for the two models, an average value was used. The permeability $K$ of the liquid-saturated porous medium is dependent on the matrix porosity and sphere diameter and was calculated by the following empirical formula (Ergun, 1952):

$$K = \frac{d_p^2\, \phi^3}{175(1-\phi)^2} \tag{3}$$

The pressure gradient was determined by measuring the differential manometer height and the horizontal differential length, while the free-stream velocity component was an average value based on flow rate and porosity.

The experimental thermal boundary-layer thickness $\Delta_T$ was approximated from the vertical temperature measurements. Eleven thermocouple stations, which consisted of 10–14 thermocouples, were positioned along the heated test section. By comparing the free-stream (inlet) temperature and the vertical thermocouple readings, $\Delta_T$ was estimated. The experimental local Nusselt number was determined as follows:

$$\mathrm{Nu_X} = \left(\frac{\partial T}{\partial Y}\right)_{Y=0} \frac{X}{T_w - T_\infty} \tag{4}$$

where $X$ is the horizontal spatial coordinate from the heated test section entrance. The local wall temperature gradient $(\partial T/\partial Y)_{Y=0}$ was evaluated by using the plate temperature and the reading of the thermocouple in the porous medium nearest to the wall (1.5 mm from the surface), at each station. The local Nusselt number was also evaluated by calculating and nondimensionalizing the heat flux (power) produced by the strip heaters at the wall. The product of the measured current and voltage determined the heat flow across the transfer surface. Good agreement (within 5 percent) between the two methods was found.

## Background on Previous Theoretical Work

Figure 2 shows a schematic of the problem of interest, namely, forced convection from an isothermal horizontal plate to a bed of glass spheres through which a fluid is flowing. The free-stream fluid temperature at the heated section inlet is isothermal and designated as $T_\infty$ ($T_\infty < T_w$). The coordinate system is also defined in Fig. 2.

Three different models will be compared to the experimental results. These models include the Darcy model, a general model that includes the boundary and inertia effects, and a general model with variable porosity. Only the final results of the theoretical solutions will be transferred here. All of the details of the mathematical modeling, the governing equations, and the analysis are found in Vafai and Tien (1981), Beckermann and Viskanta (1987), Vafai et al. (1985), Cheng (1977), and Bejan (1984).

The classical Darcy model is the most popular model used to describe porous media convective heat transfer because of its simplicity and good performance within the range of its validity. For the two-dimensional system of Fig. 2, this model yields (Cheng, 1977; Bejan, 1984):

$$\theta = \mathrm{erf}\left(\frac{\eta}{2}\right) \tag{5}$$

$$\mathrm{Nu_X} = 0.5641\ \mathrm{Pe_X^{1/2}} \tag{6}$$

where

$$\theta = \frac{T_w - T}{T_w - T_\infty} \tag{7}$$

$$\eta = \left(\frac{U_\infty X}{\alpha_e}\right)^{1/2} \frac{Y}{X} \tag{8}$$

$$\mathrm{Pe_X} = \frac{U_\infty X}{\alpha_e} \tag{9}$$

Vafai and Tien (1981) report the following approximation for the dimensionless thermal boundary-layer thickness $\delta_T$:

$$\delta_T \simeq 7 \left(\frac{XL}{\mathrm{Pr_m Re K_\infty}}\right)^{1/2} \tag{10}$$

where

$$\mathrm{Re} = \frac{-K_\infty L}{\rho \nu^2} \frac{dP}{dX} \tag{11}$$

$$\mathrm{Pr_m} = \frac{\nu\phi}{\alpha_e} \tag{12}$$

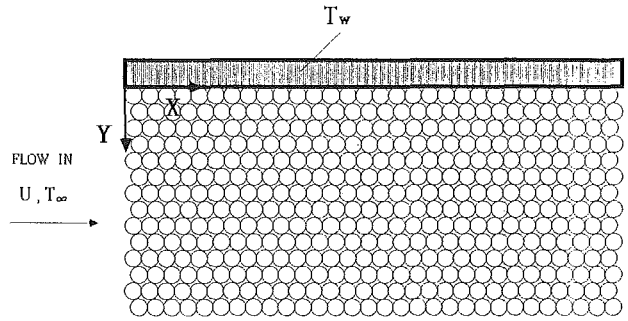


**Fig. 2 Schematic of mathematical model: liquid-saturated packed bed of spheres bounded by an isothermal plate**

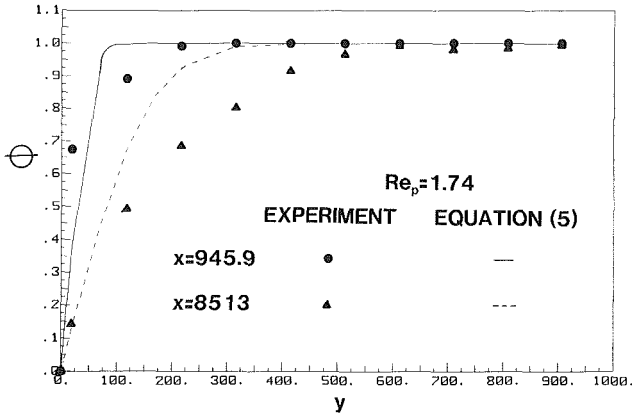


Fig. 3 Comparison of experimental dimensionless temperature distribution with the temperature distribution based on equation (5) for $Re_p$ = 1.74 at two downstream locations

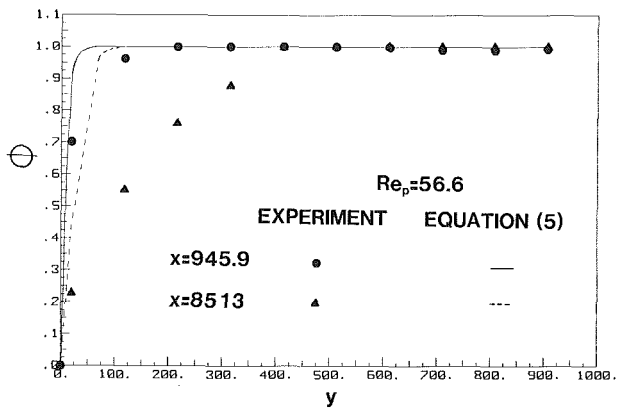


Fig. 4 Comparison of experimental dimensionless temperature distribution with the temperature distribution based on equation (5) for $Re_p$ = 56.6 at two downstream locations

and $L$ is the horizontal extent of the external boundary. The above simplified relation, equation (10), is for the limited case of negligible boundary and inertia effects (Darcy model), which allows for a closed-form solution of the governing equations.

Unlike the Darcy model, the general flow model does not neglect the effects of macroscopic shear and inertia on fluid flow and heat transfer through porous media. Due to the complicated nature of the velocity profile, two approximate solutions using this model were presented by Beckermann and Viskanta (1987) for the cases of very small and very large Prandtl numbers. In the case where the thermal boundary-layer thickness is much larger than the velocity boundary-layer thickness ($Pr_e \to 0$), the following relations were obtained:

$$\delta_T \simeq 6.0 \left(\frac{x}{\mathrm{Re_m Pr_e} u_\infty}\right)^{1/2} \tag{13}$$

$$\mathrm{Nu_X} = (x\mathrm{Re_m Pr_e}\, u_\infty/\pi)^{1/2} \tag{14}$$

where

$$\mathrm{Re_m} = \frac{U_c\sqrt{K_\infty}C}{\nu} \tag{15}$$

$$U_c = \frac{-K_\infty}{\mu}\frac{dP}{dX} \tag{16}$$

$$\mathrm{Pr_e} = \frac{\nu}{\alpha_e C} \tag{17}$$

$$u_\infty = \frac{(1+4\ \mathrm{Re_m})^{1/2}-1}{2\mathrm{Re_m}} \tag{18}$$

For the case of large Prandtl number ($Pr_e \to \infty$), the following local Nusselt number relation was obtained:

$$\mathrm{Nu_X} = 0.5384\,(x^2\mathrm{Re_m Pr_e}\tau_w)^{1/3} \tag{19}$$

where

$$\tau_w = \left[2u_\infty - u_\infty^2 - \frac{2}{3}\ \mathrm{Re_m}\ u_\infty^3\right]^{1/2} \tag{20}$$

is the dimensionless wall shear stress for the fully developed velocity field. The differences in the Nusselt number expressions for the two limiting cases are fairly small at modified Prandtl numbers of the order of one. Equation (14) can be used for Prandtl numbers up to about 0.5, while equation (19) can be used for Prandtl numbers greater than about 10.0.

The last model to be considered, in addition to the effects of flow inertia and macroscopic shear, accounts for variable porosity. No closed-form solutions can be obtained by using this model and for the comparisons we will rely on the numerical results displayed graphically by Vafai et al. (1985).

## Discussion of Results

In this section, the main results of the forced convection boundary-layer experiment are reported and compared to the solutions of the three mathematical models discussed in the last section. In obtaining the experimental results and comparing them to the theoretical models, the following physical parameters were measured: the external boundary and water-saturated porous matrix composite temperatures, the pressure gradient within the porous medium, the water flow rate, the core porosity of the packed bed of spheres, and the voltages and currents of the heating elements. A constant value of effective thermal conductivity of fluid-saturated porous medium is calculated (Weaver and Viskanta, 1986; Combarnous and Bories, 1975; Veinberg, 1967). The experimental results are presented and compared for uniform 3-mm-dia. soda lime glass spheres, except where noted. Presented in Figs. 3 and 4 are the results for the temperature distribution for two different values of $Re_p$ at two representative downstream locations. The experimental results are compared with the analytical solution of the Darcy model, equation (5). The temperature in the porous bed decreases monotonically as we move away from the heated wall. Near the leading edge of the plate ($x = 945.9$) the thermal boundary layer is sharp as the heating effect of the wall is hardly felt by the porous bed. Farther downstream, the thermal boundary layer thickens, reflecting the fact that the heating effect of the wall is communicated within the porous bed.

The theoretical solution is in better agreement with the experimental findings for "slow" flow (Fig. 3, $Re_p = 1.74$). As the flow rate increases (Fig. 4, $Re_p = 56.6$) the agreement deteriorates. This result indicates that the validity of the Darcy flow model becomes questionable for $Re_p = 0(1)$ or greater. An additional observation from Figs. 3 and 4 is that agreement between equation (5) and the experimental data deteriorates as we move away from the leading edge of the plate. It appears that near the leading edge the velocity distribution is close to the "uniform" velocity profile predicted by the Darcy flow model. Another reason for the deterioration of the agreement between theory and experiment downstream is that the Darcy flow model neglects possible variations of porosity, which are important in the near-wall region, for they cause "flow channelling." To this end, all the resulting variations in the thermal diffusivity with porosity were neglected as well in deriving equation (5).

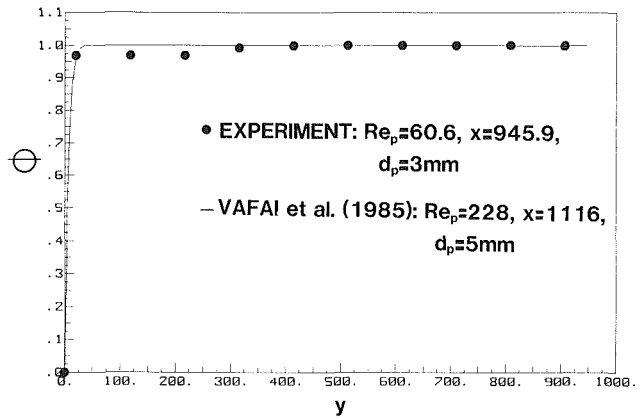


Fig. 5 Comparison of experimental dimensionless temperature distribution with the temperature distribution based on the general model with variable porosity (Vafai et al., 1985)

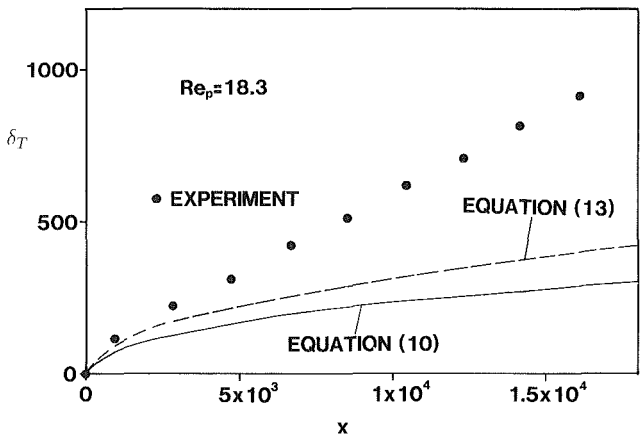


Fig. 7 Comparison of experimental dimensionless thermal boundary-layer thickness with equations (10) and (13) for $Re_p = 18.3$

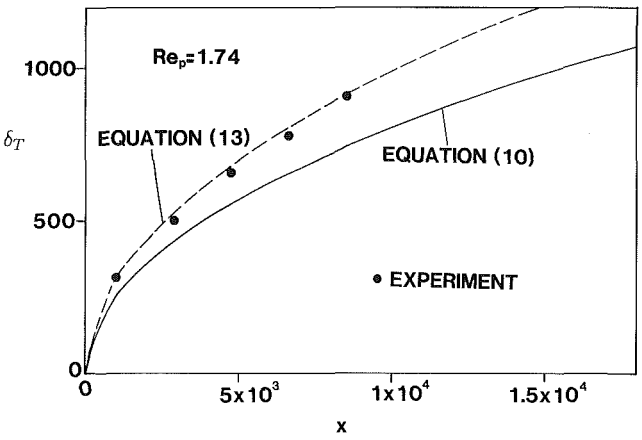


Fig. 6 Comparison of experimental dimensionless thermal boundary-layer thickness with equations (10) and (13) for $Re_p = 1.74$

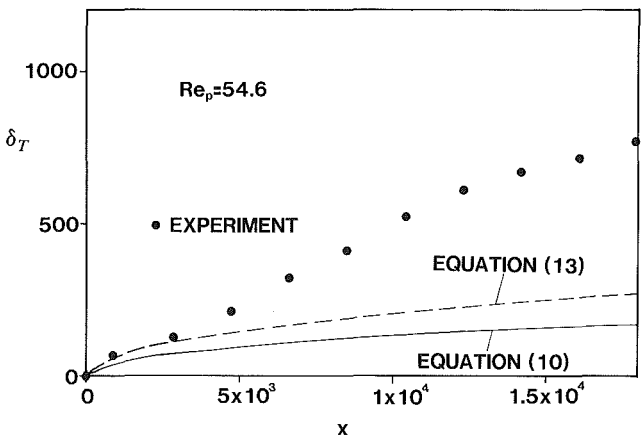


Fig. 8 Comparison of experimental dimensionless thermal boundary-layer thickness with equations (10) and (13) for $Re_p = 54.6$

Figure 5 shows a comparison betwen the present experiment and the theoretical findings of Vafai et al. (1985) who accounted for variable porosity, Brinkman friction, and flow inertia. Note that the $x$-location, the values of $Re_p$, and the bead diameter (5 mm in the theoretical solution) are different for the theory and the experiment. However, the parameters chosen represent the best feasible match. Despite the above discrepancies the agreement appears to be very good. A necessity for the inclusion of variable porosity together with Brinkman friction and flow inertia is indicated; however, no definite conclusions are drawn due to limited theoretical results available in Vafai et al. (1985).

Figures 6-8 present the dependence of the dimensionless thermal boundary-layer thickness $\delta_T$ on the Reynolds number $Re_p$. The experimental thermal boundary-layer thickness was determined by comparing the thermocouple readings at each station to the reading of the free-stream temperature. Since the temperature measurements were taken at select horizontal and vertical locations, it was estimated that the thermal boundary-layer thickness values were accurate within 10 percent. The theoretical model used by Beckermann and Viskanta (1987), equation (13), and that of Darcy's model equation (10), are included for comparison. In all of the Figs. 6-8, the thermal boundary layer thickens as we move downstream. Equation (13) predicts the growth of the thermal boundary layer quite well for $Re_p = 1.74$ (Fig. 6). As $Re_p$ increases to $Re_p = 18.3$ and the $Re_p = 54.6$ (Figs. 7 and 8, respectively) both equations (10) and (13) seriously underpredict the growth of $\delta_T$. The Darcy model underpredicts $\delta_T$ even for $Re_p$ as low as $Re_p = 1.74$ (Fig. 6). Note that in deriving equation (13) variations of porosity and associated variations of the thermal conductivity are neglected. These variations as well as thermal dispersion are of importance for high values of $Re_p$ and probably contribute to the disagreement between theoretical modeling and experiment.

Figures 9-11 show experimental and theoretical results for the local Nusselt number. The estimated overall error for the experimental values of Nu was 5.5 percent. Three theoretical predictions are presented, which include the general model with constant porosity for the cases of very small, equation (14), and very large, equation (19), Prandtl numbers and the Darcy model, equation (6). In all cases (Figs. 9–11) the experiments support the fact that the Nusselt number increases almost linearly with distance from the leading edge of the plate. The Darcy flow model agrees the best with the experiments for $Re_p = 1.90$ (Fig. 9). As the Reynolds number increases, it appears that equation (14) gives the most realistic prediction of the value of $Nu_X$. This is especially true for $Re_p = 32.8$ (Fig. 10). As $Re_p$ increases further all equations overpredict the value of $Nu_X$. Equation (19) performs clearly the worst in Figs. 10 and 11. The physical explanation for the above results is speculated as follows: equation (14) corresponds to the case where $Pr \to 0$ or the momentum equation accounts for inertia and Darcy friction (the Brinkman friction term is negligible). As $Re_p$ increases, inertia becomes important and equation (14) represents the physical situation (Fig.

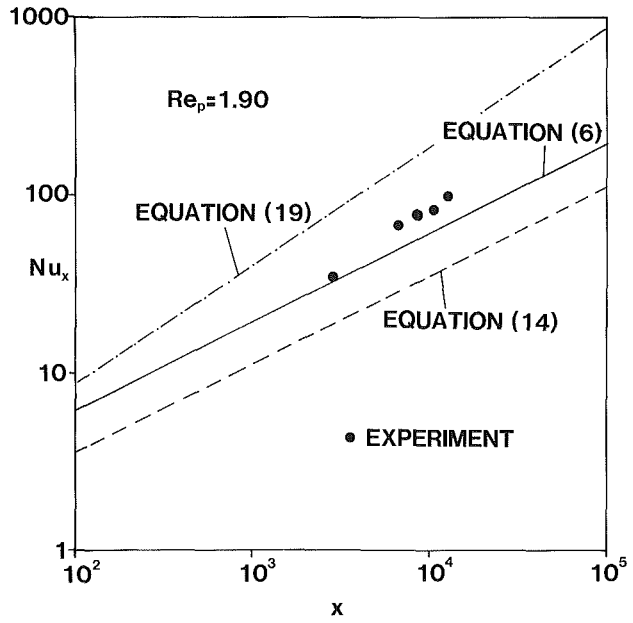


Fig. 9 Nusselt number variation with horizontal coordinate for $Re_p = 1.90$

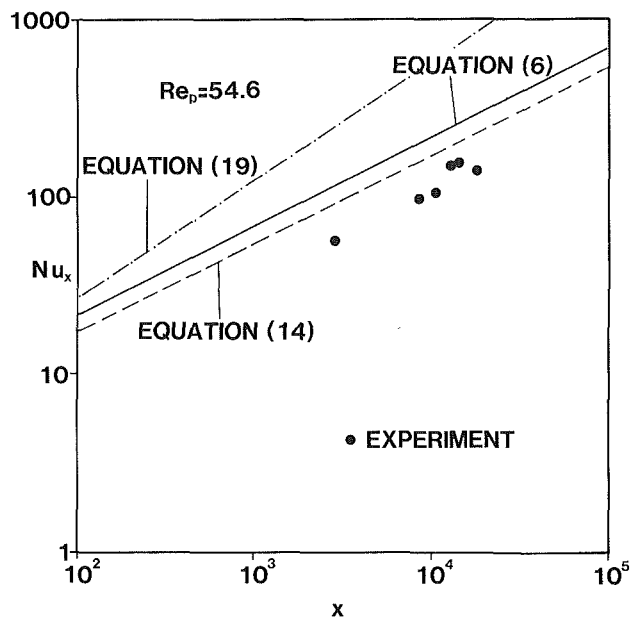


Fig. 11 Nusselt number variation with horizontal coordinate for $Re_p = 54.6$

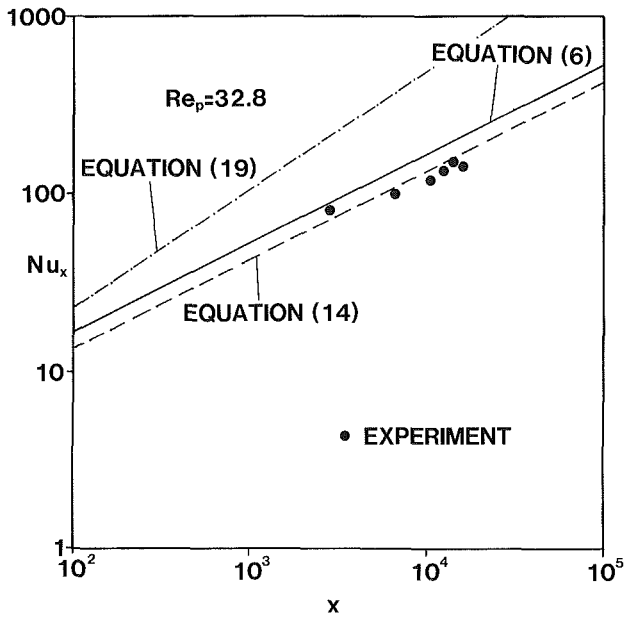


Fig. 10 Nusselt number variation with horizontal coordinate for $Re_p = 32.8$

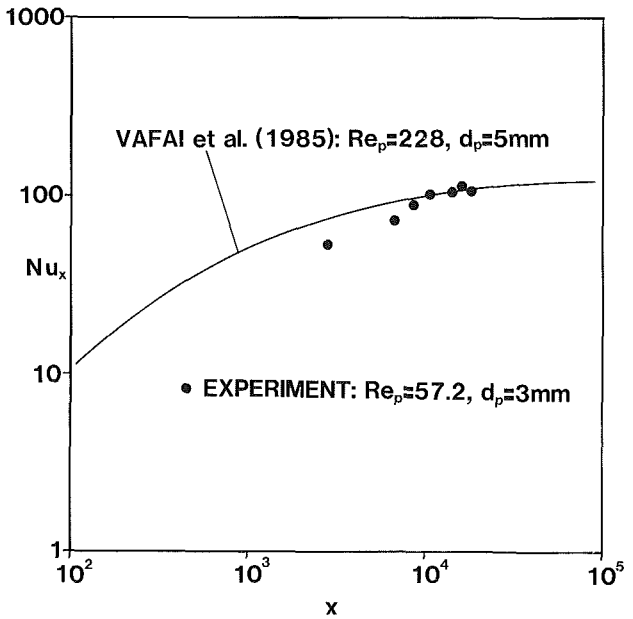


Fig. 12 Comparison of Nusselt number variation to the predictions of Vafai et al. (1985)

10) better. For even larger values of $Re_p$, other phenomena, such as channelling effects caused by porosity variations and dispersion that are not accounted for in equation (14) (Fig. 11), probably become of importance. Equation (19), on the other hand, represents the case where $Pr \rightarrow \infty$ or in physical terms, the case where macroscopic shear (Brinkman friction) dominates the momentum equation. This is never the case in the experiments; the main resistance to the flow is offered by the presence of the bed of spheres (Darcy friction). Macroscopic shear plays only a minor role; hence, equation (19) cannot match the experimental findings for Nu.

Lastly, the experimental results for the local Nussel number are compared to the numerical predictions of Vafai et al. (1985), who, in addition to flow inertia and macroscopic shear, accounted for variable porosity (Fig. 12). Despite the fact that the values of $Re_p$ and the bead diameter in Vafai et al. (1985) are different from the present study, the agreement is quite good. This indicates that inclusion of the effect of porosity variation together with inertia at large values of $Re_p$ (fast flows) is necessary. No further comparisons were possible because of the limited numerical results and the different conditions used for the numerical solution and the present experiments.

## Conclusions

This paper presented an experimental investigation for the problem of forced convection from a flat isothermal plate in a packed bed of glass spheres. The results document the temperature distribution in the porous bed, the growth of the

thermal boundary layer, and the variation of the local heat flux (represented by the local Nusselt number) with distance from the leading edge of the plate.

Several comparisons were made between the experimental findings and existing theoretical results. It was found that the Darcy model predicts the temperature distribution, the growth of the thermal boundary layer, and the Nusselt number quite well for flows with $Re_p \sim 0(1)$ or smaller. In addition, the Darcy model can be used with reasonable success near the leading edge of the plate even for higher Reynolds numbers. Including the effect of flow inertia improves agreement between theory and experiment as $Re_p$ increases. If, in addition to flow inertia, the porosity variation near the wall is accounted for, this agreement is further improved. Assuming that the macroscopic shear is dominant ($Pr \rightarrow \infty$) misrepresents the real situation in the present experiments and is inappropriate for heat transfer predictions.

Finally, the present study presents a solid body of experimental data, which, taking into account the fact that experimental studies are scarce in the porous media heat transfer literature, can provide future modeling attempts with a valuable tool for model validation.

## Acknowledgements

Financial support for this research provided by the National Science Foundation through Grant No. ENG-8451144 and by the University of Illinois at Chicago Abraham Lincoln Graduate Fellowship is greatly appreciated.

## References

Beckermann, C., and Viskanta, R., 1987, "Forced Convection Boundary Layer Flow and Heat Transfer Along a Flat Plate Embedded in a Porous Medium," *Int. J. Heat Mass Transfer*, Vol. 30, pp. 1547–1551.

Bejan, A., 1984, *Convection Heat Transfer*, Wiley, New York.

Benenati, R. F., and Brosilow, C. B., 1962, "Void Fraction Distribution in Packed Beds," *AIChE J.*, Vol. 8, pp. 359–361.

Chandrasekhara, B. C., and Vortmeyer, D., 1979, "Flow Model for Velocity Distribution in Fixed Beds Under Isothermal Conditions," *Thermo and Fluid Dynamics*, Vol. 12, pp. 105–111.

Chellaiah, S., and Viskanta, R., 1988, "Freezing of Saturated and Superheated Liquid in Porous Media," *Int. J. Heat Mass Transfer*, Vol. 31, pp. 321–330.

Cheng, P., 1977, "Combined Free and Forced Convection Flow About Inclined Surfaces in Porous Media," *Int. J. Heat Mass Transfer*, Vol. 20, pp. 807–814.

Combarnous, M. A., and Bories, S. A., 1975, "Hydrothermal Convection in Saturated Porous Media," *Advances in Hydroscience*, Academic Press, NY, Vol. 10, pp. 231–307.

Ergun, S., 1952, "Fluid Flow Through Packed Columns," *Chem. Eng. Prog.*, Vol. 48, pp. 89–94.

Poulikakos, D., and Renken, K. 1987, "Forced Convection in a Channel Filled With a Porous Medium Including the Effects of Flow Inertia, Variable Porosity and Brinkman Friction," ASME JOURNAL OF HEAT TRANSFER, Vol. 109, pp. 880–888.

Renken, K. J., and Poulikakos, D., 1988, "Experiment and Analysis of Forced Convective Heat Transport in a Packed Bed of Spheres," *Int. J. Heat Mass Transfer*, Vol. 31, No. 7, pp. 1399–1408.

Schertz, W. M., and Bischoff, K. B., 1969, "Thermal and Material Transport in Non-isothermal Packed Beds," *AIChE J.*, Vol. 15, pp. 597–604.

Schwartz, C. E., and Smith, J. M., 1958, "Flow Distribution in Packed Beds," *Ind. Eng. Chem.*, Vol. 45, pp. 1209–1218.

Vafai, K., 1984, "Convective Flow and Heat Transfer in Variable Porosity Media," *J. Fluid Mechanics*, Vol. 147, pp. 233–259.

Vafai, K., and Thiyagaraja, R., 1987, "Analysis of Flow and Heat Transfer at the Interface Region of a Porous Medium," *Int. J. Heat Mass Transfer*, Vol. 30, pp. 1391–1405.

Vafai, K., and Tien, C. L., 1981, "Boundary and Inertia Effects on Flow and Heat Transfer in Porous Media," *Int. J. Heat Mass Transfer*, Vol. 24, pp. 195-203.

Vafai, K., Alkire, R. L., and Tien, C. L., 1985, "An Experimental Investigation of Heat Transfer in Variable Porosity Media," ASME JOURNAL OF HEAT TRANSFER, Vol. 107, pp. 642–647.

Veinberg, A. K., 1967, "Permeability, Electrical Conductivity, Dielectric Conclusions," *Soviet Physics—Doklady*, Vol. 11, pp. 593–595.

Weaver, J. A., and Viskanta, R., 1986, "Freezing of Liquid-Saturated Porous Media," ASME JOURNAL OF HEAT TRANSFER, Vol. 108, pp. 654-659.

# Free-Stream Turbulence Effects on Convex-Curved Turbulent Boundary Layers

**S. M. You**
Research Assistant.

**T. W. Simon**
Associate Professor.

**J. Kim**
Research Assistant.

University of Minnesota, Minneapolis, MN 55455

*Free-stream turbulence intensity effects on a convex-curved turbulent boundary layer are investigated. An attached fully turbulent boundary layer is grown on a flat plate and is then introduced to a downstream section where the test wall is convexly curved, having a constant radius of curvature. Two cases, with free-stream turbulence intensities of 1.85 and 0.65 percent, are discussed. They were taken in the same facility and with the same strength of curvature, $\delta/R = 0.03$–$0.045$. The two cases have similar flow conditions upon entry to the curve, thus separating the free-stream turbulence effects under study from other effects. The higher turbulence case displayed stronger curvature effects on the skin friction coefficient $C_f$, and on streamwise-normal and shear stress profiles, than observed in the lower turbulence case. Observations of this are: (1) As expected, the higher turbulence case has a higher $C_f$ value ($\sim 5$ percent) upstream of the curve than does the lower turbulence case, but this difference diminishes by the end of the curve. (2) Streamwise turbulence intensity profiles, differing upstream of the curve for the two cases, are found to be similar near the end of the curve, thus indicating that the effect of curvature is dominating over the effect of free-stream turbulence intensity. Many effects of curvature observed in the lower turbulence intensity case, and reported previously, e.g., a dramatic response to the introduction of curvature and the rapid assumption of an asymptotic shape within the curve, are also seen in the higher turbulence case.*

## 1 Introduction and Review of Previous Work

The present experimental study was conducted to enhance the knowledge of curved turbulent flows and to expand the data base used for development of computational models. Despite the considerable work on the effects of curvature, the present study is the first showing the effects of free-stream turbulence intensity (or disturbance level) on a convex-curved turbulent boundary layer. It is important to investigate the effect of turbulence intensity with curvature since accurate predictions of skin friction and heat transfer, under the combined effects of curvature and free-stream turbulence intensity, are needed in the design of many important devices, e.g., fluid machinery where airfoils are operated in a highly turbulent environment. The present study is a continuation of the convex curvature turbulent boundary layer study presented by You et al. (1986) in which two lower turbulence cases with different radii of convex curvature were tested ($\delta/R = 0.013$ and 0.03). The stronger curved case of the two ($\delta/R = 0.03$) is the base case for the present study, which isolates the turbulence intensity effect. The following, then, presents high free-stream turbulence data for the first time and compares these data to previously presented data taken on the same facility with nearly the same $\delta/R$ value but with a lower disturbance level. The higher disturbance case has a free-stream turbulence intensity level of 1.85 percent. This is lower than would be experienced in some practical devices, e.g., turbomachinery, but is shown herein to be sufficiently high to display the effect of increased turbulence intensity on momentum and heat transport. It is felt that cases with higher levels of free-stream turbulence intensity, though interesting, may be less useful for this particular comparison in that they would suffer from a rather high degree of nonisotropy and, possibly, nonhomogeneity of free-stream turbulence, confusing the study and requiring considerably more detailed characterization of the free-stream turbulence (e.g., scales and turbulence intensity values in the three principal directions).

Bradshaw (1973) published a comprehensive survey of the literature on the effects of streamwise curvature showing that the ratio of boundary layer thickness to radius of wall curvature, $\delta/R$, was an appropriate descriptor for the strength of curvature. Carefully controlled and detailed experiments on mild ($\delta/R = 0.01$) and strong ($\delta/R > 0.05$) convex-curved boundary layers were subsequently performed by So and Mellor (1973), Mayle et al. (1979), Gibson et al. (1982, 1984), Gibson and Verriopoulos (1984), Simon and Moffat (1982, 1983), Gillis and Johnston (1983), Muck et al. (1985), and Hoffmann et al. (1985). They confirmed that streamwise curvature has a marked effect on turbulence structure, heat transfer and skin friction.

You et al. (1986) added heat transfer and fluid mechanics data on a mildly curved convex surface, with recovery from curvature, to the data base. This test was designed so that $\delta/R$ could be changed by varying $R$ in a single test facility from mild ($\delta/R = 0.013$) to moderately strong ($\delta/R = 0.03$). Although their measurements showed the same trends for both cases, the effects of the different strengths of curvature were clearly observable. Some of these effects are:

1 The percentage decrease in St and $C_f$ from expected flat-wall values is almost an order of magnitude greater than the magnitude of $\delta/R$; 10 percent decrease for $\delta/R = 0.013$ and 20 percent for $\delta/R = 0.03$. Bradshaw (1973) stated that this should be expected.

2 The turbulent Prandtl number deduced from the mean velocity and temperature profiles increases within the curve about 20 percent for $\delta/R = 0.013$ and 25 percent for $\delta/R = 0.03$.

3 Shear stress profiles, plotted as $-\overline{u'v'}/U_{pw}^2$ versus $y/\delta$, show a self-similar shape within the curve, even for the weaker curvature case.

A more detailed discussion of this data set is given by You (1986), You et al. (1986), and Kim (1986).

Contributed by the Heat Transfer Division and presented at the ASME Winter Annual Meeting, Anaheim, California, December 7–12, 1986. Manuscript received by the Heat Transfer Division February 19, 1987. Paper No. 86-WA/HT-46. Keywords: Forced Convection, Turbulence.

Many investigators have reported on the effect of free-stream turbulence in noncurved flows; some of the recent ones are Meier and Kreplin (1980), Simonich and Bradshaw (1978), and Blair (1983a, 1983b). Meier and Kreplin (1980) concluded that increased free-stream turbulence levels increase skin friction and boundary layer growth rate and that mean velocity profiles become similar in shape to those of pipe flow. They also suggested that, for turbulence levels less than 1 percent, $C_f$ changes proportionally to $(u'/U)^2_\infty$ and for turbulence levels higher than 1 percent, $C_f$ changes proportionally to $(u'/U)_\infty$.

Simonich and Bradshaw (1978) investigated the effect of free-stream turbulence on heat transfer. Their measurements, with turbulence intensities up to 7 percent, showed that Stanton numbers increased with increasing free-stream turbulence.

In 1983, several tests were conducted by Blair (1983a, 1983b) in a zero pressure gradient two-dimensional channel and with turbulence intensities varying from 0.25 to 7 percent, showing the effects of free-stream turbulence on turbulent boundary layer heat transfer and hydrodynamics. He concluded that a free-stream turbulence intensity of 6 percent increased skin friction and heat transfer rates approximately 14 and 18 percent, respectively. He also found that the Reynolds analogy factor ($2St/C_f$) increased by just over 1 percent for each 1 percent increase in free-stream turbulence intensity.

## 2 Experimental Apparatus

The present experiment was conducted in an open-circuit, blown-type wind tunnel constructed with an upstream developing section, a curved section, and a downstream straight section (Fig. 1). Details of this wind tunnel are given by You (1986). The test channel is rectangular, 68 cm wide and 11.4 cm deep. The heated test wall consists of a 1.4-m-long developing section and a 1.4-m-long curved section of 0.9 m radius of curvature followed by a straight section.

The laminar boundary layer was tripped in the lower-turbulence case, with a 1.0-mm-high, 12.7-mm-wide strip that spanned the full channel width. It was installed 10 cm downstream of a suction slot so that a spanwise-uniform turbulent boundary layer was established in the measurement area. Higher turbulence levels were obtained by inserting a coarse grid constructed of 2.5 cm aluminum strips in a square array on 10 cm centers at the entrance of the nozzle. A turbulence intensity, normalized by $U_{pw}$, of 1.85 percent was achieved in the test region. In the higher turbulence case, the boundary layer trip was removed and the boundary layer was allowed to pass naturally through transition. In both cases, Stanton numbers measured using embedded thermocouples and uniform heating of the test wall were spanwise uniform upstream of the curve to within 4 percent of the mean.

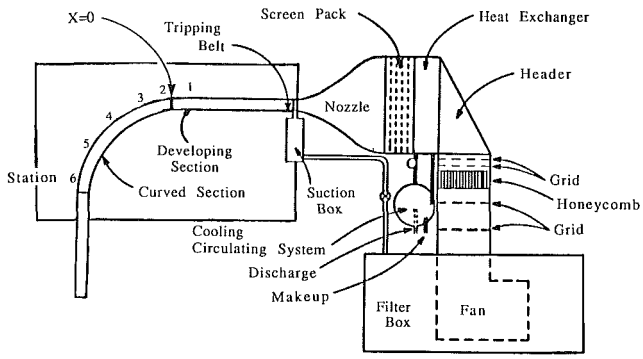


**Fig. 1 Plan view of the curved boundary layer facility**

The test wall was heated to nominally 8°C above the free-stream temperature with a uniform heat flux 255 W/m$^2$. Stanton number data were corrected for back-side heat loss, radiation loss, streamwise conduction loss, recovery effects, and the effects of temperature and humidity on fluid properties. The uncertainty in the Stanton number data was approximately 5 percent. Details of these corrections and the uncertainty analysis are given by You (1986), Wang and Simon (1987, 1988), and Wang et al. (1985).

Static pressures were measured through 0.64-mm-dia taps in the opposite wall and side walls. In the curved region, these pressures were used to estimate the static pressure at the test wall assuming potential flow. In all cases, the concave wall was adjusted to give a uniform static pressure on the convex wall. Mean velocity profiles were measured with a 0.34 mm i.d. pitot tube. Mean temperature profiles were measured with a two-dimensional boundary layer thermocouple probe. Turbulence measurements were taken in an isothermal flow with constant-temperature hot-wire anemometry: a horizontal wire for normal stress measurements and a cross wire for shear stress measurements. Uncertainties of the normal and shear stress measurements were estimated to be less than 5 and 10 percent, respectively. The digitized anemometer signals were linearized and processed within the computer. Signals from

## Nomenclature

$C_f$ = skin friction coefficient
$C_p$ = static pressure coefficient $= 2(P_{s,w} - P_{s,ref})/\rho U^2_{pw,ref}$
$c_p$ = specific heat
$H$ = shape factor
$P$ = pressure
Pr = Prandtl number
$Pr_t$ = turbulent Prandtl number
$q_t$ = heat flux
$R$ = wall radius of curvature
Re = Reynolds number
St = Stanton number
$2St/C_f$ = Reynolds analogy factor
$T$ = mean temperature
$T^+$ = normalized mean temperature $= (T_w - T)U\tau/(q''_w/\rho c_p)$
T.I. = turbulence intensity $= u'_\infty/U_{pw}$
$U$ = streamwise mean velocity
$U^+$ = normalized streamwise velocity $= U/U_\tau$
$U_\tau$ = shear velocity $= \sqrt{\tau_w/\rho}$
$t'$ = fluctuating component of temperature
$u'$ = fluctuating component or root mean square of fluctuating streamwise velocity
$-\overline{u'v'}$ = Reynolds shear stress
$v'$ = fluctuating component of velocity normal to the test wall
$x$ = streamwise distance
$y$ = distance normal to the test wall
$Y^+$ = normalized distance normal to the test wall $= yU_\tau/\nu$
$Y^+_{Cl}$ = conduction layer thickness in inner coordinates
$\delta$ = boundary layer thickness based on 99.5 percent of potential flow velocity
$\theta$ = momentum thickness
$\kappa$ = Karman constant = 0.41
$\nu$ = kinematic viscosity
$\rho$ = density
$\tau$ = shear stress

**Subscripts**

$pw$ = potential flow value at the wall
$ref$ = reference
$s$ = static
$w$ = wall value
$\infty$ = free-stream value

the cross-wire probe were digitized simultaneously. Averages were taken over a period of 40 s. Wall skin friction ($C_f$) measurements were made using the Clauser technique whereby $C_f$ is chosen so that the velocity data agreed with the law of the wall.

The time-averaged velocity measured in the potential core of the developing section, nominally 16 m/s, was uniform to within 0.2 percent of the mean and the time-averaged temperature, nominally 26°C, was uniform to within 0.03°C of the mean. Heat flux on the test wall was uniform to within 1 percent of the nominal value and $C_p$ was uniform to within 3 percent of the nominal value. Normalized free-stream turbulence intensity values, $u'_\infty/U_{pw}$, were 0.65 and 1.85 percent over the streamwise length in which data were taken. Turbulence quantities in the other two directions $v'$ and $w'$ were not measured, but because the grid was well upstream of the first station and because the turbulence levels were not extremely high, it is expected that the turbulence is reasonably isotropic at the measurement stations. Spanwise variations of Stanton numbers, measured within the central span of 30 cm, were typically less than 5 percent from the mean. Secondary flow measurements, taken with a Conrad probe, showed skew angles of less than 2 deg within the curve. Energy and momentum balances over the full test region showed closure to within 5 and 3 percent, respectively. This assured that the boundary layer was sufficiently two-dimensional and that secondary flow effects were minimal.

## 3 Results and Discussion

Descriptors of the two cases compared in the present paper and the locations of profile measurement stations are listed in Tables 1 and 2. Case 1 refers to the lower free-stream turbulence intensity case (T.I. = 0.65 percent). The results of this case have been reported earlier by You et al. (1986). Case 2 (T.I. = 1.85 percent) results have not been reported previously. Measurements of the mean velocity profiles at station 1 were compared with the measurements of Purtell et al. (1981), and were found to be in excellent agreement. Streamwise normal turbulence intensity profiles at station 1 are compared with the data of Erm et al. (1987) on Fig. 2. It was concluded from the excellent agreement of case 1 with these data sets that the boundary layer achieved by artificial tripping has the characteristics of a turbulent boundary layer with zero pressure gradient on a smooth wall.

**Table 1 Descriptors of Cases 1 and 2**

| | CASE 1 | CASE 2 | |
|---|---|---|---|
| R | 90 | 90 | (cm) |
| $U_{pw}$ | 16.32 | 15.83 | (m/s) |
| T.I. | 0.65 | 1.85 | (%) |
| δ/R at B.O.C.* | 0.03† | 0.039† | |
| δ/R at E.O.C.* | 0.04† | 0.045† | |
| $Re_\theta$ at B.O.C.* | 3405† | 3030† | |

*B.O.C. -- Beginning of Curvature (x=0 cm)

*E.O.C. -- End of Curvature (x=125 cm)

† Estimated Values

**A Summary of the Base Case (Case 1): $R = 90$ cm, $\delta/R = 0.03$–$0.046$, and T.I. = 0.65 percent.** The effects of streamwise convex curvature on a turbulent boundary layer, as seen in the base case and documented by You et al. (1986), are:

1 Mean velocity and temperature profiles show shortened log-linear regions and enhanced wake regions in the curve.

2 Curvature increases the turbulent Prandtl number, deduced from the mean velocity and temperature profiles, by about 25 percent.

3 Reduced momentum thickness growth rate and increased shape factor $H$ within the curve are observed.

4 A rapid decrease of St and $C_f$ at the beginning of the curve is observed followed by a slow decrease within the curve. They become 20 percent lower than the expected flat-wall values.

5 Streamwise-normal turbulence intensity profiles show a fast response to the introduction of curvature with a large reduction of the near-wall peak. A self-similar shape is attained midway through the curve and continues throughout the curve.

The effect of varying the radius of curvature on curved two-dimensional boundary layers, including the process of recovery from curvature, was previously investigated and reported by You et al. (1986). In that study, the base case for the present study was compared to a second case, which had stronger curvature and the same free-stream turbulence intensity. In the present paper, this base case is compared to a higher-turbulence comparison case to discuss the effect of turbulence intensity on curved turbulent boundary layer flows of equal strengths of curvature.

**The Effect of Turbulence Intensity: Introduction of a Comparison Case With $R = 90$ cm; $\delta/R = 0.039$–$0.045$, and T.I. = 1.85 percent (Case 2).** The comparison case has similar flow conditions to the base case except that the tur-

**Table 2 Locations of stations**

| Stations | x (cm)* | Case 1 $Re_\theta$ (T.I.) [H] | Case 2 $Re_\theta$ (T.I.) [H] |
|---|---|---|---|
| 1 (Dev.) | -29.9 | 2737 (0.74) [1.42] | 2531 (1.85) [1.37] |
| 3 (Cur.) | 26.2 | 3987 (0.65) [1.47] | 3468 (1.88) [1.42] |
| 4 (Cur.) | 52.8 | 4287 (0.64) [1.48] | 3814 (1.82) [1.43] |
| 5 (Cur.) | 79.8 | 4602 (0.68) [1.51] | 4131 (2.10) [1.48] |
| 6 (Cur.) | 106.7 | 5056 (0.75) [1.52] | 4290 (2.55) [1.51] |
| End of Curve. | 125.0 | | |

bulence intensity, nomalized on the free-stream velocity, was 1.85 percent instead of 0.65 percent (see Table 1). Although measurements were taken and could have been reported for the straight section downstream of the curve, rapid growth of the boundary layers due to the higher free-stream disturbance for case 2 resulted in the disappearance of the potential core within this recovery region. Therefore, a comparison of the two cases in the recovery region to show the free-stream turbulence intensity effect, assuming that both were external boundary layers, would not have been accurate. For this reason, no data downstream of the curve are discussed in the present paper.

Mean velocity profiles at station 1 for the two cases (T.I. = 0.65 and 1.85 percent) are presented in Fig. 3. They demonstrate that free-stream turbulence mainly affects the outer part of the boundary layer (wake region). Despite the considerable depression of the wake region of case 2, the log-linear regions of the two velocity profiles are similar and obey the law of the wall. At station 1, the Reynolds numbers based on the momentum thickness are 2737 and 2531 and the shape factors are 1.42 and 1.37 for cases 1 and 2, respectively. The momentum thickness Reynolds numbers therefore match to within 10 percent for the two cases. The shape factors are expected to differ due to the effect of different turbulence intensities. The streamwise evolutions of the mean velocity and temperature profiles are shown in Figs. 4 and 5. One can observe the effects of curvature: enhanced wake regions and shortening of the log-linear regions. A comparison of flat-wall profiles (Fig. 3) shows that elevated free-stream turbulence intensity results in a reduction of the wake strength. It is interesting to note that the curvature influence is sufficiently

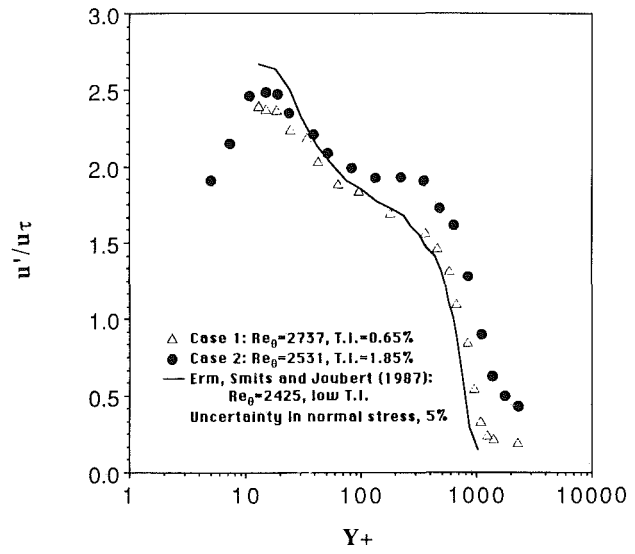


Fig. 2 Comparison of streamwise-normal turbulence intensity profiles at Station 1 (Cases 1 and 2) with the data of Erm et al. (1987)

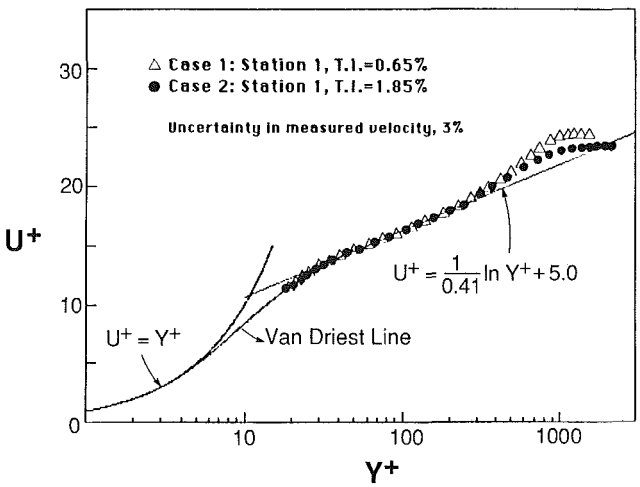


Fig. 3 Comparison of mean velocity profiles at Station 1 (Cases 1 and 2)

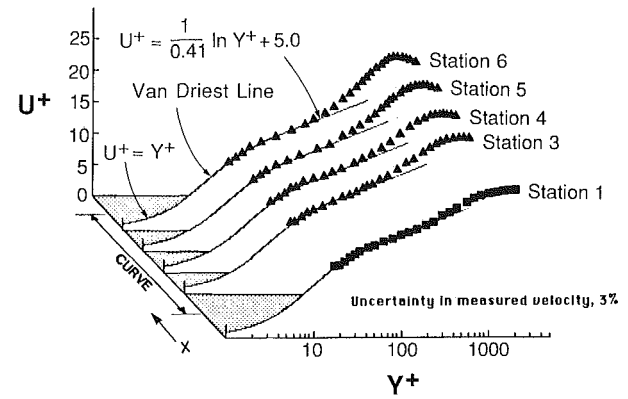


Fig. 4 Mean velocity profiles, Case 2 (T.I. = 1.85 percent)

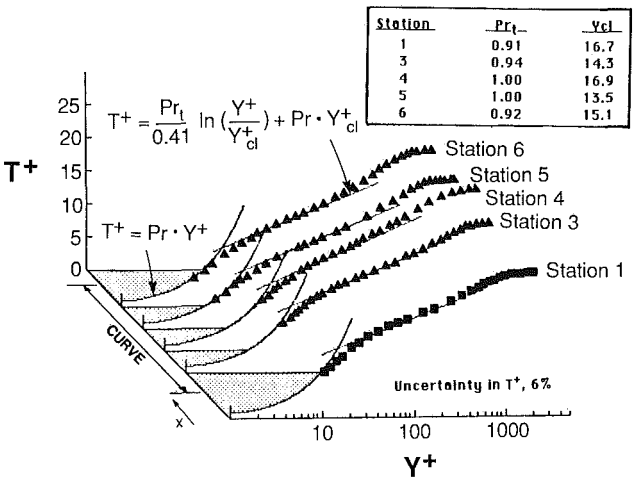


Fig. 5 Mean temperature profiles, Case 2 (T.I. = 1.85 percent)

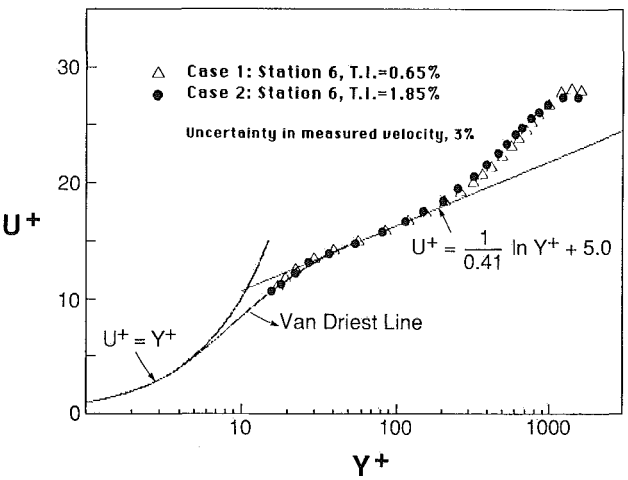


Fig. 6 Comparison of mean velocity profiles at Station 6 (Cases 1 and 2)

strong to nearly eliminate this suppressed wake by station 6 (Fig. 6). This is shown further by a comparison of the shape factor (Fig. 7). At station 1, it is lower for the higher disturbance case; but the two become comparable by the end of the curve. This disappearance of the high free-stream turbulence characteristics within the curve will also be seen in the wall values and the turbulence profiles.

Stanton numbers and skin friction coefficients are compared in Fig. 8. St and $C_f$ for the higher free-stream turbulence case (T.I. = 1.85 percent) measured at station 1 are about 5 percent larger than those of the low T.I. case. Curvature is seen to affect the higher free-stream turbulence $C_f$ data more than it does the corresponding lower turbulence data. Although $C_f$ is higher for the higher T.I. case at the entrance to the curve, there is no difference in the values by the end of the curve. In contrast, Stanton numbers for the two cases were reduced equally by curvature. Supporting this trend, turbulent Prandtl number $Pr_t$ values decrease near the end of the curved region in case 2 (Fig. 9), while in case 1 they increase continuously throughout the curve. This rise in turbulent Prandtl number within the convex curve for the low free-stream turbulence level cases has been documented by others, e.g., Gibson et al. (1982) and You et al. (1986). Direct measurements of turbulent Prandtl number have been made in both the high and low T.I. flows and are reported by Kim and Simon (1988). They were taken with a three-wire, hot-wire anemometer probe that allowed local measurements of $U$, $T$, $\overline{u'v'}$, and $\overline{v't'}$. The large uncertainty in $Pr_t$ computed from these measurements prevents the use of the measurements for support of the deduced $Pr_t$ values presented herein, however. A comparison of the profiles of $\overline{u'v'}$ and $\overline{v't'}$ presented by Kim and Simon (1988) for the high and low T.I. cases does show some differences, which tend to support the trends observed in $C_f$ and St. For example, for the low T.I. case, $\overline{u'v'}$ and $\overline{v't'}$ are of the same sign throughout the boundary layer. But, for the higher T.I. case, a sign reversal is observed in the outer portions of the $\overline{u'v'}$ profile but not in the $\overline{v't'}$ profile. This is a hint that the high T.I. $C_f$ values may be more affected by curvature than are the low T.I. $C_f$ values or the high or low T.I. Stanton number values. Turbulent Prandtl numbers are found by forcing the mean temperature profile to obey the thermal law of the wall by choosing the appropriate values of $Pr_t$ and $Y_{Cl}^+$, as discussed in You (1986). This evaluation presumes that momentum and thermal laws of the wall have not been violated by curvature. Most researchers agree that it is appropriate to do so, e.g., Muck et al. (1985). There has been some recent discussion about the possibility that curvature invalidates the laws, however.

Streamwise-normal turbulence intensity profiles in case 2 are shown in Fig. 10. The response to the introduction of convex curvature shows the same trends as in the base case: an immediate reduction and the establishment of an asymptotic profile in the upstream portion of the curve. The reduction of turbulence in the inner half of the boundary layer as the profiles

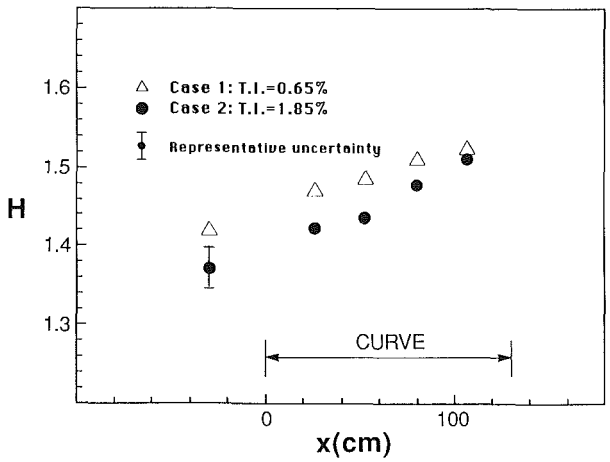


Fig. 7 Shape factor versus streamwise distance (Cases 1 and 2)

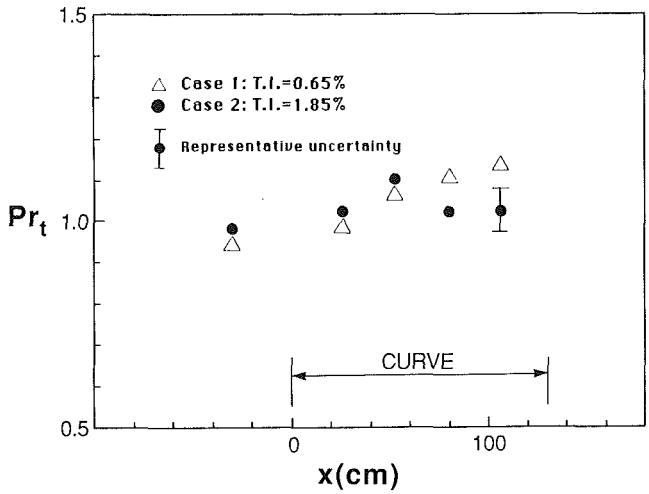


Fig. 9 Turbulent Prandtl number versus streamwise distance (Cases 1 and 2)

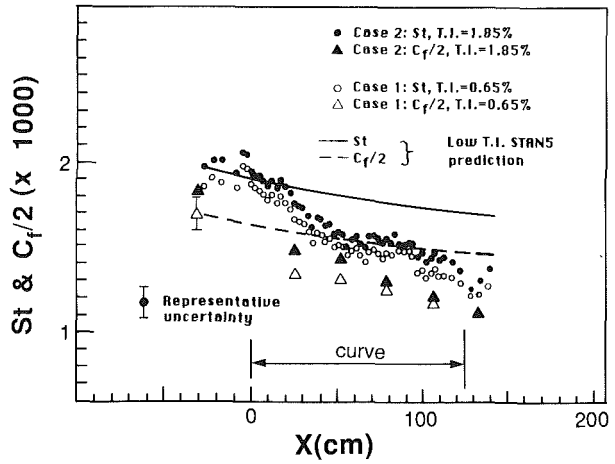


Fig. 8 Stanton number and skin friction coefficient versus streamwise distance, comparison between Cases 1 and 2

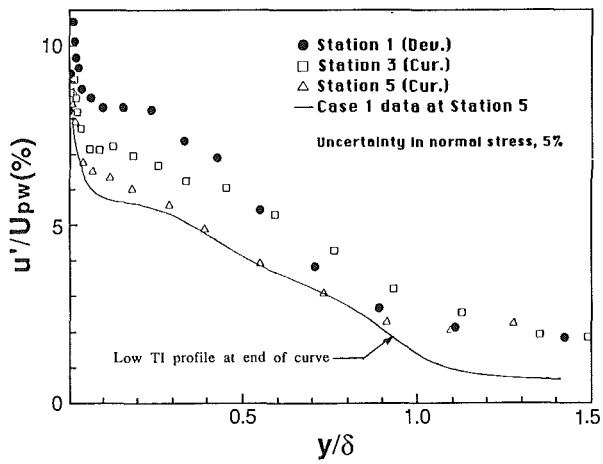


Fig. 10 Streamwise-normal turbulence intensity profiles, Case 2 (T.I. = 1.85 percent)

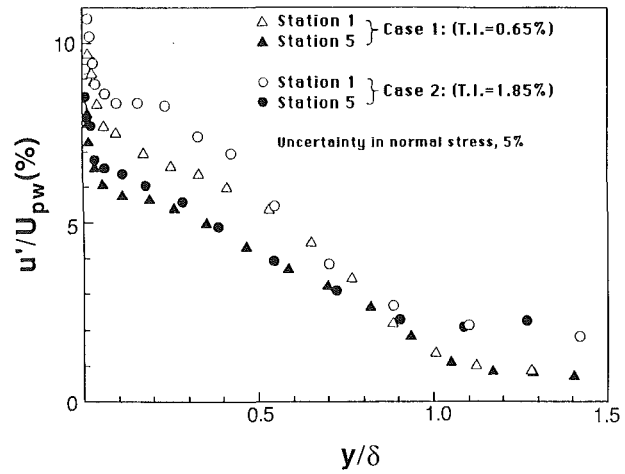


Fig. 11 Streamwise-normal turbulence intensity profiles at Stations 1 and 5, comparison between Cases 1 and 2

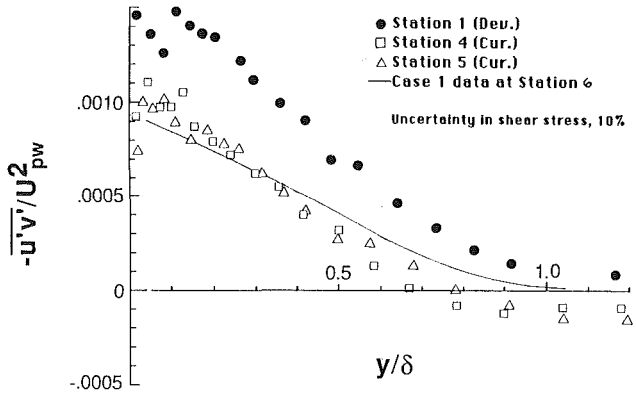


Fig. 12 Reynolds shear stress profiles, Case 2 (T.I. = 1.85 percent)

evolve from flat-plate to asymptotic-curved is much larger for case 2 than for case 1 (Fig. 11). Even though the shapes of the turbulence intensity profiles at station 1 are different, the curved self-similar profiles (stations 5) for cases 1 and 2 are nearly equal. The stabilizing effect of curvature, which reduces the profiles to the asymptotic shape within the curve, is apparently dominating the free-stream turbulence intensity effect (see Fig. 11) over the entire boundary layer thickness.

Reynolds shear stress data are plotted in Fig. 12. The dramatic response to the introduction of curvature and the appearance of an asymptotic profile are similar to those observed in case 1. The shear stress profile at station 1 in case 2 shows an extended "tail"; the turbulent shear stress extends well beyond $\delta$. The effect of curvature on shear stress profiles within the curve is dramatic. In the outer 30 percent of the boundary layer, the Reynolds shear stress reverses in sign downstream of station 3. This was not observed in the lower turbulence case (case 1). Similar profiles, including reversal of sign, were previously reported for more strongly curved cases (Gillis and Johnston, 1983; So and Mellor, 1973; Smits et al., 1979; Kim and Simon, 1988). The number of studies reporting the reversal of sign in the shear stress profiles makes it unlikely that the observed negative shear stress is due merely to uncertainties in the measurement. As discussed by Gillis and Johnston (1983), the dominant production terms of the Reynolds-stress transport equation are

$$P = \overline{v'^2}\frac{\partial U}{\partial y} - (2\overline{u'^2} - \overline{v'^2})\frac{U}{R}$$

For an attached flat-wall boundary layer, only the first term is

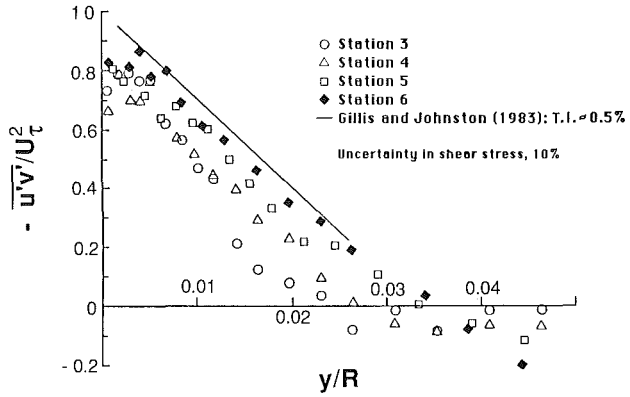


Fig. 13 Turbulence shear stress profiles within the curved section, Case 2 (T.I. = 1.85 percent)

nonzero and positive. The production of turbulence in convexly curved boundary layers tends to decrease due to the second term. As the curvature increases, this term may lead to negative production and negative $-\overline{u'v'}$ values in the outer part of the boundary layer. This was shown by Gillis and Johnston (1983). Negative production in the present study is obtained by an increased $(2\overline{u'^2} - \overline{v'^2})$ for the higher free-stream turbulence case with moderate curvature. Therefore, the Reynolds shear stress can reverse in sign for cases of strong curvature and low turbulence intensity as well as for cases of moderate curvature and high turbulence intensity (present study). It is interesting that there is a self-similar profile for $y/\delta < 0.5$ at stations 4 and 5 in this higher turbulence intensity case (Fig. 12), while the outer part of the boundary layer shows a reversal in sign of $\overline{u'v'}$. In Fig. 13, the shear stress data ($-\overline{u'v'}/U_\tau^2$ versus $y/R$) approaches the "asymptotic" line for strong curvature suggested by Gillis and Johnston (1983), as $\delta/R$ grows. The shear stress profiles at station 6 for both of the cases discussed herein were close to, but not on, this line.

## 4 Summary and Conclusions

Two different free-stream turbulence intensity cases were studied to investigate the effect of free-stream turbulence intensity on boundary layers over convex-curved surfaces.

The main conclusions about the effects of free-stream turbulence are:

1 The curvature effect dominates the free-stream turbulence effect for the cases studied.

2 Flat-plate data upstream of the curve show reduced wake strength with 1.85 percent turbulence intensity and about a 5 percent increase in St and $C_f$ compared to the lower turbulence intensity case (0.65 percent).

3 The skin friction coefficient decreases more for the higher turbulence case than for the lower turbulence case within the convex-curved section. This relative change was not observed with the Stanton number data, consistent with the lower $Pr_t$ of the higher turbulence case than of the lower turbulence case near the end of the curved section.

4 Profiles of turbulence intensity show the same trends for the two cases: dramatic response to the introduction of curvature and the appearance of asymptotic turbulent shear stress profiles.

5 Similar streamwise normal turbulence intensity profiles for the two cases were found near the end of the curve in spite of the different profiles upstream of the curve.

6 Reynolds shear stress profiles for the higher turbulence case are dramatically influenced by curvature; shear stress reverses sign for $y/\delta > 0.7$ within the curve. This behavior was previously reported in strongly curved convex-wall cases. A

self-similar shear stress profile in $-\overline{u'v'}/U_{pw}^2$ versus $y/\delta$ coordinates on the curved wall was realized for both cases inside 50 percent of the boundary layer thickness.

## Acknowledgments

This study was supported by the Air Force Office for Scientific Research grant number F49620-83-C0062. The grant monitor was Dr. James D. Wilson. Additional support was provided by the Graduate School of the University of Minnesota and by the AMOCO Foundation.

## References

Blair, M. F., 1983a, "Influence of Free-Stream Turbulence on Turbulent Boundary Layer Heat Transfer and Mean Profile Development, Part I—Experimental Data," ASME JOURNAL OF HEAT TRANSFER, Vol. 105, pp. 33–40.

Blair, M. F., 1983b, "Influence of Free-Stream Turbulence on Turbulent Boundary Layer Heat Transfer and Mean Profile Development, Part II—Analysis of Results," ASME JOURNAL OF HEAT TRANSFER, Vol. 105, pp. 41–47.

Bradshaw, P., 1973, "Effects of Streamline Curvature on Turbulent Flow," AGARDograph No. 169.

Erm, L. P., Smits, A. J., and Joubert, P. N., 1987, "Low Reynolds Number Turbulent Boundary Layers on a Smooth Flat Surface in a Zero Pressure Gradient," *Turbulent Shear Flows 5*, Springer-Verlag, New York, pp. 186–196.

Gibson, M. M., and Verriopoulos, C. A., 1984, "Turbulent Boundary Layers on a Mildly Curved Convex Surface, Part 2: Temperature Field Measurements," *Experiments in Fluids 2*, Springer-Verlag, New York, pp. 73–80.

Gibson, M. M., Verriopoulos, C. A., and Nagano Y., 1982, "Measurements in the Heated Turbulent Boundary Layer on a Mildly Curved Convex Surface," *Turbulent Shear Flows 3*, Springer-Verlag, New York, pp. 80–89.

Gibson, M. M., Verriopoulos, C. A., and Vlachos, N. S., 1984, "Turbulent Boundary Layer on a Mildly Curved Convex Surface, Part 1: Mean Flow and Turbulence Measurements," *Experiments in Fluids 2*, Springer-Verlag, New York, pp. 17–24.

Gillis, J. C., and Johnston, J. P., 1983, "Turbulent Boundary-Layer Flow and Structure on a Convex Wall and its Redevelopment on a Flat Wall," *J. Fluid Mechanics*, Vol. 135, pp. 123–153.

Hoffmann, P. H., Muck, K. C., and Bradshaw, P., 1985, "The Effect of Concave Curvature on Turbulent Boundary Layers," *J. Fluid Mechanics*, Vol. 161, p. 371.

Kim, J., 1986, "The Development of a Turbulent Heat Flux Probe and Its Use in a 2-D Boundary Layer Over a Convex Surface," M.S.M.E. Thesis, Department of Mechanical Engineering, University of Minnesota, Minneapolis, MN.

Kim, J., and Simon, T. W., 1988, "Measurements of the Turbulent Transport of Heat and Momentum in Convexly Curved Boundary Layers: Effects of Curvature, Recovery and Free-Stream Turbulence," ASME *Journal of Turbomachinery*, Vol. 110, No. 1, pp. 80–87.

Mayle, R. E., Blair, M. F., and Kopper, F. C., 1979, "Turbulent Boundary Layer Heat Transfer on Curved Surfaces," ASME JOURNAL OF HEAT TRANSFER, Vol. 101, No. 3.

Meier, H. V., and Kreplin, H. P., 1980, "Influence of Freestream Turbulence on Boundary Layer Development," *AIAA Journal*, Vol. 18, No. 1.

Muck, K. C., Hoffmann, P. H., and Bradshaw, P., 1985, "The Effect of Convex Surface Curvature on Turbulent Boundary Layers," *J. Fluid Mechanics*, Vol. 161, pp. 347–369.

Purtell, L. P., Klebanoff, P. S., and Buckley, F. T., 1981, "Turbulent Boundary Layer at Low Reynolds Number," *Phys. Fluids*, Vol. 24, No. 5, pp. 802–811.

Simon, T. W., and Moffatt, R. J., 1982, "Convex Curvature Effects on the Heated Turbulent Boundary Layer," *Proceedings of the VIIth International Heat Transfer Conference*, Vol. 3 pp. 295–301.

Simon, T. W., and Moffatt, R. J., 1983, "Turbulent Boundary Layer Heat Transfer Experiments: A Separate Effects Study on a Convexly Curved Wall," ASME JOURNAL OF HEAT TRANSFER, Vol. 105, No. 4, pp. 835–840.

Simonich, J. C., and Bradshaw, P., 1978, "Effect of Free-Stream Turbulence on Heat Transfer Through a Turbulent Boundary Layer," ASME JOURNAL OF HEAT TRANSFER, Vol. 100, No. 4, pp. 671–677.

Smits, A. J., Young, S. T. B., and Bradshaw, P., 1979, "The Effect of Short Regions of High Surface Curvature on Turbulent Boundary Layers," *J. Fluid Mechanics*, Vol. 94,, p. 209.

So, R. M. C., and Mellor, G. L., 1973, "Experiment on Convex Curvature Effects in Turbulent Boundary Layers," *J. Fluid Mechanics*, Vol. 60, Part 1, pp. 43–62.

Wang, T., and Simon, T. W., 1987, "Heat Transfer and Fluid Mechanics Measurements in Transitional Boundary Layers on Convex-Curved Surfaces," ASME *Journal of Turbomachinery*, Vol. 109, No. 3, pp. 443–452.

Wang, T., and Simon, T. W., 1988, "Development of a Special Purpose Test Surface Guided by Uncertainty Analysis: Introduction of a New Uncertainty Analysis Step," presented at the AIAA 26th Aerospace Sciences Meeting, Paper No. AIAA-88-0169.

Wang, T., Simon, T. W., and Buddhavarapu, J., 1985, "Heat Transfer and Fluid Mechanics Measurements in Transitional Boundary Layer Flows," ASME *Journal of Engineering for Gas Turbines and Power*, Vol. 107, No. 4, pp. 1007–1015.

You, S. M., 1986, "Turbulent Boundary Layer Heat Transfer and Fluid Mechanics Measurements on a Curved Convex Wall," M.S.M.E. Thesis, Department of Mechanical Engineering, University of Minnesota, Minneapolis, MN.

You, S. M., Simon, T. W., and Kim, J., 1986, "Boundary Layer Heat Transfer and Fluid Mechanics Measurements on a Mildly-Curved Convex Wall," *Proceedings of the VIIIth International Heat Transfer Conference*, Vol. 3, pp. 1089–1094.

# Cavity Heat Transfer on a Transverse Grooved Wall in a Narrow Flow Channel

**D. E. Metzger**

**R. S. Bunker**

**M. K. Chyu**

Mechanical and Aerospace Engineering Department,
Arizona State University,
Tempe, AZ 85287

*Measurements are presented of local convection heat transfer for the case of flow through a narrow slot-type channel where one of the bounding walls contains a transverse rectangular cavity. The experimental situation is a stationary modeling of some salient features of flow through the clearance gap at the grooved tips of axial turbine blades. Cavity depth-to-width ratios of 0.1, 0.2, and 0.5 are included for each of clearance-to-width ratios of 0.05, 0.10, and 0.15. Overall heat transfer on the cavity floor is in general reduced as cavity depth is increased, but reduction with the deepest cavity tested is essentially the same as that of the intermediate depth cavity. Resistance to flow through the gap is increased as cavity depth is increased, but again the change between the deepest and intermediate depth cavities is small. In addition to the stationary experiments, heat transfer in the cavity with a moving as well as stationary shroud is modeled with a finite-difference method. The numerical results indicate that, within the range of parameters considered, heat transfer characteristics in the cavity are virtually unaffected by the shroud movement. This is in agreement with a previous finding for heat transfer on ungrooved blade tips.*

## Introduction

The clearance gap between the tip of an axial turbine blade and the adjacent stationary shroud provides a narrow flow passage between the pressure and suction sides of the blade. Although the resulting leakage flow is undesirable, it is impractical to elminate the gap entirely because the clearance must accommodate centrifugal growth of the blade as well as differential thermal expansion between the blade and shroud through a variety of operating conditions [1].

The primary detrimental effect of the tip leakage flow is on the blade aerodynamic performance, but a second important and less well-understood effect concerns the convection heat transfer associated with the leakage flow. The surface area at the blade tip in contact with the hot working gas represents an additional thermal loading on the blade which, together with heat transfer to the suction and pressure side surface area, must be removed by the blade internal cooling flows. These cooling flows impose a thermodynamic penalty on engine performance, and in this general sense the blade tip heat transfer acts to degrade turbine performance.

Also, heat transfer rates at the tip can be among the highest experienced over the entire blade surface, potentially leading to large local temperature and/or temperature gradients and related durability problems. As a result, blade tips have traditionally been one of the turbine areas most susceptible to structural damage. Structural damage to the blade tips can have a severe effect on turbine performance. Loss of material from the tip increases the clearance gap, increases the flow and heat transfer across the tip, and in general exacerbates all of the above problems.

Despite its importance, turbine blade tip heat transfer is one of the least studied and least understood aspects of turbine airfoil heat transfer. In present turbine design procedures, strategies for reducing the leakage flow and its associated tip heat transfer are largely empirical, based more in observation of durability with actual turbine blades than on an understanding of the phenomena involved.

One strategy commonly employed to reduce tip flow and heat transfer is to groove a single rectangular cavity chordwise along the blade tip. The groove acts like the cell of a labyrinth seal to increase the flow resistance and thus reduce the flow for a given pressure differential across the tip. The reduction of flow will tend to reduce heat transfer, and heat transfer rates on the bottom of the groove are expected to be less than those present for the same flow over an ungrooved surface. However, available cavity heat transfer information suggests that the total blade tip heat transfer may actually be increased by grooving because of the additional heat transfer area created by the sides of the groove. In [2], for example, a groove with depth-to-width ratio of 0.5 was found to have 22 percent higher total heat transfer than the ungrooved surface in the same flow.

A blade tip geometry of the grooved type is depicted in Fig. 1, where the blade is shown stationary and the relative motion of the shroud with respect to the blade is indicated by the right-pointing arrow. The direction of the leakage flow will be in opposition, from pressure to suction side across the tip. Previous studies of this flow phenomenon, in the absence of heat transfer [3, 4], have shown that leakage through the clearance gap is basically an inviscid, pressure-driven flow whose magnitude can be calculated from knowledge of the suction and pressure side pressures. Normal clearance gap heights are, in effect, small enough to uncouple the flow through the gap from the details of the flow fields on either side and to render it essentially two-dimensional.

A more recent study with heat transfer [5] conducted for the case of a flat ungrooved blade tip has shown that, for clearances normally employed, the relative motion of the shroud has a negligible effect on the blade tip heat transfer. In effect, the influence of the shroud countermotion is restricted

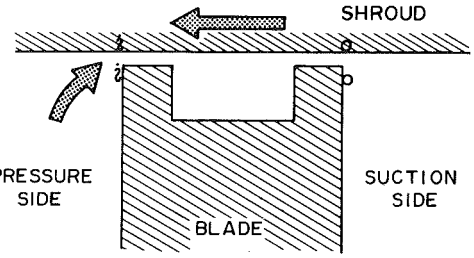


**Fig. 1 Grooved turbine blade tip cross section**

Contributed by the Heat Transfer Division and presented at the National Heat Transfer Conference, Denver, Colorado, August 1985. Manuscript received by the Heat Transfer Division May 16, 1986. Paper No. 85-HT-57. Keywords: Forced Convection, Numerical Methods, Turbines.

to a thin boundary layer on the shroud, and the main fluid motion is pressure driven as if the flow were through a stationary gap. It seems plausible to expect that similar circumstances will prevail in the presence of a grooved tip, and that major features of heat transfer on grooved tips can be studied on a stationary cavity with cavity entrance and exit provided through narrow slots. This speculation, in fact, will be justified from the numerical results of this study, at least for the parameter ranges presently studied.

Flow and heat transfer in rectangular cavities have been the subjects of continuous investigation during the past thirty years [eg. 2, 6, 7]. In all cases, the cavities studied have been installed in wind tunnel walls where the cavity is open to a well-developed, zero pressure gradient flow over an otherwise smooth surface. The present case differs from these by virtue of the confined nature of the geometry. It is, in effect, a completely enclosed rectangular volume both supplied and relieved from narrow short slots at the top side corners. The degree of similarity between the heat transfer characteristics for this case and those of previous cavity studies is unclear at present. The purpose of the present study is to investigate these characteristics both experimentally and numerically, to compare them with previous cavity studies, and to interpret the findings in terms of the turbine blade tip application.

## Experimental Apparatus and Procedures

The present study utilizes the melting patterns of thin replaceable coatings on the test surfaces in the presence of a heated air stream to determine the local surface heat transfer rates. Details of the method and the procedures used have been given previously [8, 9], so only a brief description will be repeated here.

Figure 2 shows a schematic of the test apparatus. Laboratory compressed air, filtered and dried, is metered through an ASME standard orifice and supplied to a heating section and following diverter ball valve. In operation the heated air is first diverted away from the test section and at the same time the test section is shielded from the heated flow so that it remains uniformly at the laboratory ambient temperature. The ball valve remains in the diverted position until a steady-state temperature (above the melting point of the coating applied to the test surfaces) has been achieved in the diversion channel. At that time the valve is used suddenly to route the heated air flow through the test section.

The test section construction is entirely transparent acrylic plastic and consists of a plenum chamber and interchangeable adjacent cavities held between two endwall plates and sealed with O-rings. Figure 3 shows a cross-sectional view of one of the cavities indicating measuring locations and coordinate orientation. Three different cavities of depth $D$ equal to 5.08,

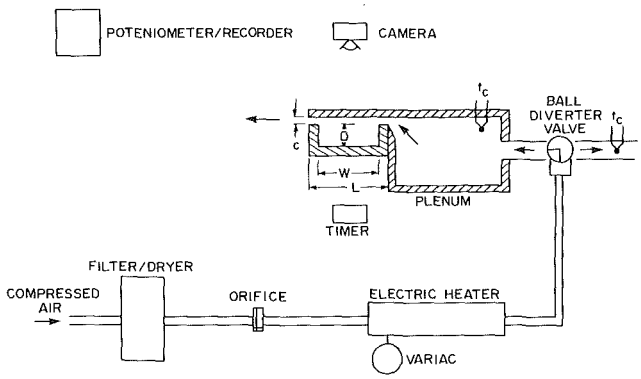


Fig. 2 Schematic of test apparatus

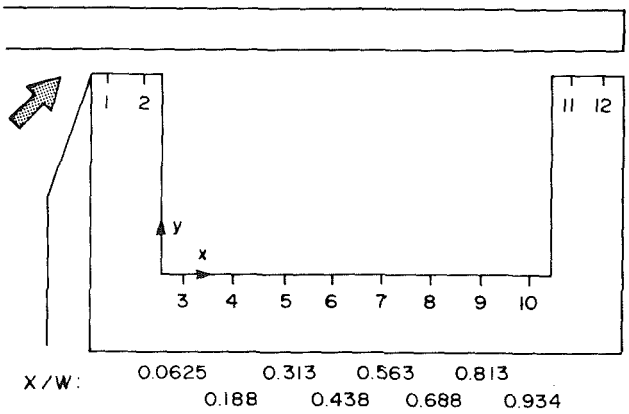


Fig. 3 Typical test cavity cross section

10.16, and 25.4 mm were used in the present tests, each in conjunction with clearance gaps $C$ of 2.54, 5.08, and 7.62 mm. A flat surface, $D=0$, was also used with the same three clearances. The cavity width in the mean flow direction $W$ is in all cases 50.8 mm. The span of the cavities in the direction normal to the cross section shown in Fig. 3 is 76.2 mm. Cavity wall thickness in all cases in 9.5 mm.

A thin layer of the coating material (approximately $5\times10^{-2}$ mm) is sprayed evenly on the cavity bottom, in the case of $D/W=0.5$, on the cavity sides, before each test. Coating was also applied to the top of the cavity side walls (locations 1, 2 and 11, 12). The coating material is a commercially available product (Tempil Industries, S. Plainfield, NJ) with a specified melting point of 109° F. Calibration tests were performed with the coating batch used in the tests with a resulting measured

## Nomenclature

$A$ = heat transfer surface area
$c_p$ = fluid specific heat
$C$ = clearance height at gap
$D$ = cavity or groove depth
$f$ = pressure loss coefficient $=\Delta PC/2L\rho V^2$
$h$ = convection heat transfer coefficient $=q/A\,(t_p-t)$
$k$ = test surface thermal conductivity
$k_f$ = fluid thermal conductivity
$L$ = gap length in flow direction
Nu = local Nusselt number $=hC/k_f$
$Nu_m$ = average nusselt number over the cavity floor
$P$ = pressure
$q$ = surface heat transfer rate
Re = Reynolds number $=\rho VC/\mu$
$t$ = local test surface temperature
$t_1$ = initial temperature
$t_p$ = plenum temperature
$U$ = fundamental solution, see equation (3)
$U_b$ = mean velocity at gap
$U_s$ = shroud velocity relative to cavity
$W$ = cavity width in streamwise direction
$x$ = cavity floor coordinate
$y$ = cavity side wall coordinate
$\alpha$ = test surface thermal diffusivity
$\theta$ = time
$\mu$ = fluid dynamic viscosity
$\rho$ = fluid density
$\tau$ = time step

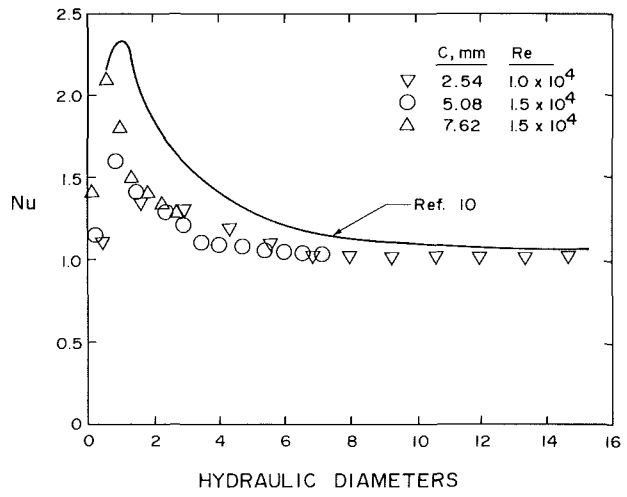


**Fig. 4 Flat surface ($D = 0$) results**

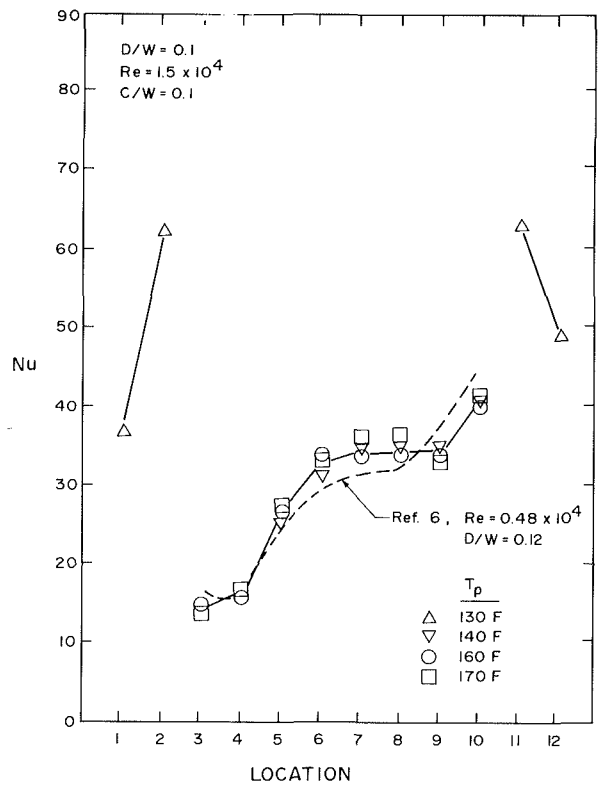


**Fig. 5 Results of repeated testing at $D/W = 0.1$, $C/W = 0.1$**

mean melting point temperature of 109.5°F for 15 samples. The lowest and highest melting temperatures measured were 109.1 and 109.6°F. In both the calibration tests and in subsequent test program use, the melting is determined visually from the property of the coating to change from opaque white to transparent upon melting. A black background facilitates the melting determination.

The test is started by diversion of the heated flow to the test section. The resulting conduction of heat into the test section walls has been numerically simulated [8] on a finite element code using specified heat transfer coefficients of the magnitude and spatial variation expected for the experiments. For these conditions together with physical properties for acrylic plastic, the simulations show that the depth of heating into the wall over the expected test duration is less than the wall thickness. In addition, lateral conduction in the wall has a negligible effect on the local surface temperature response. At any surface point, the wall temperature can thus be represented by the classical one-dimensional response of a semi-infinite medium to the sudden step application of a convecting fluid at temperature $t_p$

$$(t-t_1)/(t_p-t_1) = 1-\exp(h^2\alpha\theta/k^2)\operatorname{erfc}(h\sqrt{\alpha\theta}/k) \tag{1}$$

If each surface point of interest were subjected to a true step increase in $t_p$, then measurement of the required times to reach the known phase change temperature allows solution of equation (1) for the heat transfer coefficients. This is the essence of the method, with the thin coating of phase change material providing a means of acquiring an array of temperature–time pairs over the surface.

However, in actual internal flow experiments, the wall surfaces will not experience a pure step change in air temperature because of the transient heating of the upstream plenum chamber and duct walls. Nevertheless, equation (1) is a fundamental solution that can be used to represent the response to a superposed set of elemental steps in $t_p$ arranged to represent the actual air temperature rise

$$t-t_1 = \sum_{i=1}^{N} U(\theta-\tau_i)\Delta t_p \tag{2}$$

where

$$U(\theta-\tau_i) = 1-\exp\left[\frac{h^2\alpha(\theta-\tau_i)}{k^2}\right]\operatorname{erfc}\left[\frac{h\sqrt{\alpha(\theta-\tau_i)}}{k}\right] \tag{3}$$

In the present experiments, air temperature $t_p$ is determined from the plenum thermocouple measurement. The $t_p$ variation with time is recorded and approximated by steps, and the resulting superposed solution, equations (2) and (3), is solved for the local surface heat transfer coefficients, using observed local melting times. Melting patterns were recorded photographically at discrete times with a motor-driven camera during the test transient. The time required for melting at a given location was determined from visual comparisons between pairs of adjacent photographs in the sequence.

## Experimental Results and Discussion

Figure 4 presents the present results obtained with the flat test surface in the absence of any cavity. The Nusselt numbers have been normalized with expected fully developed channel values, $Nu_0 = 0.023\,Re^{0.8}Pr^{0.4}$, and are presented as a function of the distance, in hydraulic diameters, downstream from the gap entrance. For comparison, the solid line shows results from [10], as presented in [11], for an abrupt contraction entrance. The present results display a similar maximum heat transfer location downstream of the entrance, but they are in general not as high above fully developed values. This behavior seem reasonable in view of the fact that the present geometry has an abrupt entrance on only one side of the channel. The good agreement with expected values in the downstream region provides confidence in the present experimental technique. A detailed treatment of the uncertainties in the technique is given in [8], based on the methods of [12]. For the present tests, the uncertainty in the local Nusselt number is estimated to be ±10 percent.

For most of the present tests, repeatability is considerably better than ±10 percent. This is illustrated in Fig. 5, which presents results for the shallow cavity, $D/W = 0.1$, obtained with four separate tests, utilizing four different plenum temperatures. In general, the experimental uncertainty in a given locality can be minimized by choosing a temperature potential that is appropriate for the level of heat transfer rate at the location. Temperature potentials that are too large result in short melting times and larger uncertainties. Those that are too small result in melting times larger than the time required for the thermal transient to penetrate the test wall

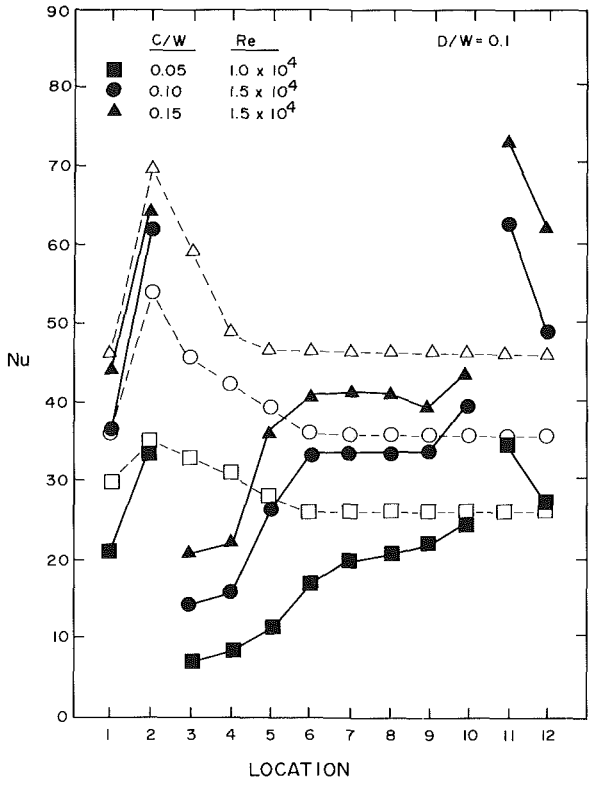


Fig. 6 Results at $D/W = 0.1$ compared to flat surface

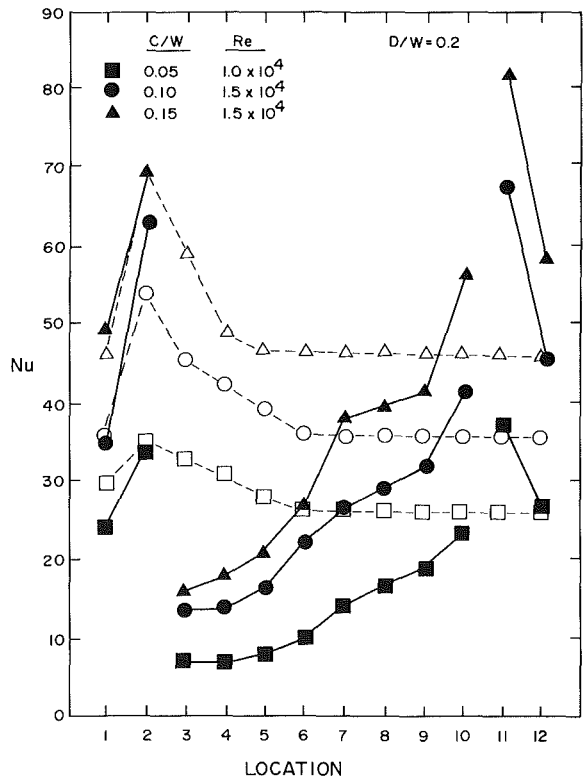


Fig. 7 Results at $D/W = 0.2$ compared to flat surface

thickness, compromising the validity of the assumed semi-infinite wall response. During the test program, if too short or too long melting times are found on a surface region of interest, the test is re-run with a different plenum temperature. Good agreement between overlapping points, as shown in Fig. 5, is typical of the present study and provides additional confidence in the results.

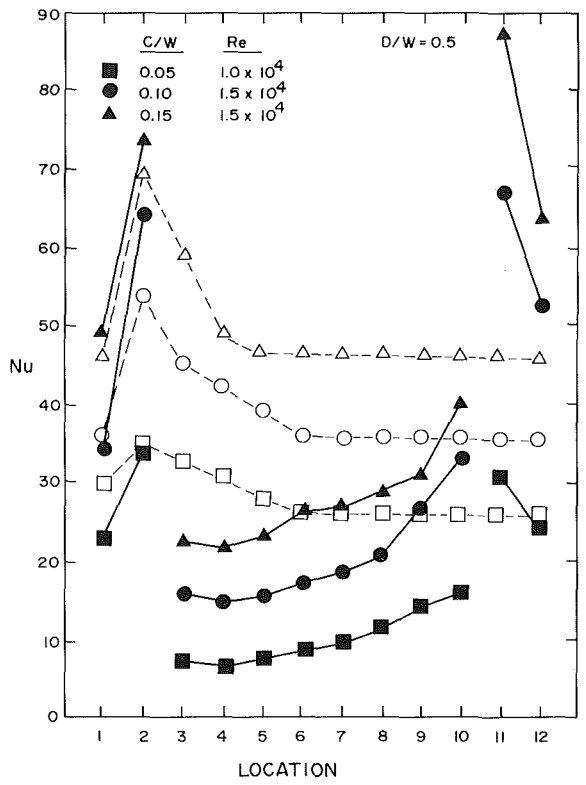


Fig. 8 Results at $D/W = 0.5$ compared to flat surface

The distribution of heat transfer on the test surfaces shown in Fig. 5 is also typical of the entire present study. Very high heat transfer rates are present on the top surface of the upstream wall, and these have the same general magnitude and character as those measured with the flat test surface. From location 2 on the top surface to location 3 at the upstream end of the groove floor, heat transfer decreases by a factor of four. It then increases rapidly, levels at midfloor, and increases again at the downstream end of the floor.

Heat transfer on the top of the downstream wall is back up to its level on the top of the upstream wall. In this case, however, the highest value of Nu is on the upstream end, rather than on the downstream end as is the case for the top of the upstream wall. This behavior supports the notion that the source of the downstream gap flow is largely fluid moving downstream adjacent to the shroud, partially impinging on and flowing down the downstream cavity wall toward the cavity floor. Thus there would be little or no separation at the downstream gap entrance as is the case in the upstream gap.

Figure 5 also shows comparison with the cavity floor results for the unshrouded cavity experiments of [6]. These results are in quite good agreement with the present findings in both magnitude and streamwise distribution. This agreement with [6] is typical of the present results at $D/W = 0.1$ for all three of the $C/W$ values investigated. However, as the relative depth of the cavity is increased, the results of [6] increasingly underpredict the heat transfer levels for the enclosed cavity, as will be shown in a later figure.

Figures 6–8 present composites of all of the present side wall, top, and cavity floor measurements for $D/W = 0.1$, 0.2, and 0.5, shown with solid symbols and solid connecting lines. For comparison, the corresponding measured values on the flat surface without cavity ($D = 0$) are shown on the same figures with open symbols. As $D/W$ is increased, heat transfer levels on the cavity floor decreases, although the reduction is less pronounced as $C/W$ increases. To show this reduction quantitatively, mean Nusselt number values, averaged over

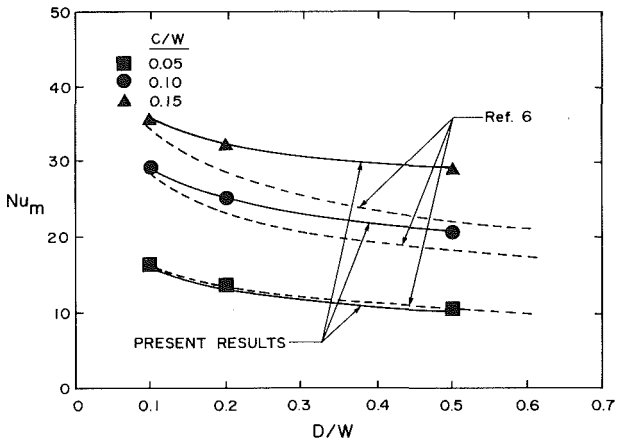


Fig. 9 Mean cavity floor Nusselt numbers

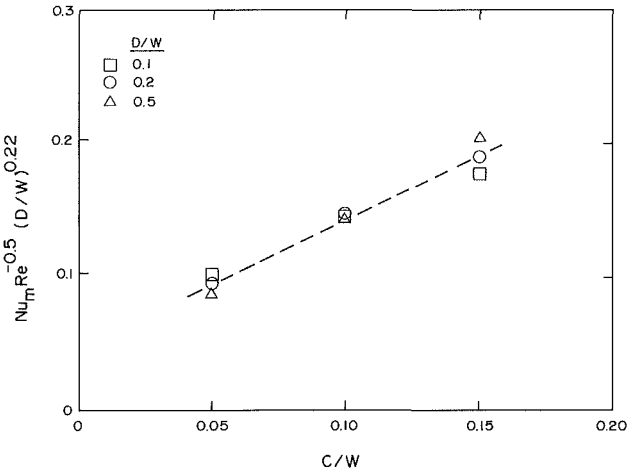


Fig. 10 Effect of $C/W$ on $Nu_m$

the cavity floor, are presented in Fig. 9, along with similar results from [6] for unshrouded cavities. As mentioned previously, the agreement with [6] is very good at $D/W=0.1$, but worsens as both $C/W$ and $D/W$ increase.

The present results displayed as in Fig. 9 suggest that the relative clearance $C/W$ has a larger influence on cavity heat transfer than does the relative depth $D/W$; however, the mixed values of Reynolds number act to obscure the independent $C/W$ effect. In [6], $Nu_m$ was found to vary as the 0.5 power of Reynolds number. This same Re dependence, together with a $-0.22$ power of $D/W$, is found to group the present results quite well, as shown in Fig. 10. The $-0.22$ power on $D/W$ also agrees well with the $-0.27$ power dependence reported in [6]. In this Fig. 10 presentation, a strong dependence of $Nu_m$ on $C/W$ is apparent, at least in the $C/W$ range covered by the present experiments.

For the $D/W=0.5$ cavity, heat transfer was also measured in the present study on the cavity sides. Figure 11 shows typical results for the intermediate case $C/W=0.1$. On the upstream side wall, heat transfer rates are nearly as low as those on the upstream end of the floor. The small variation is monotonic, with the highest value at the bottom and the lowest at the top. This is in agreement with behavior observed in a recent cavity study that included measurements on the side walls [7]. On the downstream side wall, a larger variation exists, again monotonic, but with the highest value at the top.

These side wall variations are again consistent with convection expected from a cavity flow that first impinges on and flows down the downstream side wall, then flows upstream along the cavity floor and up the upstream side wall. These

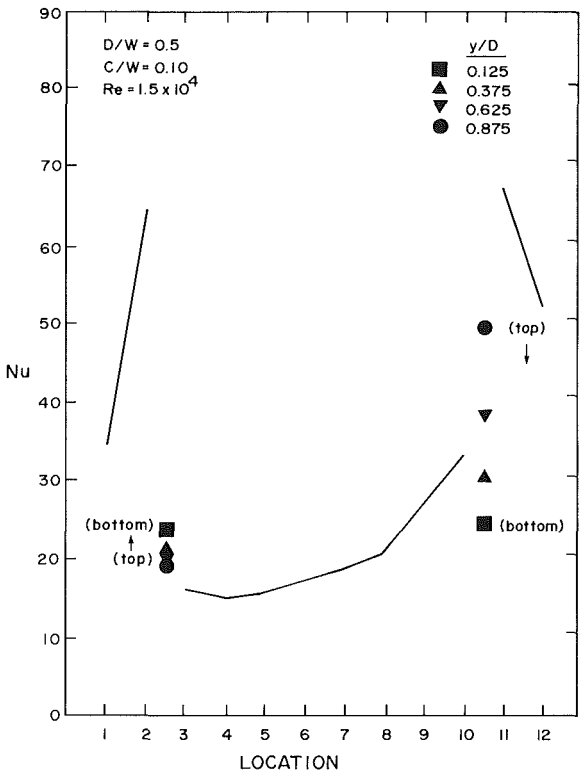


Fig. 11 Side wall results for $D/W=0.5$, $C/W=0.1$

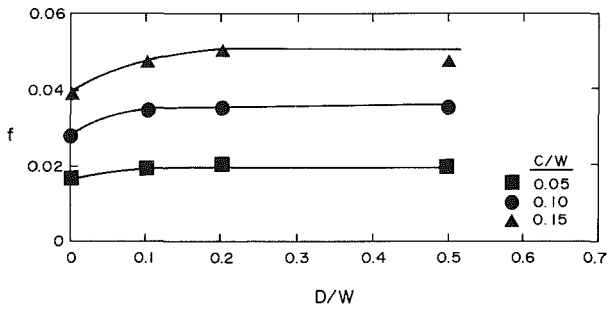


Fig. 12 Measured pressure loss coefficients

side wall Nusselt number distributions, relative to the adjacent floor values, are virtually identical to those reported in [2].

It is apparent in Fig. 9 that in terms of the cavity floor values alone, there is only small turbine blades tip heat transfer reduction to be gained from a groove depth greater than $D/W=0.2$, for a given flow rate through the upstream gap. Taking into account the additional heat transfer area associated with longer side walls strengthens this conclusion. Deepening the groove could have a heat transfer benefit if it further reduced the flow across the tip for a given pressure-to-suction side pressure differential. This does not appear to be the case, however. Figure 12 shows pressure loss coefficients calculated from the measured pressure differentials for the present tests. In all cases investigated, deepening the groove beyond $D/W=0.5$, for a given clearance gap, will not further reduce the flow.

## Numerical Computation and Results

The main objective of this portion of the study is to investigate numerically the effect of the relative cavity–shroud motion on heat transfer. A control volume based finite-difference method is employed for solving a system of partial differential equations governing the conservation of mass, momentum, energy, and turbulent flow parameters. The

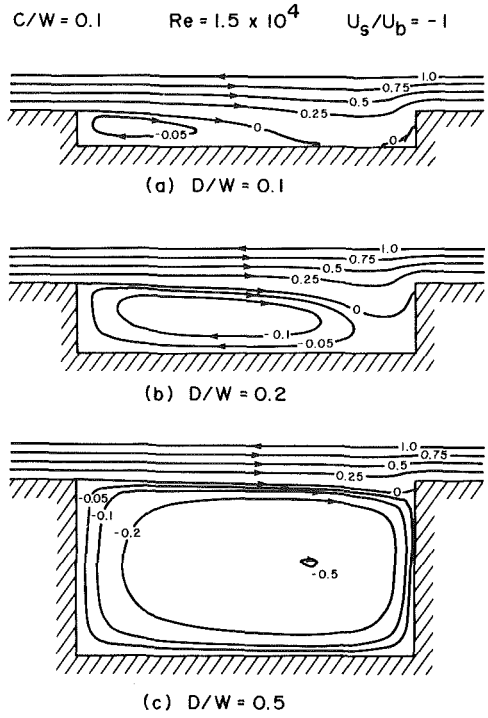


**Fig. 13 Contours of stream function; $U_s/U_b = -1$, $C/W = 0.1$, $Re = 1.5 = 10^4$**

SIMPLER algorithm [13] is used to solve explicitly for the velocity and pressure fields. Turbulent parameters are determined by a two-equations high-Reynolds-number, $k$–$\epsilon$ model in association with a ramp-type wall function [14]. The momentum, continuity, and turbulence equations, together with their coupling characterisitics, constitute five equations to be solved simultaneously for the converged velocity field. This is followed by a separate solution for the energy equation. The computational domain, similar to that shown in Fig. 1, is a two-dimensional, shrouded rectangular cavity. The computation uses a $40 \times 26$ grid for all cases studied, and a nonuniform spacing with dense placement near solid walls. For a typical run, approximately 250 iterations are required to obtain the converged velocity field, and an additional 30 steps are required for the temperature computation.

For obtaining information on grid independence and determining the optimal grid size, three additional grid configurations of $20 \times 11$, $50 \times 36$, and $60 \times 41$ were also run for the case $C/W = 0.1$, $D/W = 0.1$, $Re = 1.5 \times 104$, and $U_s/U_b = 0$. The value of $f \cdot Re$ resulting from these three runs deviates from that obtained using at $40 \times 26$ grid by 11, 2.7, and 3.5 percent, respectively. The $40 \times 26$ grid was thus chosen to limit the computing costs and time.

For the flow field computation, no-slip boundary conditions are imposed along the solid walls, a zero normal gradient at the outlet of the computational domain (plane 0–0 in Fig. 1), and a uniform velocity profile $U_b$ is specified at the inlet (plane $i$–$i$ in Fig. 1). For the temperature computation, an isothermal surface condition is assumed for the entire tip and shroud. $Pr = 0.7$ is used for air as the flow medium.

The heat transfer effect created by variation of relative shroud motion is investigated by computing two cases, $U_s/U_b = 0$ and $-1$, where $U_s$ is the shroud speed relative to the cavity. In Fig. 13, contours of the computed stream function are drawn for $C/W = 0.1$, $Re = 1.5 \times 10^4$, $U_s/U_b = -1$, and $D/W = 0.1$, 0.2, and 0.5, respectively. For a given $U_s/U_b$, the computed flow pattern is found to be strongly dependent on values of $D/W$ and little influenced by variations in either $C/W$ or Reynolds number. As seen in Fig. 13, a recirculating region, enveloped by the dividing streamline separating from the top edge of the cavity upstream wall and the solid wall boundary, exists immediately downstream of the cavity upstream wall. For an unshrouded cavity, in general the dividing streamline reattaches at the cavity floor provided that the cavity is sufficiently wide, say $D/W = 0.12$ [11], otherwise it will re-attach at the cavity downstream sidewall. The present flow patterns, even with the presence of the shroud, agree favorably with the findings for the unshrouded cavities.

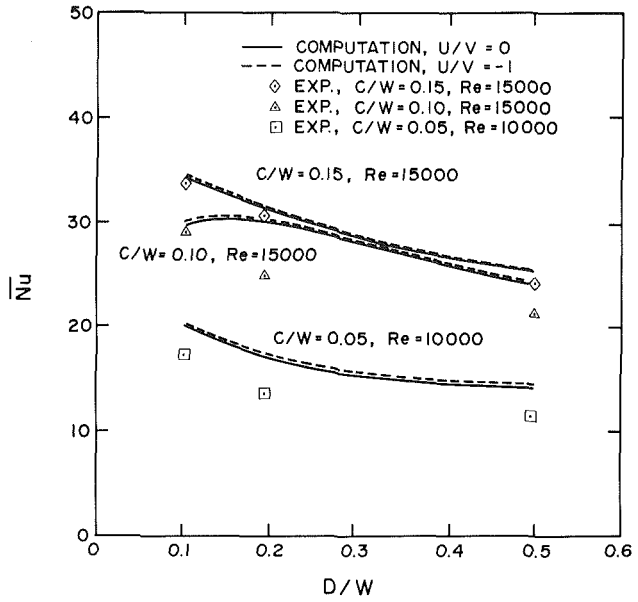


**Fig. 14 Area-averaged Nu over cavity floor**

For the present range of parameters, the relative shroud motion is found to have virtually no effect on the flow pattern and heat transfer characteristics in the cavity. Except for regions very close to the shroud, the computed stream function contours shown in Fig. 13 can also be regarded as the characteristic flow patterns for the cases with stationary shroud, i.e., $U_s/U_b = 0$. This finding is also reflected in the heat transfer results; at most a 3 percent variation in corresponding local values of Nu exists between $U_s/U_b = 0$ and $-1$. Hence, the speculation in [5] that relative shroud motion has an insignificant effect on the ungrooved blade tip is also supported for the grooved tip, at least for $-1 \le U_s/U_b \le 0$.

Figure 14 shows area-averaged heat transfer results on the cavity floor, $Nu_m$, for both computed relative velocities along with the corresponding measured results for a stationary shroud. Agreement between the computed and measured $Nu_m$ appears to be good, although the computational results are, in general, higher. Excellent agreement exists for the cases with higher $C/W$ and lower $D/W$.

## Summary

The convection heat transfer in a rectangular cavity, situated in one wall of a narrow flow channel, has been measured as a stationary model of leakage flow through the clearance gap of a grooved turbine blade tip. Grooving of turbine blade tips is a commonly used strategy for reducing the undesirable clearance gap flow, and hopefully for reducing the heat transfer from this hot flow to the blade tip. However, very little quantitative information is presently available on blade tip heat transfer, and the present study is an attempt to provide some understanding of the phenomenon.

Previous studies have shown that stationary modeling is valid for a plain ungrooved blade tip, since the effect of the relative motion between tip and shroud is confined to a thin boundary layer along the shroud. The present study assumes

that the same circumstances will prevail in the presence of grooves on the tip, and presents results from numerical computations that support the assumption. It should be experimentally verified in future studies. In the meantime, the following principal findings for stationary enclosed cavities in the ranges $0.1 \leq D/W \leq 0.5$m $0.05 \leq C/W \leq 0.15$ can be considered tentative for application to blade tips:

1 Local Nusselt numbers distributions have similar characteristics to those of unenclosed cavities. On the cavity floor, Nu values are lowest at the upstream end and increase monotonically to the downstream end. On the upstream cavity side wall, Nu values are nearly as low as those on the upstream floor, and exhibit only a small variation from bottom to top. On the downstream cavity side wall a larger variation in Nu prevails, with the highest values occurring at the top and the lowest at the bottom.

2 Average values of Nusselt numbers on the cavity floor are in good agreement with those of unshrouded cavities for the smallest values of $D/W$ and $C/W$ investigated. As either or both $D/W$ and $C/W$ increase, the floor averages for the enclosed cavities increase over those for unshrouded cavities. At the combined largest values of $D$ and $C$ tested, the increase over the unenclosed case is approximately 30 percent.

3 For a given pressure differential across the gap, flow will be reduced by deepening the cavity up to $D/W = 0.2$. Beyond this depth, no further flow reduction will occur.

4 Overall heat transfer on the cavity wall is reduced by the presence of a cavity. However, reduced heat transfer levels on the cavity floor are substantially offset by high heat transfer rates associated with redeveloping flow in the downstream gap and by the additional heat transfer area created by the cavity side walls. Because of this additional heat transfer area and the fact that deepening of the cavity provides little or no further flow reduction, shallow cavities are preferred if overall heat transfer reduction on the cavity wall is the goal.

## References


1 Henneke, D. K., "Heat Transfer Problems in Aero-Engines," *Heat and Mass Transfer in Rotating Machinery*, D. E. Metzger and N. H. Afgan, eds., Hemisphere, Washington, DC, 1984, pp. 353-379.

2 Seban, R. A., "Heat Transfer and Flow in a Shallow Rectangular Cavity With Subsonic Turbulent Air Flow," *International Journal of Heat and Mass Transfer*, Vol. 8, 1965, pp. 1353-1368.

3 Booth, T. C., Dodge, P. R., and Hepworth, H. K., "Rotor-Tip Leakage: Part I—Basic Methodology," ASME *Journal of Engineering for Power*, Vol. 104, 1982, pp. 154-161.

4 Wadia, A. R., and Booth, T. C.,"Rotor-Tip Leakage: Part II—Design Optimization Through Viscous Analysis and Experiment," ASME *Journal of Engineering for Power*, Vol. 104, 1982, pp. 162-169.

5 Mayle, R. E., and Metzger, D. E., "Heat Transfer at the Tip of an Unshrouded Turbine Blade," *7th International Heat Transfer Conference*, Munich, Vol. 3, 1982, pp. 87-92.

6 Yamamoto, H., Seki, N., and Fukusako, S., "Forced Convection Heat Transfer on Heated Bottom Surface of a Cavity," ASME JOURNAL OF HEAT TRANSFER, Vol. 101, 1979, pp. 475-479.

7 Chyu, M. K., and Goldstein, R. J., "Local Mass Transfer in Rectangular Cavities With Separated Turbulent Flow," 8th International Heat Transfer Conference, San Francisco, CA, 1986, Paper No. 86-IHTC-230.

8 Larson, D. E., "Transient Local Heat Transfer Measurements in 90° Bends Using Surface Coatings Having Prescribed Melting Points," MS Thesis, Arizona State University, Tempe, AZ, 1983.

9 Metzger, D. E. and Larson, D. E., "Use of Melting Point Surface Coatings for Local Convection Heat Transfer Measurements in Rectanglar Channel Flows With 90 Deg Turns," ASME JOURNAL OF HEAT TRANSFER, Vol. 108, 1986, pp. 48-54.

10 Boelter, L. M. K., Young, G., and Iverson, H. W., "An Investigation of Aircraft Heaters XXVII—Distribution of Heat Transfer Rate in the Entrance Region of a Tube," NACA TN 1451, 1948.

11 Kays, W. M., and Crawford, M. C., *Convection Heat and Mass Transfer*, 2nd ed., McGraw-Hill, New York, 1980.

12 Kline, S. J., and McClintock, F. A., "Describing Uncertainties in Single Sample Experiments," *Mechanical Engineering*, Vol. 75, Jan. 1953.

13 Patankar, S. V., *Numerical Heat Transfer and Fluid Flow*, McGraw-Hill, New York, 1980.

14 Launder, B. E., and Spalding, D. B., "The Numerical Computation for Turbulent Flows," *Computer Methods in Applied Mechanics and Engineering*, Vol. 3, 1974, pp. 269-289.

# Numerical Solution of an Open Cavity, Natural Convection Heat Exchanger

**D. A. Richmond**
Polysar Limited,
Sarnia, Canada

**K. G. T. Hollands**
Centre for Solar Thermal Engineering,
Department of Mechanical Engineering,
University of Waterloo,
Waterloo, Ontario, Canada

*An "open-cavity" natural convection heat exchanger is one in which the flow on one side is driven by buoyancy forces and in which the effect of associated piping, valves, and fittings on that side can be ignored, since the exchanger is effectively exposed there to an extensive fluid of uniform temperature. This paper reports a finite volume numerical solution of the full set of equations governing the flow on the natural convection side of such a heat exchanger. The exchanger's dimensionless performance is shown to depend on five dimensionless groups: a modified Rayleigh number Ra*, a flow number F describing the forced convection heat capacity, a Biot number Bi describing the effect of forced convection side heat transfer coefficient, an aspect ratio $A_R$, and the Prandtl number Pr. A parametric study is performed for suitable ranges of Ra*, F, and Bi, and for Pr = 6 and AR = 0.1. The results are presented in terms of a Nusselt number, a dimensionless flow rate, and the exchanger effectiveness as a function of these variables.*

## 1 Introduction

Natural convection heat exchangers use the buoyancy force to drive the fluid through one side of the exchanger, eliminating the need for a pump on that side. Buoyancy-driven flow, sometimes called a thermosyphon, has been used successfully, for example, in solar collector loops and transformer cooling loops. There is little published information, however, indicating its use for heat exchangers, *per se*, although it appears to have some potential there. Equations permitting the rational design of these exchangers are not available in the literature. It appears that where a design has been done, forced convection relations have (incorrectly) been used to obtain the heat transfer coefficients and the shear stress at the wall.

In the exchanger analyzed in this paper, the buoyancy-driven fluid (fluid B) is contained in a set of identical equi-elevation vertical tubes, like the tubes in a vertical single-tube-pass shell-and-tube heat exchanger. The other fluid (fluid A) is assumed to be in forced flow and pure counterflow to stream B, and a known, constant heat transfer coefficient $h'$ is assumed to apply locally between stream A and the outside tube wall. The required output of the analysis is the outlet temperature of the two streams and the flow rate of stream B for prescribed values of the inlet temperatures of the two streams, the flow rate of stream A, the coefficient $h'$, the thermal conductance of the tube wall (which can be lumped with $h'$, giving $h$), the tube length $L$ and radius $R$, the relevant fluid properties, and the pressure difference $\Delta P$ from end to end of tube on the stream B side.

Previous related work (Dyer, 1968, 1975; Davis and Perona, 1971) has been restricted to the case where the tube wall, as seen by stream B, is either at uniform (constant) temperature (CWT) or receives uniform heat flux (CHF), in which case stream A does not enter the problem. The more realistic "heat exchanger type" boundary condition of the present study has not been previously examined, although Anderson and Bejan (1980) have analyzed the somewhat related problem of two counterflowing natural convection streams, but not in a cavity situation. In the present study, the problem with the heat exchanger type boundary condition was analyzed, using a finite volume representation of the governing equations, and a numerical solver.

## 2 Problem Formulation

**Physical Modeling.** One cannot complete the analysis of a natural convection heat exchanger without also analyzing the remaining part of the natural convection loop. In the well-known "open cavity" problem of natural convection (Fig. 1), the rest of the loop takes on its simplest form. In this problem (recently reviewed by Raithby and Hollands, 1985), a body containing one or more cylindrical vertical cavities is immersed in an extensive fluid of uniform temperature $T_\infty$. This problem becomes a heat exchanger problem if we posit that what keeps the wall temperature $T_W$ greater than $T_\infty$ is a second fluid (fluid A), which is driven by forced convection through passages fully interior to the body. An exchanger of this type is analyzed in this paper.

Existing solutions to the open cavity problem(s) have generally neglected certain terms in the governing equations: namely the pressure variation term in the radial direction and the terms representing axial diffusion of heat and momentum. This reduces the governing differential equations to a parabolic form, which can be solved numerically using a downstream marching technique. Thus Davis and Perona (1971) solved the circular CWT cavity problem and Dyer (1968, 1975) solved the circular CHF and CWT cavities.

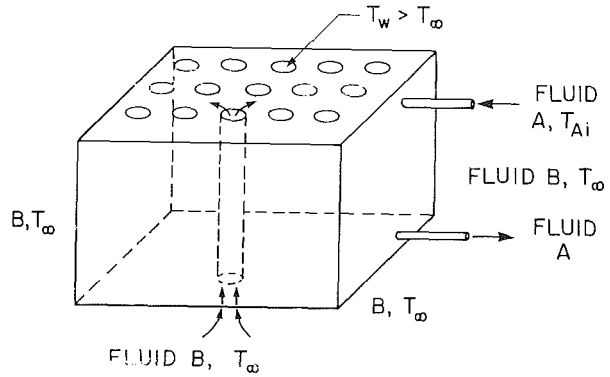


**Fig. 1 An "open cavity," counterflow, natural convection heat exchanger**

Contributed by the Heat Transfer Division and presented at the National Heat Transfer Conference, Pittsburgh, Pennsylvania, August 9-12, 1987. Manuscript received by the Heat Transfer Division August 24, 1987. Keywords: Heat Exchangers, Natural Convection, Numerical Methods.

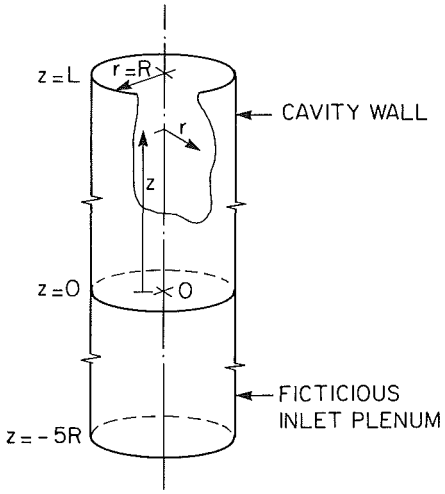


**Fig. 2 Coordinate system used for analysis of flow in singe tube**

Shewen (1986), however, has recently shown that at very low Rayleigh number, the neglect of radial variation in pressure and of the axial diffusion terms results in substantial errors in the heat transfer: At low flow rates, the fluid is preheated by axial conduction before it enters the cavity. This means that properly predicting low Rayleigh number behavior requires the solution of elliptic equations with these terms left in, and, moreover, the solution domain must be extended to include the region in front of the entrance region.

An exchanger having low values of Ra was thought to be of practical interest, so it was decided to leave in all the terms in the governing equations, solve the elliptic equations, and to extend the solution domain. For the latter it was assumed that each cavity is one of a large number of identical, closely spaced, circular heat exchanger tubes. For this condition the following extension seemed relevant and was therefore adopted: a fictitious inlet plenum is constructed, which is simply an extension of the cavity into the entrance region (see Fig. 2). The plenum length is five times the tube radius $R$, and its walls are impermeable but have zero shear and zero heat transfer. At the inlet to this plenum, the fluid is assumed to be at uniform temperature $T_i = T_\infty$ and to have a uniform velocity profile. Thus the insertion of this fictitious plenum allows for the effects of upstream conduction to be included without permitting flow across its sides. Following Aihara (1973) and Dyer (1975), the average pressure at the inlet to the plenum is set at $-\rho v_i^2/2$, where $v_i$ is the inlet velocity to the plenum. The pressure at the tube outlet at the top is made zero at the centerline. These pressures are relative to those, at the same elevation, of fluid B far from the exchanger.

The forced convection stream A enters the exchanger at inlet temperature $T_{Ai} > T_\infty$ and then flows through the interior passages in the heat exchanger in pure counterflow to stream B, which rises through the cavities or tubes. (These last two terms will be used interchangeably.) We do not solve for the velocity and temperature field on the stream A side. Rather, as is customarily done on *both* sides of a heat exchanger, this stream is represented by its bulk mean temperature $T_A$, which is taken to be a function only of the axial distance $z$, and by a convective heat transfer coefficient, which is assumed to be independent of $z$. In series with this latter convective resistance is the thermal resistance of the tube wall. We let $h$ represent the overall heat transfer coefficient, based on cavity wall area, between stream A and the inner surface of the cavity wall.

**Governing Equations.** Since all tubes are identical, it suffices to analyze one tube. Figure 2 shows the tube and the coordinate system. At any axial distance $z$, an elementary heat balance gives

$$k2\pi R\frac{\partial T}{\partial r}\Big|_{r=R} = h2\pi R(T_A - T|_{r=R}) = C_A\frac{dT_A}{dz} \tag{1}$$

where $T = T(r, z)$ is the temperature of stream B, $k$ is its thermal conductivity, and $C_A$ is stream A's total heat capacity rate divided by the number of tubes in the heat exchanger.

Fluid B is assumed to move through the tube in axisymmetric steady laminar flow, with constant $k$, viscosity $\mu$, and density $\rho$, except where $\rho$ occurs in the gravity force term, in which term it is assumed to obey the equation of state: $\rho = \rho_\infty(1 - \beta(T - T_\infty))$ where $\beta$ is a constant. According to these assumptions the governing equations are

## Nomenclature

$A$ = area of tube $= 2\pi RL$
$A_R$ = aspect ratio $= R/L$
Bi = Biot number $= h\,R/k$
$C_A$ = total heat capacity rate of side A divided by the number of tubes
$C_p$ = fluid B specific heat
$F$ = flow number $= C_A R/kA$
$g$ = gravitational acceleration
$h'$ = convective heat transfer coefficient of side A
$h$ = overall heat transfer coefficient from fluid A to inside surface of tube wall
$H_c$ = apparent mean convective heat transfer coefficient on side B, see equation (22)
$k$ = thermal conductivity of fluid B
$L$ = tube length (Fig. 2)
$\dot{m}$ = total mass flow rate on side B
$M$ = dimensionless flow rate on side B $= \dot{m}C_pR/kA$
Nu = Nusselt number $= h_c(R)/k$
$\mathrm{Nu}_w$ = $QR/(kA(T_w - T_\infty))$
$P$ = local pressure of fluid B
$P_d$ = pressure defined by equation (6)
$\bar{P}_d$ = $P_d$ averaged over tube cross-sectional area
Pr = Prandtl number of fluid B
$Q$ = heat transferred to stream B
$R$ = radius of tube (Fig. 2)
Ra* = modified Rayleigh number, see equation (13)
$\mathrm{Ra}_w^*$ = value of Ra* with $T_w$ replacing $T_{Ai}$
$r$ = radial coordinate (Fig. 2)
$T$ = local temperature of fluid B
$T_A$ = bulk mean temperature of fluid A
$T_\infty$ = temperature of fluid B far from the exchanger
$T_w$ = temperature of the cavity surface
$T_i$ = inlet temperature of fluid B
$\bar{T}_o$ = bulk mean outlet temperature of fluid B
$T_{Ai}$ = fluid A inlet temperature
$U$ = exchanger overall apparent heat transfer coefficient, based on inside area
$u$ = fluid velocity in the radial direction
$v$ = fluid velocity in the axial direction
$v_i$ = value of $v$ at entrance to plenum
$z$ = axial coordinate (Fig. 2)
$Z$ = exchanger heat capacity rate ratio $= C_A/C_B$
$\beta$ = thermal expansion coefficient of fluid B
$\epsilon$ = heat exchanger effectiveness
$\bar{\theta}$ = dimensionless outlet temperature of fluid B
$\mu$ = viscosity of fluid B
$\rho$ = local density of fluid B
$\rho_\infty$ = density of fluid B at ambient temperature $T_\infty$

$$\frac{1}{r}\frac{\partial}{\partial r}(ur)+\frac{\partial v}{\partial z}=0 \tag{2}$$

$$\rho_\infty\left(u\frac{\partial u}{\partial r}+v\frac{\partial u}{\partial z}\right)=-\frac{\partial P_d}{\partial r}+\mu\left[\frac{\partial}{\partial r}\left(\frac{1}{r}\frac{\partial}{\partial r}(ru)\right)+\frac{\partial^2 u}{\partial z^2}\right] \tag{3}$$

$$\rho_\infty\left(u\frac{\partial v}{\partial r}+v\frac{\partial v}{\partial z}\right)=-\frac{\partial P_d}{\partial z}+\mu\left[\frac{1}{r}\frac{\partial}{\partial r}\left(r\frac{\partial v}{\partial r}\right)+\frac{\partial^2 v}{\partial z^2}\right]-\rho_\infty g\beta(T-T_\infty) \tag{4}$$

$$\rho_\infty c_p\left[u\frac{\partial T}{\partial r}+v\frac{\partial T}{\partial z}\right]=k\left[\frac{1}{r}\frac{\partial}{\partial r}\left(r\frac{\partial T}{\partial r}\right)+\frac{\partial^2 T}{\partial z^2}\right] \tag{5}$$

where $u$ and $v$ are the fluid's radial and axial velocities, respectively, and

$$P_d=P-\rho_\infty g(z+5R) \tag{6}$$

where $P$ is the fluid's local pressure, and $g$ is the acceleration of gravity. Equations (1)-(5) are to be solved subject to the following boundary conditions:

$$r=0,\ -5R\le z\le L,\ u=0,\ \frac{\partial v}{\partial r}=0,\ \frac{\partial T}{\partial r}=0 \tag{7}$$

$$r=R,\ 0\le z\le L,\ u=0,\ v=0,\ k\frac{\partial T}{\partial r}=h(T_A-T) \tag{8}$$

$$r=R,\ -5R\le z\le 0,\ u=0,\ \frac{\partial v}{\partial r}=0,\ \frac{\partial T}{\partial r}=0 \tag{9}$$

$$z=-5R,\quad 0\le r\le R,\quad u=0,$$

$$\bar{P}_d=-\frac{1}{2}\rho v^2,\quad T=T_i=T_\infty,\quad v=\text{const} \tag{10}$$

$$z=L,\quad 0\le r\le R,\quad \frac{\partial u}{\partial z}=0,\quad \frac{\partial v}{\partial z}=0,$$

$$\frac{\partial T}{\partial z}=0,\quad T_A=T_{\mathrm{Ai}},\quad P_d|_{r=0}=0 \tag{11}$$

In arriving at the boundary condition covered by equation (11), it was noted that the fluid is at outflow, and Patankar's (1980) discussion of outflow boundaries at high Rayleigh number (high Peclet number) were assumed to apply. At very low Ra*, the flow should be fully developed, so the gradients should, in any event, be essentially zero at the end of tube. In reality the flow continues as a plume, and further investigation of this boundary condition may be warranted.

(It should be noted that the outflow boundary conditions are not correct if recirculation is taking place at the exit. After simulation of the flow using the above equations and boundary conditions had been complete, two observations were made that tend to support the hypothesis that such recirculation does not in fact, take place. First, downward velocities were never observed in the flow field, including the top; second, there was no indication in the numerical convergence process of the oscillations that often accompany recirculating flow, which is often bistable; convergence was generally monotonic and required few iterations. Experimental evidence would, of course, help to settle the matter of recirculation, and although such evidence is not yet available for all aspects of the present problem, the evidence relating to the special case of the CWT boundary condition tends to negate the possibility of recirculation existing, or (if it does exist), of appreciably affecting the heat transfer. In particular, Dyer (1968) observed that his Nusselt number predictions—which he computed without allowing for recirculation—match closely the experimental Nusselt numbers obtained by Ellenbaas (1942). To account for the possibility of recirculation in the present analysis would require the extension of the region modeled to include part of the region outside the heat exchanger tube, and, as found by Ormiston et al. (1986), who worked on a somewhat similar problem, this may require modeling the heat transfer surfaces that bring fluid B back to $T_\infty$ after leaving the exchanger. The problem with recirculation is far more complicated than the problem without circulation.

The main quantities of interest, once $T$, $u$, and $v$ have been solved for, are the total flow rate $\dot{m}$ (obtained by integrating $v$ across the cavity) and the bulk mean temperature $\bar{T}_o$ at the outlet.

**Nondimensionalization of Governing Equations.** The governing equations and boundary conditions may be nondimensionalized, with the following dimensionless groups emerging:

$$\mathrm{Ra}^*=\frac{\rho_\infty^2 g\beta c_p(T_{Ai}-T_\infty)R^3}{\mu k}\frac{R}{L} \tag{13}$$

$$\mathrm{Pr}=\frac{\mu c_p}{k} \tag{14}$$

$$F=\frac{C_A R}{kA} \tag{15}$$

$$\mathrm{Bi}=\frac{hR}{k} \tag{16}$$

$$A_R=R/L \tag{17}$$

In equation (15), $A=2\pi RL$ is the tube area.

From engineering considerations, a range of interest of Ra* $F$, and Bi was determined. The range for Ra($1\le \mathrm{Ra}^*\le 1000$) was established by examining the conditions for good heat transfer in the known CWT solution. When the thermal boundary layers overlap, the temperature profile across the tube becomes flat and the potential for heat transfer is subsequentially reduced; the lower bound of Ra* was determined by avoiding "fully developed flow" over a majority of the tube. The upper bound is determined by estimating the lowest value of Ra* at which there is no interaction between the thermal boundary layers over the tube length; this "separate flow" is undesirable for a heat exchanger because the buoyancy force is used to carry a core of unheated, or parasitic, fluid in the center of the tube. The flow number $F$ represents the amount of energy available in stream A relative to the ability of the stream B to absorb the energy. The range of flow number $F$ considered in this study was $0.25\le F\le 10$. The range of Biot numbers considered was $1\le \mathrm{Bi}\le 1000$; the condition $\mathrm{Bi}=1000$ should be equivalent to $\mathrm{Bi}=\infty$; the condition $\mathrm{Bi}=1$ would represent very poor heat transfer on the forced convection side.

The aspect ratio $A_R$ is only a variable if the axial diffusion terms are important (it multiplies these terms in the nondimensionalized equations). Thus it is expected to be unimportant except at low Ra*. In this study, $A_R$ was kept constant at 0.1. The Prandtl number Pr was kept constant at 6, its value for water at moderate temperatures.

The nondimensionalized output variables of the analysis are nondimensionalized outlet temperature

$$\bar{\theta}=(\bar{T}_o-T_\infty)/(T_{Ai}-T_\infty) \tag{20}$$

and the dimensionless flow rate

$$M=\frac{\dot{m}c_p R}{kA} \tag{21}$$

Other output parameters of interest are the capacity rate ratio $Z$ given by

$$Z = C_A/\dot{m}c_p = \frac{F}{M}$$

and a Nusselt number Nu, defined as follows. From the outlet temperature $\bar{T}_o$ and the flow rate $\dot{m}$, one can calculate an exchanger effectiveness $\epsilon$, using standard heat exchanger equations. Assuming counterflow, one can then determine an NTU for the exchanger, from which a UA can be determined. Now

$$\frac{1}{U} = \frac{1}{h} + \frac{1}{h_c} \tag{22}$$

where $h$, of course, is the thermal conductance from stream A to tube wall. It follows that $h_c$ must be the apparent mean convective heat transfer coefficient for the free convective flow. From this $h_c$, a Nusselt number can be readily formed:

$$\mathrm{Nu} = h_c R/k \tag{23}$$

Dimensional analyses show that $\theta$, $M$, $Z$, heat exchanger effectiveness $\epsilon$, and Nu are each functions of the list of five variables given by equations (13)-(17). The equations were solved in their primitive, dimensional form using the properties of water at 300 K, and afterwards the results were put into dimensionless form.

## 3 Numerical Solution Method

The solution approach followed here was to discretize the domain into a finite number of control volumes using a nonuniform, two-dimensional, axisymmetric mesh, whose perimeter grid lines coincided with the physical boundaries of the system. The conservation equations were then integrated over each control volume, approximating the resulting integral terms, as required, to yield a discrete set of algebraic equations. This set of algebraic equations was then solved numerically. The general discretization procedure and approximations used were direct analogies to those of Patankar (1980). The basic FORTRAN coding of the discretized equations and the numerical solution method used were obtained from a community code at the University of Waterloo called WATSHARE. The WATSHARE code consists of a set of subroutines written to facilitate the finite volume solution of incompressible fluid flow and heat transfer problems. Details of the finite volume formulation and the resulting equations are given by Richmond (1985).

After all input data had been read, the solution procedure first initialized all field quantities $T$, $u$, $v$, $P_d$ to zero. The continuity and energy equation coefficients and source terms were then calculated. A modified version of the Alternating Direction Implicit (ADI) method from VanDoormaal and Raithby (1984) was applied to the energy equation, to solve for $T$. Each line of the ADI sweep was solved with the Thomas Algorithm (TDMA). The momentum equation coefficients and source terms were then calculated and the SIMPLEC pressure–velocity coupling solution method from VanDoormaal and Raithby (1984) was followed. (SIMPLEC is an enhanced version of the SIMPLE method of Patankar, 1980.) Both the temperature and pressure fields were checked for convergence. If the convergence criterion was met, the final solution fields were processed to obtain the desired gross information. If convergence was not met, the control shifted to the recalculation of coefficients and source terms based on the most recent solution fields, and iteration continued.

Iteration was required to determine, by trial and error, the inlet velocity $v_i$ (and hence the flow rate $\dot{m}$) that makes $P_d$ satisfy the boundary condition given by equation (11). The central point in establishing the convergence criterion for this process was ensuring that the flow generated by any pressure difference associated with $\bar{P}_{d,o}$ (the value of $\bar{P}_d$ at plenum inlet), being different from $-1/2\rho v_i^2$, constituted a negligibly small part of the total flow. This turns out to be essentially equivalent to ensuring that the force $F_p = (\bar{P}_{d,o} + 1/2\rho v_i^2)\pi R^2$ is much smaller than the net buoyancy force $F_B$ on the cylinder of fluid. A criterion $F_p < 0.01 F_B$ was decided upon. Thus the iteration procedure ran as follows: $v_i$ was guessed and the flow solved for ; $\bar{P}_{do}$, $F_p$, and $F_B$ were calculated, the first by integrating $P_d$ across the inlet plenum cross section, the last by integrating $\rho_\infty(T - T_\infty)g$ over the entire cylindrical volume. If $F_p/F_B < 0.01$, the procedure ends. If not, a new $v_i$ is guessed and iterated on, and $F_p/F_B$ is again compared to 0.01. If this $v_i$ does not produce results that satisfy the criterion, linear interpolation (or extrapolation) of $F_p/F_B$ versus $v_i$ is used to estimate the value of $v_i$ that makes $F_p/F_B = 0$. Generally this value of $v_i$ gave results that satisfied the criterion, but if not, interpolation was repeated with the last two values of $v_i$, and so on. (Plots of $F_p/F_B$ versus $v_i$ gave straight lines over the range $|F_p/F_B| \le 0.2$.)

A nonuniform grid, with closer spacing near the wall, was used. Studies were carried out to determine the size of grid required for 1 percent accuracy on the heat transfer. The most demanding condition was at the high Rayleigh number $\mathrm{Ra}^* = 1000$. Here it was found that 22 divisions in the radial direction and 33 divisions in the axial direction were required to produce a value of Nu within 1 percent of the exact Nu value. This latter value was calculated by extrapolating, on a curve of Nu versus the number ($N$) of control volumes, to infinite $N$, assuming an exponential shape to the curve.

The solution procedure was verified on a number of test problems for which the solution was known (e.g., forced convection in a tube). As further verification, the program was used to simulate the CWT boundary condition open cavity problem analyzed by Davis and Perona (1971) and Dyer (1968). Both these workers used $P_d = 0$ at the inlet rather than $P_d = -1/2\rho v_i^2$ and neither used an inlet plenum. Thus, to be consistent, the boundary condition on $\bar{P}_d$ was changed to $\bar{P}_d = 0$ and the inlet plenum was deleted. The results are shown in Table 1 for three values of $\mathrm{Ra}_w^*$, which is Ra* with $T_{Ai}$ replaced by $T_w$. At $\mathrm{Ra}_w^* = 100$ and 1000, agreement on the Nusselt number with both Davis and Perona, and Dyer was within 1 percent, which is well within the error of reading the graphs from their papers. At $\mathrm{Ra}^* = 10$, agreement with both other workers is within 3 percent.

**Table 1 Comparison of Solutions for CWT boundary condition**

| $\mathrm{Ra}_w^*$ | $\mathrm{Nu}_w$ | | |
|---|---|---|---|
| | Dyer* (1968) | Davis and Perona* (1971) | Present study |
| 1000.0 | 3.2 | 3.2 | 3.24 |
| 100.0 | 1.5 | 1.5 | 1.51 |
| 10.0 | 0.47 | 0.44 | 0.45 |

*Values read from graphs for which the reading error is estimated at ± 1.5 percent.

Runs for the heat exchanger boundary condition were then made, simulating each point in the following three-dimensional matrix in $F$, Bi, and Ra*:

$$\mathrm{Ra}^* = 10, 100, 1000$$

$$\mathrm{Bi} = 1, 10, 1000$$

$$F = 0.25, 1, 2, 5, 10$$

## 4 Results

The Nusselt number results are shown in Fig. 3, in which (as in subsequent plots) cubic splines have been used for interpolation between the Ra* values simulated. The triangular markers indicate the heat transfer for the CWT boundary condition with $\mathrm{Ra}^* = \mathrm{Ra}_w^*$. For $\mathrm{Bi} = 1000$, the curves pass directly through CWT points for $F > 5$. This is as expected: For $\mathrm{Bi} = \infty$ and $F = \infty$ the heat exchanger problem reduces to the CWT problem with $T_w = T_{Ai}$; apparently values of Bi and $F$ of 1000 and 5 are sufficiently close to infinity to meet this condition.

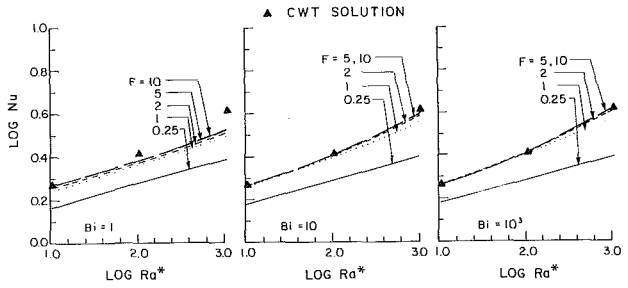


**Fig. 3 Plot of Nusselt number as a function of dimensionless groups. CWT refers to the solution for constant wall temperature. Note: Values have been calculated only at three values of Ra*: 10, 100, 1000; cubic spline interpolation has been used between these points.**

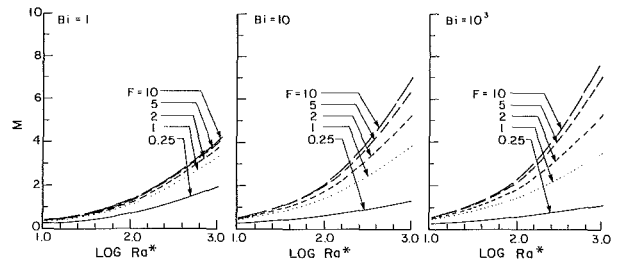


**Fig. 4 Plot of dimensionless free convective flow rate M as a function of dimensionless groups**

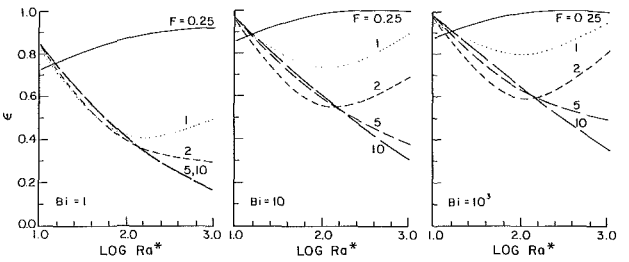


**Fig. 5 Plot of heat exchanger effectiveness ε as a function of dimensionless groups**

The curves for Bi = 1000 are independent of $F$ when Ra* < 100 and $F \geq 1$. The same is roughly true for Bi = 10. But for Bi = 1, the heat transfer is affected by both Ra* and $F$ over the full Ra* range. Thus, heat transfer is insensitive to $F$ and Bi for Ra* < 100 provided Bi ≥ 10, and the effects of Ra* and $F$ are greatest at Bi = 1.

The dimensionless natural convection flow $M$ is shown in Fig. 4. These figures illustrate the dramatic increase in flow rate that accompanies increasing Ra*. This trend may be explained by the balance of forces in the momentum equations, namely the viscous and buoyancy forces. At low Ra* the shear stresses are large and easily balance the buoyancy forces, thus limiting the flow rate. At a higher Ra*, corresponding to a larger radius duct, the shear produced by viscous forces will be smaller, and will only balance the buoyancy when the flow rate becomes very high. Flow rate $F$ has a significant effect on $M$ at all Bi, especially at high Ra*. At Ra* = 10, $F$ has little effect on $M$, and its effect increases with Ra*. The spread in the curves for Ra* > 100 shows that Ra* and $F$ have a much more severe influence on the thermosyphon flow rate than they have on the Nusselt number.

The influence of flow rate $F$ and Biot number Bi shown in Figs. 3 and 4 is largely a reflection of the fact that smaller values for these numbers have the effect of reducing the temperature difference $\bar{T}_w - T_\infty$ driving the buoyant flow, by reducing the mean wall temperature $\bar{T}_w$. For example, at very small values of $F$, the forced convection fluid will, because of its low heat capacity, essentially reach $T_\infty$ after having traveled only a very short axial distance, so that most of the tube

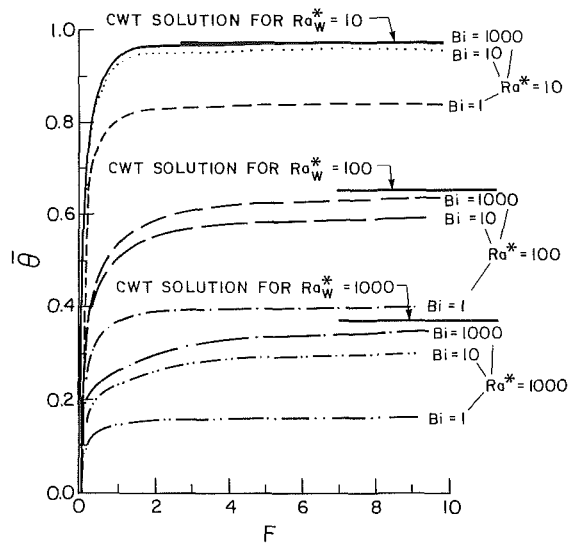


**Fig. 6 Plot of dimensionless free convective stream outlet temperature as a function of dimensionless groups. CWT refers to solution for constant wall temperature.**

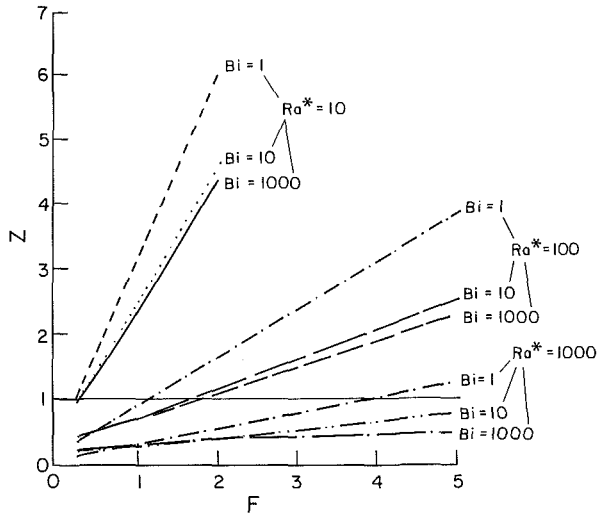


**Fig. 7 Plot of ratios of forced convective (stream A) to free convective (stream B) flow rates as a function of dimensionless groups**

wall will be essentially at $T_\infty$. Very low values of $h$ (or Bi) will produce a large temperature difference between the forced convection fluid and the wall temperature, again driving the wall temperature toward $T_\infty$. With only a small value of $T_w - T_\infty$, the buoyant flow $M$ will be very small and the heat transfer Nu will consequently be low.

Figure 5 shows the exchanger effectiveness ε plotted as functions of Ra*, $F$, and Bi. The peculiar shape of these curves is a consequence of the fact that the definition of ε changes when $C_A/C_B$ passes through unity. (Even for a standard exchanger, a plot of ε versus capacity rate on one side, other variables held constant, passes through a minimum when the capacity rates are equal.) Figure 6 shows the same data plotted as $\bar{\theta}$ versus $F$ for various Bi and Ra*. This plot shows, as horizontal lines, the CWT solution, which forms upper bounds for the plots. Figure 7 shows a similar plot for $Z$.

## 5 Conclusions

The natural convection heat exchanger is an important problem worthy of full-scale analysis. This paper has presented a start on this needed work, by formulating the problem and presenting solutions for particular set of conditions. Because of the large range of parameters on which the

heat transfer and flow rate depend, a completely general solution does not seem possible. For design purposes, it may be necessary to run a full-scale finite-volume numerical code, such as that described here. The code will have to include the external part of the loop, but the most difficult part to analyze will be the heat exchanger itself. By inter-comparing solution at the same sets of dimensionless parameters, and by comparing against experimental results, workers in different labs can validate the accuracy of these programs.

## 6 Acknowledgments

The authors are indebted to the Natural Sciences and Engineering Research Council of Canada for financial support and to G. D. Raithby for a great deal of guidance in the carrying out of the work. Thanks also to Jo Brooks for her excellent typing of the manuscript and Dr. A. V. Hassani for careful editorial work, and Dr. Theo Van der Meer for several contributions.

## References

Aihara, T., 1973, "Effect of Inlet Boundary Conditions on Numerical Solutions of Free Convection Between Vertical Parallel Plates," *9th Heat Transfer Symposium of Japan, Rep. Inst. High Speed Mech.*, Tohoku University, No. 258, Vol. 28.

Anderson, R., and Bejan, A., 1980, "Natural Convection on Both Sides of a Vertical Wall Separating Fluids at Different Temperatures," ASME JOURNAL OF HEAT TRANSFER, Vol. 102, pp. 630–635.

Davis, L. P., and Perona, J. J., 1971, "Development of Free Convection Flow of a Gas in a Heated Vertical Open Tube," *Int. J. Heat Mass Transfer*, Vol. 14, pp. 889–903.

Dyer, J. R., 1968, "The Development of Natural Convection in a Vertical Circular Duct," *Mech. Chem. Engng. Trans.*, I. E. Aus., MC4(1), pp. 78–86.

Dyer, J. R., 1975, "Development of Laminar Natural Convective Flow in a Vertical Uniform Heat Flux Duct," *Int. J. Heat Mass Transfer*, Vol. 18, pp. 1455–1465.

Elenbaas, W., 1942, "Heat Dissipation of Parallel Plates by Free Convection," *Physica*, Vol. IX, No. 1, pp. 2–28.

Ormiston, S. J., Raithby, G. D., and Hollands, K. G. T., 1986, "Numerical Predictions of Natural Convection in a Trombe Wall System," *Int. J. Heat Mass Transfer*, Vol. 29, No. 6, pp. 869–877.

Patankar, S. V., 1980, *Numerical Heat Transfer and Fluid Flow*, McGraw-Hill, New York.

Raithby, G. D., and Hollands, K. G. T., 1985, "Natural Convection," in: *Handbook of Heat Transfer Fundamentals*, Rohsenow, Hartnett, and Ganic, eds., McGraw-Hill, New York, Chap. 6, pp. 6–33 to 6–41.

Richmond, D. A., 1985, "Numerical Solution of Buoyancy Driven Flows in Tubular Heat Exchangers," M.A.Sc. Thesis, Department of Mechanical Engineering, University of Waterloo, Waterloo, Canada.

Shewen, E. C., 1986, "A Peltier-Effect Technique for Natural Convection Heat Flux Measurement Applied to the Rectangular Open Cavity," Ph.D. Thesis, Department of Mechanical Engineering, University of Waterloo, Waterloo, Canada.

VanDoormal, J. P., and Raithby, G. D., 1984, "Enhancements of the SIMPLE Method for Predicting Incompressible Fluid Flows," *J. of Numerical Heat Transfer*, Vol. 7, pp. 147–163.

**D. N. Jones**
Development Scientist,
Union Carbide Corporation,
Bound Brook, NJ 08805

**D. G. Briggs**
Associate Professor,
Department of Mechanical and Aerospace Engineering,
Rutgers College of Engineering,
Piscataway, NJ 08855-0909

# Periodic Two-Dimensional Cavity Flow: Effect of Linear Horizontal Thermal Boundary Condition

## Introduction

A two-dimensional air-filled cavity with isothermal vertical walls adiabatic top and bottom surfaces has been extensively studied both numerically and experimentally. When the aspect ratio is of order one and the Rayleigh number is less than about $10^9$ this geometry produces a highly stable and reproducible laminar flow.

The result is quite different when the upper and lower surfaces are subjected to a destabilizing boundary condition, i.e., a linear temperature variation between the hot and cold vertical walls. At a critical Rayleigh number between $10^6$ and $10^7$ the flow becomes periodic and thus appears to fall into the category of instability of the type known as Hopf bifurcation. Briggs and Jones (1985) report velocity variations measured near the vertical surfaces that vary by nearly ± 20 percent about the mean. Other unexplained behavior reported by Briggs and Jones (1985) consisted of jumps in the periodic frequency as the Rayleigh number increased. These jumps exhibited hysteresis effect, which resulted in some overlap between regimes.

This paper presents the results of additional measurements, which indicate that the periodic flow is characterized by the convection of hot and cold pairs of thermals around the enclosure.

## Experimental Apparatus and Techniques

Figure 1 illustrates the key features of the experimental apparatus. It consisted of an experimental enclosure, two constant temperature circulating baths, $x$-$y$-$z$ traversing table, Thermo-Systems single color laser-Doppler velocimeter (LDV), temperature measurement apparatus, and Gould Model 1600 stripchart recorder. Figure 2 illustrates details of the free convective enclosure, which measured 150 mm wide, 150 mm high, and was 186 mm deep. This apparatus is described in more detail in Briggs and Jones (1985) and in Jones (1987).

During experimentation, the apparatus was brought to equilibrium temperature and then allowed to stabilize for a time ranging from thirty minutes to one hour prior to taking data. Details of this procedure are also summarized in Briggs and Jones (1985).

Schlieren studies were conducted using a single beam system with the experimental apparatus placed to expose the entire cross section to the incident beam. This provided an excellent picture of the thermal processes underway within the cavity. Under nonoscillatory conditions, a distinct boundary layer structure was visible along all horizontal and vertical surfaces. This varied in thickness from the "leading edge" of these surfaces in the usual manner. When operating in the oscillating regime, thermal events that circulated with the primary flow were clearly visible. The periodic events visualized were correlated and compared with temperature fluctuations, thereby indicating that these events were the source of the fluctuations.

The frequency of velocity fluctuation was measured at various locations within the cavity, and for a wide range of Rayleigh number. This is reported by Briggs and Jones (1985) and the results are repeated in Fig. 3.

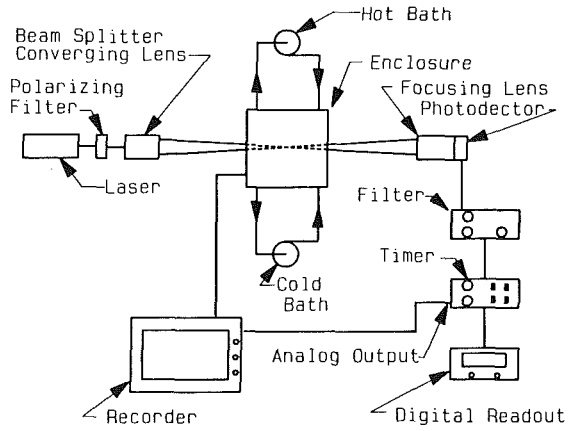


**Fig. 1 Schematic of apparatus**

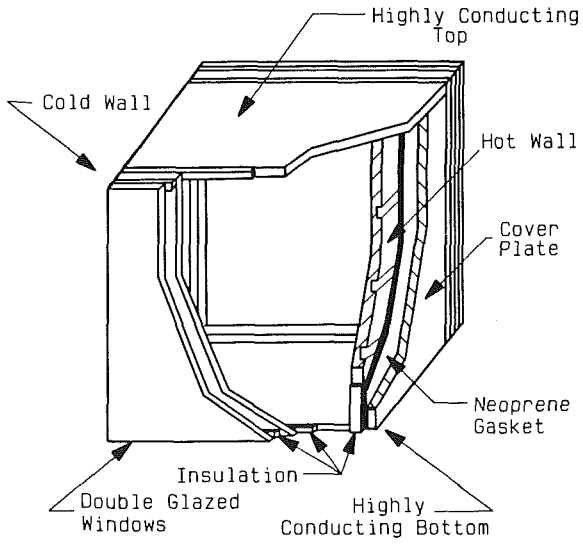


***Fig. 2 Cutaway view of enclosure***

Contributed by the Heat Transfer Division and presented at the ASME Winter Annual Meeting, Anaheim, California, December 7-12, 1986. Manuscript received by the Heat Transfer Division February 23, 1987. Keywords: Enclosure Flows, Natural Convection, Transient and Unsteady Heat Transfer.

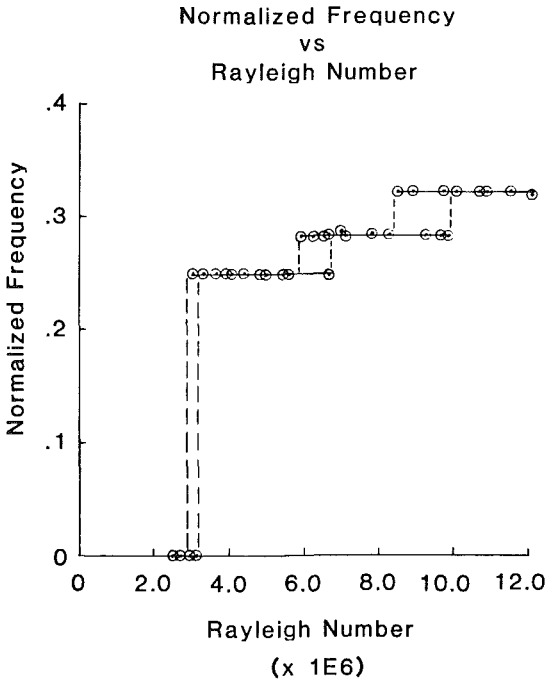


**Fig. 3 Normalized frequency variation with Rayleigh number**

In order to compare the velocity at the same instant in time at various positions around the enclosure, the laser-Doppler velocimeter was used in conjunction with a small thermocouple, which could be moved to various locations within the enclosure. When held at a fixed location, the thermocouple provided a periodic temperature variation in time, which permitted correlation of the measured velocities at other locations within the enclosure to the same point in the time cycle.

The combination of the thermocouple and velocimeter also made it possible to correlate local temperature variations with a fixed velocity time base, and to correlate local temperature variations with local velocity variations.

## Experimental Results and Discussion

Schlieren photographs (Jones, 1987) were made at specific stages during the fluid oscillation, i.e., at the onset of a cycle, 1/4, 1/2, 3/4, and 1 cycle later. This was accomplished by continuously monitoring the oscillations via the use of a strip-chart recording of the fluid temperature at a reference point within the fluid boundary layer, and using it as reference for the periodic variation with time. Thus, specific stages within the oscillation cycle were repeatedly identified and the schlieren photographs taken at the desired stage of fluid oscillation. This procedure was repeated for a variety of Rayleigh numbers and revealed much about the flow behavior.

For Rayleigh numbers within the first regime of periodic motion($3.0\times10^6<\mathrm{Ra}<6.8\times10^6$), the peak of the oscillation occurred at exactly the same instant in both the lower hot wall corner and the upper cold corner. Discharges of fluid went up the hot wall and down the cold wall perfectly in phase with each other. These discharges both traveled the length of the vertical walls and reached the opposing horizontal surfaces in about 1/2 cycle. They then appeared to dissipate somewhat while flowing along the horizontal surfaces. This process was followed by repeated vertical discharges every cycle. During the vertical flow, the discharges had almost a plumelike appearance. Just prior to the discharge, the Schlieren revealed two vertical bulges in the thermal boundary layers along the horizontal surfaces. The second bulge was the source of the discharge.

For Rayleigh numbers within the second regime of periodic motion ($6.0\times10^6<\mathrm{Ra}<9.0\times10^6$), a phase shift occurred such that the vertical discharge at the hot vertical wall occurred 1/2 cycle out of phase with the downward flowing discharge at the cold vertical wall. Thus the hot discharge arrived at the top of the enclosure just about the same time that the cold discharge was starting to travel down the cold wall.

For Rayleigh numbers greater than about $9.0\times10^6$, the flow became more disorganized with cold wall discharges leaving at various times relative to the hot discharge. In addition, discharges were initiated up the hot wall before the prior hot discharge had reached the top. It was much more difficult to correlate and time the stages within a cycle of these oscillations since not all cycles were identical. However, in general it appeared that the hot discharges occurred at about the same time (symmetrically) as the cold discharges. The double bulge was also noted along the horizontal surfaces before a discharge took place.

In addition to the Schlieren photographs, correlation of the velocity at points along the path of the primary circulatory flow were recorded using the LDV in conjunction with the reference thermocouples. The results at Rayleigh numbers of $5.0\times10^6$ and $8.75\times10^6$ are shown in Fig. 4 and 5, respectively. Figure 4 illustrates the velocity correlation with position at the same time in a typical cycle. The position is measured along a path located 10 mm inside the enclosure walls beginning near the lower cold corner and proceeding in the direction of flow; thus 130 mm corresponds to a point near the bottom corner of the hot wall, 260 mm corresponds to a point near the top corner of the hot wall, etc. Along both horizontal surfaces, there are three points within the fluid that are simultaneously at the local velocity maximum. These regions of maxima are separated by two other regions experiencing local velocity minima, and regions in transition. On the vertical walls, at the same time, only one velocity maximum and minimum were present. Since studies had shown that all points within the boundary layer experienced fluctuating velocities, it became apparent that these local maxima and minima must move around the cavity. Measurements indicated no phase shift in a direction perpendicular to the flow at a given location.

## Nomenclature

$Ar$ = aspect ratio of the enclosures $= H/L$
$f$ = frequency in cycles per second
$f_{ND}$ = normalized frequency $= fL/\sqrt{g\beta\Delta TH}$
$g$ = gravitational constant
$H$ = height of the enclosure
$L$ = width of the enclosure
Pr = Prandtl number $= \nu/\alpha$
Ra = Rayleigh number based on width $= g\beta\Delta TL^3/\nu\alpha$
$T_H$ = hot wall temperature
$T_C$ = cold wall temperature
$U_c$ = convection scaling velocity $= \sqrt{g\beta\Delta TH}$
$\alpha$ = thermal diffusivity
$\beta$ = volumetric expansion coefficient
$\Delta T$ = temperature difference $= T_H - T_C$
$\Delta\tau$ = dimensionless time increment
$\mu$ = dynamic viscosity
$\nu$ = kinematic viscosity $= \mu/\rho$
$\rho$ = density of air
$\tau$ = dimensionless time $= \alpha t/L^2$

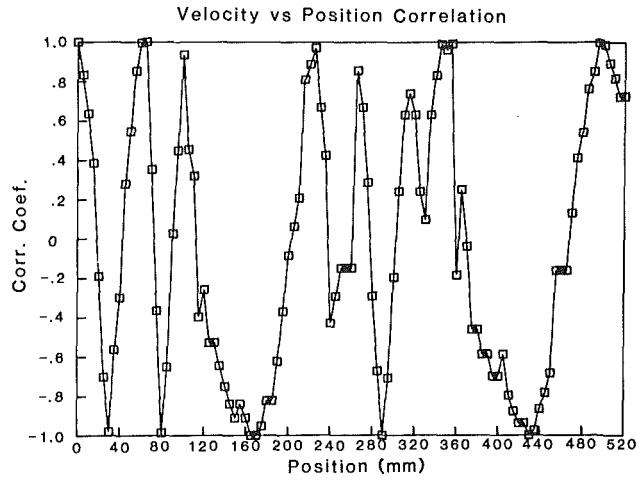


Fig. 4 Velocity correlation with position at $Ra = 5.0 \times 10^6$

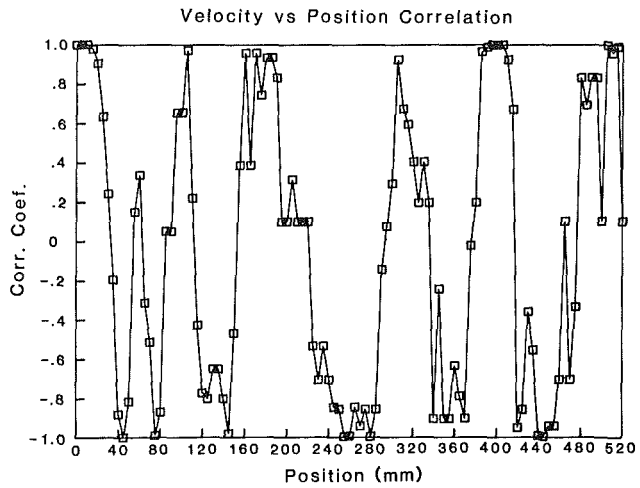


Fig. 5 Velocity correlation with position at $Ra = 8.75 \times 10^6$

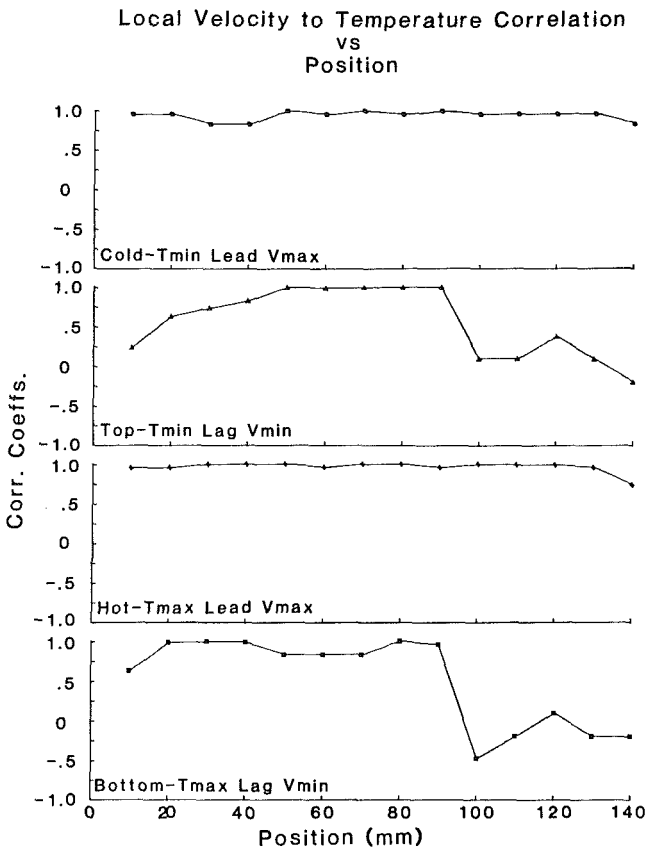


Fig. 6 Local velocity/temperature correlation with position at $Ra = 5.0 \times 10^6$

This data showed that the velocity fluctuations measured were not the result of a cavity wide oscillation, or similar to a thermosyphon where all velocity variations take place simultaneously. The measurements at the vertical walls showed that the distance separating the high and low velocity regions was considerably stretched as the fluid traveled up (or down) the walls.

At the higher Rayleigh number of $8.75 \times 10^6$ (Fig. 5) similar correlations of velocity maxima and minima were found on the horizontal surfaces, but a pronounced reversal of phase angle occurred between the lower hot corner and the upper cold corner. In this case the velocity maximum occurred at the same instant that the velocity minimum occurred in the cold corner. This was consistent with the Schlieren photographic observations, which had revealed a phase shift in the discharging of plumes at these two corners at this Rayleigh number. Short spikes also appeared with the correlation along the horizontal surfaces indicating some anomalous motion, not completely in phase with the primary peaks. In addition, the spikes were not part of a smooth transition between phases but appeared suddenly as independent regions. In spite of this, the behavior on the vertical walls was consistent with what had been seen at the lower Rayleigh numbers, i.e., only one pair of high and low velocity regions was present.

In order better to understand the nature of the flow, thermal information was recorded as a function of time and position around the cavity. These data were then correlated with the velocity data at the same positions, thereby defining the local relations between the thermal and momentum processes. Typical results of these correlations are depicted in Figs. 6 and 7 at the indicated Rayleigh numbers. These show that the temperature extremes were in phase with the velocity extremes along the vertical walls, i.e., the most buoyant fluid produced the highest vertical velocity. The same conclusion about the least buoyant fluid was observed at the cold wall.

A different behavior was noted along the horizontal surfaces, however. Along the bottom, the temperature maximum was initially in phase with the velocity minimum. This is reasonable, since the hot fluid would possess the least momentum down the cold wall, translating into slow initial motion across the horizontal surface. Conversely, the lowest temperature initially was in phase with the highest velocity along the bottom surface. This corresponded to fluid which had the highest velocity during its descent down the cold wall. Near the midpoint of the bottom, a phase shift occurred such that the maximum temperature became in phase with the maximum velocity. This phase correlation then continued to and up the vertical hot wall.

Figures 8 and 9 plot the variation of temperature correlation with position around the cavity. It may be seen from these figures that it is difficult to determine exactly the number of circulating hot and cold pairs, but it appears to be five at $Ra = 5 \times 10^6$ and six at $Ra = 8.75 \times 10^6$. Symmetric or in-phase passage of hot thermals up the hot wall and cold thermals down the cold wall requires the number of hot-cold pairs to be an odd number.

## Numerical Simulation Method and Results

A two-dimensional numerical solution of the problem was performed. The objective of this exercise was to see how close-

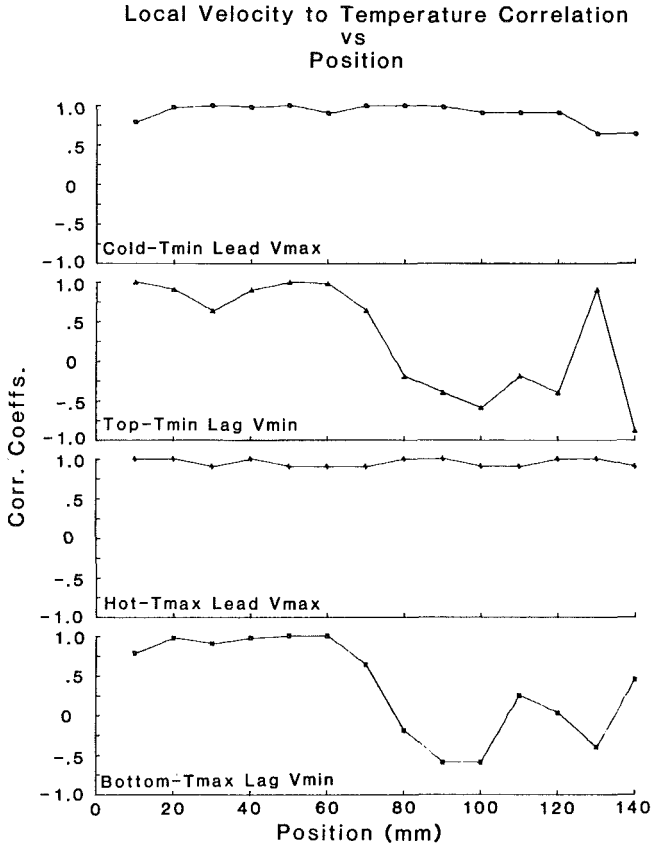


**Fig. 7 Local velocity/temperature correlation with position at $Ra = 8.75 \times 10^6$**

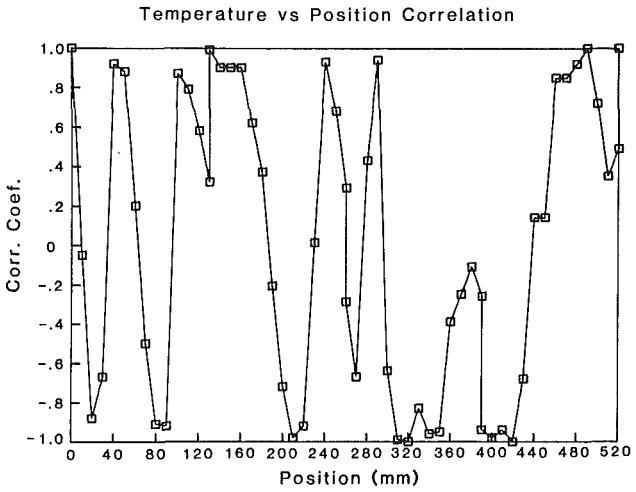


**Fig. 8 Temperature correlation with position at $Ra = 5.0 \times 10^6$**

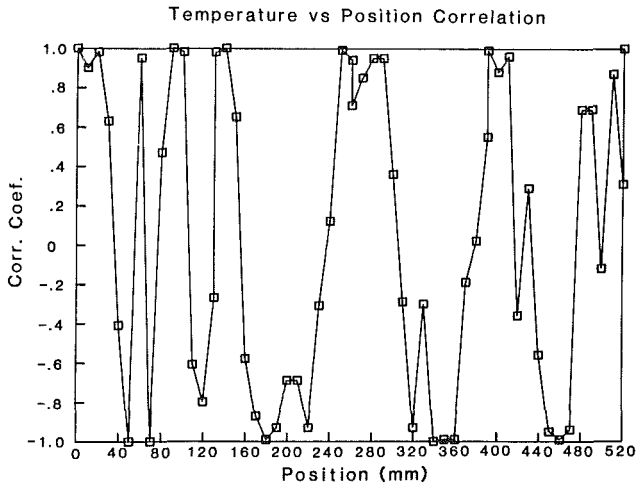


**Fig. 9 Temperature correlation with position at $Ra = 8.75 \times 10^6$**

ly the purely two-dimensional calculations would compare with the apparently two-dimensional behavior of the experiment. Although it was realized that three-dimensional effects must be present, and affecting the experimental flow, these effects were believed to be minimal, and it was hoped that the numerical simulation would provide additional insight into the transient variation of temperature and velocity throughout the cavity during the oscillations. These global instantaneous measurements would have been extremely difficult to perform experimentally with the equipment available. Some of the key results of the numerical experiments are summarized here.

The numerical scheme used was a variation of the Patankar SIMPLER method (Patankar, 1980) in which the equations of motion and the coupled energy equation are written in explicit form. The continuity equation permits the formation of a Poisson equation in pressure, which is solved at each time step by a fast solver. The velocity and temperature fields are then advanced. The incompressible form of the momentum equation was used and the Boussinesq approximation was employed in the energy equation. The method is first-order accurate in time.

The boundary conditions were isothermal vertical walls with a linear temperature variation on the horizontal surfaces. The Prandtl number used was 0.72. Interestingly, above a critical Rayleigh number, the numerical simulation produced periodic motion possessing features similar to those observed experimentally. However, the critical Rayleigh number for the onset of the periodic motion was about $2.2 \times 10^6$ rather than the experimental value of $3.2 \times 10^6$, and the computations did not indicate a sharp cutoff in periodic flow at the critical Rayleigh number as observed experimentally. Instead, the amplitude of the fluctuating velocities decreased as the Rayleigh number was reduced below about $3.0 \times 10^6$ with the fluctuations disappearing at $2.2 \times 10^6$. The Rayleigh number at which the fluctuations disappeared depended on grid size down to a spacing of about $100 \times 100$. Further grid refinement had no effect on the Rayleigh number at which the fluctuations disappeared.

The nondimensional frequency obtained from the numerical simulation was similar to that found experimentally, although this also only became independent of the grid size and the Rayleigh number for fine grids. A value of 0.249 was obtained at a Rayleigh number of $2.2 \times 10^6$ using a uniform grid of $127 \times 127$. This frequency decreased slowly with increasing Rayleigh number, reaching a value of 0.240 at a Rayleigh number of $6.25 \times 10^6$. The experimentally obtained value appeared to be constant at 0.248 as shown earlier in Fig. 3. Introduction of a symmetric temperature disturbance into the temperature field at a Rayleigh number of $6.25 \times 10^6$ produced a jump in the nondimensional frequency to a value of 0.320. This value agrees well with that measured experimentally (0.321 from Fig. 3) at Rayleigh numbers above approximately $9.0 \times 10^6$.

Introduction of an artificial nonsymmetrical thermal condition within the boundary layer can cause the numerical equations to simulate the intermediate frequency value observed experimentally, as reported by LeQuere and de Roquefort (1986a).

Numerically obtained velocities were qualitatively similar to those measured experimentally. There were small differences in magnitude and spatial variation that can be attributed to three-dimensional effects present in the experimental results. For example, it was noted that the experimental steady

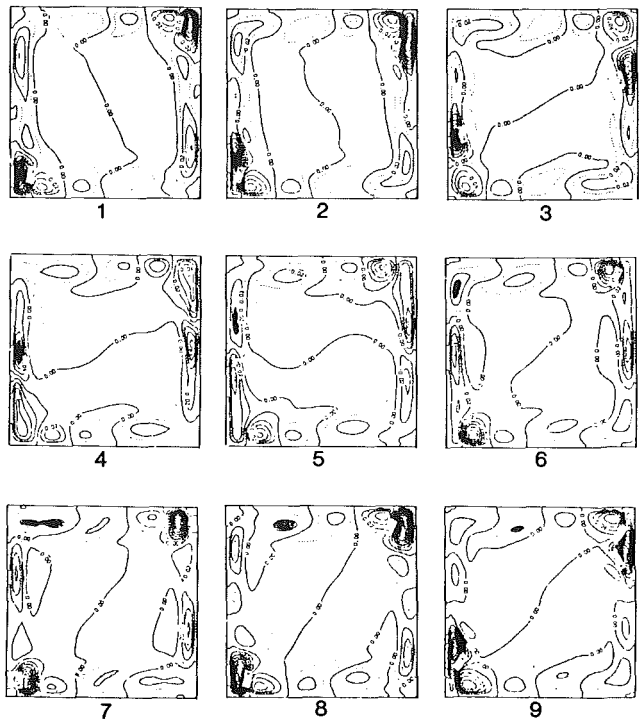


**Fig. 10 Temperature difference field at successive times at $Ra = 5.0 \times 10^6$**

horizontal centerline velocity profile was nearly 20 percent larger than the two-dimensional numerically calculated velocity, but that the vertical wall experimental centerline velocity and its numerically calculated counterpart differed by less than 3 percent. Measurements confirmed that the sidewall boundary layers for the horizontal flow on the top and bottom were significantly thicker than were the sidewall boundary layers on the two vertical surfaces within the experimental cavity. The side-wall boundary layers appear to cause a narrowing of the flow area on these surfaces, resulting in the increased centerline velocity.

The numerical results also provided a means of gaining a more thorough understanding of the observed phenomenon in a manner not possible through experiment. Specifically, the calculations permitted the collection of temperature values over the whole flow field and the computation of a local average temperature at each cell location by averaging over many periods of oscillation. By subtracting this average from the instantaneous temperature at each location one creates a temperature difference field, which can be plotted as seen in the various views of Fig. 10. These nine views show the progression of the local temperature maxima and minima through one cycle for $Ra = 5.0 \times 10^6$ using a $63 \times 63$ uniform grid.

The cycle begins with a local maximum temperature (hot cell) starting up the hot left-hand wall (shaded cell seen in the lower left-hand corner in view 1) and a local minimum (cold cell) starting down the cold right wall.

The hot element rises rapidly up the left wall staying relatively coherent. Its progression may be followed as it is shaded in each of the nine views. It passes part of the preceding cold cell and consumes a recently formed weak warm cell in views 2, 3, and 4.

A cold cell (located squarely in the lower left corner in view 3) begins to ascend the hot wall in views 4 and 5. By view 6 it has begun to break into two cold parts. One continues on to the top but the other barely moves. The next hot cell pushes it aside and begins its ascent in views 7, 8, and 9. By view 8 the field has virtually returned to the condition of view 1, thus completing a single period. Each view is separated by nearly the same time increment ($\Delta\tau \simeq 2.55 \times 10^{-4}$).

It may be seen that there are essentially five pairs of hot and cold cells convecting around the enclosure with some formation and destruction taking place along the vertical wall. At least one of the jumps in nondimensional frequency observed experimentally and numerically can be ascribed to an increase in the number of circulating hot and cold pairs of cells from ten to fourteen.

A recent paper by LeQuere and Roquefort (1986b) discussed a similar numerical experiment. They propose that the phenomenon observed is due to a Hopf bifurcation (Drazin, 1981). They report a measured numerical nondimensional frequency of 0.255 at a Rayleigh number of $2.2 \times 10^6$, and indicate five circulating pairs of hot and cold fluid elements as also found in this current work. Their numerical experiments indicate a critical Rayleigh number for the onset of the periodic motion to be $2.1 \times 10^6$. This is also in agreement with the current numerical work but considerably lower than the experimental value. The difference must be tentatively ascribed to three-dimensional effects in the experiments.

It should be pointed out that even though there are some discrepancies between the numerical calculations and the experimental results, the agreement that does exist is surprising. Most of the literature dealing with stability of a laminar flow heated from below predicts or reports an instability in the form of rolls aligned with the flow direction. This type of flow could not be simulated by a two-dimensional computation and the experiments clearly indicated that such an instability was not present in this geometry.

## Proposed Physical Model of the Phenomenon

The experimental and numerical results summarized within the preceding sections describe an interesting and unusual physical phenomenon. Few references were found in which similar behavior has been observed and/or predicted for cavity flow. Unlike many transient flow phenomena, the repeatability of the flow provided the opportunity to obtain a detailed picture of this time-dependent behavior especially at Rayleigh numbers near the onset of the periodic motion. Analysis of the Schlieren slides, numerical data, and experimental measurements leads to the following description of the phenomenon.

The driving force behind the oscillating flow lies in the horizontal boundary conditions imposed. The thermally conducting boundary surface results in a heated from below (or cooled from above) heat transfer situation as the cavity Rayleigh number is increased. At a critical Rayleigh number the combination of residence time, flow velocity, and diffusion rate results in an unstable heated from below situation. The instability results in some vertical motion in the fluid flowing across the horizontal surfaces. The horizontal flow separates into slightly warmer and slightly colder fluid cells, which are carried along to a vertical surface at which their temperature difference results in accentuated velocity differences. These tend to separate the hot and cold temperature elements even more and result in building up the periodic flow to steady state.

The experimental and numerical evidence indicate the phenomenon is essentially two-dimensional for Rayleigh numbers less than $5.0 \times 10^6$.

The experimentally observed jumps in frequency, which occur at Rayleigh numbers near $6.8 \times 10^6$ and $9.0 \times 10^6$, can be attributed to an increase in the number of circulating cells. The numerical solution predicts a jump in frequency at a lower Rayleigh number and it also indicates that the onset of the periodic flow should take place at a lower Rayleigh number than found experimentally. These differences are probably caused by as yet undefined three-dimensional effects.

The numerical and experimental velocity data taken showed there were significant phase differences in velocity for cavity

periodic flow, whereas thermosyphon flow is always in phase. It would appear that the large stagnant central area of the cavity permits vertical flows and thus phase differences whereas the construction of the thermosyphon precludes such a phenomenon.

The magnitude and stability of this periodic cavity flow suggests it may appear in previously unsuspected situations.

## References


Briggs, D. G., and Jones, D. N., 1985, "Two-Dimensional Periodic Natural Convection in a Rectangular Enclosure of Aspect Ratio One," ASME JOURNAL OF HEAT TRANSFER, Vol. 107, pp. 850–854.

Drazin, P. G., and Reid, W. H., 1981, *Hydrodynamic Stability*, Cambridge University Press, Cambridge, United Kingdom, pp. 402–405.

Jones, D. N., 1987, "Periodic Natural Convection in a Rectangular Enclosure of Low Aspect Ratio," Ph.D. Thesis, Department of Mechanical and Aerospace Engineering, Rutgers University, New Brunswick, N.J.

LeQuere, P., and de Roquefort, T. A., 1986a, "Transition to Unsteady Natural Convection of Air in Differentially Heated Vertical Cavities," presented at the 1986 ASME Winter Annual Meeting, Anaheim, CA.

LeQuere, P., and de Roquefort, T. A., 1986b, "Transition to Unsteady Natural Convection of Air in Vertical Differentially Heated Cavities: Influence of Thermal Boundary Conditions on the Horizontal Walls," presented at the 8th International Heat Transfer Conference, San Francisco, CA.

Patankar, S. V., 1980, *Numerical Heat Transfer and Fluid Flow*, McGraw-Hill, New York, pp. 133–134.

# Transient Destratification in a Rectangular Enclosure

**C. Gnafakis**
Graduate Student.
Assoc. Mem. ASME

**V. P. Manno**
Assistant Professor.
Mem. ASME

Department of Mechanical Engineering,
Tufts University,
Medford, MA 02155

*An experimental study of transient destratification in a rectangular air-filled enclosure is described. The test cell, which is 1 m high, 0.5 m wide, and 0.25 m deep, is made of plexiglass with a variety of side and bottom thermal boundary conditions. The initial vertical stratification is 30°C. A number of transient tests are reported in which a destabilizing heat source is introduced after the initial stratification. Temperature maps of the middepth plane are recorded and analyzed. Basic enclosure destratification dynamics are described in terms of developing thermal and flow fields. Separate effects of horizontal partitioning, stabilizing side heating, and asymmetric heating are studied. Certain large fractional horizontal blockages are shown to enhance destratification, while side heating is demonstrated to be a stablizing effect that produces a steady-state inversion.*

## Introduction

Stratification phenomena concurrent with natural convective flow are of substantial current interest due to their relevance to engineering design issues and the understanding of natural phenomena. Illustrative engineering applications include solar collector design, building fire analysis, passive solar optimization, electronic component cooling layout, and nuclear reactor containment postaccident performance. The analysis of real geometries challenges the knowledge gained from idealized studies of simple arrangements and boundary conditions in that the results are often not directly transferable. The burgeoning utilization of sophisticated numerical models for the analysis of complex problems produces an associated problem of predictions without adequate verification vis-à-vis data comparison.

The purpose of this work is to investigate relatively complex physical arrangements with the primary goals of producing qualitative understanding of phenomena and to add to the rather scarce validation data base. The specific focus of the investigation is transient destratification in an air-filled enclosure due to the imposition of destabilizing heating from below under a variety of boundary and internal conditions. This paper describes a preliminary investigation with subsequent goals of experimental refinement and validating simulation.

## Brief Overview of Past Work

The pertinent literature is extensive and only an overview of the most relevant work is attempted. Natural convection in general and enclosure flows in particular are the subjects of entire monographs (Kakac et al., 1985) and review articles (Ostrach, 1972). The earlier literature is dominated by experimental and analytical investigations of relatively simple problems with the goal of developing a basic understanding of the underlying phenomena. The important dimensionless groups (e.g., Gr, Ra, $AR$, etc.) were identified, variation in basic flow regimes (conductive, boundary layer, laminar/turbulent) were demarcated, and heat transfer relations, usually in the form of Nusselt number equations, were obtained. Knowledge of steady-state phenomena preceded the study of transient phenomena. The more recent work that is the focus of this review is the extension to complex arrangements, transient phenomena, and spatial nonuniformity, specifically, stratification.

Chu et al. (1976) presented one of the first studies of the effect of variable and nonidealized boundary conditions through variation of heater location and size, aspect ratio, and boundary conditions in a laminar flow confined in a rectangular geometry. The specific issue of the effect of discrete heat sources in rectangular enclosures and their effect on the local flow field as well as integral heat transfer has been the focus of Oosthuizen and his co-workers (Kuhn and Oosthuizen, 1986; Oosthuizen and Paul, 1987). Relevant information from these studies includes the interaction of closely placed heat sources, the importance of three-dimensional effects, and the significant variation in heat transfer. Poulikakos and co-workers (Filis and Poulikakos, 1985; Poulikakos, 1986) studied the effect of variable side wall temperature both experimentally and numerically. The most striking features of their results for cases in which the arrangement is intrinsically stable is the production of a vertical stratification and the partitioned vortex flow that is produced. Internal flow structures such as partitions (especially vertical) have been the focus of recent work (Nansteel and Greif, 1981; Kelkar and Patankar, 1987). These studies emphasize the importance of both partition placement and thermal properties in the alteration of the open flow field. Inactive regions can be produced as well as convective enhancement due to the formation of preferential flow loops.

Transient effects are important in engineering design due to the observation that steady-state operation is an idealization that is realized rarely in practice. In addition to the transient aspects of destratification, which are the present focus, the most important aspect of transient enclosure natural convection is the variable approach to steady state. Specifically, the transient can be either monotonic or oscillatory with the critical parameters being Ra, $AR$, and Pr. This point was argued heuristically on the basis of scaling laws and predicted numerically by Patterson and Imberger (1980) and verified experimentally by Ivey (1984). Numerous additional studies (mostly numerical) also verify this qualitative behavior but definitive quantitative criteria remain to be established (see Nicolette et al., 1985, for example).

The existence of spatial heterogeneity in the form of density gradients is one of the most important considerations in the analysis of a natural convective flow, either confined or immersed. The recent review article of Jaluria (1985) provides an excellent articulation of this aspect. Stable stratification (i.e., an existing fluid field that tends to suppress convective motion) can alter dynamic time responses by orders of magnitude and produce flow phenomena that are quite unique from the homogeneous results. Fusegi and Farouk (1985) studied numerically the problem of enclosure heating from below with side walls with a linear stable temperature gradient. The thermal (and flow) patterns show the increased stratification

Contributed by the Heat Transfer Division for publication in the JOURNAL OF HEAT TRANSFER. Manuscript received by the Heat Transfer Division January 14, 1988. Keywords: Enclosure Flows, Natural Convection, Stratified Flows.

causes the convective transport to be confined to the lower portion of the enclosure. In addition the side heating suppressed the horizontal spreading of the counterrotating central vortex flow from the heated walls. Similar effects were noted by Quarini (1985) who added the complication of partial vertical partitioning. Kirkpatrick and Bohn (1985) investigated experimentally three-dimensional flow and developed correlating stability criteria to predict which situations would or would not destratify based on the relative strengths of the bottom (destabilizing) heating and the side (stabilizing or destabilizing depending on arrangement) heating as embodied in their respective Ra numbers. The criteria also involve the aspect ratio. This latter effect is obtained from the intrinsic turbulence suppression of narrower (i.e., high $AR$) enclosures. Torrance (1979) had predicted effects similar to those reported by Fusegi and Farouk (1985) as well as the stability criteria of Kirkpatrick and Bohn (1985) in a numerical study.

The transient aspects of destratification in unbounded geometries (e.g., atmosphere and large bodies of water) have been a focal interest of the penetrative convective literature of the past 20 years (see Deardorff et al., 1969; Denton and Wood, 1981, for example). This literature, while not directly applicable due to the importance of the side walls in enclosures, does describe the relevant physics of the density interface as well as the qualitative aspects of the core flow in a stratified geometry. Finally, Jaluria and Gupta (1982) studied stratification decay in a tank that modeled a thermal storage device. Three directly relevant results from this are the importance of side boundary conditions, initial stratification, and the observation that destratification times were on the order of $10^{-2}$ when time is normalized to the thermal diffusivity and enclosure size.

## Experimental Description

**Apparatus.** The apparatus is designed to achieve the following conditions: establishment of a specified initial vertical thermal stratification, imposition of a variety of thermal boundary and internal conditions, and environmental isolation. The basic features of the experiment are illustrated in Fig. 1. The depth of the enclosure is 0.25 m. This shallow depth is selected to produce data that may be influenced significantly by three-dimensional effects and hence challenge numerical simulations. Further the depth and width aspect ratios are integral multiples. The overall scaling is specifically representative of certain regions of nuclear reactor containment buildings. The initial measurement system as well as the data to be presented (see below) are focused upon the mid-depth plane thermal fields.

The walls of the enclosure are constructed of 1.2-cm-thick plexiglass ($k = 1$ W/m°C). The bottom surface is constructed of 1.9-cm-thick oak panel with three independently controlled heated plates imbedded in the upper surface, which produces a smooth lower boundary with regionally discrete heat sources. The wooden base isolates the heaters and also provides good insulation ($k = 0.19$ W/m°C). The vertical sidewalls are constructed of plexiglass sheets that are machined to accept two

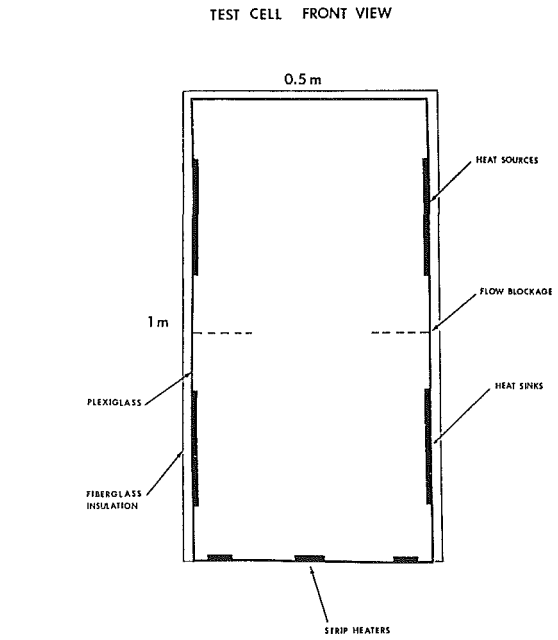


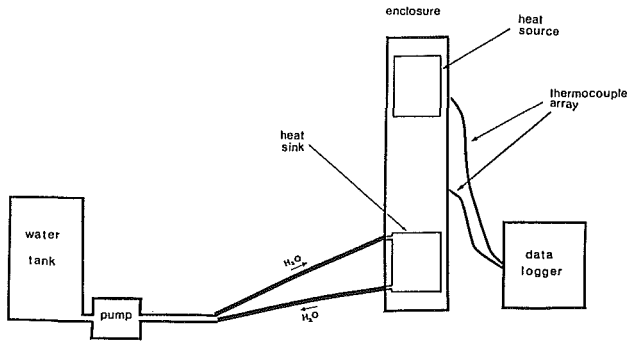


**Fig. 1 Test cell and experimental apparatus**

types of localized boundary condition units in a manner that produces a resultant smooth surface. The heat sources consist of heaters identical to those of the bottom plate while the heat sink units are finned, water-cooled, heat exchangers press fit to a flat aluminum plate. A large variety of side boundary conditions can be imposed using these basic units.

The heaters employed both to establish the vertical boundary conditions and to provide the destabilizing heating from below were controlled to dissipate constant power over the course of the experiment. When the heaters were operated in the vertical orientation, the surfaces were not isothermal due to the lengthwise variation in local heat transfer coefficient. The variation is also temporal as the local ambient temperature varies over the course of an experiment. For

## Nomenclature

$AR$ = aspect ratio (height to width)
Gr = Grashof number $= g\mathrm{B}\Delta TL^3/\nu^2$
$g$ = gravitational acceleration
$H$ = height
$k$ = thermal conductivity
$L$ = characteristic length
Pr = Prandtl number $= \nu/\alpha$
Ra = Rayleigh number $= g\mathrm{B}\Delta TL^3/\alpha\nu$
S.I. = stratification index
$T$ = temperature, °C
$t^*$ = characteristic destratification time constant, (s)
$\alpha$ = thermal diffusivity
B = coefficient of thermal expansion, $°C^{-1}$
$\nu$ = kinematic viscosity
$\tau$ = dimensionless destratification time constant

**Subscripts**

$avb$ = average of bottom region
$avt$ = average of top region
$h$ = horizontal length and temperature difference
$o$ = initial condition
$v$ = vertical length and temperature difference

modeling or quantitative data analysis, a reasonable estimate of the average temperature, based on experimental observation, is 75°C for the vertical configuration. Vertical temperature variations of 5 to 6°C were typical (hotter at top). In the horizontal placement, the average heater surface temperature was approximately 80°C and the typical positional variation was 2 to 4°C. Note that the entire lower boundary is not at all isothermal due to the discrete nature of the heater placement. The surface temperature of the insulator (oak) sections of the lower boundary was not monitored. The heat sink/heat exchanger units were designed to achieve a surface temperature uniformity of 1 to 2°C. This was achieved through the use of an extensively finned heat exchanger surface and high pressure (good thermal contact) mounting of a thin aluminum plate, which provides the actual bounding surface.

The internal geometry of the enclosure is variable in that a midheight horizontal flow blockage in the form of 1.2 cm cedar sliders can be positioned to achieve variable degrees of upper and lower region isolation. The cedar material provides a nearly adiabatic divider. Two experimental considerations deserve attention. First, the plexiglass does affect the experiment especially due to its role as an additional heat sink. Also, radiative heat transfer cannot be neglected a priori in comparison to convection due the utilization of air as a working fluid. Rough estimates of radiative (surface to surface) heat transfer based on bounding temperature values leads to an estimation that radiative transfer can represent 10–15 percent of the total internal heat transfer. These two effects should be noted both in the interpretation of results and any subsequent numerical simulation.

**Data Acquisition.** Temperature data were obtained from a matrix of copper-constantan thermocouples positioned in the middepth plane. The thermocouples were inserted through thin (4 mm) glass tubes, which penetrated the back enclosure face. The matrix was basically a square-pitched pattern with spacings of over 10 cm. Additional thermocouples measured the heat sources/sinks and ambient temperatures. Temperatures within 4 cm of the near walls were not monitored. The approximately 60 thermocouples were monitored simultaneously using a Kaye Digistrip IV data logger. The data were postprocessed on a VAX superminicomputer to produce the desired graphic output, which included isotherm contours and $X$–$Y$ plots.

The data acquisition did have limitations, which should be noted and addressed in future work. First, the square pitch and thermocouple density leads to concerns as to the intrusive nature of the probes. The probe density was determined as a compromise of resolution and intrusion. The probe tubing thinness helped minimize the local perturbation. A calculation of wake effects (Blevins, 1984) using expected natural convective flow parameters results in an expected wake velocity deficit of less than 10 percent in the worst case. Most measurement regions are expected to have less than a 2 percent effect. Nonetheless, a triangular pitch would have been preferable. Second, the midplane focus leaves the third dimension of the thermal field unmonitored. Finally, no flow visualization was performed in this set of experiments. One limitation in this regard is that visualization tests involve removing the insulation blanket, which perturbs the boundary conditions significantly.

Some of the figures presented in the results discussion involve plots of a stratification index (S.I.). S.I. is defined as

$$\text{S.I.} = (T_{avt} - T_{avb})/(T_{avt} - T_{avb})_o \quad (1)$$

where the average regional temperatures are arithmetic means of thermocouple measurements in the upper and lower regions, respectively. It is used as a normalized measure of the transient strength of the stratification and is useful in the comparison of the various experimental runs. The subsequent isotherm contours are produced using curve-fitting software. Therefore, in the near wall regions where data are sparse, the curvature of the contour lines are not accurate.

**Procedure.** The initial stable stratificiation is obtained through the imposition of the upper heaters. A significant fraction of the energy is absorbed in the heating of the plexiglass walls. Before the heating is initiated, the internal geometry is set, the enclosure secured and insulated, and the various instrumentation is checked and synchronized. This includes cooling the water in the controlled thermal bath to 7°C, which takes about 20 min. Roughly 50 min are required to achieve a stratification of 30°C as measured by the difference between the upper thermocouple string and lowest bank. Once this is achieved, the upper heaters are de-energized (if consistent with that particular experiment) and the lower heat sources (and heat sinks if desired) are energized. The time constants of these new boundary conditions are on the order of 1 min. Data acquisition is active throughout the experiment. Periodic thermal maps are obtained until the stratification is destroyed, as indicated by temperature differences of 1 to 2°, or "steady-state" conditions are reached. (The editorial modification of the term "steady-state" will become evident in the results discussion.)

**Errors and Repeatability.** The temperature measurement errors are affected by the basic thermocouple resolution, the calibration of the data logger, positional error, and parasitic effects of radiative transfer from hot surfaces directly to the thermocouple and the wake effect mentioned above. The thermocouples and data logger were calibrated to an accuracy of 0.1°C and positional errors were about 1 mm. Radiation effects were studied as separate effects and found to be 0.3°C in the interior of the enclosure and about 1°C in the vicinity of a heated surface. These errors combined with the wake effect lead to average temperature errors of about 1°C with a maximum of about 2°C.

Repeatability is a more substantive concern. Due to the complexity of the arrangement, the difficulties of air as a working fluid and the fact that this represents a first generation experiment, the repetition of apparently identical experiments did yield measurable variation. After some fine tuning (enclosure sealing, water mixing, etc.) repeatability on the order of 5 percent of S. I. was achieved in the reported experiments. Parasitic heating of the plexiglass wall is a particularly troublesome aspect, which requires better quanitification as to its temporal behavior. Both experimental and numerical investigations of this effect are planned.

In retrospect, the experimental design was not optimal especially in the areas of easily definable boundary conditions and the minimization of parasitic effects. This situation is not unexpected since the primary goals of the reported work were to develop qualitative understanding and to identify undocumented behavior in configurations that begin to approach the complexity of real applications. The more important observations made on the basis of this study serve to set the goals and design of the next generation of experiments, which is currently under way.

## Results and Discussion

A list of the experiments performed is provided in Table 1. A characteristic time is defined for each experiment. This time has the general definition as the time required for the S. I. to decrease from its initial value of 1 to 0.37 ($e^{-1}$). In the cases of Experiments 7 through 10 when the S. I. never decreases to that level, the definition is modified to that time when the S. I. has decreased to within 37 percent of its approximate steady-state value. The dimensionless time constant is defined as

$$\tau = t^* \alpha / H^2 \quad (2)$$

**Table 1 Experimental matrix**

| Experiment | Flow Blockage[1] | Upper BC[2] | Lower BC[2] | Bottom BC[3] | $\tau^4$ |
|---|---|---|---|---|---|
| 1 | 0 | NN | NN | All | 0.0133(562) |
| 2 | 0 | NN | NN | Left | 0.0319(1399) |
| 3 | 50 | NN | NN | All | 0.0153(630) |
| 4 | 90 | NN | NN | All | 0.0122(503) |
| 5 | 0 | NN | NN | Center | 0.0579(2471) |
| 6 | 25 | NN | NN | All | 0.0283(1173) |
| 7 | 0 | HH | NN | All | 0.0503(1943) |
| 8 | 0 | HH | CC | All | 0.0461(1814) |
| 9 | 50 | HH | CC | All | 0.0450(1800) |
| 10 | 90 | HH | CC | All | 0.0418(1700) |
| 11 | 0 | HN | NN | All | 0.0393(1613) |

[1]Percent horizontal blockages. All cases are symmetric except Experiment 6, where blockage is imposed on left side only.
[2]H = hot, C = cold, N = neutral. Format is left-right.
[3]All = 3 heaters, Left = left only, Center = center only.
[4]Normalized time constant (see equation (2)). Format is dimensionless time followed by time in seconds in parentheses.

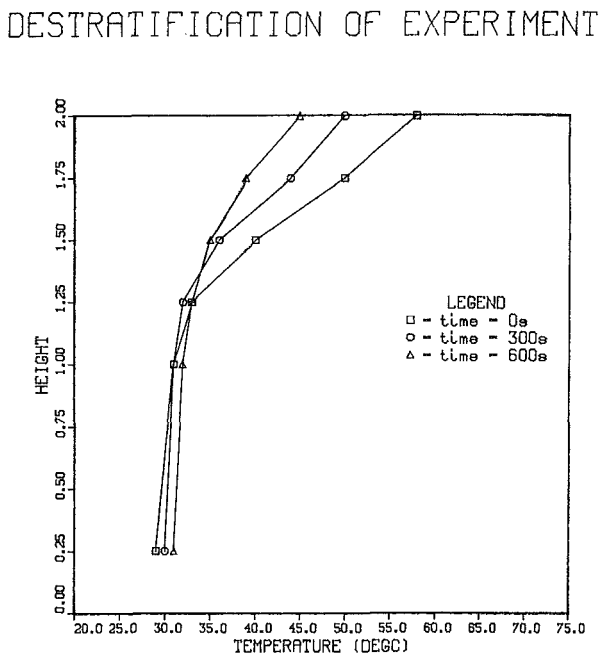


Fig. 2 Destratification of Experiment 1

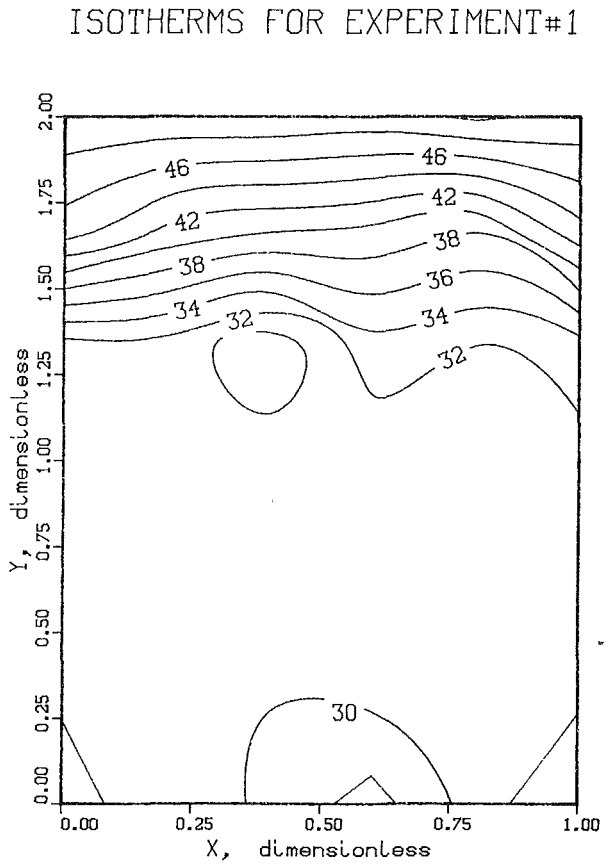


Fig. 3 Isotherm contours during Experiment 1

where $\alpha$ is the thermal diffusivity and $H$ is the enclosure height. This nondimensionalized measure is useful for experimental comparison and was also utilized by Jaluria and Gupta (1982) in their destratification study. Not all of the experiments are considered here but instead the focal points of the discussion are the destratification process, the effect of flow blockages, the effect of side heating and some consideration of asymmetric conditions.

**Basic Destratification Dynamics.** The basic dynamics of the destratification process in this geometry can be obtained from an analysis of Experiment 1. The vertical centerline temperature profiles at selected times are presented in Fig. 2. The initial stratification is actually linear in the upper region. The entire domain is destratified in approximately 2400 s. The flow pattern can be inferred from Fig. 3. which is a temperature contour map during the destratification. The lower region contains two counterrotating flows, which at the time of this contour penetrate to the 1.25 (normalized) elevation. The slight asymmetries of the contours are typical for the experiments performed. The upper region is believed to contain weaker counterrotating circulations as indicated by the downslope of the contours near the upper sidewalls. Two driving forces are postulated for this upper region flow pattern. First, some of the buoyant plume penetrates into the hotter region and turns at the roof. This is consistent with some recent salt solution experiments reported by Kulkarni and Murphy (1987). Second, some side wall heat losses produce a negative buoyancy downflow. As the experiment progresses, the main recirculation involves more of the enclosure until the classic two-cell recirculation is achieved. This is evidenced by the progression upward of temperature uniformity and the compression of the isotherm contours toward the top of the enclosure.

The evolution of this flow and thermal pattern is very

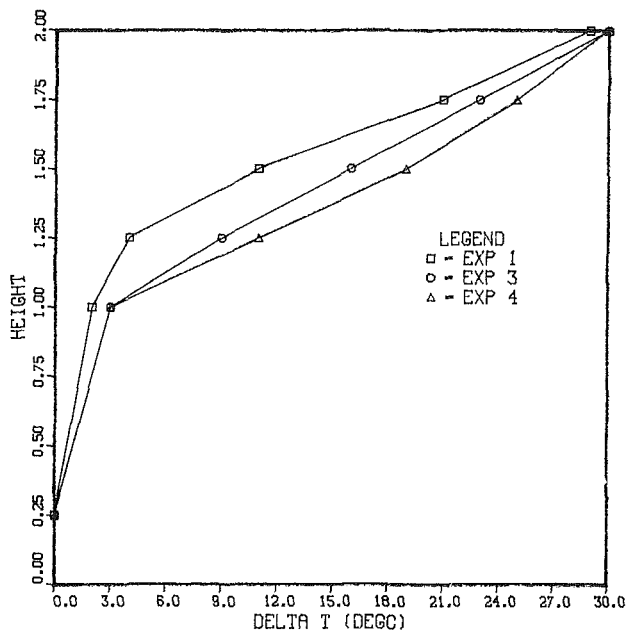


Fig. 4 Initial stratification of Experiments 1, 3, and 4

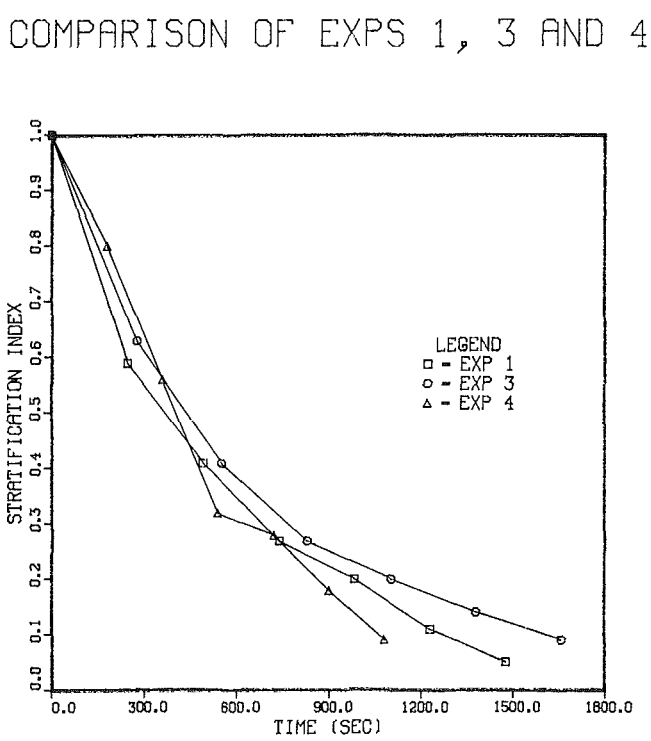


Fig. 5 Stratification index transients of Experiments 1, 3, and 4

similar to the various steady-state conditions predicted by Fusegi and Farouk (1985). In addition the destratification time scale of $10^{-2}$ is in agreement with the experiments of Jaluria and Gupta (1982). In Experiment 5, only the lower central heated surface is utilized. This test progressed in a manner similar to Experiment 1, except the time constant increased by a factor of 4.

**Horizontal Flow Blockage.** The effect of horizontal flow blockage can be studied through a comparison of Experiments

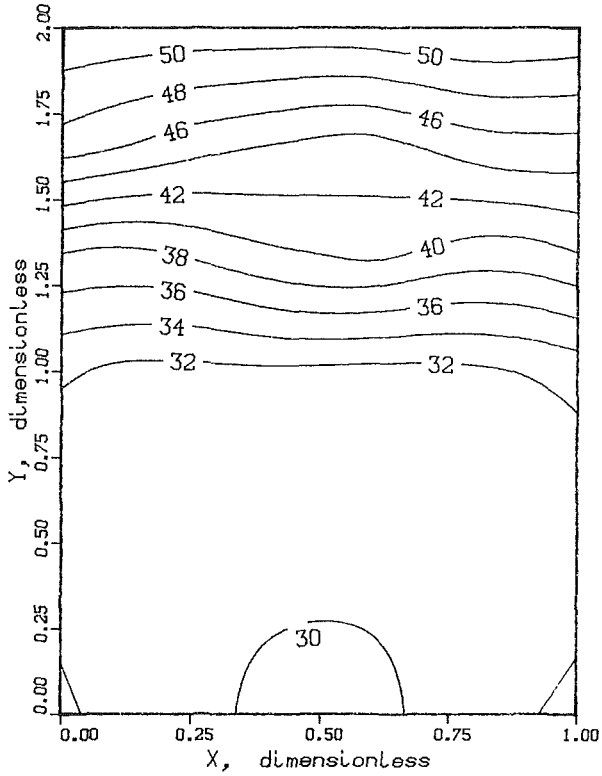


Fig. 6 Isotherm contours during Experiment 4

1, 3, and 4. In addition, Experiments 8, 9, and 10 test this effect concurrent with stabilizing heating from above. As stated in Table 1, Experiments 3 (and 9) and 4 (and 10) have 50 percent and 90 percent midplane flow blockages, respectively. One important distinction is obtained from the initial stratification achieved. Figure 4 illustrates that the nearly blocked configuration can achieve a much steeper vertical stratification. The horizontal partitions suppress the mixing of the heated upper air that occurs in the open configuration due to the relatively strong flow induced from the upper heaters when they are energized.

The destratification time scales can be ascertained from a review of both Table 1 and Fig. 5. Two observations are noteworthy. First, the partitions do not change the destratification times dramatically. The second and more interesting result is that the 90 percent blockage case destratified faster than the more open geometries. The difference is admittedly small given the repeatability limitations, but this destratification enhancement was repeatable in that the characteristic time constant is approximately 20 percent smaller than the open geometry. The 50 percent blockage cases are less definitive and the only valid comment is that a partial blockage of smaller extent is of negligible global importance.

A plausible physical explanation of this unexpected behavior can be constructed from an analysis of the isotherm contour evolution. Consider Fig. 6, which depicts the isotherms at an intermediate time during Experiment 4. The bowing of the isotherms at the 1.50 elevation is a characteristic that persisted throughout the duration of the experiment. This pattern is indicative of vertically stacked counterrotating cells. This flow pattern is consistent with the following destratification enhancement mechanism. The more buoyant warmer air rises from the lower heated surfaces. In the low blockage experiments (1 and 3), this rising plume is relatively broad at the time it interacts with the upper density change. In Experiment

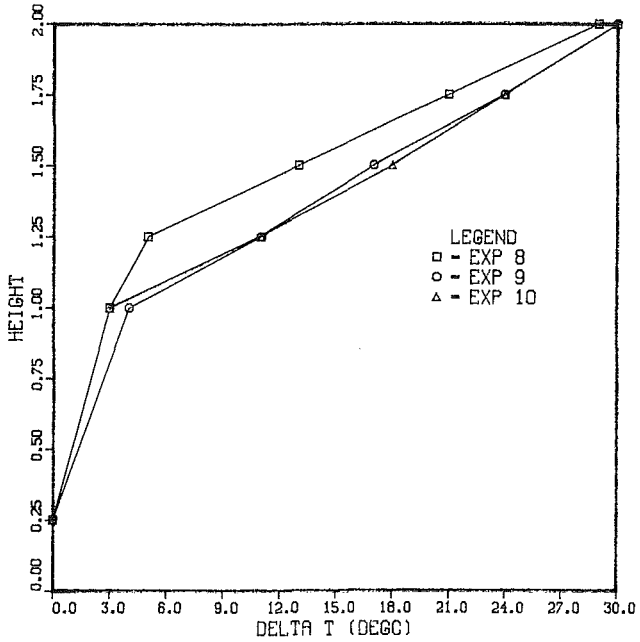


Fig. 7 Initial stratification of Experiments 8, 9, and 10

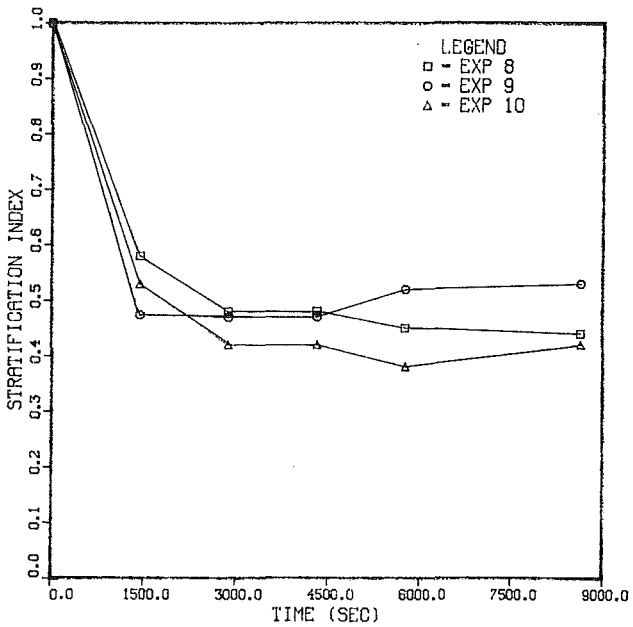


Fig. 9 Stratification index transients of Experiments 8, 9, and 10

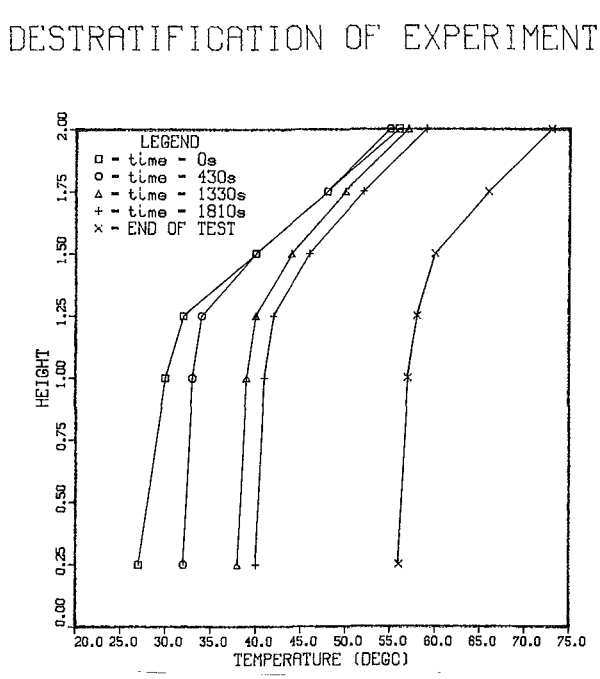


Fig. 8 Destratification of Experiment 8

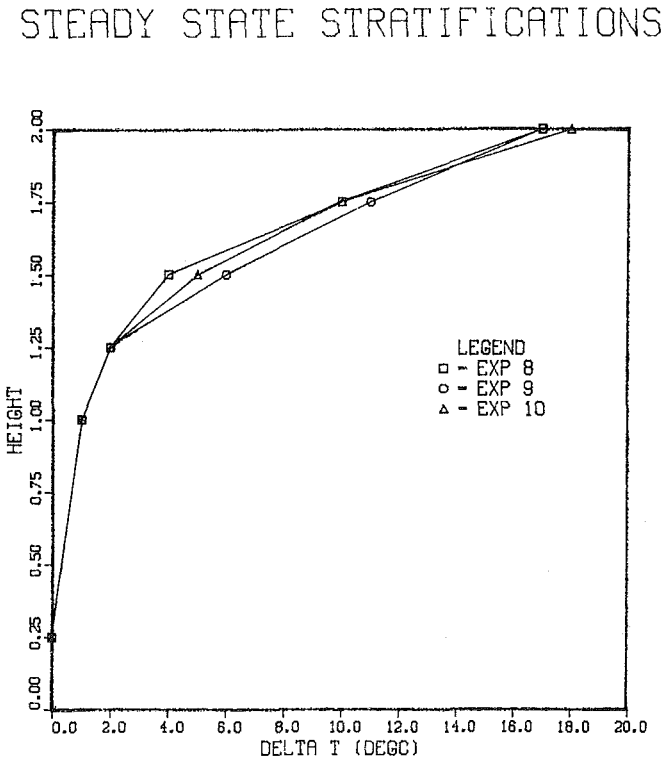


Fig. 10 Terminal stratification profiles for Experiments 8, 9, and 10

4, the tight opening causes a spatial acceleration of the plume as it tries to penetrate into the upper layer. Note the total upward flow of the three cases is similar since it is more a function of the lower heater strength than the internal geometry. The higher velocity plume cannot penetrate the entire upper region due to its depressed relative buoyancy and is forced to turn in the direction of the vertical side walls. This creates a rather flat circulation in the region just above the partitions, which has the same circulation sign as the stronger flow in the lower region. This upper region recirculation is strong enough to induce a counterrotating flow in the top portions of the upper region through a shear interaction. These multiple cells produce a mixing process that is more effective than the baseline open geometry flow. This hypothesis is clearly in need of demonstration, but a relevant reference is that similar phenomena (critical horizontal orifice size) were observed in large-scale hydrogen transport testing at the Battelle Frankfurt Institute (Langer, 1980).

**Side Heating.** A series of experiments (7 through 10) was performed to test the effect of stabilizing side heating of the

upper region. The imposition of an additional stabilizing influence of lower side heat sinks did not change the enclosure dynamics in a significant way and therefore only Experiments 8 through 10 are utilized in this discussion. The initial stratification patterns depicted in Fig. 7 are very similar to those associated with Experiments 1, 3, and 4 (i.e., Fig. 4) as is expected. The evolution of Experiment 8 can be contrasted with Experiment 1 since the side heating is the only distinguishing difference. As can be seen from the destratification transient illustrated in Fig. 8, the side heating does cause the stratification to persist throughout the experiment. Typical total test times were on the order of 4 h. The slope of the stratification does diminish, which is indicative of some interregional mixing, and the continued imposition of the side heating also produces a linear stratification similar to the initial condition. The overall enclosure average temperature increases due to the fact that the heat sources are significantly stronger than the heat sinks.

Figure 9 illustrates the stratification index transients for the three side heating cases with progressively increasing horizontal blockages. The stratification profiles at the termination of the experiments are shown in Fig. 10. A "steady-state" stratification is achieved in terms of stratification index. In the cases of these experiments, this steady-state index is about half the initial value. Other experiments indicate that the relative value of the steady-state stratification is a strong function of the relative strengths (i.e., heat input) of the lower and side heat sources. Also note that a timing hierarchy vis-à-vis the effect of blockage extent is similar to the earlier results. In fact, the bowed temperature profile was also observed in these data (see Fig. 11).

As mentioned earlier, Kirkpatrick and Bohn (1985) developed a stratification stability criterion statement of the following form

$$\mathrm{Ra}_v \mathrm{Ra}_h^{-3/5} AR^{-3} < 3400 \qquad (3)$$

where the two Rayleigh numbers represent the competing destabilizing ($\mathrm{Ra}_v$) and stabilizing ($\mathrm{Ra}_h$) effects, respectively. In these experiments, typical values are on the order of 2000 to 5000 and hence, the particle destratification obtained is consistent with equation (3).

**Asymmetric Heating.** Two cases (Experiment 2 and 11) of localized asymmetric heating are investigated. In Experiment 2, only the left side lower heater is energized. The resultant temperature patterns show that the left 2/3 of the enclosure is involved in a strong recirculation while the right side remains relatively quiescent. This pattern is reminiscent of the Kirkpatrick and Bohn (1985) data. In the asymmetric side heating test (Experiment 11), the enclosure did destratify nearly completely, but a small asymmetric stratification does persist for the experimental duration. The total temperature differences that persisted were roughly 2°C.

## Concluding Remarks

An important general conclusion is that destratification of an enclosure involves fairly complex thermal-fluid phenomena even in cases of relatively mild deviation from idealized geometries and conditions. Many of the experimental results are consistent with existing separate effects studies in the literature. In some cases, phenomena predicted by numerical experimentation are verified. The sensitivity of stratification dynamics to the interaction of competing boundary conditions is evidenced. The data should be significant challenges for existing simulation models. Of the effects noted, the destratification behavior as a function of horizontal partitioning is the most intriguing and important from an engineering design standpoint.

Some very important tasks remain to be done. Flow visualization is a high priority so that the postulated flow

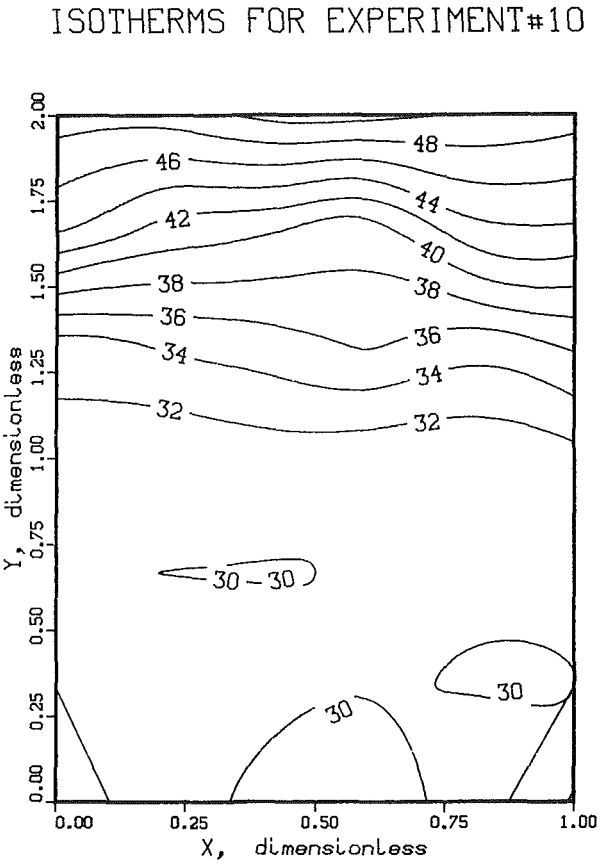


**Fig. 11 Terminal isotherm contours of Experiment 10**

phenomena can be tested. The third-dimensional (i.e., depth) dependencies and fields are not measured, yet their structure is of great importance. As stated in the earlier discussion, the experimental apparatus should be improved especially in the areas of verifiable boundary conditions, parasitic and uncontrollable effects, and nonintrusive instrumentation. Finally, numerical simulation of similar transients would help in achieving a better understanding of the destratification and mixing transient.

## References


Blevins, R. D., 1984, *Applied Fluid Dynamics Handbook*, van Nostrand Reinhold, New York.

Chu, H. H.-S., Churchill, S. W., and Patterson, C. V. S., 1976, "The Effect of Heater Size, Location, Aspect Ratio and Boundary Conditions on Two-Dimensional, Natural Convection in Rectangular Channels," ASME JOURNAL OF HEAT TRANSFER, Vol. 98, pp. 194–201.

Deardorff, J. W., Willis, G. E., and Lilly, D. K., 1969, "Laboratory Investigation of Non-steady Penetrative Convection," *Journal of Fluid Mechanics*, Vol. 35, pp. 7–31.

Denton, R. A., and Wood, I. R., 1981, "Penetrative Convection at Low Peclet Number," *Journal of Fluid Mechanics*, Vol. 113, pp. 1–21.

Filis, P., and Poulikakos, D., 1986, "An Experimental Study on the Effect of Wall Temperature Nonuniformity on Natural Convection in an Enclosure Heated From the Side," *International Journal of Heat and Fluid Flow*, Vol. 7, pp. 258–265.

Fusegi, T., and Farouk, B., 1985, "Natural Convection in a Thermally Stratified Square Cavity With Localized Heating From Below," ASME Paper No. 85-HT-34.

Ivey, G. N., 1984, "Experiments on Transient Natural Convection in a Cavity," *Journal of Fluid Mechanics*, Vol. 144, pp. 389–401.

Jaluria, Y., 1985, "Convective Flow in a Stably Stratified Environment," in: *Natural Convection: Fundamentals and Applications*, S. Kakac et al., eds., Hemisphere, Washington, DC, pp. 413–441.

Jaluria, Y., and Gupta, S. K., 1982, "Decay of Thermal Stratification in a Water Body for Solar Energy Storage," *Solar Energy*, Vol. 28, pp. 137–143.

Kakac, S., Aung, W., and Viskanta, R., eds., 1985, *Natural Convection: Fundamentals and Applications*, Hemisphere, Washington, DC.

Kelkar, K. M., and Patankar, S. V., 1987, "Numerical Prediction of Natural

Convection In Partitioned Enclosures," in: *Numerical Methods in Thermal Problems*, R. W. Lewis et al., eds., Pineridge Press, New York, pp. 63–71.

Kirkpatrick, A. T., and Bohn, M., 1985, "Flow Visualization and Stratification in High Rayleigh Number Mixed Cavity Natural Convection," ASME Paper No. 85-HT-38.

Kuhn, D., and Oosthuizen, P. H., 1986, "Three-Dimensional Transient Natural Convective Flow in a Rectangular Enclosure With Localized Heating," in: *Natural Convection in Enclosures*, R. S. Figliola and I. Catton, eds., ASME HTD-Vol. 63, pp. 55–62.

Kulkarni, A. K., and Murphy, F., 1987, "Onset of Circulation Due to Buoyant Jet in a Two-Layer Stratified Medium," in: *Natural Circulation*, J. H. Kim and Y. A. Hassan, eds., ASME FED-Vol. 61/HTD-Vol. 92, pp. 313–318.

Langer, G., et al., 1980, "Experimental Investigation of Hydrogen Distribution in a Containment of a Light Water Reactor Following a Loss of Coolant Accident," BF-63.363-3, Battelle Institute e. V., Frankfurt, Federal Republic of Germany.

Nansteel, M. W., and Greif, R., 1981, "Natural Convection in Undivided and Partially Divided Rectangular Enclosures," ASME JOURNAL OF HEAT TRANSFER, Vol. 103, pp. 623–629.

Nicolette, V. F., Yang, K. T., and Lloyd, J. R., 1985, "Transient Cooling by Natural Convection in a Two-Dimensional Square Enclosure," *International Journal of Heat and Mass Transfer*, Vol. 28, pp. 1721–1732.

Oosthuizen, P. H., and Paul, J. T., 1987, "Natural Convective Heat Transfer Across a Cavity With Elliptical Ends," in: *Numerical Methods in Thermal Problems*, R. W. Lewis et al., eds., Pineridge Press, New York, pp. 356–367.

Ostrach, S., 1972, "Natural Convection in Enclosures," *Advances in Heat Transfer*, Vol. 8, pp. 161–227.

Patterson, J., and Imberger, J., 1980, "Unsteady Natural Convection in a Rectangular Enclosure," *Journal of Fluid Mechanics*, Vol. 100, pp. 65–86.

Poulikakos, D., 1985, "Natural Convection in a Confined Fluid-Filled Space Driven by a Single Vertical Wall With Warm and Cold Regions," ASME JOURNAL OF HEAT TRANSFER, Vol. 107, pp. 867–876.

Quarini, G. L., 1987, "Buoyancy Induced Flows Caused by Inert Solids Immersed in Stratified Fluids," in: *Numerical Methods in Thermal Problems*, R. W. Lewis et al., eds., Pineridge Press, New York, pp. 461–471.

Torrance, K. E., 1979, "Natural Convection in Thermally Stratified Enclosures With Localized Heating From Below," *Journal of Fluid Mechanics*, Vol. 95, pp. 477–495.

# Convection Near the Temperature of Maximum Density for High Rayleigh Number, Low Aspect Ratio, Rectangular Cavities

G. N. Ivey[1]

P. F. Hamblin

National Water Research Institute,
Burlington, Ontrario, Canada L7R 4A6

*Natural convection in rectangular cavities with the vertical endwalls differentially heated about the temperature of maximum density of water was studied in the laboratory. In order to control heat losses, the experiments were conducted in a large cold room with the air temperature maintained at 4°C. The Rayleigh number was varied over the range $10^5$ to $10^8$ and the aspect ratio over the range 0.1 to 0.5. The flow field consisted of a double cellular circulation, and the observed temperature field, flow field, and heat transfer rates were compared with analytical predictions in the diffusive regime. The experiments demonstrated that the interior sinking flow was unstable for $Ra > 10^7$.*

## Introduction

The appearance of a frontal structure, characterized by vertical isotherms near the temperature of maximum density (approximately 4°C) is often observed in freshwater lakes. This structure is most clearly observed during the spring warming period either separating the warmer, shallow, coastal water from the body of the lake (e.g., Spain et al., 1976; Legeckis, 1978), or at the point of entry of discharges such as rivers into lakes (Carmack, 1979). The fronts, commonly known as thermal bars, are important in the geophysical context due to their controlling influence on the horizontal mixing between the nearshore and offshore regions, the mixing of inflowing rivers with lake water, and the mixing of thermal discharges from power stations with lake water.

These situations are characterized by horizontal temperature gradients driving the motion, by high Rayleigh numbers, and by relatively low aspect ratio $A$ (depth/length) for the circulation. With these applications in mind, this laboratory study uses a rectangular box model with vertical endwalls differentially heated about the temperature of maximum density in order to examine the induced temperature and velocity fields and the overall heat transfer of the system, during both transient and steady states. Two previous laboratory studies investigated the steady-state flow in cavities with $A > 1$ and high Rayleigh number (Lankford and Bejan, 1986), and for cavities with $A = 1$ and with Rayleigh numbers of order $10^4$ (Inaba and Fukuda, 1984). The present laboratory experiments cover the previously unexplored regime with aspect ratios down to $A = 0.1$ and Rayleigh numbers up to $10^8$.

## Experiments

The laboratory tank was made of a molded fiberglass construction and the working space had dimensions of: 1 m in length ($2l$), 1 m in breadth ($b$) and a height ($h$) that could be varied between 5 cm and 25 cm. At each end of the tank, 1.27-cm-thick, aluminum plates separated the working space from two water jackets. At the hot end, a constant temperature water bath circulated water through the water jacket. At the cold end, an immersion cooler, mounted on a frame above the tank to eliminate vibration, maintained the set temperature. For most runs the cold wall water jacket temperature was 0°C and the hot wall water jacket temperature was 8°C, and both were maintained to within 0.1°C. The front wall of the tank was made of lexan for flow visualization. In order to control heat losses, the working space, including the back of the viewing port, was encased with a 30-cm-thick styrofoam insulation, and the entire assembly placed in a large cold room with the air temperature maintained at 4°C.

The adjustable lid was closely fitted to the vertical sidewalls, with a tolerance of about 1 mm, and contained nine access ports along the centerline of the lid. Temperatures were measured by inserting thermistors through these ports. The thermistors, mounted at the tips of 80 cm lengths of thin-walled 3.2 mm stainless steel shaft, were calibrated using the technique described by Stienhart and Hart (1968) and the accuracy of temperature measurement in the tank then estimated at 0.01°C. Two types of temperature probes were used: a straight probe and a second type with a right-angle bend about 10 cm from the thermistor. Most temperatures were measured with the first type as the probe was traversed downward and the vertical spatial relations was about 1 mm. The second type of probe was used by placing it at a fixed depth and rotating it through an arc. From the measured angular positions it was then possible to measure temperatures with a horizontal resolution of about 3 mm. Flow visualization was accomplished by the injection of dye, and the details are given below.

With the simplified form of the equation of state over the range 0 to 8°C suggested by Simons (1980), given by

$$\rho = \rho_0(1 - \alpha(T - T_0)^2) \tag{1}$$

where $\alpha = 6.8 \times 10^{-6}$ $(°C)^{-2}$ and $T_0$ is the reference temperature of 4°C, the relevant dimensionless parameters are then the Rayleigh number $Ra = g\alpha(\Delta T)^2 h^3/\nu\kappa$ and the aspect ratio $A = h/1$. The parameters of the various runs are summarized in Table 1.

## Results

**Temperature Field.** An experiment was conducted by filling the tank with water and allowing the whole system to come to equilibrium with the air temperature in the cold room at 4°C. A run was initiated by simultaneously starting to heat and cool the water in the water jackets. In practice, it took about 5 to 10 min for the fluid in these water jackets to reach

[1]Current address: Centre for Water Research, University of Western Australia, Nedlands, W.A., Australia 6009.

Contributed by the Heat Transfer Division for publication in the JOURNAL OF HEAT TRANSFER. Manuscript received by the Heat Transfer Division February 26, 1987. Keywords: Geophysical Heat Transfer, Natural Connection, Stratified Flows.

Table 1 Summary of experimental runs (Pr = 11.6 at 4°C)

| Run No. | $\Delta T$, °C | $h$, cm | Ra | $A$ |
|---|---|---|---|---|
| 1 | 1.5 | 5.9 | $1.4\times10^5$ | 0.118 |
| 2 | 4.0 | 5.7 | $9.3\times10^5$ | 0.114 |
| 3 | 4.0 | 6.7 | $1.5\times10^6$ | 0.134 |
| 4 | 4.0 | 7.0 | $1.7\times10^6$ | 0.141 |
| 5 | 4.0 | 7.0 | $1.7\times10^6$ | 0.141 |
| 6 | 4.0 | 7.7 | $2.3\times10^6$ | 0.154 |
| 7 | 4.0 | 16.2 | $2.1\times10^7$ | 0.324 |
| 8 | 4.0 | 20.0 | $4.0\times10^7$ | 0.400 |
| 9 | 4.0 | 26.5 | $9.3\times10^7$ | 0.530 |

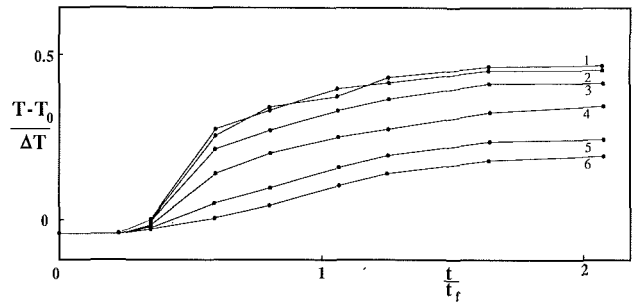


Fig. 1 Temperatures as a function of time at $x/l = 0.45$ ($l = 1$ m) for run 1 showing the asymptotic approach to steady state ($t_f = hl/\kappa \mathrm{Ra}^{1/4}$)

| Trace | 1 | 2 | 3 | 4 | 5 | 6 |
|---|---|---|---|---|---|---|
| Depth ($z/h$) | 0.08 | 0.25 | 0.42 | 0.59 | 0.76 | 0.93 |

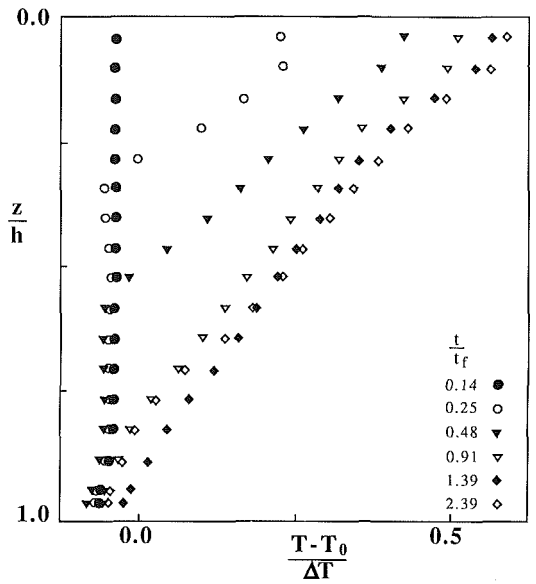


Fig. 2 Temperatures as a function of time at $x/l = 0.45$ for run 7 showing the development of the stratification in the cavity

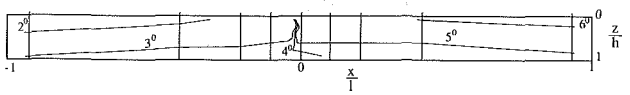


Fig. 3 Steady-state temperature distribution for the cavity for run 4; temperatures in °C

the desired temperatures of 0 and 8°C. In response to this heating and cooling, buoyant fluid rises along the two vertical endwalls, is turned at the lid, and flows out into the cavity as a horizontal buoyant outflow under the lid. The two oppositely directed intrusions emanating from each endwall meet in the center of the tank, turn, and sink toward the bottom. At the bottom, the sinking flow divides symmetrically into two now oppositely directed flows along the bottom toward the base of the respective endwalls to complete the circuit. Thus two counterrotating cellular circulations arise—one in each half of the cavity—that set up the temperature structure in the initially isothermal cavity.

The evolution of the interior temperature structure for two representative runs is shown in Figs. 1 and 2 where all times are nondimensionalized by the time to steady state suggested by Patterson and Imberger (1980) of $t_f \sim hl/\kappa \mathrm{Ra}^{1/4}$. Figure 1 demonstrates the asymptotic approach to steady state. The vertical temperature profiles in Fig. 2 clearly show the effect of the intrusion of warm buoyant fluid through the measurement section (after nondimensionalized time 0.25), the final steady-state temperature profile with little variation in temperature near the top and bottom boundaries, and a gradient region over much of the cavity. Both figures indicate that steady state is approached in time $2t_f$, in good agreement with the predicted time scale.

Figure 3 depicts a typical steady-state temperature distribution for the entire tank. The important points to note are: the symmetric temperature distribution about $x = 0$, the midpoint of the cavity; the essentially horizontal isotherms away from either the endwalls or the thermal front around $x = 0$; and finally, the vertically oriented isotherms near the front centered around 4°C. The temperature distribution around $x = 0$ is shown in more detail in Fig. 4. The isotherms indicate both an overshoot of the isotherms before they tend toward the horizontal far from the front, and a weakening of the temperature front with depth—there are, in fact, only very weak horizontal temperature gradients near the bottom.

**Velocity Field.** The basic flow field is a double cellular circulation, much as observed by Inaba and Fukuda (1984), and described above. At the high Rayleigh numbers obtained in the present study, however, this double cellular circulation was not always stable. Dye studies were made by injecting dye into the flow at the base of the hot wall. The dyed fluid was drawn up the wall by the ascending buoyant fluid, and around the half-cavity in the cellular motion described above. Injection of dye at different positions across the breadth of the tank confirmed the basic two-dimensional nature of the flow field. Figure 5 shows the central portion of the cavity as this dye is swept down through the central sinking region. Beyond a critical depth, the flow becomes unstable and undergoes a series of large-scale horizontal meanders while sinking. An apparently similar feature was reported by Lankford and Bejan

## Nomenclature

$A$ = aspect ratio of cavity $= h/l$
$b$ = breadth of the cavity
$g$ = gravitational constant
$h$ = height of the cavity
$l$ = length of the half cavity
$l_f$ = thickness of the front
Gr = Grashof number $= \alpha(\Delta T)^2 g h^3/\nu^2$
Pr = Prandtl number $= \nu/\kappa$
Ra = Rayleigh number $= \alpha(\Delta T)^2 g h^3/\nu\kappa$
$t$ = time
$t_f$ = time to steady state
$T$ = temperature
$T_0$ = reference temperature of 4°C
$u$ = horizontal velocity
$w$ = vertical velocity
$w_f$ = vertical velocity in the front
$x$ = horizontal coordinate
$z$ = vertical coordinate
$\alpha$ = nonlinear coefficient of thermal expansion
$\theta$ = nondimensionalized temperature
$\kappa$ = thermal diffusivity
$\nu$ = kinematic viscosity
$\rho$ = density
$\omega$ = vorticity
$\Delta T$ = 1/2 the difference in endwall jacket temperatures

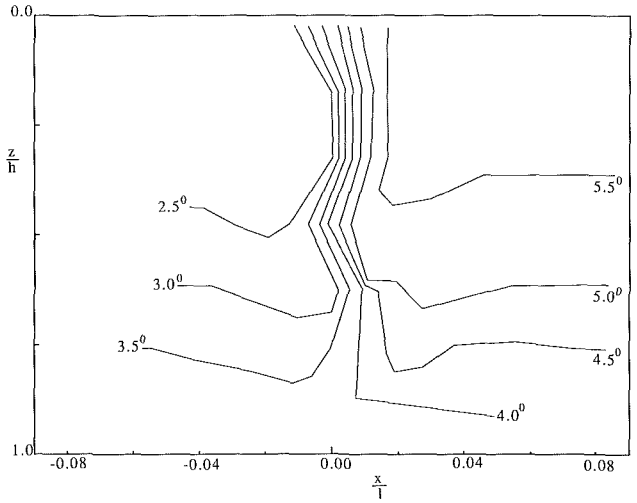


Fig. 4 Steady-state temperature distribution for the central portion of the cavity for run 3; temperatures in °C

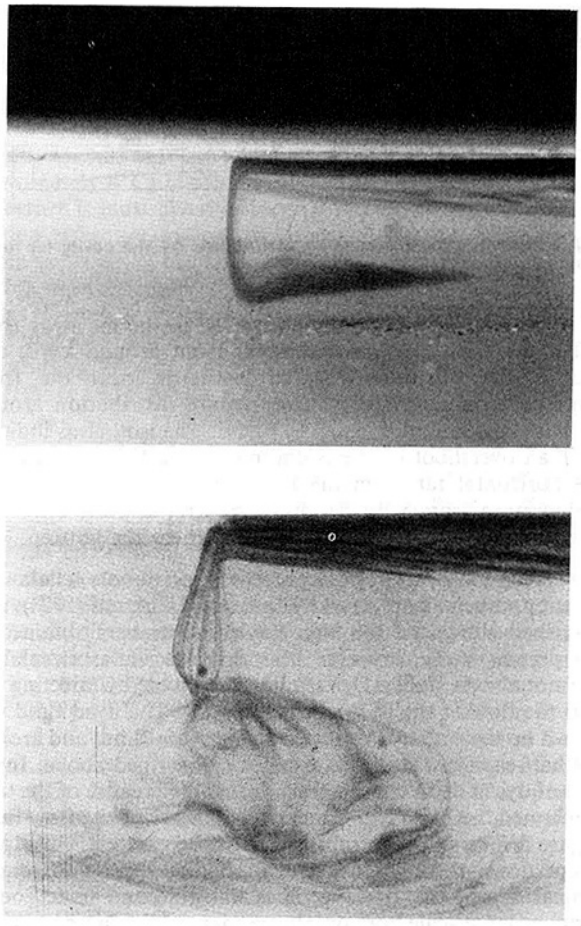

Fig 5 (a)Dye injection study for run 2 ($Ra = 9.3 \times 10^5$) with stable sinking flow in the central region; (b) dye injection study for run 8 ($Ra = 4.0 \times 10^7$) with unstable sinking flow in the central region

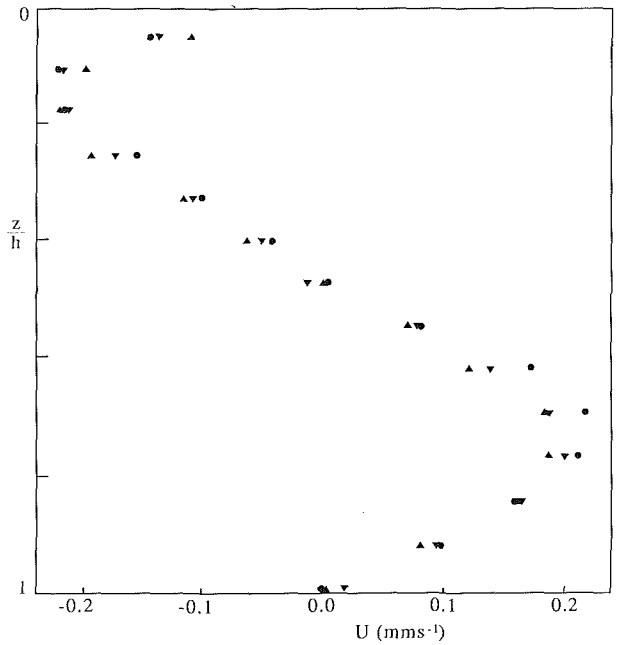


Fig. 6 Horizontal velocities at $x/l = 0.45$ for run 3; symbols correspond to three separate estimates of the profile

(1986) in their experiments with $A > 1$. The net effect of this instability in the present experiments is that the frontal region no longer acts as a barrier to horizontal transport: Some leakage of the flow now occurs across the thermal front near the bottom.

Some estimates of the flow characteristics in this sinking region can be made in terms of the external parameters. In particular, there is a local balance between the vertical convection of heat and the horizontal diffusion of heat. The dynamic balance in the sinking region is thus the same as against a heated or cooled wall as studied, for example, by Gill (1966) and Patterson and Imberger (1980). Following their arguments, as $Pr > 1$ we therefore expect that the width of the sinking region should be $l_f \sim h/Ra^{1/4}$, and the characteristic velocity in the sinking region $w_f \sim \kappa Ra^{1/2}/h$. From the temperature observations in experiments 1, 3, and 4, $l_f \approx 6h/Ra^{1/4}$, although no front could be defined clearly beyond a depth of $z/h \approx 0.7$. From 16 mm movie film taken of dye studies of experiments 5 and 8, the maximum sinking velocities were $w_f \approx 0.3\ \kappa Ra^{1/2}/h$. These estimates are limited, but are in accord with the predicted scales, and are representative of the sinking region before the descending flow becomes unstable. The sinking flow was observed to go unstable in runs 7, 8, and 9, and from the data in Table 1, this suggests unstable flow may be expected when the Rayleigh number $Ra \geq 10^7$.

Estimates were also made of the flow velocities in the central portion of the half-cavity away from either the central sinking region or the endwalls. The flow is horizontal in this region and, following the technique used by Bejan et al. (1981), velocities were inferred from the distortion of dye streaks. Figures 6 and 7 show typical results for two runs with Rayleigh numbers of $1.5 \times 10^6$ and $2.1 \times 10^7$, respectively. Figure 6 is similar, but not identical, to the cubic function in $z$ observed by Imberger (1974). In particular, he observed for a fluid with a linear equation of state a profile symmetric about $z/h = 0.5$. The profile in Fig. 6 is weakly asymmetric with the point of flow reversal at $z/h \approx 0.46$, in agreement with the predictions of the analytical solution in the diffusive limit in equation (A8) below. For the Rayleigh number shown in Fig 7, the profiles are again asymmetric but the new feature is the appearance of weak counterflows in the interior.

Bejan et al. (1981) have argued that if $Ra > A^{-4}$ then the horizontal convection of heat dominates over the vertical diffusion of heat and one would then expect to see jetlike structures in the velocity field. On the other hand, if we consider the horizontal momentum equations directly, then the horizontal flux of momentum in the core $\sim (u\Delta)u$, where $u$ and $\Delta$ are the characteristics velocity and thickness, respectively, of an intrusion into the core, and the vertical diffusion of momentum $\sim \nu u l/h$. Equating the two estimates, and noting that $(u\Delta) \sim \kappa Ra^{1/4}$ (Patterson and Imberger, 1980; Simpkins

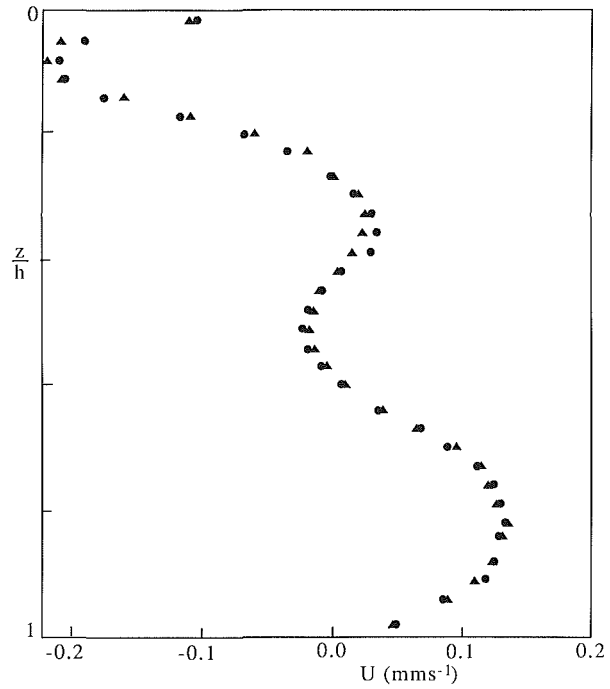


**Fig. 7 Horizontal velocities at $x/l = 0.45$ for run 7; symbols correspond to two separate estimates of the profile**

and Chen, 1986) yields the criterion that the horizontal flux of momentum dominates over the vertical diffusion of momentum if $\mathrm{Ra} > \mathrm{Pr}^4 A^{-4}$. The interpretation here is that if $\mathrm{Ra} > \mathrm{Pr}^4 A^{-4}$, the vertical diffusion of momentum occurs over a vertical scale less than $h$. The criterion $\mathrm{Ra} > A^{-4}$ predicts jetlike flows in both experiments, whereas the criterion $\mathrm{Ra} > \mathrm{Pr}^4 A^{-4}$ predicts jetlike flows only in the higher Rayleigh number experiment in Fig. 6, consistent with the observations. The experimental observations described by Simpkins and Chen (1986) are also consistent with this latter criterion, and thus $\mathrm{Ra} > \mathrm{Pr}^4 A^{-4}$ appears a better predictor of the appearance of jetlike flows in the core region of cavities.

**Heat Transfer.** It is possible to obtain an analytical expression for the Nusselt number using a perturbation expansion in the small parameter $A$. Following this technique, first described by Cormack et al. (1974) for a fluid with a linear equation of state, we can write (see equation (A14) in the appendix) correct to second order that

$$\mathrm{Nu} = 1 + K(\mathrm{Ra}A)^2 \tag{2}$$

where the constant $K = 3.67 \times 10^{-6}$ and equation (2) is valid provided $(\mathrm{Ra}A)^2 < 10^5$.

Nusselt numbers were computed for several experiments once the flow had reached steady state, taken as $t = 2t_f$. If the thermal bar was stable (i.e., $\mathrm{Ra} < 10^7$) the Nusselt number was computed directly from the temperature measurements across the bar. For higher Rayleigh numbers, the Nusselt number was computed from the velocity profiles and in situ temperatures in the same manner as used by Imberger (1974) and Bejan et al. (1981). A comparison of the two methods for run 3 yielded $\mathrm{Nu} = 32.5$ and $\mathrm{Nu} = 34.2$, respectively. The overall accuracy of the estimates of Nu is thus estimated as about 10 percent. The results are shown in Fig. 8 where the straight line is a plot of equation (2), and the data suggest a roll-off from this prediction as $\mathrm{Ra}A$ increases.

## Conclusions

Heating and cooling the respective vertical endwalls drove a double cellular circulation, which set up a steady-state

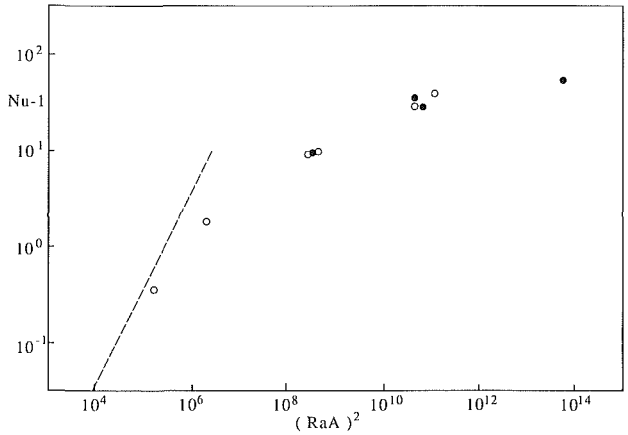


**Fig 8 Heat transfer as a function of $(\mathrm{Ra}A)^2$. The line is from equation (1), experimental values are denoted by • and the numerical values from Hamblin (1988) are denoted by ○.**

temperature structure in time $2t_f$ in the initially isothermal interior of the rectangular cavity. The steady-state flow field and temperature structure were symmetric about the midpoint of the cavity. Away from this central point, the isotherms and local velocities were essentially horizontal. Unlike the case for a fluid with a linear equation of state, the horizontal velocity was observed to be asymmetric about the middepth and this is consistent with the predictions of an analytical solution in the diffusive limit. When $\mathrm{Ra} > \mathrm{Pr}^4 A^{-4}$, the form of the velocity profiles changed to one with jetlike flows.

At the midpoint of the cavity, the isotherms were vertically oriented and a strong, vertical sinking flow was observed at this thermal front. The width and sinking velocity within the front were in accord with the predictions of scaling arguments. The thermal front was unstable for $\mathrm{Ra} > 10^7$, some leakage of flow then occurred across the front near the bottom, and the expression thermal bar was really a misnomer in this limit.

## Acknowledgments

The authors thank Dr. John Patterson for many helpful discussions during the course of this work.

## References

Bejan, A., and Tien, C. L., 1978, "Laminar Natural Convection Heat Transfer in a Horizontal Cavity With Different End Temperatures," ASME JOURNAL OF HEAT TRANSFER, Vol. 100, pp. 641–647.

Bejan, A., Al-Homound, A., and Imberger, J., 1981, "Experimental Study of High Rayleigh Number Convection in a Horizontal Cavity With Different End Temperatures," *J. Fluid Mech.*, Vol. 109, pp. 283–299.

Carmack, E. C., 1979, "Combined Influence of Inflow and Lake Temperatures on Spring Circulation in a Riverine Lake," *J. Phys. Oceanogr.*, Vol. 9, pp. 422–434.

Cormack, D., Leal, L., and Imberger, J., 1974, "Natural Convection in a Shallow Cavity With Differentially Heated End Walls. Part 1. Asymptotic Theory," *J. Fluid Mech.*, Vol. 65, pp. 209–229.

Hamblin, P. F., 1988, "Convection Near the Temperature of Maximum Density Due to Horizontal Temperature Differences," in preparation.

Hart, J. E., 1972, "Stability of Thin Non-Rotating Hadley Circulations," *J. Atmos. Sci.*, Vol. 29, pp. 687–697.

Imberger, J., 1974, "Natural Convection in a Shallow Cavity With Differentially Heated End Walls. Part 3. Experimental Results," *J. Fluid Mech.*, Vol. 65, pp. 247–260.

Inaba, I., and Fukuda, T., 1986, "Natural Convection in an Inclined Square Cavity in Regions of Density Inversion of Water," *J. Fluid Mech.*, Vol. 142, pp. 363–381.

Ivey, G. N., 1983, "Experiments on Convection Near the Temperature of Maximum Density and Their Application," *Proceedings, 8th Australasian Fluid Mechanics Conference*, University of Newcastle, Vol. 1, pp. 2A.4–2A.6.

Lankford, K. E., and Bejan, A., 1986, "Natural Convection in a Vertical Enclosure Filled With Water Near 4°C," ASME JOURNAL OF HEAT TRANSFER, Vol. 108, pp. 755–673.

Legeckis, R., 1978, "A Survey of Worldwide Sea Surface Temperature Fronts Detected by Environmental Satellites," *J. Geophys. Res.*, Vol. 83, pp. 4501–4522.

Patterson, J., and Imberger, J., 1980," Unsteady Natural Convection in a Rectangular Cavity," *J. Fluid Mech.*, Vol. 100, pp. 65-86.

Simons, T. J., 1980, "Circulation Models of Lakes and Inland Seas." *Can. Bul. Fish. Aquatic Sci.*, Vol. 203, pp. 1-146.

Steinhart, J. S., and Hart, S. R., 1968, "Calibration Curve for Thermistors," *Deep Sea Res.*, Vol. 15, pp. 497-503.

Simpkins, P. G., and Chen, K. S., 1986, "Convection in Horizontal Cavities," *J. Fluid Mech.*, Vol. 166, pp. 21-39.

Spain, J. D., Wernert, G. M., and Hubbard, D. W., 1976, "The Structure of the Spring Thermal Bar in Lake Superior," *J. Great Lakes Res.*, Vol. 2, pp. 296-306.

## APPENDIX

The solution is appropriate for cavities with small aspect ratios (see Hart, 1972) and the technique follows that of Cormack et al. (1974). For the case of small aspect ratio $A$, the nondimensional core variables (i.e., away from the end regions) in the diffusive limit are $x'=x/l$, $z'=z/h$, $y'=yl/\mathrm{Gr}\nu h$, $\omega'=\omega lh/\kappa\mathrm{Ra}$, and $\Theta=(T-T_0)/\Delta T$ (where primes denote nondimensional core variables). The governing equations then become (subsequently dropping primes for clarity)

$$A^2\frac{\partial^2\Psi}{\partial x^2}+\frac{\partial^2\Psi}{\partial z^2}=-\omega \tag{A1}$$

$$\frac{\mathrm{Ra}}{\mathrm{Pr}}A^2\frac{\partial(\omega,\Psi)}{\partial(x,z)}=\frac{\partial\theta^2}{\partial x}+A^2\frac{\partial^2\omega}{\partial x^2}+\frac{\partial^2\omega}{\partial z^2} \tag{A2}$$

$$\mathrm{Ra}A^2\frac{\partial(\theta,\Psi)}{\partial(x,z)}=A^2\frac{\partial^2\theta}{\partial x^2}+\frac{\partial^2\theta}{\partial z^2} \tag{A3}$$

The novel feature in the present configuration is thus the nonlinear form of the buoyancy term on the right-hand side of equation (A2).

The boundary conditions on $z=0$, 1 are

$$\Psi=\frac{\partial\Psi}{\partial z}=\frac{\partial\theta}{\partial z}=0 \tag{A4}$$

on $x=0$ (where the coordinate origin is taken at the center of the cavity)

$$\Psi=\frac{\partial^2\Psi}{\partial x^2}=\theta=0 \tag{A5}$$

and on $x=1$ (the endwall)

$$\Psi=\frac{\partial\Psi}{\partial x}=0,\quad \theta=1 \tag{A6}$$

Following Cormack et al. (1974), we assume all variables can be expressed in the form of a regular expansion in the small parameter $A$

$$\begin{aligned}\theta&=\theta_0+A\theta_1+A^2\theta_2+\ldots\\ \Psi&=\Psi_0+A\Psi_1+A^2\Psi_2+\ldots\\ \omega&=\omega_0+A\omega_1+A^2\omega_2+\ldots\end{aligned} \tag{A7}$$

Substituting equation (A7) into equations (A1), (A2), and (A3), applying the boundary conditions (A4), (A5), and (A6), and using the centrosymmetry condition that $\theta=0$ at $x=0$ (see Gill, 1966) we obtain

$$\theta=c_0x+c_1Ax+A^2\left[2\,\mathrm{Ra}x\left(\frac{z^5}{120}-\frac{z^4}{48}+\frac{z^3}{72}\right)-\frac{\mathrm{Ra}^2}{45360}\left(\frac{x^3}{6}+c_2x\right)\right]+\mathrm{O}(A^3)$$

$$\Psi=[2c_0+2c_0c_1]\left(\frac{z^4}{24}-\frac{z^3}{12}+\frac{z^2}{24}\right)x+A^2\Psi_2(x,z)+\mathrm{O}(A^3) \tag{A8}$$

where $c_0$, $c_1$, and $c_2$ are unknown constants.

The unknown constants may be determined by matching with the flow in the end regions. Following Cormack et al. (1974), the problem in the end regions must be rescaled since now $x\sim h$. The correct nondimensional variables in the end regions are $x^*=x/h$, $z^*=z/h$, $\Psi^*=\Psi l/\mathrm{Gr}\nu h$, $\omega^*=\omega lh/\kappa\mathrm{Ra}$ and $\theta^*=(T-T_0)/\Delta T$ (where * denotes nondimensional end region variables). The nondimensionalized equations valid in the end regions then becomes (subsequently dropping * for clarity)

$$\nabla^2\Psi=-\omega \tag{A9}$$

$$\mathrm{Gr}A^2\frac{\partial(\omega,\Psi)}{\partial(x,z)}=\frac{\partial\theta^2}{\partial x}+A\nabla^2\omega \tag{A10}$$

$$\mathrm{GrPr}A\frac{\partial(\theta,\Psi)}{\partial(x,z)}=\nabla^2\theta \tag{A11}$$

and the boundary conditions valid in the end region near the hot wall are

$$\theta(0,z)=1,\quad \Psi(0,z)=0$$

$$\frac{\partial\theta}{\partial z}(x,0)=\frac{\partial\theta}{\partial z}(x,1)=\Psi(x,0)=\Psi(x,1)=0 \tag{A12}$$

In the limit as $x\to-\infty$, the $\theta$ and $\Psi$ must match the core solutions in (A8) above, suitably expressed in end region scaling, where we note that the transformation between the nondimensional variables is given by $x'=Ax^*+1$. As before we assume a regular expansion of all functions in the end regions in the small parameter $A$.

At order $A^0$ we obtain from (A10) and (A11)

$$\frac{\partial\theta_0^2}{\partial x}=0 \text{ and } 0=\nabla^2\theta_0$$

and with boundary conditions $\theta_0(0,z)=1$, $\partial\theta_0/\partial z(x,0)=\partial\theta_0/\partial z(x,1)=0$ and in $\lim x\to-\infty\ \theta_0=c_0$, this yields $c_0=1$.

At order $A^1$ we obtain from (A11)

$$\mathrm{GrPr}\frac{\partial(\theta_0,\Psi_0)}{\partial(x,z)}=\nabla^2\theta_1$$

and with boundary conditions $\theta_1(0,z)=0$, $\partial\theta_1(x,0)/\partial z=\partial\theta_1(x,1)/\partial z=0$ and $\lim x\to-\infty\ \theta_1=x+c_1$, this yields $c_1=0$.

These results imply that $\theta_0=1$ and $\theta_1=x$ and hence at order $A^2$ we obtain from (A11) that

$$\mathrm{GrPr}\left(\frac{\partial\Psi_0}{\partial z}\right)=\nabla^2\theta_2 \tag{A13}$$

Using the integral matching technique introduced by Bejan and Tien (1978), we then integrate (A13) by $\int_0^1 dz$ and also the boundary conditions such that $\int_0^1\theta_2(0,z)dz=0$ and $\lim x\to-\infty\ \int_0^1\theta_2(x,z)dz=\mathrm{GrPr}/720-(\mathrm{GrPr})^2/45360\ (1/6+c_2)$, finally to obtain $c_2=63/\mathrm{GrPr}-1/6$.

The Nusselt number may then be written in dimensionless core variables as

$$\mathrm{Nu}=\int_0^1\left[\frac{\partial\theta}{\partial x}-(\mathrm{Ra})u\theta\right]dz$$

$$\text{i.e., } \mathrm{Nu}=1+(\mathrm{Ra}A)^2/272{,}160=1+(3.67\times10^{-6})(\mathrm{Ra}A)^2 \tag{A14}$$

Finally demanding that the second term in the expansion in $\theta$ be small compared to the first requires that

$$(\mathrm{Ra}A)^2<10^5$$

As noted in the introduction, the primary motivation for the present study was to model convection in lakes. The boundary condition on the upper surface is a free-slip boundary in such cases, and Ivey (1983) has generalized the above analysis to examine this effect. Specifically, instead of equation (A4), he applied the boundary condition

$$\Psi = \frac{\partial^2 \Psi}{\partial z^2} = \frac{\partial \theta}{\partial z} = 0 \text{ on } z = 1 \tag{A15}$$

Following the same procedure as above, the heat transfer is then given by

$$\text{Nu} = 1 + (1.745 \times 10^{-5})(\text{Ra}A)^2 \tag{A16}$$

providing $(\text{Ra}A)^2 < 10^4$. Comparing (A14) and (A16), it is clear that the effect of the free surface is to increase the effectiveness of horizontal heat transfer for given values of Ra and A, although the Nu is still of order 1 in both cases. Due to the unwanted effects of surface tension, it is not possible to examine this configuration in the laboratory. Other factors, such as heat transfer across the top boundary and ambient turbulence, also complicate the description of the flow in the field. As Ivey (1983) demonstrated, however, the effect of these complications can be assessed, and the present laboratory results do yield predictions that compare favorably with the available field data.

**B. R. Morton**
Department of Mathematics,
Monash University,
Melbourne, Australia

**D. B. Ingham**

**D. J. Keen**

Department of Applied Mathematical Studies,
University of Leeds,
Leeds, United Kingdom

**P. J. Heggs**
Schools of Chemical Engineering,
University of Bradford,
Bradford, United Kingdom

# Recirculating Combined Convection in Laminar Pipe Flow

*Investigations are conducted into situations where flow recirculation occurs in laminar combined convection flows in vertical circular tubes. Particular attention is given to flows in which finite sections of the tube wall are maintained at constant temperatures, which may be either hotter or colder than the temperature of the fluid at the entrance of the tube. A numerical study is carried out in which the governing elliptic partial differential equations are expressed in finite difference form and solved using a relaxation technique. The values of the governing parameters, namely the Reynolds, Prandtl, and Grashof numbers, and the thermal and viscous boundary conditions are chosen to correspond as closely as possible to an experimental investigation that involves water being forced along a perspex vertical circular tube, which is heated and/or cooled over finite sections. It is found that the numerical model is able to predict quite accurately the location, shape, and size of the recirculation regions observed in the experiments.*

## 1 Introduction

The problem of obtaining theoretical solutions for axisymmetric steady laminar combined convection flows in vertical tubes has been investigated in detail. It is of great interest because of its relevance to the modeling of, for example, heat exchangers in industry and the cooling processes in nuclear reactors. An interesting feature of these investigations is the effect that natural convection has on the axial velocity profile of the fluid in the tube. In flows with sufficiently large Grashof numbers, the distortion produced in the axial velocity profiles can often be great enough to produce either flow recirculation inside the pipe or a transition to turbulent flow at some point along the pipe. The first of these two phenomena has, until now, received little attention either experimentally or numerically, and it is in this area that the investigations in this paper are concentrated.

There are two general approaches to the modeling of problems of heat transfer to a fluid flowing along a duct of constant cross section, these being either the inclusion or the exclusion of the axial diffusion terms in the governing momentum and energy equations. In situations where the Reynolds and Peclet numbers are relatively large, Re, Pe $\gg 1$, it can be seen, using a suitable nondimensionalization, that the radial diffusion terms in the governing momentum and energy equations, respectively, become far more important than the axial diffusion terms. Under certain circumstances when both Re and Pe are large the axial diffusion terms may be neglected and the governing equations become parabolic in nature. However in the situations considered in this paper Re is relatively small and flow reversals are present in the fluid, so neglecting the axial diffusion in the momentum equations is not a valid assumption and the full elliptic equations are considered. For the solution of these types of problem, downstream and upstream boundary conditions must be specified and the solution technique involves solving a set of finite difference equations, derived from the governing equations, using a standard relaxation technique. The investigations of Zeldin and Schmidt (1972) and Chow et al. (1984) give a good description of the method of solution of these types of problem and ideas similar to those used by Zeldin and Schmidt (1972) and Chow et al. (1984) are employed in the solution of the finite difference equations in this paper.

Contributed by the Heat Transfer Division and presented at the International Symposium on Natural Circulation, ASME Winter Annual Meeting, Boston, Massachusetts, December 13–18, 1987. Manuscript received by the Heat Transfer Division January 21, 1988. Keywords: Flow Visualization, Heat Pipes and Thermosyphons, Mixed Convection.

One of the aims of this paper is to model mathematically a number of steady-state experimental situations involving water being forced upward through a vertical perspex tube of circular cross section. The experimental apparatus, which is illustrated schematically in Fig. 1, consists of a length of straight perspex tube (A), which is encased by a water bath. The water bath consists of two sections, (B) and (C), through which water of different temperatures can be pumped at a rate significantly greater than the rate at which the water is pumped through the vertical tube (A), in order to enforce constant-temperature boundary conditions over certain parts of the tube wall. The dimensions of the water bath are as indicated in Fig. 1. When it is desired first to heat and then to cool the water flowing up the tube, the water bath is positioned so that the large section (B), is placed below the small section (C), and $T_B$ is chosen to be greater than both $T_A$ and $T_C$. However if it is desired first to cool the water in the tube, the bath is then positioned with the small section (C) below the large section (B), and the temperatures are then maintained so that $T_A > T_C$ and $T_B > T_C$. The reason for having both heating and cooling sections in the water bath is to restrict any recirculation regions formed in the first section of the bath, thus allowing the experimental investigations to remain stable. The longer section is used for heating in both situations because flow reversals at the center of the pipe need more distance to develop than those adjacent to the wall. The water streams being pumped up the vertical tube and into the two water baths are maintained at constant temperatures by storing prior to pumping in tanks that are held at specified temperatures. The temperature $T_A$ is very close to the temperature of the room so that little or no heat transfer can take place until the water enters the section of the tube encased by the water bath. The straight length of the tube preceding the heat transfer region is long enough so that fully developed flow can be set up before the fluid velocity is affected by the heat transfer region. Beyond the region encased by the water bath there is a long length of straight vertical pipe where the fluid velocity is able to return to being fully developed. The average velocities for each individual situation were found by using a flow meter, which was situated in the section of the pipe preceding the heat transfer region. The results presented for these experimental situations are in terms of streamline patterns in the region of the duct encased by the water bath. The streamlines were revealed by adding aluminum powder to the water in the tube and the patterns formed were photographed for comparison with the numerical investiga-

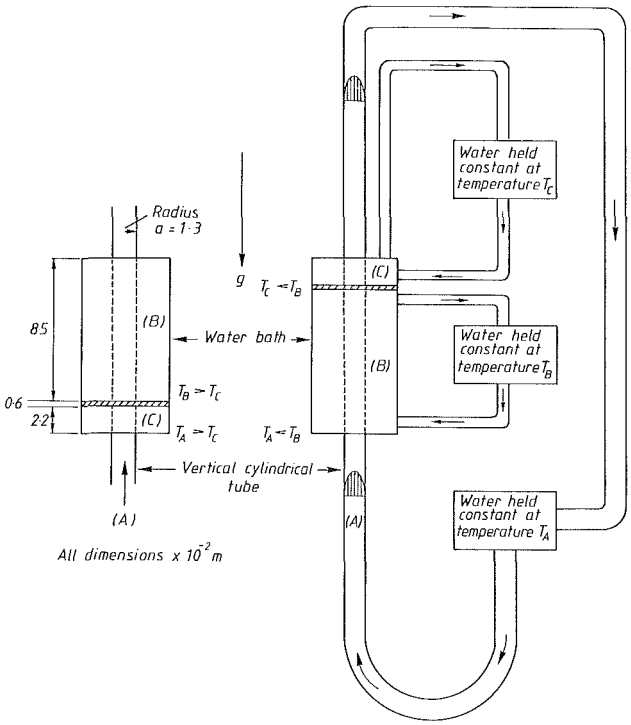


**Fig. 1 Schematic view of the experimental apparatus**

tion. In the experimental results the flow appeared to be laminar, although a small amount of turbulence was present at the closure of the recirculation regions. In such a simple experimental apparatus there is bound to be a certain amount of uncertainty in any conclusions drawn, and this will be discussed in more detail later.

The mathematical model includes an entry length, which the fluid enters with a fully developed parabolic velocity profile, the walls of this entry length being maintained at the same temperature as the fluid at the entry. The entry length precedes a heated/cooled section where the wall of the tube is maintained at a constant temperature greater/less than the entry temperature and beyond the heated/cooled section the fluid is cooled/heated again. In the mathematical model this final section is assumed to be infinite in extent and a fully developed boundary condition can be applied at infinity by using a scaling in the axial direction. The geometry of the numerical problem is illustrated in Fig. 2. This arrangement is similar to that used by Chow et al. (1984) for a parallel plate channel where insulated entry and exit lengths are used to investigate the effect of axial conduction from a heat transfer section where the walls are maintained at a constant temperature. However, the investigations carried out by Chow et al. (1984) did not cover situations where the ratio |Gr/Re| was sufficiently large to produce a flow reversal at some point within the vertical tube.

In this study it is found, by experimental investigation, that flows, with Reynolds numbers of the order of 50 and |Gr/Re| of the order of 500, can exhibit laminar flow with substantial

## Nomenclature

$a$ = radius of the tube
$A$ = area of tube wall through which heat transfer takes place
$A_c$ = flow cross-sectional area $= \pi a^2$
$b$ = axial location of the beginning of the water bath
$c$ = axial location of the divide in the water bath
$C$ = transformation parameter
$d$ = position at which scaling in the axial direction is introduced
$f$ = friction factor
$g$ = acceleration due to gravity
Gr = Grashof number $= g\beta(T_e - T_h)a^3/\nu^2$
$G^Z$ = finite difference grid for $0 \le Z \le d$
$G^\xi$ = finite difference grid for $d \le Z \le \infty$
$h$ = local heat transfer coefficient
$k$ = thermal conductivity of the fluid
$K$ = finite difference step size in the $Z$ direction on $G^Z$
$L$ = characteristic length
$N$ = number of finite difference steps in the $R$ direction
$NN$ = number of finite difference steps in the $Z$ direction on $G^Z$
$N^\xi$ = number of finite difference steps in the $Z$ direction on $G^\xi$
Nu = local Nusselt number $= hL/k$
$\mathrm{Nu_{AV}}$ = average Nusselt number between $Z = 0.3$ and $Z = L$
$p$ = pressure
$P$ = dimensionless pressure $= p/\rho_0 u_m^2 - gz\,[\beta(T_h - T_e) - 1]/u_m^2$
Pe = Peclet number = RePr
Pr = Prandtl number $= \nu/\alpha$
$r$ = radial coordinate
$R$ = dimensionless radial coordinate $= r/a$
Re = Reynolds number $= au_m/\nu$
$T$ = temperature
$u$ = axial velocity
$U$ = dimensionless axial velocity $= u/u_m$
$v$ = radial velocity
$V$ = dimensionless radial velocity $= v/u_m$
$z$ = axial coordinate
$Z$ = dimensionless axial coordinate $= z/a\mathrm{Re}$
$\alpha$ = molecular thermal diffusivity
$\beta$ = coefficient of thermal expansion $= (-1/\rho)(\partial\rho/\partial T)$
$\epsilon$ = convergence criterion parameter
$\theta$ = dimensionless temperature $= (T - T_h)/(T_e - T_h)$
$\nu$ = kinematic viscosity
$\xi$ = dimensionless axial coordinate on $G^\xi$ $= 1 - 1/(1 + C(Z - d))$
$\rho$ = variable density
$\rho_0$ = density at $T = T_e$
$\psi$ = dimensionless stream function
$\Omega$ = dimensionless vorticity

### Subscripts

$A$ = experimental entry value
$B$ = value in the large section of the water bath
$C$ = value in the small section of the water bath
$e$ = entry value
$h$ = wall value for $b < z < c$
$i$ = radial finite difference suffix
$j$ = axial finite difference suffix
$m$ = flow average value
$NN$ = value at axial location $j = NN$
$w$ = wall value
$\infty$ = infinity value

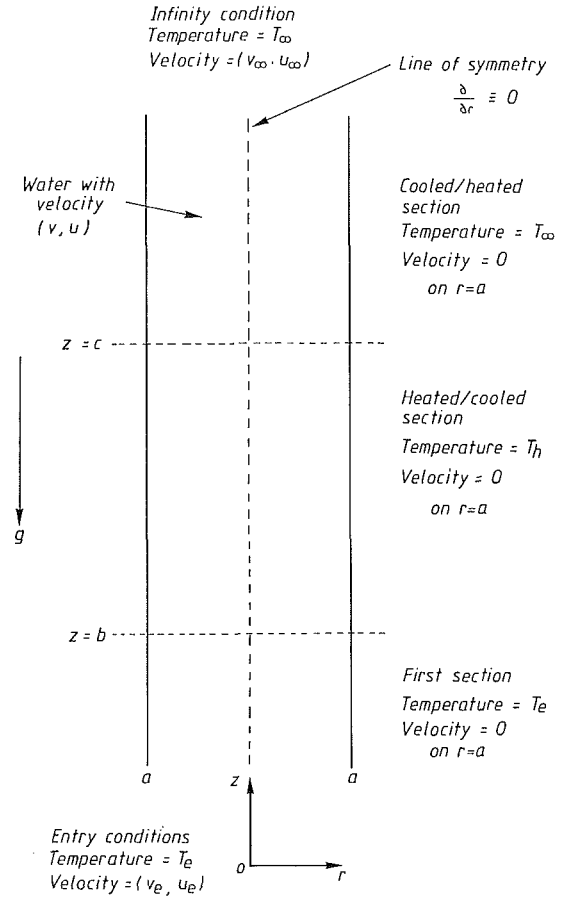


**Fig. 2 Schematic view of mathematical model**

regions of recirculating flow. The model derived in the numerical investigation is able to reproduce the experimental observations of the size, shape, and location of the recirculation regions quite accurately.

## 2 Model and Governing Equations

Steady laminar combined convection of a fluid with velocity $(v, u)$ inside a vertical circular tube as illustrated in Fig. 2 is the situation under consideration. In the model an entry section between $z=0$ and $z=b$ is employed where the temperature of the wall for $0 < z < b$ is held constant at $T=T_e$. The value of $b$ is chosen so that the boundary condition at $z=0$ is a good approximation to $z=-\infty$ where fully developed parabolic flow, $(v_e, u_e)$, at constant temperature is assumed. A heated/cooled section is situated between $z=b$ and $z=c$ where the temperature of the tube wall is maintained at $T=T_h$ and beyond $z=c$ the temperature of the wall is reduced/increased to $T_\infty$, which is the temperature that the fluid attains as $z$ tends to infinity. It should be noted at this point that in the mathematical model the region beyond the second section of the water bath is being treated as if that part of the bath extends to infinity. This is a fair assumption to make for both orientations of the water bath for the following reasons. In the situation where the bath is such that the large section is uppermost it is reasonable to assume that most of the heat transfer takes place inside the length of the tube encased by the water bath, and in the situation where the small section of the water bath is uppermost the fluid is cooled by the small water bath to a temperature that is very similar to the room temperature. No changes occur in the azimuthal direction, so the solution domain can be reduced to $0 < r < a$, $0 < z < \infty$ where $a$ is the radius of the tube and the condition $\partial/\partial r \equiv 0$ applies along $r = 0$. The acceleration due to gravity, $g$, acts vertically downward in the direction opposite to the forced convection. The fluid is considered to be Newtonian with constant dynamic viscosity, thermal conductivity, specific heat capacity, and coefficient of expansion. Density variations are assumed to be negligible except in the buoyancy term of the vertical momentum equation (Boussinesq approximation). The above assumptions are made in order to keep the model as simple as possible, although inclusion of variations in some of the physical parameters should not in theory be difficult to introduce into the following numerical theory. Viscous dissipation is ignored in the energy equation as it was shown to have only a small effect (Collins, 1975).

The governing equations are the continuity, axial momentum, radial momentum, and energy equations and these can be written in the form (Collins, 1980)

$$\frac{\partial u}{\partial z}+\frac{\partial v}{\partial r}+\frac{v}{r}=0 \tag{1}$$

$$u\frac{\partial u}{\partial z}+v\frac{\partial u}{\partial r}=-\frac{1}{\rho}\frac{\partial p}{\partial z}+\nu\left[\frac{\partial^2 u}{\partial z^2}+\frac{1}{r}\frac{\partial}{\partial r}\left(r\frac{\partial u}{\partial r}\right)\right]-g \tag{2}$$

$$u\frac{\partial v}{\partial z}+v\frac{\partial v}{\partial r}=-\frac{1}{\rho}\frac{\partial p}{\partial r}+\nu\left[\frac{\partial^2 v}{\partial z^2}+\frac{1}{r}\frac{\partial}{\partial r}\left(r\frac{\partial v}{\partial r}\right)-\frac{v}{r^2}\right] \tag{3}$$

$$u\frac{\partial T}{\partial z}+v\frac{\partial T}{\partial r}=\alpha\left[\frac{\partial^2 T}{\partial z^2}+\frac{1}{r}\frac{\partial}{\partial r}\left(r\frac{\partial T}{\partial r}\right)\right] \tag{4}$$

where $\alpha$ is the molecular thermal diffusivity, $\nu$ the kinematic viscosity, $\rho$ the density, and $p$ the pressure of the fluid. The boundary conditions for the problem are as follows:

$$\text{At } r=0,\quad 0\le z<\infty:\quad v=0,\quad \frac{\partial u}{\partial r}=0,\quad \frac{\partial T}{\partial r}=0 \tag{5}$$

$$\left.\begin{aligned}&\text{At } r=a,\quad 0\le z<\infty:\quad v=0,\quad u=0\\ &0\le z<b:\quad T=T_e\\ &b\le z<c:\quad T=T_h\\ &c\le z<\infty:\quad T=T_\infty\end{aligned}\right\} \tag{6}$$

$$\text{At } z=0,\quad 0\le r\le a:\quad v=v_e,\quad u=u_e,\quad T=T_e \tag{7}$$

$$\text{As } z\to\infty,\quad 0\le r\le a:\quad v=v_\infty,\quad u=u_\infty,\quad T=T_\infty \tag{8}$$

The velocities $v_e=v_\infty=0$ and $u_e=u_\infty$ correspond to parabolic velocity profiles.

The Boussinesq approximation involves replacing $\rho$ by $\rho_0[1-\beta(T-T_e)]$ in the buouyancy term of equation (2) and by $\rho_0$ elsewhere. Here $\beta = (-1/\rho)(\partial\rho/\partial T)$ is the coefficient of expansion with respect to $T$, and $\rho_0$ is the density at $T=T_e$. The nondimensional variables $V, U, R, Z, P$, and $\theta$ are defined as follows:

$$v=u_m V,\quad u=u_m U,\quad r=aR,\quad z=a\mathrm{Re}Z,$$

$$p=g\rho_0 z[\beta(T_h-T_e)-1]+\rho_0 u_m^2 P,\quad T=T_h+(T_e-T_h)\theta$$

where $u_m$ is a characteristic velocity taken in this study to be the mean velocity and $\mathrm{Re} = au_m/\nu$ is the Reynolds number. Now introduce a stream function $\psi$, which satisfies the continuity equation (1):

$$V=\frac{1}{\mathrm{Re}}\frac{1}{R}\frac{\partial\psi}{\partial Z},\quad U=-\frac{1}{R}\frac{\partial\psi}{\partial R} \tag{9}$$

and define the vorticity as follows:

$$\Omega = \frac{1}{\mathrm{Re}}\frac{\partial V}{\partial Z} - \frac{\partial U}{\partial R} \tag{10}$$

Combining equations (9) and (10) leads to

$$\Omega R = \frac{1}{\mathrm{Re}^2}\frac{\partial^2 \psi}{\partial Z^2} + \frac{\partial^2 \psi}{\partial R^2} - \frac{1}{R}\frac{\partial \psi}{\partial R} \tag{11}$$

and if $P$ is eliminated between equations (2) and (3), equations (2)–(4) become

$$\frac{1}{R}\frac{\partial \psi}{\partial Z}\frac{\partial \Omega}{\partial R} - \frac{1}{R}\frac{\partial \psi}{\partial R}\frac{\partial \Omega}{\partial Z} - \frac{\Omega}{R^2}\frac{\partial \psi}{\partial Z}$$

$$= \frac{1}{\mathrm{Re}^2}\frac{\partial^2 \Omega}{\partial Z^2} + \frac{\partial^2 \Omega}{\partial R^2} + \frac{1}{R}\frac{\partial \Omega}{\partial R} - \frac{\Omega}{R^2} - \frac{\mathrm{Gr}}{\mathrm{Re}}\frac{\partial \theta}{\partial R} \tag{12}$$

$$\frac{1}{R}\frac{\partial \psi}{\partial Z}\frac{\partial \theta}{\partial R} - \frac{1}{R}\frac{\partial \psi}{\partial R}\frac{\partial \theta}{\partial Z}$$

$$= \frac{1}{\mathrm{Pr}}\left\{\frac{1}{\mathrm{Re}^2}\frac{\partial^2 \theta}{\partial Z^2} + \frac{\partial^2 \theta}{\partial R^2} + \frac{1}{R}\frac{\partial \theta}{\partial R}\right\} \tag{13}$$

where $\mathrm{Pr} = \nu/\alpha$ is the Prandtl number and $\mathrm{Gr} = g\beta(T_e - T_h)a^3/\nu^2$ is the Grashof number. The boundary conditions (5)–(8) become

$$\text{At } R=0,\quad 0 \le Z < \infty:\quad \psi = 0.5,\quad \Omega = 0,\quad \frac{\partial \theta}{\partial R} = 0 \tag{14}$$

$$\left.\begin{aligned} &\text{At } R=1,\quad 0 \le Z < \infty:\quad \psi = 0,\quad \frac{\partial \psi}{\partial R} = 0 \\ &0 \le Z < b/a\mathrm{Re}:\quad \theta = 1 \\ &b/a\mathrm{Re} \le Z < c/a\mathrm{Re}:\quad \theta = 0 \\ &c/a\mathrm{Re} \le Z < \infty:\quad \theta = \theta_\infty \end{aligned}\right\} \tag{15}$$

$$\text{At } Z=0,\quad 0 \le R \le 1:\quad \psi = \frac{1}{2}(1-R^2)^2,\quad \Omega = 4R,\quad \theta = 1 \tag{16}$$

$$\text{As } Z \to \infty,\quad 0 \le R \le 1:\quad \psi = \frac{1}{2}(1-R^2)^2,\quad \Omega = 4R,\quad \theta = \theta_\infty \tag{17}$$

where $\theta_\infty = (T_\infty - T_h)/(T_e - T_h)$.

The elliptic equations (11)–(13) give the desired description of the flow under consideration and these must be solved subject to the boundary conditions (14)–(17). The governing parameters in the problem are thus the Reynolds number Re, the Prandtl number Pr, the ratio of the Grashof to the Reynolds numbers Gr/Re, the nondimensional axial locations $b/a$Re and $c/a$Re, and the nondimensional temperature $\theta_\infty$.

## 3 Solution Technique

The solution of the mathematical problem is achieved by expressing the governing nondimensional equations (11)–(13) in finite difference form and solving them using a relaxation procedure subject to the boundary conditions (14)–(17). In order to do this boundary conditions (17) must be satisfied as $Z \to \infty$; this is achieved by using a scaling in the axial direction. This scaling is only applied over the region $d < Z < \infty$ where $Z = d$ is a station sufficiently far along the final section of the tube where most of the heat transfer has already taken place. The scaling of the axial coordinate, as used by Zeldin and Schmidt (1972), is defined as follows:

$$\xi = 1 - 1/(1 + C(Z-d)) \text{ or } Z = (\xi/C)/(1-\xi) + d$$

where $\xi$ is a new axial variable that lies in the range $0 \le \xi \le 1$ and $C$ is a transformation parameter to be defined later. Equations (11)–(13) under this transformation become

$$\Omega R = \frac{1}{\mathrm{Re}^2}\left[\frac{\partial^2 \psi}{\partial \xi^2}\left(\frac{\partial \xi}{dZ}\right)^2 + \frac{\partial \psi}{\partial \xi}\frac{d^2\xi}{dZ^2}\right] + \frac{\partial^2 \psi}{\partial R^2} - \frac{1}{R}\frac{\partial \psi}{\partial R} \tag{18}$$

$$\frac{1}{R}\frac{d\xi}{dZ}\left[\frac{\partial \psi}{\partial \xi}\frac{\partial \Omega}{\partial R} - \frac{\partial \psi}{\partial R}\frac{\partial \Omega}{\partial \xi} - \frac{\Omega}{R}\frac{\partial \psi}{\partial \xi}\right] = \frac{1}{\mathrm{Re}^2}\left[\frac{\partial^2 \Omega}{\partial \xi^2}\left(\frac{d\xi}{dZ}\right)^2 + \frac{\partial \Omega}{\partial \xi}\frac{d^2\xi}{dZ^2}\right] + \frac{\partial^2 \Omega}{\partial R^2} + \frac{1}{R}\frac{\partial \Omega}{\partial R} - \frac{\Omega}{R^2} - \frac{\mathrm{Gr}}{\mathrm{Re}}\frac{\partial \theta}{\partial R} \tag{19}$$

$$\frac{1}{R}\frac{d\xi}{dZ}\left[\frac{\partial \psi}{\partial \xi}\frac{\partial \theta}{\partial R} - \frac{\partial \psi}{\partial R}\frac{\partial \theta}{\partial \xi}\right] = \frac{1}{\mathrm{Pr}}\left\{\frac{1}{\mathrm{Re}^2}\left[\frac{\partial^2 \theta}{\partial \xi^2}\left(\frac{d\xi}{dZ}\right)^2 + \frac{\partial \theta}{\partial \xi}\frac{d^2\xi}{dZ^2}\right] + \frac{\partial^2 \theta}{\partial R^2} + \frac{1}{R}\frac{\partial \theta}{\partial R}\right\} \tag{20}$$

The solution domain of the problem can now be split into two regions, namely $0 \le Z \le d$ where equations (11)–(17) are expressed in finite difference form on a regular rectangular grid, $G^Z$, of $N+1$ points in the radial direction and $NN+1$ points in the axial direction, and $d \le Z < \infty$ where equations (18)–(20) and (14)–(17) are expressed in finite difference form on a regular rectangular grid, $G^\xi$, of $N+1$ points in the radial direction and $N^\xi + 1$ points in the $\xi$ direction. The value of the parameter $C$ is chosen so that the step size between the axial locations $Z_{NN+2}$ and $Z_{NN+1} = d$ is the same as the distance between axial locations $Z_{NN+1}$ and $Z_{NN}$. Thus if $\xi_{NN+2} = 1/N^\xi = 1 - 1/(1 + C(Z_{NN+2} - d))$ and $Z_{NN+2} - Z_{NN+1} = K$ where $K = d/NN$ it must hold that

$$C = 1/((N^\xi - 1)K)$$

and hence for $Z \ge d$

$$Z = (\xi(N^\xi - 1)K)/(1-\xi) + d \tag{21}$$

Central differences are employed in the radial direction for both first and second derivatives; however attempts to do the same in the axial direction, as in the model of Zeldin and Schmidt (1972), produce oscillations in the solution that can be attributed both to the discontinuities in the temperature on the wall of the tube and the presence of reverse flow at some point in the tube. These oscillations are overcome by using either backward or forward differencing in the axial first derivative terms, depending upon whether the flow at a particular point is in the positive or negative $Z$ direction, respectively. The vorticity on the boundary is determined to second-order accuracy using Taylor series expansions of $\psi$ and $\Omega$ at $R = 1$, the fact that $\partial\psi/\partial R = 0$ at $R = 1$, and equations (11) and (18) evaluated at $R = 1$. The temperature at the centerline is given to second-order accuracy using $\partial\theta/\partial R = 0$ at $R = 0$ and equations (13) and (20) evaluated at $R = 0$. The solution to the problem is obtained iteratively by sweeping across the grids $G^Z$ and $G^\xi$ from $Z = 0$ to $\xi = 1$, relaxing the finite difference equations at each point on the two grids. The solution is in this way matched between the two grids at $Z = d$ during each iteration. It is found that different relaxation parameters are desirable for each of the finite difference variables $\psi$, $\Omega$, and $\theta$, with $\Omega$ and $\theta$ needing to be under-relaxed, $\Omega$ more so than $\theta$, and $\psi$ having a relaxation parameter of unity. It is also found that the relaxation parameters for $\Omega$ and $\theta$ decrease as the Reynolds number increases.

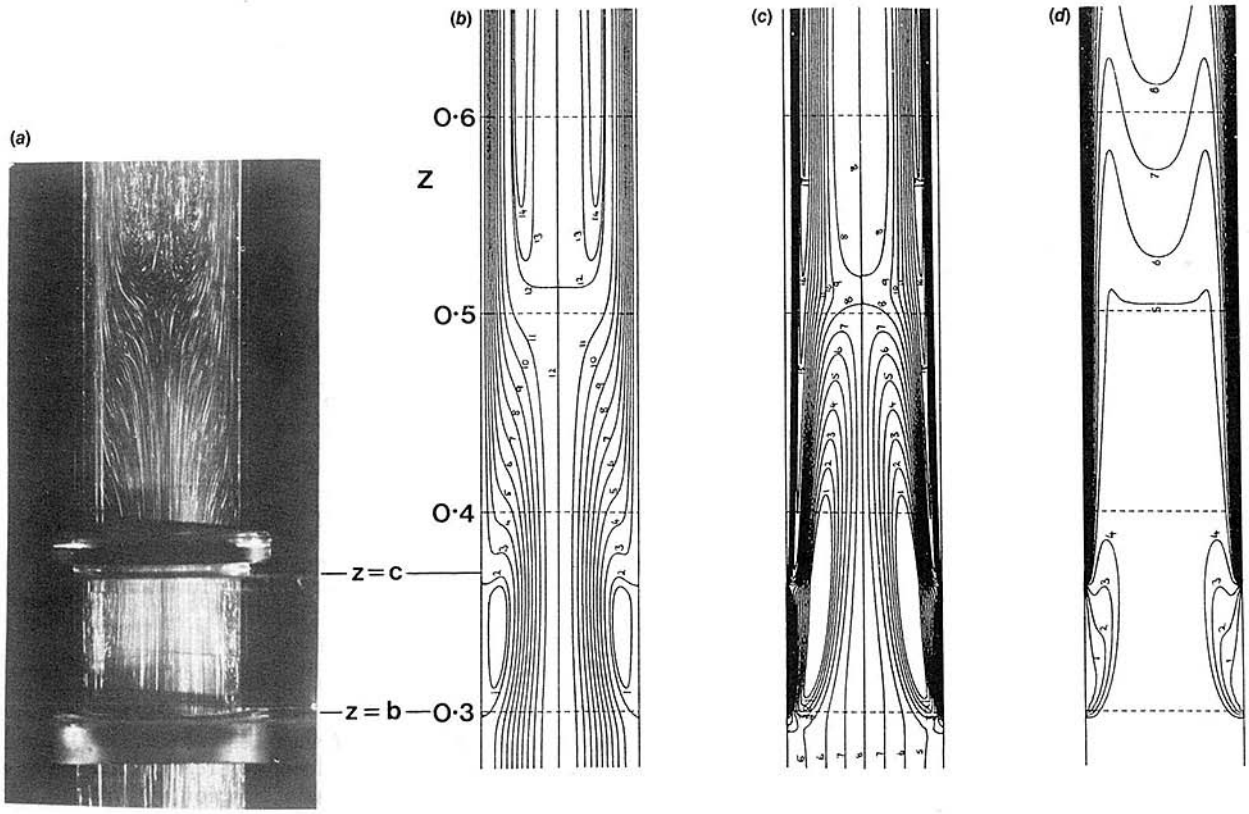


Fig. 3 Case (I): (*a*) photograph of experimental observation, (*b*) contour plot of streamlines, (*c*) contour plot of vorticity, (*d*) contour plot of temperature

Convergence is assumed to have occurred when the following criterion is satisfied:

$$\frac{\left[\sum_{i,j}\{|\psi_{i,j}^{I+1}-\psi_{i,j}^{I}|+|\Omega_{i,j}^{I+1}-\Omega_{i,j}^{I}|+|\theta_{i,j}^{I+1}-\theta_{i,j}^{I}|\}\right]}{[(3N-1)(NN+N^{\xi}+1)]}<\epsilon \quad (22)$$

where $(3N-1)(NN+N^{\xi}+1)$ is the total number of finite difference variables used in the solution of the problem, the subscripts $i$ and $j$ are the finite difference suffices in the radial and axial directions, respectively, the superscript $I$ refers to values calculated at the $I$th iteration, and $\epsilon$ is a small number usually taken to be $10^{-6}$. Convergence is achieved more quickly by using previous solutions as an initial guess for new calculations.

The values of $N$ and $NN$ are usually 30 and 120, respectively, with $N^{\xi}$ equal to 40. Calculations with $N=20$ and $NN=80$ suggest that the combined $30\times160$ grid is fine enough to give an accurate solution, and calculations with $N=60$ and $NN=240$ suggest that the results presented here for the stream function are correct to within $5\times10^{-3}$ at every point on the two grids $G^{Z}$ and $G^{\xi}$. Also a set of results obtained using the solution techniques described above and continuous temperature boundary conditions was found to be graphically indistinguishable from the results of Zeldin and Schmidt (1972).

## 4 Results and Comparisons

Two different situations are considered, the first involving water being cooled and then heated (I), and the second involving water being heated and then cooled (II). In each case the forced convection is in the upward direction. For case (I) the length of the cooled section, $c-b$, is equal to $2.2\times10^{-2}$ m and the temperatures $T_e$, $T_h$, and $T_\infty$ are taken to be 22, 21, and 25°C, respectively. The average velocity $u_m$ is $1.82\times10^{-3}$ m/s and the parameters $\nu$, $\beta$, and Pr are given their values at 22°C, these being $0.95\times10^{-4}$ m/s, $2.3\times10^{-4}$°C$^{-1}$, and 6.6, respectively, as given by Raznjevic (1976). The above assumptions coupled with the facts that the radius of the tube $a$ is $1.3\times10^{-2}$ m and $g$ is 9.8 m/s$^2$ give approximate values for the parameters Re, Gr, and $\theta_\infty$ of 25, 5000, and 4, respectively. For case (II) the length of the heated section $c-b$ is $8.5\times10^{-2}$ m and the temperatures $T_e$, $T_h$, and $T_\infty$ are taken to be 22, 32, and 22°C respectively. The average velocity $u_m$ is $4.17\times10^{-3}$ m/s and $\nu$, $\beta$, Pr, $a$, and $g$ have the same values as in case (I) so that Re, Gr, and $\theta_\infty$ take the values 55, $-50{,}000$, and 1, respectively.

Consider first case (I). The photograph displayed in Fig. 3(*a*) shows an experimental situation corresponding to the values of the governing parameters indicated above. In Fig. 3(*b*) the streamlines produced from the numerical investigation are illustrated on a scale that corresponds exactly to that in the photograph. The streamlines correspond to values of $\psi$ in the set $\{-0.02, 0.0, 0.05, 0.1, \ldots, 0.45, 0.5, 0.505, 0.51\}$ and are numbered so that 1 corresponds to $\psi=-0.02$, 2 to $\psi=0.0$, etc. The value $Z=0.3$ is chosen to correspond to the beginning of the cooling section, $z=b$. It can be seen from the streamlines that little deviation from fully developed flow occurs for $Z<0.3$. The end of the cooling section is $Z=0.37$, which corresponds closely to the dimensional value $z=c=b+2.2\times10^{-2}$ m. The value of $d$ is chosen to be 1.0, which allows a fairly long region between $Z=0.37$ and $Z=1.0$ for both hydrodynamic and thermal development to take place before the axial scaling is introduced. In the cooled region it is expected that the velocity of the water near the center of the tube will increase because the water there is warm relative to

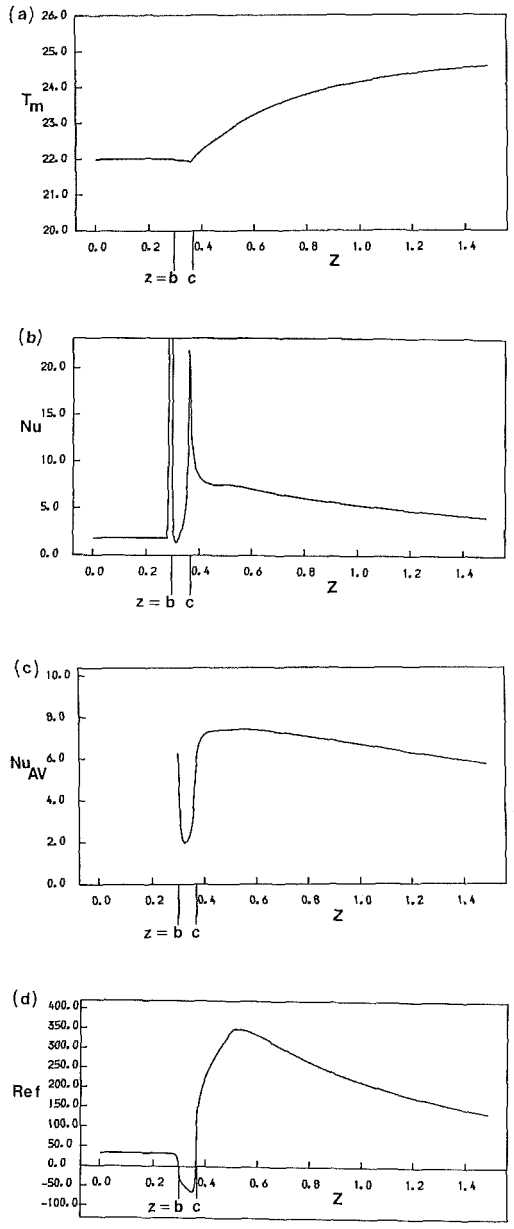


Fig. 4 Case (I): (*a*) bulk temperature, (*b*) local Nusselt number, (*c*) average Nusselt number, (*d*) friction factor times Reynolds number, all plotted against axial distance

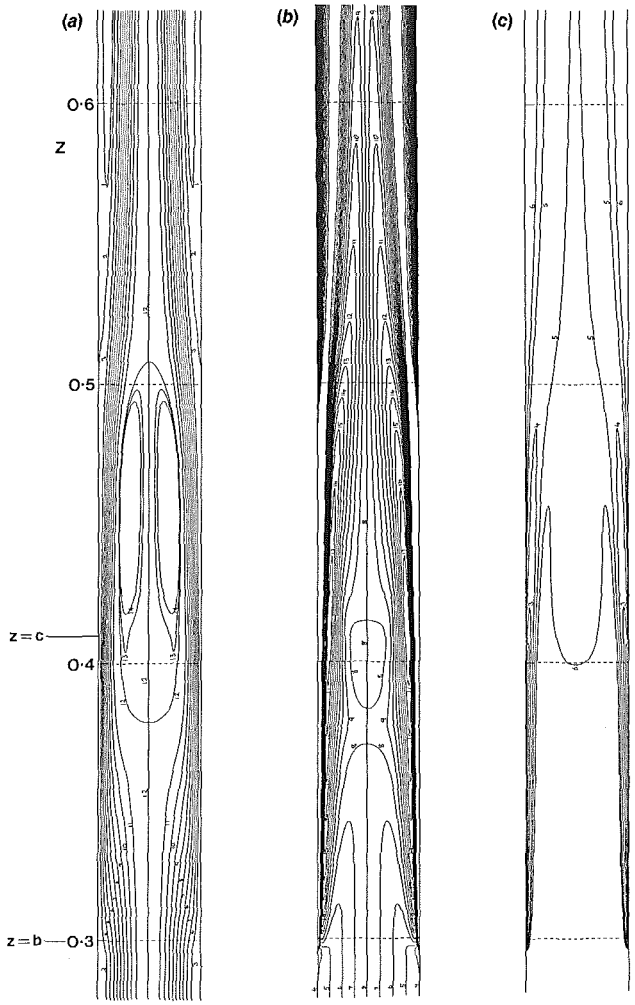


Fig. 5 Case (II), contour plots of: (a) streamlines, (*b*) vorticity, (*c*) temperature

the water near the wall. Hence by continuity the velocity of the water near the wall is expected to decrease and it may in fact become negative. This phenomenon is illustrated in both Figs. 3(*a*) and 3(*b*). In the heated region the opposite effect to that described above is anticipated, with reverse flow being expected near the center of the pipe. This flow reversal will take longer to develop in the heated section since the velocity of the water at the center of the pipe is relatively large when the water enters that section. This is also confirmed in Figs. 3(*a*) and 3(*b*). The agreement between Figs. 3(*a*) and 3(*b*) is very good and, in particular, the location size and shape of the recirculation regions are extremely close. This agreement is better than may have been expected bearing in mind the relative simplicity of the mathematical model. Plots of vorticity and temperature contours for situation (I) for values of $\Omega$ and $\theta$ of {7.0, 6.0, 5.0, . . . , −10.0, −11.0} and {0.2, 0.4, 0.6, . . . , 3.6, 3.8} respectively are displayed in Figs. 3(*c*) and 3(*d*). The contours in Figs. 3(*c*) and 3(*d*) are numbered in the same way as those in Fig. 3(*b*). From Fig. 3(*c*) it is evident that the greatest change in vorticity occurs near the wall in the heating region and this is associated with the large changes in axial velocity near the wall. From Fig. 3(*d*) it can be seen that the colder temperature on the wall of the cooling section does not penetrate through the area of recirculation into the strong flow at the center of the pipe to any great extent.

The flow average or mixing cup temperature at any particular axial location is defined by (Shah and London, 1975)

$$T_m = \frac{1}{A_c u_m} \int_{A_c} uT \, dA_c$$

where $A_c$ is the flow cross-sectional area. In the situation under consideration $A_c = \pi a^2$ and $dA_c = 2\pi a^2 R dR$ so that

$$T_m = -2 \int_0^1 \frac{\partial \psi}{\partial R} T \, dR \tag{23}$$

Simpson's rule is used to evaluate $T_m$ and the results are plotted against $Z$ in Fig. 4(*a*). It is observed from Fig. 4(*a*) that the bulk temperature drops only slightly over the cooled section, $0.3 < Z < 0.37$, as would be expected from Fig. 3(*d*), before rising fairly rapidly in the heated section toward its fully developed value of 25°C.

The local Nusselt number is defined as (Özişik, 1985) Nu = $hL/k$, where $L$ is a characteristic length which may be taken to be $a$. A simple heat balance at the wall of the duct gives the following:

$$hA(T_m - T|_{r=a}) = kA \left.\frac{\partial T}{\partial r}\right|_{r=a}$$

where $A$ is the area of the wall through which heat transfer takes place. Expressing $T$ in terms of $\theta$ leads to

$$\mathrm{Nu} = -\frac{\partial\theta}{\partial R}\bigg|_{R=1} / (\theta_m - \theta|_{R=1}) \tag{24}$$

A plot of Nu against $Z$ is displayed in Fig. 4($b$). At $Z = 0.3$ and $Z = 0.37$ the temperature boundary condition at the tube wall is discontinuous, so according to equation (24) the local Nusselt number is expected to be infinite at these two points. It can be seen from Fig. 4($b$) that the local Nusselt number is in fact very large at these two points and as the finite difference grid is reduced, so that $1/N$ and $1/NN$ both tend to zero, it is observed from the numerical experiments that Nu tends to infinity at $Z = 0.3$ and $Z = 0.37$. Beyond $Z = 0.37$ the local Nusselt number is seen to decrease toward the fully developed value of 1.83, as given by Shah and London (1975).

The average Nusselt number between the points $Z = 0.3$ and $Z = L$ is defined by

$$\mathrm{Nu_{AV}} = \frac{1}{L-0.3}\int_{0.3}^{L} \mathrm{Nu}\, dZ \tag{25}$$

This integral is calculated using Simpson's rule and $\mathrm{Nu_{AV}}$ is plotted against $Z$ in Fig. 4($c$). As would be expected from Fig. 4($b$) $\mathrm{Nu_{AV}}$ takes a relatively large value at $Z = 0.3$ before falling as $Z$ increases and then rising steeply again at $Z = 0.37$. It then decays toward its expected fully developed value of 1.83 as $Z$ becomes large.

The friction factor $f$ at a particular axial location is defined as follows (Özişik, 1985):

$$f = -\frac{8\nu}{u_m^2}\frac{\partial u}{\partial r}\bigg|_{r=a}$$

Putting $u = u_m U$ and $r = aR$ and using equation (11) the above expression reduces to

$$\mathrm{Re}f = 8\Omega|_{R=1} \tag{26}$$

Re$f$ is plotted against $Z$ in Fig. 4($d$). As would be expected the friction factor is negative over the part of the wall where the flow is separated and positive everywhere else. The maximum value of Re$f$ occurs at the point where the flow reversal at the center of the pipe begins. As $Z$ tends to infinity Re$f$ approaches its asymptotic value of 32.

One major factor that is not accounted for in the mathematical model is the effects of axial conduction of heat in the wall of the tube. Although this is not too important at $z = c$ where the continuous flow of water through the two sections of the water bath maintains a fairly rapid temperature change, at $z = b$ the cooling for $z > b$ is conducted down the tube wall to cause precooling of the water in the tube before it enters the region encased by the water bath. In the above example the effects of axial wall conduction are obviously not great enough to cause a significant change in the streamline patterns; however in the next example a flow situation occurs in which axial wall conduction is clearly important.

The streamlines from the second case to be considered, case (II), are displayed in Fig. 5($a$) with the numbers on each streamline corresponding to the same values of $\psi$ as in case (I). In Fig. 5($a$) $Z = 0.3$ corresponds to the beginning of the heating section and the beginning of the cooling section is taken to be at $Z = 0.41$, which corresponds very closely to the dimensional value $z = c = b + 8.5 \times 10^{-2}$ m. The value of $d$ is again chosen to be 1.0. As in case (I) the heating section is expected to produce a flow reversal near the center of the pipe and the cooling section is expected to produce reverse flow adjacent to the wall of the pipe. It can be seen from Fig. 5($a$) that these two phenomena are both features of the numerical model. In case (II), however, it is found that the mathematical model is not quite as good at predicting the position of the recirculating region at the center of the pipe as in case (I), although the shape and length of the recirculation region are still predicted fairly well. In the experimental situation it is found that this recirculating region occurs farther upstream in the flow than is predicted by the numerical model. This is thought to be due to the axial conduction of heat in the wall of the tube causing the fluid to be heated before it enters the heating section. Heating of the wall upstream of $z = b$ causes the centerline velocity of the fluid to be retarded before the fluid enters the heated section and hence the reverse flow region begins sooner than predicted. This problem is not encountered in case (I) because the boundary condition between the cooled and heated sections at $z = c$ is satisfied very much more rigidly because in this case it is between the two sections of the water bath. The critical distance in case (I) is the distance between the start of the heating section, $z = c$, and the start of the recirculation region at the center of the tube, and as was indicated earlier the agreement between the experimental and numerical investigations is excellent. The problem of heat conduction in the wall can be overcome by including a wall solution domain, in which heat can be con-

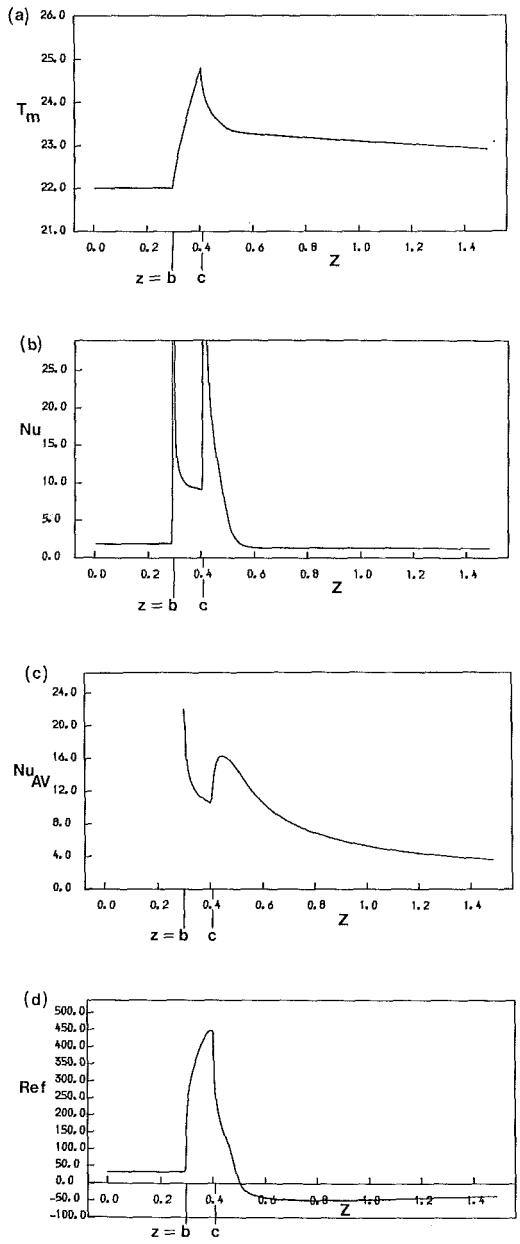


**Fig. 6 Case (II): (*a*) bulk temperature, (*b*) local Nusselt number, (*c*) average Nusselt number, (*d*) friction factor times Reynolds number, all plotted against axial distance**

ducted in the axial direction, in the numerical model; this however is beyond the scope of the present investigation. The vorticity and temperature contours for situation (II) are presented in Figs. 5(*b*) and 5(*c*), the vorticity contours being numbered exactly as in case (I) and the temperature contours in this case being for values of $\theta$ in the set {0.2, 0.4, 0.6, 0.8, 0.9, 0.95}. Again the penetration of heat from the heated section can be seen from Fig. 5(*c*) to be fairly insubstantial.

A plot of bulk temperature against axial distance for case (II) is displayed in Fig. 6(*a*). In this situation the bulk temperature rises relatively steeply as the fluid enters the heated section of the tube before falling rather more gradually back toward its original value. This steep rise is due to the fact that all of the incoming fluid is forced to move close to the wall of the tube by the recirculation region, thus making the heat transfer process more efficient. The plots illustrated in Figs. 6(*b*) and 6(*c*) show local Nusselt number and average Nusselt number against axial distance. Figure 6(*b*) illustrates extremely well the expected singularities in the local Nusselt number at $Z = 0.3$ and $Z = 0.41$, and although beyond $Z = 0.5$ the local Nusselt number appears to settle down to a constant value below the expected value of 1.83 it does in fact approach this value for large $Z$. In Fig. 6(*c*) $\mathrm{Nu}_{\mathrm{AV}}$ starts with a relatively large value at $Z = 0.3$ before falling and then rising again at $Z = 0.41$ and as $Z$ becomes large $\mathrm{Nu}_{\mathrm{AV}}$ falls toward its fully developed value of 1.83. Figure 6(*d*) illustrates a plot of Re*f* against axial distance for case (II). There is a very sharp peak in this profile corresponding to the beginning of the reverse flow region at the center of the pipe and the profile becomes negative at about $Z = 0.5$, which is the point at which separation from the wall occurs. Although development of the flow profile is very slow for $Z > 0.5$ the value of Re*f* approaches its asymptotic value of 32 as $Z$ becomes large.

It should be noted that the formulation presented in this paper is valid for all values of the Reynolds and Peclet numbers. However in the two cases discussed in detail the Peclet number is large enough that the axial heat conduction term in the energy equation may safely be neglected, but the Reynolds number is not sufficiently large for the axial conduction term in the vorticity equation to be ignored. Thus the problem is elliptic with respect to the vorticity; there is therefore no advantage to be gained in neglecting the axial heat conduction term and it is therefore retained.

## 5 Conclusion

New numerical and experimental results are presented for situations in combined convection flows that include substantial regions of reverse flow. In situations of upflow heated sections produce flow reversals near the center of the pipe and cold sections produce reverse flows adjacent to the wall of the pipe. Results are presented from the numerical investigation for stream function, vorticity, and temperature distributions and plots of bulk temperature, Nusselt number, average Nusselt number, and friction factor times Reynolds number against axial distance are displayed. The comparison between the streamline patterns from the numerical model and the observed patterns from experiments is remarkably good.

In the future it is intended to modify the numerical model to include axial conduction in the wall of the tube in order to assess the length to which axial conduction causes a significant change in the wall temperature. It is also hoped to increase the speed of the solution procedure by using multigrid techniques in the solution of the finite difference equations. The use of multigrids would also allow a wider range of problems to be considered. Another improvement to the techniques used in this paper would be the accommodation of variations in the physical properties such as $\alpha$, $\nu$, and $\beta$. Even over the small range of temperatures considered in this paper the above quantities could change fairly substantially. Using these modifications it will be possible to produce a much more comprehensive model of the various experimental situations.

## Acknowledgments

D. J. Keen thanks the SERC for providing a research studentship for the duration of his studies.

## References

Chow, L. C., Husain, S. R., and Campo, A., 1984, "Effects of Free Convection and Axial Conduction on Forced Convection Heat Transfer Inside a Vertical Channel at Low Peclet Number," ASME JOURNAL OF HEAT TRANSFER, Vol. 106, pp. 297–303.

Collins, M. W., 1975, "Viscous Dissipation Effects on Developing Laminar Flow in Adiabatic and Heated Tubes," *Proceedings of the Institution of Mechanical Engineers*, Vol. 189, pp. 129–137.

Collins, M. W., 1980, "Finite Difference Analysis for Developing Laminar Flow in Circular Tubes Applied to Forced and Combined Convection," *International Journal for Numerical Methods in Engineering*, Vol. 15, pp. 381–404.

Özişik, M. N., 1985, *Heat Transfer, A Basic Approach*, McGraw-Hill, New York.

Raznjevic, K., 1976, *Handbook of Thermodynamic Tables and Charts*, McGraw-Hill, New York.

Shah, R. K., and London, A. L., 1975, *Advances in Heat Transfer, Supplement 1, Laminar Flow Forced Convection in Ducts*, Academic Press, London.

Zeldin, B., and Schmidt, F. W., 1972, "Developing Flow With Combined Forced-Free Convection in an Isothermal Vertical Tube," ASME JOURNAL OF HEAT TRANSFER, Vol. 94, pp. 211–223.

A. S. Lavine

M. Y. Kim

C. N. Shores

Mechanical, Aerospace and
Nuclear Engineering Department,
University of California,
Los Angeles, CA 90024-1597

# Flow Reversal in Opposing Mixed Convection Flow in Inclined Pipes

*An experimental investigation of opposing mixed convection in an inclined pipe has been conducted. Dye injection reveals the existence of flow reversal regions. There is an optimal tilt angle that yields maximum flow reversal length. Flow reversals are seen to cause early transition to turbulence. Temperature profiles are measured across the tube cross section near the entrance to the heated section, and show the effect of tube inclination. Temperature measurements exhibit periodic behavior in the flow reversal region under some conditions, generally characterized by low tilt angle and moderate to high Reynolds and Grashof numbers. Flow visualization indicates that this periodic behavior is due to the intermittent breakdown of the flow reversal region.*

## Introduction

Many situations arise in heat transfer applications in which both forced and free convection play a role in determining the velocity and temperature fields. Free convection can act with the forced flow or in opposition to it. This paper concerns mixed convection in an inclined tube, with buoyancy (free convection) opposing the forced flow. The experimental apparatus is shown in Fig. 1. Water flows downward through the inclined tube and enters a constant wall temperature heating section. Heated fluid rises toward the upper tube wall, and may flow upstream in a "flow reversal." The general pattern of a flow reversal for the case of a low tilt angle (close to horizontal) is shown in Fig. 2. For large tilt angles, the flow reversal becomes distributed around a greater portion of the tube periphery. Flow reversals are significant because they affect wall shear stress, heat transfer, occurrence of temperature extremes, and stability of the flow. Applications in which flow reversal could occur include the transport of heated or cooled fluids, heat exchangers, solar water heaters, and thermosyphons.

Several previous studies have been performed on related subjects. Turbulent flow in vertical tubes with opposing buoyancy has been studied experimentally by Eckert and Diaguila (1954), Brown and Gauvin (1965), and Herbert and Sterns (1972). The Nusselt number was found to be greater than for turbulent forced convection. Hanratty et al. (1958), Scheele et al. (1960), and Scheele and Hanratty (1962, 1963) performed an extensive evaluation of the effect of natural convection upon the stability of flow at low Reynolds number in vertical tubes. Flow reversal was observed experimentally and was believed to result in sudden transition to turbulence due to flow separation.

Flow through inclined ducts with buoyancy aiding the flow has been studied by several researchers, but the opposing case has barely been addressed. Bohne and Obermeier (1986) performed an experimental investigation of aiding and opposing mixed convection in an inclined cylindrical annulus. Lavine (1987, 1988) analyzed fully developed flow between inclined parallel plates for both the aiding and opposing cases.

To summarize, work has been done on flow through vertical tubes with the buoyancy opposing the main flow, and has been seen to yield gains in heat transfer due in part to flow reversal. Aiding flows in inclined ducts, where no reversal occurs at the wall, have also been examined. Very little work has been done on opposing mixed convection in inclined tubes. This paper addresses this topic by examining the influence of tilt angle, Grashof number, and Reynolds number upon the temperature field, the occurrence of flow reversals, early transition to turbulence, and the occurrence of periodic behavior. This paper gives selected portions of the more detailed results reported by Shores (1986) and Kim (1986).

## Apparatus

The test section (Fig. 1) is a 3.66-m-long polycarbonate tube with i.d. = 0.0381 m, o.d. = 0.0445 m, and thermal conductivity of 0.019 W/m-K. Cold water is supplied from the main water line. The flow is downward in the present experiments. Surrounding the test section is a plexiglass jacket divided into two compartments, the hot water jacket (downstream half), and the cold water jacket (upstream half), each 1.52 m long. The test section and jacket assembly is mounted on a pivot, and a winch is used to raise or lower the upstream end of the test section, to vary the tilt angle. A pump circulates water between a water heater and the hot water jacket. The cold water jacket is an open-loop system with cold water supplied from the main water line. For the present experiments, the water temperature is the same for both cold water jacket and test

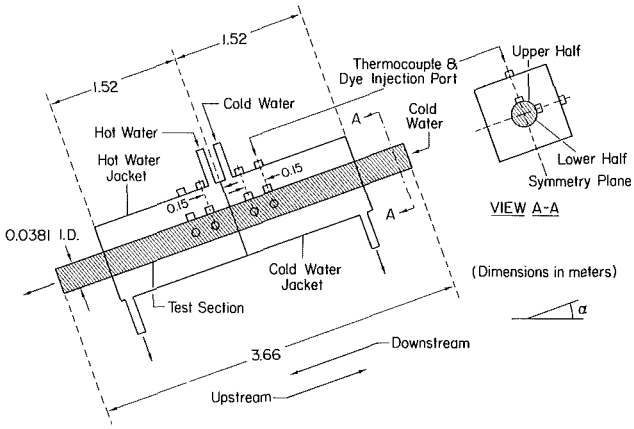


**Fig. 1 Experimental apparatus**

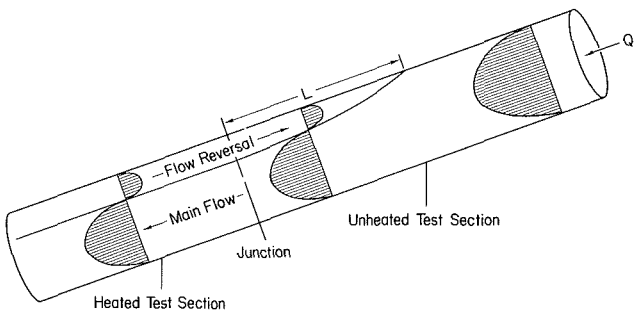


**Fig. 2 Sketch of flow reversal**

Contributed by the Heat Transfer Division for publication in the JOURNAL OF HEAT TRANSFER. Manuscript received by the Heat Transfer Division September 21, 1987. Keywords: Mixed Convection, Natural Convection.

section inlet. In each half of the test section (heated and unheated), an approximately constant-wall-temperature boundary condition is provided at the outer wall of the polycarbonate tube.

Dye is injected using hypodermic needles 0.15 m long with 0.79 mm o.d.; the thermocouples are type-T probes with the same dimensions. There are eight ports for dye injection and temperature measurement, four in the heated section and four in the unheated section (see Fig. 1). The probes or hypodermic needles are inserted through these ports and can traverse the tube cross section.

Figure 1 also illustrates the meanings of the terms "symmetry plane," "upper" and "lower" halves, and "downstream" and "upstream" directions.

## Independent Parameters

Independent system variables to be considered are flow rate, tilt angle, and water temperature of the hot water jacket. The flow rate through the test section is represented by $\mathrm{Re} = 4Q/\pi D\nu$. For the current experiments, Reynolds numbers between 100 and 3500 were used. The tilt angle $\alpha$ is defined as the angle between a horizontal plane and the test section axis, and was varied from 0 to 80 deg. Since the Grashof number based on local wall-to-bulk temperature difference would vary throughout the test section, a characteristic Grashof number (Gr) is defined. The difference between the hot water jacket temperature and the test section inlet water temperature is used. Characteristic Grashof numbers between $1.0\times10^6$ and $7.0\times10^6$ were obtained. It should be noted that for the polycarbonate tube, the temperature difference across the tube wall was quite large. Therefore, a Grashof number based on the temperature difference between the inner wall and test section inlet fluid would be substantially smaller (about an order of magnitude less) than the characteristic Grashof number defined above. All fluid properties were evaluated at 22°C because it represented a reasonable average temperature in the region where temperature measurements were made.

## Experimental Procedures

For a given hot water temperature, the experiment was run for at least an hour to achieve thermal equilibrium. To maintain steady-state flow after a change in flow rate or tilt angle, at least 15 min were allowed to elapse before any measurement was made.

**Flow Reversals.** Dye injection using red dye was an effective method to visualize the flow reversals. In general, flow reversals started from downstream at the end of the heated test section and extended to some upstream location that depended on various flow parameters. Figure 2 shows the general reversal pattern for the case of a low tilt angle. When the reversal extended as far upstream as the port locations or beyond, dye could be injected directly into the flow reversal region. The dye would then follow the reversed flow, and clearly mark the extent of the flow reversal region. If the flow reversal did not extend as far upstream as the port locations, a different visualization method was used. Dye was injected at a high flow rate for a few seconds to flood the flow field; then, water flowing through the test section purged the dye from the main flow, while dye remained in the flow reversal region for a longer period of time. The resulting dye pattern marked the reversal region. See Fig. 3 for an example of this method.

The junction where hot and cold jackets are joined is defined as an origin. The axial distance between the upstream end of the flow reversal and the junction (normalized by the tube diameter) is termed the flow reversal length $L^*$ (see Fig. 2). Positive values correspond to flow reversals that penetrated into the unheated test section, while negative values indicate that the extent of reversal is confined to the heated test section. The repeatability of the length measurements is about $\pm 2.7$ diameters.

A qualitative indication of the velocity profile in the symmetry plane could be obtained as follows. A hypodermic needle was inserted downward through a port such that its tip touched the tube wall opposite the port. It was then quickly pulled up while injecting dye. An example is shown in Fig. 4; flow is clearly to the left in the lower region (main flow), and to the right in the upper region (reversed flow).

**Flow Regimes.** Dye injection was also used to determine the flow regime, i.e., laminar, unstable, or turbulent. To determine the flow regime of the main flow, dye was injected at the tube centerline in the heated portion of the test section. The flow was considered laminar if the injected dye formed a straight filament, with little mixing. If the dye filament became wavy, the flow would be termed unstable. Turbulent flow was characterized by extensive mixing and eddy motion, resulting in rapid diffusion of injected dye. Similarly, the flow regime of the reversed flow could be independently determined by injecting dye into the flow reversal region.

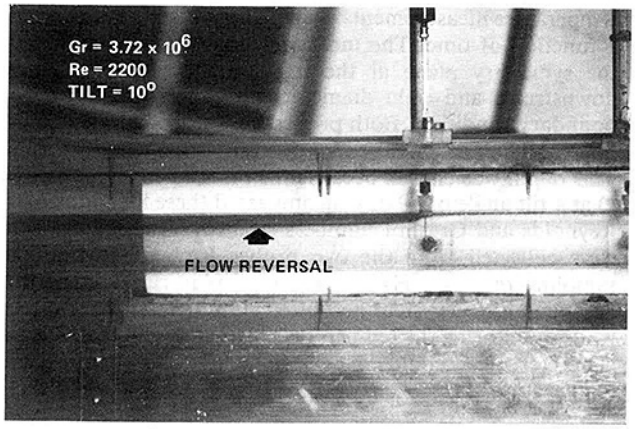


Fig. 3 Photograph of flow reversal region

## Nomenclature

$D$ = tube inside diameter
$g$ = gravitational acceleration
Gr = Grashof number $= g\beta(T_{HJ}-T_i)D^3/\nu^2$
$L$ = flow reversal length
$L^*$ = $L/D$
$p$ = fluid pressure
$Q$ = volumetric flow rate
Re = Reynolds number $= 4Q/\pi D\nu$
$T$ = temperature
$T_{HJ}$ = hot water jacket temperature
$T_i$ = test section inlet water temperature or cold water jacket temperature
$X$ = axial coordinate starting at the junction where boundary condition changes
$Y$ = transverse coordinate, measured along the pipe diameter which is vertical when the pipe is horizontal
$Y^*$ = $Y/(D/2)$
$\alpha$ = tilt angle, angle between tube axis and horizontal plane
$\beta$ = volumetric thermal expansion coefficient
$\theta$ = $(T-T_i)/(T_{HJ}-T_i)$
$\nu$ = kinematic viscosity
$\rho$ = fluid density

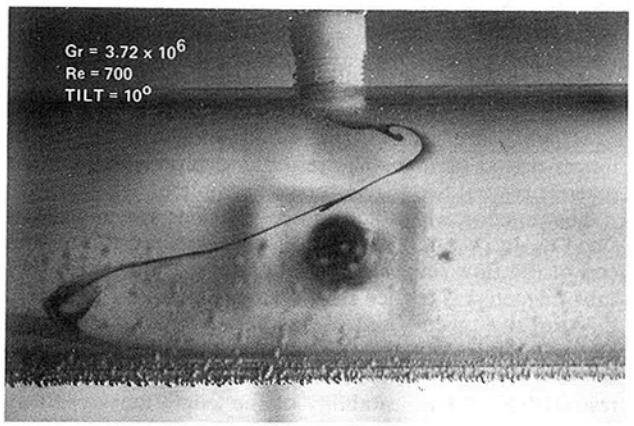


Fig. 4 Photograph of velocity profile

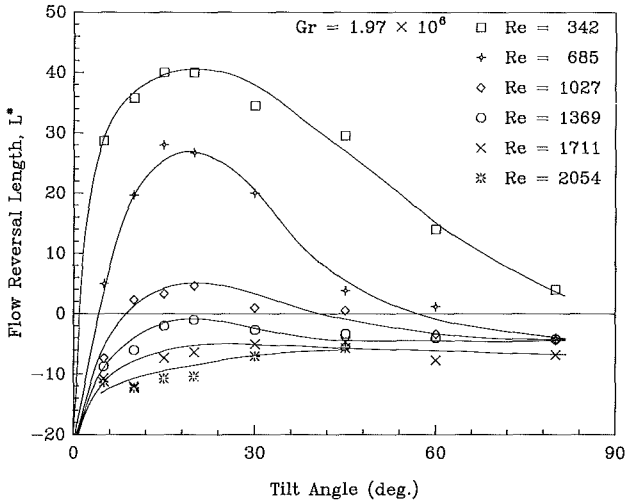


Fig. 5 Flow reversal length versus tilt angle for $Gr = 1.97 \times 10^6$

**Temperature Profiles.** Temperature measurements were made across the tube diameter at a location three diameters downstream from the change in thermal boundary condition. A thermocouple was inserted in the port located four diameters downstream of the change in boundary condition. The probe was then bent to form an **L** with respect to the wall so that the leads from the thermocouple junction would lie approximately in a single isotherm, thus minimizing conduction errors in temperature readings. The probe was then traversed from the lower to the upper tube wall through the symmetry plane (see view *A-A*, Fig. 1). At any particular radial location 300 sample points were collected at a rate of 1 Hz, and were then analyzed for the sample mean and standard deviation. Several tests under similar conditions were conducted using the above technique, and were seen to yield good repeatability.

**Temporal Characteristics.** At a tilt angle of 10 deg, dye injection in the reversal region revealed the existence of a periodic flow, for some combinations of Re and Gr. For this reason, a series of experiments was conducted in which temperature measurements were made in the reversal region as a function of time. Thermocouple probes were positioned in the symmetry plane at the injection ports four diameters downstream and eight diameters upstream of the change in boundary condition. Both probes were placed at $Y^* = 0.67$ (in the upper half of the tube, 2/3 of a radius from the centerline). This depth was chosen because the reversal envelope (see Fig. 2) at a tilt angle of 10 deg encompassed these locations for the Reynolds and Grashof numbers studied. Temperature values were collected from the two probes for half an hour at a sampling rate of 1 Hz. Real-time display capabilities of the data acquisition system permitted simultaneous dye injection while monitoring the temperature history. In this fashion flow characteristics could be correlated with variation in temperature.

## Discussion of Results

**Flow Reversals.** Flow reversals were found to occur over some part of the test section for all experimental cases investigated, except for the zero tilt angle case. As mentioned earlier, all flow reversals originated at the downstream end of the heated test section. (It is anticipated that if the tube were long enough, the flow reversal would terminate at some downstream location, since the cross-sectional temperature variation in the fluid diminishes for a constant wall temperature boundary condition). The distance to which the flow reversal extends upstream is a function of Re, Gr, and $\alpha$.

Before the flow reversal length results are presented, it is helpful to consider the mechanisms that contribute to flow reversals. Since flow reversals are caused by buoyancy effects, they would of course be expected to be enhanced by large Grashof and small Reynolds numbers. Next, consider the effect of tilt angle on flow reversals. The axial flow is driven by the combined effect of the axial pressure gradient and the axial body force, $-\partial p/\partial X + \rho g \sin \alpha$. This quantity must be locally positive over that portion of the cross section where the axial velocity is positive, and locally negative where the flow reverses. Thus, for flow reversal to occur, either $\partial p/\partial X$ or $\rho$ (or both) must vary over the cross section. Now, the larger the cross-stream component of gravity, $g \cos \alpha$, the greater will be the cross-sectional variations of $\partial p/\partial X$ and $\rho$ (as explained in the next paragraph). However, the larger the *axial* component of gravity, $g \sin \alpha$, the more effect a variation in $\rho$ has on the quantity $-\partial p/\partial X + \rho g \sin \alpha$. Thus the potential for flow reversal is affected by tilt angle in two competing ways. Small tilt angles promote large cross-sectional variations in $\partial p/\partial X$ and $\rho$, and large tilt angles magnify the effect of variations in $\rho$. It will be seen that this leads to the existence of an optimal tilt angle for which flow reversals are longest.

The fact that a cross-stream component of gravity gives rise to cross-sectional variations in $\partial P/\partial X$ and $\rho$ can most easily be demonstrated by considering a tube near horizontal. The cross-stream component of gravity causes a cross-stream pressure variation with pressure lower in the upper region of the tube. This cross-stream pressure variation decreases as the flow proceeds downstream and the fluid gets hotter and less dense. This in turn causes the axial pressure gradient to be less negative (or even to become positive) in the upper region of the tube cross section. Thus, as stated in the previous paragraph, the cross-stream component of gravity gives rise to a cross-sectional variation in $\partial p/\partial X$. Furthermore, since $\partial P/\partial X$ is less negative in the upper region of the cross section, the axial velocity will be lower in the upper region. If the fluid moves more slowly in the upper region, it will be hotter, having been in contact with the heated wall for a longer time. Thus, the density $\rho$ also varies over the cross section. There is an additional reason why the fluid will be hotter and less dense in the upper region of the tube. When the tube is near horizontal, it is well known that a secondary motion arises. The heated fluid near the wall rises upward along the wall to the upper region of the tube and the cooler fluid in the core moves downward toward the lower region of the tube. Thus, it has been seen that the cross-stream component of gravity, $g \cos \alpha$, gives rise to cross-stream variations in both the axial pressure gradient and the density, for a variety of reasons.

Flow reversal length is now presented in Fig. 5 as a function of tilt angle, with Re as a parameter. The figure is for $Gr = 1.97 \times 10^6$, but is representative of the results for other Grashof numbers. Recall that for a zero tilt angle, there was

no flow reversal; therefore, the flow reversal length, as defined, would be $-\infty$. As expected, the figure shows that reversal length is a decreasing function of Re. While the data are not shown here, it has also been seen that flow reversal length increases with Gr. The figure clearly shows that there is some "optimal" tilt angle for which flow reversal length is maximum, as was just discussed. Another factor that may contribute to the decreasing flow reversal length for higher tilt angles is that the flow was found to be more turbulent at the higher tilt angles, based on flow visualization. Turbulent mixing tends to make both the temperature and velocity more uniform over the cross section, thereby reducing the tendency for flow reversals.

Flow reversal length is shown as a function of $Gr/Re^2$ in Fig. 6 for various tilt angles. Other variations on the independent parameter, of the form of $Gr/Re^n$, did not appear to collapse the data any better. Note that the use of $\sin\alpha$ or $\cos\alpha$ multiplying either the independent or dependent parameters cannot be expected to remove the dependence on tilt angle, since this dependence is nonmonotonic. For tilt angles of 10 and 80 deg, the parameter $Gr/Re^2$ accounts for most of the variation, although for 45 deg, there is significant spread in the data. Unfortunately, due to the small Grashof number range investigated, it is unrealistic to conclude from this figure that flow reversal length does or does not depend on $Gr/Re^2$ and $\alpha$, as opposed to Gr, Re, and $\alpha$ separately. (Of course, even if $L^*$ does depend on $Gr/Re^2$, other aspects of the flow can, and do, depend on Gr and Re independently).

**Flow Regimes of the Main Flow.** Dye injection was used to determine whether the main flow was laminar, unstable, or turbulent. These experiments were carried out over a Reynolds number range from about 300 to 3000, for four Grashof numbers, $Gr = 1.97\times10^6$, $3.72\times10^6$, $5.12\times10^6$, and $6.64\times10^6$. The results are indicated in Figs. 7 through 9 for three different tilt angles, 10, 45, and 80 deg. Each experimental case is represented by a letter *L*, *U*, or *T*, depending on whether the main flow was found to be laminar, unstable, or turbulent. The curves were drawn in to separate the various regions in an approximate way. The results shown in these figures will be compared to a base case for which the tilt angle is zero degrees and the Grashof number is zero. For this base case, there is of course no flow reversal. The flow is found to be laminar for Re less than 1600, unstable in the range Re = 1600 to 2400, and turbulent for Re greater than 2400.

For $\alpha = 10$ deg (Fig. 7), early transition is observed at low Re for the two higher Grashof numbers ($Gr = 5.12\times10^6$ and $6.64\times10^6$). As Re is increased at these Grashof numbers, the flow becomes laminar once again. As Re is increased still further, the transitions to an unstable and then a turbulent flow regime occur at about the same Reynolds numbers as for the base case. No early transition is seen at the two lower Grashof numbers ($Gr = 3.72\times10^6$ and $1.97\times10^6$). (As mentioned

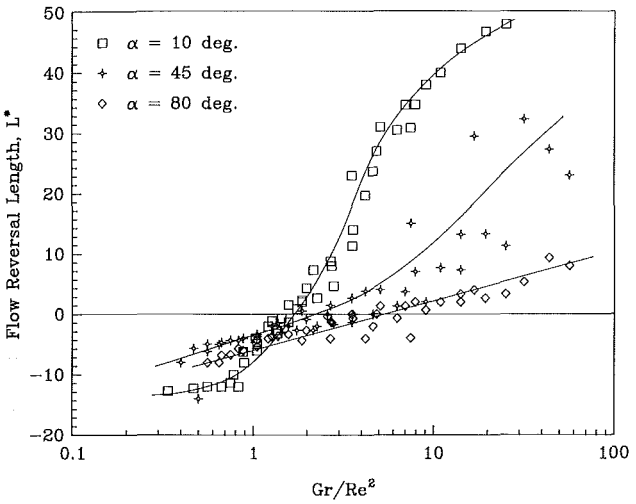


Fig. 6 Flow reversal length versus $Gr/Re^2$

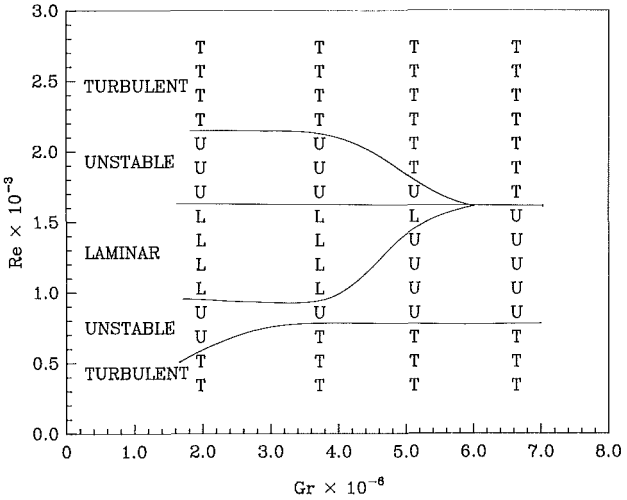


Fig. 8 Flow regimes, $\alpha = 45$ deg

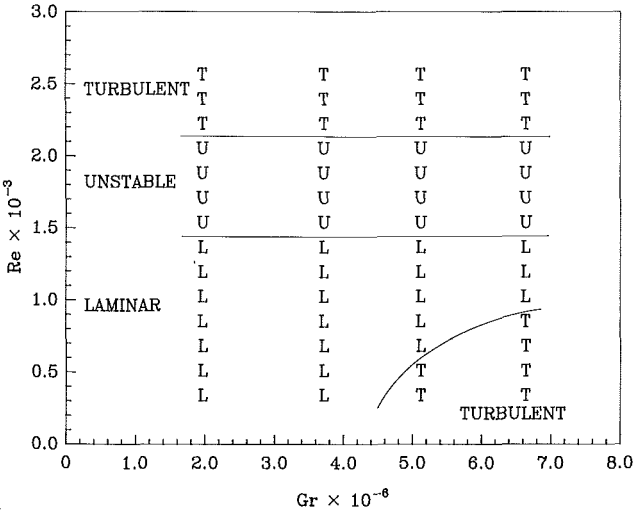


Fig. 7 Flow regimes, $\alpha = 10$ deg

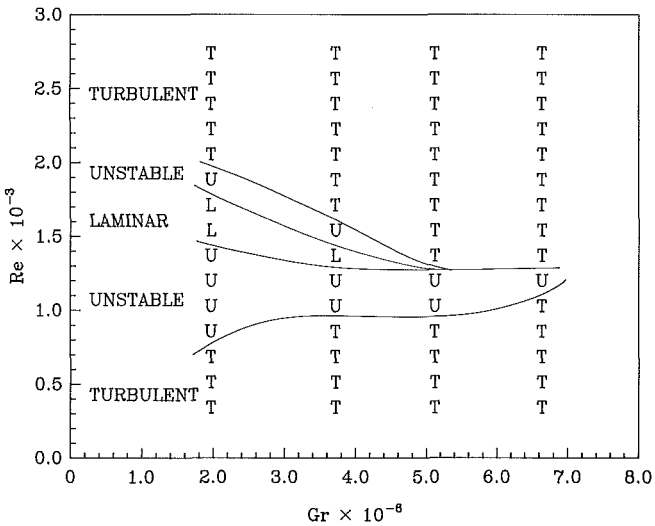


Fir. 9 Flow regimes, $\alpha = 80$ deg

previously, the flow exhibits periodic behavior for some combinations of Re and Gr at a 10 deg tilt angle. The flow regimes given in Fig. 7 are the predominant flow regimes. Even for experimental cases labeled as laminar or unstable, turbulence would sometimes sweep through the flow. This will be discussed in more detail in a later section).

For $\alpha = 45$ deg (Fig. 8), early transition is observed for all four Grashof numbers. At the two lower Grashof numbers, the flow is turbulent for Re below about 700, and unstable for Re between 700 and 900. As Re is increased at these lower Grashof numbers, the transition to unstable and turbulent regimes is much like the base case. For the two higher Grashof numbers, the flow is again turbulent for Re below about 700; as Re is increased the flow becomes unstable, but does not become laminar again. Turbulence sets in once again at a slightly decreased Reynolds number as compared to the base case.

For $\alpha = 80$ deg (Fig. 9), the extent of the laminar and unstable regimes is diminished. Laminar flow exists only in a small Reynolds number range for the two lower Grashof numbers.

In summary, at low tilt angles, early transition to turbulence occurs for high Gr and low Re. As the tilt angle increases, the early transition extends to lower Gr and higher Re.

**The Mechanism of Early Transition to Turbulence.** At the upstream tip of the flow reversal region, the main flow separates from the wall to flow around the reversal region; hence the upstream tip of the flow reversal is a separation point. The interface between the main and reversed flow regions, which has zero axial velocity, will be termed the "shear interface." Early transition to turbulence is believed to be related to separation at the tip of the flow reversal region and the instability of the shear interface separating the main and reversed flows. Dye injection revealed that, for low and moderate Reynolds numbers, vortical motion is generated at the interface between the main and reversed flows near the separation point, and propagates downstream. (For Reynolds number above about 1700, the flow reversal is confined to a narrow region near the wall, and vortical motion near the separation point becomes increasingly difficult to detect). When vortical motion occurs, it may decay or grow, depending on the values of Re, Gr, and $\alpha$. If vortical motion decays, the shear interface downstream remains intact and stable, and the main and reversed flow regions remain laminar. On the other hand, early transition to turbulence is associated with amplified vortical motion, which destroys the shear interface as it propagates downstream; in the process, turbulence occurs throughout the test section.

Recall that Hanratty et al. (1958), Scheele et al. (1960), and Scheele and Hanratty (1962, 1963) found that opposing mixed convection in vertical tubes caused transition to turbulence at low Reynolds numbers. They suggested that the transition was caused by separation of the flow due to flow reversals. The current experiments support the hypothesis that early transition is related to separation; however, the mere presence of separation does not guarantee that the flow will become turbulent. Recall that all flows discussed here do exhibit flow reversal, but not all of them are turbulent.

**Flow Regimes of the Reversed Flow.** Dye injection revealed that when early transition to turbulence occurs in the main flow, the reversed flow becomes turbulent as well. This makes sense in light of the fact that early transition appears to be caused by amplified vortical motion, which destroys the interface between the main and reversed flows. However, when the main flow becomes turbulent at higher Reynolds numbers (on the order of 2000), the reversed flow can be unstable, or even laminar. Turbulence of the main flow at higher Reynolds numbers is not due to flow reversal, but to the usual amplification of flow disturbances. At higher Reynolds numbers, the reversed flow is confined to a narrow region near the wall, and probably has a lower velocity than the main flow. Thus, an effective Reynolds number for the reversed flow would be less than for the main flow. This probably accounts for the fact that the reversed flow can be more stable than the main flow at these higher Reynolds numbers.

**Temperature Profiles.** Temperature profiles in the symmetry plane were measured three diameters downstream of the change in thermal boundary condition. The time-averaged nondimensional temperature ($\bar{\theta}$) and the standard deviation of $\theta$ are presented in Figs. 10 and 11 for a representative case with a Grashof number of $6.64 \times 10^6$ and a Reynolds number of 409. The ordinate represents the nondimensional displacement from the tube centerline in the symmetry plane. Positive $Y^*$ corresponds to the "upper" half of the tube, negative $Y^*$ to the "lower" half. Data are presented for tilt angles of 0, 10, 45, and 80 deg. For the horizontal case ($\alpha = 0$ deg) the temperature is much hotter at the upper wall ($Y^* = 1$) than at the lower wall, due to the mechanisms described earlier. (As noted previously, the inner wall temperature differs substantially from the hot water jacket temperature. Therefore, $\bar{\theta}$ is not necessarily close to 1 at the wall). For this horizontal case, flow visualization revealed a laminar flow. Standard deviation may be interpreted as an indicator of the degree of fluctuation in the flow and is seen to be low and uniform for this tilt angle

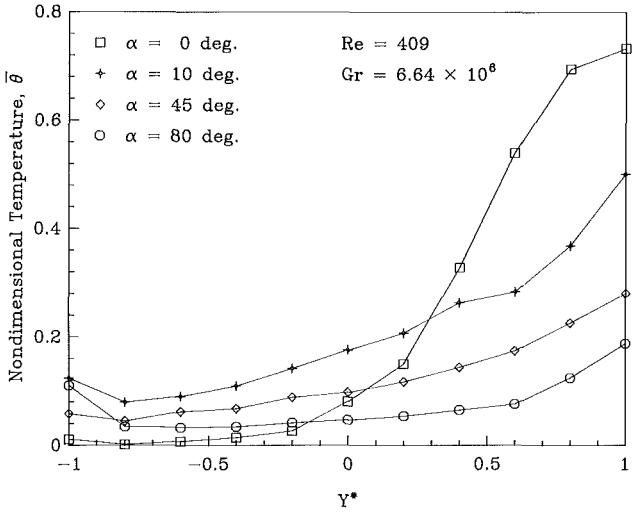


**Fig. 10 Nondimensional temperature profile, Re = 409, Gr = 6.64 x $10^6$**

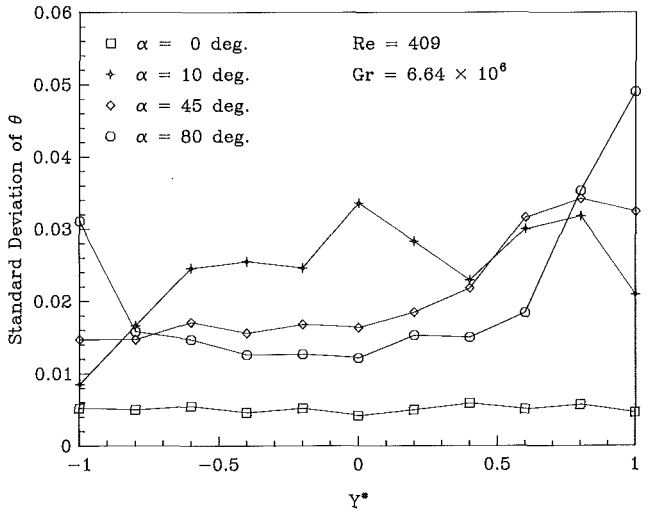


**Fig. 11 Standard deviation of nondimensional temperature, Re = 409, Gr = 6.64 x $10^6$**

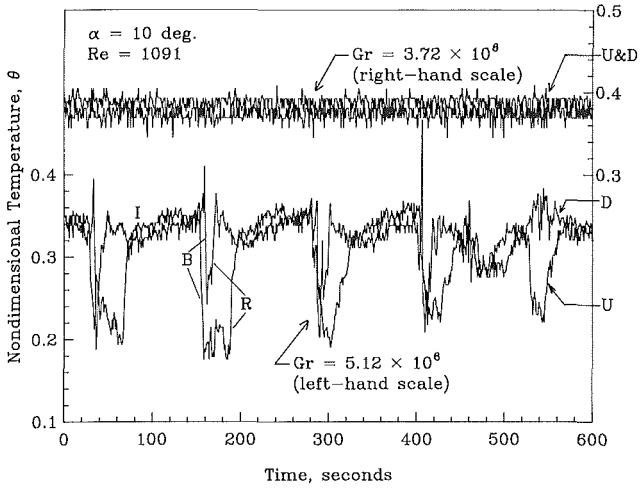


**Fig. 12 Nondimensional temperature versus time**

(see Fig. 11). As the tilt angle increases, the temperature profile becomes more symmetric, due to the diminishing cross-stream component of gravity. As discussed previously, the higher tilt angle cases were found to be more turbulent. An indication of this can be seen in the standard deviations, which are higher than for the horizontal case. This increased turbulence may also contribute to the more uniform temperature distributions for the nonhorizontal cases. At a tilt angle of 10 deg, strong flow reversals were observed. Vortex motion was present at the interface of the reversal and main flow regions, as described above. This explains the presence of a maximum in the standard deviation near the centerline. For the 80 deg case, a weak flow reversal was present and was distributed around the complete tube periphery. The instability associated with flow reversal may account for the large rise in standard deviation near the wall.

**Temporal Characteristics of the Flow Reversal Region.** As previously mentioned, dye injection revealed the existence of periodic behavior in the flow reversal region at a tilt angle of 10 deg. Therefore a series of experiments was conducted to obtain an understanding of the time-dependent characteristics of the flow reversal. These experiments are reported in detail in Shores (1986). In general, periodic conditions were found to occur for low tilt angles (10 and 30 deg). They were not present at the lowest Reynolds and Grashof numbers, but appeared as either Re or Gr was increased. For instance, at a tilt angle of 10 deg, for $Re = 409$, the flow was not periodic for any value of Gr studied. For $Re = 750$, the flow was not periodic for $Gr = 3.72 \times 10^6$ or $5.12 \times 10^6$, but was periodic for $Gr = 6.64 \times 10^6$. For $Re = 1091$, the flow was not periodic for $Gr = 3.72 \times 10^6$, but was for $Gr = 5.12 \times 10^6$ and $6.64 \times 10^6$. Only two selected cases will be presented here. These two cases are for $Re = 1091$, $\alpha = 10$ deg, and two different Grashof numbers, $Gr = 3.72 \times 10^6$ and $5.12 \times 10^6$.

As explained in the experimental procedures section, thermocouple probes were inserted both upstream and downstream of the change in boundary condition. For the two cases presented here, the flow reversal region encompassed both probes. In Fig. 12 the nondimensional temperature is plotted as a function of time for the last 10 min of both 30 min runs. Note that the left and right-hand scales apply to the higher and lower Grashof number cases, respectively. Both the upstream and downstream probe traces (denoted "*U*" and "*D*," respectively) are included.

For the lower Grashof number case (upper curve), the overlap between the two traces indicates that the fluid temperatures are nearly equal, even though the upstream probe is located within the unheated section. This result is due solely to the transport of heated fluid upstream by the flow reversal.

For the higher Grashof number (lower curve), the flow appears periodic. To confirm this observation, the Fourier spectrum of the last 1024 data points was generated using a Fast Fourier Transform algorithm. A distinct spike appeared in the Fourier spectrum for both the upstream and downstream probe traces for this case, corresponding to a characteristic period of 128 seconds for both locations. This period agrees well with a visual inspection of the traces.

Dye injection was used to observe the periodic nature of this flow. The observations parallel the measured temperature variation quite well. Suppose that upon initial dye injection the reversal region can be clearly identified, and there is little mixing between it and the main flow. An "*I*" denotes this point in time in Fig. 12. As time increases, the reversal velocity is observed to increase slowly, along with the fluid temperature. At a distinct point in time the reversal breaks up, as turbulence spreads from the separation point downstream past the two probes. This event is marked by the large drop in temperature seen in the traces when mixing occurs between the reversal and the cool main flow ("*B*"). Since the breakdown of the flow reversal region spreads from upstream to downstream, the drop in temperature is noticed first for the upstream probe. The reversal reforms after a waiting period required for cool fluid at the wall to be heated and rise towards the upper half of the tube. It gradually increases in strength as more fluid is added to it. When the reversal envelope encompasses a probe there is a rapid rise in temperature ("*R*"). It can be seen that this event occurs earlier for the downstream probe since the reformed reversal reaches that location first. The same cycle is then repeated with the characteristic period mentioned earlier.

## Conclusions

This experimental investigation has revealed some interesting features of opposing mixed convection in inclined tubes. Flow reversals were observed for all experimental cases (except for zero tilt angle). The length of the flow reversal region is an increasing function of Gr and a decreasing function of Re. The flow reversal length is also a function of tilt angle, with an optimal tilt angle for which flow reversal length is maximum. The existence of an optimal tilt angle is due to the tradeoff between two effects: Large tilt angles imply a large axial component of gravity, whereas small tilt angles cause large density and pressure variations over the cross section. The optimal tilt angle was generally small (less than 20 deg).

At low tilt angles, early transition to turbulence is observed when the Reynolds number is low and the Grashof number is high. As the tilt angle increases, the early transition extends to lower Grashof numbers and higher Reynolds numbers. It is believed that this early transition is related to flow separation occurring at the upstream end of the flow reversal region, and to the instability of the shear interface between the main and reversed flow regions. Under some conditions, vortical motion near the separation point has been observed to amplify as it propagates downstream along the shear plane; in the process, turbulence occurs throughout the test section. However, the mere presence of separation associated with flow reversal does not guarantee that the flow will become turbulent.

The temperature profiles demonstrate that at low tilt angles, there is a large temperature rise near the upper wall. As $\alpha$ increases, the profile becomes more symmetric. The standard deviation of temperature measurements is larger for cases with flow reversal than for horizontal cases, due to early transition to an unstable or turbulent flow.

Temperature measurements in the flow reversal region exhibited periodic behavior under conditions characterized by

low tilt angle and high Reynolds and Grashof numbers. Concurrent dye injection revealed a distinct cycle in which the reversal would gradually build in strength, and then break down as turbulence swept through it.

The experiments described here have indicated that tube inclination angle can have a strong effect on the occurrence of flow reversals, extreme temperatures, and flow stability. Further experimental and analytical investigation is recommended to gain a better understanding of these phenomena.

## Acknowledgments

The authors would like to thank Harold Kasper and Stanley Chen for their help in construction of the apparatus, and both Stanley Chen and Kai-Choong Leong for their invaluable assistance in the gathering and interpretation of data.

## References

Bohne, D., and Obermeier, E., 1986, "Combined Free and Forced Convection in a Vertical and Inclined Cylindrical Annulus," *Proceedings, 8th International Heat Transfer Conference*, Vol. 3, pp. 1401–1406.

Brown, C. K., and Gauvin, W. H., 1965, "Combined Free and Forced Convection II. Heat Transfer in Opposing Flow," *Canadian Journal of Chemical Engineering*, Vol. 43, pp. 306–318.

Eckert, E. R. G., and Diaguila, A. J., 1954, "Convective Heat Transfer for Mixed, Free, and Forced Flow Through Ducts," *Transactions of ASME*, Vol. 76, pp. 498–504.

Hanratty, T. J., Rosen, E. M., and Kabel, R. L., 1958, "Effect of Heat Transfer on Flow Field at Low Reynolds Number in Vertical Tubes," *Industrial and Engineering Chemistry*, Vol. 50, pp. 815–820.

Herbert, L. S., and Sterns, U. J., 1972, "Heat Transfer in Vertical Tubes—Interaction of Forced and Free Convection," *Chemical Engineering Journal*, Vol. 4, pp. 47–52.

Kim, M. Y., 1986, "Visualization of Flow Reversals in Mixed Convection Flow in an Inclined Tube," M. S. Thesis, University of California, Los Angeles, CA.

Lavine, A. S., 1987, "Analysis of Fully Developed Opposing Mixed Convection Between Inclined Parallel Plates," in: *Mixed Convection Heat Transfer—1987*, ASME HTD-Vol. 84, pp. 29–35.

Lavine, A. S., 1988, "Analysis of Fully Developed Aiding Mixed Convection Between Inclined Parallel Plates," in: *ASME Proceedings of the 1988 National Heat Transfer Conference*, ASME HTD-96, Vol. 2, pp. 87–94.

Scheele, G. F., Rosen, E. M., and Hanratty, T. J., 1960, "Effect of Natural Convection on Transition to Turbulence in Vertical Pipes," *Canadian Journal of Chemical Engineering*, Vol. 38, pp. 67–73.

Scheele, G. F., and Hanratty, T. J., 1962, "Effect of Natural Convection on Stability of Flow in a Vertical Pipe," *Journal of Fluid Mechanics*, Vol. 14, pp. 244–255.

Scheele, G. F., and Hanratty, T. J., 1963, "Effect of Natural Convection Instabilities on Rates of Heat Transfer at Low Reynolds Numbers," *AIChE Journal*, Vol. 9, pp. 183–185.

Shores, C. N., 1986, "Thermal Characteristics of Flow Reversal in Mixed Convection Flow in Inclined Tubes," M. S. Thesis, University of California, Los Angeles, CA.

# An Experimental Study of Transition to Turbulence in Vertical Mixed Convection Flows

**R. Krishnamurthy**
Department of Mechanical Engineering,
The Catholic University of America,
Washington, DC 20064

**B. Gebhart**
Department of Mechanical Engineering
and Applied Mechanics,
University of Pennsylvania,
Philadelphia, PA 19104

*Results are reported from an experimental study of a mixed convection flow, that is, combined forced and natural convection, undergoing transition to turbulence, adjacent to a vertical, uniform-heat-flux surface. Small and aiding forced convection effects were studied. The measurements, in air, were made at pressure levels ranging from 4.4 bars to 8 bars, at flux levels* q″ *in the range 14–1300 W/m². The imposed free-stream velocities* $U_\infty$ *were around 5 cm/s. One objective was to determine any quantitative parameters that would predict the bounds of the transition region. Another was to measure disturbance growth characteristics during transition. Results show that, at a given* $U_\infty$*, the beginning of transition is not correlated by the local Grashof number* $Gr_x^*$ *alone. An additional dependence on both the downstream location and pressure level was found. Thermal and velocity transitions were found to begin when the mixed convection parameter* $\epsilon_M$ *reached a value of 0.18. Transition was found to be complete when the nondimensional convected energy in the boundary region,* $\beta q'' x/5k$*, reached a value of 7.10. These experimental results confirm the prediction of linear stability analysis, that aiding mixed convection stabilizes the flow, compared to pure natural convection flow. The data also support a physical explanation of these mechanisms.*

## 1 Introduction

Mixed convection very commonly arises in the environment and in technological applications. It results from an interaction of a moving ambient medium with a buoyancy driven flow. The two characteristic velocities, $U_\infty$ and $U_c$, may be in the same or opposite directions in a vertical flow. This results in aiding and opposed effects, respectively. Chao et al. (1983) report the role of mixed convection in loss of coolant situations in nuclear reactors. Mixed convection is also of fundamental importance in electronic cooling, as evident from the discussions in Incropera (1986).

For purely buoyancy-driven flows, much is now known of the initial instability, the growth of disturbances, and the transition region; see the recent review by Gebhart and Mahajan (1982). However, very little is known about the transition of mixed convection flows. Analyses of the stability of this flow (Carey and Gebhart, 1983) have shown that in aiding mixed convection, downstream growth of disturbances is less compared to that in pure natural convection. The aiding mixed convection flow is more stable. This stabilization is expected to affect the location of the beginning and end of the transition region. Since both the heat transfer and the shear stress characteristics are very different in laminar and turbulent flows, prediction of the bounds of the transition region is usually a very important matter.

The experiments reported here are with relatively small forced convection effects. Therefore, the sequence of downstream events leading to developed turbulence is expected to be similar to that in purely buoyancy-driven flows. An example of this sequence of transition from a laminar flow to developed turbulence is illustrated in Fig. 1. This example applies to a natural convection flow in water with a surface heat flux of 1000 W/m². The laminar boundary region first becomes unstable to background disturbances at some distance downstream. Initial amplification then follows closely the predictions of linear stability theory. Eventually, nonlinear effects arise. A principal result is the generation of alternate sets of double longitudinal mean flow vortices. These form regions of high shear and increase the growth rate of the disturbances; see Jaluria and Gebhart (1974) and Audunson and Gebhart (1976).

In water, the velocity boundary layer is thicker than the thermal boundary layer. Turbulent bursts first occur in the velocity layer. These then diffuse into the thermal layer. Farther downstream, the measured maximum level of the base-flow velocity grows less rapidly than in a continuing laminar flow. This signals the beginning of velocity transition. Simultaneously, the mean velocity profile also deviates from its laminar form. Farther downstream, the mean temperature profile changes, marking the beginning of thermal transition.

Thereafter, the velocity and thermal boundary layers thicken rapidly. The end of transition is taken as the downstream location beyond which there is no appreciable further change in the local distributions of velocity and temperature intermittency factors, $I_v$ and $I_t$. These are defined as the fraction of the time the flow is locally turbulent, in its velocity and temperature fields, respectively. The end of transition is followed by a regime of spectral development leading toward developed turbulence (Bill and Gebhart, 1979).

In air, the overall mechanisms are largely similar. However, since the thermal and velocity boundary layers are of comparable extent, some differences arise. Both the velocity and thermal transitions occur almost simultaneously. Based on the data in air, reported by Smith (1972), Gebhart and Mahajan (1982) suggest that a well-defined region of spectral development may not exist beyond the end of transition.

Historically, there have been many differences and ambiguities in defining the physical criteria for the downstream bounds of the transition region. The various such criteria in use in buoyancy-induced flows have been reviewed by Gebhart and Mahajan (1982). The following criteria were recommended. The beginning of velocity transition is taken as the location where the downstream growth of $U_{max}$, the measured maximum of the base flow velocity, begins to decrease from the calculated trend in laminar flow. The beginning of thermal transition is similarly defined in terms of $(t_o - t_\infty)$, the temperature difference across the boundary region. The general criterion for the end of transition is the absence of downstream variations in the forms of the intermittency factor

Contributed by the Heat Transfer Division for publication in the JOURNAL OF HEAT TRANSFER. Manuscript received by the Heat Transfer Division October 30, 1987. Keywords: Mixed Convection, Turbulence.

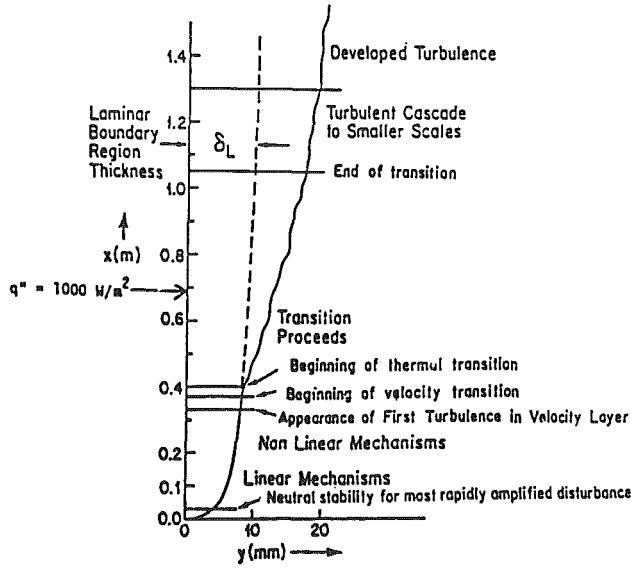


**Fig. 1 Sequence of downstream events during transition in a natural convection flow in water adjacent to a vertical uniform heat flux surface (Gebhart, 1979)**

distributions. However, this latter measure could not be used in this study because the hot-wire and thermocouple probes could not be traversed in the downstream direction. Instead, alternative criteria have been used. This matter is further discussed in Section 3. Next the various studies in the literature related to mixed convection are reviewed.

**Laminar Mixed Convection.** Extensive theoretical analyses of flows adjacent to a vertical surface have appeared. For a vertical uniform heat flux surface, a detailed analysis was given by Wilks (1974). Following the earlier study by Merkin (1969) for isothermal surface conditions, three distinct downstream regions in the flow were recognized. The region near the leading edge is dominated by forced convection mechanisms. The region far downstream of the leading edge is dominated by natural convection. Between these lies a region where the two effects are comparable. The relative importance of the forced and natural convection mechanisms is indicated by $U_\infty/U_c$. This parameter is expressed in terms of $\epsilon_M$ as

$$\epsilon_M = 5U_\infty/U_c = \mathrm{Re}_x/(\mathrm{Gr}_x^*/5)^{2/5} \quad (1)$$

A value of $\epsilon_M \ll 1$ indicates dominance of natural convection and $\epsilon_M \gg 1$ a dominance of forced convection.

There have been two experimental studies of laminar mixed convection adjacent to a vertical uniform flux surface. Babezha et al. (1981) reported measurements of surface heat transfer coefficients over a wide range of $\epsilon_M$, for aiding mixed convection. Carey and Gebhart (1982) measured velocity and temperature fields for $\epsilon_M < 1$, finding agreement between calculations and experiment. Armaly et al. (1987) have reported numerically computed values of local and average Nusselt numbers in laminar mixed convection on flat plates with uniform flux. The configurations considered included horizontal, inclined, and vertical plates. Correlating equations are given for the Nusselt number in all the flow configurations and show good agreement with numerical results.

**Instability.** Mucoglu and Chen (1978) report a linear stability analysis for mixed convection adjacent to a vertical isothermal surface. The results relate to the region near the leading edge, since buoyancy effects were taken to be relatively small. Buoyancy was found to stabilize the flow by inducing a favorable pressure gradient. Carey and Gebhart (1983) studied the stability for the uniform heat flux surface condition. The region far from the leading edge was considered, where the forced convection effects, and therefore $\epsilon_M$, are small. Calculated disturbance growth rates and some supporting experimental measurements were also given. The

## Nomenclature

$a$ = acceleration of a fluid element (equation (19))
$A$ = disturbance amplitude (equation (18))
$B^*$ = nondimensional frequency $= 2\pi f \sqrt{g\beta q''/k}$
$C_1, C_2, C_3$ = constants defined in equations (6), (7), and (15), respectively
$f$ = frequency
$F(f)$ = fraction of total disturbance energy up to a frequency $f$
$g$ = acceleration due to gravity
$\mathrm{Gr}_x^*$ = $g\beta q'' x^4/k\nu^2$
$G^*$ = $5(\mathrm{Gr}_x^*/5)^{1/5}$
$I_v$ = intermittency factor for velocity
$I_t$ = intermittency factor for temperature
$k$ = thermal conductivity
$K$ = wave number
$P$ = pressure
$q''$ = convective heat flux from the surface
$Q(x)$ = mean convected thermal energy in the boundary region
$\mathrm{Re}_x$ = Reynolds number $= U_\infty x/\nu$
$t$ = temperature
$T$ = mean temperature
$u$ = local fluid velocity in the $x$ direction
$U$ = mean fluid velocity in the $x$ direction
$U_c$ = characteristic laminar natural convection velocity $= \nu G^{*2}/5x$
$v$ = local fluid velocity in the $y$ direction
$x$ = distance along the surface from the leading edge
$y$ = distance normal to the surface
$\alpha_i$ = spatial exponential disturbance amplification rate
$\beta$ = coefficient of thermal expansion $= (1/v)(\partial v/\partial t)_p$
$\Gamma$ = strength of a vortex element (equation (19))
$\delta$ = $5x/G^*$
$\epsilon_M$ = laminar mixed convection parameter $= \mathrm{Re}_x/(G^*/5)^2$
$\zeta$ = mean flow vorticity $= -\partial U/\partial y$
$\eta$ = $yG^*/5x$
$\mu$ = dynamic viscosity
$\rho$ = density
$\tau$ = time
$\phi$ = spectral energy density of disturbance

**Subscripts**

BTT = beginning of thermal transition
BVT = beginning of velocity transition
$ET$ = end of transition
$L$ = laminar
max = maximum
$MC$ = mixed convection
$o$ = at the surface
$P$ = at constant pressure
$s$ = selected
$u$ = velocity
$t$ = temperature
$x$ = characteristic length scale
$\infty$ = quantity evaluated at a large distance from the surface

**Superscripts**

$'$ = disturbance quantity

presence of a free stream was found to have a stabilizing effect even at small values of $\epsilon_M$.

**Turbulent Mixed Convection.** Hall and Price (1970) measured the effect of superimposing an aiding upward flow on a turbulent natural convection boundary layer, adjacent to a vertical uniform flux surface. The experiment was in air at atmospheric pressure in a vertical wind tunnel at various levels of free-stream velocity. At low velocities the heat transfer coefficient was less than that for natural convection alone. It did increase, as the free-stream velocity was increased. The minimum heat transfer coefficient arose when the imposed free-stream velocity was about the same as the peak measured velocity for pure natural convection. Some turbulence intensity measurements were also reported. Details of velocity and temperature fields in the boundary region were not reported. No data were given for disturbance growth rates in the transition region. A tentative model was proposed to explain this unexpected behavior. Oosthuizen (1974) reported numerical calculations for the same circumstance, using a mixing length postulate. By choosing the empirical constants in the resulting model suitably, agreement was obtained with the data of Hall and Price (1970). Chen et al. (1987) report an analysis of turbulent mixed convection adjacent to a vertical, isothermal plate. A modified Van Driest mixing length model was used to calculate the eddy diffusivities. A simple correlation for the Nusselt number was given based on numerically obtained values. The predictions based on this correlation are expected to be accurate in the forced-flow dominated regime.

Kitamura and Inagaki (1987) have reported experimental results for aiding turbulent mixed convection flow of water adjacent to a vertical uniform flux surface. Local Nusselt numbers in the combined convection region were found to decrease by as much as 25 percent from those for pure forced and natural convection, corroborating earlier findings of Hall and Price (1970). By employing flow visualization techniques, in addition to sensor measurements, it was established that in the combined convective region the velocity fluctuations are suppressed. This suppression of turbulent fluctuations was shown to result in reduced heat transfer. Three distinct regions in the flow were identified based on a comparison of the experimentally determined values of the Nusselt numbers with those calculated from traditional forced and natural convection correlations. The forced convection regime applies for $\xi$ $(\equiv \mathrm{Gr}_x^*/\mathrm{Nu}_x\mathrm{Re}_x^{2.7}) < 4 \times 10^{-4}$ and the natural convection region for $\xi > 3\times10^{-2}$. The region in between is the true mixed convection region. The onset of turbulence was taken to be marked by fluctuations in the velocity and temperature signals. Spectral characteristics of the turbulent velocity and temperature fields are not discussed.

The experiments of Brown and Gauvin (1966), Khosla et al. (1974), Kenning et al. (1974), and Tanaka et al. (1987) concerned internal, vertical mixed convection flows. The imposed mean flow pressure gradient causes different mechanisms. Townsend (1972) reported measurements for turbulent mixed convection over a horizontal plane surface. Then the effects of thermal instability arise. The study reported here, in vertical flows, concerns instability, which is largely due to the presence of a point of inflection in the velocity profile. This is discussed in detail in Section 4.

This first study of transition in mixed convection adjacent to vertical plane surfaces had several objectives. One was to develop quantitative predictive parameters for the beginning and end of the transition region. The other was to determine the disturbance form and growth, for comparisons with the linear stability predictions in Carey and Gebhart (1983).

Detailed mean velocity and temperature distributions, along with disturbance data, were determined at various levels of pressure $P$ and surface convective heat flux $q''$; see Table 1. The ranges were $P$ = 4.4 to 8 bars and $q''$ = 14 to 1300 W/m$^2$. Higher than atmospheric pressures were used primarily to obtain sufficiently large values of Grashof and Reynolds numbers. The free-stream velocity was constant at about 5 cm/s. Sensor measurements were made at a downstream location of $X$ = 28.4 cm. The apparatus is described next, followed by a presentation and discussion of the results.

**Table 1 Experimental conditions and symbols for the data; $G^*$, $U_c$, and $\epsilon_M$ values for each experiment correspond to $X = 28.4$ cm**

| Expt. No. | P(bars) | $U_\infty$(cm/s) | q"(W/m$^2$) | G* | $U_c$(cm/s) | $\epsilon_M$ | Symbol |
|---|---|---|---|---|---|---|---|
| 1 | 4.4 | 4.8 | 14 | 357 | 31.6 | 0.75 | ✤ |
| 2 | 4.4 | 4.5 | 51 | 445 | 52.1 | 0.43 | ⊞ |
| 3 | 4.4 | 5.2 | 529 | 677 | 130 | 0.18 | ◪ |
| 4 | 4.4 | 4.6 | 712 | 700 | 145 | 0.16 | ■ |
| 5 | 6.1 | 4.3 | 800 | 821 | 142 | 0.15 | ◭ |
| 6 | 6.1 | 4.2 | 904 | 828 | 148 | 0.14 | ◮ |
| 7 | 6.1 | 4.0 | 1010 | 846 | 156 | 0.14 | ◬ |
| 8 | 6.1 | 5.1 | 1136 | 855 | 166 | 0.13 | ▲ |
| 9 | 6.1 | 0 | 782 | 805 | 140 | 0 | △ |
| 10 | 6.8 | 4.7 | 1130 | 898 | 159 | 0.16 | ◓ |
| 11 | 6.8 | 4.5 | 1262 | 913 | 166 | 0.13 | ◒ |
| 12 | 7.9 | 4.0 | 596 | 885 | 122 | 0.17 | ● |
| 13 | 7.9 | 4.2 | 895 | 942 | 142 | 0.15 | ◑ |
| 14 | 7.9 | 5.2 | 1262 | 984 | 194 | 0.13 | ◐ |
| 15 | 7.9 | 0 | 787 | 913 | 135 | 0 | ○ |

## 2 Experiment

Compressed air was filtered for impurities. A regulator held a constant pressure downstream, at levels up to 8 bars, with a maximum fluctuation of ±0.03 bar. A receiver tank downstream damped these fluctuations. The air then entered the test section, a cylindrical pressure vessel 33 cm in diameter and 76 cm high. At the bottom of the test vessel, air expanded from a 1-cm-dia inlet to the 33-cm-dia test section. In order to distribute this flow, and to dampen any large-scale turbulence, a series of baffles was placed just above the inlet. These baffles consisted of a thin plywood surface with holes, followed by a honeycomb structure made of 6-mm-dia straws of 25 mm length. The last elements were two fine meshed wire screens, 62 to a square centimeter. A plywood surface with holes and a similar wire screen were placed below the exit from the test section. The leading edge of the surface was 5 cm above the topmost screen. The surface was located in the middle of the test section with the air flowing over its both sides. The uniformity of the flow was verified by hot-wire transverses, to be within 1 percent of the average free-stream velocity $U_\infty$. The design of the baffle system was based on the recommendations of Loehrke and Nagib (1972).

The test surface consisted of two layers of resin-impregnated fabric, sandwiched between the folds of an Inconel 600 foil, 0.0013 cm thick. Seven Copper Constantan thermocouples were placed between the two layers of the fabric, to measure the downstream surface temperature distribution. The entire assembly was bonded in a press, at high pressure and temperature. The resulting surface assembly was 40 cm high, 15 cm wide, and 0.018 cm thick. The test section is 76 cm high.

The electrical heating circuit consisted of 0–40 A, 0–40 V, regulated d-c power supply, connected in series with the test surface and a 0.01 Ω precision resistor, to measure the current. The voltage drop across the surface was independently measured by a digital voltmeter. These two measurements give the total electrical energy input to the surface. By measurement of the surface temperature distribution, by the embedded copper-constantan thermocouples, the radiation correction for the surface heat flux was obtained. The correction amounted to less than 15 percent of the total electrical energy dissipation in the surface assembly. In this paper $q''$ is taken to be the net convective heat flux from the surface on each side.

Boundary region velocity and temperature distributions

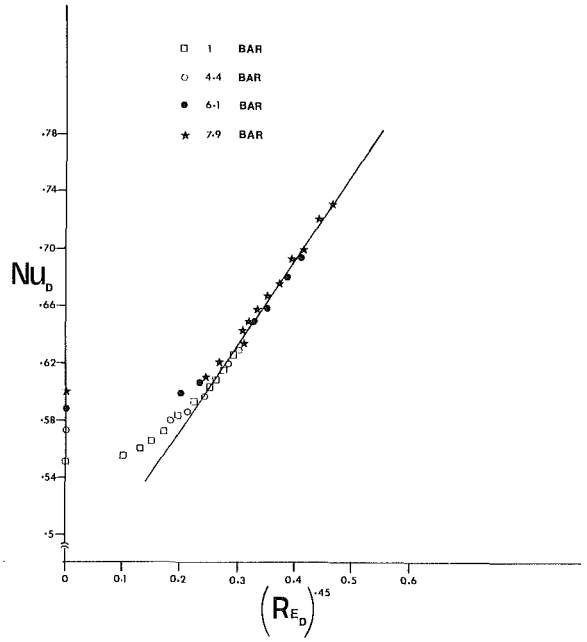


Fig. 2 Heat transfer correlation for the hot wire in the forced flow regime, for an overheat ratio of 1.6

were measured by a horizontally traversing probe assembly. The sensors were a 0.05-mm-dia copper-constantan thermocouple and a calibrated DISA 55 P14 hot-wire probe. The sensor outputs, as well as those from the surface thermocouples, were acquired and stored by a data acquisition system consisting of an HP 3497A Scanner, an HP 3450A Digital Voltmeter, and an HP 9845B Microcomputer. The instrumentation had recording rates of about 45 per second, with an accuracy of 1 $\mu$V. The boundary region probes were traversed in $y$, normal to the heated surface, by a DISA 55 H01 remote-controlled traversing mechanism.

The hot-wire probes were calibrated at atmospheric pressure using the test rig of Shaukatullah (1977). At higher pressures, the method developed by Mahajan and Gebhart (1979) was employed. That method consists of generating a natural convection boundary layer at the desired pressure level and calibrating the hot-wire voltage output against the velocity distribution obtained from the similarity solution. The resulting calibration curve, shown in Fig. 2, applies for an overheat ratio of 1.6 at an ambient temperature $t_\infty$ of 25°C. As the hot wire, at a particular overheat ratio, is traversed across the thermal boundary layer, it encounters a series of different local "ambient" temperatures. Thus, the voltage output of the hot wire changes, due to both the variation in the velocity and the varying local temperature. The latter effect was accounted for by using the relations developed by Mahajan (1977). These relations simulate the changes in local ambient temperature, in terms of changes in the resulting "effective" overheat ratio.

The error in temperature measurements is estimated to be about 1 percent. The errors in the measurement of boundary region velocity and surface heat flux are 5 percent each. Further details on the error estimation are given in Krishnamurthy (*1985*).

## 3 Results and Discussion

The measurements in the region of laminar mixed convection are considered first. Figure 3 shows the velocity and temperature profiles for $\epsilon_M = 0.75$ and 0.43, for $G^* = 357$ and 445. Good agreement is seen with the calculations of Carey and Gebhart (1982).

**First Mean Flow Deviations.** The laminar boundary layer

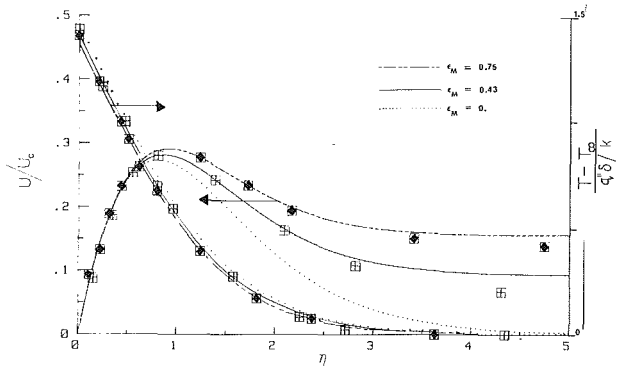


Fig. 3 Measured velocity and temperature profiles in laminar mixed convection air flow. Experimental conditions and symbols are listed in Table 1. Also shown are curves based on the laminar flow calculations of Carey and Gebhart (1982).

first becomes unstable to background disturbances at some downstream location. Thereafter, amplification follows, as predicted by linear theory. The disturbance characteristics depend only on $G^*$ and $U_\infty$, as shown, for example, in the study of Carey and Gebhart (1983). Eventually, nonlinear effects arise and cause a more rapid growth of the disturbances. The local mean profiles begin to deviate from laminar boundary region behavior, as a result of the transfer of energy from the mean flow to the disturbances, through nonlinear processes.

Figures 4(*a*) and 4(*b*) show the data comparison for $G^*$ in the range 885 to 984, where $U$ and $U_{max}$ are the average values of the local velocity $U$ and of its maximum value, respectively. The measurements are in large disagreement with the laminar flow calculations. The peak region in the velocity profile has broadened and the boundary region has thickened. These flows are clearly no longer laminar. This comparison also indicates that the amounts of these departures from laminar flow do not depend on $G^*$ and $\epsilon_M$ only. For example, consider the velocity and temperature distribution at $G^* = 913$, $P = 6.8$ bars, and $q'' = 1262$ W/m$^2$, with that at $G^* = 942$, $P = 7.9$ bars, and $q'' = 895$ W/m$^2$, experiments 11 and 13 in Table 1. Although the $G^*$ value for the latter is higher, the data at $G^* = 913$ deviate more from the laminar flow calculations. The difference in the values of $\epsilon_M$ for these two conditions is small. It is therefore clear that the form of mean transitional profiles, and hence their deviation from laminar flow, depends on both $G^*$ and $P$.

All mean boundary region profiles of temperature and velocity were determined at a single downstream location, $x = 28.4$ cm. Thus, the $x$ dependence of the progressive downstream deviations from laminar flow calculations were not determined directly. However, the actual downstream surface temperature distribution, $t_o(x)$, was measured for all the experimental conditions, $q''$ and $P$. In Fig. 5 the measured local temperature difference across the boundary region, $(t_o(x) - t_\infty)$, normalized by the corresponding calculated laminar value $(t_o(x)_L - t_\infty)$, is plotted as a function of $G^*$, for experiments 4 and 11–14. In each experiment this ratio decreases from 1.0 at some point downstream. The value of $G^*$ at which this begins depends on both $x$ and $P$. Thus, predictive parameters for the bounds of the transition region would also depend on these quantities. The fact that $G^*$ alone does not correlate the bounds of the transition region is apparent from measurements in natural convection flows reported by Regnier and Kaplan (1963), Godaux and Gebhart (1974), and others. The quantitative parameters for the beginning of transition are next considered.

**Beginning of Transition.** Various criteria have been applied to data to locate the beginning of transition. Two conventional ones are a modification of local heat transfer characteristics and the presence of significant aperiodic fluc-

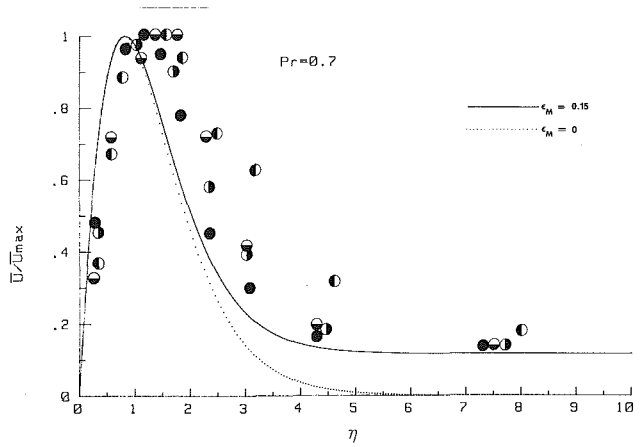


**Fig. 4(a) Measured mean velocity profiles in mixed convection flow of air. Experimental conditions are listed in Table 1. Also shown are curves based on laminar flow calculations of Carey and Gebhart (1982).**

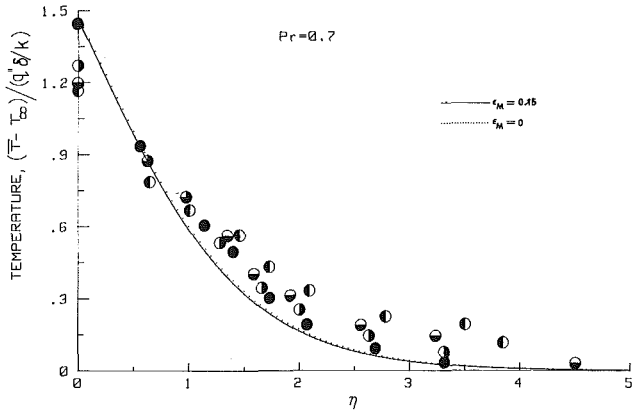


**Fig. 4(b) Measured mean temperature profiles in mixed convection flow of air. Experimental conditions and symbols are listed in Table 1. Also shown are laminar flow calculations of Carey and Gebhart (1982).**

tuations in the local velocity and temperature levels. Both have been shown to be imprecise measures.

In natural convection flows, Eckert and Soehngen (1951), Dring and Gebhart (1969), and others have shown that, during the early stages of disturbance growth, the flow selectively amplifies disturbance components. The highly amplified components downstream lie in a very narrow frequency range. In measurements, it may amount, essentially, to a single frequency. However, as turbulence arises, it quickly generates components of many additional frequencies. Thereby, it is reasonable to define the beginning of transition as the appearance of such components, superimposed on the single selected laminar frequency. This criterion was adopted by Jaluria and Gebhart (1974) from data in a water ambient.

However, Mahajan and Gebhart (1979) found that this spectral criterion is not definitive in gases. That study showed the velocity transition begins when the downstream growth of $U_{max}$, the measured mean maximum value of the tangential velocity, begins to decrease from its calculated laminar trend of increase downstream. The beginning of thermal transition is similarly taken to be the downstream location where the measured rate of increase of the local temperature difference across the boundary region begins to decrease from its calculated laminar trend. This procedure is followed here. Hereafter, local values of $G^* = 5(\mathrm{Gr}_x^*/5)^{1/5}$, at the beginning of velocity and thermal transition, will be designated as $G^*_{\mathrm{MC,BVT}}$ and $G^*_{MC,\mathrm{BTT}}$, respectively.

**Predictive Parameters.** The experimental values of $G^*_{MC,\mathrm{BTT}}$ at pressure levels of 6.1, 6.8, and 7.9 bars are plotted in Fig. 6, the upper three lines. The points shown were deter-

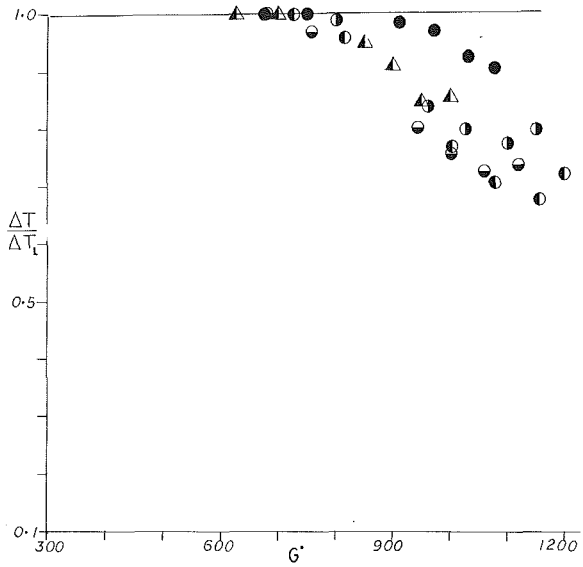


**Fig. 5 Measured downstream surface temperature excess compared with corresponding laminar flow calculations, for mixed convection flow of air. See Table 1 for experimental conditions and symbols.**

mined from departures such as those seen in Fig. 5. The results, for different $q''$, show a systematic variation of $G^*$ with respect to $x$. At each pressure the variation is

$$G^*_{MC,\mathrm{BTT}} \propto x^{1/2} \tag{2}$$

The effect of pressure is also seen in Fig. 6. The variation is

$$G^*_{MC,\mathrm{BTT}} \propto P^{1/2} \propto \rho^{1/2} \propto \nu^{-1/2} \tag{3}$$

Similarly on $G^*$, for the beginning of velocity transition, as indicated by $U_{max}$, the pressure effect is seen from Fig. 6 to be

$$G^*_{MC,\mathrm{BVT}} \propto P^{1/2} \propto \rho^{1/2} \propto \nu^{-1/2} \tag{4}$$

In equations (3) and (4) the proportionality of $P$, $\rho$, and $1/\nu$ to each other results from the reasonable assumption of taking air to be a perfect gas. Additionally, the dynamic viscosity $\mu$ is assumed to be independent of pressure. The determination of the $x$ dependence of $G^*_{MC,\mathrm{BVT}}$ requires the measurement of downstream variation of $U_{max}$ at a given pressure level. This was not possible in our apparatus. The $x$ dependence of $G^*_{MC,\mathrm{BVT}}$ is taken to be the same as that determined for $G^*_{MC,\mathrm{BTT}}$ as is the case in natural convection; see Jaluria and Gebhart (1974) and Mahajan and Gebhart (1979). That is

$$G^*_{MC,\mathrm{BVT}} \propto x^{1/2} \tag{5}$$

Relations (2)–(5) together indicate that the beginning of thermal and velocity transition occur when

$$G^*_{MC,\mathrm{BTT}} = C_1(x/\nu)^{1/2} \tag{6}$$

$$G^*_{MC,\mathrm{BVT}} = C_2(x/\nu)^{1/2} \tag{7}$$

where $C_1$ and $C_2$ are dimensional constants, each with dimensions of (velocity)$^{1/2}$. $G^*$ is related to $U_c$, the characteristic buoyancy-induced velocity (defined implicitly in equation (1)) as

$$G^* = (5U_c x/\nu)^{1/2} \tag{8}$$

Combining equations (6), (7), and (8) with equation (1), the criterion for the beginning of thermal and velocity transitions is recast in terms of $\epsilon_M$ as follows:

$$\epsilon_{M,\mathrm{BTT}} = 25\ U_\infty/C_1^2 = 25\ U_\infty/(G^{*2}_{MC,\mathrm{BTT}}/(x/\nu)) \tag{9}$$

and

$$\epsilon_{M,\mathrm{BVT}} = 25\ U_\infty/C_2^2 = 25\ U_\infty/(G^{*2}_{MC,\mathrm{BVT}}/(x/\nu)) \tag{10}$$

Based on our measurements, the right-hand sides of equations (9) and (10) turn out to be 0.183 and 0.185, respectively. However, the inherent uncertainties in velocity and

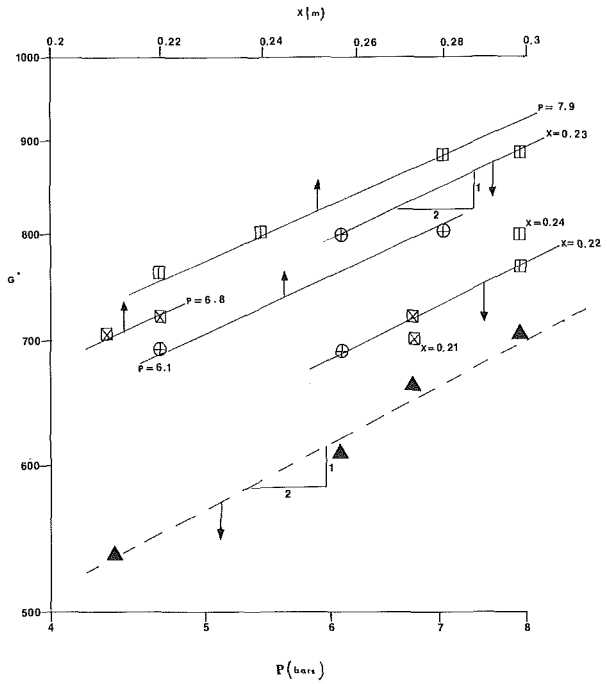


Fig. 6 The dependence of $G^*$ on $x$ and $P$ at the beginning of thermal (————) and velocity transitions (— — —). For velocity transition, 0.8 times the actual value of $G^*$ has been plotted.

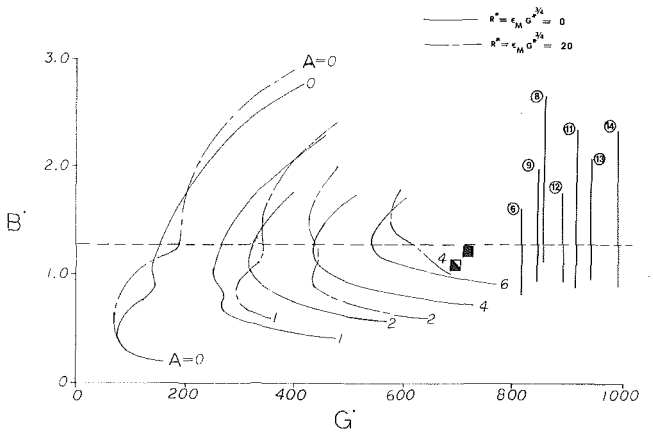


Fig. 7 Measured disturbance frequencies in mixed convection flow of air undergoing transition to turbulence. Each vertical line represents the measured *range* of frequencies. The circled number next to each line denotes the experiment. Experimental conditions and symbols are listed in Table 1. The horizontal dashed line at $B^* = 1.2$ represents the selected frequency. Also shown are disturbance amplification contours from the linear stability calculations of Carey and Gebhart (1983).

temperature measurements imply an uncertainty of about 10 percent in the value of $\epsilon_{MC,\mathrm{BVT}}$. The difference between these values is therefore insiginificant. Thus, the result is that velocity and thermal transitions begin when $\epsilon_M = 0.18$. This result is based on a limited set of measurements and therefore should not be regarded as conclusive.

**End of Transition.** As indicated in Section 1, transition would be taken to be complete at the downstream location beyond which the form of the local distributions of the intermittency factors $I_v$ and $I_t$ cease to change. This criterion could not be used in this experiment, since streamwise probe traverses were not possible.

Alternative criteria have been used instead. As indicated earlier, for a purely buoyancy-induced flow, the most amplified disturbance components lie in a very narrow frequency range. In mixed convection, with small forced convection effects, this was also predicted by the calculations of Carey and Gebhart (1983). A disturbance growth plane is plotted in Fig. 7, in terms of $B^* = 2\pi f\sqrt{g\beta q''/k}$ versus $G^*$. Constant $B^*$ lines correspond to lines of constant physical frequency downstream, $f$, for a given heat flux $q''$. $A = 0$ is the neutral curve. The other values of $A$ indicate the downstream disturbance amplitude, $e^A$, relative to its value at the neutral curve, see equation (18). With increasing values of $G^*$ (that is increasing distance downstream for a given $P$ and $q''$) the range of amplified frequencies decreases. Experimentally, often, only a single frequency-selected frequency is observed for amplifying disturbances. The horizontal line in Fig. 7 represents the estimated value of this selected frequency in terms of $B^*$. The two points from experiments 3 and 4 plotted in Fig. 7 agree in frequency with the selected frequency of $B^* = 1.2$. It is to be noted that in these two experiments for which $\epsilon_M = 0.18$ and 0.16, respectively, the transition to turbulence was just beginning. Recall that $\epsilon_{MC,\mathrm{BTT}} \cong \epsilon_{MC,\mathrm{BVT}} = 0.18$.

On the other hand, turbulence generates many disturbance frequency components. Thus, as transition proceeds, a spectral development of the flow occurs. The frequency data, also shown at higher $G^*$ in Fig. 7 for seven experiments, indicates that a wide range of amplified frequencies has arisen. Each vertical line represents the actual range of measured frequencies at that value of $G^*$. The circled number refers to the listing in Table 1.

This downstream spectral development may be qualitatively characterized by the fraction of the total disturbance energy contained in the frequency range above the favored frequency $f_s$. This fraction was found to be 7 percent at the end of transition and 15 percent in developed turbulence, by Bill and Gebhart (1979) in a natural convection flow in water. The disturbance energy data from the present study are next considered.

**Energy Spectrum of Disturbances.** Instantaneous velocities $U(\tau)$ and temperatures $t(\tau)$, where $\tau$ is the time, were measured. They are decomposed as follows:

$$U(\tau) = U + u'(\tau) \text{ and } t(\tau) = T + t'(\tau) \tag{11}$$

Fourier transform of the data determined the spectral energy density functions $\phi_u$ and $\phi_t$. These are defined as the contributions to $u'^2$ and $t'^2$, respectively, in the frequency range $f$ to $f + df$. The amount of disturbance kinetic energy in any frequency $f_1$ to $f_2$ is then $\int_{f_1}^{f_2} \phi_u\, df$. The fraction of the total disturbance energy contained up to a frequency level $f$ is given by

$$F(t) = \int_{f_l}^{f} \phi_u df \Big/ \int_{f_l}^{f_h} \phi_u df$$

Here $f_l$ is the lowest measured frequency, 0.22 Hz and $f_h$ is the highest measurable frequency, the Nyquist limit, 22.5 Hz. A plot of $F(f)$ is shown in Fig. 8, for three experimental conditions, 3, 11, and 13. For experiment 3, $\epsilon_M = 0.18$. This is close to the beginning of transition. For the others, $\epsilon_M = 0.15$ and 0.13. These flows are in the later stages of the transition.

The spectral development of the flow is characterized by the value of $F(f)$ at the favored frequency $f_s$. This selected frequency, determined from linear stability theory, corresponds to $u'$. Since $u'$ is assumed to be sinusoidal, the frequency of $u'^2$ is twice that of $u'$. The small arrows on the frequency axis in Fig. 8 indicate locations of $2f_s$ for the data shown. $F(2f_s)$ is about 0.95 for experiment 3. This means that only 5 percent of the disturbance energy lies above $f_s$, in experiment 3.

For experiments 11 and 13 ($\epsilon_M = 0.15$ and 0.13, respectively), $F(2f_s)$ has decreased to about 0.85. This indicates small-scale turbulence in the boundary region. However, these small scales do not necessarily assure developed turbulence. This would be signalled, for example, by the spectral behavior of quantities such as $\phi_u$ becoming like those in regions of locally isotropic turbulence.

**Decay of Spectral Energy Density.** Kolmogorov (1941) showed that $\phi_u$ decays with wave number $K$, as $K^{-5/3}$ in the inertial subrange, in fluids of uniform density. Obhukov (1949) and Corrsin (1951) showed the existence of a convection subrange, where $\phi_t$ decays as $K^{-5/3}$. This applied in flows in which temperature is a passive scalar. In our experiments temperature effects actively contribute to the generation of velocity fluctuations. A rigorous analysis of the spectral energy dynamics for such flows was given by Lumley (1964). It was shown that a buoyancy subrange exists in which $\phi_u$ decays as $K^{-3}$. This is followed by a $K^{-5/3}$ subrange. In the buoyancy subrange $\phi_u$ and $\phi_t$ are proportional to each other. Further theoretical work on the spectral decay of $\phi_u$ and $\phi_t$ was undertaken by Phillips (1965) and Weinstock (1978, 1985). Experimental observations of the existence of a buoyancy subrange have been reported by Papailiou and Lykoudis (1974) and Bill and Gebhart (1979) in studies of turbulent natural convection adjacent to vertical surfaces.

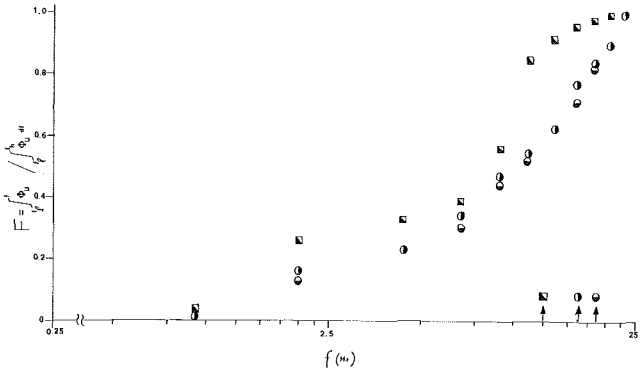

Fig. 8 Cumulative spectral distribution of disturbance energy in three experiments. See Table 1 for experimental conditions and symbols. Arrows on the frequency axis indicate the selected frequency for $u'^2$ as inferred from linear stability theory.

Experimentally, $\phi_u$ is determined in terms of the frequency $f$. The decay relations of $\phi_u$ are in terms of $K$. Therfore, to detect the presence of developed turbulence from measurements, a relation between $f$ and $K$ is needed. To this end, the hypothesis of Taylor (1938) is frequently invoked. It proposes to substitute $f$ and $K$, by regarding turbulence as a frozen pattern of eddies being swept past an observer. However, the frozen pattern hypothesis must be interpreted with care, in the presence of appreciable mean shear and turbulence intensity.

Lin (1953), Fisher and Davies (1964), and Lumley (1966) have considered this question in detail. Several mechanisms may preclude a direct application of Taylor's hypothesis. These include (*i*) the various wave number components of a disturbance being convected at different velocities and (*ii*) the intrinsic time variation/fluctuation of the convective velocity. The effects of these mechanisms are small when (*i*) $U > U'$ $2\pi/K$, where $U$ is the mean velocity and $U'$ its gradient in the direction normal to the surface, and (*ii*) if the turbulence intensities are small. In our experiments the turbulence intensities are quite high. Thus, while Taylor's hypothesis may not be valid across much of the boundary region, it is indeed applicable near the outer edge of the boundary region. There, the above conditions are met.

In Fig. 9, $\phi_u$ is plotted against frequency $f$ for experiments 11, 14, and 8. For each condition, results are given for three different $y$ locations. Experiments 11 and 14 indicate that the expected $f^{-3}$ behavior occurs only at large $\eta = yG/5x$, that is, near the outer edge of the boundary region. At small $\eta$, the spectra are irregular and develop no specific trend in terms of frequency. Thus, in experiments 11 and 14, the flow is in a state of developed turbulence, whereas in 8 it is not.

**Structure of Turbulence.** The distribution of turbulence intensity $\sqrt{u'^2}/U_{\max}$ across the boundary region is shown in Fig. 10, for experiments 7, 8, 11, 13, and 14. For 11, the turbulence intensity is significantly lower than for 8 and 14. Turbulence intensity is less in developed turbulence than in the

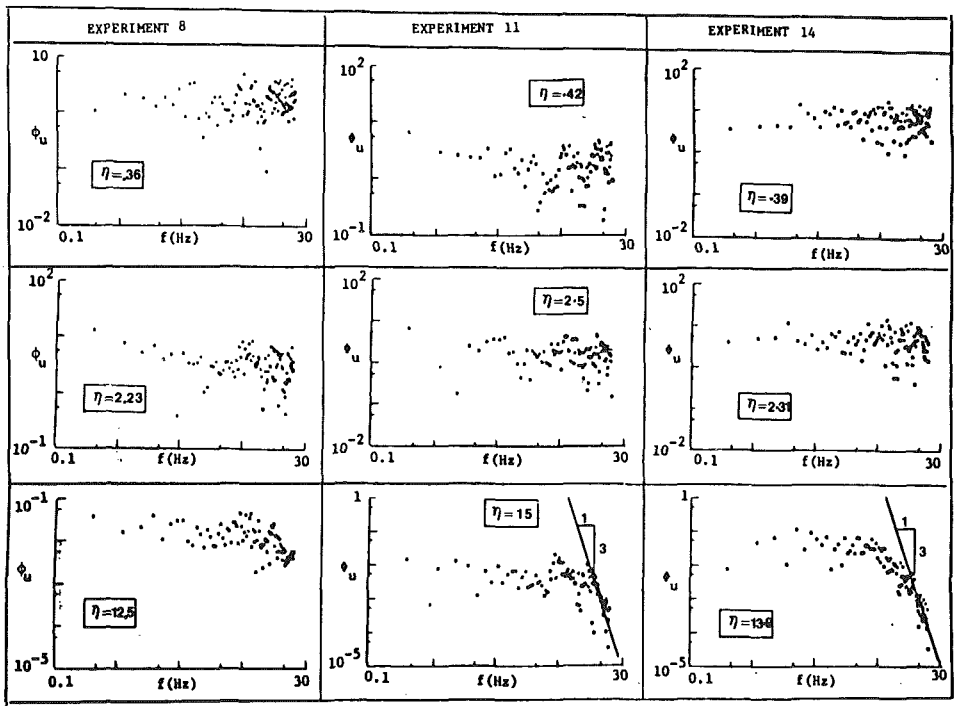


Fig. 9 Spectral distribution of the spectral energy density $\phi_u$ ((Cm/s)/Hz) in experiments 8, 11, and 14; see Table 1 for experimental conditions

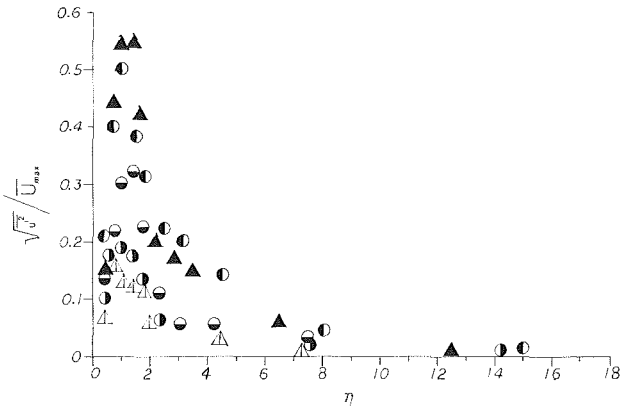


*Fig. 10 Measured turbulence intensities in five experiments; see Table 1 for experimental conditions and symbols*

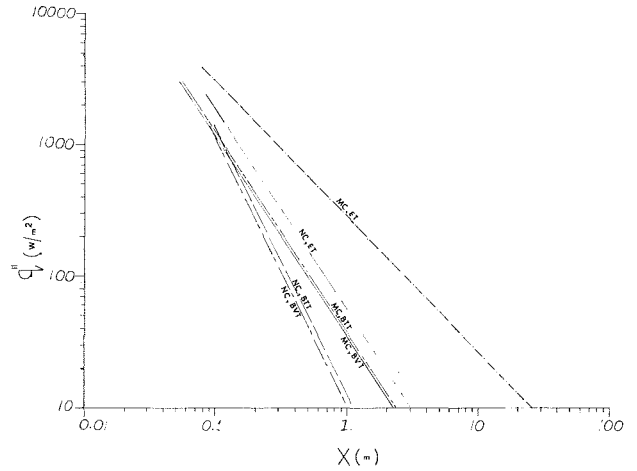


*Fig. 11 A comparison of the predictive correlations for the beginning and end of transition in natural and mixed convection flows of air, at P = 1 bar; here, NC stands for natural convection*

transition region upstream. However, turbulence intensity need not decrease monotonically as the vigor of the flow is increased, as indicated, for example, by $U_c$. This is evident in Fig. 10. The value of $\epsilon_M$ for experiments 14, 11, and 8 is 0.13. Yet, the turbulence intensity in experiments 14 and 8 is much greater than in 11. Thus, unlike for the beginning of transition, $\epsilon_M$ does not predict the beginning of developed turbulence.

A sharp rise in turbulence intensity slightly upstream of the developed turbulent region was also measured by Klebanoff et al. (1962), their Fig. 22. This was a study of transition to turbulence in forced convection boundary layer flow over a flat plate. Bill and Gebhart (1979) have also reported higher turbulence intensity levels upstream of the turbulent region. This sharp rise in turbulence intensity was seen in experiments 8 and 14.

Thus, in experiments 8, 11, and 14 at pressure levels of 6.1, 6.8, and 7.9 bars, respectively, the flow characteristics are those usually associated with the end of transition/beginning of developed turbulence. At each of these pressure levels, in experiments 7, 10, and 13, which are at flux levels lower than those in 8, 11, and 14, developed turbulence or high turbulence intensity levels were not observed. Thus, the achievement of developed turbulence or the end of transition is in terms of a parameter $G^*_{MC,ET}$, which would correlate the flow conditions of experiments 7, 10, and 13.

**Predictive Parameter for Developed Turbulence.** The measurements in experiments 7, 10, and 13 were at the same downstream location, but at different pressure levels. For the achievement of developed turbulence, the pressure effect is

$$G^*_{MC,ET} \propto P^{2/5} \propto \nu^{-2/5} \tag{13}$$

where $G^*_{MC,ET}$ represents the local value of $G^*$. The dependence of $G^*_{MC,ET}$ on $x$ at a given level of $P$ could not be determined. For the purpose of nondimensionalization, the following $x$ dependence is assumed:

$$G^*_{MC,ET} \propto x^{3/5} \tag{14}$$

Relations (13) and (14) are combined to yield

$$G^*_{MC,ET} = C_3[g\, x^3/\nu^2]^{1/5} \tag{15}$$

where the constant $g$ (acceleration due to gravity) has been introduced for convenience. Based on the flow conditions of experiments 7, 10, and 13, $C_3 = 1.48$, with an rms deviation of about 1 percent. From equation (15)

$$C_3 = G^*_{MC,ET}/(gx^3/\nu^2)^{1/5} = (\beta q'' x/5k)^{1/5} \propto Q(x) \tag{16}$$

where

$$Q(x) = q'' x = \int_0^\infty \rho c_p \{U(t - t_\infty) + \overline{u't'}\}\, dy \tag{17}$$

*Here* $Q(x)$ represents the total convected energy in the boundary region. This result indicates that the onset of developed turbulence arises as the nondimensional convected energy $\beta q'' x/5k$ $(= C_3^5)$ attains a value of 7.10.

**Comparisons of Mixed and Natural Convection.** The predictive parameters for the bounds of the transition region that have been developed in this study will now be compared with those applicable to pure natural convection flows, given in Gebhart and Mahajan (1982). In this comparison, shown in Fig. 11, in interpreting the correlation for $G^*_{MC,BTT}$ and $G^*_{MC,BVT}$, $U_\infty$ is taken to be 4.8 cm/s. For comparison, consider the flux $q'' = 100$ W/m$^2$. Downstream locations are along the horizontal line shown. The $x$ locations at which transition begins and ends are seen to be greater in mixed convection. The mixed convection effect stabilizes the flow and delays transition.

Several other important features of the enhanced stability also arise. Consider the stability plane in Fig. 7. There $B^*$ is directly proportional to the disturbance frequency $f$. The nondimensional parameter $A$ is a measure of the local downstream amplitude $A_L$, relative to its amplitude at the neutral curve $A_N$. For any frequency, it is defined as

$$e^A = A_L/A_N;\ A = -1/4\left(\int_{G_N^*}^{G_L^*} \alpha_i dG^*\right) \tag{18}$$

where $\alpha_i$ is the spatial exponential amplification rate. The integration is at constant $B^*$. The $A$ contours show that the downstream amplification rate is appreciably smaller in mixed convection.

Figure 12 compares the measured turbulence intensities across the boundary region in mixed and natural convection flows, for $P = 6.1$ and 7.9 bars. At each pressure level, the turbulence intensity is significantly lower. The physical reasons for the stabilizing effect of the imposed forced flow are considered next.

## 4 Stabilizing Effect

This observed stabilization is in accord with the well-known instability considerations arising at an inflection point in the velocity profile of a parallel flow of an inviscid fluid. The application of this consideration here follows the formulation of Lin (1945). According to this criterion, $U''(y) = 0$ implies instability for symmetric or boundary layer velocity distributions. The criterion was formulated for the parallel flow of an inviscid fluid. However, experimental measurements have repeatedly shown the importance of this same instability mechanism in developing viscous, natural convection boundary region flows. Here, for example, the measured velocity

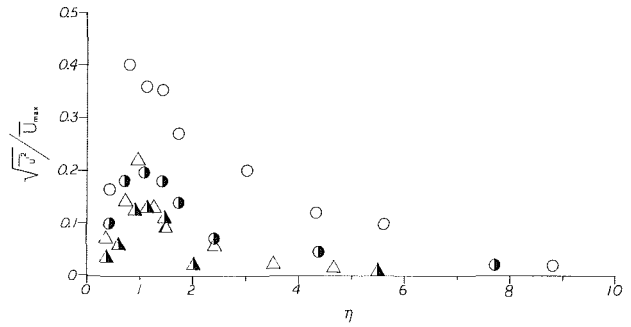

Fig. 12 A comparison of measured turbulence intensities in natural and mixed convection flows of air; see Table 1 for experimental conditions and symbols

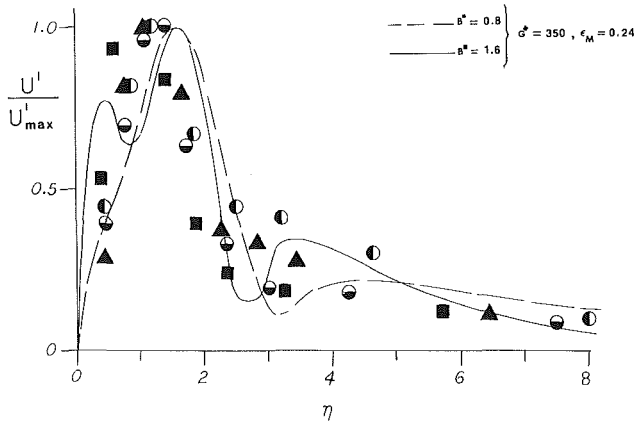

Fig. 13 Measured velocity disturbance profiles in mixed convection flow of air. Also shown are calculations based on linear stability theory from Carey and Gebhart (1983). See Table 1 for experimental conditions and symbols.

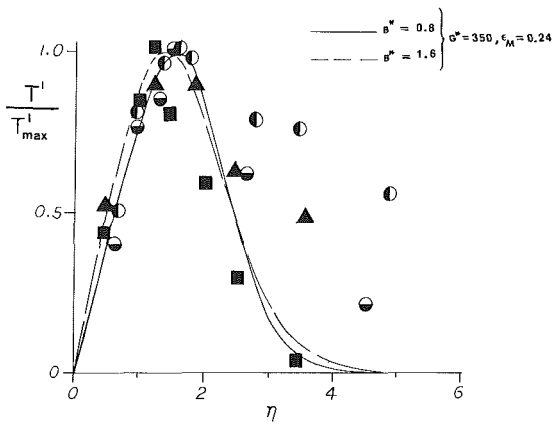

Fig. 14 Measured temperature disturbance profiles in mixed convection flow of air. Also shown are calculations based on linear stability theory from Carey and Gebhart (1983). See Table 1 for experimental conditions and symbols.

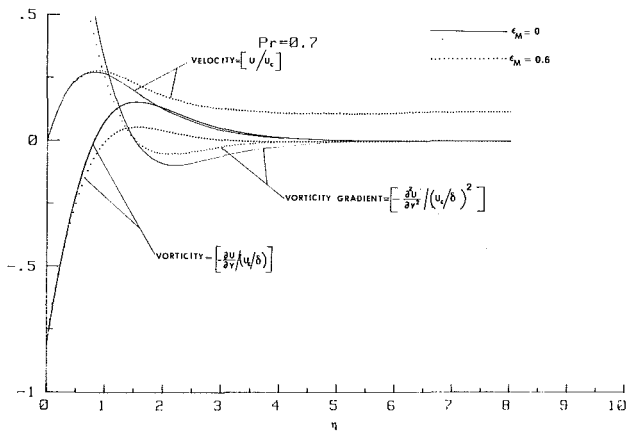

Fig. 15 A comparison of the velocity, vorticity, and vorticity gradient distributions in natural and mixed convection flows

and temperature disturbance amplitudes show a maximum near the point of inflection of $U(y)$; see Figs. 13 and 14. Also, see Polymeropolous and Gebhart (1967), their Figs. 7 and 9 and Dring and Gebhart (1969), their Figs. 1, 2, and 6.

A disturbance in a shear layer may be regarded as an exchange of fluid elements, or vortex filaments, from two adjacent layers, each with different vorticity. If one of the elements has an excess or deficiency of vorticity over that of the base flow, the exchange leads to a distortion of the vorticity distribution in the flow. This redistribution leads to an acceleration of the fluid element, as follows:

$$a = \Gamma^{-1} \int\int \{v'(x, y)\}^2 \zeta'(y) dxdy \tag{19}$$

Here, $a$ is positive outward from the surface, $\Gamma$ is the strength of the vortex, including the conventional sign, $\zeta'(y)$ is the base flow vorticity gradient, and $v'$ is the velocity in the $y$ direction due to the disturbance. In a shear flow where $\zeta'(y)$ does not vanish, the displaced fluid element would return to the original location, thereby rendering the flow stable. When the base velocity profile has an inflection point, $\zeta'(y)$ has opposite signs on the two sides of the inflection point. Thus, an exchange of fluid elements from opposite sides, where the magnitudes of vorticity and different, could result in the fluid element tending to move away from its layer of origin; see equation (19). If the fluid elements originate from layers where the vorticity is same, the exchanged elements tend to persist in their new locations. In either event there will be an exchange of momentum. Under such circumstances fluid motion is not necessarily stable.

Vertical natural convection flow adjacent to a surface has an inflection point. Thus, it is not necessarily stable to small disturbances. In the presence of small forced convection effects, the slope of the velocity profile, and also the magnitude of $\zeta'(y)$ on either side of the point of inflection, is reduced; see Fig. 15. Therefore, the tendency of fluid elements to move away from their region of origin is not as strong as in a purely buoyancy-driven flow. This implies that mixed convection is more stable, even for small forced flow effects.

## 5 Conclusions

Experimental measurements are reported for mixed convection flow adjacent to a vertical uniform flux surface, with small forced convection effects. The region of transition from laminar flow to turbulence has been considered in detail. Quantitative predictive parameters for the beginning and end of the transition region have been formulated. The experimental measurements show that transition events may not be correlated by $G^*$ only. An additional dependence on the downstream location and pressure level arises. The beginning of both thermal and velocity transition has been found to occur when the laminar mixed convection parameter $\epsilon_M = 0.18$. Previously used criteria for the end of transition, based on local distributions of intermittency factors $I_v$ and $I_t$, were not used here. Alternative criteria, based on the spectral properties of developed turbulence, have been used instead. The data indicate that the end of transition occurs when nondimensional convected energy, $\beta q'' x/5k$, in the boundary region, attains a value of 7.10. These quantitative criteria apply for the conditions of the experiment, that is, for $0.13 < \epsilon_M < 0.2$. It should be pointed out that these quantitative criteria are based on

limited data. Mixed convection flow was found to be considerably more stable than the corresponding pure natural convection flow.

## Acknowledgments

The authors wish to acknowledge support for this study by the National Science Foundation under grant No. CBT 8418517.

## References

Armaly, B. F., Chen, T. S., and Ramachandran, N., 1987, "Correlations for Laminar Mixed Convection on Vertical Inclined and Horizontal Flat Plates With Uniform Surface Heat Flux," *Int. J. Heat Mass Transfer*, Vol. 30, pp. 405-408.

Audunson, T., and Gebhart, B., 1976, "Secondary Mean Motions Arising in Buoyancy-Induced Flow," *Int. J. Heat Mass Transfer*, Vol. 19, pp. 337-350.

Babezha, A. V., Gimbutis, G. I., and Shvenchyanas, P. P., 1981, "Heat Transfer at a Vertical Flat Surface With the Combined Effect of Forced and Free Convection in the Same Direction," *Int. Chem. Engr.*, Vol. 21, pp. 135-138.

Bill, R. G., and Gebhart, B., 1979, "The Development of Turbulent Transport in a Vertical Natural Convection Boundary Layer," *Int. J. Heat Mass Transfer*, Vol. 22, pp. 267-277.

Brown, C. K., and Gauvin, W. H., 1966, "Temperature Profiles and Fluctuations in Combined Free- and Forced-Convection Flows," *Chemical Engr. Sci.*, Vol. 21, pp. 961-970.

Carey, V. P., and Gebhart, B., 1982, "Transport at Large Downstream Distances in Mixed Convection Flow Adjacent to a Vertical Uniform Heat Flux Surface," *Int. J. Heat Mass Transfer*, Vol. 25, pp. 255-266.

Carey, V. P., and Gebhart, B., 1983, "The Stability and Disturbance Amplification Characteristics of Vertical Mixed Convection Flow," *J. Fluid Mech.*, Vol. 127, pp. 185-201.

Chao, B. T., Chen, S. J., and Yao, L. S., 1983, "Mixed Convection Over a Vertical Zircaloy Plate in Steam With Simultaneous Oxidation," *Int. J. Heat Mass Transfer*, Vol. 26, pp. 73-82.

Chen, T. S., Armaly, B. F., and Ali, M. M., 1987, "Turbulent Mixed Convection Along a Vertical Flat Plate," ASME JOURNAL OF HEAT TRANSFER, Vol. 109, pp. 251-253.

Corrsin, S., 1951, "On the Spectrum of Isotropic Temperature Fluctuations in Isotropic Turbulence," *J. Appl. Phys.*, Vol. 22, pp. 469-473.

Dring, R. P., and Gebhart, B., 1969, "An Experimental Investigation of Disturbance Amplification in External Laminar Natural Convection Flow," *J. Fluid Mech.*, Vol. 36, pp. 447-464.

Eckert, E. R. G., and Soehngen, E., 1951, "Interferometric Studies on the Stability and Transition to Turbulence of a Free Convection Boundary Layer," *Proc. Gen. Disc. Heat Transfer*, London, pp. 321-323.

Fisher, M. J., and Davies, P. O. A. L., 1964, "Correlation Measurements in a Non-frozen Pattern of Turbulence," *J. Fluid Mech.*, Vol. 18, pp. 97-116.

Gebhart, B., 1979, "Buoyancy Induced Fluid Motions Characteristic of Applications in Technology," ASME *Journal of Fluids Engineering*, Vol. 101, pp. 5-28.

Gebhart, B., and Mahajan, R. L., 1982, "Instability and Transition in Buoyancy-Induced Flows," *Adv. Appl. Mech.*, Vol. 22, pp. 231-315.

Godaux, F., and Gebhart, B., 1974, "An Experimental Study of the Transition of Natural Convection Flow Adjacent to a Vertical Surface," *Int. J. Heat Mass Transfer*, Vol. 17, pp. 93-107.

Hall, W. B., and Price, P. H., 1970, "Mixed, Forced and Free Convection From a Vertical Heated Flat Plate to Air," *Proceedings of the 4th International Heat Transfer Conference*, Versailles, Paris V, NC 3.3.

Incropera, F. P., ed., 1986, "Research Needs in Electronic Cooling," *Proceedings of a workshop* sponsored by National Science Foundation and Purdue University, Dec.

Jaluria, Y., and Gebhart, B., 1974, "On Transition Mechanisms in Vertical Natural Convection Flow," *J. Fluid Mech.*, Vol. 66, pp. 309-337.

Kenning, D. B. R., Shock, R. A. W., and Poon, J. Y. M., 1974, "Local Reductions in Heat Transfer Due to Buoyancy Effects in Upward Turbulent Flow," *Proceedings of the 5th International Heat Transfer Conference*, Tokyo, Japna III, NC 4.3.

Khosla, J., Hoffman, T. W., and Pollock, K. G., 1974, "Combined Forced and Natural Convective Heat Transfer to Air in a Vertical Tube," *Proceedings of the 5th International Heat Transfer Conference*, Tokyo, Japan III, NC 4.4.

Kitamura, K., and Inagaki, T., 1987, "Turbulent Heat and Momentum Transfer of Combined Forced and Natural Convection Along a Vertical Flat Plate-Aiding Flow," *Int. J. Heat Mass Transfer*, Vol. 30, pp. 23-41.

Klebanoff, P. S., Tidstrom, K. D., and Sargent, L. M., 1962, "The Three-Dimensional Nature of Boundary Layer Instability," *J. Fluid Mech.*, Vol. 12, pp. 1-34.

Kolmogorov, A. N., 1941, "The Local Structure of Turbulence in Incompressible Viscous Fluid for Very Large Reynolds Numbers," *Doklady Akad. Nauk. SSSR*, Vol. 30, pp. 301-305.

Krishnamurthy, R., 1985, "An Experimental Study of Transition to Turbulence in Vertical Mixed Flows and Analyses of Laminar Mixed Convection in Plumes and in Wall Plumes," Ph.D. Dissertation, University of Pennsylvania, Philadelphia, PA.

Lin, C. C., 1945, "On the Stability of Two-Dimensional Parallel Flows—Part II," *Quart. Appl. Math.*, Vol. 3, pp. 218-234.

Lin, C. C., 1953, "On Taylor's Hypothesis and the Acceleration Terms in the Navier-Stokes Equations," *Quart. Appl. Math.*, Vol. 10, p. 295.

Loehrke, R. I., and Nagib, H. M., 1972, "Experiments on the Management of Free Stream Turbulence," AGARD Report #598, M. V. Morkovin and D. Kuchemann, eds.

Lumley, J. L., 1964, "The Spectrum of Nearly Inertial Turbulence in a Stably Stratified Fluid," *J. Atmos. Sci.*, Vol. 21, pp. 99-102.

Lumley, J. L., 1966, "Interpretation of Time Spectra Measured in High-Intensity Shear Flows," *Physics Fluids*, Vol. 8, pp. 1053-1062.

Mahajan, R. L., 1977, "Higher Order Effects, Stability and Transition in Vertical Natural Convection Flow," Ph.D. Dissertation, Cornell University, Ithaca, NY.

Mahajan, R. L., and Gebhart, B., 1980, "Hot-Wire Anemometer Calibration in Pressurized Nitrogen at Low Velocities," *J. Phys. E.: Sci. Instrm.*, Vol. 13, pp. 1110-1118.

Mahajan, R. L., and Gebhart, B., 1979, "An Experimental Determination of Transition Limits in a Vertical Natural Convection Flow Adjacent to a Surface," *J. Fluid Mech.*, Vol. 91, pp. 131-154.

Merkin, J. H., 1969, "The Effect of Buoyancy Forces on the Boundary Layer Flow Over a Semi-infinite Vertical Flat Plate in a Uniform Free Stream," *J. Fluid Mech.*, Vol. 35, pp. 439-450.

Mucoglu, A., and Chen, T. S., 1978, "Wave Instability of Mixed Convection Flow Along a Vertical Flat Plate," *Num. Heat Transfer*, Vol. 1, pp. 267-283.

Oboukhov, A. M., 1949, "Structure of the Temperature Field in Turbulent Flows," *Izvestiya Akademii Nauk SSSR, Geogr. and Geophys.*, Ser. 13, p. 58.

Oosthuizen, P. H., 1974, "Turbulent Combined Convective Flow Over a Vertical Plane Surface," *Proceedings of the 5th International Heat Transfer Conference*, Tokyo, Japan III, NC 4.1.

Papailiou, D. D., and Lykoudis, P. S., 1974, "Turbulent Free Convection Flow," *Int. J. Heat Mass Transfer*, Vol. 17, pp. 161-172.

Phillips, O. M., 1965, "On the Bolgiano and Lumley-Shur Theories of the Buoyancy Subrange," *Atmospheric Turbulence and Radio Wave Propagation*, A. M. Yaglom and V. I. Tatarsky, eds., Nauka, Moscow, pp. 121-128.

Polymeropoulos, C. E., and Gebhart, B., 1967, "Incipient Instability in Free Convection Laminar Boundary Layers," *J. Fluid Mech.*, Vol. 30, Pt. 2, pp. 225-239.

Regnier, G. M., and Kaplan, C., 1963, "Visualization of Natural Convection on a Plane Wall and in a Vertical Gap by Differential Interferometry: Transitional and Turbulent Regimes," *Proc. 1963 Heat Transfer and Fluid Mech. Inst.*, Stanford University Press, Stanford, CA, pp. 94-110.

Shaukatullah, H., 1977, "An Experimental Investigation of the Natural Convection Boundary Layer Over a Uniform Flux Inclined Surface," Ph.D. Dissertation, Cornell University, Ithaca, NY.

Smith, R. R., 1972, "Characteristics of Turbulence in Free Convection Flow Past a Vertical Plate," Ph.D. Thesis, University of London, Queen Mary College, United Kingdom.

Tanaka, H., Maruyama, S., and Hatano, S., 1987, "Combined Forced and Natural Convection Heat Transfer for Upward Flow in a Uniformly Heated Vertical Pipe," *Int. J. Heat Mass Transfer*, Vol. 30, pp. 165-174.

Taylor, G. I., 1938, "The Spectrum of Turbulence," *Proc. Roy. Soc. London*, Ser. A., Vol. 164, p. 476.

Townsend, A. A., 1972, "Mixed Convection Over a Heated Horizontal Plane," *J. Fluid Mech.*, Vol. 55, pp. 209-227.

Weinstock, J., 1978, "On the Theory of Turbulence in the Buoyancy Subrange of Stably Stratified Flows," *J. Atmos. Sci.*, Vol. 35, pp. 634-649.

Weinstock, J., 1985, "On the Theory of Temperature Spectra in a Stably Stratified Fluid," *J. Phys. Oceanogr.*, Vol. 15, pp. 475-477.

Wilks, G., 1974, "The Flow of a Uniform Stream Over a Semi-infinite Vertical Flat Plate With Uniform Surface Heat Flux," *Int. J. Heat Mass Transfer*, Vol. 17, pp. 743-753.

# Band Radiation From a Fluctuating Medium

**D. A. Nelson**
The Aerospace Corporation,
El Segundo, CA 90245

*A simple model of band radiation from a fluctuating medium, which emulates fluctuations in a turbulent diffusion flame, has been studied to determine the relative importance of the many mean and fluctuation parameters. The importance of fluctuations is largely confined to variation in the Planck function, which is strongly dependent upon the mean and variance of the mixture fraction and upon the band fundamental wavenumber.*

## Introduction

The effect of fluctuations on the radiation emerging from a medium is of importance in turbulent flows with combustion. It is particularly relevant to flows in large heat exchange devices fired with typical fuels and to the evolution of large-scale fires and the associated hazards.

The earliest studies, which treat the effect of radiation on fluctuations (Spiegel, 1960; Shved, 1978), have relied on linearization and, therefore, have been restricted to small amplitudes. These works have served to clarify the role of radiation in the damping of fluctuations but give no information about fluxes at flow boundaries. Because of the small amplitudes and lack of boundaries the relevance to many turbulent flows of particular interest is not great.

Subsequent to the completion of the present work the earlier studies by Cox (1977), Kabashnikov and Kmit (1979), and Grosshandler and Joulain (1986) came to light. Cox studies the total emergent radiation and discovers a significant effect of fluctuations of sufficient amplitude. He does not present a model of the gas emissivity, however, and so the results are tentative and incomplete. Kabashnikov and Kmit similarly find a possibly large effect but restrict themselves to monochromatic radiation and introduce some rather strong assumptions, once again making it difficult to relate their work to combustion problems. The work of Grosshandler and Joulain has much in common with the present study but the point of view is somewhat different and they do not isolate the primary phenomenon leading to significant effects of fluctuations on emergent radiation. This study and the latter one are complementary; there is some overlap but each makes it own contributions to the full problem.

Jeng et al. (1984) have shown that a stochastic analysis of radiation from reacting jets, using an approach similar to that of Grosshandler, is presently possible if the radiation is decoupled from the fluid mechanics. Virtually all other works on radiation from turbulent flows have ignored fluctuations and as yet there is no generally known criterion, or criteria that would allow one to make an a priori judgment of the circumstances under which this might be appropriate.

Formulation of such criteria is certainly a desirable goal and it is toward this that the present paper is directed. The approach is to follow the formalism of band radiation, as described by Edwards (1976), and to emulate as closely as possible the statistical approach to turbulent combustion as outlined by Bilger (1980). Certain idealizations are adopted to remove extraneous influences of real but, nevertheless, secondary concern. Furthermore, the simplified model makes it possible to study the relative importance of the many mean and fluctuating parameters in a setting that promotes generalized conclusions.

Contributed by the Heat Transfer Division and presented at the AIAA/ASME 4th Thermophysics and Heat Transfer Conference, Boston, Massachusetts, June 2–4, 1986. Manuscript received by the Heat Transfer Division August 24, 1987. Keywords: Radiation Interactions, Reacting Flows, Turbulence.

## Analysis

The idealized model of interest consists of an instantaneously homogeneous medium, which absorbs and emits band radiation along a particular line of sight of length $x$. The thermodynamic state is determined uniquely by the mixture fraction, which is defined as the mass fraction of fluid that originated in a pure fuel stream, the other stream being air at standard conditions. A single-step, irreversible reaction of fuel and oxidizer yields a radiating product. For simplicity all thermodynamic properties including temperature, overall specific volume, and concentrations are taken as sectionally linear functions of the mixture fraction. (This may not be appropriate for $H_2$ where $f > f_s$ due to a strong variation of mixture molecular weight.) Fluctuations in the mixture fraction are described by a two-parameter pdf, which depends only on the mean and variance. Instantaneous values of other properties depend upon the instantaneous mixture fraction, the initial values in fuel and air streams, and the stoichiometric properties of the reaction.

The instantaneous radiative flux emerging from the medium within band $k$ can be written

$$q_k^r = \omega_k E_{kb}(T, \nu_k) A(\tau_k) \tag{1}$$

where $E_{kb}(T, \nu_k)$ is the Planck emissive power at wavenumber $\nu_k$ and temperature $T$, $A(\tau_k)$ is the band absorption, and

$$\tau_k = \rho_k \alpha_k x / \omega_k \tag{2}$$

is the band optical depth with $\rho_k$ the partial density of the species radiating at wavenumber $\upsilon_k$, $\alpha_k$ is the band integrated intensity, and $\omega_k$ is the band width parameter (Edwards, 1976).

Since in general all physical parameters except the wavenumber are fluctuating, the mean radiative flux is given by

$$\bar{q}_k^r = \int_{L-\delta}^{L+\delta} \int_0^1 \omega_k E_{kb}(T, \nu_k) A(\tau_k) p(f) p(x) df\, dx \tag{3}$$

where $L$ is the mean path length, $\delta$ its amplitude, and $f$ is the mixture fraction, while $p(f)$ and $p(x)$ are the appropriate pdf's whose form remains to be specified.

The partial density $\rho_k$ can be expressed as

$$\rho_k = c_k \rho$$

where $c_k$ is the mass fraction, and if we assume that

$$\rho = \bar{\rho} \bar{T} M / T \bar{M}$$

then mean properties naturally enter as parameters. Moreover, many molecular-gas band properties are given by (Edwards, 1976)

$$\alpha_k(T) = \alpha_k(\bar{T}) = \bar{\alpha}_k$$

$$\omega_k = \bar{\omega}_k (T/\bar{T})^{1/2}$$

If we write

$$q_k^r(\bar{P}) = \bar{\omega}_k E_{kb}(\bar{T}, \nu_k) A(\bar{\tau}_k) \qquad 10^{-3} \le \bar{\tau}_k \le 10^3$$

$$\bar{\tau}_k = \bar{\rho}_k \bar{\alpha}_k L/\bar{\omega}_k \qquad 0.5 \le u_k \le 6$$

$$\psi_k = \overline{q_k^r}/q_k^r(\bar{P}) \qquad 0.36 f_s \le \bar{f} \le 3 f_s$$

$$0.35\bar{f} \le g^{1/2} \le 0.55\bar{f}$$

where $\bar{P}$ is a shorthand for all relevant mean properties, then

$$\psi_k = \frac{\int_{1-\eta}^{1+\eta} \int_0^1 (T/\bar{T})^{1/2} E_{kb}[u_k(\bar{T}/T)] A[\bar{\tau}_k \xi (\rho_k/\bar{\rho}_k)(\bar{T}/T)^{1/2}] p(f) p(\xi) df d\xi}{E_{kb}(u_k) A(\bar{\tau}_k)} \tag{4}$$

where $\xi = x/L$, $\eta = \delta/L$, and $u_k = hc\nu_k/k\bar{T}$ is a dimensionless wavenumber.

Equation (4) gives the ratio of the mean radiative flux to the flux computed using mean thermodynamic and radiative properties. The parameters that must be specified to evaluate equation (4) are the mean mixture fraction and variance, the path length amplitude, the mean optical depth, the band frequency parameter $u_k$, and values of temperature, density, and mixture fraction for the initial conditions of fuel and air and the stoichiometric products of reaction. In addition the mathematical expressions for the pdf's and the band absorption are required.

## Results and Discussion

The band absorption function was chosen as

$$A(\tau_k) = \ln(1 + \tau_k) \tag{5}$$

which is representative of the known behavior of many molecular-gas bands at both small and large values of $\tau_k$ (Nelson, 1974).

The pdf for path length was chosen as the uniform distribution, which implies a time-dependent triangular waveform for the boundaries of the medium. The pdf for mixture fraction was either a uniform or beta distribution, but since the results were relatively insensitive to the particular choice only those for the uniform distribution are reported. Thus one has

$$p(\xi) = 1./2\eta; \qquad 1 - \eta \le \xi \le 1 + \eta \tag{6}$$

and

$$p(f) = 1./2.\sqrt{3g}; \qquad \bar{f} - \sqrt{3g} \le f \le \bar{f} + \sqrt{3g} \tag{7}$$

where $g$ is the mixture fraction variance. Outside the indicated ranges each pdf is zero.

The initial conditions were taken as 300 K and 1 atm for both fuel and air. The fuel stream was assumed pure and consisted of either $H_2$, $CH_4$, or CO because of low or no propensity for soot formation.

For each fuel the parameter variations covered the ranges and equation (4) was evaluated by Monte Carlo using 50,000 samples for each case. The results are summarized in Fig. 1 and 2 and in Tables 1-3. The figures show results only at a value of $\tau_k = 1$ because this parameter had a very weak influence. This is clear from a comparison of the last two rows of the tables, which represent results for $\tau_k \to 0$ and $\tau_k \to \infty$, respectively. There was also only a weak effect of fluctuations in the path length so that the figures and Table 1 are for no path length fluctuations. Table 2 illustrates the effect of path length fluctuation. The effect of fluctuations in the thermodynamic and radiative properties was also rather weak but are included in the results. The rather strong dependence upon band wavenumber and mixture fraction variance is due almost entirely to fluctuations in the Planck function alone, which

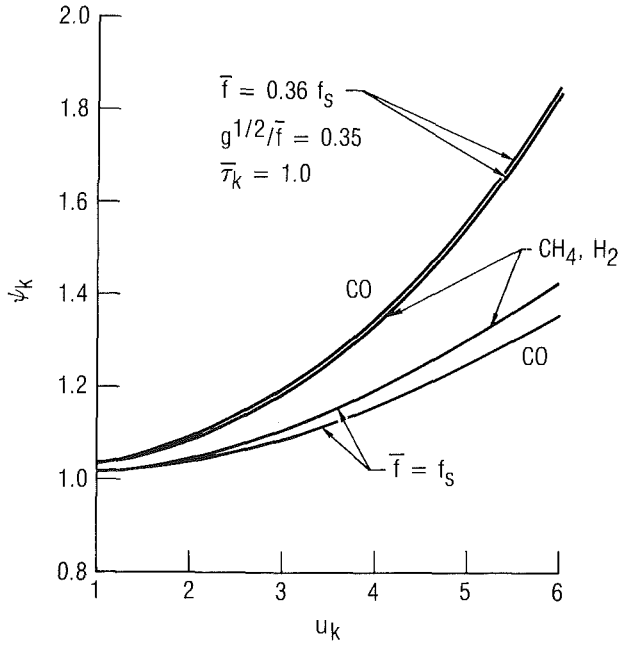


**Fig. 1 Emergent radiative flux ratio for a moderate fluctuation intensity**

## Nomenclature

$A(x)$ = band absorption for optical path $x$
$c$ = speed of light
$c_k$ = mass fraction of species radiating in band $k$
$E_{kb}$ = Planck emissive power at wavenumber $\nu_k$
$f$ = mixture fraction
$f_s$ = stoichiometric mixture fraction
$g$ = mixture fraction variance
$h$ = Planck constant
$k$ = Boltzmann constant
$L$ = mean path length
$M$ = molecular weight
$P$ = generic symbol for thermodynamic and radiative properties
$p(x)$ = probability density function
$q_k^r$ = radiative flux for band $k$
$T$ = absolute temperature
$u_k$ = dimensionless wavenumber $= hc\nu_k/kT$
$x$ = instantaneous path length
$\alpha_k$ = band intensity
$\delta$ = amplitude of path length fluctuations
$\eta$ = $\delta/L$
$\nu_k$ = wavenumber for bank $k$
$\xi$ = $x/L$
$\rho$ = density
$\rho_k$ = density of species radiating in band $k$
$\tau_k$ = optical depth for band $k$
$\psi_k$ = dimensionless mean radiative flux
$\omega_k$ = band width parameter for band $k$
$(\,)'$ = denotes an rms value

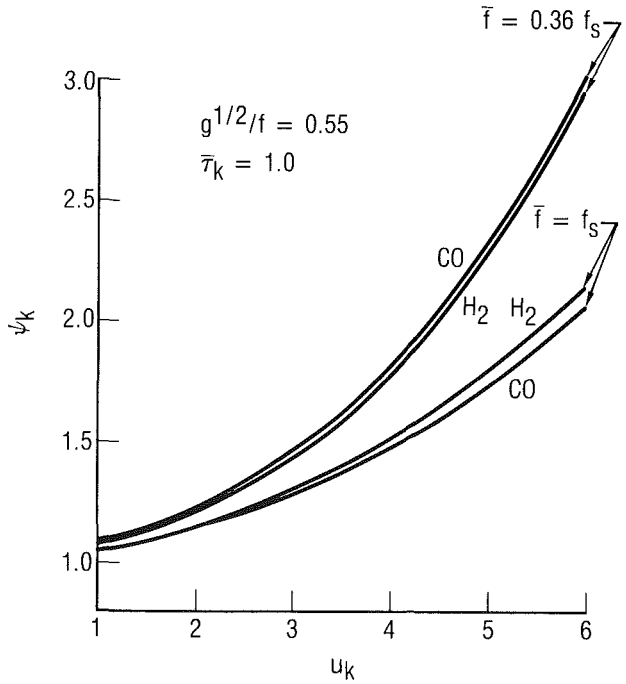


**Fig. 2 Emergent radiative flux ratio for a large fluctuation intensity**

can be easily seen by reference to the tabular results. At small values of $u_k$ the Planck function approaches linearity in $T$, but at large values it behaves as $\exp(-hc\nu_k/kT)$ and this accounts for the large effect at high wavenumbers (frequencies). The effect of mean mixture fraction is also quite strong. Reference to Table 3 shows that the underlying cause is the intensity of the temperature fluctuations, which also accounts for the weaker response of CO at $\bar{f}=f_s$. One should not conclude from the figures that diffusion flames of the various fuels considered would show similar behavior in the emitted radiation. In general the parameter values appropriate for one flame may be quite different from those for another. However, when parameter sets do match, the type of fuel is not especially important.

Before discussing possible implications of these findings it is worth some effort to identify what connection, if any, the present model might have with real turbulent flows. It is easier to make a connection with some experimental observations than with current modeling methods. Some years ago observations were reported on turbulent mixing layers that suggested a nearly uniform conditional mean scalar, specifically temperature distribution, through the transverse dimension of the large eddies (Fiedler, 1975). More recently (Koochesfahani et al., 1985) similar observations have been made for the instantaneous structure. The present model is consistent with these observations and the mean values should, therefore, be interpreted as the conditional values consistent with the model assumptions. Typically, however, predictive methods for turbulent flows are confined to unconditional means and it must be anticipated that predicted radiative flux $q_k^r(\bar{P})$ using these values will be different from that obtained from the present model. One should expect, however, that the use of unconditional means and pdf's that properly account for intermittency will properly predict the effect of fluctuations on the radiative flux. This means that with regard to the present results the value of $q_k^r(\bar{P})\psi_k$ should be independent of the conditioned or unconditioned point of view, while the values of $\psi_k$ might differ. Grosshandler and Joulain (1986) used unconditioned means and an intermittency of one so their results are not directly comparable to those given herein but are, nevertheless, fully consistent with the present findings.

Finally, it is mentioned that the present model produces unconditional mean mixture fraction profiles that are uniform over a flow core width of $1-\eta$ and that decrease linearly and symmetrically to zero on either side within a total width of $1+\eta$. Thus, the idealizations adopted do not appear to be too far afield from real turbulent flows. Moreover, by allowing path length fluctuations (Table 2) intermittency is taken into account.

Perhaps the most significant observation produced by this analysis is that it should be possible to predict adequately the effect of fluctuations on radiative transfer by accounting for variations in the Planck function alone and replacing all other fluctuating parameters by their mean values. This approximation reduces a very complicated problem to a tractable one and would require only single point pdf's for temperature alone. The parameter set would also be reduced to $u_k$ and $T'/\bar{T}$.

In view of the small difference between optically thin and

**Table 1 Selected mean values for band radiation from a fluctuating medium with hydrogen–air combustion parameters**

**Table 1(*a*) $H_2$–air, $g^{1/2}/\bar{f}=0.35$, $\bar{\tau}_k=1$, $\bar{f}=f_s$**

| Normalized mean values | Wavenumber parameter, $u_k=hc\nu_k/k\bar{T}$ | | |
|---|---|---|---|
| | 1 | 3 | 6 |
| $\psi_k$ | 1.015 | 1.104 | 1.427 |
| $\overline{E_{kb}(T)}/E_{kb}(\bar{T})$ | 1.007 | 1.084 | 1.392 |
| $\overline{A(\tau_k)}/A(\bar{\tau}_k)$ [i] | 1.003 | 1.003 | 1.003 |
| $\overline{\omega_k(T)}/\omega_k(\bar{T})$ [i] | 0.995 | 0.995 | 0.995 |
| $\overline{\omega_k(T)A(\tau_k)}/\omega_k(\bar{T})A(\bar{\tau}_k)$ [i] | 0.993 | 0.993 | 0.993 |
| $\overline{\rho_k E_{kb}(T)}/\bar{\rho}_k E_{kb}(\bar{T})$ [ii] | 1.010 | 1.094 | 1.411 |
| $\overline{\omega_k E_{kb}(T)}/\bar{\omega}_k E_{kb}(\bar{T})$ [iii] | 1.032 | 1.131 | 1.472 |

[i] These values are independent of $u_k$.
[ii] The optically thin limit of $\psi_k$.
[iii] The optically thick limit of $\psi_k$.

**Table 1(*b*) $H_2$–air, $g^{1/2}/\bar{f}=0.35$, $\bar{\tau}_k=1$, $\bar{f}=0.36f_s$**

| Normalized mean values | Wavenumber parameter, $u_k=hc\nu_k/k\bar{T}$ | | |
|---|---|---|---|
| | 1 | 3 | 6 |
| $\psi_k$ | 1.030 | 1.181 | 1.822 |
| $\overline{E_{bk}(T)}/E_{bk}(\bar{T})$ | 1.010 | 1.125 | 1.690 |
| $\overline{A(\tau_k)}/A(\bar{\tau}_k)$ | 0.986 | 0.986 | 0.986 |
| $\overline{\omega_k(T)}/\omega_k(\bar{T})$ | 0.993 | 0.993 | 0.993 |
| $\overline{\omega_k(T)A(\tau_k)}/\omega_k(\bar{T})A(\bar{\tau}_k)$ | 0.978 | 0.978 | 0.978 |
| $\overline{\rho_k E_{kb}(T)}/\bar{\rho}_k E_{kb}(\bar{T})$ | 1.023 | 1.171 | 1.802 |
| $\overline{\omega_k E_{kb}(T)}/\bar{\omega}_k E_{kb}(\bar{T})$ | 1.049 | 1.208 | 1.874 |

**Table 1(*c*) $H_2$–air, $g^{1/2}/\bar{f}=0.55$, $\bar{\tau}_k=1$, $\bar{f}=f_s$**

| Normalized mean values | Wavenumber parameter, $u_k=hc\nu_k/k\bar{T}$ | | |
|---|---|---|---|
| | 1 | 3 | 6 |
| $\psi_k$ | 1.056 | 1.305 | 2.132 |
| $\overline{E_{bk}(T)}/E_{kb}(\bar{T})$ | 1.026 | 1.250 | 2.032 |
| $\overline{A(\tau_k)}/A(\bar{\tau}_k)$ | 0.989 | 0.989 | 0.989 |
| $\overline{\omega_k(T)}/\omega_k(\bar{T})$ | 0.982 | 0.982 | 0.982 |
| $\overline{\omega_k(T)A(\tau_k)}/\omega_k(\bar{T})A(\bar{\tau}_k)$ | 0.963 | 0.963 | 0.963 |
| $\overline{\rho_k E_{kb}(T)}/\bar{\rho}_k E_{kb}(\bar{T})$ | 1.041 | 1.281 | 2.089 |
| $\overline{\omega_k E_{kb}(T)}/\bar{\omega}_k E_{kb}(\bar{T})$ | 1.099 | 1.371 | 2.253 |

**Table 1(*d*) $H_2$–air, $g^{1/2}/\bar{f}=0.55$, $\bar{\tau}_k=1$, $\bar{f}=0.36f_s$**

| Normalized mean values | Wavenumber parameter, $u_k=hc\nu_k/k\bar{T}$ | | |
|---|---|---|---|
| | 1 | 3 | 6 |
| $\psi_k$ | 1.077 | 1.431 | 2.953 |
| $\overline{E_{kb}(T)}/E_{kb}(\bar{T})$ | 1.026 | 1.304 | 2.618 |
| $\overline{A(\tau_k)}/A(\bar{\tau}_k)$ | 0.936 | 0.936 | 0.936 |
| $\overline{\omega_k(T)}/\omega_k(\bar{T})$ | 0.980 | 0.980 | 0.980 |
| $\overline{\omega_k(T)A(\tau_k)}/\omega_k(\bar{T})A(\bar{\tau}_k)$ | 0.929 | 0.929 | 0.929 |
| $\overline{\rho_k E_{kb}(T)}/\bar{\rho}_k E_{kb}(\bar{T})$ | 1.062 | 1.407 | 2.895 |
| $\overline{\omega_k E_{kb}(T)}/\bar{\omega}_k E_{kb}(\bar{T})$ | 1.122 | 1.496 | 3.114 |

**Table 2 The effect of a large path length fluctuation on band radiation from a fluctuating medium**

**Table 2(*a*) $CH_4$-air, $g^{1/2}/\bar{f}=0.55$, $\bar{\tau}_k=1.$, $\bar{f}=f_s$, $L'=0.55L$, $\delta=0.953L$**

| Normalized mean values | Wavenumber parameter, $u_k=hc\nu_k/k\bar{T}$ | | |
|---|---|---|---|
| | 1 | 3 | 6 |
| $\psi_k$ | 0.993 | 1.224 | 1.989 |
| $\overline{E_{kb}(T)}/E_{kb}(\bar{T})$ | 1.024 | 1.242 | 2.004 |
| $\overline{A(\tau_k)}/A(\bar{\tau}_k)$ | 0.925 | 0.925 | 0.925 |
| $\overline{\omega_k(T)}/\omega_k(\bar{T})$ | 0.982 | 0.982 | 0.982 |
| $\overline{\omega_k(T)A(\tau_k)}/\omega_k(\bar{T})A(\bar{\tau}_k)$ | 0.903 | 0.903 | 0.903 |
| $\overline{\rho_k x E_{kb}(T)}/\bar{\rho}_k L E_{kb}(\bar{T})$ | 1.039 | 1.277 | 2.071 |
| $\overline{\omega_k E_{kb}(T)}/\bar{\omega}_k E_{kb}(\bar{T})$ | 1.095 | 1.359 | 2.219 |

**Table 2(*b*) $CH_4$-air, $g^{1/2}/\bar{f}=0.55$, $\bar{\tau}_k=1.$, $\bar{f}=0.36f_s$, $L'=0.55L$, $\delta=0.953L$**

| Normalized mean values | Wavenumber parameter, $u_k=hc\nu_k/k\bar{T}$ | | |
|---|---|---|---|
| | 1 | 3 | 6 |
| $\psi_k$ | 1.014 | 1.350 | 2.793 |
| $\overline{E_{kb}(T)}/E_{kb}(\bar{T})$ | 1.024 | 1.302 | 2.619 |
| $\overline{A(\tau_k)}/A(\bar{\tau}_k)$ | 0.878 | 0.878 | 0.878 |
| $\overline{\omega_k(T)}/\omega_k(\bar{T})$ | 0.979 | 0.979 | 0.978 |
| $\overline{\omega_k(T)A(\tau_k)}/\omega_k(\bar{T})A(\bar{\tau}_k)$ | 0.872 | 0.872 | 0.872 |
| $\overline{\rho_k x E_{kb}(T)}/\bar{\rho}_k L E_{kb}(\bar{T})$ | 1.061 | 1.410 | 2.909 |
| $\overline{\omega_k E_{kb}(T)}/\bar{\omega}_k E_{kb}(\bar{T})$ | 1.120 | 1.495 | 3.118 |

thick limits it is virtually certain that these findings will not change if the form of the absorption function is altered, say to one more appropriate for soot. In that case equation (4) would be altered by deleting the $(T/\bar{T})^{1/2}$ terms and using the spectral form, $A(\tau_\nu)=1-\exp(-\tau_\nu)$, for the absorption function. The optically thin limit is unaltered by these changes but the optically thick limit would become equal to $\overline{E_{\nu b}(T)}/E_{\nu b}(\bar{T})$. As can be seen from Table 1 the results for thin and thick limits are then not significantly different from those for band radiation of molecular gases except that monotonicity in optical depth no longer holds.

## Conclusions

Band radiation from a fluctuating medium is affected almost entirely by variations in the Planck function alone.

**Table 3 Intensity of temperature fluctuations, $T'/\bar{T}$**

| $g/\bar{f}$ | $\bar{f}$ | Fuel | | |
|---|---|---|---|---|
| | | $H_2$ | $CH_4$ | CO |
| 0.35 | $f_s$ | 0.192 | 0.190 | 0.171 |
| 0.35 | $0.36f_s$ | 0.243 | 0.244 | 0.243 |
| 0.55 | $f_s$ | 0.331 | 0.328 | 0.308 |
| 0.55 | $0.36f_s$ | 0.382 | 0.384 | 0.382 |

Other fluctuating parameters can be replaced with their mean values with little loss in accuracy. The effects predicted by the present analysis should be detectable if band radiation measurements can be made at the higher frequencies of absorbing-emitting gases such as $CO_2$ for comparison with measurements made at a sufficiently lower frequency. The ratio would not satisfy predictions based upon a nonfluctuating Planck's Law.

## References


Bilger, R. W., 1980, "Turbulent Flows With Nonpremixed Reactants," *Turbulent Reacting Flows*, P. A. Libby and F. A. Williams, eds., Springer-Verlag, New York, pp. 65–113.

Cox, G., 1977, "On Radiant Heat Transfer From Turbulent Flames," *Comb. Sci. and Tech.*, Vol. 17, pp. 75–78.

Edwards, D. K., 1976, "Molecular Gas Band Radiation," *Advances in Heat Transfer*, Vol. 12, T. F. Irvine, Jr. and J. P. Hartnett, eds., Academic Press, New York, pp. 115–193.

Fiedler, H. E., 1975, "On Turbulence Structure and Mixing Mechanism in Free Turbulent Shear Flows," *Turbulent Mixing in Nonreactive and Reactive Flows*, S. N. B. Murthy, ed., Plenum Press, New York, pp. 381–409.

Grosshandler, W. L., and Joulain, P., 1986, "The Effect of Large-Scale Fluctuations on Flame Radiation," *Dynamics of Reactive Systems. Part II: Modeling and Heterogeneous Combustion*, J. R. Bowen, J.-C. Leyer, and R. I. Soloukhin, eds., AIAA, New York, pp. 123–152.

Jeng, S.-M., Lai, M.-C., and Faeth, G. M., 1984, "Nonluminous Radiation in Turbulent Buoyant Axisymmetric Flames," *Comb. Sci. and Tech.*, Vol. 40, pp. 41–53.

Kabashnikov, V. P., and Kmit, G. I., 1979, "Influence of Turbulent Fluctuations on Thermal Radiation," *J. Appl. Spectroscopy*, Vol. 31, pp. 963–967.

Koochesfahani, M. M., Dimotakis, P. E., and Broadwell, J. E., 1985, "A Flip Experiment in a Chemically Reacting Turbulent Mixing Layer," *AIAA Journal*, Vol. 23, pp. 1191–1194.

Nelson, D. A., 1974, "A Study of Band Absorption Equations for Infrared Radiative Transfer in Gases—I. Transmission and Absorption Functions for Planar Media," *J. Quant. Spect. Radiat. Transfer*, Vol. 14, pp. 69–80.

Shved, G. M., 1978, "Influence of Radiative Transfer on Certain Types of Motions in Planetary Atmospheres," *Advances in Heat Transfer*, Vol. 14, T. F. Irvine, Jr. and J. P. Hartnett, eds., Academic Press, New York, pp. 249–280.

Spiegel, E. A., 1960, "The Convective Instability of a Radiating Fluid Layer," *Astrophysical Journal*, Vol. 132, pp. 716–728.

# Reduction of Computing Time and Improvement of Convergence Stability of the Monte Carlo Method Applied to Radiative Heat Transfer With Variable Properties

**M. Kobiyama**
Associate Professor,
Faculty of Engineering,
Muroran Institute of Technology,
Muroran, 050 Japan

*A modified Monte Carlo method is suggested to reduce the computing time and improve the convergence stability of iterative calculations without losing other excellent features of the conventional Monte Carlo method. In this method, two kinds of radiative bundle are used: energy correcting bundles and property correcting bundles. The energy correcting bundles are used for correcting the radiative energy difference between two successive iterative cycles, and the property correcting bundles are used for correcting the radiative properties. The number of radiative energy bundles emitted from each control element is proportional to the difference in emissive energy between two successive iterative cycles.*

## 1 Introduction

There are many kinds of heat transfer systems where radiative heat transfer is important. The energy equation regarding problems, including radiative heat transfer, is an integral equation, or an integro-differential equation, which is solved by some numerical method. The Monte Carlo method is one of those numerical techniques, and has the excellent feature of easy application to models in which thermal radiative properties are not uniform or system geometries are complex. However, the Monte Carlo method has a defect in requiring long computing times when radiative heat transfer coexists with the other heat transfer mechanisms, or when the energy equation is nonlinear due to the dependency of thermal properties on temperature and other quantities. To resolve this defect, the author and his co-workers have already suggested a technique called the DPE method (the Differential Emissive Power Emission method) (Kobiyama et al., 1979) in which the number of radiative bundles emitted from a control element is taken to be proportional to the difference of emissive power between two successive iterative cycles. However, this method has the restriction of a lack of applicability to variable property problems. In this paper, the author modifies the PDE method so that it can be applied to problems with variable properters where the medium and walls exhibit constant directional emissive characteristics. An examination is included to examine the features of the new modified Monte Carlo method.

## 2 Calculating Procedure

**Basic Equations.** Consider the heat transfer field, composed of radiation, convection, and other heat transfer mechanisms. For the sake of facilitating the discussion, consider the coordinate system shown in Fig. 1 where the flow field is already known. The values of the radiative properties, the absorption coefficient of the medium $\kappa$ and the emissivity of a wall surface $\epsilon$, depend on other independent variables such as temperature. In Fig. 1 a radiative ray emitted from a wall or medium element is reflected $k$ times by the walls with angle $\phi$ and its energy is absorbed by the walls and medium until arriving at the wall or medium element considered. Then the energy equations regarding the medium and the wall are expressed as follows:

$$c_p\rho \frac{DT}{Dt} = \lambda \nabla^2 T + \Phi - \text{div } \mathbf{q}_{Rg} \tag{1}$$

$$q_w = -\lambda \nabla T - q_{Rw} \tag{2}$$

where $D/Dt$ is the material differential operator of the fluid dynamics, and $\nabla^2$ and $\nabla$ are the Laplacian and gradient operators, respectively. In equations (1) and (2), $-\text{div}\mathbf{q}_{Rg}$ and $-q_{Rw}$ are expressed as follows:

$$-\text{div } \mathbf{q}_{Rg} = -4\kappa_0 E_{g0} + \int_V \kappa E_g P_{gg} dV + \int_A \epsilon E_w P_{wg} dA \tag{3}$$

$$-q_{Rw} = -\epsilon_0 E_{w0} + \int_V \kappa E_g P_{gw} dV + \int_A \epsilon E_w P_{ww} dA \tag{4}$$

$$\left.\begin{aligned} P_{gg} &= \kappa_0 P_g \\ P_{wg} &= \kappa_0 \cos\phi_0 P_g \\ P_{gw} &= \epsilon_0 P_w \\ P_{ww} &= \epsilon_0 \cos\phi_0 P_w \end{aligned}\right\} \tag{5}$$

$$\left.\begin{aligned} P_g &= \frac{\exp(-\int_0^l \kappa dl)}{\pi l^2} + \sum_{k=1}^{\infty} \left[\Pi_k^*(1-\epsilon_k)\cos\phi_k \frac{\exp(-\int_0^l \kappa dl)}{\pi l^2}\right] \\ P_w &= \frac{\exp(-\int_0^l \kappa dl)}{\pi l^2}\cos\phi_1' + \sum_{k=2}^{\infty} {}^*\Pi_k^* \\ \Pi_k^* &= \frac{\exp(-\int_0^l \kappa dl}{\pi l^2}\cos\phi_1' \times \left[\prod_{j=1}^{k-1}(1-\epsilon_j)\cos\phi_j'\cos\phi_{j+1}' \frac{\exp(-\int_0^{l_j} \kappa dl)}{\pi l_j^2}\right] \end{aligned}\right\} \tag{6}$$

where the symbol $\Sigma^*$ means that the summaton is taken only for $k$'s that correspond to the heat receiving wall considered.

Here, equations (3) and (4) are constituted assuming that the medium and the walls are gray and that the walls are isotropic and diffuse. These assumptions are not restrictions for the present method. However, only problems with variable properties of constant directional emissive character are considered here. That is, the directions of the radiative rays emit-

Contributed by the Heat Transfer Division for publication in the JOURNAL OF HEAT TRANSFER. Manuscript received by the Heat Transfer Division October 6, 1987. Keywords: Numerical Methods, Radiation.

ted from medium or wall element are not dependent on the other variables.

The following quantities are introduced to facilitate the numerical treatments:

$$\left.\begin{aligned} B_{g0} &= \lambda \nabla^2 T + \Phi - c_p \rho \frac{DT}{Dt} \\ B_{w0} &= -\lambda \nabla T - q_w \end{aligned}\right\} \quad (7)$$

Equations (1) and (2) are rewritten as follows by substituting equations (3), (4), and (7):

$$4\kappa_0 E_{g0} = \int_V \kappa E_g P_{gg} dV + \int_A \epsilon E_w P_{wg} dA + B_{g0} \quad (8)$$

$$\epsilon_0 E_{w0} = \int_V \kappa E_g P_{gw} dV + \int_A \epsilon E_w P_{ww} dA + B_{w0} \quad (9)$$

**Suggested Method.** In general, the Monte Carlo method is not suitable to numerical calculations with iteration because this method requires long computing times to arrive at the solutions. Therefore, the author modified it and obtained a method named the DPE method. By means of this method, the computing time is much shortened and the covergence stability is improved remarkably. However, the method cannot be applied to an iterative calculation in which radiative properties vary at each iterative cycle. In this paper, the author suggests a modified DPE method called the DPEVC method (Differential Emissive Power Emission Method Applied to Variable Property Problems with Constant Directional Emissive Character), which is applicable to problems with variable properties and constant directional emissive characteristics.

The $N$ method (Standard Method Applied to Nonlinear Problems) (Kobiyama et al., 1979) is used at the first iterative cycle or in the first several cycles in the execution of the DPEVC method. Applying the $N$ method, a solution at the $i$th iterative cycle is calculated from the following equations, which are equations (8) and (9) rewritten in the form of an iterative calculation. The 0th value of temperature $T^0$ is given and the $\Phi^i$ and $B^i$ values are calculated using $T^i$ or other dependent variables by some numerical technique such as the finite difference method.

$$4\kappa_0^{i-1} E_{g0}^i = \int_V \kappa^{i-1} E_g^{i-1} P_{gg}^i dV + \int_A \epsilon^{i-1} E_w^{i-1} P_{wg}^i dA + B_{g0}^{i-1} \quad (10)$$

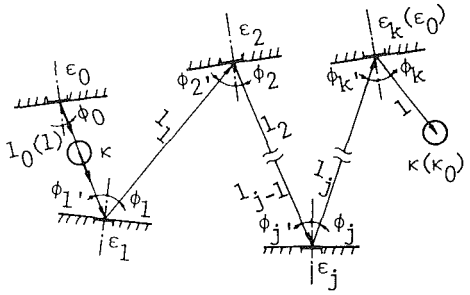


Fig. 1 Coordinate system

$$\epsilon_0^{i-1} E_{w0}^i = \int_V \kappa^{i-1} E_g^{i-1} P_{gw}^i dV + \int_A \epsilon^{i-1} E_w^{i-1} P_{ww}^i dA + B_{w0}^{i-1} \quad (11)$$

where

$$\left.\begin{aligned} B_{g0}^{i-1} &= \lambda^{i-1} \nabla^2 T^{i-1} \Phi^{i-1} - c_p^{i-1} \rho^{i-1} \frac{DT^{i-1}}{Dt} \\ B_{w0}^{i-1} &= -\lambda^{i-1} \nabla T^{i-1} - q_w^{i-1} \end{aligned}\right\} \quad (12)$$

$i \geq 1$

The $P^i$ values are the radiative heat transfer probabilities calculated by the Monte Carlo method through equations (5). During these computations, the radiative heat onto the wall is absorbed in proportion to the emissivity of the wall. This treatment of the absorption of radiative energy differs from those of Howell (1964) and Taniguchi (1967) and is introduced to reduce the use of random numbers and the quantity of radiative energy carried by a radiative bundle. The radiative energy of an emitted bundle $S^i$ is calculated by

$$S^i = [{}_{\text{all}}\Sigma_{\Delta V} 4\kappa^{i-1} E_g^{i-1} \Delta V + {}_{\text{all}}\Sigma_{\Delta A} \epsilon^{i-1} E_w^{i-1} \Delta A]/N_t \quad (13)$$

where $N_t$ is the total number of radiative bundles, and $\Delta V$ and $\Delta A$ are the control element volume and wall element area, respectively. From this equation, the number of bundles emitted from a given control element $N^i$ is calculated by the following equations:

$$\left.\begin{aligned} N_g^i &= 4\kappa^{i-1} E_g^{i-1} \Delta V / S^i \\ N_w^i &= \epsilon^{i-1} E_w^{i-1} \Delta A / S^i \end{aligned}\right\} \quad (14)$$

## Nomenclature

$A$ = total wall area
$\Delta A$ = area of a wall element
$B$ = defined by equation (7)
$C$ = transferred radiative energy, defined by equation (18)
$c_p$ = specific heat at constant pressure
$E$ = emissive power $= \sigma T^4$
$\Delta E$ = difference of emissive power between successive iterative cycles, defined by equation (16)
$k$ = incident or reflected time of a bundle
$l$ = distance
$L$ = traced distance of a bundle
$N$ = the number of bundles emitted from a control element
$N_t$ = total number of bundles
$P$ = radiative heat transfer probability
$q_{in}$ = heat generation rate
$q_R$ = radiative heat flux
$q_w$ = wall heat flux
$S$ = emitted radiative energy of an energy correcting bundle in the DPEVC method; emitted radiative energy of a bundle in the $N$ method
$S^*$ = transferred radiative energy of a energy correcting bundle in the DPEVC method; transferred radiative energy of a bundle in the $N$ method
$s$ = emitted radiative energy of a property correcting bundle
$s^*$ = transferred radiative energy of a property correcting bundle
$t$ = time
$T$ = temperature
$V$ = total volume of the medium
$\Delta V$ = volume of a control element
$y$ = coordinate
$y_0$ = distance between walls
$\Delta Z$ = changing rate of absorption probability, defined by equation (17)
$\epsilon$ = wall emissivity
$\kappa$ = absorption coefficient
$\lambda$ = thermal conductivity
$\rho$ = density
$\sigma$ = Stefan-Boltzmann constant
$\phi, \phi'$ = incident and reflected angles of a radiative ray at a wall
$\Phi$ = rate of heat generation by friction

### Superscripts

$i$ = iterative cycle

### Subscripts

0 = control element
$f$ = medium (flame)
$g$ = medium (gas)
$w$ = wall

The radiative energy transported to the medium or the wall $S^{*i}$ is calculated by the following equations:

$$\left.\begin{aligned} S_g^{*i} &= S^i\left[\prod_{j=1}^{k}(1-\epsilon_j^{i-1})\right] \\ S_w^{*i} &= \sum_{k'=1}^{k}{}^{*}\left\{S^i\left[\prod_{j=1}^{k'}(1-\epsilon_j^{i-1})\right]\right\} \end{aligned}\right\} \tag{15}$$

For the first several cycles, the iterative calculation is performed by the $N$ method described above. Thereafter, the DPEVC method is used.

In describing the DPEVC formation, the quantities $\Delta E$ and $\Delta Z$ are defined as

$$\Delta E_g^i = \kappa^{i-1}E_g^{i-1} - \kappa^{i-2}E_g^{i-2} \tag{16a}$$

$$\Delta E_w^i = \epsilon^{i-1}E_w^{i-1} - \epsilon^{i-2}E_w^{i-2} \tag{16b}$$

$$\Delta Z_{gg}^i = 1 - P_{gg}^{i-1}/P_{gg}^i \tag{17a}$$

$$\Delta Z_{wg}^i = 1 - P_{wg}^{i-1}/P_{wg}^i \tag{17b}$$

$$\Delta Z_{gw}^i = 1 - P_{gw}^{i-1}/P_{gw}^i \tag{17c}$$

$$\Delta Z_{ww}^i = 1 - P_{ww}^{i-1}/P_{ww}^i \tag{17d}$$

$$i \geq 2$$

The radiative energy transferred $C^i$ is calculated by the following equations using $\Delta E^i$, $\Delta Z^i$, and $P^i$.

$$\left.\begin{aligned} C_{g0}^i = C_{g0}^{i-1} &+ \int_V (\Delta E_g^i + \kappa^{i-2}E_g^{i-2}\Delta Z_{gg}^i)P_{gg}^i dV \\ &+ \int_A (\Delta E_w^i + \epsilon^{i-2}E_w^{i-2}\Delta Z_{wg}^i)P_{wg}^i dA \\ C_{w0}^i = C_{w0}^{i-1} &+ \int_V (\Delta E_g^i + \kappa^{i-2}E_g^{i-2}\Delta Z_{gw}^i)P_{gw}^i dV \\ &+ \int_A (\Delta E_w^i + \epsilon^{i-2}E_w^{i-2}\Delta Z_{ww}^i)P_{ww}^i dA \end{aligned}\right\} \tag{18}$$

$$i \geq 2$$

The values of the first term in the parentheses on the right-hand side of equations (18) are calculated just as in the $N$ method, except that the number of radiative bundles is proportional to $\Delta E$ given by equations (16); this kind of bundle is called an energy correcting bundle because the quantities of emissive power emitted at each iterative cycle are corrected with these bundles. For the calculation of the second term, the radiative bundle and the quantities involved in $\Delta Z$ are used; this kind of bundle is called a property correcting bundle because the values of the radiative properties used at each iterative cycle are corrected with these bundles. Equations (8) and (9) are rewritten as the following equations by means of equations (18):

$$4\kappa_0^{i-1}E_{g0}^i = C_{g0}^i + B_{g0}^{i-1} \tag{19}$$

$$\epsilon_0^{i-1}E_{w0}^i = C_{w0}^i + B_{w0}^{i-1} \tag{20}$$

The temperatures or the emissive powers of the control element at the $i$th iterative cycle are calculated by equations (19) and (20) after the integration are performed over the region considered. Furthermore, from equations (16)–(18), it is clear that if the radiative properties are not affected by the iteration cycle, that is $P^i = P^{i-1}$, then the relation $\Delta Z = 0$ is satisfied and the DPEVC method is reduced to the DPE method.

The radiative energy of the energy correcting bundle $S^i$ is defined by the following equation:

$$S^1 = \left[\sum_{\text{all }\Delta V} 4\kappa^0 E^0 \Delta V + \sum_{\text{all }\Delta A} \epsilon^0 E^0 \Delta A\right]/N_t \tag{21}$$

$$S^i = S^{i-1} \tag{22}$$

$$i \geq 2$$

The number of radiative bundles $N^i$ assigned to each element is calculated by the following equation, which is deduced from equations (22) and (16):

$$\left.\begin{aligned} N_g^i &= |\Delta E_g^i|\Delta V/S^i \\ N_w^i &= |\Delta E_w^i|\Delta A/S^i \end{aligned}\right\} \tag{23}$$

where $S^i$ takes the following values according to the sign of $\Delta E^i$:

$$\left.\begin{aligned} \Delta E^i \geq 0 &: \quad S^i = |S^i| \\ \Delta E^i < 0 &: \quad S^i = -|S^i| \end{aligned}\right\} \tag{24}$$

The radiative heat transferred by an energy correcting radiative bundle is calculated from equation (15).

Next, consider the property correcting bundles. In the Monte Carlo method, the most time-consuming steps are those that trace the radiative bundles and generate the random numbers. Thus the number of property correcting bundles is set to the same value as the number of energy correcting bundles. In addition, the property correcting bundles trace the same geometric trajectories as does the energy correcting bundle in order to avoid overlap in the use of bundles and to reduce the computing time. That is to say, the calculations of $\Delta Z^i$ are done in accordance with those of $P^i$. When a radiative bundle is reflected $k$ times until it is absorbed, $\Delta Z^i$ is given as follows:

$$\left.\begin{aligned} \Delta Z_{gg}^i &= 1 - \frac{\kappa_0^{i-2}Z_g^{i-2}}{\kappa_0^{i-1}Z_g^{i-1}} \\ \Delta Z_{wg}^i &= 1 - \frac{\kappa_0^{i-2}\cos\phi_0^{i-2}Z_g^{i-2}}{\kappa_0^{i-1}\cos\phi_0^{i-1}Z_g^{i-1}} \\ \Delta Z_{gw}^i &= 1 - \frac{\epsilon_0^{i-2}Z_w^{i-2}}{\epsilon_0^{i-1}Z_w^{i-1}} \\ \Delta Z_{ww}^i &= 1 - \frac{\epsilon_0^{i-2}\cos\phi_0^{i-2}Z_w^{i-2}}{\epsilon_0^{i-1}\cos\phi_0^{i-1}Z_w^{i-1}} \end{aligned}\right\} \tag{25}$$

where

$$\left.\begin{aligned} Z_g^i &= \left[\prod_{j=1}^{k}\{(1-\epsilon_j^i)\cos\phi_j^i\cos\phi_j'^i/\pi(l_{j-1}^i)^2\}\right] \\ &\quad\times\left[\exp\left(-\int_0^{L^i}\kappa^i dl\right)\Big/\pi(L^i)^2\right] \\ Z_w^i &= \left[\prod_{j=1}^{k'-1}\{(1-\epsilon_j^i)\cos\phi_j^i\cos\phi_j'^i/\pi(l_{j-1}^i)^2\}\right] \\ &\quad\times\left[\cos\phi_{k'}\exp\left(-\int_0^{L_{k'-1}^i}\kappa^i dl\right)\Big/\pi(L_{k'-1}^i)^2\right] \end{aligned}\right\} \tag{26}$$

$L^i$ indicates the total length of the locus of the radiative bundle absorbed by the medium, and $L_{k'-1}^i$ that locus to the $(k'-1)$th incident on the wall. In the DPEVC method, the geometrical loci of the radiative bundles at the $(i-1)$th iteration cycle are the same as those of the $i$th. However the properties along those loci take different values between $i$th and $(i-1)$th. That is, $l^{i-2}$, $\phi^{i-2}$ and $\phi'^{i-2}$ take the same values as $l^{i-1}$, $\phi^{i-1}$, and $\phi'^{i-1}$. The second terms on the right-hand sides of equations (25) are then written as follows:

$$\left.\begin{aligned}
\Delta Z_g^i &= \Delta Z_{gg}^i = \Delta Z_{wg}^i \\
&= 1 - \left(\frac{\kappa_0^{i-2}}{\kappa_0^{i-1}}\right)\left[\prod_{j=1}^{k}\frac{(1-\epsilon_j^{i-2})}{(1-\epsilon_j^{i-1})}\right] \\
&\quad \times \exp\left[-\int_0^L (\kappa^{i-2}-\kappa^{i-1})dl\right] \\
\Delta Z_w^i &= \Delta Z_{gw}^i = \Delta Z_{ww}^i \\
&= 1 - \left(\frac{\epsilon_0^{i-2}}{\epsilon_0^{i-1}}\right)\left[\prod_{j=1}^{k'-1}\frac{(1-\epsilon_j^{i-2})}{(1-\epsilon_j^{i-1})}\right] \\
&\quad \times \exp\left[-\int_0^{L_{k'-1}} (\kappa^{i-2}-\kappa^{i-1})dl\right]
\end{aligned}\right\} \quad (27)$$

When the energy of a bundle $s^i$ is expressed by equations (28), the quantities of the heat transferred to the medium and wall by the property correcting bundle $s^{*i}$ is expressed by equations (29):

$$\left.\begin{aligned}
s_g^i &= \kappa^{i-2}E_g^{i-2}\Delta V/N_g^i \\
s_w^i &= \epsilon^{i-2}E_w^{i-2}\Delta A/N_w^i
\end{aligned}\right\} \quad (28)$$

$$\left.\begin{aligned}
s_g^{*i} &= s_g^i\left[\prod_{j=1}^{k}(1-\epsilon_j^{i-1})\right]\Delta Z_g^i \\
s_w^{*i} &= \sum_{k'=1}^{k} {}^{*}\left\{s_w^i\left[\prod_{j=1}^{k'}(1-\epsilon_j^{i-1})\right]\Delta Z_w^i\right\}
\end{aligned}\right\} \quad (29)$$

To simplify the discussion of the proof of the equivalence of the DPEVC method with the $N$ method, the following quantities are introduced:

$$C_{gg0}^i = C_{gg0}^{i-1} + \int_V (\Delta E_g^i + \kappa^{i-2}E_g^{i-2}\Delta Z_g^i)P_{gg}^i dV \quad (30a)$$

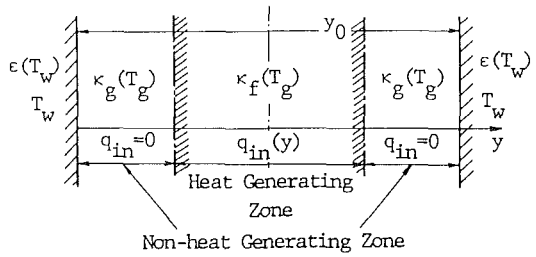


**Fig. 2 Heat transfer model with internal heat generation**

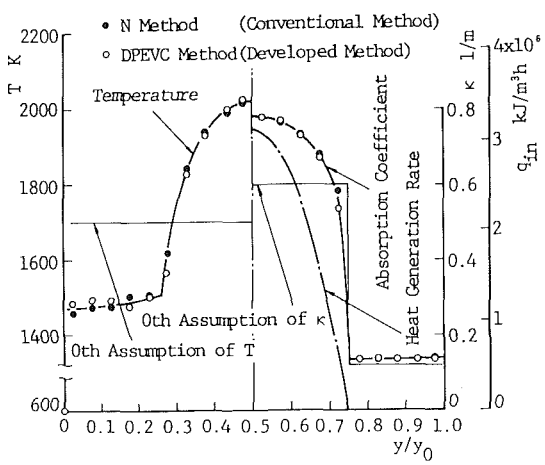


**Fig. 3 Temperature distribution and values used in the calculation**

$$C_{wg0}^i = C_{wg0}^{i-1} + \int_A (\Delta E_w^i + \epsilon^{i-2}E_w^{i-2}\Delta Z_g^i)P_{wg}^i dA \quad (30b)$$

$$C_{gw0}^i = C_{gw0}^{i-1} + \int_V (\Delta E_g^i + \kappa^{i-2}E_g^{i-2}\Delta Z_w^i)P_{gw}^i dV \quad (30c)$$

$$C_{ww0}^i = C_{ww0}^{i-1} + \int_A (\Delta E_w^i + \epsilon^{i-2}E_w^{i-2}\Delta Z_w^i)P_{ww}^i dA \quad (30d)$$

Then, equations (18) can be rewritten as follows:

$$\left.\begin{aligned}
C_{g0}^i &= C_{gg0}^i + C_{wg0}^i \\
C_{w0}^i &= C_{gw0}^i + C_{ww0}^i
\end{aligned}\right\} \quad (31)$$

Here, for example, the following equation can be deduced from the expansion of equation (30$a$) using equations (16$a$) and (17$a$):

$$\begin{aligned}
C_{gg0}^i &= \\
&\int_V (\Delta E_g^i + \kappa^{i-2}E_g^{i-2}\Delta Z_{gg}^i)P_{gg}^i dV \\
&+ \int_V (\Delta E_g^{i-1} + \kappa^{i-3}E_g^{i-3}\Delta Z_{gg}^{i-1})P_{gg}^{i-1} dV \\
&+ \ldots + \int_V (\Delta E_g^2 + \kappa^0 E_g^0 \Delta Z_{gg}^2)P_{gg}^2 dV + \int_V \kappa^0 E_g^0 P_{gg}^1 dV \\
&= \int_V \kappa^{i-1}E_g^{i-1}P_{gg} dV \\
&+ \int_V (\kappa^{i-2}E_g^{i-2}P^{i-1} - \kappa^{i-2}E_g^{i-2}P_{gg}^i + \kappa^{i-2}E_g^{i-2}\Delta Z_{gg}^i]dV \\
&+ \ldots + \int_V (\kappa^0 E_g^0 P_{gg}^1 - \kappa^0 E_g{}^0 P_{gg}^0 + \kappa^0 E_g^0 \Delta Z_{gg}^2 P_{gg}^2)dV \\
&= \int_V \kappa^{i-1}E_g^{i-1}P_{gg}^i dV \\
&+ \sum_{i'=2}^{i}\left\{\int_V [\kappa^{i'-2}E_g^{i'-2}(P_{gg}^{i'-1}/P_{gg}^{i'} - 1 + \Delta Z_{gg}^{i'})P_{gg}^{i'} dV]\right\} \quad (32)
\end{aligned}$$

From equation (17$a$), the second term on the right-hand side of equation (32) becomes zero. Therefore, equation (32) reduces to

$$C_{gg0}^i = \int_V \kappa^{i-1}E_g^{i-1}P_{gg}^i dV \quad (33a)$$

Similarly, equations (30$b$)–(30$d$) are rewritten as follows:

$$C_{wg0}^i = \int_A \epsilon^{i-1}E_w^{i-1}P_{wg}^i dA \quad (33b)$$

$$C_{gw0}^i = \int_V \kappa^{i-1}E_g^{i-1}P_{gw}^i dV \quad (33c)$$

$$C_{ww0}^i = \int_A \epsilon^{i-1}E_w^{i-1}P_{ww}^i dA \quad (33d)$$

By the substition of equations (33) into equations (31), the following equations are obtained:

$$\left.\begin{aligned}
C_{g0}^i &= \int_V \kappa^{i-1}E_g^{i-1}P_{gg}^i dV + \int_A \epsilon^{i-1}E_w^{i-1}P_{wg}^i dA \\
C_{w0}^i &= \int_V \kappa^{i-1}E_g^{i-1}P_{gw}^i dV + \int_A \epsilon^{i-1}E_w^{i-1}P_{ww}^i dA
\end{aligned}\right\} \quad (34)$$

Substituting equations (34) into equations (19) and (20), it is made clear that the solution by the DPEVC method coincides with that by the conventional $N$ method.

The DPEVC method has a larger memory requirement of

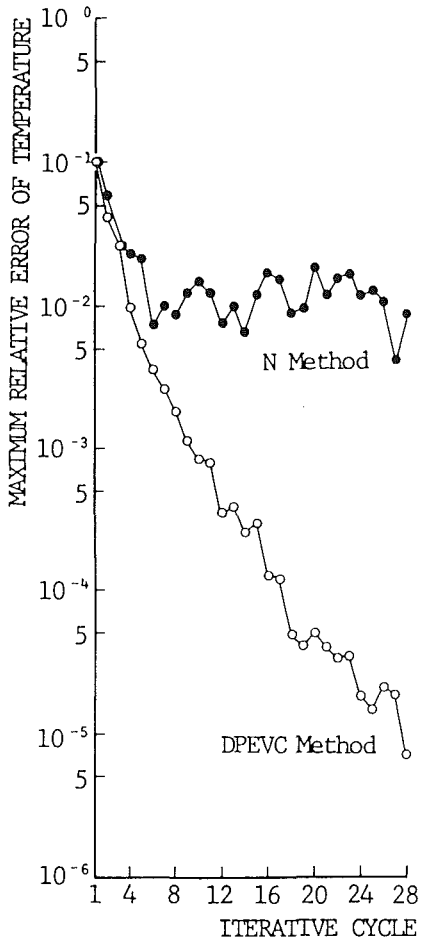


Fig. 4 Convergence of the maximum relative error of temperature

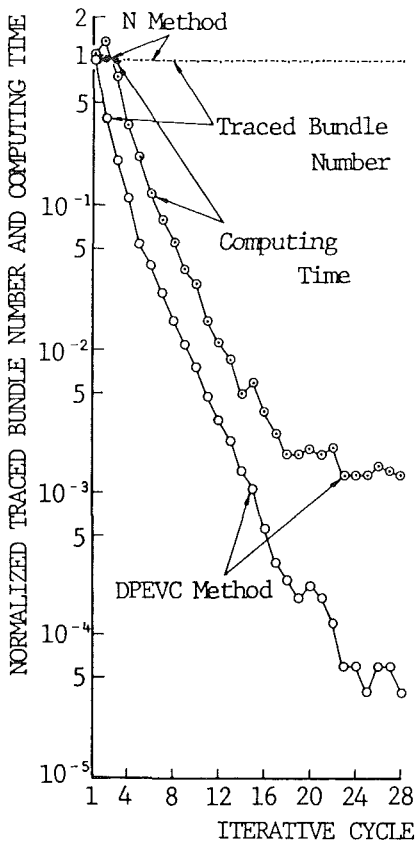


Fig. 5 Traced bundle number and computing time

the computer than the $N$ method for variables $E^{i-2}$ and $C^i$, defined by equations (16) and (18), respectively.

## 3 Example of the Application of the DPEVC Method

A one-dimensional heat transfer model with internal heat generation, shown in Fig. 2, is considered here to exhibit the reduction of the computing time and the improvement of the convergence stability by the DPEVC method. In this model, a radiative medium fills the space between two parallel plates with infinite length, and heat generating zone is placed in the center of the medium.

It is assumed that the medium is gaseous and gray with respect to thermal radiative properties. The value of the absorption coefficient at a particular location depends on whether heat generation is present or not. It is also assumed that the walls are isothermal and diffuse. The system is at steady state and convection, conduction, and energy dissipation can be ignored. Substitution of these conditions into equations (1) and (2) leads to the following energy equations:

$$q_{in} - \text{div}\, \mathbf{q}_{Rg} = 0 \tag{35}$$

$$q_w + q_{Rw} = 0 \tag{36}$$

where $-\text{div}\mathbf{q}_{Rg}$ and $-q_{Rw}$ are obtained from the transformation of equations (3) and (4) into one-dimensional forms. Although there are many functions proposed for the temperature dependence of the radiative absorption coefficient $\kappa$ and the emissivity $\epsilon$, in this paper the following functions are employed:

$$\left.\begin{aligned} &\text{Heat generating zone:} && \kappa_f = 0.5(T_g/1500)^{1.5}\ \text{m}^{-1} \\ &\text{Non-heat generating zone:} && \kappa_g = 0.2(T_g/1000)^{-1}\ \text{m}^{-1} \\ &\text{Wall:} && \epsilon = 0.8(T_w/600)^{0.1} \end{aligned}\right\} \tag{37}$$

The heat generation is described by a parabolic distribution with the maximum value at the center point between the two parallel plates and a value of zero at the interfaces of the heat generating and non-heat generating zones as shown in Fig. 3. The mean value of the heat generating rate is $2.09\times10^6$ kJ/(m$^3$h) [$5\times10^5$ kcal/(m$^3$h)], the wall temperature 600 K, the distance between the two plates $y_0 = 1$ m, the total number of elements in the medium $n = 20$, the total number of radiative bundles $N_t = 10^5$ and the criterion of convergence $10^{-5}$. Here, the maximum value of the relative error of the temperature in each iterative cycle $|T^i - T^{i-1}|/T^i$ is used as the criterion of convergence for this iterative calculation. The solutions by the methods used in this paper were verfied by comparison with the solutions by Usiskin (1960) for constant radiative properties and heat generation rate, and with the solutions by Taniguchi (1967), which took into account wave dependence of the radiative absorption coefficient and the wall emissivity.

The temperature distribution calculated is shown in the left half of Fig. 3. The distribution of temperature by the $N$ method is the result of the 28th iterative cycle at which the iterative solution by the DPEVC method is considered to converge. Although the probability calculations exhibit some peculiar values in the region near the wall, the solutions of DPEVC method generally agree with those of the $N$ method, irrespective of the presence of heat generation. Figure 3 also show the 0th profiles of the temperature and radiative absorption coefficient.

The maximum value of the relative error of the temperature

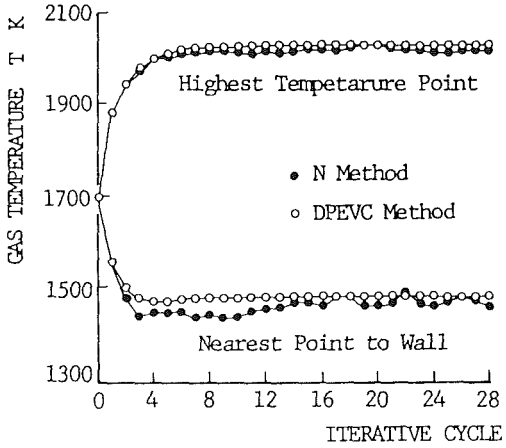


**Fig. 6 Convergence of temperature**

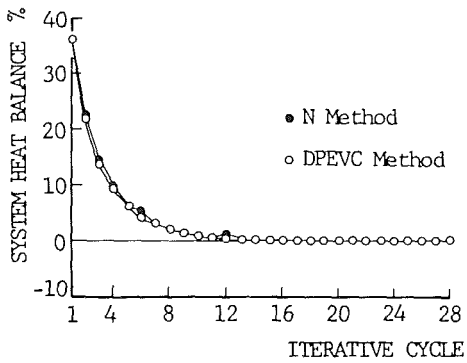


**Fig. 7 Convergence of the heat balance**

in each iterative cycle is shown in Fig. 4. Because the relative error corresponding to the $N$ method suffers oscillatory behavior in the vicinity of $10^{-2}$, which is a prescribed value by the law of large numbers and is in inverse proportional to $\sqrt{N_t}$, as the iterative cycle advances. Thus the $N$ method does not seem to be applicable to numerical analyses that requires higher convergence accuracy. The convergence process of the relative error in the DPEVC method is very smooth and stable even if the same value of a radiative bundle energy as used in the $N$ method is applied. In the DPEVC method, integration terms in equation (18), which are composed of $\Delta E$ and $\Delta Z$, are calculated at each iteration cycle by the Monte Carlo method. When the iteration advances, $\Delta E$ and $\Delta Z$ take smaller values as shown in equation (17) and the quantities of the integration terms become much smaller than $C^{i-1}$. Accordingly, the convergence by the DPEVC method is smooth and the relative error converges below $10^{-2}$ as shown in Fig. 4.

In Fig. 5, the number of the traced bundles and the computing time at each iterative cycle are shown in the form of the ratio to the mean values of those in the $N$ method. In the DPEVC method, the number of traced bundles decrease roughly as an exponential function with the advance of iterative cycles and this value becomes less than 1/1000 of its initial size at the 16th iterative cycle. The decrease in computing time is directly related to the decrease in the number of traced bundle. At the second iterative cycle, the computing time for the DPEVC method increases in spite of the decrease of the traced bundle number. This is because one radiative bundle in the DPEVC method does double tasks in energy and property correction. Therefore, the computing time of the DPEVC method can be reduced by using the $N$ method at the second iterative cycle too. For the result shown in Fig. 5, the total computing time for radiative heat transfer by the DPEVC method is less than 15 percent of that by the $N$ method.

The convergence of the temperature at different zones is shown in Fig. 6. At the highest temperature zone, the convergence of the $N$ method is smooth and shows the same behavior as that of the DPEVC method. But at the lower temperature zone, the $N$ method solution reveals a peculiar oscillation in the probability calculation. This is because the number of radiative bundles absorbed in the lower temperature region is proportional to the absolute value of the emissive power in the case of the $N$ method. Thus the bundle number absorbed is typically small. However, in the case of the DPEVC method, the number of absorbed bundles is proportional to the difference of the emissive powers and such a peculiar oscillation absent in the same manner as the result shown in Fig. 4. This stability of convergence is an excellent feature of the DPEVC method and allows the method to be easily applied to multidimensional problems even when the total radiative bundle number is small.

In Fig. 7, the convergence of the system heat balance, $\sum_{\text{all } \Delta A} q_w \Delta A / \sum_{\text{all } \Delta V} q_{in} \Delta V$, is shown. In this example, the stability of convergence seems to be satisfactory for the $N$ method because many radiative bundles are used.

From the above discussion, it is clear that the DPEVC method performs well with respect to stability of convergence and reduction of computing times. These features of the DPEVC method would be of value in numerically solving a system of simultaneous equations composed of the momentum equation of complex flow, the energy equation including radiative heat transfer, etc.

## 4 Conclusions

In this paper, a modified Monte Carlo method is presented that reduces the calculating time and improves the convergence stability of the conventional method, while retaining other excellent features of the Monte Carlo method such as flexibility for easy application to the numerical analysis of problems with variable thermal properties and complex geometries. In this method, the number of radiative bundle emitted from a control element and transferred by probabilistic means is proportional to the difference of the emissive powers of two successive iterative cycles. Those same radiative bundles correct the radiative properties at each iterative cycle.

An application example of the method demonstrates the reduction of calculation time and the improvement in convergence stability. This method can be of great utility in numerically solving heat transfer problems where radiation is combined with the other heat transfer mechanisms or where the radiative properties depend on other variables.

## References

Howell, J. R., and Perlmutter, M., 1964, "Monte Carlo Solution of Thermal Transfer Through Radiant Media Between Gray Walls," ASME JOURNAL OF HEAT TRANSFER, Vol. 86, pp. 116–122.

Kobiyama, M., et al., 1979, "The Numerical Analysis of Heat Transfer Combined With Radiation and Convection," *Bull. of JSME*, Vol. 122, No. 167, pp. 707–714.

Taniguchi, H., 1967, "Temperature Analysis on Radiative Gas by the Monte Carlo Method," *Journal of JSME*, Vol. 33, No. 247, pp. 406–419.

Usiskin, C. M., and Sparrow, E. M., 1960, "Thermal Radiation Between Parallel Plates Separated by an Absorbing-Emitting Nonisothermal Gas," *Int. Journal Heat Mass Transfer*, Vol. 1, pp. 28–36.

# Radiative Heat Transfer in Multidimensional Emitting, Absorbing, and Anisotropic Scattering Media—Mathematical Formulation and Numerical Method

**Zhiqiang Tan**[1]
Department of Thermal Engineering,
Northeast University of Technology,
Shenyang, People's Republic of China

*Thermal radiative transmission in multidimensional emitting, absorbing, and anisotropic scattering media is studied in this paper. In the first part, starting from basic formulae of radiative heat transfer, a set of integral equations for the problem is derived. Then the product-integration method is applied to discretize the integral equations. This method, while analogous to Hottel's zonal method or Razzaque's finite element method, requires evaluation of only three or two-dimensional integrals for three-dimensional systems. Finally the formulation and the numerical technique are applied to the problems of thermal radiation in emitting, absorbing, and linearly anisotropic scattering planar and square media with gray surfaces and with or without internal heat generations. Computed results are discussed and compared with available data.*

## 1 Introduction

Radiation heat transfer in absorbing, emitting, and scattering media plays an important role in engineering. Some applications are in boilers and industrial furnaces, rocket propulsion, plasma generators for nuclear fusion, and so on. In recent years, much attention has been paid to numerical solution of radiation in multidimensional participating media and radiation with anisotropic scattering.

For multidimensional radiation transfer, most works are related to non-scattering or isotropic scattering problem. Of all the numerical methods, the zonal method (Hottel and Cohen, 1958) and the finite element method (Razzaque et al., 1984) give good results, and the former has been widely used in multidimensional problems. Unfortunately, these methods often need to compute many six, five, and four-dimensional integrals for three-dimensional problems. This is quite time consuming and thus restricts their use. The Monte Carlo technique (Taniguchi, 1969), despite its flexibility to deal with complex problems, is also a time-consuming method and can be inaccurate under certain conditions. The *P-N* approximation (Ratzel and Howell, 1983), which may not encompass both accuracy and simplicity, does not apply well to general problems. The point allocation method was applied by Yuen and Wong (1984) to radiation transfer in an absorbing and emitting rectangular medium. Because it requires evaluation of integrals of only three or two dimensions for three-dimensional problems, this method generates results rapidly. However, as is known, the point allocation method using a polynomial approximation may become unstable at higher orders (see, e.g., Szidarovszky and Yakowitz, 1978; or Baker, 1977), and thus may not apply to complex geometries. Another technique, which solves the original integro-differential transport equation, is the discrete-ordinates method (Fiveland, 1984). For problems in which scattering is dominant, this method works very well, but errors may arise if it is applied to absorption-dominated problems due to the "ray effect" (Lathrop, 1968).

For anisotropic scattering radiation, because of the complexity of this problem, most of the previous works are concerned with one-dimensional problems (see, e.g., Dayan and Tien, 1975; Modest and Azad, 1980; Boffi and Spiga, 1977; Beach et al., 1971). The methods presented in the literature are often hard to apply to multidimensional problems with anisotropic scattering.

In this paper, the mathematical formulation and the related numerical method for general multidimensional radiation in absorbing, emitting, and anisotropic scattering media will be studied. It contains three parts. In the first the thermal radiation transmission problem shall be represented by a set of integral equations. In the second part of this study, an efficient numerical method to discretize those equations is to be applied. Finally, the formulation and numerical method will be applied to problems of radiation in one and two-dimensional participating media, including linearly-anisotropic scattering and gray surface reflecting. Some of the results will be compared with available data.

## 2 Mathematical Formulation

The system considered is an absorbing, emitting, and scattering medium $\Omega$, which is bounded by a gray and diffusely reflecting enclosure $\partial\Omega$ (Fig. 1). For simplicity, it is assumed that the radiant properties, the absorption coefficient $a$, the scattering coefficient $\sigma$, and the emissivity of the enclosure $\epsilon$ are constants. The $\partial\Omega$ is assumed to be convex; that is, there is no radiation shade by the surface in the system. Another assumption is that the scattering in the medium can be described by Mie's theory, so that its phase function $\phi$ can be expressed as (Chu and Churchill, 1955)

$$\phi(\omega, \omega') = \sum_{n=0}^{N} a_n P_n(\omega \cdot \omega') \tag{1}$$

[1]Present address: Department of Mechanical Engineering, The University of Texas at Austin, Austin, TX 78712.

Contributed by the Heat Transfer Division for publication in the JOURNAL OF HEAT TRANSFER. Manuscript received by the Heat Transfer Division June 12, 1986. Keywords: Numerical Methods, Radiation.

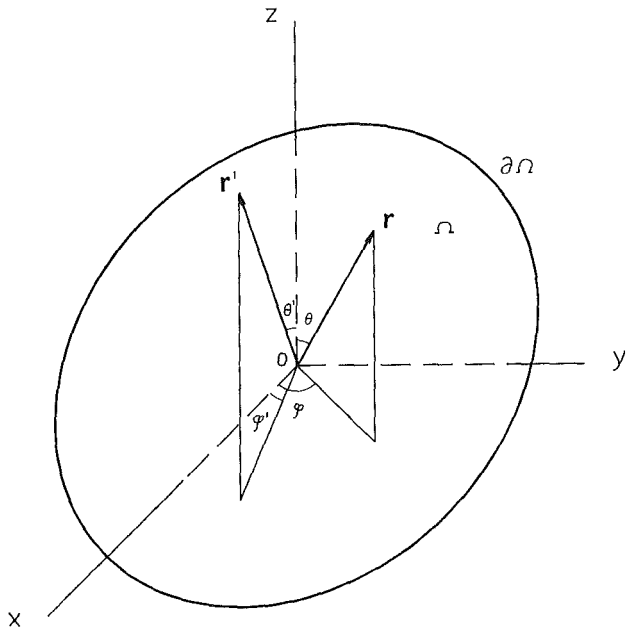


**Fig. 1 Geometry for derivative of the integral equations**

where $a_n$ ($n=0, 1, \ldots, N$) are constants with $a_0=1$, and the $P_n$ are Legendre polynomials.

Using the addition theorem for Legendre functions (see Gradshteyn and Ryzhik, 1980), equation (1) can be rearranged as

$$\phi(\omega, \omega') = \sum_{k=0}^{M} \beta_k S_k(\omega)\, S_k(\omega') \tag{2}$$

where $M=N(N+2)$, $\beta_k$ is a constant, and $S_k$ is a function of the form $P_n^m(\cos\theta)\cos m\varphi$ or $P_n^m(\cos\theta)\sin m\varphi$. For example, $\beta_0=1$, $\beta_1=\beta_2=\beta_3=a_1$ and $S_0(\omega)=1$, $S_1(\omega)=\sin\theta\cos\varphi$, $S_2(\omega)=\sin\theta\sin\varphi$, $S_3(\omega)=\cos\theta$.

Now substituting equation (2) into the radiant transfer equation (Siegel and Howell, 1981) yields

$$\frac{di(\mathbf{r}, \omega)}{ds} = -ki(\mathbf{r}, \omega) + ai_b(\mathbf{r}) + \frac{\sigma}{4\pi}\sum_{k=0}^{M} \beta_k S_k(\omega)\, w_k(\mathbf{r}) \tag{3}$$

where $w_k$ is defined by

$$w_k(\mathbf{r}) = \int_{\omega=4\pi} S_k(\omega)\, i(\mathbf{r}, \omega)\, d\omega \tag{4}$$

When $k=0$, 1, 2, and 3, the $w_k$ have the physical significances that $w_0$ is the integrated intensity, and $w_1$, $w_2$, $w_3$ are the radiation fluxes in the $x$, $y$, and $z$ directions in the Cartesian coordinate system, respectively, i.e.,

$$w_0 = \int_{\omega=4\pi} i(\mathbf{r}, \omega)\, d\omega, \quad w_1 = q_{rx}, \quad w_2 = q_{ry}, \quad w_3 = q_{rz}$$

Integrating the equation of radiant transfer with respect to $\omega$ over $\omega = 0-4\pi$ gives

$$\nabla\cdot\mathbf{q}_r(\mathbf{r}) = -a\int_{4\pi} i(\mathbf{r}, \omega)\, d\omega + 4ae_g(\mathbf{r})$$

$$= a[4e_g(\mathbf{r}) - w_0(\mathbf{r})] \tag{5}$$

Equation (3) has the solution

$$i(\mathbf{r}, \omega) = i(\mathbf{r}', \omega)e^{-k|\mathbf{r}-\mathbf{r}'|} + \int_0^{|\mathbf{r}-\mathbf{r}'|} e^{-kt}\left[ai_b(\mathbf{r}_t) + \frac{\sigma}{4\pi}\sum_{k=0}^{M}\beta_k S_k(\omega)\, w_k(\mathbf{r}_t)\right] dt \tag{6}$$

where $\mathbf{r}_t = \mathbf{r} - t(\mathbf{r}-\mathbf{r}')/|\mathbf{r}-\mathbf{r}'|$.

Take $\mathbf{r}'$ to be on $\partial\Omega$. Because $\partial\Omega$ is gray and reflects diffusely, its outgoing intensity is independent of direction and thus $i(\mathbf{r}', \omega) = i_o(\mathbf{r}')$. Multiplying equation (6) by $S_i(\omega)$ ($i=0$, 1,. . ., $M$) and integrating it over $4\pi$ solid angles gives

$$w_i(\mathbf{r}) = a\iiint_\Omega \frac{e^{-k|\mathbf{r}-\mathbf{r}'|}}{|\mathbf{r}-\mathbf{r}'|^2} i_b(\mathbf{r}')\, S_i(\omega)\, dV(\mathbf{r}') + \frac{\sigma}{4\pi}\sum_{k=0}^{M}\beta_k \iiint_\Omega \frac{e^{-k|\mathbf{r}-\mathbf{r}'|}}{|\mathbf{r}-\mathbf{r}'|^2} \times w_k(\mathbf{r}')\, S_k(\omega)\, S_i(\omega)\, dV(\mathbf{r}') + \iint_{\partial\Omega} \frac{e^{-k|\mathbf{r}-\mathbf{r}'|}}{|\mathbf{r}-\mathbf{r}'|^2} i_0(\mathbf{r}')\, S_i(\omega)\cos(\mathbf{r}-\mathbf{r}', \mathbf{n}')\, dA(\mathbf{r}'),$$

$$i=0, 1, \ldots, M, \quad \mathbf{r}\in\partial\Omega \tag{7}$$

after some mathematical manipulations. In the equation, $\omega = (\mathbf{r}-\mathbf{r}')/|\mathbf{r}-\mathbf{r}'|$.

## Nomenclature

- $a$ = absorption coefficient
- $a_n$ = coefficient in the scattering phase function expansion (equation (1))
- $e_g$ = radiative emissive power of medium
- $e_s$ = radiative emissive power of enclosure
- $i$ = radiation intensity
- $i_b$ = intensity of blackbody
- $k$ = extinction coefficient = $a+\sigma$
- $K$ = function defined by equation (11)
- $\mathbf{n}$, $\mathbf{n}'$ = inward unit normal vectors at $\mathbf{r}$ and $\mathbf{r}'$, respectively
- $P_n$ = Legendre polynomial
- $P_n^m$ = associated Legendre function
- $\mathbf{q}_r$ = radiation flux vector
- $q_s$ = heat flux on $\partial\Omega$
- $\mathbf{r}$ = position vector
- $s$ = coordinate along path of radiation
- $u_i$, $v_i$ = interpolating functions in $\Omega$ and on $\partial\Omega$, respectively
- $w_k$ = function defined by equation (4)
- $x, y, z$ = coordinates in Cartesian system
- $\epsilon$ = emissivity
- $\theta, \varphi$ = polar and azimuth angles in spherical coordinate system
- $\sigma$ = scattering coefficient
- $\tau_o$ = optical thickness
- $\phi$ = scattering phase function
- $\omega$ = solid angle
- $\boldsymbol{\omega}$ = direction vector
- $\omega_o$ = albedo for scattering
- $\Omega$ = medium
- $\partial\Omega$ = boundary of $\Omega$

**Subscripts**

- $i$ = incident; incoming
- $o$ = outgoing
- $(\bullet)_i$ = the value of $\bullet$ at node $\mathbf{r}=\mathbf{r}_i$

Similarly, note that

$$q_i(\mathbf{r}) = \int_{2\pi} i\,(\mathbf{r},\,\omega)\cos\,(\omega,\,\mathbf{n})\,d\omega, \quad \mathbf{r}\in\partial\Omega \tag{8}$$

where $q_i$ is the incident heat flux on the boundary. After taking $\mathbf{r}\in\partial\Omega$, multiplying equation (6) by cos $(\omega, \mathbf{n})$ and integrating it over $\omega = 0-2\pi$, one obtains the following equation:

$$q_i(\mathbf{r}) = a\iiint_\Omega \frac{e^{-k|\mathbf{r}-\mathbf{r}'|}}{|\mathbf{r}-\mathbf{r}'|^2}\, i_b\,(\mathbf{r}')\cos\,(\mathbf{r}'-\mathbf{r},\,\mathbf{n})\,dV\,(\mathbf{r}')$$

$$+\frac{\sigma}{4\pi}\sum_{k=0}^{M}\beta_k\iiint_\Omega \frac{e^{-k|\mathbf{r}-\mathbf{r}'|}}{|\mathbf{r}-\mathbf{r}'|^2}$$

$$\times w_k\,(\mathbf{r}')\,S_k\,(\omega)\cos\,(\mathbf{r}'-\mathbf{r},\,\mathbf{n})\,dV\,(\mathbf{r}')$$

$$+\iint_{\partial\Omega}\frac{e^{-k|\mathbf{r}-\mathbf{r}'|}}{|\mathbf{r}-\mathbf{r}'|^2}\, i_o\,(\mathbf{r}')$$

$$\cos\,(\mathbf{r}'-\mathbf{r},\,\mathbf{n})\cos\,(\mathbf{r}-\mathbf{r}',\,\mathbf{n}')\,dA\,(\mathbf{r}'),\ \mathbf{r}\in\partial\Omega \tag{9}$$

Now, because

$$i_b = \frac{1}{\pi}\,e_g$$

$$w_0 = 4e_g - \frac{1}{a}\,\nabla\cdot\mathbf{q}_r$$

$$i_o = \frac{1}{\pi}\left(e_s - \frac{1-\epsilon}{\epsilon}\,q_s\right)$$

and

$$q_i = \pi i_o - q_s = e_s - \frac{1}{\epsilon}\,q_s$$

equations (7) and (9) can be rewritten as

$$4e_g(\mathbf{r}) - \frac{1}{a}\,\nabla\cdot\mathbf{q}_r\,(\mathbf{r}) = \iiint_\Omega K(\mathbf{r},\,\mathbf{r}')$$

$$\times\left[ke_g\,(\mathbf{r}') - \frac{\sigma}{4a}\nabla\cdot\,\mathbf{q}_r\,(\mathbf{r}')\right]dV\,(\mathbf{r}')$$

$$+\frac{\sigma}{4}\sum_{k=1}^{M}\beta_k\iiint_\Omega K(\mathbf{r},\,\mathbf{r}')$$

$$\times w_k\,(\mathbf{r}')\,S_k\,(\omega)dV\,(\mathbf{r}')$$

$$+\iint_{\partial\Omega}K(\mathbf{r},\,\mathbf{r}')\left[e_s\,(\mathbf{r}')\right.$$

$$\left.-\frac{1-\epsilon}{\epsilon}\,q_s\,(\mathbf{r}')\right]\cos\,(\mathbf{r}-\mathbf{r}',\,\mathbf{n}')\,dA\,(\mathbf{r}'),\quad \mathbf{r}\in\Omega \tag{10a}$$

$$w_i(\mathbf{r}) = \iiint_\Omega K(\mathbf{r},\,\mathbf{r}')\left[ke_g\,(\mathbf{r}')\right.$$

$$\left.-\frac{\sigma}{4a}\nabla\cdot\,\mathbf{q}_r\,(\mathbf{r}')\right]S_i\,(\omega)\,dV\,(\mathbf{r}')$$

$$+\frac{\sigma}{4}\sum_{k=1}^{M}\beta_k\iiint_\Omega K(\mathbf{r},\,\mathbf{r}')$$

$$\times w_k\,(\mathbf{r}')\,S_k\,(\omega)S_i\,(\omega)\,dV\,(\mathbf{r}')$$

$$+\iint_{\partial\Omega}k(\mathbf{r},\,\mathbf{r}')\left[e_s\,(\mathbf{r}')\right.$$

$$\left.-\frac{1-\epsilon}{\epsilon}\,q_s\,(\mathbf{r}')\right]S_i\,(\omega)\cos\,(\mathbf{r}-\mathbf{r}',\,\mathbf{n}')\,dA\,(\mathbf{r}'),$$

$$i=1,\,2,\ldots,\,M,\quad \mathbf{r}\in\Omega \tag{10b}$$

$$e_s(\mathbf{r}) - \frac{1}{\epsilon}\,q_s\,(\mathbf{r}) = \iiint_\Omega K(\mathbf{r},\,\mathbf{r}')\left[ke_g\,(\mathbf{r}')\right.$$

$$\left.-\frac{\sigma}{4a}\nabla\cdot\,\mathbf{q}_r\,(\mathbf{r}')\right]\cos(\mathbf{r}'-\mathbf{r},\,\mathbf{n})\,dV\,(\mathbf{r}')$$

$$+\frac{\sigma}{4}\sum_{k=1}^{M}\beta_k\iiint_\Omega K(\mathbf{r},\,\mathbf{r}')$$

$$w_k\,(\mathbf{r}')\,S_k\,(\omega)\cos\,(\mathbf{r}'-\mathbf{r},\,\mathbf{n})\,dV\,(\mathbf{r}')$$

$$+\iint_{\partial\Omega}K(\mathbf{r},\,\mathbf{r}')\left[e_s\,(\mathbf{r}')\right.$$

$$\left.-\frac{1-\epsilon}{\epsilon}\,q_s\,(\mathbf{r}')\right]\cos\,(\mathbf{r}-\mathbf{r}',\,\mathbf{n}')$$

$$\times\cos\,(\mathbf{r}'-\mathbf{r},\,\mathbf{n})\,dA\,(\mathbf{r}'),\quad \mathbf{r}\in\partial\Omega \tag{10c}$$

In equation (10) $e_g$ and $e_s$ are the blackbody emissive powers of the medium and the boundary, respectively; $q_s$ is the net heat flux on wall. The kernel $K$ is defined by

$$K(\mathbf{r},\,\mathbf{r}') = \frac{e^{-k|\mathbf{r}-\mathbf{r}'|}}{\pi|\mathbf{r}-\mathbf{r}'|^2}\,. \tag{11}$$

Equation (10) is just the integral equation formulation for radiative heat transfer in an emitting, absorbing, and Mie-anisotropic scattering enclosure with a gray boundary.

In each of the equations, the first integral on the right-hand side relates to the denotation of the emitting and isotropic scattering of the medium to radiative transfer, the summation is the denotation of the anisotropic scattering without the isotropic part to radiant transfer, and the last integral denotes the effect of surface emission and reflection.

If $\nabla\cdot\mathbf{q}_r$ and $e_s$ are known, examining equation (10) together with the energy equation shows that the number of equations is one more than that of unknowns. Hence these equations must not be independent of each other. In fact, from equations (10*a*) and (10*b*) for $i = 1$, 2, and 3, it can be proved that

$$\left(\frac{\partial w_1}{\partial x} + \frac{\partial w_2}{\partial y} + \frac{\partial w_3}{\partial z}\right) = -aw_0 + 4ae_g$$

or

$$\nabla\cdot\mathbf{q}_r(\mathbf{r}) = -aw_0(\mathbf{r}) + 4ae_g(\mathbf{r})$$

This is just equation (5).

Therefore, one of the first three equations in equation (10*b*) should be eliminated to get a closed equation system. This can be done by substituting into equation (10) the energy equation

$$\nabla\cdot\mathbf{q}_r(\mathbf{r}) = F(T) + Q(\mathbf{r}) \tag{12}$$

where $F(T)$ is the conductive and convective terms and $Q$ is the internal heat generation, or simply by regarding $\nabla\cdot\mathbf{q}_r$ as an unknown independent of $w_1$, $w_2$, and $w_3$.

The complexity of an anisotropic scattering problem is determined mainly by the number of terms $N$ in the phase function expansion (equation (1)). For numerical solution to the integral equations, a large value of $N$ would lead to a large amount of computing time and storage, although the similarity among the integrals with different $S_i$ can be utilized to reduce the work of integral computations. Fortunately, in most engineering problems, the scattering phase functions can be approximated by expansions of a few terms without causing much error.

In the cases of one or two-dimensional problems, the number of integrals appearing in equation (10) is reduced further, because many terms in equation (2) vanish. Especially, in the one-dimensional case, equation (10) is similar to those given by Modest and Azad (1980).

If isotropic scattering problems ($\beta_k = 0$, $k = 1, 2, \ldots, M$) are encountered, equations (10*a*) and (10*c*) reduce to the following form:

$$4e_g(\mathbf{r}) - \frac{1}{a}\nabla\cdot\mathbf{q}_r(\mathbf{r}) = \iiint_\Omega K(\mathbf{r}, \mathbf{r}')\left[ke_g(\mathbf{r}') - \frac{\sigma}{4a}\nabla\cdot\mathbf{q}_r(\mathbf{r}')\right] dV(\mathbf{r}')$$

$$+ \iint_{\partial\Omega} K(\mathbf{r}, \mathbf{r}')\left[e_s(\mathbf{r}') - \frac{1-\epsilon}{\epsilon} q_s(\mathbf{r}')\right] \cos(\mathbf{r}-\mathbf{r}', \mathbf{n}')\, dA(\mathbf{r}'), \quad \mathbf{r}\in\Omega$$

$$e_s(\mathbf{r}) - \frac{1}{\epsilon} q_s(\mathbf{r}) = \iiint_\Omega K(\mathbf{r}, \mathbf{r}')\left[ke_g(\mathbf{r}') - \frac{\sigma}{4a}\nabla\cdot\mathbf{q}_r(\mathbf{r}')\right] \cos(\mathbf{r}'-\mathbf{r}, \mathbf{n})\, dV(\mathbf{r}') + \iint_{\partial\Omega} K(\mathbf{r}, \mathbf{r}')\left[e_s(\mathbf{r}') - \frac{1-\epsilon}{\epsilon} \times q_s(\mathbf{r}')\right] \cos(\mathbf{r}-\mathbf{r}', \mathbf{n}') \cos(\mathbf{r}'-\mathbf{r}, \mathbf{n})\, dA(\mathbf{r}'), \quad \mathbf{r}\in\partial\Omega$$

Note that the number of integrals appearing in these equations is the same as that in the case of a nonscattering medium ($\sigma = 0$) and a nonreflecting wall ($\epsilon = 1$). This is significant to numerical solution to the equations, since it means that the number of multidimensional integral computations in the isotropic scattering case is the same as that in the nonscattering, nonreflecting case.

## 3 Numerical Method

The linear integral equations (10*a*)–(10*c*) are the second kind of Fredholm type. There exist many numerical methods to solve them (see, e.g., Baker, 1977). Among these, the Galerkin-type methods have been widely used in radiant heat transfer computations. For examples, Hottel's zonal technique and Razzaque's finite element method, which can be extended to solve equations (10*a*)–(10*c*), are of this type. Because it is necessary to calculate six, five, or four-dimensional integrals for a three-dimensional problem, this method consumes a large amount of computer time. Another type of numerical method needs to evaluate only three or two-dimensional integrals. Yuen and Wong's (1984) point allocation technique is an example of this one.

In this study, the product-integration method (see Chaps. 4 and 5 of Baker, 1977) is utilized to discretize equation (10), because this method is as flexible as the finite element method or the zonal method, which apply to complex geometries and, mentioned more importantly, it belongs to the latter type of solution method mentioned above.

Now we select $N_d$ points, $r_1, r_2, \ldots, r_{N_d}$ in $\Omega$ and $N_b$ points on $\partial\Omega$. Set

$$e_g(\mathbf{r}) = \sum_{i=1}^{N_d} u_i(\mathbf{r})(e_g)_i, \quad \nabla\cdot\mathbf{q}_r(\mathbf{r}) = \sum_{i=1}^{N_d} u_i(\mathbf{r})(\nabla\cdot\mathbf{q}_r)_i$$

$$w_k(\mathbf{r}) = \sum_{i=1}^{N_d} u_i(\mathbf{r})(w_k)_i, \quad k = 1, 2, \ldots, M \tag{13}$$

$$e_s(\mathbf{r}) = \sum_{j=1}^{N_b} v_j(\mathbf{r})(e_s)_j, \quad q_s(\mathbf{r}) = \sum_{j=1}^{N_b} v_j(\mathbf{r})(q_s)_j$$

where $u_i$ and $v_j$ are interpolating functions and $(\cdot)_i$ denotes the value of $\cdot$ at $\mathbf{r} = \mathbf{r}_i$. Substituting into the integral equations yields

$$4E_g - \frac{1}{a}Q_g = A_{00}\left[kE_g - \frac{\sigma}{4a}Q_g\right] + \frac{\sigma}{4}\sum_{k=1}^{M}\beta_k A_{0k}W_k + B_0\left[E_s - \frac{1-\epsilon}{\epsilon}Q_s\right]$$

$$W_i = A_{0i}\left[kE_g - \frac{\sigma}{4a}Q_g\right] + \frac{\sigma}{4}\sum_{k=1}^{M}\beta_k A_{ik}W_k + B_i\left[E_s - \frac{1-\epsilon}{\epsilon}Q_s\right], \quad i = 1, 2, \ldots, M$$

$$E_s - \frac{1}{\epsilon}Q_s = C_0\left[kE_g - \frac{\sigma}{4a}Q_g\right] + \frac{\sigma}{4}\sum_{k=1}^{M}\beta_k C_k W_k + D\left[E_s - \frac{1-\epsilon}{\epsilon}Q_s\right]$$

or in matrix form

$$\begin{bmatrix} 4E_g - \frac{1}{a}Q_g \\ W_1 \\ W_2 \\ \vdots \\ W_M \\ E_s - \frac{1}{\epsilon}Q_s \end{bmatrix} = \begin{bmatrix} A_{00} & A_{01} & \ldots & A_{0M} & B_0 \\ A_{10} & A_{11} & \ldots & A_{1M} & B_1 \\ A_{20} & A_{21} & \ldots & A_{2M} & B_2 \\ \vdots & \vdots & \vdots & \vdots & \vdots \\ A_{M0} & A_{M1} & \ldots & A_{MM} & B_M \\ C_0 & C_1 & \ldots & C_M & D \end{bmatrix} \times \begin{bmatrix} kE_g - \frac{\sigma}{4a}Q_g \\ \frac{\sigma}{4}\beta_1 W_1 \\ \frac{\sigma}{4}\beta_2 W_2 \\ \vdots \\ \frac{\sigma}{4}\beta_M W_M \\ E_s - \frac{1-\epsilon}{\epsilon}Q_s \end{bmatrix} \tag{14}$$

where

$$E_g \equiv [(e_g)_1, (e_g)_2, \ldots, (e_g)_{N_d}]^T,$$

$$Q_g \equiv [(\nabla\cdot\mathbf{q}_r)_1, (\nabla\cdot\mathbf{q}_r)_2, \ldots, (\nabla\cdot\mathbf{q}_r)_2, \ldots, (\nabla\cdot\mathbf{q}_r)_{N_d}]^T$$

$$W_i \equiv [(w_i)_1, (w_i)_2, \ldots, (w_i)_{N_d}]^T, \quad i = 1, 2, \ldots, M$$

$$E_s \equiv [(e_s)_1, (e_s)_2, \ldots, (e_s)_{N_b}]^T,$$

$$Q_s \equiv [(q_s)_1, (q_s)_2, \ldots, (q_s)_{N_b}]^T$$

and $A_{lm}$ ($l, m = 0, 1, \ldots, M$), $B_l$ ($l = 0, 1, \ldots, M$), $C_l$ ($l = 0, 1, \ldots, M$) and $D$ are matrices with elements

**Table 1 Comparative fluxes for radiation in one-dimensional planar media**

| $\omega_0 a_1$ / $\tau_0$ | −0.7 | | | | 0.0 | | | | 0.7 | | | |
|---|---|---|---|---|---|---|---|---|---|---|---|---|
| | Zonal method | Present method | Dayan and Tien | $E$,* percent | Zonal method | Present method | Dayan and Tien | $E$, percent | Zonal method | Present method | Dayan and Tien | $E$, percent |
| 0.1 | 0.901 | 0.901 | 0.901 | 0.0 | 0.916 | 0.916 | 0.916 | 0.0 | 0.931 | 0.931 | 0.931 | 0.0 |
| 0.5 | 0.664 | 0.664 | 0.663 | 0.1 | 0.705 | 0.705 | 0.704 | 0.1 | 0.751 | 0.751 | 0.750 | 0.1 |
| 1.0 | 0.506 | 0.506 | 0.505 | 0.3 | 0.555 | 0.555 | 0.553 | 0.4 | 0.614 | 0.614 | 0.611 | 0.5 |
| 3.0 | 0.269 | 0.271 | 0.260 | 4.1 | 0.310 | 0.311 | 0.301 | 3.2 | 0.365 | 0.366 | 0.358 | 2.1 |

*The error of the results by this method compared with the exact method.

$$(a_{lm})_{ij} = \int\int\int_{\Omega} K(\mathbf{r}_i, \mathbf{r}')\, u_j(\mathbf{r}')\, S_l(\omega)\, S_m(\omega)\, dV(\mathbf{r}'),$$

$$i, j = 1, 2, \ldots, N_d$$

$$(b_l)_{ij} = \int\int_{\partial\Omega} K(\mathbf{r}_i, \mathbf{r}')\, v_j(\mathbf{r}')\, S_l(\omega) \cos$$

$$(\mathbf{r}_i - \mathbf{r}', \mathbf{n}')\, dA(\mathbf{r}'),\ i = 1, 2, \ldots, N_d,\quad j = 1, 2, \ldots, N_b$$

$$(c_l)_{ij} = \int\int\int_{\Omega} K(\mathbf{r}_i, \mathbf{r}')\, u_j(\mathbf{r}')\, S_l(\omega) \cos$$

$$(\mathbf{r}' - \mathbf{r}_i, \mathbf{n}_i)\, dV(\mathbf{r}'),\ i = 1, 2, \ldots, N_b,\quad j = 1, 2, \ldots, N_d$$

$$(d)_{ij} = \int\int_{\partial\Omega} K(\mathbf{r}_i, \mathbf{r}')\, v_j(\mathbf{r}') \cos(\mathbf{r}_i - \mathbf{r}', \mathbf{n}')$$

$$\cos(\mathbf{r}' - \mathbf{r}_i, \mathbf{n}_i)\, dA(\mathbf{r}'),\ i, j = 1, 2, \ldots, N_b$$

respectively. It is noted that $A_{lm} = A_{ml}$ $(l, m = 0, 1, \ldots, M)$.

There are $(M+1)$ $N_d + N_b$ equations and $(M+2)N_d + 2N_b$ variables in equation (14). When the $N_d$ discretized equations of the energy equation (12) are substituted into or combined with equation (14), together with the $N_b$ boundary conditions, the radiation problem can be readily solved.

As it is done in the finite element or zonal method, the medium $\Omega$ and its boundary $\partial\Omega$ are divided into a number of elements. The interpolating functions $u_i(\mathbf{r})$ and $v_i(\mathbf{r})$ are taken to be piecewise polynomials or piecewise constants, which are continuous in each element. In the piecewise polynomial interpolating function case, this method is analogous to the finite element method of Razzaque et al. (1983, 1984), and in the piecewise-constant case it is analogous to the zonal method.

## 4 Applications

As illustrations, the abovementioned formulation and computing method were applied to thermal radiation in one and two-dimensional geometries. For briefness, all the notations used hereafter have been nondimensionalized.

**One-Dimensional Problem.** Thermal radiation in an infinite planar medium that emits, absorbs, and linear-anisotropically scatters radiant energy, which was studied by Dayan and Tien (1975), was recomputed using the present formulation. The resulting integral equations were solved numerically by the zonal method and the present technique using piecewise-constant interpolating functions. For comparison, the medium is divided in the same manner (eight equal segments) for both methods.

In Table 1, numerical radiation fluxes are compared with the exact ones listed in Dayan and Tien (1975). It is seen that in the ranges of optical thickness ($\tau_0$) and anisotropic scattering parameter ($\omega_0 a_1$) concerned, the present numerical method gives excellent data comparing with both the zonal and Dayan and Tien's results. It is also noted that both the zonal and the present method overestimate the radiant fluxes when the optical thickness and anisotropic scattering parameter increase. Further, radiation fluxes computed by the zonal method and the present method are almost the same for all optical thicknesses considered, except in the case of $\tau_0 = 3$, where the zonal method is 0.001–0.002 more accurate than the present technique.

Other data computed by the zonal method and the present technique are also compared with Dayan and Tien's figures. It is found that the results are indistinguishable with the figures and hence are not given here.

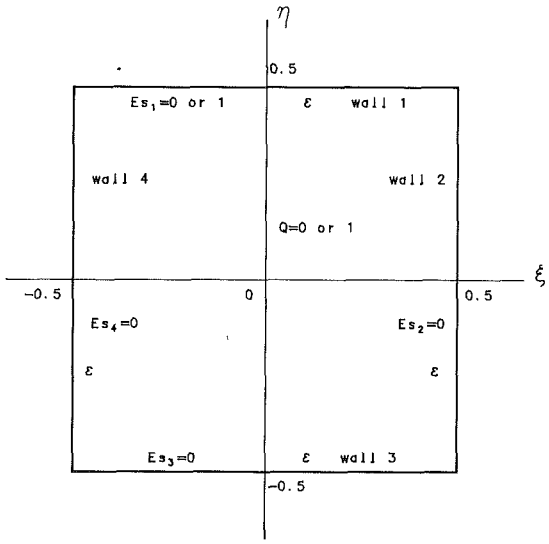


**Fig. 2 Geometry of a two-dimensional square enclosure and the boundaries**

**Two-Dimensional Problem.** Radiation heat transfer in a two-dimensional medium is studied as the second application of the present method. The system is composed of a square emitting, absorbing, and scattering medium with unit optical thickness along each side, and four gray boundaries. For simplicity, it is assumed that the scattering is linear-anisotropic, and all the walls have the same emissivity $\epsilon$. Heat conduction and convection are neglected. There may be a uniform energy generation in the medium (Fig. 2).

Two cases are considered: (*i*) $E_{s_1} = 1$, $E_{s_2} = E_{s_3} = E_{s_4} = 0$, $Q = 0$; (*ii*) $E_{s_1} = E_{s_2} = E_{s_3} = E_{s_4} = 0$, $Q = 1$, where $E_{s_i}$ is the emissive power of the $i$th wall, $Q$ is the internal energy generation rate.

The symmetry of the system can be utilized so that we can consider only the right half of the medium and the related boundaries. In the calculations, the half region is divided into $8 \times 4$ square elements, and the corresponding walls are divided into 16 equal segments. For comparison with the zonal results, the interpolating functions are chosen to be piecewise constant again.

All the computations were performed on an IBM Personal Computer/XT. For a typical problem, about 8 min are required to generate results; of which 4 min are for numerical integrations and 4 min are for solving equations.

Figures 3 and 4 show the comparison between the present

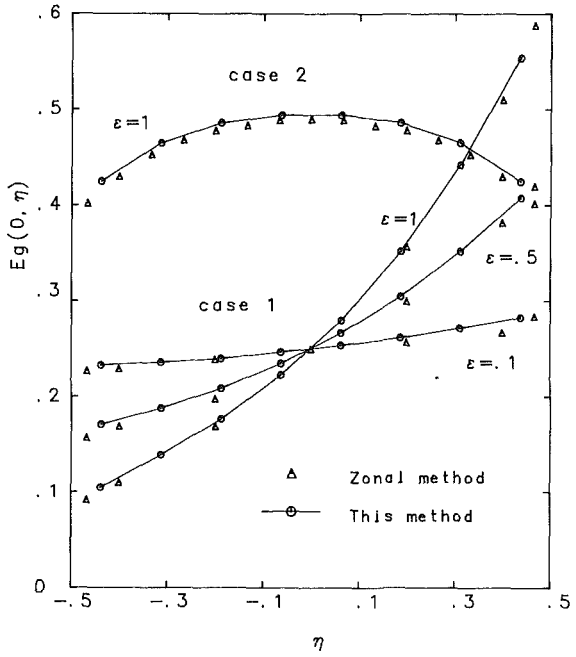


Fig. 3 Comparative results for the dimensionless centerline emissive power (interpolated) in a square enclosure

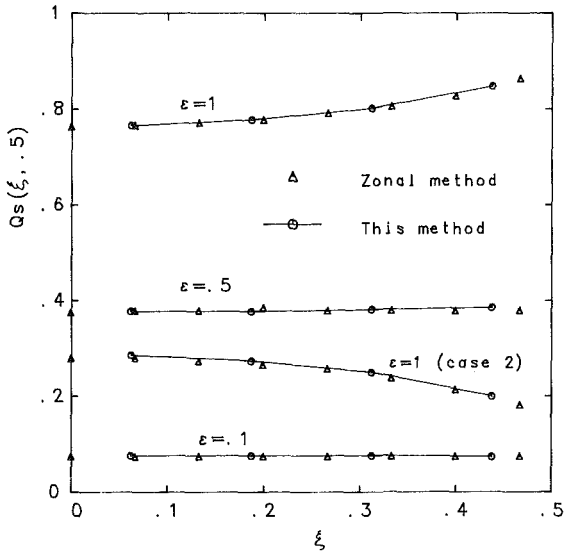


Fig. 4 Comparative results for the dimensionless heat flux on wall 1

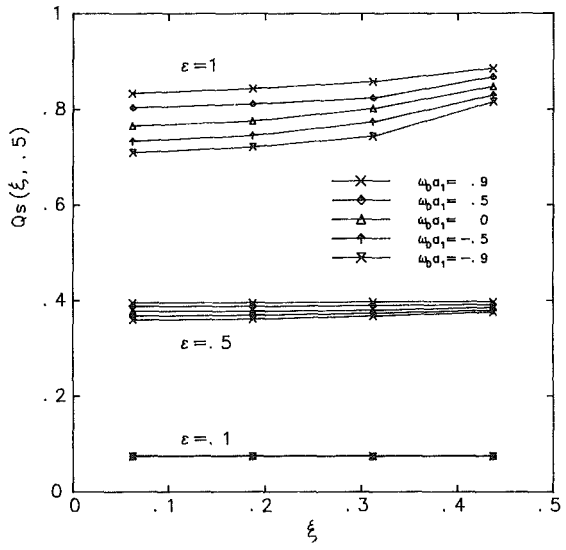


Fig. 5 Effects of anisotropic scattering and surface reflecting on the dimensionless heat flux on wall 1 when $E_{s_1}=1$, $E_{s_2}=E_{s_3}=E_{s_4}=0$, $Q=0$, $\eta=0.5$

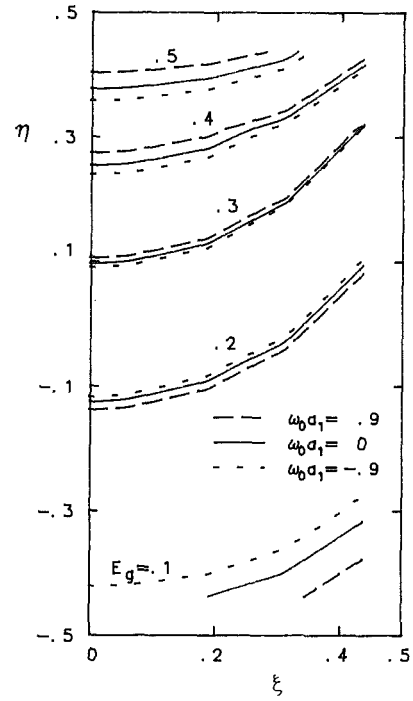


Fig. 6 Effect of anisotropic scattering on emissive power distributions in a square enclosure when $E_{s_1}=1$, $E_{s_2}=E_{s_3}=E_{s_4}=0$, $Q=0$, $\epsilon=1$

results and the available zonal data. It is found that compared with existing zonal data (from Ratzel and Howell, 1983; Yuen and Ho, 1985) with $15\times7.5$ elements in a half-region, the product-integration technique with 32 space elements gives excellent centerline emissive powers (interpolated) and hot-wall fluxes, except that the centerline emissive powers in the second case are slightly higher than the zonal data. If more elements or higher order interpolating functions are used, more accurate results can be expected.

The hot-wall surface heat flux distributions for case 1 are shown in Fig. 5. The influence of anisotropic scattering on the emissive power profiles is shown in Fig. 6. It is found that the higher the surface emissivity, the greater the influence of anisotropic scattering on radiant heat transfer, and increasing $\omega_0 a_1$ will always increase hot surface flux. This is because strong forward scattering "speeds up" the radiant heat transmission rate while strong backward scattering causes it to "slow down." Consequently, the emissive power near wall 1 will decrease and that near wall 3 increase as $\omega_0 a_1$ increases (Fig. 6).

Figures 7 is for case 2. The results show that the influences of scattering albedo $\omega_0$ on the centerline emissive power are great, but the influences of coefficient $a_1$ are almost indistinguishable. The influences of $a_1$ on surface heat fluxes (not shown here) are also very small. Thus case 2 can be approximated excellently by the isotropic scattering model.

## 5 Summary

1 The integration equations for thermal radiation in a general three-dimensional absorbing, emitting, and Mie-anisotropic scattering medium with diffusely reflecting

enclosure was accurately formulated. Because of this, anisotropic scattering problems can be treated using the numerical method presented in the second part of the paper or other methods such as the zonal method, the finite element method, and so on.

2 The product-integration technique applied in this paper for the integral equations is much faster than Hottel's zonal method or the finite element method since it evaluates integrals of fewer dimensions. The numerical computations for both one and two-dimensional problems show that compared with existing data, this method gives excellent results. To improve the accuracy of computation, more grid points or higher order interpolating functions should be applied.

3 The formulation and the numerical method can be extended to radiation in nongray participating media in the same way as the zonal method had been. Extension to radiation with angular dependent wall reflections is being studied.

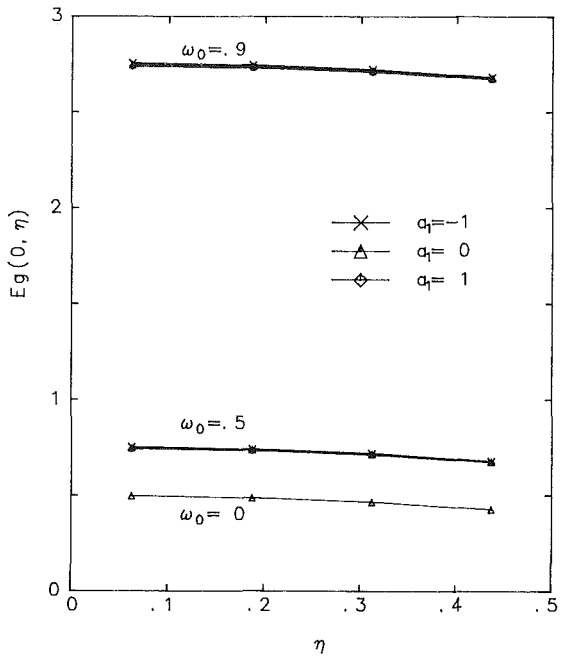


**Fig. 7 Effect of anisotropic scattering on interpolated centerline emissive power in a square enclosure when $E_{s_1} = E_{s_2} = E_{s_3} = E_{s_4} = 0$, $Q = 1$, $\epsilon = 1$**

## References


Baker, C. T. H., 1977, *The Numerical Treatment of Integral Equations*, Clarendon Press, Oxford, pp. 396–398.

Beach, H. L., Özişik, M. N., and Siewert, C. E., 1971, "Radiative Transfer in Linearly Anisotropic-Scattering, Conservative and Non-conservative Slabs With Reflective Boundaries," *Int. J. Heat Mass Transfer*, Vol. 14, pp. 1551–1565.

Boffi, V. C., and Spiga, G., 1977, "Integral Theory of Radiative Heat Transfer With Anisotropic Scattering and General Boundary Conditions," *J. Math. Phys.*, Vol. 18, pp. 2448–2455.

Chu, C. M., and Churchill, S. W., 1955, "Representation of an Angular Distribution of Radiation Scattered by a Spherical Particle," *J. Opt. Soc. Amer.*, Vol. 45, pp. 958–962.

Dayan, A., and Tien, C. L., 1975, "Heat Transfer in a Gray Planar Medium With Linear Anisotropic Scattering," ASME JOURNAL OF HEAT TRANSFER, Vol. 97, pp. 391–396.

Fiveland, W. A., 1984, "Discrete-Ordinates Solutions of the Radiative Transport Equation for Rectangular Enclosures," ASME JOURNAL OF HEAT TRANSFER, Vol. 106, pp. 613–619.

Gradshteyn, I. S., and Ryzhick, I. M., 1980, *Table of Integrals, Series, and Products*, Academic Press, New York, pp. 1013.

Hottel, H. C., and Cohen, E. S., 1958, "Radiant Heat Transfer in a Gas-Filled Enclosure: Allowance for Non-uniformity of Gas Temperature," *AIChE J.*, Vol. 4, pp. 3–14.

Lathrop, K. D., 1968, "Ray Effects in Discrete-Ordinates Equations," *Nucl. Sci. Eng.*, Vol. 32, pp. 357–369.

Modest, M. R., and Azad, F. H., 1980, "The Influence and Treatment of Mie-Anisotropic Scattering in Radiative Heat Transfer," ASME JOURNAL OF HEAT TRANSFER, Vol. 102, pp. 92–98.

Ratzel, A. C., III, and Howell, J. R., 1983, "Two-Dimensional Radiation in Absorbing-Emitting Media Using the *P-N* Approximation," ASME JOURNAL OF HEAT TRANSFER, Vol. 105, pp. 333–340.

Razzaque, M. M., Howell, J. R., and Klein, D. E., 1984, "Coupled Radiative and Conductive Heat Transfer in a Two-Dimensional Rectangular Enclosure With Gray Participating Media Using Finite Elements," ASME JOURNAL OF HEAT TRANSFER, Vol. 106, pp. 613–619.

Razzaque, M. M., Klein, D. E., and Howell, J. R., 1983, "Finite Element Solution of Radiative Heat Transfer in a Two-Dimensional Rectangular Enclosure With Gray Participating Media," ASME JOURNAL OF HEAT TRANSFER, Vol. 105, pp. 933–936.

Siegel, R., and Howell, J. R., 1981, *Thermal Radiative Heat Transfer*, 2nd ed., McGraw-Hill, New York.

Szidarovszky, F., and Yakowitz, S., 1978, *Principles and Procedures of Numerical Analysis*, Plenum Press, New York–London, Chap. 3.5.

Taniguchi, H., 1969, "The Radiative Heat Transfer of Gas in a Three Dimensional System Calculated by Monte Carlo Method," *Bull. JSME*, Vol. 12, pp. 67–78.

Yuen, W. W., and Wong, L. W., 1984, "Analysis of Radiative Equilibrium in a Rectangular Enclosure With Gray Medium," ASME JOURNAL OF HEAT TRANSFER, Vol. 106, pp. 433–440.

Yuen, W. W., and Ho, C. F., 1985, "Analysis of Two-Dimensional Radiative Heat Transfer in a Gray Medium With Internal Heat Generation," *Int. J. Heat Mass Transfer*, Vol. 28, pp. 17–23.

E. Gutmark

T. P. Parr

D. M. Parr

K. C. Schadow

Naval Weapons Center,
China Lake, CA 93555-6001

# Planar Imaging of Vortex Dynamics in Flames

*The interaction between the fluid dynamics and the combustion process in an annular diffusion flame was studied experimentally using the Planar Laser Induced Fluorescence (PLIF) technique. The local temperature and OH radical fluorescence signals were mapped in the entire flame cross section. The flame was forced at different instability frequencies, thus enabling the study of the evolution and interaction of large-scale structures in the flame shear layer. The present study of the effect of fluid dynamics on combustion is part of a more comprehensive program aimed at understanding and controlling the effect of heat release, density variations, and reaction parameters on the shear layer evolution.*

## Introduction

The effectiveness of many combustion systems depends critically on the ability to maintain a stable flame at reasonably high combustion efficiency. Both aspects are closely related to the flow characteristics inside the combustor and the degree of mixing obtained between the injected fuel and the air. The mixing involves two important processes. The large-scale structures bring into the mixing layer large amounts of the reacting components from the two separated streams. The fine-scale eddies enhance the mixing at the molecular level between the reactants, which is a necessary condition to initiate the chemical reaction. The understanding of this complex gas-dynamic process requires analysis of the interactions between fluid dynamics, chemical reaction, acoustic waves, and heat release of the reactive system (Broadwell and Dimotakis, 1986; Ballal, 1986).

The fluid dynamics involved in various types of flames are related to the mixing layer flow, which is governed by large-scale vortices. The roll-up and growth of these vortices are determined by instability forces and mutual interactions (Brown and Roshko, 1974). The large-scale structures entrain flow from the two sides of the shear layer and mix the flow at both large and small scales, leading to the molecular mixing necessary for reaction. Recent developments (Brown and Roshko, 1974) in the understanding of the important role of large coherent structures in mixing layer dynamics opened up the possibility of controlling the flow in combustors to improve their performance. The development of large-scale vortices in a shear layer is influenced by the reaction through heat release and density gradients. In turn, the vorticity controls the reaction by the turbulent mixing process (Mungal and Dimotakis, 1984). The physical mechanisms involved in this interaction are not fully understood. Although many of these phenomena have been observed in nonreactive or reactive, but noncombusting, flow or postulated on the basis of modeling, experimental results in combusting flows are limited. One of the few papers that discuss the detailed structure of turbulent diffusion flames is that of Vandsburger et al. (1986). They used OH PLIF and Mie scatter from $TiO_2$ particles to study an acoustically forced jet flame and obtained the time history of the flame structure via phase angle sampled images. Chen and Roquemore (1986) have also used planar sheet imaging of Mie scatter from $TiO_2$ particles generated in the flame to study slow-speed unforced diffusion flames. Strawa and Cantwell (1985) have studied slow-speed acoustically forced diffusion flames using Schlieren and photographic imaging. In all these cases buoyancy was a significant factor in controlling the large-scale structures in the flame. In the present work buoyancy is much less a factor. Our Richardson number (Ri) is estimated to be 0.03 while for the abovementioned studies $Ri > 1$.

By using the OH PLIF technique discussed later, a detailed instantaneous picture of the combustion process inside the flow structures can be followed. The possibility of getting simultaneous temperature and species concentration fields is crucial to the understanding of the combustion process.

In the present work, the flame of a circular burner was excited at the preferred mode and its first harmonic. The relative amplitudes and phase difference of the two frequencies could be varied, as well as the phase relative to the diagnostic laser pulse. The details of the combustion reaction inside the vortices were visualized and analyzed. The effects of vortex interaction, forcing frequency, and amplitude on the combustion dynamics were studied. It is shown that knowledge of the flow dynamics is important for understanding the flame combustion process.

## Planar Laser Fluorescence Imaging

In this paper we used the Planar Laser Induced Fluorescence (PLIF) technique (developed by Crosley and Dyer, 1982, and Kychakoff et al., 1982, and recently reviewed by Hanson, 1986) to study the evolution and interaction of vortices in the initial mixing region of air and fuel in an annular diffusion flame. The OH radical produced by combustion reactions was used to study the temperature field of the flame structures as well as to provide an indicator of the presence of combustion or hot combustion products. The OH molecule is an important flame radical participating in combustion reactions in the flame front, but it is also present as an equilibrium product in the hot burnt gas region. Thus OH PLIF images might show not only the active combusting zones, but regions of burnt gases as well. However, several studies have shown superequilibrium concentrations of OH in the flame front region. Cattolica (1982), Cattolica et al. (1982), and Cattolica and Vosen (1984) showed OH concentrations in the flame front of lean and stoichiometric methane air flat flames as much as 6 to 8 above equilibrium, and up to 40 times above equilibrium for rich flames. Drake et al. (1984) show 4 to 5 times superequilibrium concentrations of OH in turbulent non-premixed flames. Thus OH concentration maps would be expected to favor the flame front in turbulent combusting flows, and OH PLIF images should give a good indication of regions of active combustion. This is especially true if, in addition to superequilibrium effects, the OH concentration in the burnt gas regions are reduced by cooling caused by entrainment of surrounding cool air.

Contributed by the Heat Transfer Division and presented at the 24th National Heat Transfer Conference, Pittsburgh, Pennsylvania, August 9–12, 1987. Manuscript received by the Heat Transfer Division September 4, 1987. Paper No. 87-HT-37. Keywords: Fire/Flames, Flow Visualization, Turbulence.

PLIF imaging is an established technique for following combustion and mixing in turbulent flows. Cattolica and Vosen (1986) used OH imaging to study the interaction of flame with vortex structure in an unsteady jet flame. Masutani and Bowman (1986) employed PLIF of NO in a nonreacting plane shear layer to visualize the concentration structure of the mixing layer. Kychakoff et al. (1984) used OH PLIF to study laminar, transitional, and turbulent non-premixed flames. Their PLIF images showed that the flame front thickness decreased with increasing Re and that at high Re the flame front was broken.

**OH Imaging.** The system for PLIF imaging of OH radicals in flames using a XeCl excimer laser at 308 nm used in the present experiments is shown in Fig. 1. The laser beam was expanded into a planar sheet, passed through the flame along the chosen axis, and the resonance fluorescence from OH selected by a 310 nm (10 nm bandwidth) interference filter was imaged with a gated intensified diode array camera. Although 98.6 percent of the 70 mJ wide bandwidth excimer output is wasted, sufficient overlap existed between one of the two major excimer "lines" and the $Q_1(3)$, $P_1(1)$, and $R_2(18)$ lines of the (0,0) $A^2\Sigma^+ - X^2\Pi$ system of OH to give low-noise single-shot images even with the laser expanded into a 13-cm high sheet. The $Q_1(3)$ line, which has the best overlap with the excimer output, drops in sensitivity by only 33 percent in going from 1500 K to 2500 K. The $Q_1(6)$ line would have been a better choice for minimum temperature sensitivity, but it is not accessible with the excimer output. The sheet was approximately 0.5 mm wide for a spectral power density (of the 308 nm component) of about 0.2 $MW/cm^2cm^{-1}$. This is not enough to saturate the transition (Eckbreth et al., 1977). Since only visualization of the flame structure was of interest, no attempt was made to calibrate for absolute sensitivity and quenching for use in absolute number density calculations.

Because the off-diagonal elements of the Frank–Condon matrix for the A-X transition of OH are all much smaller than the on-diagonal, it was necessary to monitor resonance fluorescence. This limits the use of the excimer laser OH PLIF to clean flames as Mie scattering by soot would overwhelm the OH LIF signal. All of the images shown here are from OH LIF, not Mie or Rayleigh scattering, as emission spectra, taken with a 0.75 meter double monochrometer, showed only OH lines. Mie or Rayleigh scatter due to the other major XeCl excimer "line," which contains about half the energy and occurs between the $Q_1(1)$ and $Q_1(2)$ OH transition, was insignificant compared to the fluorescence output. If the mixture ratio was enriched to the point of producing a bright yellow flame, however, Mie scatter from soot caused serious interferences. Natural flame emission was removed from the images by gating the intensifier on for only a short period encompassing the laser pulse (about 100 ns). The intensifier luminous gain for most of these experiments was about $10^4$. To reduce noise, at a minimal loss of resolution, the signal for each pixel was calculated as a weighted average with its nearest neighbors (the central pixel with weight 1, 4 perpendicular neighbors at 0.5 and 4 diagonal at 0.25).

The spatial sensitivity (excimer laser sheet intensity profile convoluted with the detector gain map), was relatively flat (less than 20 percent variation), as measured with Rayleigh scattering. Therefore no sensitivity correction was applied to the images presented here. Fixed pattern detector background, however, was subtracted out (but is typically insignificant at less than 4 percent of the peak signals).

The excimer system can frame at up to 200 Hz and the YAG (mentioned below) is limited to 20 Hz. Both of these rates, however, are too slow for real-time imaging of turbulent flow structure for all but the slowest buoyancy-driven oscillations. To construct the turbulent structure time history, both laser systems were phase locked to acoustic excitation of the flame

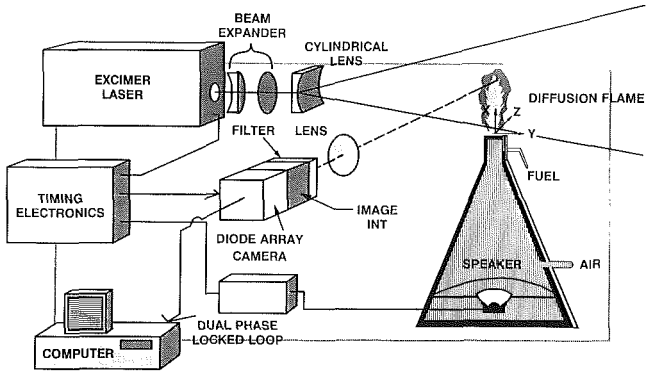


**Fig. 1 OH planar laser-induced fluorescence imaging setup**

jet. This allowed stroboscopic time dependence to be obtained in multiple frames and allowed two images to be taken at the same "equivalent" time, i.e., the same phase angle in the cycle, for PLIF temperature calculations.

**Temperature Imaging.** Seitzmann et al. (1985) have presented instantaneous temperature field measurements using single laser shot PLIF images of NO seeded into a rod-stabilized premixed flame. Here the concentration of NO is assumed constant throughout the flame obviating the need for ratioing images. Long et al. (1985) made use of Rayleigh scattering for single-shot temperature field measurements (as well as Raman imaging for major species concentration maps). This technique, however, is limited to extremely clean flow systems. The temperature field of a premixed flame was imaged by Cattolica and Stephenson (1985) using OH PLIF. They mapped the temperature field with an accuracy of 10 percent for OH temperature above 1800 K.

For the OH rotational temperature measurements presented here, a YAG-pumped, tunable dye laser with tracking doubling system was used. By pumping two rotational levels of OH (via the $R_2(17)$ and $P_2(4)$ transitions of the (1,0) $A^2\Sigma^+ - X^2\Pi$ system) and ratioing the separate PLIF images, the temperature could be calculated from Boltzmann population distributions. The same camera and filter were used for temperature as for excimer-driven OH PLIF. Although it is possible to remove the need for consideration of the rotational level dependence of the collisional quenching rate from the analysis via selection of transitions pumped (Cattolica, 1981), the assumption is made here that the rotational level dependence of the collisional quenching does not lead to serious errors in the calculated temperature. For example, the OH quenching cross sections (with $H_2O$) for $N=0$ and $N=7$ differ by only 20 percent (Copeland et al., 1985). Furthermore, rapid rotational energy transfer in the $A^2\Sigma^+$ state thermalizes the rotational levels, further reducing the dependence of emitted fluorescence on particular rotational level pumped (in our emission spectra the lines that come from emission directly pumped from the levels are only marginally stronger than "thermal" and the vast majority of the fluorescence emission is from thermalized rotational levels). Finally, our greatest interest lies in the shape of the measured PLIF temperature images, not the exact quantitative values. Therefore rotational dependence of collisional quenching was not taken into account in the analysis for temperature. Calibration of the laser technique in a steady laminar premixed propane/air flame produced measured temperatures that were about 100 K below thermocouple measurements.

It is important to note that the temperature images presented here are calculated from *two* PLIF images at different times (although at constant phase angles in the periodic flame cycle). This is required because of the use of only one laser system and one detector, and leads to a possible source of

error in the technique: Any nonreproducibility of the shape of the flame from cycle to cycle will lead to errors in the temperature calculated from the ratio of the two images. Since the flames being studied are turbulent, there are variations of shape from cycle to cycle. Therefore the temperature images presented here are only qualitative, but do show significant trends. Experiments using two laser systems and two detectors are planned for the future to obtain "near simultaneous" images (i.e., separated by a time short compared to the evolution of the flow).

The doughnut YAG-pumped dye laser beam profile yields a highly nonuniform laser sheet. Because the temperature is calculated from a ratio of two images, however, the laser power profile, which does not change over the very narrow wavelength range between the $P_2(4)$ and $R_2(17)$ lines, is ratioed out. Another limitation is that the technique gives temperature only for those regions of the flame that have a significant concentration of the OH radical. The temperature images reported here are blank for any pixel for which LIF signal from pumping for $R_2(17)$ or $P_2(4)$ is less than 5 percent of the largest average signal level in either image. This is done to reduce clutter in the images from regions that don't have sufficient OH LIF signal to form a meaningful ratio.

**Burner.** The fuel used was propane and the flame studied was an annular diffusion flame. The fuel was injected circumferentially parallel to the air flow into the initial shear layer. The fuel velocity was 0.2 m/s at a flow rate of 0.55 1/min. The air issued at a velocity of $u$ = 5 m/s (81 1/min) from a $d$ = 22 mm diameter circular nozzle yielding a Reynolds number of 7000, based on the exit diameter. The fuel and air issued at an initial temperature of 300 K. The initial velocity rms level measured at the exit of the nozzle on the centerline was 3.6 percent.

The flame was excited by a set of four speakers mounted in an acoustic resonating chamber, which was used as a setting chamber as well. The speakers were driven at a frequency $f$ to give a Strouhal number ($St = fd/u$) of 0.44, the preferred mode of the jet, and St = 0.88, its first harmonic using a dual phase locked loop and audio power amplifier. The preferred mode of the jet was determined to be 100 Hz using a hot-wire probe on the centerline at $x/D$ = 2.5, for unforced flow. The phase angle jitter was less than 7 deg. Excitation waveforms were usually triangular but little or no difference was seen with filtered triangles (approximating sine waves). A combination of forcing using two different frequencies with varying amplitude ratio and phased locked together was also applied. The phase angles between the two forcing signals and the laser could be varied in a full cycle range. The forcing frequencies, amplitudes, and relative phase angles were monitored (in cold flow) by using a calibrated hot-wire anemometer. The maximum forcing level corresponded to 14 percent rms modulation of the centerline free-stream velocity.

The data were taken in two different modes. Short-time exposures were taken yielding instantaneous OH LIF signal level images (18 ns) or "two-shot" temperature images (i.e., from the ratio of two 18 ns images taken at constant phase angle but at different times). Alternately, multiple frames (usually about 100) were averaged together for each image to reduce the chaotic nature of the flow and bring out the coherent portion. The "averaged " temperature results suffer from the added source of error arising from the inequality between the average of a ratio and the ratio of an average. Future experiments with two laser/camera systems for near simultaneous measurement of the two images will alleviate this problem.

## Results and Discussion

**Vortex Roll-Up.** The initial instability of the jet's shear layer leads to the amplification of disturbances in a certain wavelength range and to the roll-up of the shear layer into vortices. The roll-up process can be enhanced and stabilized by applying forcing to the jet. The best response is achieved when the jet is forced at its preferred mode frequency $f_j$, which, when scaled with the jet's exit diameter $D$ and exit velocity $U_0$, yields a Strouhal number $St_j = f_j D/U_0 = 0.25 \rightarrow 0.5$ (Crow and Champagne, 1971; Gutmark and Ho, 1983). Much previous work done using hot-wire measurements and flow visualization in cold flow (Crow and Champagne, 1971; Ho and Huerre, 1984) showed the highly coherent large-scale structures generated by this forcing. Different forcing frequencies produce structures of different wavelengths.

The circular flame in our experiment was acoustically excited at different instability modes of the jet. The phase angle between the forcing signal and the laser pulse was varied so that the flame temperature field and OH concentration could be followed at different stages of the vortices' development.

Figure 2 shows a sequence of pictures taken in an annular

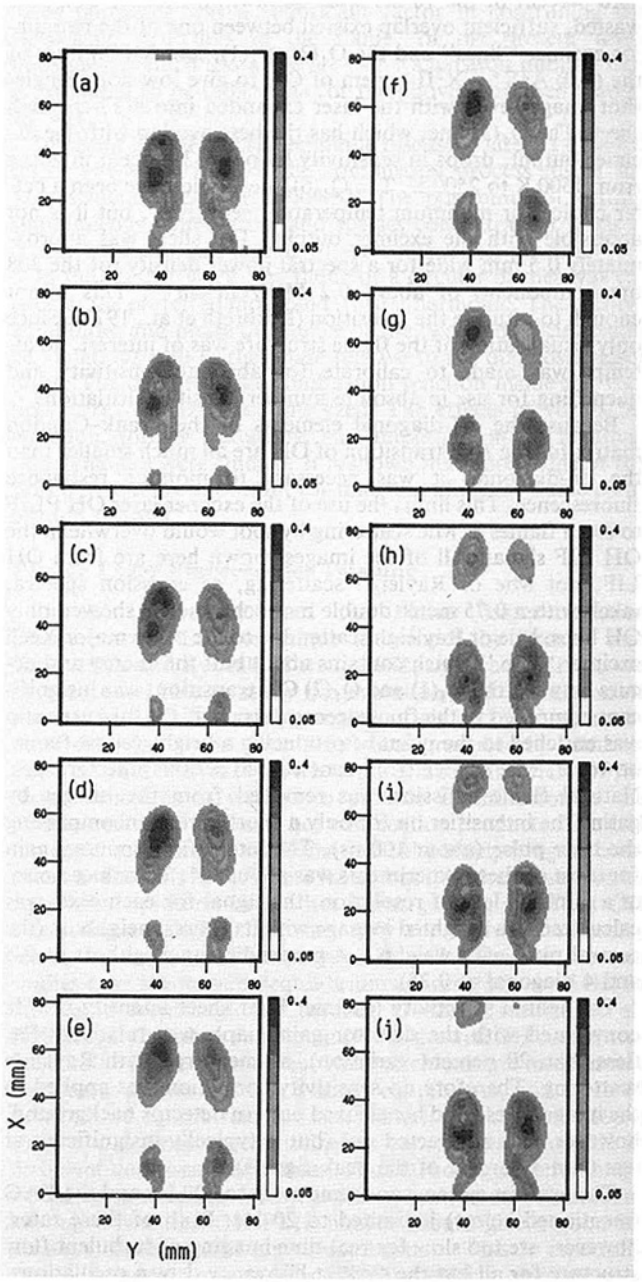


Fig. 2 A sequence of vortex roll-up in an annular diffusion flame ($St_{Forcing}$ = 0.44, $f$ = 100 Hz); time step between each frame is 1 ms

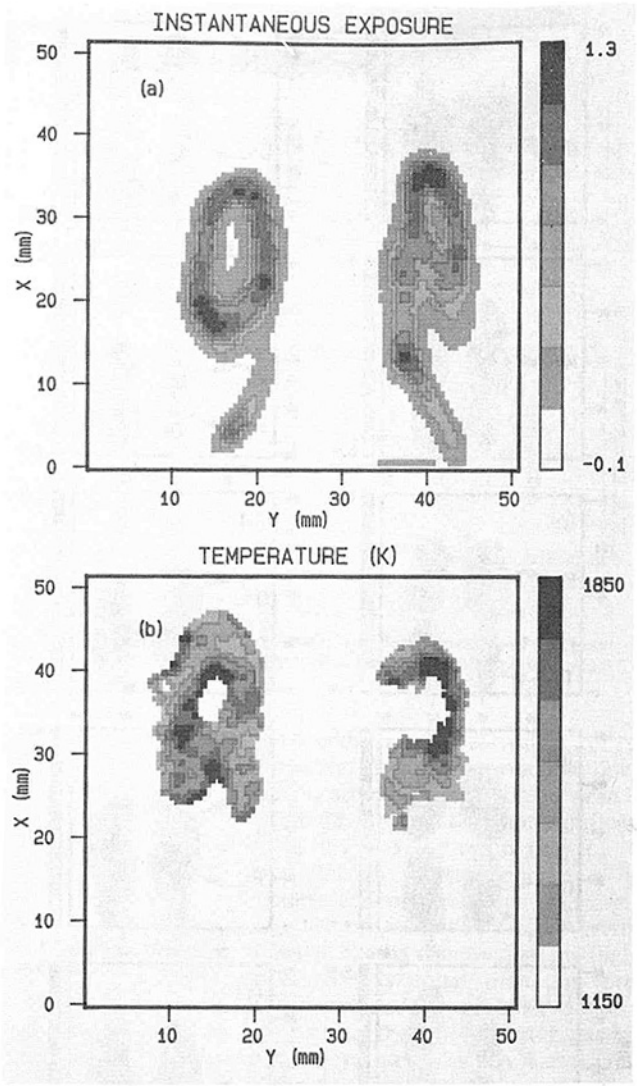


**Fig. 3 Short time exposure (18 ns) of a circular flame vortex: (*a*) OH concentration, (*b*) temperature**

diffusion flame that was acoustically excited at the preferred mode of the jet (St = 0.44). The phase angle between the forcing signal and the laser pulse was varied in steps of 18 deg. The time difference ($\Delta t$) between the forcing signal and the laser pulse is given for each frame. The sequence shows the detailed process of combustion during the vortices' roll-up, convection, and subsequent burn-through. The combustion reaction is traced here during the various stages of the vortical structure of the flame, by using the OH radical concentration mapping. Each frame has a color scale attached to it with values (voltages) corresponding to the upper and lower limits indicated. These voltages are proportional to the fluorescence intensity from the OH radicals in the flame. The phase-controlled sampling technique used to obtain the time-dependent sequence shown in Fig. 2 requires an averaging process over about 100 single realizations.

The OH fluorescence intensity seems to be nearly uniform inside the vortex. The structures are highly coherent in shape and location, but the internal details are smeared by the averaging process. An example of a single shot of 18 ns duration is shown in Fig. 3 for OH fluorescence along with a "two-shot" determination of temperature. It is shown here that following the initial roll-up, the combustion is most intense in the vortex circumference. Time sequences of "instantaneous" images show that as the vortex is convected downstream, the

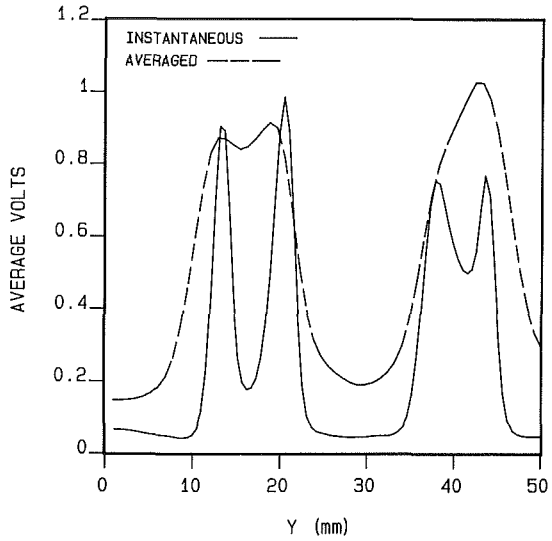


**Fig. 4 Combustion intensity distribution across the circular flame vortex: instantaneous and averaged**

combustion proceeds into the vortex core while the reaction at the circumference is completed. The difference between the instantaneous combustion intensity in the flame vortex and the averaged intensity is emphasized in Fig. 4. The radial variation of the OH concentration (represented here by voltage level) in the vortex center is compared for the two cases. The combustion process details inside the vortices are lost by the averaging process.

An efficient combustion reaction occurs in regions where molecular mixing between the fuel and the oxygen is obtained. In a diffusion flame the fuel and air are mixed together initially by the large-scale structures. The reaction requires additional small-scale mixing. The small-scale turbulence production was shown to be concentrated at the circumference of the large-scale structures following the roll-up process (Fiedler, 1975; Oster and Wygnanski, 1982; Hussain, 1984). This previous observation, obtained in cold nonreacting flows, can explain the present results concerning the reaction zones in the flame vortices.

Givi et al. (1986) investigated the conditions leading to local flame extinction due to the high dissipation rates at the braids formed during the vortices' roll-up. Their findings agree well with the present measurements. Both the average and the instantaneous OH fluorescence maps (Figs. 2 and 3, but especially in the latter) show the quenching of the flame in the braid region.

Temperature mapping of the same vortical structure in the flame revealed similar characteristics. The average temperature distribution of the vortices during one cycle of the vortex roll-up is shown in Fig. 5. The scale represents seven temperature levels in degrees Kelvin between 1150 and 1850. The temperature mapping of the structures reveals similar average features of the forced flame. The highest temperatures were measured in the cores of the vortices. While the OH measurements via the averaged technique showed maximum signal in the center of the vortices, the temperature measurements of Fig. 3 show a minimum temperature in the center. It is important to note that the white region is not defined by temperature but rather the region where the OH signal was too low to allow the reliable calculation of temperature via the ratio of two images. The temperature field represents the cumulative effect of the heat release during the combustion process. The flame extinction in the braid region is evident from the low temperatures at this location.

Similar features of the forced flame were observed for higher frequency forcing. Figures 6 and 7 show the averaged

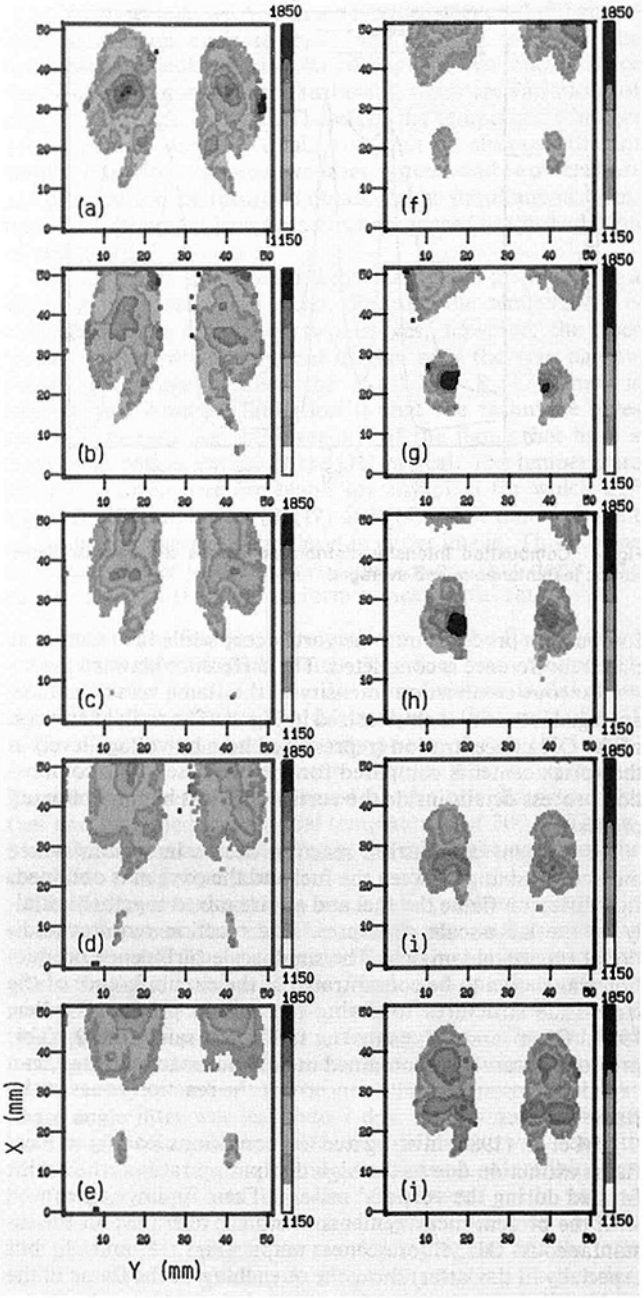


Fig. 5 The temperature distribution of the flame vortices in a sequence of vortex roll-up ($St_{Forcing}$ = 0.44); time step between each frame is 1 ms

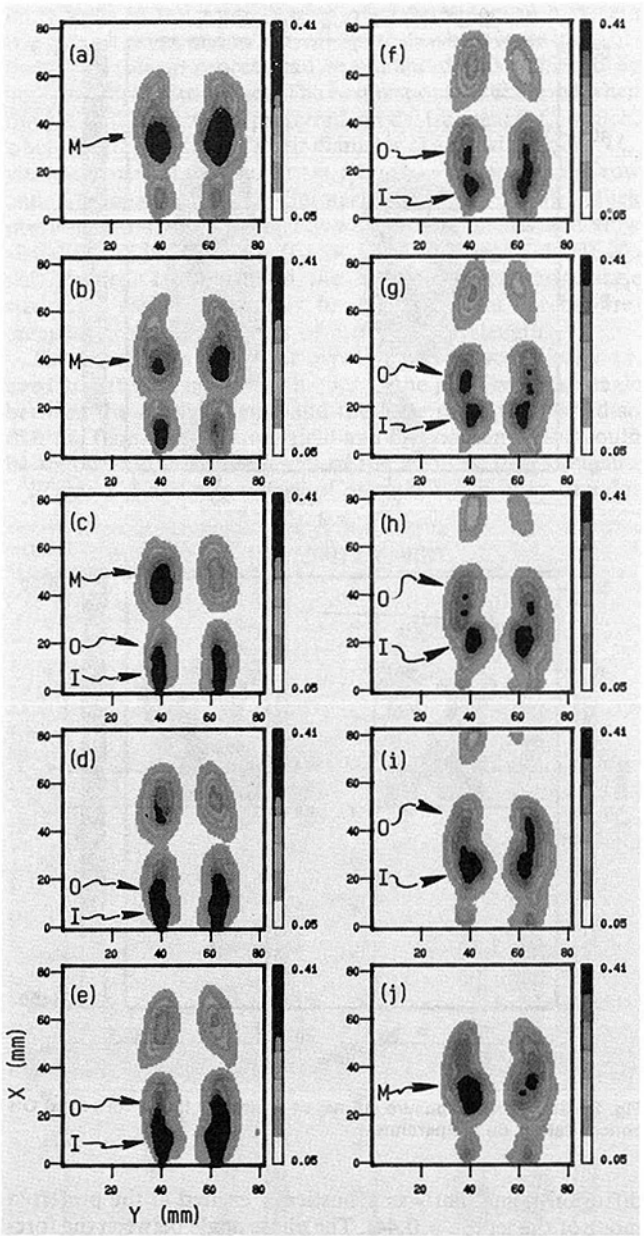


Fig. 6 A sequence of vortex roll-up in an annular diffusion flame ($St_{Forcing}$ = 0.88, $f$ = 200 Hz); time step between each frame is 0.5 ms

combustion intensity and temperature distributions, respectively, of the flame forced at 200 Hz, corresponding to the first harmonic of the preferred mode frequency. The vortices' evolution process can be tracked during more than one cycle. The extinction of the flame in the braid region is demonstrated not only for the initial roll-up braids but also for the braids between adjacent vortices.

**Vortex Interaction.** The growth of the flame shear layer is characterized not only by the previously discussed vortex generation but also by various interactions between the vortices that merge together to produce new large-scale structures. This interaction process is important for the understanding of the flow dynamics because it determines the shear layer growth and the evolution of both the large- and small-scale turbulence. One such interaction process is the pairing of two vortices, which was studied and is described in this section.

It was possible to follow vortex pairing in the flame by forcing the flame with a combination of two frequencies – the preferred mode and its first harmonic (Zhang et al., 1984). The harmonic frequency phase was at 120 deg at 0 deg phase of the fundamental. Figure 8 shows a sequence of the pairing process. The merging process of vortices in the flame is very similar to that observed in cold flows (Ho and Huerre, 1984). The lower frequency (subharmonic) displaces the small vortices, alternating between the high and low-velocity sides of the shear layer. The vortices in the higher velocity region (labeled I in Fig. 8) catch up with the slower moving vortices (labeled as O in Fig. 8) and merge by mutual induction forces (labeled as M). The high strain rates and the small-scale turbulence generated during the merging process enhance the combustion, and the burning through of the new combined vortex is accelerated. The "two-shot" temperature mapping of the vortices during the merging process is shown in Fig. 9 together with the hydroxyl fluorescence intensity, as given by the image from the $P_2(4)$ line measured as part of the two-shot temperature determination.

The $P_2(4)$ OH image, taken with the YAG pumped-dye laser

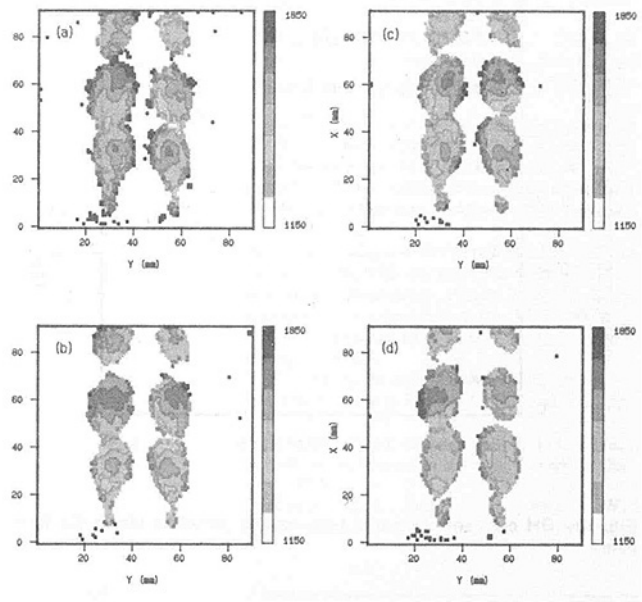


Fig. 7 Temperature distribution of the flame vortices in a sequence of vortex roll-up ($St_{Forcing}$ = 0.88); time step between each frame is 0.5 ms

system instead of the excimer, is not corrected for the doughnut laser profile variation. The major correction, due to the doughnut hole minimum, occurs in the region between the two major vortices (at about 55 mm) and does not significantly change the shape shown in Fig. 9. By comparing the two pictures it is possible to find the correspondence of the temperature field to the individual vortices during the merging process. Prior to pairing, the vortices have different average temperature levels. The vortex that is displaced to the higher velocity side (into the jet core) is hotter than the vortex displaced outside, into the lower velocity and cooler section of the shear layer. Following pairing, the unified vortex gets hotter due to the turbulence augmentation, which accompanies the merging process and the resulting increase in the combustion intensity.

**Controlling the Flame Reaction Rate.** The possibility of controlling the growth rate of both two-dimensional and three-dimensional shear layers was demonstrated by many previous works in cold flows (Ho and Huerre, 1984; Oster and Wygnanski, 1982). It was shown that the nonlinear interaction and energy transfer between the mean flow and amplified disturbances can change the growth rate of the shear flow. The saturation in the mixing layer growth, or the region where the width of the shear layer does not increase in the downstream direction, is associated with the disturbances reaching their neutral stability point, where they are no longer amplified. Roberts (1985) showed that in a chemically reacting but noncombusting mixing layer (acid-base reaction), when the shear layer ceases to grow, the chemical reaction ceases too.

In the present work we used methods comparable to those used to control cold flows to modify the flame structure and to control the combustion location. By forcing the flame at the first subharmonic of the fundamental instability frequency with sufficiently high energy, the flame growth saturated when the subharmonic frequency reached its neutral stability point due to the growth of the flame's shear layer. Figure 10 compares this forced flame with an unforced one. The left ordinate in the plot describes the cumulated OH production due to the combustion reaction. This value was obtained by integrating the OH signal intensity across the radial coordinate of the flame at each axial position starting from the exit. The integrated values were then accumulated along the axial coordinate. The images used for this were unphaselocked and averaged over many laser shots. Thus they show the time-average OH signal intensity. In the unforced case (dashed line), the amount of OH production grows linearly in the downstream direction, until the fuel is fully consumed. In the forced case, as explained above, the combustion stops at $X$ = 1.5 $D$, which is where the flame's shear layer saturates. The plateau between $X$ = 1.4 $D$ and $X$ = 2.2 $D$ shows that no additional combustion products are being generated in this range. Only farther downstream the shear layer growth and the combustion resume and more OH radicals are being produced. Figure 10 also shows the variation of the radially averaged flame temperature along the flame axis for the forced flame. The temperature reaches a maximum in the plateau area. This behavior might be related to the fact that in this region no cold air is entrained into the flame, contrary to the two shear-layer spreading zones upstream and downstream of the plateau location. This demonstrates the significance of the shear layer evolution to the combustion process and shows

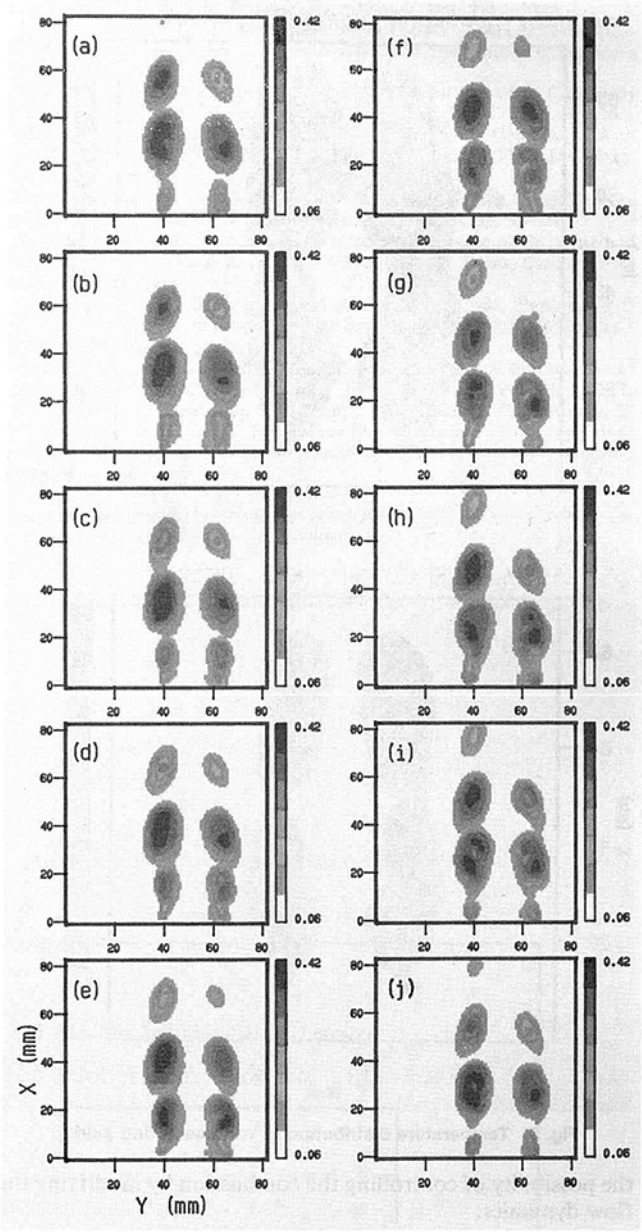


Fig. 8 A pairing process in the circular flame; time step between each frame is 1 ms; notation: I = inside vortex (shed toward inside of shear layer), O = outside vortex (shed toward outside of shear layer), M = merged vortex

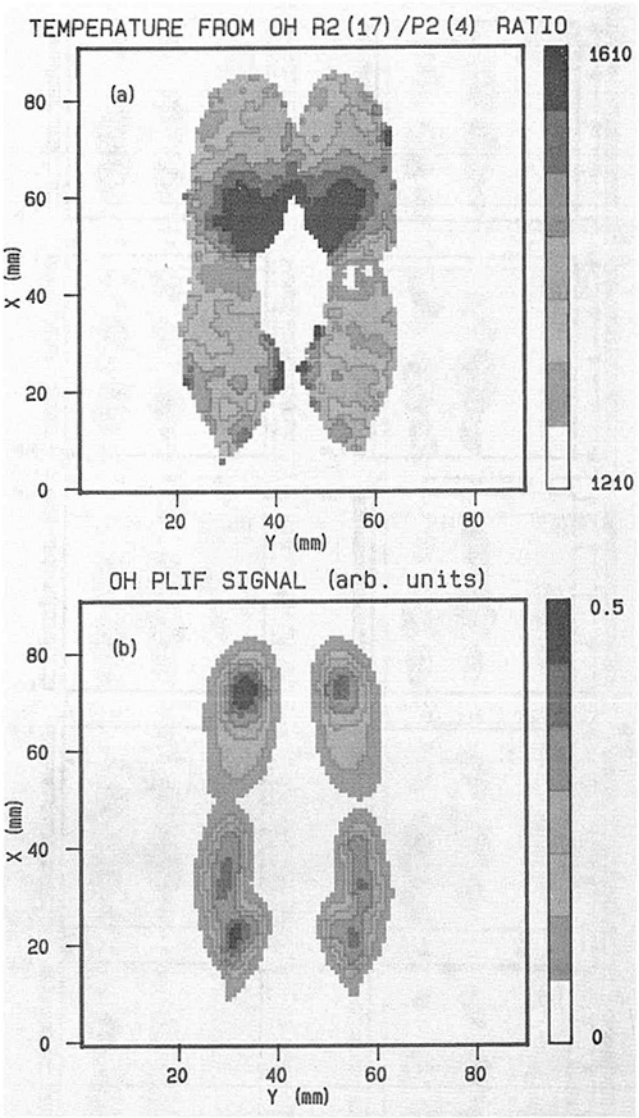


Fig. 9 Temperature distribution of vortices during pairing

the possibility of controlling the combustion by modifying the flow dynamics.

## Conclusions

The interaction between flow structures and the combustion process in an annular diffusion flame was investigated using imaging laser induced fluorescence. Methods that were developed for nonreacting flows to control the shear layer evolution actively were used in a combustion flow. The combustion process associated with vortex roll-up and merging dynamics as well as the similarity between the nonreactive and reactive mixing layer large-scale structures were observed.

The evolution of the flame vortices was studied by mapping the OH radical concentration and the temperature field of the same structures. The vortices formed in the flame are very similar in shape and evolution process to large-scale structures in cold flows. Instantaneous pictures show that the reaction starts in the circumference of the vortices and proceeds into the core as the vortices are being convected in the downstream direction. The temperature distribution confirms this observation by the lower initial temperature levels measured in the initial vortex core. Both OH concentration and the temperature measurements show the flame extinction at the high strain rate regions at the braids of the vortices during roll-up or between adjacent vortices.

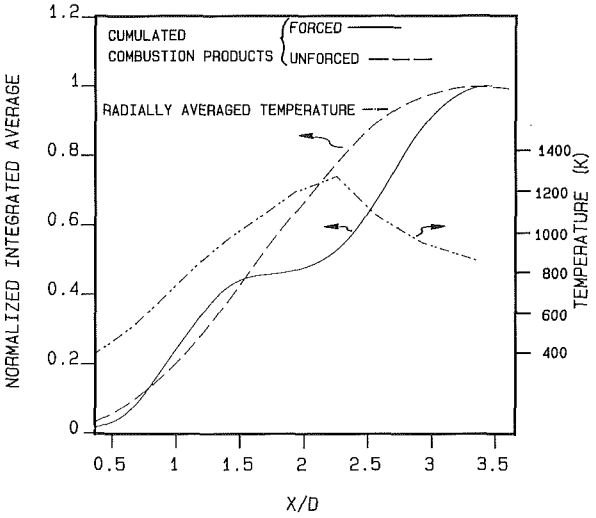


Fig. 10 OH concentration and temperature variation along the flame axis

The merging of two vortices in the flame was found to be very similar to that in cold flow process. The similarity of various shear flow dynamics in nonreacting and reacting flows suggested the possibility of controlling the combustion process by using similar methods applied to cold flows. By altering the spreading rate of the flame shear layer the combustion rate was changed. This underlines the importance of the role of the large-scale structures on the chemical reaction in general and in the combustion process in particular.

The effects of the heat release and the chemical reaction parameters on the shear layer dynamics are currently being studied as well as the influence of the various turbulent scales on the combustion process. Future experiments with simultaneous measurements of the "two-shot" temperature will improve our understanding of the relation between heat release and chemical reaction in the flow structures.

## References


Ballal, D. R., 1986, "Studies of Turbulent Flow-Flame Interaction," *AIAA Journal*, Vol. 24, No. 7, pp. 1148–1154.

Broadwell, J. E., and Dimotakis, P. E., 1986, "Implications of Recent Experimental Results for Modeling Reaction in Turbulent Flows," *AIAA Journal*, Vol. 24, No. 6, pp. 875–889.

Brown, G. L., and Roshko, A., 1974, "On Density Effects and Large Structures in Turbulent Mixing Layers," *Journal of Fluid Mechanics*, Vol. 64, No. 4, pp. 775–816.

Cattolica, R., 1981, "OH Rotational Temperature From Two-Line Laser Excited Fluorescence," *Applied Optics*, Vol. 20, pp. 1156–1166.

Cattolica, R. J., 1982, "OH Radical Nonequlibrium in Methane-Air Flat Flames," *Combustion Science and Technology*, Vol. 44, p. 43.

Cattolica, R. J., Yoon, S., and Knuth, E. L., 1982, "OH Concentration in an Atmospheric-Pressure Methane-Air Flame From Molecular Beam Mass Spectrometry and Laser-Absorption Spectroscopy," *Combustion Science and Technology*, Vol. 28, p. 225.

Cattolica, R. J., and Vosen, S., 1984, "Two-Dimensional Measurements of the [OH] in a Constant Volume Combustion Chamber," *20th Symposium (International) on Combustion*, pp. 1273–1282.

Cattolica, R. J., and Stephenson, D., 1985, "Two-Dimensional Imaging of Flame Temperature Using Laser-Induced Fluorescence," *Dynamics of Flames and Reactive Systems*, Progress in Astronautics and Aeronautics, Vol. 95, pp. 714–721.

Cattolica, R. J., and Vosen, S., 1986, "Fluorescence Imaging of a Flame-Vortex Interaction," *Combustion and Flame*, Vol. 48, p. 77.

Chen, L. D., and Roquemore, W. M., 1986, "Visualization of Jet Flames," *Combustion and Flame*, Vol. 66, pp. 81–86.

Copeland, R. A., Dyer, M. J., and Crosley, D. R., 1985, "Rotational-Level-Dependent Quenching of $A^2\Sigma^+$ OH and OD," *Journal of Chemical Physics*, Vol. 82, p. 4022.

Crow, S. C., and Champagne, F. H., 1971, "Orderly Structure in Jet Turbulence," *Journal of Fluid Mechanics*, Vol. 48, pp. 547–591.

Drake, M. C., Pitz, R. W., Lapp, M., Fenimore, C. P., Lucht, R. P., Sweeney, D. W., and Laurendeau, N. M., 1984, "Measurements of Super-equilibrium Hydroxyl Radical Concentrations in Turbulent Premixed Flames

Using Saturated Fluorescence," *20th Symposium (International) on Combustion*, p. 327.

Eckbreth, A. C., Bonczyk, P. A., and Verdieck, J. F., 1977, "Review of Laser Raman and Fluorescence Techniques for Practical Combustion Diagnostics," U.S. Environmental Protection Agency Report #EPA-600/7-77-066 (NTIS PB-269 653).

Fiedler, H. E., 1975, "On Turbuelnce Structure and Mixing Mechanism in Free Turbulent Shear Flows," in: *Turbulent Mixing in Nonreactive and Reactive Flows*, S. N. B. Murthy, ed., Plenum Press, New York, pp. 381–417.

Givi, P., Jou, W. H., and Metcalfe, R. W., 1986, "Flame Extinction in a Temporally Developing Mixing Layer," *21st International Symposium on Combustion*, Munich, Federal Republic of Germany.

Gutmark, E., and Ho, C. M., 1983, "On the Preferred Modes and the Spreading Rates of Jets," *Physics of Fluids*, Vol. 26, pp. 2932–2938.

Hansen, R. K., 1986, "Combustion Diagnostics: Planar Imaging Techniques," *21st Symposium (International) on Combustion*, pp. 1677–1691.

Ho, C. M., and Huerre, P., 1984, "Perturbed Free Shear Layers," *Annual Review of Fluid Mechanics*, 1984, pp. 365–424.

Hussain, A. K. M. F., 1984, "Coherent Structures and Incoherent Turbulence," *Turbulence and Chaotic Phenomena in Fluids*, T. Tatsumi, ed., pp. 453–460.

Kychakoff, G., Howe, R. D., Hanson, R. K., and McDaniel, J. C., 1982, "Quantitative Visualization of Combustion Species in a Plane," *Applied Optics*, Vol. 21, pp. 3225–3227.

Kychakoff, G., Howe, R. D., Hanson, R. K., Drake, M. C., Pitz, R. W., Lapp, M., and Penney, C. M., 1984, "Visualization of Turbulent Flame Fronts With Planar Laser-Induced Fluorescence," *Science*, Vol. 224, p. 382.

Long, M. B., Levin, P. S., and Fourguette, D. C., 1985, "Simultaneous Two-Dimensional Mapping of Species Concentration and Temperature in Turbulent Flames," *Optics Letter*, Vol. 10, p. 267.

Masutani, S. M., and Bowman, C. T., 1986, "The Structure of a Chemically Reacting Mixing Layer," *Journal of Fluid Mechanics*, Vol. 172, pp. 93–126.

Mungal, M. G., and Dimotakis, P. E., 1984, "Mixing and Combustion With Low Heat Release in a Turbulent Shear Layer," *Journal of Fluid Mechanics*, Vol. 148, pp. 349–382.

Oster, D., and Wygnanski, I., 1982, "The Forced Mixing Layer Between Parallel Streams," *Journal of Fluid Mechanics*, Vol. 123, pp. 91–130.

Roberts, F. A., 1985, "Effects of a Periodic Disturbance on Structure and Mixing in Turbulent Shear Layers and Wakes," Ph.D. Thesis, California Institute of Technology.

Seitzmann, J. M., Kychakoff, G., and Hanson, R. K., 1985, "Instantaneous Temperature Field Measurements Using Planar Laser-Induced Fluorescence," *Optics Letters*, Vol. 10, p. 267.

Strawa, A. W., and Cantwell, B. J., 1985, "Visualization of the Structure of a Pulsed Methane–Air Diffusion Flame," *Physics of Fluids*, Vol. 28, p. 2317.

Vandsburger, U., Lewis, G., Seitzmann, J. M., Allen, M. G., Bowman, C. T., and Hanson, R. K., 1986, "Flame-Flow Structure in an Acoustically-Driven Jet Flame," *Proceedings Western States Section Combustion Institute Meeting*, Paper No. 86-19.

Zhang, Y. Q., Ho, C. M., and Monkewitz, P., 1984, "The Mixing Layer Forced by Fundamental and Subharmonics," *Proceedings IUSAM Symposium on Laminar-Turbulent Transition*, USSR.

# Convective Boiling in Vertical Channels With Different Offset Strip Fin Geometries

**G. D. Mandrusiak**

**V. P. Carey**

Department of Mechanical Engineering,
University of California,
Berkeley, CA 94720

*Newly obtained local heat transfer data are presented for flow boiling of liquids in two partially heated vertical channels with different offset strip fin geometries operating at low to moderate wall superheat levels. Experiments were conducted in special test sections that permitted direct visual observation of the boiling process while simultaneously measuring the heat transfer coefficient along the channel. Data for which nucleate boiling appeared to be completely suppressed were analyzed together with similar results for other offset fin geometries to assess the effects of channel geometry variations on the two-phase heat transfer coefficient during annular film-flow evaporation. For all geometries considered, the data for annular film-flow evaporation were found to correlate well in terms of modified versions of the F and Martinelli parameters used by Bennett and Chen (1980) to correlate similar data for round tubes. For fin matrices of similar size and configuration, the forced convective component of the two-phase heat transfer coefficient was found to be well represented by a single F-parameter correlation curve. However, F-factor correlations for matrices having significant differences in fin and channel dimensions were found to differ substantially. An approximate superposition method for including the contribution of nucleate boiling to the two-phase heat transfer coefficient at low to moderate wall superheat levels is also proposed.*

## Introduction

In recent years, the reduced size and enhanced performance offered by compact heat exchangers with offset strip fins have made them increasingly attractive for use on the phase-change side of both evaporators and condensers in refrigeration, air-conditioning, and chemical processing applications. Interest in these and other applications has prompted a series of experimental and theoretical studies of the boiling and two-phase flow characteristics of offset strip fin geometries.

Galezha et al. (1976) reported heat transfer data obtained in experimental studies of flow boiling of R-12 and R-22 in several compact heat exchangers, each having a different offset fin surface. Robertson (1979) and Robertson and Lovegrove (1983) presented measured local heat transfer data for flow boiling of nitrogen and R-11, respectively, in a channel with offset strip fins. For these tests, the base wall superheat was sufficiently low that nucleate boiling effects were negligible and the dominant mechanism of heat transfer was annular film-flow evaporation.

The results of a finite difference analysis of a fin in a stagnant fluid were used in a model presented by Panitsidis et al. (1975) for predicting the total heat duty of a commercial offset fin matrix. This study focused on high wall superheat conditions for which the dominant heat transfer mechanism was nucleate boiling. Chen et al. (1981) refined this model to include the effects of fluid velocity on the energy transport. This improved model predicted values of the thermal performance of offset fin heat exchangers that were in good agreement with measurements reported in Chen et al. (1981) and Chen and Westwater (1984).

Yung et al. (1981) developed an analytical model for computing the two-phase heat transfer coefficient during annular film-flow boiling in offset fin matrices. Predictions made using this model were in good agreement with measurements reported for nitrogen by Robertson (1979). Robertson (1982, 1984) also developed two different models for predicting local heat transfer coefficients for annular flow in these geometries. Local two-phase heat transfer coefficients predicted with these models generally agreed well with measurements reported by Robertson (1979) and Robertson and Lovegrove (1983).

In a very recent study, Carey and Mandrusiak (1986) developed a closed-form expression for computing the two-phase heat transfer coefficient for annular film-flow boiling in an offset strip fin matrix heated from only one side. Predictions made using this model were in good agreement with measurements obtained by these authors for water, butanol, and methanol.

While each of the above studies has provided valuable insight into the boiling and two-phase flow characteristics of channels with offset strip fins, several aspects of flow boiling in these geometries have not been fully explored. Although they may be useful design tools, the predictive methods presented in the literature have been verified only for one or two specific geometries. A detailed comparison of the performance characteristics of several different geometries would help to define the important geometric parameters controlling two-phase heat transfer. Additional data would also provide the means to evaluate more fully methods of predicting the boiling heat transfer performance of offset fin geometries.

In addition, the effect of nucleate boiling on the local flow boiling heat transfer coefficient at low to moderate wall superheat levels has not been investigated in detail. Flow visualization photographs (see Carey et al., 1986) indicate that, while nucleate boiling may be completely absent at high qualities, it may be the dominant mechanism of heat transfer at low qualities. Consequently, in applications where low-quality performance is important, predictive techniques that do not include nucleate boiling effects may have limited accuracy.

The present study was undertaken to achieve two main objectives. The primary objective was to examine the effects of channel geometry on the local heat transfer coefficient for flow boiling in vertical channels with different offset fin configurations. We specifically sought to determine how the forced convective component of the two-phase heat transfer

Contributed by the Heat Transfer Division for publication in the JOURNAL OF HEAT TRANSFER. Manuscript received by the Heat Transfer Division March 11, 1987. Keywords: Boiling, Forced Convection, Multiphase Flows.

coefficient was affected by changes in the fin geometry. A second objective was to attempt to quantify the contribution of nucleate boiling to the overall two-phase heat transfer coefficient at low to moderate wall superheat levels.

In order to explore the effects of channel geometry on transport, experiments were conducted to obtain flow boiling performance data for two new offset strip fin geometries. The resulting data were then analyzed together with previously reported data for a third geometry (see Carey et al., 1986). This study specifically focused on flow boiling in finned channels heated on only one side. Therefore the results of this study are most directly related to electronics cooling and other applications in which a coolant passage is heated from only one side. Trends in the data for the partially heated channels are also compared to those in the data reported by Robertson (1979) and Robertson and Lovegrove (1983) for an offset fin matrix heated on both sides. Two different correlation methods for predicting the heat transfer coefficient during annular film flow boiling in offset fin geometries are evaluated using the measured data. An approximate technique for computing the contribution of nucleate boiling to the overall heat transfer coefficient at low wall superheat and quality levels is also proposed.

## Experimental Apparatus

The characteristics of boiling and two-phase flow in partially heated vertical channels with offset strip fins were studied using test sections similar to that illustrated in Fig. 1(*a*). The main channel and fin dimensions indicated in Fig. 1(*b*) are summarized in Table 1. Surface 1 in Table 1 is the geometry tested in an earlier study (Carey et al., 1986). Also shown in this table are the dimensions of the surface used by Robertson and his co-workers (1979, 1983) to be considered later in this paper. The equipment used in this study and the fabrication details of test surface 1 are identical to those described in detail in the paper by Carey et al. (1986). Since the test sections for surfaces 2 and 3 are essentially the same as that for surface 1 (with the exception of the fin geometry), the description of the equipment in this paper will be brief.

Each offset strip fin surface is machined from one edge of a rectangular slab of oxygen-free pure copper. The side walls of each test section are Teflon to minimize lateral heat losses, and the top wall is formed by a 6.35-mm-thick glass plate that per-

**Table 1 Dimensions of offset strip fin geometries tested**

| DIMENSION (mm) | SURFACE 1 | SURFACE 2 | SURFACE 3 | ROBERTSON AND CO-WORKERS |
|---|---|---|---|---|
| t | 1.59 | 1.91 | 1.59 | 0.203 |
| H | 3.81 | 9.52 | 1.91 | 6.35 |
| L | 12.7 | 12.7 | 12.7 | 3.18 |
| B | 7.94 | 8.26 | 7.94 | 1.49 |
| $d_h$ | 5.15 | 8.84 | 3.07 | 2.41 |
| $d_{hp}$ | 7.78 | 11.52 | 5.15 | 2.41 |
| $W_c$ | 19.05 | 25.4 | 19.05 | 76.2 |
| $L_H$ | 456 | 762 | 456 | 3400 |
| NUMBER OF THERMOCOUPLE BANKS | 3 | 8 | 3 | 12 |

## Nomenclature

$A$ = constant in equation (3)
$A_F$ = surface area of fins in channel section of length $L_c$
$A_o$ = cross-sectional open area of channel
$A_P$ = prime surface area of channel of length $L_c$
$B$ = cross-stream fin spacing
$c_p$ = specific heat at constant pressure
$d_h$ = hydraulic diameter based on wetted perimeter $= 4A_o/P_W$
$d_{hp}$ = hydraulic diameter based on heated perimeter $= 4A_o/P_H$
$F$ = convective boiling parameter $= h_c/h_{fp}\mathrm{Pr}_f^{0.296}$
$g$ = acceleration due to gravity
$G$ = mass flux
$h$ = heat transfer coefficient
$h_c$ = heat transfer coefficient due to forced convective effects alone (no nucleate boiling)
$h_{FZ}$ = heat transfer coefficient predicted by the Forster-Zuber relation
$H$ = dimension of fins from root to tip
$i_{fg}$ = latent heat of vaporization of coolant
$k$ = fluid thermal conductivity
$k_c$ = conductivity of copper
$L$ = length of fin in the downstream direction
$L_c$ = length of channel section
$L_H$ = heated length of channel
$n$ = exponent in equation (3)
$N_B$ = bubble growth parameter $= \frac{h_c}{k}\left[\frac{\sigma}{g(\rho_f-\rho_g)}\right]^{1/2}$
$p$ = pressure
$\Delta p$ = difference in saturation pressure for change in saturation temperature equal to $\Delta T$
$P_H$ = heated perimeter
$P_W$ = wetted perimeter
$\mathrm{Pr}_f$ = liquid Prandtl number
$Q$ = surface heat transfer rate
$\mathrm{Re}_f$ = liquid Reynolds number $= G(1-x)d_h/\mu_f$
$\mathrm{Re}_{fp}$ = liquid Reynolds number based on heated perimeter $= G(1-x)d_{hp}/\mu_f$
$S$ = suppression factor
St = Stanton number $= h/Gc_p$
$t$ = fin thickness
$T_w$ = wall temperature of primary surface of channel
$T_m$ = bulk mean temperature of the coolant
$T_{SAT}$ = saturation temperature of coolant
$W_c$ = width of copper slab
$x$ = mass quality
$X_{tt}$ = Martinelli parameter for turbulent-turbulent flow $= [(dp/dz)_{Ff}/(dp/dz)_{Fg}]^{1/2}$
$\eta$ = fin efficiency
$\mu$ = absolute viscosity
$\rho$ = density
$\sigma$ = liquid surface tension
$\Psi$ = parameter defined in equation (10*a*)

### Subscripts

$f$ = liquid properties or corresponding to liquid flow alone in the channel
$fp$ = corresponding to liquid flow alone in the channel heated on one side only
$F$ = corresponding to the fins
$FR$ = friction component of pressure gradient
$g$ = vapor properties or corresponding to vapor flow alone in the channel
$n$ = corresponding to nucleate boiling effects
$ne$ = effective value for nucleate boiling
$tp$ = corresponding to two-phase flow conditions

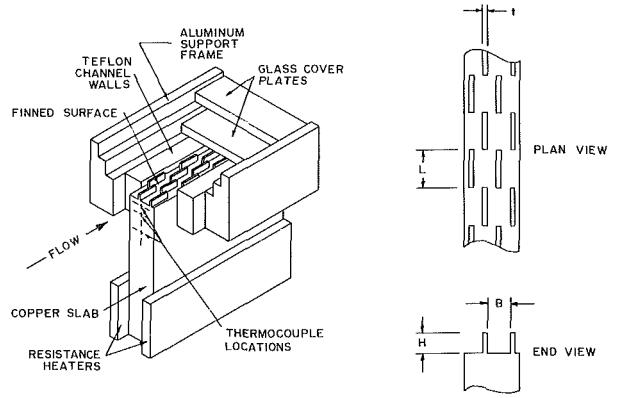


**Fig. 1 (a) Cutaway view of test section; (b) drawing of fin geometry**

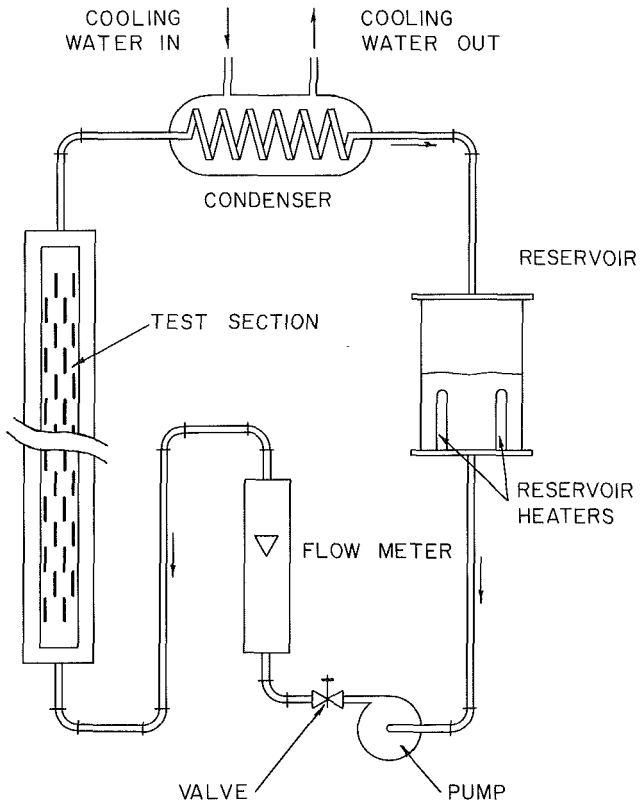


**Fig. 2 Test system used in convective boiling experiments**

mitted direct visual observation of the boiling process all along the channel. A second glass plate covers the inner plate as shown in Fig. 1(*a*) to reduce heat losses from the top of the assembly.

Two resistance heaters clamped to the bottom of each copper slab as indicated in Fig. 1(*a*) provided an essentially uniform heat input along the entire heated length of each channel. Temperatures measured with precisely located copper-constantan thermocouples, embedded in the copper slab as shown in Fig. 1(*a*), were used to determine the heat flux and wall temperature at several locations along the heated length of each channel. A fourth thermocouple was installed through the channel wall at each bank to measure the local flow temperature. This quantity was combined with the measured heat flux and wall temperature to compute the local heat transfer coefficient.

In addition to providing local values of heat flux and wall temperature, the banks of thermocouples made it possible to compute the magnitude of any flow of heat axially along the copper slab. For single-phase flow, the slab temperature tended to increase in proportion to the bulk fluid temperature along the entire heated length of the channel. However, calculations indicate that the error in the local heat flux at each thermocouple station caused by axial conduction effects was less than 4 percent for the conditions explored here. For two-phase flow, the slab temperature near the channel surface was virtually uniform, and axial conduction effects were negligible.

A schematic diagram of the test loop used in the present study is presented in Fig. 2. A centrifugal pump was used to provide a steady flow of subcooled liquid to each test section. The level of subcooling at the test section inlet could be controlled by varying the condenser water flow rate and/or the power input to two auxiliary heaters in the reservoir. The flow rate was measured upstream of the test section using a variable area flowmeter calibrated over a wide range of temperatures for each fluid tested.

Prior to running each series of heat transfer measurements, the copper surface of each test section was cleaned using a mild acid solution. This procedure, which was repeated on a regular basis, kept the copper surfaces free of tarnish and insured that the nucleation properties of each surface were consistent from one test to the next.

Although Fig. 1(*a*) depicts the finned surface positioned horizontally, all tests were performed with each test section mounted in a vertical support frame with the flow upward.

## Experimental Procedure

Before running the convective boiling experiments, the single-phase heat transfer characteristics of the two new offset strip fin surfaces were determined using the technique described in detail in Carey et al. (1986). The measured single-phase heat transfer data for each surface, obtained using water as the test fluid, are plotted in terms of the Colburn *j*-factor and Reynolds number in Fig. 3. The data presented in Fig. 3, which were measured at locations at least 40 hydraulic diameters downstream of the inlet to the test section, correspond to local values of the heat transfer coefficient averaged over the heated perimeter at each thermocouple station. The local heat transfer coefficient was determined by iteratively solving the energy balance relation

$$W_c L_c k_c \nabla T_c = h[A_P + \eta_F A_F][T_w - T_m] \tag{1}$$

where $\nabla T_c$ is the measured local temperature gradient in the copper slab, and $\eta_F$ is the fin efficiency for the finned portion of the surface given by

$$\eta_F = \frac{\tanh(MH)}{MH}, \qquad M = \left[\frac{2h(t+L)}{k_c tL}\right]^{1/2} \tag{2}$$

It has been assumed throughout this paper that the tortuous path followed by the flow and interactions between the flow and the fins would give the flow at least a weakly turbulent nature, even at Reynolds numbers below 1000. As such, curves have only been fit to experimental data that lie in the turbulent regime for the three surfaces shown in Fig. 3. The three curves indicated in Fig. 3 are of the form

$$\mathrm{St}_{fp}\mathrm{Pr}_f^{2/3} = A\,\mathrm{Re}_{fp}^{-n} \tag{3}$$

where

$$\mathrm{Re}_{fp} = \frac{G(1-x)d_{hp}}{\mu_f} \tag{4}$$

and $x$ is the local quality, taken to be zero for single phase flow. The coefficients $A$ and $n$ have been chosen to provide least-squares curve fits to the measured turbulent heat transfer data. As the results in Fig. 3 show, these curves are actually in reasonable agreement with the experimental data over the en-

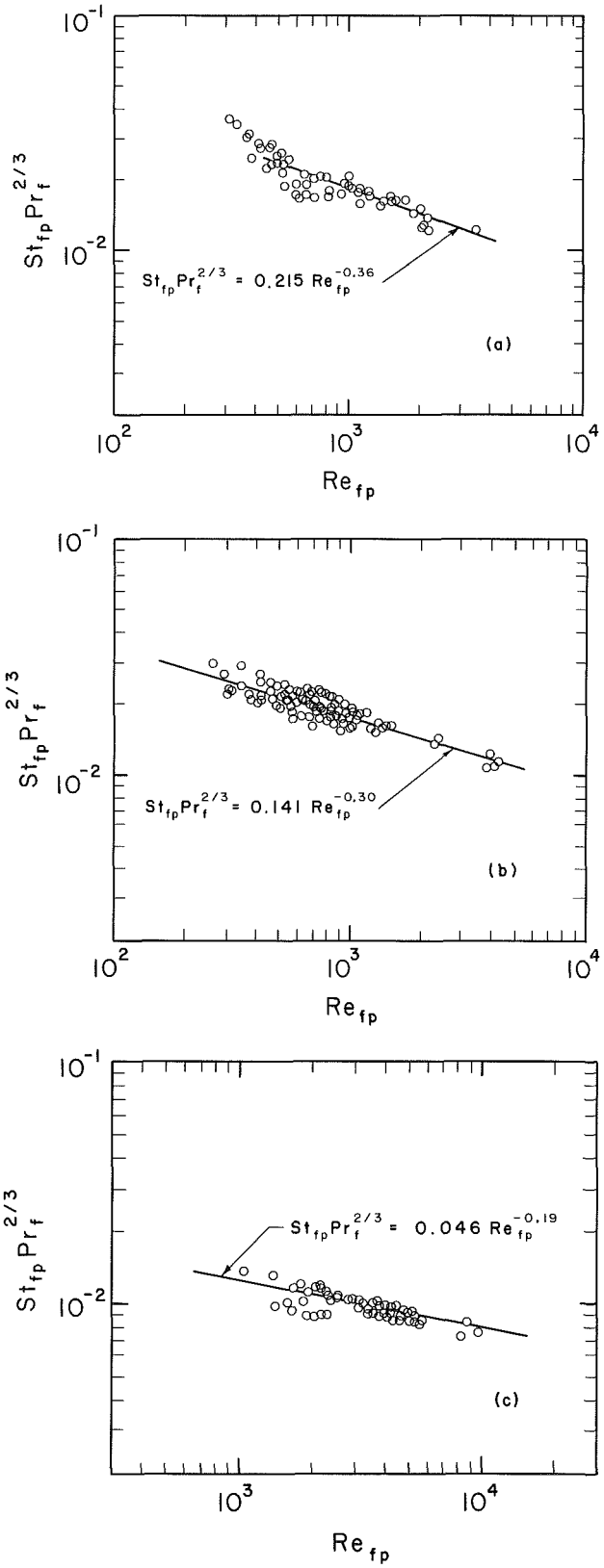


**Fig. 3 Single-phase heat transfer data for each test surface: (*a*) surface 1; (*b*) surface 2; (*c*) surface 3**

tire range of conditions explored here, including conditions for which the flow was laminar. It should be noted that attempts to correlate the single-phase heat transfer data for all three surfaces using a single curve were not very successful. Correlations like that proposed by Joshi and Webb (1984), for example, are best suited to small-scale commercial geometries heated from both sides and may not yield accurate results when used for the surfaces of the present study.

For the flow boiling experiments, the system was allowed to stabilize at the selected power and flow settings for at least 10–15 min before any thermocouple readings were recorded. The local two-phase heat transfer coefficient was determined at each thermocouple location where boiling was observed to occur using the method described above for single phase flow, with the mean flow temperature in equation (1), $T_m$, now equal to $T_{SAT}$, the measured saturation temperature of the coolant. The boiling heat transfer coefficient calculated in this manner is the average value over the heated perimeter of the channel at each thermocouple station, and corresponds to specific values of mass flux and local quality.

The banks of thermocouples embedded in the copper slab provided the local variation of the surface heat flux along the entire heated length of the channel. This information was combined with the measured mass flow rate in an energy balance to compute the local quality at each thermocouple station downstream of the onset of saturated boiling. The downstream location where saturated nucleate boiling began was determined by visually inspecting the flow. This zero quality point was taken to be the lowest vertical location where continuous growth and release of vapor bubbles occurred and vapor bubbles were present throughout the liquid flow in the channel. An energy balance on the fluid from the inlet of the test section to the two-phase zone yielded essentially the same location for the point of zero quality. Consequently, the quality $x$, computed from an energy balance downstream of the visually determined location of $x = 0$, will be interpreted as being the thermodynamic quality throughout this paper.

Values of the two-phase heat transfer coefficient were obtained for convective boiling of methanol, butanol, and R-113 for surface 2, and water and methanol for surface 3 (see Table 1). Two-phase heat transfer data for boiling of methanol, butanol, and water in surface 1 have already been presented by Carey et al. (1986). Overall, data have been obtained for qualities ranging from 0 to 80 percent and mass flux values ranging from 3 to 320 kg/m$^2$s. The estimated accuracy of the measurements for all three surfaces is $\pm 5$ percent for $G$, $\pm 7$ percent for $x$, and $\pm 11$ percent for $h$.

## Discussion and Analysis of Results

Measured variations of the two-phase heat transfer coefficient with quality and mass flux for flow boiling of methanol in Surfaces 1, 2, and 3 are presented in Fig. 4. The shading used in each symbol indicates the visually observed flow regime for each data point. The variation of flow regime with mass quality and mass flux shown in Fig. 4 is typical of that observed with the other test fluids. For a few points at very low mass qualities, the flow appeared to be in the bubbly or slug flow regime. At higher qualities, the flow was annular in configuration, and bubble nucleation on the heated surface appeared to be completely suppressed. A detailed description of the flow patterns observed during convective boiling in channels with offset strip fins and photographs of the different regimes present has been presented by Carey et al. (1986).

At low to moderate quality, similar trends of increasing heat transfer coefficient with increasing $x$ or $G$ are observed for all three geometries in Fig. 4. The trends in the data shown in Fig. 4 also indicate that, for a given quality and mass flux, the heat transfer coefficients for the three surfaces only differ by about 20 percent. Apparently, the three large scale offset fin geometries represented in this figure are sufficiently similar that the overall two-phase heat transfer coefficient (including contributions from both nucleate boiling and forced convec-

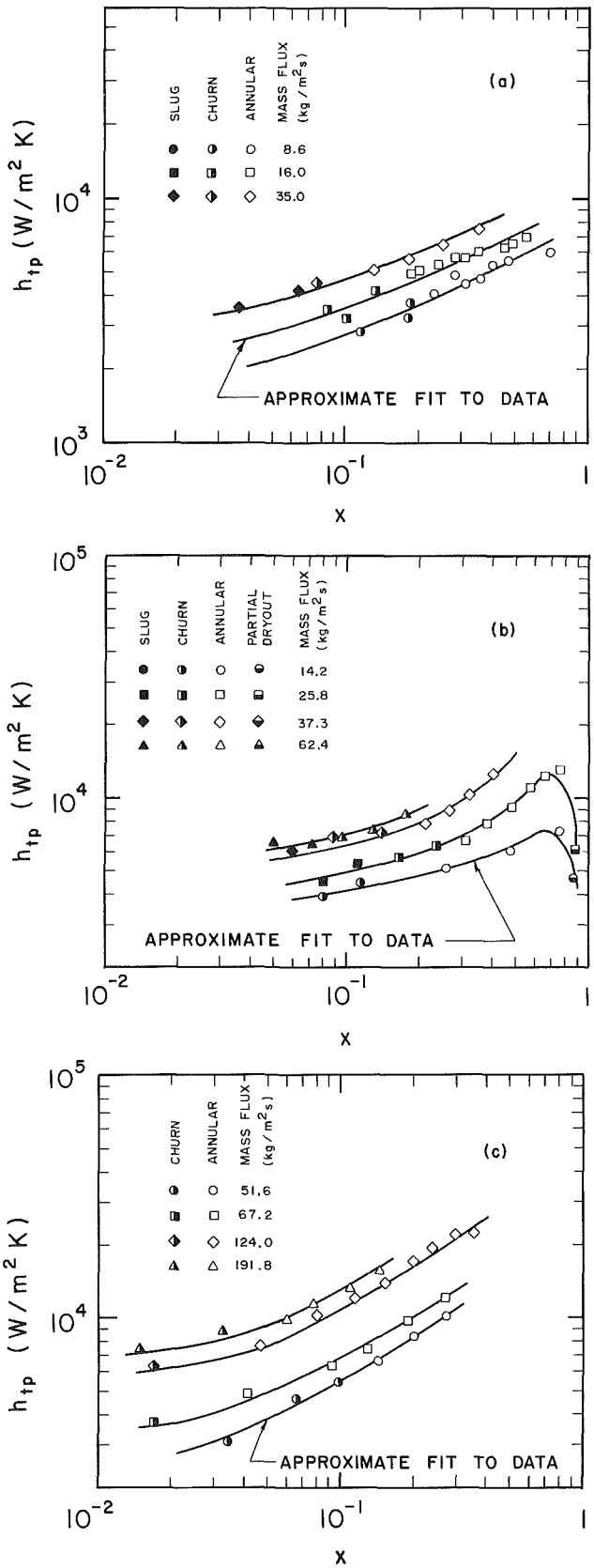


**Fig. 4 Measured local heat transfer coefficients for convective boiling of methanol in (*a*) surface 1, (*b*) surface 2, (*c*) surface 3**

tive evaporation) is not overly sensitive to changes in fin dimensions.

It is also found that at the same quality, mass flux, and base wall superheat, the measured heat transfer coefficients for these geometries were typically two to three times the values predicted by the Bennett and Chen (1980) correlation for a round tube with the same hydraulic diameter $d_h$. Hence all three of these geometries provide substantial enhancement of the flow boiling heat transfer performance relative to that for a round tube under comparable conditions. Apparently the enhancement in heat transfer performance provided by offset fin geometries during single-phase flow is even more pronounced during convective boiling.

For the two lowest mass flux levels shown in Fig. 4(*b*), the two-phase heat transfer coefficient appears to drop substantially for local mass qualities above about 75 percent. Flow visualization studies conducted in conjunction with the heat transfer measurements indicated that a substantial portion of the heated surface was dry for these flow conditions. Continuous dryout over large portions of the heated surface was invariably accompanied by a significant drop in heat transfer performance. The quality at which significant dryout and a subsequent drop in heat transfer coefficient occurred was observed to increase slightly with increasing mass flux. Partial dryout has been observed for local qualities as low as 35 percent for mass flux values below about 12 kg/m²s for Surface 1 (Carey et al., 1986). However, surface dryout for these flow conditions was often intermittent, and periodic rewet of the surface resulted in little or no drop in heat transfer coefficient. The large drop in heat transfer coefficient visible in Fig. 4(*b*) was not observed unless the local mass quality exceeded about 75 percent and a significant portion of the heated surface was dry for extended periods of time.

A substantial fraction of the heat transfer measurements reported here correspond to flow conditions in which annular film flow evaporation was the dominant heat transfer mechanism, and bubble nucleation appeared to be completely suppressed. As such, the variation of the forced convective component of the two-phase heat transfer coefficient with channel geometry will be considered first. An approximate method of accounting for the effects of weak nucleate boiling at low quality and low to moderate wall superheat will be developed later in this paper.

Two methods of correlating the annular film-flow boiling heat transfer coefficient were examined as part of this investigation. In the first method, the data were correlated in terms of a modified version of the $F$-parameter used by Bennett and Chen (1980) to correlate the forced convective effects for flow boiling in vertical round tubes

$$F = \frac{h_c}{h_{fp}} \mathrm{Pr}_f^{-0.296} \tag{5}$$

Here, $h_{fp}$ is computed from the turbulent single-phase correlation for the specific geometry used

$$h_{fp} = G(1-x)c_{pf}A\mathrm{Re}_{fp}^{n}\mathrm{Pr}_f^{-2/3} \tag{6}$$

rather than the Dittus-Boelter equation as used for round tubes. The $F$-parameter has traditionally been postulated to be a function of the Martinelli parameter $X_{tt}$. In this study, the expression for $X_{tt}$ derived in Carey et al. (1986) was used in the data analysis. In their derivation, Carey et al. (1986) assumed that the winding path followed by the two-phase flow through the fin matrix and interactions between the two phases along the gas-liquid interface would give both phases at least a weakly turbulent nature, even when the liquid Reynolds number was below about 1000. Treatment of the liquid film as being at least weakly turbulent is also consistent with its treatment in most previous analyses of annular film-flow boiling in round tubes. The liquid and vapor friction factors were determined from the turbulent heat transfer correlations given in equation (3) using the modified Reynolds analogy described in Carey et al. (1986). These assumptions, together with the definition of the Martinelli parameter, yield the following expression for $1/X_{tt}$:

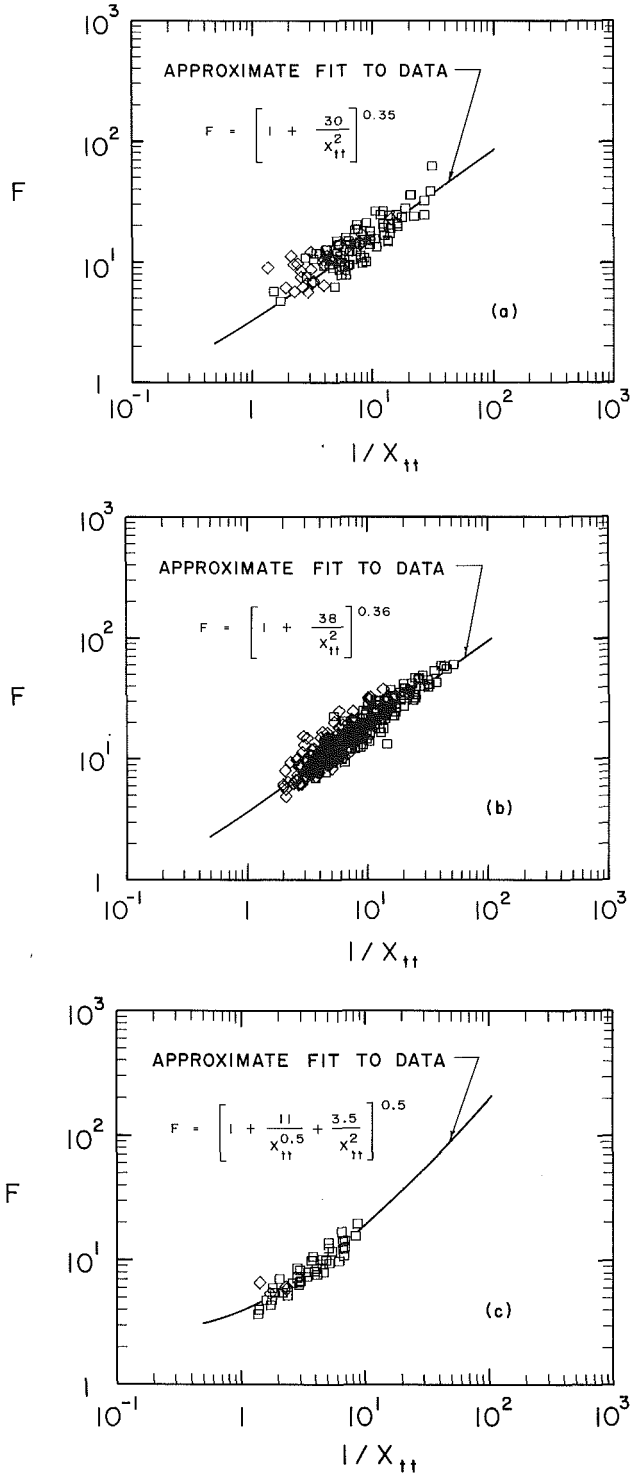


**Fig. 5 Measured forced convective heat transfer data for flow boiling in three different partially heated vertical channels with offset strip fins correlated in terms of the modified Chen *F*-parameter of equation (5): (*a*) surface 1, (*b*) surface 2, (*c*) surface 3**

$$\frac{1}{X_{tt}} = \left(\frac{\rho_f}{\rho_g}\right)^{1/2} \left(\frac{\mu_g}{\mu_f}\right)^{n/2} \left(\frac{x}{1-x}\right)^{1-n/2} \tag{7}$$

For a more detailed discussion of the derivation of this expression for $1/X_{tt}$, the reader is referred to the paper by Carey et al. (1986).

The measured forced convection heat transfer data for the three offset fin surfaces tested here are plotted separately in terms of $F$ and $1/X_{tt}$ as defined above in Fig. 5. Results for all coolants tested with each geometry are included in each plot.

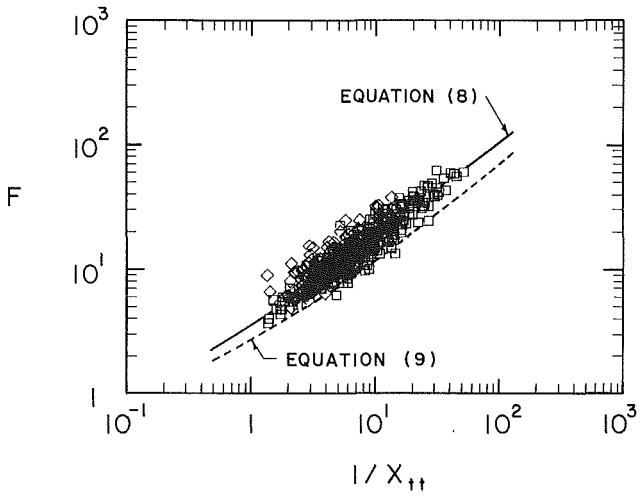


**Fig. 6 Measured forced convective heat transfer data for flow boiling in partially heated vertical channels with offset strip fins correlated in terms of the Chen *F*-parameter of equation (5). Data for all three large scale surfaces and all four test fluids are shown.**

A composite plot summarizing forced convective heat transfer data for all three surfaces and all four test fluids (water, methanol, butanol, and R-113) is shown in Fig. 6. Data corresponding to churn flow have been designated by diamond-shaped symbols, and those corresponding to annular flow have been designated by squares. Data for which bubble nucleation or partial surface dryout were observed have not been included in these plots. The equations shown in each figure represent approximate curve fits to the data points. (The functional form selected for each equation is somewhat arbitrary.)

The results shown in Fig. 5 indicate that the convective boiling component of the two-phase heat transfer coefficient for the three offset fin geometries considered here differ only slightly when correlated in terms of the $F$-parameter. Apparently, these geometries are sufficiently similar that normalizing the flow boiling data with the appropriate single-phase heat transfer coefficient very nearly collapses the data onto a single curve. Indeed, Fig. 6 indicates that all of the measured data are reasonably well represented by a single empirical relation

$$F = \left[1 + \frac{28}{X_{tt}^2}\right]^{0.372} \tag{8}$$

In fact, 70 percent of the heat transfer data shown in Fig. 6 lie within $\pm 20$ percent of equation (8).

Upon closer examination, however, the results presented in Fig. 5 indicate that small variations in the fin dimensions result in slightly different optimal curve fits to the $F$-parameter data for each geometry. As such, it seems reasonable to expect correlations for $F$-data for widely different channel geometries to vary substantially. Heat transfer data obtained for annular film-flow evaporation of nitrogen by Robertson (1979) and R-11 by Robertson et al. (1983) in a commercial offset fin matrix are plotted in terms of $F$ and $1/X_{tt}$ in Fig. 7. The agreement between the Robertson data and the optimal curve fit to the three large-scale surfaces of the present study, equation (8), is rather poor. As Table 1 indicates, the dimensions of the surface used by Robertson and his co-workers differ substantially from those of the large-scale surfaces used here. In addition, since the fin geometry used in the Robertson studies is fabricated from a formed sheet of metal sandwiched between two flat plates, an additional layer of the fin material covers the prime surface at intermittent locations along the channel. Consequently, the prime surface itself is irregular, unlike the geometries con-

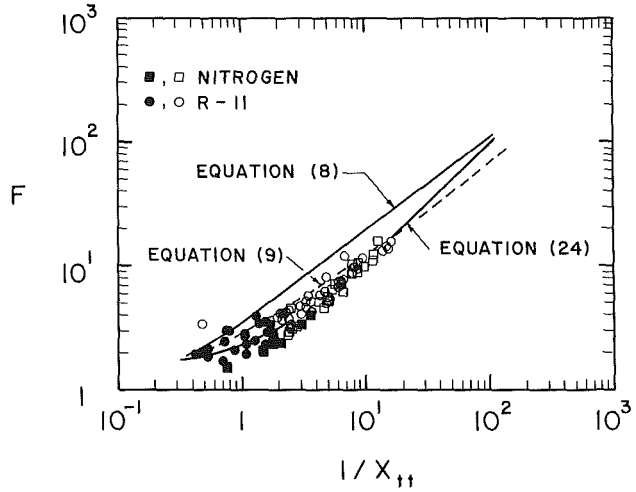


**Fig. 7 Forced convective heat transfer coefficients measured by Robertson (1979) and Robertson and Lovegrove (1983) for flow boiling of $N_2$ and R-11 in a vertical channel with offset strip fins correlated in terms of the *F*-parameter**

sidered in the present study (in which the prime surface is completely flat). As a result of these significant differences in fin and channel geometry, the large disparity between the Robertson data and equation (8) is not surprising. A similar shift in the dimensionless forced convective component of the two-phase heat transfer coefficient was also observed by Xu and Carey (1987) in tests with a partially heated channel with cross-ribbed walls.

Furthermore, none of the *F*-parameter data presented in this paper or those obtained by Robertson and his co-workers (1979, 1983) are well represented by the Chen (1966) correlation for flow boiling of liquids in round tubes (see Collier, 1981)

$$F = 2.35(1/X_{tt} + 0.213)^{0.736} \quad \text{for } 1/X_{tt} \geq 0.1 \qquad (9a)$$

$$= 1 \quad \text{for } 1/X_{tt} < 0.1 \qquad (9b)$$

Equation (9) is indicated by a broken line in Figs. 6 and 7.

These observations seem to indicate that, while it may be possible to obtain generalized correlations for groups of geometrically and dimensionally similar channels, a single, universally applicable *F*-parameter correlation for these complicated geometries does not appear to exist. It appears, therefore, that the most accurate approach would be to determine *F*-parameter correlations for each separate geometry experimentally in a manner analogous to determining individual Colburn *j*-factor curves for single phase flow. Additional two-phase heat transfer data are required for other offset fin geometries in order to quantify the effects of channel dimensions on two-phase energy transport.

A second method of correlating the convective evaporation component of the two-phase heat transfer coefficient based on the Ψ-parameter derived in Carey et al. (1986) was also considered. Using an approximate model for turbulent heat transfer in thin films, it was argued that the heat transfer coefficient data for annular film-flow boiling in partially heated vertical channels with offset strip fins could be correlated in terms of the Martinelli parameter $X_{tt}$ defined previously and the parameter Ψ defined as

$$\Psi(X_{tt}) = \frac{4.74\sqrt{A}\tan^{-1}[0.149\sqrt{\mathrm{Re}_{fp}\mathrm{Pr}_f}\sqrt{d_h/d_{hp}}]}{\mathrm{Re}_{fp}^{n/2}\mathrm{Pr}_f^{1/6}(d_{hp}/d_h)^{n/2}}\left(\frac{h_c}{h_{fp}}\right) \qquad (10a)$$

As demonstrated in the original derivation by Carey et al. (1986), the Ψ parameter is almost identical to the *F*-parameter given by equation (5), with only a slightly different Prandtl number dependence. As such, it is not surprising to find that the Ψ-parameter was not any more (or less) successful than the *F*-parameter at correlating the convective heat transfer coefficient data. The annular film-flow boiling data for all three large-scale surfaces represented in Fig. 6 were, in fact, well correlated by the empirical relation

$$\Psi = \left(1 + \frac{7.5}{X_{tt}} + \frac{3.45}{X_{tt}^2}\right)^{1/2} \qquad (10b)$$

The mean absolute deviation of the Ψ-factor data from equation (10*b*) was virtually identical to the deviation of the *F*-factor data from equation (8). The choice of using Ψ or *F* as the correlating parameter therefore appears to be somewhat arbitrary. We have selected to present the data considered here in terms of *F* because it is more conventional and more easily evaluated.

## Treatment of Nucleate Boiling Effects

Although most of the data obtained in this study correspond to flow conditions for which the heat transfer coefficient is dominated by convective evaporation effects, a number of data points were also obtained at lower qualities for which nucleate boiling effects were significant. Development of a means for predicting the effect of nucleate boiling on heat transfer for these circumstances is the subject of this section.

Most existing correlations for predicting the heat transfer coefficient for convective boiling in round tubes implicitly or explicitly incorporate a superposition approach similar to that advanced by Chen (1966). In correlations of this type, the overall heat transfer coefficient, $h_{tp}$, is assumed to equal the sum of a macroscopic or convective component, $h_c$, and a microscopic or nucleate boiling component, $h_n$

$$h_{tp} = h_c + h_n \qquad (11)$$

The effectiveness of the nucleate boiling and/or forced convective components of the two-phase heat transfer coefficient are expected to be controlled by conditions in a thin region near the heated surfaces. Since both of these mechanisms act primarily in a boundary layer region or liquid film (which is typically small compared to channel dimensions) it seems reasonable to assume that equation (11) will hold, with appropriate modifications, for the offset fin geometries considered here.

To appreciate the importance of nucleate boiling effects during flow boiling, consider the measured local heat transfer data shown in Fig. 8 for low-quality two-phase flow in the Surface 2 geometry. For these data, bubble nucleation was clearly visible on both the channel and fin walls. The predicted values of the two-phase heat transfer coefficient shown in Fig. 8 were computed assuming that the contribution from forced convective evaporation, computed using the *F*-parameter given by equation (8), dominated and that the effects of nucleate boiling were negligible (i.e., $h_n = 0$). It is clear from this plot that, for these geometries, correlations that neglect nucleate boiling effects can grossly underestimate the two-phase heat transfer coefficient for low-quality conditions.

The macroscopic component, $h_c$, of the two-phase heat transfer coefficient is traditionally correlated in terms of the *F*-parameter given by equation (5). It will be assumed that the correlations developed to fit data for annular film flow boiling presented in the previous section will appropriately predict the forced convective contribution to the overall heat transfer, even when significant nucleate boiling effects are present. This assumption is consistent with previous superposition models proposed for round tubes.

Chen (1966) proposed that the nucleate boiling, or microscopic, component of the two-phase heat transfer coeffi-

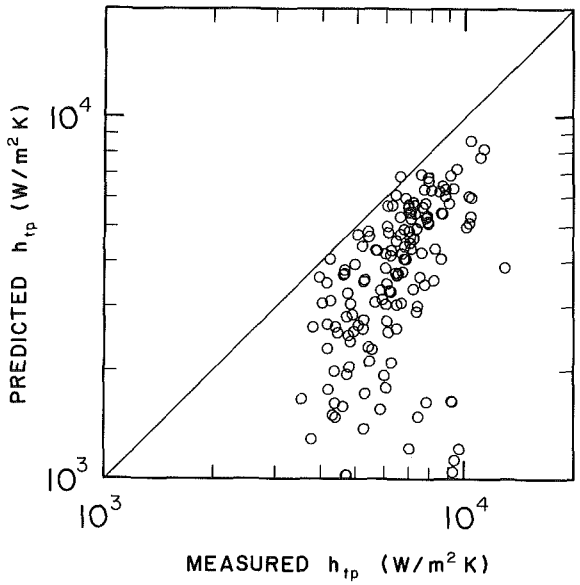


**Fig. 8 Comparison of heat transfer coefficients for low-quality convective boiling for surface 2 with values predicted assuming nucleate boiling is negligible. The convective evaporation component was computed using equation (8).**

cient for flow boiling of liquids in round tubes be predicted using a modified version of the Forster-Zuber (1955) pool boiling correlation

$$h_n = h_{FZ} S \tag{12}$$

with

$$h_{FZ} = 0.00122\left[\frac{k_f^{0.79} c_p^{0.45} \rho_f^{0.49}}{\sigma^{0.5} \mu_f^{0.29} i_{fg}^{0.24} \rho_g^{0.24}}\right] \Delta T_{SAT}^{0.24} \Delta P_{SAT}^{0.75} \tag{13}$$

The suppression factor $S$, introduced by Chen (1966), adjusts the pool boiling wall superheat $\Delta T_{SAT}$ for the effects of flow velocity.

One important difference between pool boiling on a flat surface and that on a finned surface is that the release of bubbles can be inhibited by the fin walls if the lateral spacing between the fins is of the order of the bubble departure diameter (Bondurant and Westwater, 1972). For the fluids considered here, this critical fin spacing is approximately 1 to 1.5 mm. Assuming this criterion also holds for bubble nucleation during flow boiling, bubble-fin interference is not expected to be a problem with the large-scale offset fin matrices of the present study. As such, the Chen (1966) approach for correlating nucleate boiling data will be assumed to be valid for the offset fin matrices being considered here.

The Forster-Zuber correlation applies to nucleate boiling at a specified wall temperature, which is assumed uniform over the entire surface. The use of this type of correlation is more complicated when fins are involved in the boiling heat transfer process because the temperature of each fin, in general, will not be uniform along its length. Indeed, fin efficiencies as low as 70 percent were quite common in the experimental data reported here, particularly for the tall fins of surface 2. The difference between the fin and prime surface temperatures must be taken into account in order to accurately predict the nucleate boiling contribution to the overall heat transfer coefficient.

Heat is transferred to the coolant by the nucleate and forced convective boiling mechanisms from both the prime surface and the fins. An overall energy balance thus requires

$$Q_{TOT} = (Q_c)_P + (Q_c)_F + (Q_n)_P + (Q_n)_F \tag{14}$$

where the four contributions to the total heat transfer in equation (14) represent average values for each portion of the heated surface in the channel considered.

By analogy to single-phase convection, we also expect that $Q_{TOT}$ is related to the overall convective boiling heat transfer coefficient $h_{tp}$ by

$$Q_{TOT} = h_{tp}[A_P + \eta_F A_F]\Delta T_P \tag{15}$$

where the fin efficiency $\eta_F$ is given by equation (2) (with $h = h_{tp}$) and $\Delta T_P$ is the wall superheat of the prime surface. Since the convective component of the overall heat transfer coefficient is postulated to be a function of the inverse Martinelli parameter only, and independent of the wall superheat, the convective contribution to the total heat transfer in equation (14) may immediately be written as

$$(Q_c)_P + (Q_c)_F = h_c[A_P + \eta_F A_F]\Delta T_P \tag{16}$$

with $h_c$ calculated using equation (5). For nucleate boiling, however, the heat transfer coefficient depends on the local wall superheat as indicated by equation (13). Since the temperature of the fin is not expected to be uniform, the individual contributions of the prime and fin areas to the nucleate boiling heat transfer must be computed separately

$$(Q_n)_P + (Q_n)_F = h_n(\Delta T_P) A_P \Delta T_P + h_n(\Delta T_F) A_F \Delta T_F \tag{17}$$

The functional notations $h_n(\Delta T_P)$ and $h_n(\Delta T_F)$ emphasize that the nucleate boiling heat transfer coefficients for the prime and fin areas must be computed using appropriate mean values of the wall superheat, $\Delta T_P$ and $\Delta T_F$, respectively. Since the superheat of the prime surface, $\Delta T_P$, was measured directly, the first term in equation (17) can be calculated immediately. In determining an appropriate effective value of the wall superheat of the fin surface, $\Delta T_F$, the variation in the wall temperature and the overall heat transfer coefficient along the height of the fin is assumed to be small. The latter assumption permits the fin efficiency to be computed with reasonable accuracy using the overall $h_{tp}$ value for the entire heated surface. By combining these assumptions with the definition of the fin efficiency, the mean superheat of the finned surface can be approximated by

$$\Delta T_F \approx \eta_F \Delta T_P$$

with $\eta_F$ given by equation (2). (The heat transfer coefficient $h$ in equation (2) includes the effects of both nucleate boiling and convective evaporation.) With this approximation for the wall superheat of the fin area, equation (15) is rewritten as

$$(Q_n)_P + (Q_n)_F = h_n(\Delta T_P) A_P \Delta T_P + \eta_F h_n(\eta_F \Delta T_P) A_F \Delta T_P \tag{18}$$

Combining equations (11)–(18), and solving for the two-phase heat transfer coefficient yields

$$h_{tp} = h_c + h_{ne} \tag{19}$$

where the effective nucleate boiling contribution to the heat transfer coefficient for the entire heated surface, $h_{ne}$, is given by

$$h_{ne} = \frac{h_{FZ}(\Delta T_P) A_P + h_{FZ}(\eta_F(\Delta T_P)\eta_F A_F}{A_P + \eta_F A_F} S \tag{20}$$

The values of $h_{FZ}$ associated with each part of the heated perimeter are evaluated using equation (13) with the appropriate wall superheat. Note that even though the effects of convection on nucleation for the fins and the prime surface may be somewhat different, a single mean suppression factor has been used for the entire heated surface in this treatment. Note also that if the fin surfaces are all at the same temperature as the prime surface (i.e., $\eta_F = 1.0$) or if $A_F = 0$, equation (20) reduces to the expression used by Chen (1966) for flow in round tubes with a uniform wall temperature.

The remaining unknown in equation (20) is the mean suppression factor $S$. In a recent study, Bennett et al. (1980) developed a semitheoretical expression for the suppression factor for flow boiling both in and on round tubes. An

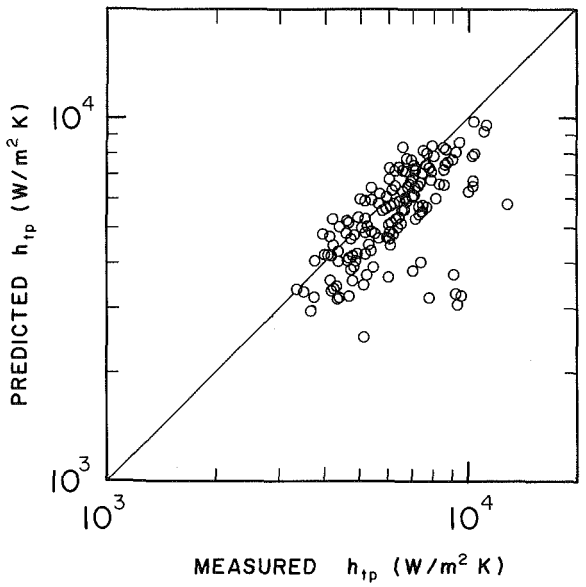


**Fig. 9 Comparison of heat transfer coefficients for low-quality convective boiling for surface 2 with values predicted using equation (19). The forced convective coefficient was calculated using equation (8) and the suppression factor was computed using equation (21).**

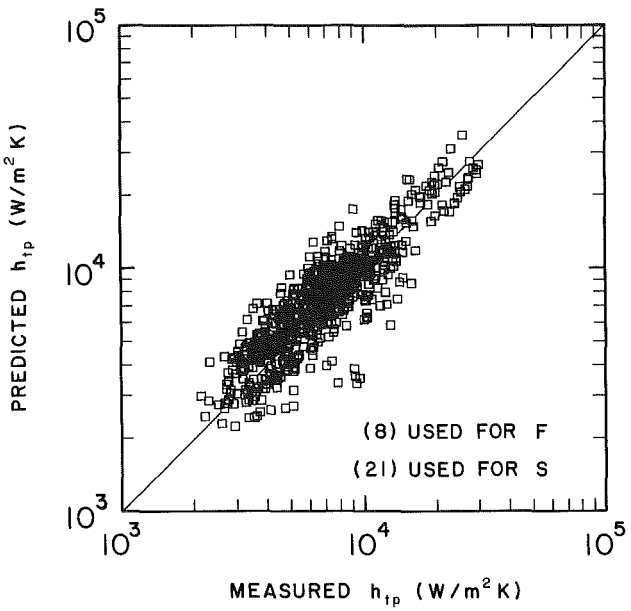


**Fig. 10 Comparison of measure boiling heat transfer coefficients with values predicted using equation (19). Data for all three large-scale surfaces and all four test fluids are shown.**

analysis of the heat transfer in the bubble growth region was used to obtain the functional form of a relation for the suppression factor, and the value of an unknown constant in the relation was chosen to optimize the fit to data for round tubes. The resulting relation can be written in terms of a bubble growth parameter $N_B$ as

$$S=\frac{24.4}{N_B}\left[1-\exp(-0.041N_B)\right] \tag{21}$$

where

$$N_B=\frac{h_c}{k_f}\left[\frac{\sigma}{g(\rho_f-\rho_g)}\right]^{1/2} \tag{22}$$

It is proposed here that the Bennett et al. (1980b) correlation for the suppression factor for flow boiling in round tubes be directly extended to boiling in the offset strip fin geometries considered in this study. This implicitly assumes that the bubble growth microlayer is sufficiently thin that the definition of the bubble growth parameter (22) does not have to be adjusted for larger scale changes in channel geometry.

To determine whether equation (21) applies to the present flow situation, equations (8) and (19)–(21) were used to predict the local two-phase heat transfer coefficient for flow conditions in the present study for which bubble nucleation was clearly visible in the channel. Values of the two-phase heat transfer coefficient predicted in this manner for these flow conditions are compared to experimental measurements in Fig. 9. Although there is considerable scatter in the data, agreement between the predicted and measured $h_{tp}$ values in Fig. 9 is fairly good, with a mean absolute error of 16 percent. Furthermore, comparisons of the results shown in Figs. 8 and 9 indicate that for these data, the inclusion of the nucleate boiling effects using the superposition method described above significantly improves the agreement between the predicted and measured values of the heat transfer coefficient.

An attempt was also made to determine experimental values of the suppression factor for those data points for which bubble nucleation was clearly visible in the channel. After using the empirical $F$-factor curve, equation (8), to compute $h_c$, the measured heat transfer coefficient $h_{tp}$ and wall superheat $\Delta T_P$ were used in equations (19) and (20) to determine the suppression factor. Suppression factor data determined in this manner showed considerable scatter when correlated in terms of the bubble growth parameter $N_B$. Two-phase heat transfer coefficients predicted using an empirical curve fit to these $S$ data

$$S=1-\frac{2}{\pi}\tan^{-1}\left[\left(\frac{N_B}{35}\right)^6\right] \tag{23}$$

were no more accurate than those predicted using the correlation developed by Bennett et al. (1980b), equation (21).

## Comparison of Correlation Predictions With Data

Heat transfer coefficients measured for the large-scale offset fin matrices of the present study are compared to values predicted using the superposition techniques described above in Fig. 10. For these predictions, the composite $F$-factor correlation, equation (8), was used to compute $h_c$, and the Bennett et al. (1980b) correlation, equation (21), was used for the suppression factor. The plot incorporates data from all three copper surfaces and all four test fluids (water, butanol, methanol, and R-113), and includes results for local qualities ranging from 1 to 70 percent. For local qualities above about 70 percent, a substantial portion of the heated surface was generally observed to be dry, and use of the methods outlined above for these circumstances is questionable. The mean absolute deviation between the predicted heat transfer coefficients and the experimental measurements is 21.5 percent.

The modified superposition technique developed above was also used to predict heat transfer coefficients for the offset fin geometry used by Robertson (1979) and Robertson et al. (1983). For this surface, the forced convective component of the two-phase heat transfer coefficient was computed using an approximate curve fit to the $F$-parameter data in Fig. 7

$$F=\left[1+\frac{3.53}{X_{tt}^{1/2}}+\frac{1.05}{X_{tt}^2}\right]^{1/2} \tag{24}$$

rather than the (inappropriate) composite curve for the large-scale surfaces, equation (8). Equation (21) was still used to calculate the suppression factor. As shown in Fig. 11, predicted values of the two-phase heat transfer coefficient are in good agreement with the experimental data, with a mean absolute deviation of 13.1 percent. The superposition correla-

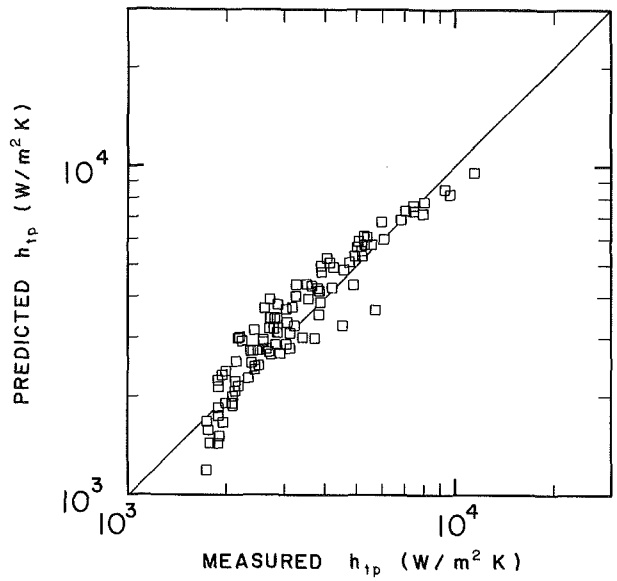


**Fig. 11 Comparison of heat transfer coefficients measured by Robertson (1979) and Robertson and Lovegrove (1983) for flow boiling of $N_2$ and R-11 with values predicted using equation (19). The forced convective coefficient was calculated using the *F*-parameter given by equation (24) and the suppression factor was computed using equation (21).**

tion technique predicts that the contribution of nucleate boiling for the surface used by Robertson and his co-workers is very small (< 5 percent) relative to the convective component. This result is consistent with the arguments of Robertson (1979) and Robertson et al. (1983) that imply that nucleate boiling effects were negligible in their convective boiling experiments.

## Conclusions

Newly obtained heat transfer data for upward flow boiling in two different offset strip fin geometries are reported in this paper. Based on our analysis of these data, together with those previously reported for other geometries of this type, the following conclusions regarding convective boiling in offset strip fin geometries at low to moderate wall superheat levels have been reached:

1 Heat transfer data for moderate to high quality conditions where bubble nucleation appeared to be completely suppressed were well correlated in terms of modified versions of the Martinelli parameter and the *F*-parameter used by Bennett and Chen (1980) for convective boiling in round tubes.

2 For a given group of geometrically and dimensionally similar surfaces, the *F*-factor data appeared relatively insensitive to small differences in channel geometry. However, *F*-factor data for surfaces having significant differences in fin and channel dimensions may differ substantially. Hence, in general, normalizing $h_{tp}$ with the single-phase heat transfer coefficient for the liquid flowing alone is not sufficient to remove all geometry dependence. These observations imply that accurate prediction of convective boiling heat transfer coefficients using this correlation technique may require a separate *F*-factor correlation for each geometry, in much the same way that each geometry requires its own Colburn *j*-factor correlation to predict single-phase heat transfer.

3 *F*-factor data for offset fin matrices do not appear to be well represented by standard correlations for the *F*-parameter for round tubes.

4 The contribution of nucleate boiling to the two-phase heat transfer coefficient for finned surfaces at low superheat levels can be computed using the Forster-Zuber correlation in a modified version of the superposition scheme proposed by Chen (1966), which incorporates an approximate treatment of the variation of the surface temperature along the fins. The expression for the nucleate boiling suppression factor for round tubes developed by Bennett et al. (1980) was found to work well in this scheme for the offset fin geometries considered in this study. Use of an empirical curve fit to measured suppression factor data offered little improvement in predictions.

## Acknowledgments

Support for this research was provided by the National Science Foundation under research grant No. CBT-8451781.

## References

Bennett, D. L., and Chen, J. C., 1980, "Forced Convective Boiling in Vertical Tubes for Saturated Pure Components and Binary Mixtures," *AIChE Journal*, Vol. 26, pp. 454-461.

Bennett, D. L., Davis, M. W., and Hertzler, B. L., 1980, "The Suppression of Saturated Nucleate Boiling by Forced Convective Flow," *AIChE Symposium Series*, Vol. 76, pp. 91-103.

Bondurant, D. L., and Westwater, J. W., 1971, "Performance of Transverse Fins for Boiling Heat Transfer," *Chem. Eng. Prog. Symp. Series*, Vol. 67, No. 113, pp. 30-37.

Carey, V. P., and Mandrusiak, G. D., 1986, "Annular Film-Flow Boiling of Liquids in a Partially Heated Vertical Channel With Offset Strip Fins," *Int. J. Heat Mass Transfer*, Vol. 29, pp. 927-939.

Chen, C. C., Loh, J. V., and Westwater, J. W., 1981, "Prediction of Boiling Heat Transfer Duty in a Compact Plate-Fin Heat Exchanger Using the Improved Local Assumption," *Int. J. Heat Mass Transfer*, Vol. 24, pp. 1907-1912.

Chen, C. C., and Westwater, J. W., 1984, "Application of the Local Assumption for the Design of Compact Heat Exchangers for Boiling Heat Transfer," ASME JOURNAL OF HEAT TRANSFER, Vol. 106, pp. 204-209.

Chen, J. C., 1966, "Correlations for Boiling Heat Transfer to Saturated Fluids in Convective Flow," *I & EC Process Design and Development*, Vol. 5, pp. 322-329.

Collier, J. G., 1981, "Forced Convective Boiling," in: *Two Phase Flow and Heat Transfer in the Power and Process Industry*, A. E. Bergles, J. G. Collier, J. M. Delhaye, G. F. Hewitt, and F. Mayinger, eds., Hemisphere Publishing Company, New York, Chap. 8.

Forster, H. K., and Zuber, N., 1955, "Dynamics of Vapor Bubbles and Boiling Heat Transfer," *AIChE Journal*, Vol. 1, pp. 531-535.

Galezha, V. B., Usyukin, I. P., and Kan, K. D., 1976, "Boiling Heat Transfer With Freons in Finned-Plate Heat Exchangers," *Heat Transfer—Soviet Research*, Vol. 8, pp. 103-110.

Joshi, H. M., and Webb, R. L., 1984, "Prediction of Heat Transfer in the Offset Strip-Fin," ASME Paper No. 84-HT-27.

Panitsidis, H., Gresham, R. D., and Westwater, J. W., 1975, "Boiling of Liquids in a Compact Plate-Fin Heat Exchanger," *Int. J. Heat Mass Transfer*, Vol. 18, pp. 37-42.

Robertson, J. M., 1979, "Boiling Heat Transfer With Liquid Nitrogen in Brazed-Aluminum Plate-Fin Heat Exchangers," *AIChE Symposium Series*, Vol. 75, pp. 151-164.

Robertson, J. M., 1982, "The Correlation of Boiling Coefficients in Plate Fin Heat Exchanger Passages With a Film-Flow Model," *Proceedings, 7th International Heat Transfer Conference*, Vol. 6, Munich.

Robertson, J. M., 1984, "The Prediction of Convective Boiling Coefficients in Serrated Plate-Fin Passages Using an Interrupted Liquid-Film Flow Model," ASME HTD-Vol. 34, pp. 163-171.

Robertson, J. M., and Lovegrove, P. C., 1983, "Boiling Heat Transfer With Freon 11 (R11) in Brazed Aluminum Plate-Fin Heat Exchangers," ASME JOURNAL OF HEAT TRANSFER, Vol. 105, pp. 605-610.

Xu, X., and Carey, V. P., 1987, "An Experimental Study of the Effects of Channel Orientation on Convective Boiling in a Partially Heated Cross-Ribbed Channel," *Proceedings of the 1987 ASME-JSME Thermal Engineering Joint Conference*, Honolulu, HI, Vol. 3, pp. 141-146.

Yung, D., Lorenz, J. J., and Panchal, C., 1980, "Convective Vaporization and Condensation in Serrated Fin Channels," ASME HTD-Vol. 23, pp. 29-37.

# Performance of a Three-Phase, Spray-Column, Direct-Contact Heat Exchanger

**T. Çoban**[1]
Research Assistant.

**R. Boehm**
Professor.
Fellow ASME

Mechanical and Industrial Engineering Department,
University of Utah,
Salt Lake City, UT 84112

*A numerical model of a three-phase, direct-contact, spray-column heat exchanger has been developed. This model has been used to calculate performance information about this type of device and to compare, where possible, to experiments. General equations are defined for distance up the column using a physically based model for the local heat transfer. This model has been used to investigate a number of characteristics of these devices, such as temperature and holdup distributions through the column. A new formulation is given for a mixed, time-averaged temperature that may be representative of measurements taken with temperature transducers in direct-contact heat exchangers. Little has been given in the literature about quantitative variations of performance as a function of the key independent variables, and information on these aspects is presented here. Although the results presented are for a specific geometry (0.61 m diameter, 3 m active column height, evaporating pentane in 85°C water), the variations shown can give insights generally into the factors affecting performance in these devices. In virtually all cases examined here, extremely good comparisons are shown between predictions and measurements. Conclusions are drawn about the applicability of the model and the important effects demonstrated.*

## Introduction

Three-phase direct-contact heat exchangers have been proposed for a variety of applications including power generation and water desalination. One of the major problems still present in this technical area is a lack of comprehensive design tools. Since only limited experiments have been performed, there is also a lack of broadly applicable data. This is in contrast to the large amount of experimental and theoretical work on physical behavior of conventional closed heat exchangers.

The key to a better understanding of these devices will almost certainly be through the development of numerical models that accurately reflect the heat transfer and fluid mechanics phenomena present. Little work has been successfully accomplished in this area. One of the more definitive efforts in this aspect has been directed toward the simulation of liquid/liquid spray columns, and this was presented by Jacobs and Golafshani (1985). They showed fair agreement between the results of their numerical model and the experimental results for the liquid/liquid portion of a three-phase direct-contact heat exchanger driven by geothermal brine.

Although there has been a large number of analytical studies of heat transfer to a single bubble reported in the literature, there have been relatively few that addressed the overall performance of three-phase spray columns. Typical of the previous work is that of Mokhtarzadeh and El-Shirbini (1979). They have analyzed droplet growth when the droplet is rising and evaporating in an immiscible liquid. They assumed the droplet was traveling through an infinite, stationary medium of constant temperature. Results given by them included transient response predictions and parametric curves of the effects of key variables.

Recently Battya et al. (1985) performed a similar type of analysis. Again the assumptions of infinite, isothermal continuous phase have been invoked, but they included a downward velocity for this fluid. A major concern of theirs was to find appropriate correlations for the Nusselt number for the heat transfer in these kinds of system.

A number of studies have focused on one of the more critical aspects of the modeling: that of defining appropriate models for droplet heat transfer rates. One of the earliest workers in this area was Sideman, and he and co-workers have both performed experiments and developed theories (Sideman and Taitel, 1964; Sideman and Isenberg, 1967). His theoretical approach is based upon a conduction-type solution in the semi-infinite (assumed) continuous fluid.

More recently Raina and co-workers have dealt with several aspects of bubble behavior on a fundamental level. Included are the analysis of the instantaneous velocity (Raina and Wanchoo, 1984) or general motion (Raina et al., 1984), a basic study of the heat transfer during change of phase (Raina and Grover, 1984) and a further analysis of heat transfer considering sloshing effects (Raina and Grover, 1985). The basis of the Raina heat transfer mechanism is to consider heat transfer only through the liquid layer in the bottom of the droplet and to assume that, other than the area effects of the layer, the heat transfer resistance exists only in the continuous phase.

Little analytical insight about the overall performance of complex systems has been given. Designers are without good numerical models to describe these kinds of systems.

The work reported here is an attempt to develop a calculational procedure to describe the flow and heat transfer of a direct-contact spray column, and to use this model to investigate the effects of different variables on the temperature profiles, total heat transfer, and holdup ratio of the column.

## Model Development

The development of the governing equations for the numerical model starts with the continuity equations. Using the assumption that the mass flow rates for both continuous and dispersed phases remain constant (this assumes, for example, that none of either the dispersed or continuous phase goes into solution in the other phase), the continuity equations for counterflow of the phases can be written as

$$m_d = \rho_d A \phi U_d \tag{1}$$

[1] Now with the Geothermal Energy Test and Utilization Service of the Mineral Research and Exploration Institute, Ankara, Turkey.

Contributed by the Heat Transfer Division and presented at the ASME-JSME Joint Thermal Engineering Conference, Honolulu, Hawaii, March 22-27, 1987. Manuscript received by the Heat Transfer Division July 28, 1986. Keywords: Direct-Contact Heat Transfer, Multiphase Flows.

$$m_c = \rho_c A (1-\phi) U_c \tag{2}$$

where $m_d$, $\rho_d$, and $U_d$ are the mass flow rate, density, and velocity of the dispersed fluid, respectively. The subscript $c$ refers to the continuous fluid. The holdup ratio $\phi$ is the volume of the dispersed fluid per unit volume of the total fluid.

A momentum equation for the total flow can be written as

$$\frac{d}{dz}[\rho_d U_d^2 \phi] + \frac{d}{dz}[\rho_c U_c^2 (1-\phi)] = -\frac{dP}{dz} - [\rho_c (1-\phi) + \rho_d \phi] g \tag{3}$$

where $z$ is the vertical coordinate measured from the bottom of the column. The variables $P$ and $g$ represent local pressure and gravitational acceleration, respectively. All of the other variables are the same as used in the continuity equations. Substituting the continuity equations (1) and (2) into equation (3), the momentum equation becomes

$$\frac{dP}{dz} = -\frac{m_d}{A}\frac{dU_d}{dz} - \frac{m_c}{A}\frac{dU_c}{dz} - [\rho_c(1-\phi) + \rho_d \phi] g \tag{4}$$

Note that the third term on the right-hand side of the equation shows the hydrostatic pressure difference. The first two terms on the right-hand side indicate the effect of velocity changes on the pressure change.

Similarly the energy equations governing one-dimensional steady-state flow for the dispersed and continuous fluids can be written as

$$\frac{d}{dz}[\rho_d \phi U_d \mathbf{h}_d] = \frac{Q_d}{V} \tag{5}$$

$$\frac{d}{dz}[\rho_c (1-\phi) U_c \mathbf{h}_c] = -\frac{\eta Q_d}{V} \tag{6}$$

In these equations $Q_d$ indicates the heat transferred to the dispersed fluid and $\eta$ defines the ratio of the heat transfer from the continuous phase divided by the heat transfer to the dispersed phase. For the case of heat loss to the surroundings, $\eta$ will be greater than unity. It is assumed that the heat loss originates from the continuous phase. Substituting the continuity equations into equations (5) and (6) results in the following relationships:

$$\frac{d\mathbf{h}_d}{dz} = \frac{A}{m_d}\frac{Q_d}{V} \tag{7}$$

$$\frac{d\mathbf{h}_c}{dz} = -\frac{A}{m_c}\frac{\eta Q_d}{V} \tag{8}$$

The heat transfer from the bubble $Q_d$ is calculated from the following equation, which is a modification of an equation given for the heat transfer through the liquid portion of the droplet (Tochitani et al., 1977) as well as conduction to the vapor portion:

$$h = (k_l/D)(\mathrm{Pr}_c \mathrm{Re}_c)^{1/3}\{0.466(\pi - \beta + 0.5\sin 2\beta)^{2/3}\}$$
$$+ (5k_v/D)\{1 - 0.466(\pi - \beta + 0.5\sin 2\beta)^{2/3}\} \tag{9}$$

The additional term not given by Tochitani et al. (1977), which accounts for the heat transfer directly to the vapor, is based upon a transient conduction formulation with a linearly varying surface temperature (Coban and Boehm, 1986).

Empirical relations are used to solve for the velocity and droplet diameter. One of the relationships for the velocity variation was given by Raina and co-workers (1984) in the following form:

$$U = \frac{1.1547\left[\left\{1 - \frac{\rho_a}{\rho_c}\left(\frac{D_0}{D}\right)^3\right\}\left(\frac{Dg}{C_D}\right)\right]^{1/2} \mathbf{D}^{\left(\frac{5}{6} - \frac{1}{T_c}\mathbf{D}\right)}}{\left[\frac{T_c^2 + T_d^2}{2T_c T_d}\right]^{\mathbf{D}} \left[\frac{Cp_c \mu_c}{k_c}\right]^{\frac{D_0}{1.6D}}} \tag{10}$$

The variable $C_D$ in equation (10) is the drag coefficient. To calculate the drag coefficient, an experimentally determined curve-fitting of data for a solid sphere is combined with a correlation for Stokes formulaton for a drag force (White, 1974). The resultant equation is given by

$$C_D = \left[\frac{24}{\mathrm{Re}} + \frac{6}{1+\mathrm{Re}^{1/2}} + 0.4\right]\left[\frac{1 + \frac{2\mu_c}{3\mu_d}}{1 + \frac{\mu_c}{\mu_d}}\right] \tag{11}$$

It is assumed that the droplets are always spherical (more discussion on this point is given later) and rigid. While there are obviously situations when droplets are not well characterized by these assumptions, it will turn out that these are not a bad approximation for the situation considered here.

The last relation needed is derived from the continuity equation. The diameter of the droplets is given as

$$D = D_o\left[\frac{n_b \rho_c U_d}{n_{b,o}\rho_{c,o} U_{d,o}}\right]^{1/3} \tag{12}$$

## Nomenclature

**A** = phase surface area
$A$ = cross-sectional area of the column
$C_D$ = drag coefficient
$C_p$ = specific heat at constant pressure
$D$ = diameter of droplet
**D** = averaged diameter $= (D^2 + D_0^2)/(2DD_0)$
$g$ = acceleration due to gravity
$h$ = heat transfer coefficient
**h** = enthalpy
$k$ = thermal conductivity
$m$ = mass flow rate
MW = molecular weight
$n_b$ = number of drops per unit volume
$P$ = pressure
Pr = Prandtl number
$Q$ = heat transfer
Re = Reynolds number
$t$ = time
$T$ = temperature
$U$ = velocity
$V$ = active volume of the column
$z$ = vertical distance along column from bottom
$\beta$ = vapor half opening angle
$\eta$ = ratio: heat transfer to the bubble to heat transfer from the continuous phase
$\mu$ = viscosity
$\rho$ = density
$\phi$ = holdup ratio

**Subscripts and Superscripts**

$av$ = average value
$c$ = continuous fluid
$cd$ = between continuous and dispersed fluids
$ct$ = between continuous fluid and thermocouple
$d$ = dispersed fluid
$dt$ = between dispersed fluid and thermocouple
$e$ = exit
$i$ = inlet
$l$ = liquid
loss = loss
mix = mixed value
$p$ = pentane
$o$ = initial
$T$ = top
$v$ = vapor
$w$ = water

where $o$ indicates the initial conditions and $n_b$ is the number of droplets per unit volume. $n_b$ is given by

$$n_b = \frac{\phi}{\pi D^3/6} \tag{13}$$

If there is no coalescence or breakup of the bubbles, $n_b$ can be approximated to be constant everywhere in the column. Therefore equation (12) reduces to

$$D = D_o \left[ \frac{\rho_c U_d}{\rho_{c,o} U_{d,o}} \right]^{1/3} \tag{14}$$

With these additional relationships, the appropriate number of equations is obtained to solve the system and to examine effects in a three-phase spray-column heat exchanger.

One final item is necessary. To be able to compare the results of any model that computes separate temperatures for both the continuous and the dispersed phases throughout the column to experimental measurements, a special formulation will often be necessary. This is because any temperature measuring device, and particularly large, shielded thermocouples, will present some degree of thermal inertia when interacting with the time-varying temperatures resulting from the dispersed and continuous phases flowing over the sensor. In the experimental studies used here for comparison to the model calculations, small amplitude temporal variations from large sensors were time averaged. Hence, the need exists to formulate a method in the model of combining the temperatures for the dispersed and continuous phases approriately for comparison to the time-averaged temperatures reported in the experimental data.

Consider a volume region monitored by the temperature measuring device. It is assumed that the statistical, time-averaged reading of the thermocouples is determined by the thermal transport to the thermocouple from the dispersed and continuous phases over some total (and arbitrarily long) amount of time. Appropriate times can be determined from the holdup ratio and each phase's velocity, although this is not necessary to be able to apply the basic idea. Assuming that there is the previously supposed one direction for the travel of the two phases (albeit opposite in sign), the total travel distance in the time $\Delta t$ should be $\Delta z_c$ plus $\Delta z_d$. There, the total volume each phase covered during this distance interval can be written as shown in the equations below, without regard to sign.

$$\text{Dispersed phase volume} = \mathbf{A}_d \Delta z_d = \mathbf{A}\phi \Delta z_d = \mathbf{A}\phi U_d \Delta t \tag{15}$$

$$\text{Continuous phase volume} = \mathbf{A}_c \Delta z_c = \mathbf{A}(1-\phi)\Delta z_c$$

$$= \mathbf{A}(1-\phi)U_c \Delta t \tag{16}$$

By combining equations (15) and (16) with an expression for an energy balance on the thermocouple, the mixed temperature is found as shown in equation (17).

$$T_{\text{mix}} = \frac{h_{dt}\phi U_d T_d + h_{ct}(1-\phi)U_c T_c}{h_{dt}\phi U_d + h_{ct}(1-\phi)U_c} \tag{17}$$

Heat transfer coefficients for the thermocouple were calculated separately either for single phase or evaporation situations from a correlation given by Churchill and Bernstein (1977).

The computational order progresses in the following manner. First the velocity of the dispersed phase is calculated. Then the holdup ratio and the continuous velocity are found from the continuity equation. Next the droplet radius is found. Initial derivatives of the velocities are assumed to be zero and new values are calculated from the stepwise change. The momentum and energy equations are solved by finding the gradients of the pressure and enthalpies and then by calculating values for these variables. In the boiling region the quality of the dispersed phase was calculated from the vertical gradient of the quality, and this is used to find the enthalpy. In all cases, bubble curvature effects on pressure were neglected. All thermodynamic and transport properties were evaluated from curve fits.

## Experiments

Experiments were performed in a 0.61-m-dia tower that measured 6.1 m high and was made entirely of conventional pipe. In all tests reported here an active tower height of approximately 3 m was used. Water entered the tower through an inlet nozzle at the midheight of the column and flowed downward, exiting through the bottom. Commercial grade $n$-pentane was used as the dispersed fluid. Pentane entered the column from the bottom through a multiple shower head ar-

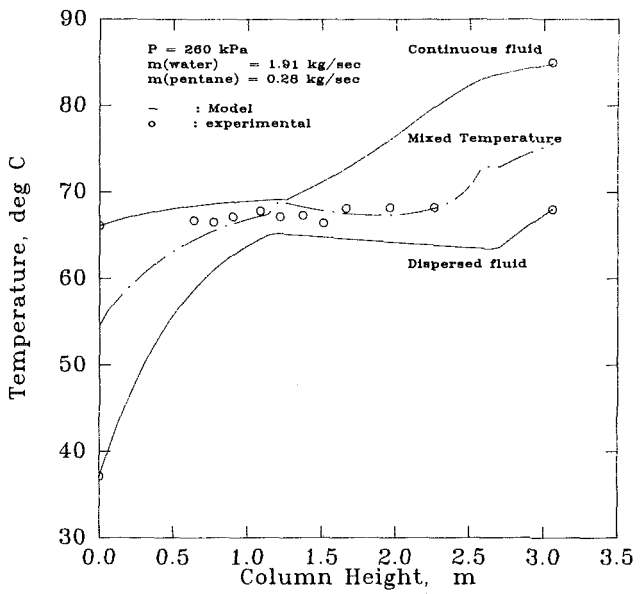


**Fig. 1 Temperature profile of dispersed and continuous fluids, mixed temperature, and experimental temperature profile data along the length of the column; $m_p = 0.28$ kg/s, $m_w = 1.91$ kg/s, $P = 260$ kPa**

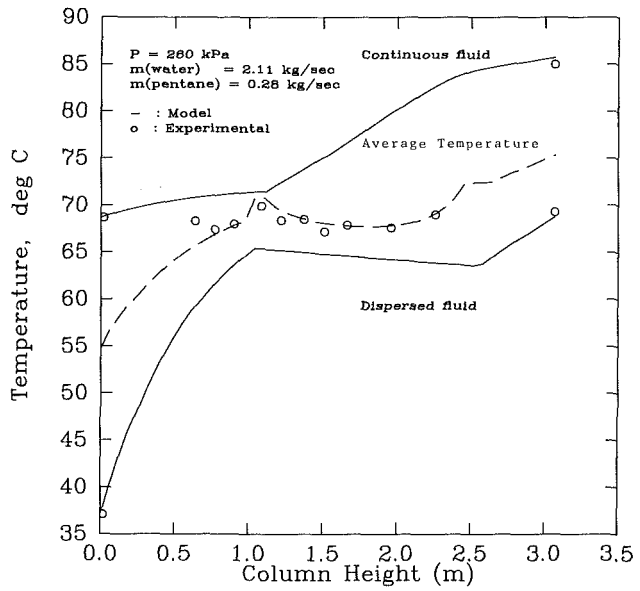


**Fig. 2 Temperature profile of dispersed and continuous fluids, mixed temperature, and experimental temperature profile data along the length of the column; $m_p = 0.28$ kg/s, $m_w = 2.11$ kg/s, $P = 260$ kPa**

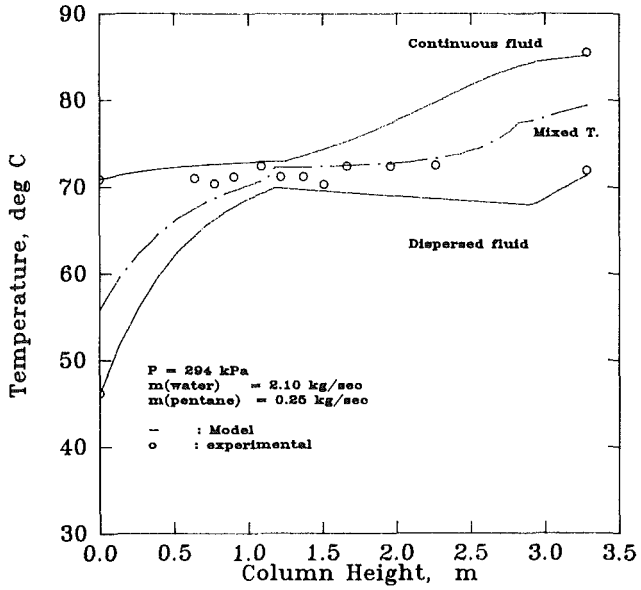


Fig. 3 Temperature profile of dispersed and continuous fluids, mixed temperature, and experimental temperature profile data along the length of the column; $m_p = 0.25$ kg/s, $m_w = 2.10$ kg/s, $P = 294$ kPa

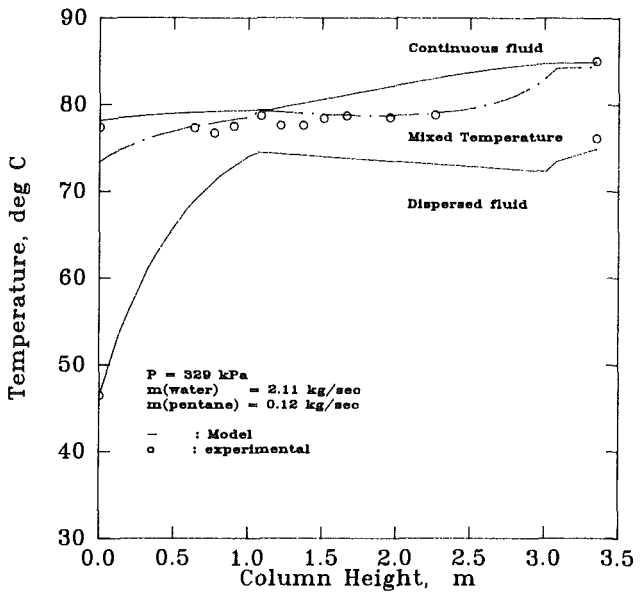


Fig. 4 Temperature profile of dispersed and continuous fluid, mixed temperature, and experimental temperature profile data along the length of the column; $m_p = 0.12$ kg/s, $m_w = 2.11$ kg/s, $P = 329$ kPa

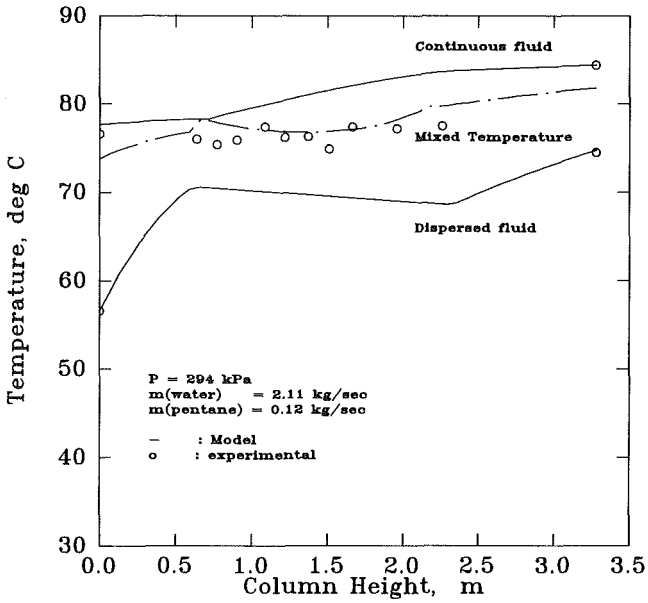


Fig. 5 Temperature profile of dispersed and continuous fluids, mixed temperature, and experimental temperature profile data along the length of the column; $m_p = 0.12$ kg/s, $m_w = 2.11$ kg/s, $P = 294$ kPa

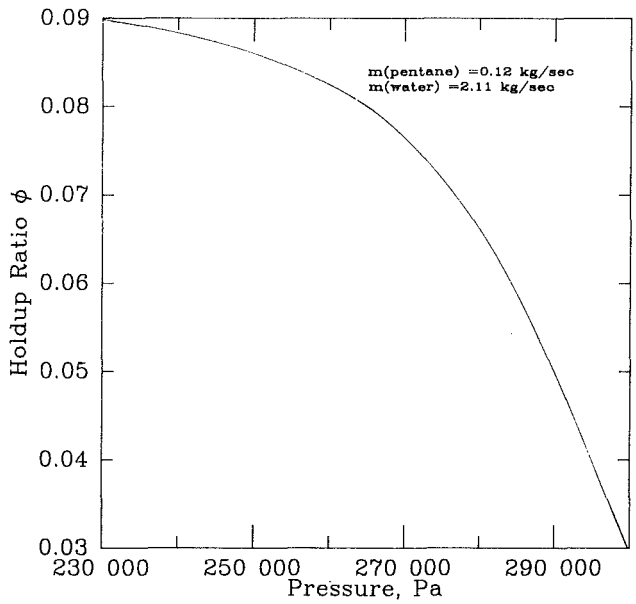


Fig. 6 The effect of pressure at the bottom of the column on the maximum holdup ratio

rangement and flowed upward in droplet form while vaporizing; the vapor formed exited at the top of the column. Design of the showerhead was such that initial pentane droplet diameters of approximately 3-4 mm were produced. Operating pressures of approximately 2-3 atmospheres were normally used in the column. Both the pentane and water loops to the direct contact heat exchanger were completely closed other than in the column where the two fluids came in contact.

Orifice plates were used to measure the flow rates of the hot water and the liquid pentane. Temperature measurements were accomplished with the use of shielded chromel-alumel thermocouples. Twenty-four thermocouples were used to determine temperatures throughout the system, including the inlet and outlet stream temperatures as well as the bulk temperatures at various locations within the column.

Data analysis for the heat transfer calculation used the following energy balance equation:

$$m^l_{w,i}\mathbf{h}^l_{w,i} + m^l_{p,i}\mathbf{h}^l_{p,i} = m^v_{p,e}\mathbf{h}^v_{p,e} + m^l_{w,e}\mathbf{h}^l_{w,e} + (m^l_{w,i} - m^l_{w,e})\mathbf{h}^v_{w,e} + Q_{\text{loss}} \tag{18}$$

The subscripts $i$ and $e$ represent inlet and exit conditions, and $w$ and $p$ stand for pentane and water, respectively. The superscripts $l$ and $v$ represent the liquid and vapor cases. $Q_{\text{loss}}$ is the heat loss. In order to estimate the water vapor mass flow rate in the exit stream at the top of the column, it is assumed that partial pressures of water and pentane vapor are proportional to the molar flow rates of the phases. The partial pressure of the pentane at the top of the column was inferred by assuming that the pentane existed at a saturated condition at the exit temperature. Thus

$$\frac{P_{w,T}(T_{p,e})}{P_{p,T}} = \frac{(m^l_{w,i} - m^l_{w,e})/\text{MW}_w}{m^v_{p,e}/\text{MW}_p} \tag{19}$$

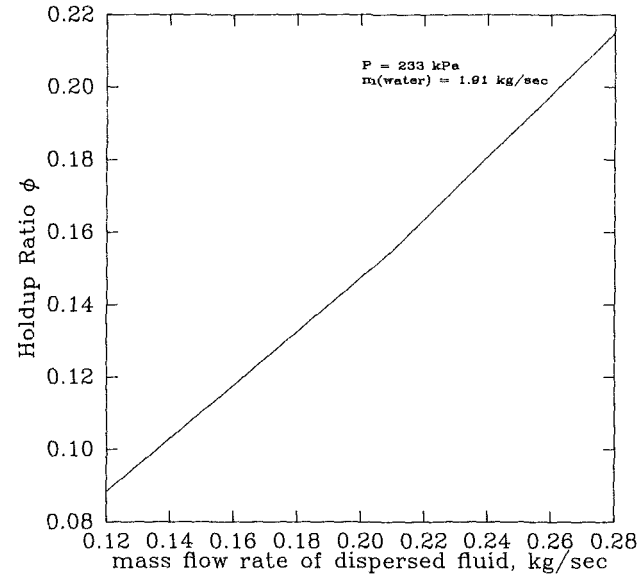


Fig. 7 The effect of dispersed fluid mass flow rate on the maximum holdup ratio

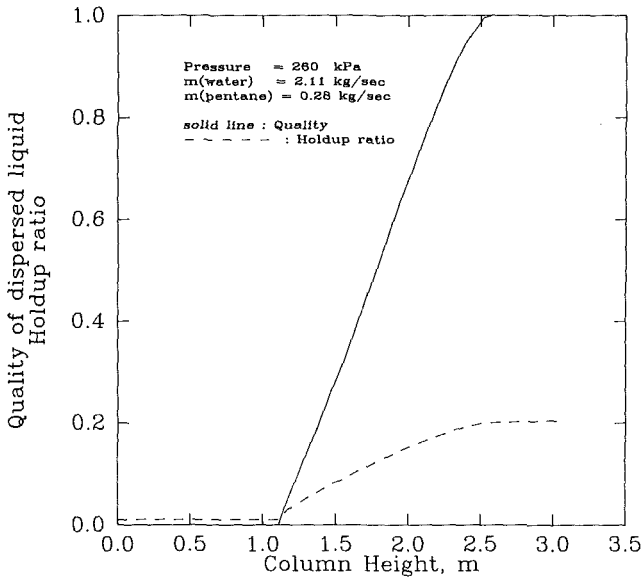


Fig. 8 Holdup ratio and quality of the column along the length of the column; $m_p = 0.28$ kg/s, $m_w = 2.11$ kg/s, $P = 260$ kPa

Here $MW_w$ and $MW_p$ are the molecular weights of water and pentane, respectively.

More information on the experimental work is available in the paper by Goodwin et al. (1985).

## Results and Discussion

The influence of various parameters on total heat transfer during the process of direct-contact evaporation has been investigated. It is necessary to ascertain how well the heat transfer model developed here describes the actual performance of such a device. Steady-state data are available for the temperature profiles from the data taken as the experimental part of this project (Goodwin et al., 1985). Experimental heat transfer was calculated from these data by the equations given previously. A numerical model is developed, and the effect of several physical parameters on the total heat transfer is investigated. All values shown refer to the same basic experimental situation: that of a 0.61-m-dia, 3-m-high spray column using water at 85°C to evaporate pentane.

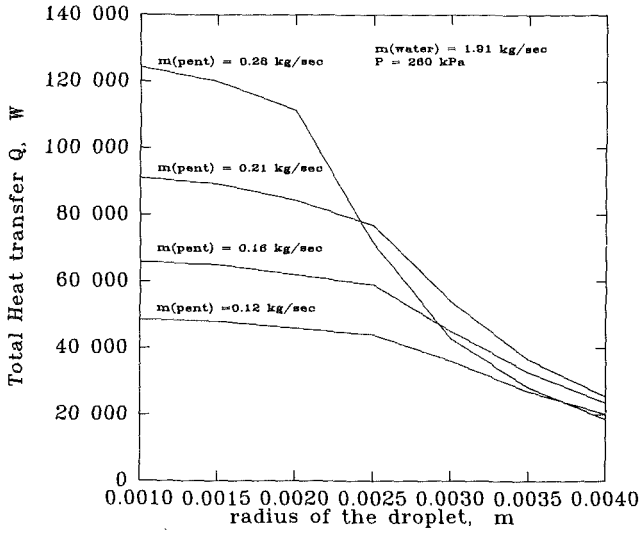


Fig. 9 The effect of initial radius of the droplet on the total heat transfer for several pentane mass flow rates

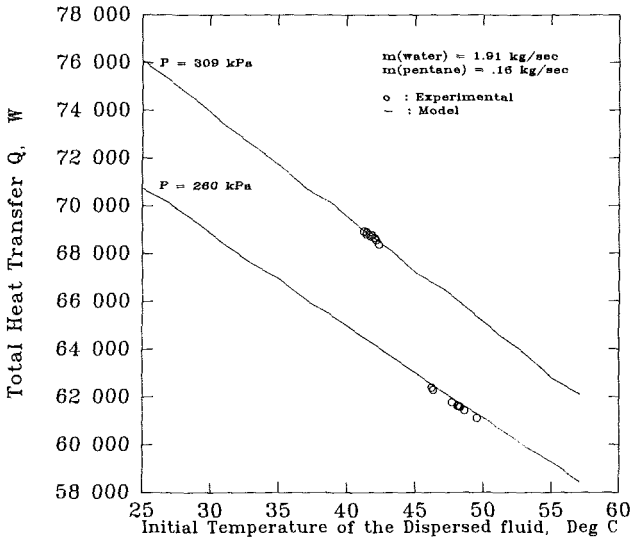


Fig. 10 Effects on initial dispersed phase temperature on the total heat transfer accomplished, for two vessel pressures

Figures 1 through 5 show a comparison of predicted temperature profiles with measured temperatures. The calculated dispersed fluid, continuous fluid, and mixed temperatures are shown in these figures. Temperature profiles for different mass flow rates and pressures can be examined through these figures. Note that decreasing the dispersed fluid flow rate, while maintaining the flow rate of the continuous fluid, causes less variation in the mixed temperature. Temperature differences between two fluids are affected by the change of continuous fluid mass flow rates. The location of the initiation of boiling is different for different values of pressure in the column. Some abrupt changes in the values for the predicted mixed temperatures at the beginning and the ending of the saturation region are the result of the effects of changes in properties on the correlation used (equation (18)).

Although other published values for temperature profiles in spray columns are quite limited, some data for a large isobutane-geothermal brine system have been reported. (Olander et al., 1983). It is shown elsewhere (Çoban, 1986) that the model described here gives a good prediction of the data reported for that system. Since that system has quite distinct characteristics from the one evaluated here, the ability

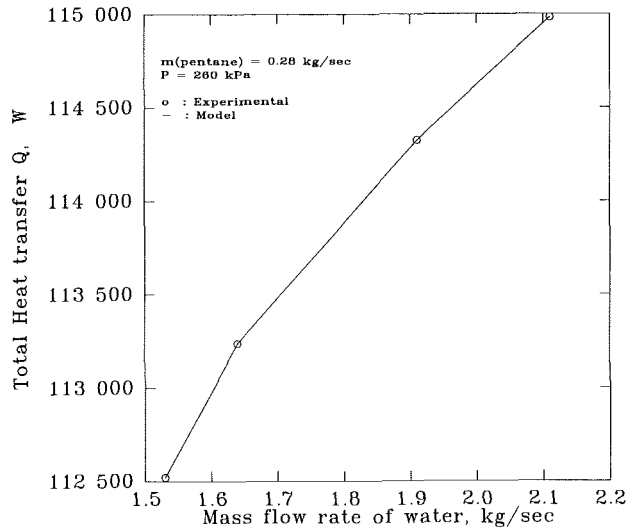


**Fig. 11 Variation of total heat transfer with continuous phase mass flow rate for specific values for pentane mass flow and vessel pressure**

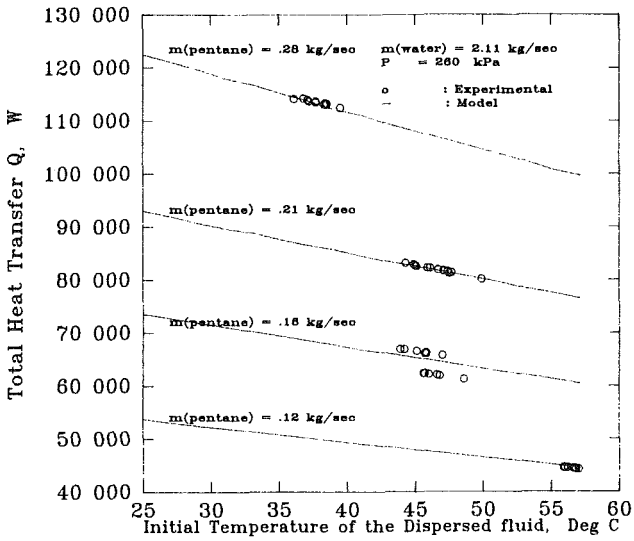


**Fig. 12 The influence of dispersed phase (pentane) mass flow and initial temperature on total heat transfer accomplished, for a specific value of continuous phase flow rate**

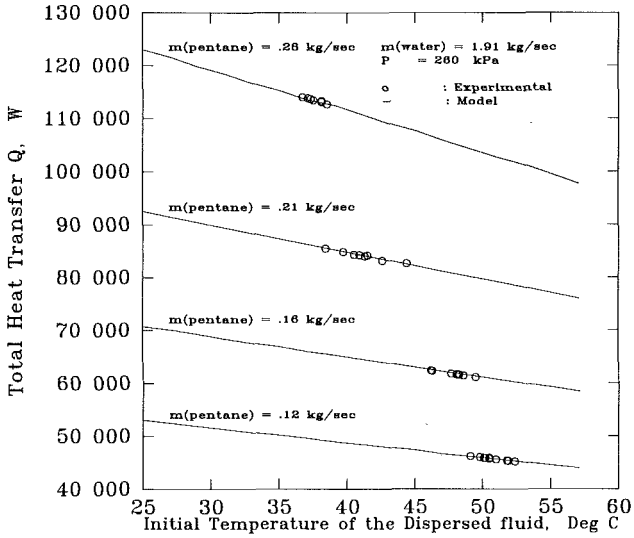


**Fig. 13 The influence of dispersed phase (pentane) mass flow and initial temperature on total heat transfer accomplished, for a specific value of continuous phase flow rate. Comparing this figure to Fig. 12 demonstrates the effects of the continuous phase mass flow.**

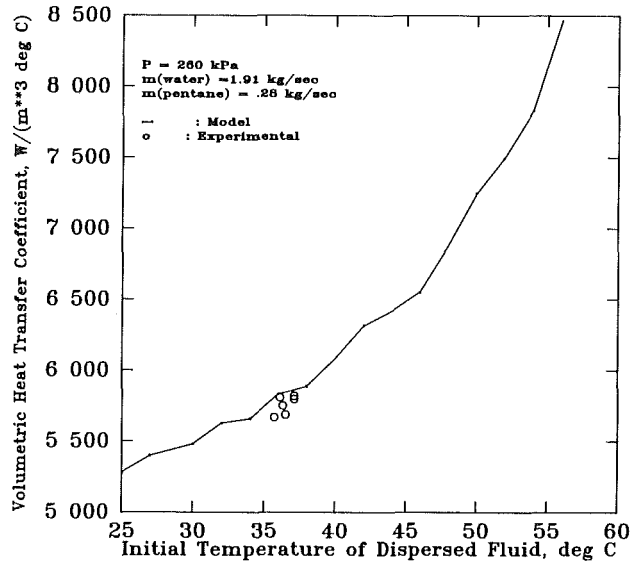


**Fig. 14 The variation of volumetric heat transfer coefficient with the initial temperature of the dispersed phase (pentane)**

of the model also to describe performance of that system is quite encouraging.

The effect of pressure on the maximum holdup ratio (at the top of the column) is shown in Fig. 6. Holdup ratio is seen to drop when the pressure increases. A smaller decrease is observed for the lower pressure range. The relationship between holdup ratio and dispersed fluid mass flow rate is given in Fig. 7. An almost linear relation is observed between these two variables.

Figure 8 shows the variation of calculated values of quality and holdup ratio throughout the column. The variation in holdup is due to the increase in bubble diameter. Not included in the model is any representation of wake effects, droplet coalescence, or droplet breakup.

Data for holdup, although very important for correlating with performance of spray columns, are very limited for heat transfer systems. Holdup was not measured in the experimental program that was carried out with this work. Comparisons with output from this model to the few reported measurements of holdup for other three-phase spray columns given in the literature show excellent agreement (Coban, 1986).

The effect of initial radius of the droplet on total heat transfer to the dispersed phase is shown in Fig. 9. Two distinct regimes are shown. The sudden change in the slope of the curves is caused by incomplete boiling that occurs for some critical initial droplet radius. The point at which this occurs is, in turn, a function of other given parameters. This figure also shows that a larger dispersed liquid mass flow rate causes a larger total heat transfer. This was an expected outcome.

In the model development, it was assumed that the bubbles were spherical. As shown by Grace (1983) the shape of the bubbles can be correlated well with droplet size. While droplet diameter was not measured in the experiment, calculated values are given. The spherical assumption was checked against plotted information of Grace (1983), and it was found that for all cases considered here, the bubbles should be spherical or deviate only slightly into the ellipsoidal regime.

In Fig. 10 relations between initial dispersed phase temperature and total heat transfer are given for two different initial pressures. As is seen from the figure, the total heat transfer decreases when the dispersed phase inlet temperature increases, and it increases when the pressure increases. The limited available experimental data (Goodwin et al., 1985) are

also shown on this plot. The data predicted by the model are nearly the same as those from the experimental situation.

Figure 11 shows a limited number of calculations used to infer the relation between total heat transfer and mass flow rate of the water. The data indicate an increasing dependence of total heat transfer on the water mass flow rate.

Figures 12 and 13 show the effects of mass flow rates of the dispersed phase, initial pentane temperature, and total heat transfer relations. Note that all parameters are the same between these two figures except that the continuous phase mass flow rate is greater in Fig. 13. The same kind of functional dependence is observed. The total heat transfer decreases linearly with an increasing initial dispersed phase temperature. A nonlinearly increasing relation with dispersed phase mass flow rate is also seen. For these cases the agreement between the experimental data and the model prediction is very good.

The effect of the initial temperature of the dispersed phase on the total heat transfer coefficient is shown in Fig. 14. Disjointed variations in slopes are a result of variations in the way the thermodynamic properties were evaluated. The volumetric heat transfer coefficient is defined here as the total heat transfer per unit volume divided by the logarithmic mean temperature difference. An exponential increase in the heat transfer coefficient is observed by increasing the inlet dispersed fluid temperature. Considering a decreasing total heat transfer for the same range of data leads to the conclusion that the volumetric heat transfer coefficient will not always reflect the general variations of the total heat transfer.

## Conclusions

A one-dimensional steady-state model of a three-phase spray-column counterflow direct-contact heat exchanger has been developed by considering a one-dimensional model of the phenomena inside the column. The numerical model was successfully applied to solve for the local variation of the heat transfer and fluid motion. Effects of several physical variables on the temperature profiles, holdup ratio, and heat transfer are investigated. It is found that the mass flow rate of the dispersed phase has a major effect on the local heat transfer, holdup ratio, and temperature profiles. Other important variables are found to be the initial droplet diameter, column pressure, and the initial droplet temperature.

Droplet diameter, as would be expected, can have a profound effect on performance due to this parameter's effect on both stored energy and heat transfer rates. The effect of this variable on the performance of a spray column is shown here. There is an implicit relationship between initial droplet diameter and the other design parameters for satisfactory operation. As would be expected, complete evaporation may not be accomplished if the initial droplet diameter is too large.

Column height is found to be an important factor, and, if it is not sufficient, incomplete boiling can result. If the column height is sufficient to complete the boiling, additional column height has only a small effect on the total heat transfer.

## Acknowledgments

The partial support by the Solar Energy Research Institute and Utah Power & Light Company of the experimental work reported here is gratefully acknowledged.

## References

Battya, P., Raghavan, V., and Seetharamu, K., 1985, "A Theoretical Correlation for the Nusselt Number in Direct Contact Evaporation of a Moving Drop in an Immiscible Liquid," *Wärme- und Stoffübertragung*, Vol. 19, pp. 61–66.

Churchill, S., and Bernstein, M., 1977, "A Correlating Equation for Forced Convection From Gases and Liquids to a Circular Cylinder in Crossflow," ASME JOURNAL OF HEAT TRANSFER, Vol. 99, pp. 300–306.

Çoban, T., 1986, "Numerical Modeling the Three Phase Direct Contact Heat Exchangers," PhD Dissertation, University of Utah, Salt Lake City, UT.

Çoban, T., and Boehm, R. 1986, "Numerical and Experimental Modelling of Three-Phase, Direct-Contact Heat Exchangers," Eighth International Heat Transfer Conference, Paper No. 5A-08.

Goodwin, P., Çoban, T., and Boehm, R., 1985, "Evaluation of the Flooding Limits and Heat Transfer of a Three-Phase, Spray-Column, Direct-Contact Heat Exchanger," ASME Paper No. 85-HT-49.

Grace, J., 1983, "Hydrodynamics of Liquid Drops in Immiscible Liquids," *Handbook of Fluids in Motion*, N. SCheremisinoff and R. Gupta, eds., Ann Arbor Science, Chap. 38, p. 1008.

Jacobs, H., and Golafshani, M., 1985, "A Heuristic Evaluation of the Governing Mode of Heat Transfer in a Liquid–Liquid Spray Column," ASME Paper No. 85-HT-50.

Mokhtarzadeh, M., and El-Shirbini, A., 1979, "A Theoretical Analysis of Evaporating Droplets in an Immiscible Liquid," *International Journal of Heat and Mass Transfer*, Vol. 22, pp. 27–38.

Olander, R., Oshmyansky, S., Nichols, K., and Werner, D., 1983, "Final Phase Testing and Evaluation of the 500 kW Direct Contact Pilot Plant at East Mesa," USDOE Report DOE/SF/11700-T1.

Raina, G., and Grover, P., 1982, "Direct Contact Heat Transfer With Change of Phase: Theoretical Model," *AIChE Journal*, Vol. 28, pp. 515–517.

Raina, G., and Grover, P., 1985, "Direct Contact Heat Transfer With Change of Phase: Theoretical Model Incorporating Sloshing Effects," *AIChE Journal*, Vol. 31, pp. 507–510.

Raina, G., and Wanchoo, R., 1984, "Direct Contact Heat Transfer With Phase Change: Theoretical Expression for Instantaneous Velocity of a Two-Phase Bubble," *International Communications in Heat and Mass Transfer*, Vol. 11, pp. 227–237.

Raina, G., Wanchoo, R., and Grover, P., 1984, "Direct Contact Heat Transfer With Phase Change: Motion of Evaporating Droplets," *AIChE Journal*, Vol. 30, pp. 835–837.

Sideman, S., and Isenberg, J., 1967, "Direct Contact Heat Transfer With Change of Phase: Bubble Growth in Three-Phase Systems," *Desalination*, Vol. 2, pp. 207–214.

Sideman, S., and Taitel, Y., 1964, "Direct Contact Heat Transfer With Change of Phase: Evaporation of Drops in an Immiscible Liquid Medium," *International Journal of Heat and Mass Transfer*, Vol. 7, pp. 1273–1289.

Tochitani, Y., Nakagawa, T., Mori, Y., and Komotori, K., 1977, "Vaporization of Single Liquid Drops in an Immiscible Liquid. Part II: Heat Transfer Characteristics," *Wärme- und Stoffübertragung*, Vol. 10, pp. 71–79.

# Sensible and Latent Heat Transfer in Cross-Counterflow Gas-To-Gas Heat Exchangers

**R. B. Holmberg**
Fläkt Evaporator AB,
S-551 84 Jönköping, Sweden

*Simultaneous heat and mass transfer during condensation in cross-counterflow gas-to-gas heat exchangers has been analyzed. The coupled heat and mass transfer equations are derived for boundary-layer controlled heat and mass transfer and include longitudinal heat conduction in the exchanger wall. A numerical method of the finite-difference type is applied to the steady-state performance. Temperature and absolute humidity distributions are calculated for exchanger parameters that are typical in air conditioning systems. Temperature and humidity efficiencies together with frosting limits are evaluated for different inlet air conditions.*

## Introduction

In gas-to-gas heat exchangers, the warmer gas often contains substances that may condense on the heat exchanger surfaces as soon as they have been cooled down to their corresponding dew points. The warmer gas may consist, for instance, of products of combustion, in which steam and sulfur dioxide are the condensable substances, or it may be ventilation air containing water vapor. In such cases, the sensible heat of the gas–vapor mixture as well as the latent heat of condensation will both be transferred.

The heat transfer process associated with the recovery of heat from humid ventilation air is studied in this paper. Plate heat exchangers of pure crossflow type are generally employed for this application, although two-pass crossflow heat exchangers are also used and are therefore covered by this analysis. The influence of the longitudinal heat conduction through the heat exchanger wall structure in the direction of the fluid flow is also taken into account when setting up the mathematical relationships. This effect has earlier been analyzed by Chiou (1978) for the transfer of sensible heat only. The mass transfer process on the hot fluid side of the plate heat exchanger is described mathematically in a way similar to the corresponding mass transfer process in the rotary heat exchanger, which was analyzed earlier by the author (Holmberg, 1977, 1979).

## Theoretical Analysis

In a plate heat exchanger in which condensation occurs on the hot fluid side, the moisture in the hot air is precipitated out on the exchanger surface when the surface temperature falls below the inlet dew-point temperature of the hot air. The condensed water vapor is then drained out of the exchanger. The latent heat is transferred through the surface together with the sensible heat. If the surface temperature falls below ice-point temperature, the moisture is deposited on the surface as frost and a frost layer will be built up. The frost will be melted and drained away as soon as the surface temperature passes above the ice-point temperature.

The different equations describing the heat transfer process in a crossflow heat exchanger, which has plates separating the two fluid streams that are flowing at right angles, will be considered for a typical element of the plate heat exchanger (Fig. 1). The equations will be given with the following main idealizations:

1 Steady-state operation is presumed.

2 The two fluids pass normal to each other in a crossflow pattern on both sides of the exchanger wall.

3 The thermal resistance of the exchanger walls is negligible in the direction normal to the fluid flows.

4 The fluid heat and mass storage capacities are negligible in comparison with the convective heat and mass transport.

5 The thermal properties of both fluids and exchanger walls do not vary with temperature.

6 The heat and mass transfer coefficients between fluids and their respective heat transfer surfaces are assumed to be constant throughout the exchanger. (However, the numerical method permits the use of different constants, for example, in the dry and wet parts of the exchanger.)

7 The heat transfer surface configuration is uniform throughout each side of the exchanger.

8 The mass velocity, inlet temperature, and humidity distributions of the fluids are uniform over their respective inlet sections.

9 Phase change due to condensation occurs only on the hot-fluid side. The thermal resistance of the condensed water is negligible.

10 No leakage between the fluids occurs.

11 No heat is generated within the exchanger.

12 No heat is transferred between the exchanger and its surroundings.

On the bases of these idealizations, a set of differential

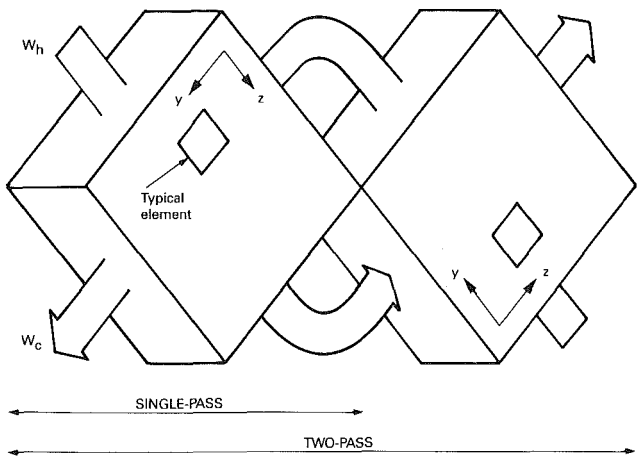


**Fig. 1 Illustrative cross-counterflow exchanger arrangement**

Contributed by the Heat Transfer Division and presented at the National Heat Transfer Conference, Houston, Texas, July 24–27, 1988. Manuscript received by the Heat Transfer Division October 15, 1987. Keywords: Condensation, Heat Exchangers, Numerical Methods.

equations describing the heat and mass transfer processes can be expressed as follows:

*Mass transfer from hot fluid to exchanger surface*

$$\frac{W_h}{L_z}\frac{\partial x_h}{\partial y} = -\frac{(\beta_x A)_h}{n L_z L_y}(x_h - x_s) \tag{1}$$

*Mass balance*

$$\frac{W_h}{L_z}\frac{\partial x_h}{\partial y} = -\frac{1}{n L_z L_y}\frac{\partial m_w}{\partial \tau} \tag{2}$$

*Heat transfer from exchanger surface to cold fluid*

$$\frac{(W c_p)_c}{L_y}\frac{\partial t_c}{\partial z} = \frac{(hA)_c}{n L_y L_z}(t_s - t_c) \tag{3}$$

*Energy transfer from hot fluid to exchanger surface*

$$\frac{W_h}{L_z}\frac{\partial i_h}{\partial y} = -\frac{(hA)_h}{n L_z L_y}(t_h - t_s) - \frac{(\beta_x A)_h}{n L_y L_z}(i_{ws} - i_{ws})(x_h - x_s) \tag{4}$$

*Energy balance*

$$\frac{W_h}{L_z}\frac{\partial i_h}{\partial y} + \frac{(Wc_p)_c}{L_y}\frac{\partial t_c}{\partial z} = -\left\{\frac{i_{ws}}{n L_z L_y}\frac{\partial m_w}{\partial \tau} - \frac{(kA_k)_h}{L_z}\frac{\partial^2 t_s}{\partial y^2} - \frac{(kA_k)_c}{L_y}\frac{\partial^2 t_s}{\partial z^2}\right\} \tag{5}$$

Along with the boundary-layer convection, the heat transfer coefficient $h$ can also take into account small transverse conduction effects within the exchanger wall.

The enthalpy of the moist hot air is defined by

$$i_h = c_{pa} t_h + i_{vh} x_h = c_{ph} t_h + r_o x_h$$

and its derivative becomes

$$\frac{\partial i_h}{\partial y} = c_{ph}\frac{\partial t_h}{\partial y} + i_{vh}\frac{\partial x_h}{\partial y} \tag{6}$$

where the specific heat of the moist air is $c_{ph} = c_{pa} + x_h c_{pv}$ and the enthalpy of the water vapor in the hot air is $i_{vh} = r_o + c_{pv} t_h$. The results are given for $c_{pa} = 1.005$ kJ/kg•°C, $c_{pv} = 1.86$ kJ/kg•°C and $r_o = 2500$ kJ/kg.

The energy transfer equation (4) together with equations (6) and (1) results with good approximation in

$$\frac{(Wc_p)_h}{L_z}\frac{\partial t_h}{\partial y} = -\frac{(hA)_h}{n L_z L_y}(t_h - t_s) \tag{7}$$

where the enthalpy of the condensed water and the enthalpy change of the water vapor during its transport through the air boundary layer are neglected.

Equation (5) together with equations (2) and (6) gives

$$\frac{(kA_k)_h}{L_z}\frac{\partial^2 t_s}{\partial y^2} + \frac{(kA_k)_c}{L_y}\frac{\partial^2 t_s}{\partial z^2} - \frac{(Wc_p)_h}{L_z}\left(\frac{\partial t_h}{\partial y} + \frac{r_o}{c_{ph}}\frac{\partial x_h}{\partial y}\right) - \frac{(Wc_p)_c}{L_y}\frac{\partial t_c}{\partial z} = 0 \tag{8}$$

Thus, the system of partial differential equations describing the actual transfer process consists of the equations (1), (3), (7), and (8). After elimination of the first derivatives in equation (8) with equations (1), (2), and (3), the equation system in normalized form can be written

$$\frac{\partial \bar{t}_c}{\partial \bar{z}} = \frac{N_{tu,c}}{n}(\bar{t}_s - \bar{t}_c) \tag{9}$$

$$\frac{\partial \bar{x}_h}{\partial \bar{y}} = -\frac{N_{tu,h}}{n\,\phi_h}(\bar{x}_h - \bar{x}_s) \tag{10}$$

## Nomenclature

$A$ = total heat transfer area, m²
$A_k$ = total solid area available for longitudinal heat conduction, m²
$c$ = specific heat, J/kg•°C
$c_p$ = specific heat of vapor–gas mixture (at constant pressure), J/kg dry gas•°C
$h$ = heat transfer coefficient, W/m²•°C
$i$ = enthalpy, J/kg; enthalpy of vapor–gas mixtures, J/kg dry gas
$k$ = thermal conductivity of exchanger wall, W/m²•°C
$L_y, L_z$ = flow length in the exchanger on cold-gas or hot-gas side, respectively, m
$m$ = mass, kg
$n$ = numbers of exchanger passes
$N_c, N_h$ = numbers of subdivisions in cold or hot-gas cross section, respectively
$p$ = pressure, Pa
$p_t$ = total pressure of vapor–gas mixture, Pa
$r_o$ = latent heat of vaporization, J/kg
$t_c, t_h$ = fluid temperature on cold-gas or hot-gas side, °C
$t_s$ = exchanger wall temperature, °C
$W$ = mass flow rate of fluid, kg dry gas/s
$x$ = absolute humidity of vapor–gas mixture, kg vapor/kg dry gas
$y, z$ = flow length coordinate measured from cold-gas or hot-gas inlet, respectively, m
$\Delta y, \Delta z$ = length of subdivisions in $y$ or $z$ directions, respectively, m
$\beta_x$ = mass transfer coefficient, kg vapor/m²•s•Δx
$\tau$ = time coordinate, s
$\varphi$ = relative humidity of vapor–gas mixture
$(i, j)$ = typical element of exchanger unit
$(f, g)$ = typical element in second part of two-pass exchanger unit
$\bar{t}$ = dimensionless temperature $= (t - t_{c1})/(t_{h1} - t_{c1})$
$\bar{x}$ = dimensionless humidity $= (x_{h1} - x)/(x_{h1} - x_{c1})$
$\bar{y}$ = dimensionless coordinate in $y$ direction $= y/L_y$
$\bar{z}$ = dimensionless coordinate in $z$ direction $= z/L_z$
$N_{tu,c}$ = number of transfer units on the cold-gas side $= (hA)_c/(Wc_p)_c$
$N_{tu,h}$ = number of transfer units on the hot-gas side $= (hA)_h/(Wc_p)_h$
$R$ = heat capacity rate ratio of gas streams $= (Wc_p)_c/(Wc_p)_h$
$W_c/W_h$ = mass flow rate ratio of gas streams
$\lambda_c$ = longitudinal heat conduction parameter defined on cold-gas side $= (kA_k)_c/(L_z(Wc_p)_c)$
$\lambda_h$ = longitudinal heat conduction parameter defined on hot-gas side $= (kA_k)_h/(L_y(Wc_p)_h)$
$\phi$ = mixing parameter $= h/(\beta_x c_p)$

### Subscripts

1 = inlet
2 = outlet
$a$ = air
$c$ = cold fluid
$h$ = hot fluid
$s$ = surface or saturation
$v$ = water vapor
$w$ = water liquid

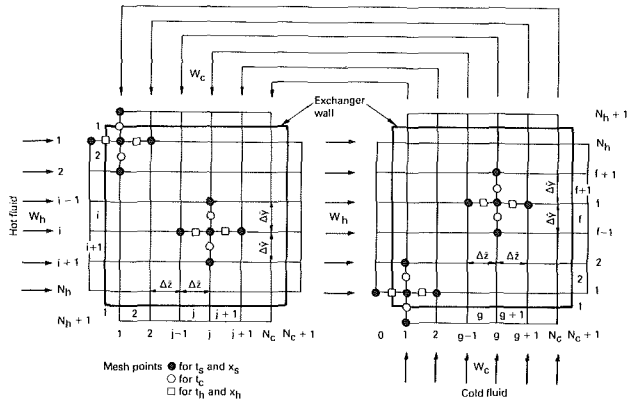


**Fig. 2 A staggered mesh representing the y-z plane of a single-pass and a two-pass cross-counterflow exchanger**

$$\frac{\partial \bar{t}_h}{\partial \bar{y}} = -\frac{N_{tu,\,h}}{n}(\bar{t}_h - \bar{t}_s) \tag{11}$$

$$\lambda_h \frac{\partial^2 \bar{t}_s}{\partial \bar{y}^2} + \lambda_c R \frac{\partial^2 \bar{t}_s}{\partial \bar{z}^2} + \frac{N_{tu,h}}{n}(\bar{t}_h - \bar{t}_s) + \frac{1}{\phi_h}\frac{r_o}{c_{ph}}(\bar{x}_h - \bar{x}_s) + \frac{N_{tu,c}}{n} R\,(\bar{t}_s - \bar{t}_c) = 0 \tag{12}$$

where $n=1$ for a single-pass exchanger and $n=2$ for a two-pass exchanger.

The mass transfer is related to the heat transfer through the mixing parameter $\phi = h/(\beta_x c_p)$, which is taken to be 0.866 for the water-air mixture in the calculated examples in accordance with Schlünder (1963).

The absolute humidity of the hot air at the exchanger surface is expressed by

$$x_s = 0.622 \cdot \frac{p_{vs}}{p_t - p_{vs}}$$

where the saturation pressure $p_{vs} = f(t_s)$ is obtained from the Goff formulas (*ASHRAE Handbook*, 1972).

When condensation occurs at surface temperatures below the ice point, that is $t_s < 0°C$, and the moisture is deposited as frost on the exchanger surface, the melting heat $r_i$ is added to the latent heat of vaporization and $r_o + r_i$ is substituted into the set of equations ($r_i = 333$ kJ/kg). On the other hand, when no condensation occurs, that is $x_s \le x_{h1}$, the absolute humidity of the hot air is maintained constant throughout the exchanger and $\partial \bar{x}_h/\partial \bar{y} = 0$ is substituted into the equations.

## Numerical Method

The equation system is solved by a finite-difference method. Figure 2 illustrates a staggered mesh representing the $z$-$y$ plane of a single-pass heat exchanger as well as a two-pass exchanger (Fig. 1).

With ordinary central differences and an implicit scheme, the equation system for the single-pass exchanger as well as for one part of the two-pass exchanger can be represented by the following equations:

$$\bar{t}_c(i+1, j) = D_1\,\bar{t}_c\,(i, j) + D_2\,\bar{t}_s\,(i, j) \tag{13}$$

$$\bar{x}_h\,(i, j+1) = D_3\,\bar{x}_h(i, j) + D_4\,\bar{x}_s\,(i, j) \tag{14}$$

$$\bar{t}_h(i, j+1) = D_5\,\bar{t}_h\,(i, j) + D_6\,\bar{t}_s\,(i, j) \tag{15}$$

$$\bar{t}_s\,(i, j) = \{D_7\,[\bar{t}_s\,(i+1, j) + \bar{t}_s(i-1, j)] + D_8\,[\bar{t}_s\,(i, j+1) + \bar{t}_s\,(i, j-1)] + D_9\,\bar{t}_c\,(i, j) + D_{10}\,\bar{t}_h\,(i, j) + D_{11}\bar{x}_h\,(i, j)\} / \{1 + D_{11}\,\bar{x}_s\,(i, j)/\bar{t}_s\,(i, j)\} \tag{16}$$

$$\bar{x}_s\,(i, j) = f(\bar{t}_s\,(i, j)) \tag{17}$$

In equation (16), an implicit trick has been used for the term $\bar{x}_s$, as it is highly dependent on $\bar{t}_s$ itself.

The constants are

$$D_1 = (1-E_1)/(1+E_1), \qquad D_2 = 2E_1/(1+E_1),$$
$$D_3 = (1-E_2)/(1+E_2), \qquad D_4 = 2E_2/(1+E_2),$$
$$D_5 = (1-E_3)/(1+E_3), \qquad D_6 = 2E_3/(1+E_3),$$
$$D_7 = E_4/E_{10}, \qquad D_8 = E_5/E_{10},$$
$$D_9 = E_6/\{E_{10}\,(1+E_1)\}, \qquad D_{10} = E_7/\{E_{10}(1+E_3)\},$$
$$D_{11} = E_8\,E_9/\{E_{10}(1+E_2)\}$$

and

$$E_1 = N_{tu,c}\Delta\bar{z}/(2n), \qquad E_2 = N_{tu,\,h}\Delta\bar{y}/(2n\phi_h)$$
$$E_3 = N_{tu,h}\Delta\bar{y}/(2n), \qquad E_4 = R\lambda_c/\Delta\bar{z}^2,$$
$$E_5 = \lambda_h/\Delta\bar{y}^2, \qquad E_6 = RN_{tu,c}/n,$$
$$E_7 = N_{tu,h}/n, \qquad E_8 = N_{tu,h}/(n\phi_h),$$
$$E_9 = r_o/c_{ph},$$
$$E_{10} = 2E_4 + 2E_5 + E_6/(1+E_1) + E_7/(1+E_3)$$

Corresponding equations with $(f, q)$ instead of $(i, j)$ represent the second part of the two-pass exchanger.

The boundary conditions of single-pass exchangers are as follows:

*For the inlet on the cold-fluid side*

$$\bar{t}_c\,(1, j) = \bar{t}_{c1}, \qquad j = 1, 2, \ldots, N_c$$

*For the inlet on the hot-fluid side*

$$\bar{t}_h\,(i, 1) = \bar{t}_{h1}, \qquad i = 1, 2, \ldots, N_h$$
$$\bar{x}_h\,(i, 1) = \bar{x}_{h1}, \qquad i = 1, 2, \ldots, N_h$$

The longitudinal heat conduction is zero at the ends of the heat exchanger walls, i.e.,

$$\bar{t}_s\,(i, 0) = \bar{t}_s\,(i, 1), \qquad i = 1, 2, \ldots, N_h$$
$$\bar{t}_s\,(i, N_c+1) = \bar{t}_s(i, N_c), \qquad i = 1, 2, \ldots, N_h$$
$$\bar{t}_s\,(0, j) = \bar{t}_s\,(1, j), \qquad j = 1, 2, \ldots, N_c$$
$$\bar{t}_s\,(N_h+1, j) = \bar{t}_s\,(N_h, j), \qquad j = 1, 2, \ldots, N_c$$

Corresponding boundary conditions for the hot unit $(i, j)$ of the two-pass exchanger are

$$\bar{t}_c\,(1, j) = \bar{t}_c\,(N_h+1, g), \qquad j = 1, 2, \ldots, N_c, \quad g = N_c + 1 - j$$

and $\bar{t}_h$, $\bar{x}_h$, and $\bar{t}_s$ according to single-pass above. The boundary conditions for the cold unit $(f, g)$ are

$$\bar{t}_c\,(1, g) = \bar{t}_{c1}, \qquad g = 1, 2, \ldots, N_c$$
$$\bar{t}_h(f, 1) = \bar{t}_h\,(i, N_c+1), \qquad f = 1, 2, \ldots, N_h$$
$$\bar{x}_h\,(f, 1) = \bar{x}_h\,(i, N_c+1), \qquad f = 1, 2, \ldots, N_h, \quad i = N_h + 1 - f$$

where unmixed air flow is assumed between the units. Furthermore

$$\bar{t}_s\,(f, 0) = \bar{t}_s\,(f, 1), \qquad f = 1, 2, \ldots, N_h$$
$$\bar{t}_s\,(f, N_c+1) = \bar{t}_s\,(f, N_c), \qquad f = 1, 2, \ldots, N_h$$
$$\bar{t}_s\,(0, g) = \bar{t}_s\,(1, g), \qquad g = 1, 2, \ldots, N_c$$
$$\bar{t}_s\,(N_h+1, g) = \bar{t}_s\,(N_h, g), \qquad g = 1, 2, \ldots, N_c$$

For the single-pass crossflow exchanger the difference equations (12)–(16) together with actual boundary conditions are solved iteratively for the grid points $(i, j)$, $i = 1, 2, \ldots, N_h$ and $j = 1, 2, \ldots, N_c$. Energy balances are made after each iteration; before a solution is accepted for a particular set of parameters, the energy balance error must be satisfied to a specified accuracy. The energy balance error is determined

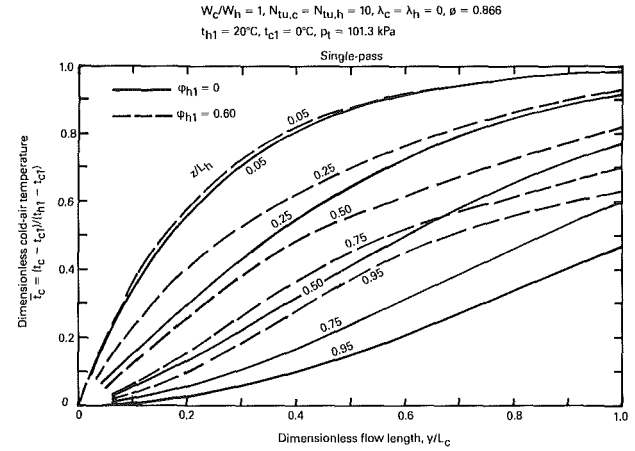


**Fig. 3 Temperature distribution of cold air in a single-pass exchanger for dry and wet condition examples**

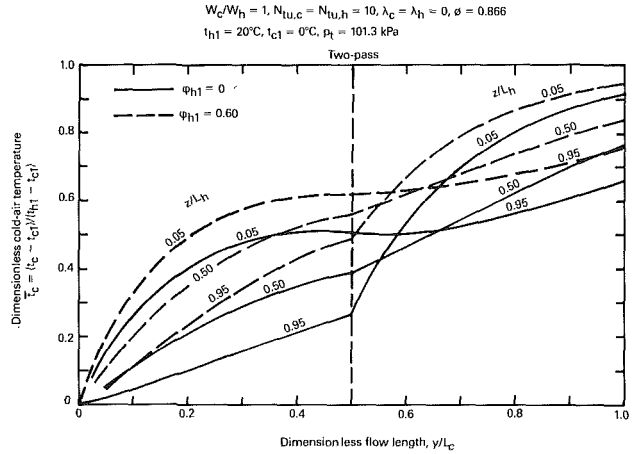


**Fig. 4 Temperature distribution of cold air in a two-pass exchanger for dry and wet condition examples**

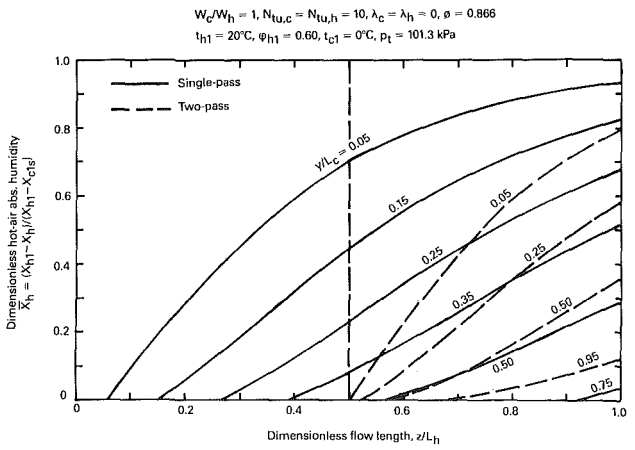


**Fig. 5 Absolute humidity distribution of hot air for single-pass and two-pass exchanger examples**

from the difference between the hot-fluid and the cold-fluid enthalpy changes compared to the difference between the hot-fluid and the cold-fluid enthalpies.

For the two-pass crossflow exchanger, the corresponding equations for ($f$, $g$) have to be included in the solution procedure.

The accuracy of the results calculated by this method depends on the error criterion as well as on the number of subdivisions. The error of 0.05 percent used for the convergence criterion gives, together with the number of subdivisions $N_h = N_c = 10$, the calculated temperature efficiency with an accuracy to three significant figures, which should be sufficient for this particular application.

## Results

In order to study how the condensed water vapor influences the heat transfer in single-pass and two-pass crossflow exchangers, the temperature distribution has been calculated with and without condensation for typical inlet air conditions. The nondimensional parameters are assumed to be $W_c/W_h = 1$, $N_{tu,c} = N_{tu,h} = 10$, $\lambda_c = \lambda_h = 0$, i.e., equal mass flow rates on each side of the exchanger, equal thermal resistance on each side, giving a heat recovery efficiency of around 75 percent, and negligible longitudinal heat conduction through the exchanger walls.

The cold-air temperature and hot-air absolute humidity distributions are represented in dimensionless form and given in Figs. 3 and 5 for the single-pass and Figs. 4 and 5 for the two-pass configuration. The dimensionless temperature is defined in an ordinary way, while the hot-air dimensionless humidity is defined with the cold-air inlet humidity $x_{c1}$ replaced by the lowest attainable hot-air humidity $x_{c1s}$ at dehumidification, which corresponds to the moist air condition ($t_{c1}$; $\varphi_{c1} = 1$).

From Figs. 3 and 4 it is clear that the latent heat of condensation will increase the temperature in wet parts of the exchanger. As the temperature increase is higher in regions where the amount of condensation is greater, that is, where the temperature is lower, the cold-air temperature distribution across the flow direction will be more uniform when condensation occurs. Thus, the latent heat increases the mean cold-air temperature, which in turn results in an increased cold-air temperature efficiency $\bar{t}_{c2}$. In the single-pass exchanger example (Fig. 3), the efficiency $\bar{t}_{c2}$ increases from 0.752 in the dry case to 0.812 in the wet case, while corresponding figures in the two-pass exchanger example (Fig. 4) are 0.776 and 0.842. The higher efficiency of the two-pass exchanger is the result of the counterflow arrangement, which can be seen in Fig. 4, where the slope of the temperature profile changes from one exchanger unit to the other.

Figure 5 shows that the mass transfer rate is highest in the cold-air inlet area, i.e., for small values of $y/L_c$. Condensation will occur as soon as the surface temperature is lower than the inlet dew-point temperature of the hot air, which is 12.0°C in this example. This condensation limit is shown in Figs. 6 and 7, where surface temperature iso-curves are given for single-pass and two-pass exchangers, respectively. Note that the condensation in the two-pass exchanger is concentrated in the "cold" unit. The hot-air humidity efficiencies $\bar{x}_{h2}$ representing the total amount of condensation are fairly close for the single-pass (0.368) and two-pass (0.397) exchangers (see Fig. 5).

In Fig. 8, the temperature and humidity efficiencies are given for typical inlet values in air conditioning. The humidity efficiencies increase with decreasing inlet temperature of the cold air and with increasing temperature and humidity of the hot air. At the same time, the temperature efficiencies increase due to condensation. It also appears that small differences in humidity efficiency are obtained between single-pass and two-pass exchangers. The frosting limits, which are marked in the figure, indicate that frosting occurs at lower inlet cold-air temperatures. The limits are somewhat lower on two-pass exchangers than on single-pass exchangers.

## Conclusions

A calculation method for analyzing the sensible and latent steady heat transfer during condensation in single-pass and

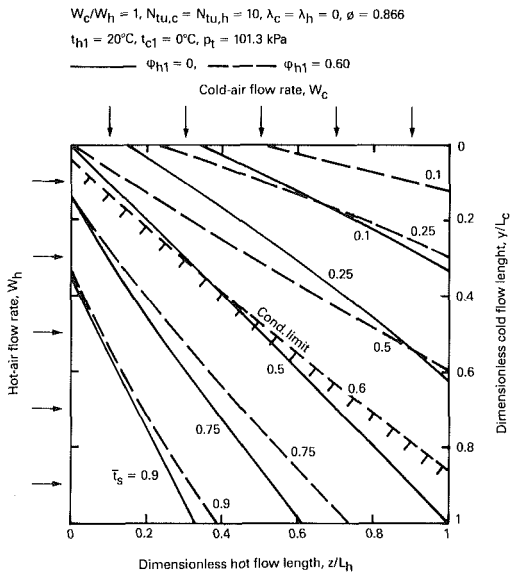


**Fig. 6 Surface temperature iso-curves in a single-pass exchanger for dry and wet condition examples**

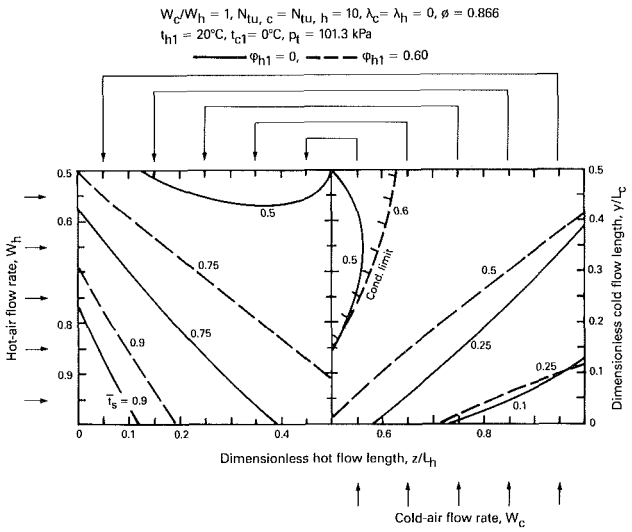


**Fig. 7 Surface temperature iso-curves in a two-pass exchanger for dry and wet condition examples**

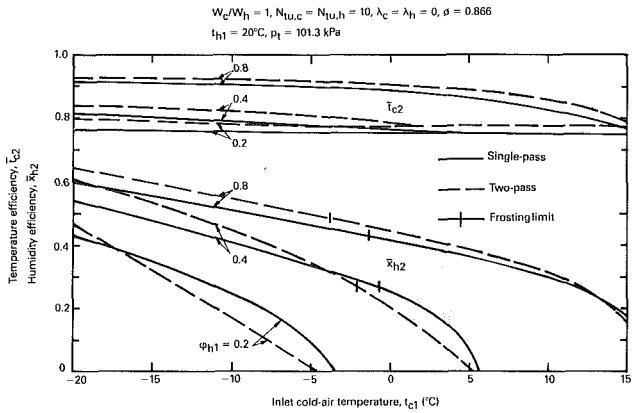


**Fig. 8 Temperature and humidity efficiencies for different inlet conditions**

two-pass cross-flow gas-to-gas heat exchangers has been presented. Calculation results from the air conditioning field show that the cold-air temperature efficiency increases with condensation rate expressed as hot-air humidity efficiency and that the condensation rate will be somewhat higher for the two-pass exchanger. Hereby follows also that frosting occurs at a slightly lower inlet cold-air temperature for the two-pass exchanger than for the single-pass exchanger.

The method is general and not restricted to equal fluid capacity rates and constant heat and mass transfer coefficients as has been assumed in the given examples. Calculations including longitudinal heat condensation will in a later published paper be shown to compare well with experimental data.

## References


ASHRAE, *Handbook of Fundamentals*, 1972, ASHRAE Inc., New York.

Chiou, J. P., 1978, "The Effect of Longitudinal Heat Conduction on Crossflow Heat Exchanger," ASME JOURNAL OF HEAT TRANSFER, Vol. 100, pp. 580–587.

Holmberg, R. B., 1977, "Heat and Mass Transfer in Rotary Heat Exchangers With Nonhygroscopic Rotor Materials," ASME JOURNAL OF HEAT TRANSFER, Vol. 99, pp. 196–202.

Holmberg, R. B., 1979, "Combined Heat and Mass Transfer in Regenerators With Hygroscopic Materials," ASME JOURNAL OF HEAT TRANSFER, Vol. 101, pp. 205–210.

Schlünder, E. U., 1963, "Einfluss molekularer Transportvorgänge auf die Zustandsänderung von Gas/Dampf-Gemischen," *Chemie Ing. Techn.*, Vol. 35, pp. 169–174.

Journal of Heat Transfer

Technical Notes

This section contains shorter technical papers. These shorter papers will be subjected to the same review process as that for full papers.

# Non-Fourier Heat Conduction in a Semi-infinite Solid Subjected to Oscillatory Surface Thermal Disturbances

W. W. Yuen[1] and S. C. Lee[2]

## 1 Introduction

Many investigators have explored the effect of non-Fourier conduction in transient heat transfer processes in recent years (Brazel and Nolan, 1966; Maurer and Thompson, 1973; Kazimi and Erdman, 1975; Luikov, 1968; Wiggert, 1977; Glass et al., 1985). Based on a relaxation model for heat conduction in solids and liquids, the traditional heat diffusion equation is replaced with a hyperbolic equation that accounts for the finite thermal propagation speed. The use of the hyperbolic equation removes the nonphysical phenomenon of the diffusion equation analysis that predicts instantaneous temperature disturbances at all points in the medium for a step heat flux at the boundary. It further removes the peculiarity of an infinite temperature gradient at the boundary as time goes to zero.

The hyperbolic equation has been used in a number of analyses. Solutions generated by these studies show that the non-Fourier effect is important only at very early times in transient heat transfer processes, such as the high-intensity electromagnetic irradiation of a solid (Brazel and Nolan, 1966), the sudden contact of two hot molten liquids such as uranium dioxide and sodium (Kazimi and Erdman, 1975), and the high-rate heat transfer in rarefied media (Luikov, 1968). In general, the non-Fourier effect is shown to decay quickly, and the conventional Fourier equation is accurate a short time after the initial transient.

The objective of this work is to show that the non-Fourier conduction effect can be important even at a "long time" after the initial transient if the thermal disturbance is oscillatory with the period of oscillation of the same order of magnitude as the thermal relaxation time. In particular, the thermal response of a semi-infinite solid subjected to a sinusoidal boundary heat flux condition is generated. The present solution illustrates readily that, in many practical situations such as the repeated irradiation of a solid by a laser with very short pulse width, heat transfer analyses using the traditional Fourier heat diffusion equation can result in significant errors. The current results also suggest that the thermal relaxation time of a solid can be determined by measuring the thermal response of the solid irradiated by a high-frequency heat flux.

[1]Department of Mechanical and Environmental Engineering, University of California, Santa Barbara, CA 93106.

[2]Thermal Control Department, The Aerospace Corporation, El Segundo, CA 90245-4691.

Contributed by the Heat Transfer Division and presented at the National Heat Transfer Conference, Pittsburgh, Pennsylvania, August 9–12, 1987. Manuscript received by the Heat Transfer Division October 14, 1987. Keywords: Conduction, Transient and Unsteady Heat Transfer.

## 2 Analysis

In one-dimensional flow of heat, the energy equation is given by

$$\rho C \frac{\partial T}{\partial t} + \frac{\partial q}{\partial x} = 0 \tag{1}$$

where $\rho$ is the solid density, $C$ is the specific heat, $T$ is the temperature, $q$ is the heat flux, and $x$, $t$ are the distance and time coordinates, respectively. The modified Fourier equation, as utilized in previous investigations (e.g., Brazel and Nolan, 1966), is

$$\tau \frac{\partial q}{\partial t} + q + k \frac{\partial T}{\partial x} = 0 \tag{2}$$

where $k$ is the thermal conductivity and $\tau$ is defined as the thermal relaxation time which, for many solids, is on the order of $10^{-12}$ to $10^{-14}$ s (Weyman, 1967). Equations (1) and (2) can be combined to form the following dissipative wave equation:

$$\tau \frac{\partial^2 T}{\partial t^2} + \frac{\partial T}{\partial t} = \alpha \frac{\partial^2 T}{\partial x^2} \tag{3}$$

For a one-dimensional semi-infinite solid subjected to a sinusoidal surface heat flux boundary condition, the boundary and initial conditions are given by

$$\begin{aligned} q(0, t) &= q_0 e^{i\omega t} \\ T(\infty, t) &= 0 \\ q(\infty, t) &= 0 \end{aligned} \tag{4}$$

and

$$\begin{aligned} T(x, 0) &= 0 \\ q(x, 0) &= 0 \end{aligned} \tag{5}$$

where $i = (-1)^{1/2}$; $q_0$ and $\omega$ are amplitude and frequency of the surface heat flux oscillation, respectively. Note the initial temperature is normalized to be zero in the above equation. The sinusoidal surface heat flux is expressed as a complex number for mathematical convenience.

The solution to equation (3) can be readily generated by the Laplace transform. Taking the Laplace transform of equations (2) and (3) yields

$$(1 + \tau s)\bar{q}(x, s) = -k \frac{d\bar{T}}{dx}(x, s) \tag{6}$$

$$\frac{d^2\bar{T}(x,s)}{dx^2} = \frac{s}{\alpha}(1+\tau s)\bar{T}(x,s) \tag{7}$$

where $\bar{q}$ and $\bar{T}$ are the Laplace transforms of $T$, respectively.

When equation (6) is evaluated at $x=0$, the boundary conditions become

$$\frac{d\bar{T}(0,s)}{dx} = -\left(\frac{1+\tau s}{s-i\omega}\right)\frac{q_0}{k}$$

$$\bar{T}(\infty,s) = 0 \tag{8}$$
$$q(\infty,s) = 0$$

The solution to equation (7) subjected to the boundary conditions as represented by equation (8) is

$$\bar{T}(x,s) = \frac{q_0(\alpha\tau)^{1/2}}{k}\frac{(s+1/\tau)^{1/2}}{s^{1/2}(s-i\omega)}e^{-x/a[s(s+1/\tau)]^{1/2}} \tag{9}$$

where

$$a = \left(\frac{\alpha}{\tau}\right)^{1/2}$$

is the thermal propagation speed. The inverse transform of equation (9) is

$$\frac{T(x,t)}{q_0(\alpha\tau)^{1/2}/k} = H(t-x/a)e^{-t/2\tau}I_0\left[\frac{(t^2-x^2/a^2)^{1/2}}{2\tau}\right]$$
$$+\left(\frac{1}{\tau}+i\omega\right)e^{i\omega t}\int_{x/a}^{t} e^{-(i\omega y+y/2\tau)}I_0\left[\frac{(y^2-x^2/a^2)^{1/2}}{2\tau}\right]dy \tag{10}$$

where $H(t)$ is the Heaviside unit step function and $I_0(x)$ is the modified Bessel function of zero order.

## 3 Results and Discussion

**(a) Temperature at x = at.** The presence of the Heaviside function $H(t)$ in equation (10) illustrates that due to the finite speed of propagation of the thermal disturbance, the temperature in the solid remains at zero for $x>at$. At $x=at$, the temperature is independent of $\omega$ and has a step discontinuity given by

$$\frac{T(at,t)}{q_0(\alpha\tau)^{1/2}/k} = e^{-t/2t} \tag{11}$$

At $t=0$, the above equation yields the surface temperature as

$$\frac{T(0,0)}{q_0(\alpha\tau)^{1/2}/k} = 1$$

which is identical to results derived in Maurer and Thompson (1973) and Wiggert (1977). Equation (11) suggests that in the limit of short time (on the order of the thermal relaxation time), the temperature at $x=at$ is significantly higher than that predicted by the conventional Fourier analysis. At a sufficiently high heat flux level, this result has important implications in the failure of structural integrity due to thermal shock.

**(b) "Steady-State" Results.** In the limit of long time ($t\to\infty$), the integral in equation (10) can be evaluated in closed form. The temperature profile can be written analytically as

$$\frac{T(x,t)}{q_0(\alpha\tau)^{1/2}/k} = \frac{(1+\omega^2\tau^2)^{1/4}}{(\omega\tau)^{1/2}}e^{i(\omega t+\gamma)-(i+1)\kappa_+ x-(i-1)\kappa_- x} \tag{12}$$

where

$$\kappa_+ = \frac{1}{2}\left[\frac{\omega}{\alpha}((1+\omega^2\tau^2)^{1/2}+1)\right]^{1/2} \tag{13a}$$

$$\kappa_- = \frac{1}{2}\left[\frac{\omega}{\alpha}((1+\omega^2\tau^2)^{1/2}-1)\right]^{1/2} \tag{13b}$$

and

$$\gamma = \frac{1}{2}\tan^{-1}\omega\tau - \frac{\pi}{4} \tag{14}$$

In the limit of $\tau\to 0$, equation (12) is reduced to

$$T(x,t) = \frac{q_0}{k\left(\frac{\omega}{\alpha}\right)^{1/2}}e^{i(\omega t-\pi/4)-(i+1)(\omega/2\alpha)^{1/2}x} \tag{15}$$

which is identical to the result generated by conventional Fourier conduction analysis as given in Carslaw and Jaeger (1980).

Physically, equation (12) represents a decaying temperature wave of wavelength $\lambda$ given by

$$\lambda = \frac{\lambda_0 2^{1/2}}{[(1+\omega^2\tau^2)^{1/2}+1]^{1/2}+[(1+\omega^2\tau^2)^{1/2}-1]^{1/2}} \tag{16}$$

where

$$\lambda_0 = \frac{2\pi}{(\omega/2\alpha)^{1/2}} \tag{17}$$

is the wavelength of the temperature wave calculated by the conventional Fourier conduction ($\tau=0$) analysis.

Equation (12) also shows that the amplitude of the temperature oscillation diminishes as $e^{-x/L}$ where

$$L = \frac{L_0 2^{1/2}}{[(1+\omega^2\tau^2)^{1/2}+1]^{1/2}-[(1+\omega^2\tau^2)^{1/2}-1]^{1/2}} \tag{18}$$

with

$$L_0 = \left(\frac{2\alpha}{\omega}\right)^{1/2} \tag{19}$$

Physically, $L$ can be interpreted as a "steady-state" penetration depth for the surface thermal disturbance, while $L_0$ is the distance predicted by the conventional Fourier analysis.

In addition to the wavelength and penetration depth of the temperature wave, the non-Fourier prediction of the actual amplitude of the temperature oscillation is also significantly different from the Fourier prediction. Evaluating at $x=0$, it can be readily shown from equation (12) that the dimensionless surface temperature is given by

$$\frac{T(0,t)}{q_0(\alpha\tau)^{1/2}/k} = Ae^{i(\omega t+\gamma)} \tag{20}$$

with

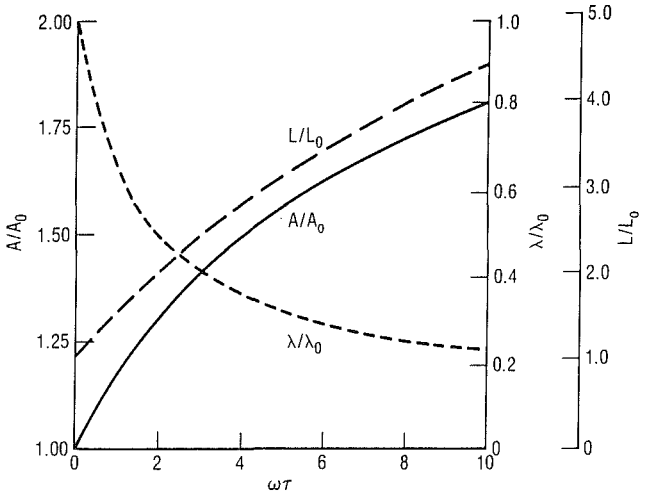


**Fig. 1 Effect of non-Fourier conduction on the amplitude $A/A_0$, penetration depth $L/L_0$, and wavelength $\lambda/\lambda_0$ of the temperature response to a sinusoidal surface heat flux for steady state**

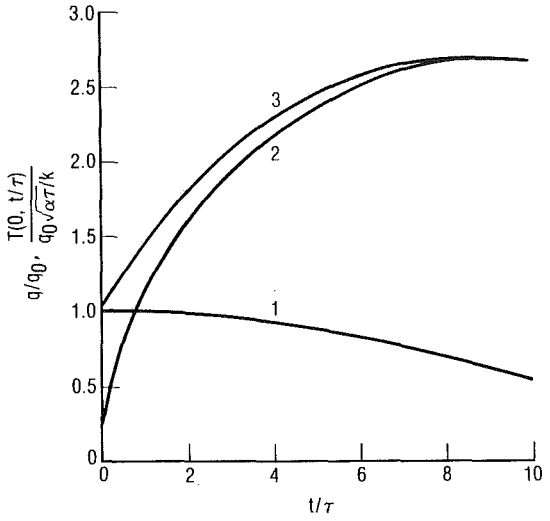


1 = DIMENSIONLESS SURFACE FLUX
2 = DIMENSIONLESS SURFACE TEMPERATURE (Fourier result)
3 = DIMENSIONLESS SURFACE TEMPERATURE (non-Fourier result)

**Fig. 2 Transient surface temperature behavior for $\omega\tau = 0.1$**

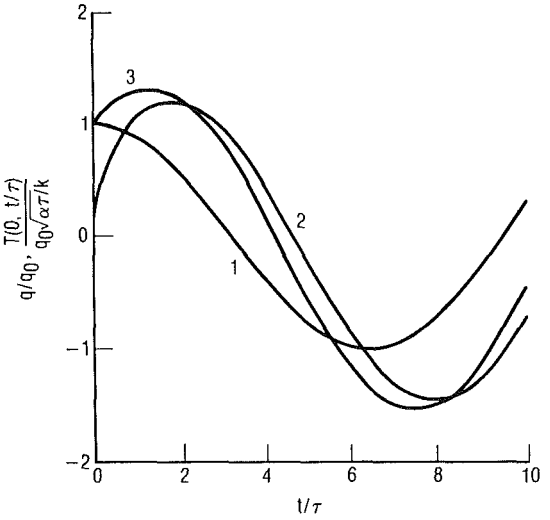


1 = DIMENSIONLESS HEAT FLUX
2 = DIMENSIONLESS SURFACE TEMPERATURE (Fourier result)
3 = DIMENSIONLESS SURFACE TEMPERATURE (non-Fourier result)

**Fig. 3 Transient surface temperature behavior for $\omega\tau = 0.5$**

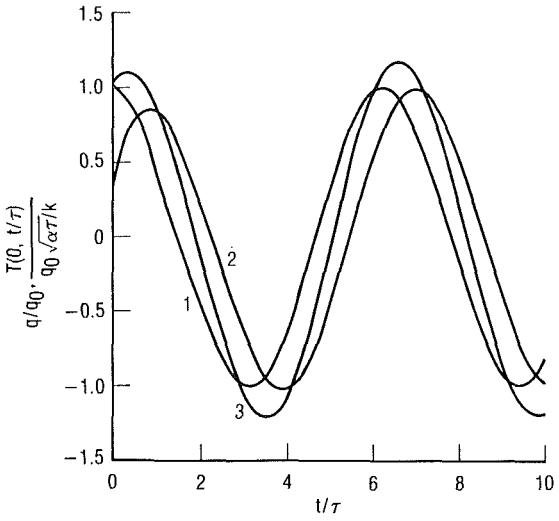


1 = DIMENSIONLESS SURFACE FLUX
2 = DIMENSIONLESS SURFACE TEMPERATURE (Fourier result)
3 = DIMENSIONLESS SURFACE TEMPERATURE (non-Fourier result)

**Fig. 4 Transient surface temperature behavior for $\omega\tau = 1.0$**

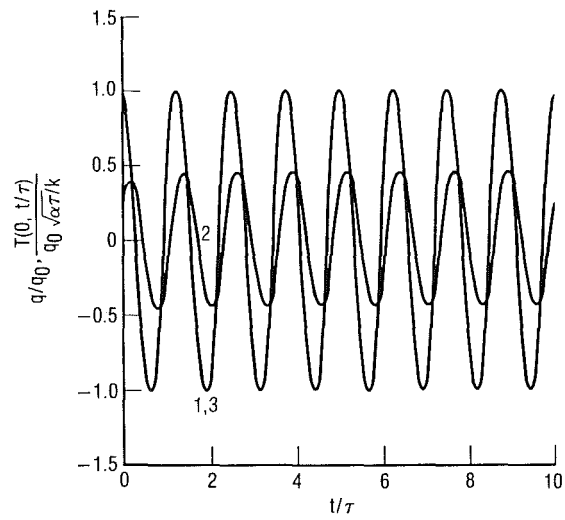


1 = DIMENSIONLESS SURFACE FLUX
2 = DIMENSIONLESS SURFACE TEMPERATURE (Fourier result)
3 = DIMENSIONLESS SURFACE TEMPERATURE (non-Fourier result)

**Fig. 5 Transient surface temperature behavior for $\omega\tau = 5.0$**

$$A = \frac{(1+\omega^2\tau^2)^{1/4}}{(\omega\tau)^{1/2}} \tag{21}$$

The corresponding surface temperature predicted by the Fourier analysis, on the other hand, is given by Glass et al. (1985)

$$\frac{T(0, t)}{q_0(\alpha\tau)^{1/2}/k} = A_0 e^{i(\omega t - \pi/4)} \tag{22}$$

with

$$A_0 = (\omega\tau)^{-1/2} \tag{23}$$

It must be reiterated that equations (20) and (22) are for large $t$.

Plots of $\lambda/\lambda_0$, $L/L_0$, and $A/A_0$ against $\omega\tau$ are shown in Fig. 1. It is readily observed that the non-Fourier effect decreases the wavelength but increases the amplitude and penetration depth of the "steady-state" temperature wave. The effect is significant when the period of oscillation $1/\omega$ is less than or equal to the relaxation time constant $\tau$. The non-Fourier effect thus has a "long time" permanent influence on the temperature response of a solid subjected to a high-frequency surface thermal disturbance.

It is noted that the product of the wavelength and penetration depth of the "steady-state" temperature wave is identical for both the Fourier and non-Fourier analysis. Specifically, the product varies inversely with the frequency of oscillation as

$$\lambda L = \lambda_0 L_0 = \frac{4\pi\alpha}{\omega} \tag{24}$$

In the limit of large frequency $\omega \to \infty$, the non-Fourier wavelength becomes

$$\lambda(\omega \to \infty) = \frac{2\pi}{\omega\tau}(\alpha\tau)^{1/2} \tag{25}$$

while the non-Fourier penetration depth is given by

$$L(\omega \to \infty) = 2(\alpha\tau)^{1/2} \tag{26}$$

The corresponding Fourier penetration depth $L_0$, on the other hand, approaches zero as $\omega \to \infty$.

**(c) General Transient Temperature Behavior.** The surface temperature $T(0, t)$ for $0 < t/\tau < 10$ with different values of $\omega\tau$ (0.1, 0.5, 1.0, 5.0) was calculated based on equation (8) and presented in Figs. 2–5. The surface heat flux is assumed to be cosine varying. The corresponding Fourier prediction and dimensionless surface heat flux are plotted on the same figures for comparison. It should be pointed out that the surface heat flux $q_0$ is regarded as negative when $q$ is negative. The negative temperature is due to the normalization by $q_0$.

For the case of small $\omega\tau$, $\gamma$ approaches $\pi/4$ and the phase difference between the Fourier and non-Fourier diminishes. The non-Fourier effect appears only when $t/\tau$ is small, and the non-Fourier temperature profile becomes identical to the Fourier result when $t/\tau \geq 10$. This transient temperature behavior is consistent with the predictions of the previous works (e.g., Brazel and Nolan, 1966). For cases with moderate and large values of $\omega\tau$, however, the non-Fourier surface temperature differs significantly from the Fourier result for all values of $t/\tau$. In the limit of large $\omega\tau$, $\gamma$ appraoches zero and the non-Fourier surface temperature oscillates in phase with the surface heat flux. The Fourier surface temperature, on the other hand, has a phase shift of $\pi/4$ relative to the surface heat flux.

## 4 Conclusion

The non-Fourier thermal response of a solid subjected to an oscillatory surface heat flux has been considered in this paper. This corresponds to the practical situation of irradiation of a solid by a pulsed laser. Results show that, for moderate and large values of the oscillation frequency, the non-Fourier effect is quite significant. In contrast to many existing results, the non-Fourier effect is demonstrated to be important even for "long times" after the initial transient. Conventional Fourier conduction analysis is shown to underestimate the steady-state penetration depth of the thermal disturbance and overestimate the wavelength of the temperature propagation. In practical calculations that involve high-frequency surface thermal disturbances, such as the irradiation of a solid by a pulsed laser, an accurate thermal analysis should, therefore, include the non-Fourier effect. Results of the present work also suggest that measurement of the relative phase shift between the surface temperature and the applied heat flux would be an effective way to determine the thermal relaxation time of a solid.

## References


Brazel, J. P., and Nolan, E. J., 1966, "Non-Fourier Effects in the Transmission of Heat," *Proceedings 6th Conference on Thermal Conductivity*, Dayton, OH, pp. 237–254.

Carslaw, H. S., and Jaeger, J. C., 1980, *Conduction of Solids*, 2nd ed., Oxford University Press, United Kingdom.

Glass, D. E., Ozisik, M. N., and Vick, B., 1985, "Hyperbolic Heat Conduction With Surface Radiation," *International Journal of Heat and Mass Transfer*, Vol. 28, No. 10, pp. 1823–1830.

Kazimi, M. S., and Erdman, C. A., 1975, "On the Interface Temperature of Two Suddenly Contacting Materials," ASME JOURNAL OF HEAT TRANSFER, Vol. 97, pp. 615–617.

Luikov, A. V., 1968, *Analytical Heat Diffusion Theory*, Academic Press, New York, pp. 245–248.

Maurer, M. J., and Thompson, H. A., 1973, "Non-Fourier Effects at High Heat Flux," ASME JOURNAL OF HEAT TRANSFER, Vol. 95, pp. 284–286.

Weymann, H. D., 1967, "Finite Speed of Propagation in Heat Conduction, Diffusion, and Viscous Shear Motion," *Am. Journal of Physics*, Vol. 35, pp. 488–496.

Wiggert, D. C., 1977, "Analysis of Early-Time Transient Heat Conduction by Method of Characteristics," ASME JOURNAL OF HEAT TRANSFER, Vol. 99, pp. 35–40.


# 1-2 *N* Shell-and-Tube Exchanger Effectiveness: a Simplified Kraus–Kern Equation


**B. S. Baclic**[1]


### Nomenclature

- $A$ = exchanger total heat transfer area on one side, m$^2$
- $C$ = heat capacity rate = $Wc_p$, W/K
- $c_p$ = specific heat at constant pressure, J/(kg K)
- $N_{tu}$ = number of heat transfer units based on the tube-side heat capacity rate = $UA/C_t$
- $P$ = temperature effectiveness of the tube-side stream = $(T_{t,o} - T_{t,i}) / (T_{s,i} - T_{t,i})$
- $R$ = heat capacity rate ratio = $C_t/C_s$
- $T$ = fluid temperature, °C
- $U$ = overall heat transfer coefficient, W/(m$^2$ K)
- $W$ = fluid mass flow rate, kg/s

### Subscripts

- $i$ = inlet to the exchanger
- $o$ = outlet to the exchanger
- $s$ = shell side
- $t$ = tube side

Kraus and Kern (1965) derived the following $P$–$N_{tu}$–$R$ relation for the heat exchangers with one shell pass and any even number $n$ of tube passes:

$$P = 2/\left\{1 + R + \frac{2}{n}\, x\, \coth(xN_{tu}/n) + \frac{2}{n} f(z)\right\} \tag{1}$$

where

$$x = (1 + n^2R^2/4)^{1/2} \tag{2}$$

$$z = \exp(2N_{tu}/n) \tag{3}$$

$$f(z) = (mz^m + (m-2)z^{m-1} + (m-4)z^{m-2} + \ldots - (m-4)z^2 - (m-2)z - m)/(1 + z + z^2 + z^3 + \ldots + z^m) \tag{4}$$

$$m = \frac{n}{2} - 1 \tag{5}$$

Using a simple relation for the sum of a geometric progression Dodd (1982) derived a more convenient expression for $f(z)$

$$f(z) = \frac{m(z^{m+2} - 1) - (m+2)z(z^m - 1)}{(z-1)(z^{m+1} - 1)} \tag{6}$$

This note is aimed at further simplification of the Kraus–Kern formula. It is sufficient to denote the even numbers

$$n = 2N, \qquad N = 1, 2, \ldots \tag{7}$$

so that equation (3) becomes

$$z = \exp(N_{tu}/N) \tag{8}$$

and Dodd's expression, equation (6), yields

$$f(z) = N\frac{z^N + 1}{z^N - 1} - \frac{z+1}{z-1} \tag{9}$$


[1]University of Novi Sad, Tehnicki fakultet "Mihajlo Pupin," 23000 Zrenjanin, Yugoslavia.



Contributed by the Heat Transfer Division for publication in the JOURNAL OF HEAT TRANSFER. Manuscript received by the Heat Transfer Division November 17, 1987. Keywords: Heat Exhangers.

while the non-Fourier penetration depth is given by

$$L(\omega \to \infty) = 2(\alpha\tau)^{1/2} \tag{26}$$

The corresponding Fourier penetration depth $L_0$, on the other hand, approaches zero as $\omega \to \infty$.

**(c) General Transient Temperature Behavior.** The surface temperature $T(0, t)$ for $0 < t/\tau < 10$ with different values of $\omega\tau$ (0.1, 0.5, 1.0, 5.0) was calculated based on equation (8) and presented in Figs. 2–5. The surface heat flux is assumed to be cosine varying. The corresponding Fourier prediction and dimensionless surface heat flux are plotted on the same figures for comparison. It should be pointed out that the surface heat flux $q_0$ is regarded as negative when $q$ is negative. The negative temperature is due to the normalization by $q_0$.

For the case of small $\omega\tau$, $\gamma$ approaches $\pi/4$ and the phase difference between the Fourier and non-Fourier diminishes. The non-Fourier effect appears only when $t/\tau$ is small, and the non-Fourier temperature profile becomes identical to the Fourier result when $t/\tau \geq 10$. This transient temperature behavior is consistent with the predictions of the previous works (e.g., Brazel and Nolan, 1966). For cases with moderate and large values of $\omega\tau$, however, the non-Fourier surface temperature differs significantly from the Fourier result for all values of $t/\tau$. In the limit of large $\omega\tau$, $\gamma$ appraoches zero and the non-Fourier surface temperature oscillates in phase with the surface heat flux. The Fourier surface temperature, on the other hand, has a phase shift of $\pi/4$ relative to the surface heat flux.

## 4 Conclusion

The non-Fourier thermal response of a solid subjected to an oscillatory surface heat flux has been considered in this paper. This corresponds to the practical situation of irradiation of a solid by a pulsed laser. Results show that, for moderate and large values of the oscillation frequency, the non-Fourier effect is quite significant. In contrast to many existing results, the non-Fourier effect is demonstrated to be important even for "long times" after the initial transient. Conventional Fourier conduction analysis is shown to underestimate the steady-state penetration depth of the thermal disturbance and overestimate the wavelength of the temperature propagation. In practical calculations that involve high-frequency surface thermal disturbances, such as the irradiation of a solid by a pulsed laser, an accurate thermal analysis should, therefore, include the non-Fourier effect. Results of the present work also suggest that measurement of the relative phase shift between the surface temperature and the applied heat flux would be an effective way to determine the thermal relaxation time of a solid.

## References


Brazel, J. P., and Nolan, E. J., 1966, "Non-Fourier Effects in the Transmission of Heat," *Proceedings 6th Conference on Thermal Conductivity*, Dayton, OH, pp. 237–254.

Carslaw, H. S., and Jaeger, J. C., 1980, *Conduction of Solids*, 2nd ed., Oxford University Press, United Kingdom.

Glass, D. E., Ozisik, M. N., and Vick, B., 1985, "Hyperbolic Heat Conduction With Surface Radiation," *International Journal of Heat and Mass Transfer*, Vol. 28, No. 10, pp. 1823–1830.

Kazimi, M. S., and Erdman, C. A., 1975, "On the Interface Temperature of Two Suddenly Contacting Materials," ASME JOURNAL OF HEAT TRANSFER, Vol. 97, pp. 615–617.

Luikov, A. V., 1968, *Analytical Heat Diffusion Theory*, Academic Press, New York, pp. 245–248.

Maurer, M. J., and Thompson, H. A., 1973, "Non-Fourier Effects at High Heat Flux," ASME JOURNAL OF HEAT TRANSFER, Vol. 95, pp. 284–286.

Weymann, H. D., 1967, "Finite Speed of Propagation in Heat Conduction, Diffusion, and Viscous Shear Motion," *Am. Journal of Physics*, Vol. 35, pp. 488–496.

Wiggert, D. C., 1977, "Analysis of Early-Time Transient Heat Conduction by Method of Characteristics," ASME JOURNAL OF HEAT TRANSFER, Vol. 99, pp. 35–40.


# 1-2 *N* Shell-and-Tube Exchanger Effectiveness: a Simplified Kraus–Kern Equation


**B. S. Baclic**[1]


### Nomenclature

- $A$ = exchanger total heat transfer area on one side, m$^2$
- $C$ = heat capacity rate = $Wc_p$, W/K
- $c_p$ = specific heat at constant pressure, J/(kg K)
- $N_{tu}$ = number of heat transfer units based on the tube-side heat capacity rate = $UA/C_t$
- $P$ = temperature effectiveness of the tube-side stream = $(T_{t,o} - T_{t,i}) / (T_{s,i} - T_{t,i})$
- $R$ = heat capacity rate ratio = $C_t/C_s$
- $T$ = fluid temperature, °C
- $U$ = overall heat transfer coefficient, W/(m$^2$ K)
- $W$ = fluid mass flow rate, kg/s

### Subscripts

- $i$ = inlet to the exchanger
- $o$ = outlet to the exchanger
- $s$ = shell side
- $t$ = tube side

Kraus and Kern (1965) derived the following $P$–$N_{tu}$–$R$ relation for the heat exchangers with one shell pass and any even number $n$ of tube passes:

$$P = 2/\left\{1 + R + \frac{2}{n}\, x\, \coth(xN_{tu}/n) + \frac{2}{n} f(z)\right\} \tag{1}$$

where

$$x = (1 + n^2R^2/4)^{1/2} \tag{2}$$

$$z = \exp(2N_{tu}/n) \tag{3}$$

$$f(z) = (mz^m + (m-2)z^{m-1} + (m-4)z^{m-2} + \ldots - (m-4)z^2 - (m-2)z - m)/(1 + z + z^2 + z^3 + \ldots + z^m) \tag{4}$$

$$m = \frac{n}{2} - 1 \tag{5}$$

Using a simple relation for the sum of a geometric progression Dodd (1982) derived a more convenient expression for $f(z)$

$$f(z) = \frac{m(z^{m+2} - 1) - (m+2)z(z^m - 1)}{(z-1)(z^{m+1} - 1)} \tag{6}$$

This note is aimed at further simplification of the Kraus–Kern formula. It is sufficient to denote the even numbers

$$n = 2N, \qquad N = 1, 2, \ldots \tag{7}$$

so that equation (3) becomes

$$z = \exp(N_{tu}/N) \tag{8}$$

and Dodd's expression, equation (6), yields

$$f(z) = N\frac{z^N + 1}{z^N - 1} - \frac{z+1}{z-1} \tag{9}$$


[1]University of Novi Sad, Tehnicki fakultet "Mihajlo Pupin," 23000 Zrenjanin, Yugoslavia.



Contributed by the Heat Transfer Division for publication in the JOURNAL OF HEAT TRANSFER. Manuscript received by the Heat Transfer Division November 17, 1987. Keywords: Heat Exhangers.

or, using equation (8)

$$f(\exp(N_{tu}/N)) = N\coth(N_{tu}/2) - \coth(N_{tu}/2N) \quad (10)$$

Also note that using equation (7), equation (2) becomes

$$x = (1+N^2R^2)^{1/2} \quad (11)$$

Thus, the Kraus-Kern equation, equation (1), can be simplified to read

$$P = 2/\left\{1+R+\coth(N_{tu}/2) - \frac{1}{N}\coth(N_{tu}/2N) + \frac{1}{N}\sqrt{1+N^2R^2}\coth\left(\frac{N_{tu}}{2N}\sqrt{1+N^2R^2}\right)\right\} \quad (12)$$

This formula is attractive for several reasons:

(*i*) One can readily prove the known results for 1-2, 1-4, 1-6, 1-8, etc., shell-and-tube exchangers, by replacing $N$ in equation (12) by 1, 2, 3, 4, etc., respectively.

(*ii*) From equation (12), for $R \to 0$,

$$\lim_{R\to 0} P = 2/(1+\coth(N_{tu}/2)) = 1-\exp(-N_{tu}) \quad (13)$$

which is true for any flow arrangement.

(*iii*) From equation (12), for $N_{tu} \to \infty$

$$\lim_{N_{tu}\to\infty} P = 2N/(N(2+R)-1+\sqrt{1+N^2R^2}) \quad (14)$$

which confirms Dodd's (1982) equation (13).

(*iv*) Since

$$\lim_{N\to\infty}\left(\frac{1}{N}\coth(N_{tu}/2N)\right) = 2/N_{tu} \quad (15)$$

from equation (12) one readily finds

$$\lim_{N\to\infty} P = 2/\{1+R+\coth(N_{tu}/2) - 2/N_{tu} + R\coth(RN_{tu}/2)\} = \left(\frac{1}{1-\exp(-N_{tu})} + \frac{R}{1-\exp(-RN_{tu})} - \frac{1}{N_{tu}}\right)^{-1} \quad (16)$$

which is a very well-known result for the effectiveness of a single-pass crossflow heat exchanger with both fluids mixed. This limiting process was intuitively considered in various texts, but an analytical proof was not available in the literature.

### References


Dodd, R., 1982, "Temperature Efficiency of Heat Exchangers With One Shell and Even Number of Tube Passes," *Trans. IChemE*, Vol. 60, pp. 364-368.

Kraus, A. D., and Kern, D. Q., 1965, "The Effectiveness of Heat Exchangers With One Shell Pass and Even Numbers of Tube Passes," ASME Paper No. 65-HT-18.


## Heat Transfer in a Channel With Uniform Injection Through a Perforated Wall


**H. Kuroda[1,2] and K. Nishioka[1]**


### Nomenclature

- $b$ = channel height
- $c_p$ = specific heat at constant pressure
- $h$ = heat transfer coefficient
- $k$ = thermal conductivity of fluid
- $K_1$ = acceleration parameter = $\nu_a(du/dx)_{max}/u^2_{max}$
- Nu = Nusselt number = $hb/k_w$
- $Pr_a$ = Prandtl number = $\mu_a c_{pa}/k_a$
- $Q$ = volumetric flow rate per unit span
- $q_w$ = heat flux
- $r$ = radius
- $R_w$ = nondimensional radius of heat transfer wall = $r_w/b$
- $Re_a$ = injection parameter = $v_a b/\nu_a$
- $T$ = temperature
- $u, v$ = velocity components parallel and normal to wall
- $v_a$ = mean injection velocity
- $x, y$ = coordinates parallel and normal to wall
- $x_0, z_0$ = nozzle spacing in streamwise and spanwise directions
- $\epsilon$ = temperature-dependent parameter = $T_w/T_a - 1$
- $\theta$ = nondimensional temperature = $(T-T_a)/(T_w-T_a)$
- $\mu, \nu$ = viscosity and kinematic viscosity
- $\xi, \eta$ = nondimensional coordinates = $x/b$, $y/b$
- $\rho$ = density

#### Subscripts

- $a$ = air
- $w$ = wall

### Introduction

Jet impingement with cross flow as applied to turbine blade cooling or various drying processes has become a well-established method of convection cooling or heating (Florschuetz et al., 1980, 1981, 1984; Gardon et al., 1966; Kercher et al., 1970; Metzger, et al., 1972, 1979; Tabakoff et al., 1972). The local heat transfer coefficient for impinging jets varies greatly over a relatively small distance for the case where the distance between jet holes and the heat transfer wall is small and the distance between jet holes is large (Florschuetz et al., 1980; Gardon et al., 1966; Kercher et al., 1970; Metzger et al., 1979). Thus, large thermal stresses and strains are induced. To alleviate this situation, it is advantageous to increase the distance between the jet holes and the heat transfer wall and reduce the distance between jet holes. Because of the accelerated fluid flow toward the downstream region of the impingement duct, "laminarization" of the flow can occur. However, laminarization of the developed flow region may occur because of the accelerated fluid flow toward the downstream region of the duct. This laminarization results in constant distributions of heat transfer coefficients (Maretti et al., 1965; Perkins et al., 1973). When turbine blades or casings are cooled by this condition the local decrease of cooling ability is not desirable. However, to alleviate the local thermal stresses and strains, it is advantageous to use laminar flow, even if the average heat transfer may be decreased. Very few studies of these phenomena have been published. Debruge and Han (1972) computed heat transfer coefficients for two-dimensional laminar flow with uniform blowing from a wall into a channel. The analysis assumes similar velocity and temperature profiles; however they did not carry out a corresponding experimental investigation, so it is not clear whether the similarities exist.

This paper reports that the flow and heat transfer characteristics are investigated experimentally for the case when an approximately uniform air flow is injected through jet holes or slots in a wall issuing into a rectangular or concentric-annular channel.


[1]Department of Aeronautical Engineering, The National Defense Academy, 1-10-20 Hashirimizu, Yokosuka 239, Japan.

[2]Assoc. Mem. ASME.



Contributed by the Heat Transfer Division for publication in the JOURNAL OF HEAT TRANSFER. Manuscript received by the Heat Transfer Division January 16, 1986. Keywords: Forced Convection, Jets.

or, using equation (8)

$$f(\exp(N_{tu}/N)) = N\coth(N_{tu}/2) - \coth(N_{tu}/2N) \quad (10)$$

Also note that using equation (7), equation (2) becomes

$$x = (1+N^2R^2)^{1/2} \quad (11)$$

Thus, the Kraus-Kern equation, equation (1), can be simplified to read

$$P = 2/\left\{1+R+\coth(N_{tu}/2) - \frac{1}{N}\coth(N_{tu}/2N) + \frac{1}{N}\sqrt{1+N^2R^2}\coth\left(\frac{N_{tu}}{2N}\sqrt{1+N^2R^2}\right)\right\} \quad (12)$$

This formula is attractive for several reasons:

(*i*) One can readily prove the known results for 1-2, 1-4, 1-6, 1-8, etc., shell-and-tube exchangers, by replacing $N$ in equation (12) by 1, 2, 3, 4, etc., respectively.

(*ii*) From equation (12), for $R \to 0$,

$$\lim_{R\to 0} P = 2/(1+\coth(N_{tu}/2)) = 1-\exp(-N_{tu}) \quad (13)$$

which is true for any flow arrangement.

(*iii*) From equation (12), for $N_{tu} \to \infty$

$$\lim_{N_{tu}\to\infty} P = 2N/(N(2+R)-1+\sqrt{1+N^2R^2}) \quad (14)$$

which confirms Dodd's (1982) equation (13).

(*iv*) Since

$$\lim_{N\to\infty}\left(\frac{1}{N}\coth(N_{tu}/2N)\right) = 2/N_{tu} \quad (15)$$

from equation (12) one readily finds

$$\lim_{N\to\infty} P = 2/\{1+R+\coth(N_{tu}/2) - 2/N_{tu} + R\coth(RN_{tu}/2)\} = \left(\frac{1}{1-\exp(-N_{tu})} + \frac{R}{1-\exp(-RN_{tu})} - \frac{1}{N_{tu}}\right)^{-1} \quad (16)$$

which is a very well-known result for the effectiveness of a single-pass crossflow heat exchanger with both fluids mixed. This limiting process was intuitively considered in various texts, but an analytical proof was not available in the literature.

### References


Dodd, R., 1982, "Temperature Efficiency of Heat Exchangers With One Shell and Even Number of Tube Passes," *Trans. IChemE*, Vol. 60, pp. 364-368.

Kraus, A. D., and Kern, D. Q., 1965, "The Effectiveness of Heat Exchangers With One Shell Pass and Even Numbers of Tube Passes," ASME Paper No. 65-HT-18.


## Heat Transfer in a Channel With Uniform Injection Through a Perforated Wall


**H. Kuroda[1,2] and K. Nishioka[1]**


### Nomenclature

- $b$ = channel height
- $c_p$ = specific heat at constant pressure
- $h$ = heat transfer coefficient
- $k$ = thermal conductivity of fluid
- $K_1$ = acceleration parameter = $\nu_a(du/dx)_{max}/u^2_{max}$
- Nu = Nusselt number = $hb/k_w$
- $Pr_a$ = Prandtl number = $\mu_a c_{pa}/k_a$
- $Q$ = volumetric flow rate per unit span
- $q_w$ = heat flux
- $r$ = radius
- $R_w$ = nondimensional radius of heat transfer wall = $r_w/b$
- $Re_a$ = injection parameter = $v_a b/\nu_a$
- $T$ = temperature
- $u, v$ = velocity components parallel and normal to wall
- $v_a$ = mean injection velocity
- $x, y$ = coordinates parallel and normal to wall
- $x_0, z_0$ = nozzle spacing in streamwise and spanwise directions
- $\epsilon$ = temperature-dependent parameter = $T_w/T_a - 1$
- $\theta$ = nondimensional temperature = $(T-T_a)/(T_w-T_a)$
- $\mu, \nu$ = viscosity and kinematic viscosity
- $\xi, \eta$ = nondimensional coordinates = $x/b$, $y/b$
- $\rho$ = density

#### Subscripts

- $a$ = air
- $w$ = wall

### Introduction

Jet impingement with cross flow as applied to turbine blade cooling or various drying processes has become a well-established method of convection cooling or heating (Florschuetz et al., 1980, 1981, 1984; Gardon et al., 1966; Kercher et al., 1970; Metzger, et al., 1972, 1979; Tabakoff et al., 1972). The local heat transfer coefficient for impinging jets varies greatly over a relatively small distance for the case where the distance between jet holes and the heat transfer wall is small and the distance between jet holes is large (Florschuetz et al., 1980; Gardon et al., 1966; Kercher et al., 1970; Metzger et al., 1979). Thus, large thermal stresses and strains are induced. To alleviate this situation, it is advantageous to increase the distance between the jet holes and the heat transfer wall and reduce the distance between jet holes. Because of the accelerated fluid flow toward the downstream region of the impingement duct, "laminarization" of the flow can occur. However, laminarization of the developed flow region may occur because of the accelerated fluid flow toward the downstream region of the duct. This laminarization results in constant distributions of heat transfer coefficients (Maretti et al., 1965; Perkins et al., 1973). When turbine blades or casings are cooled by this condition the local decrease of cooling ability is not desirable. However, to alleviate the local thermal stresses and strains, it is advantageous to use laminar flow, even if the average heat transfer may be decreased. Very few studies of these phenomena have been published. Debruge and Han (1972) computed heat transfer coefficients for two-dimensional laminar flow with uniform blowing from a wall into a channel. The analysis assumes similar velocity and temperature profiles; however they did not carry out a corresponding experimental investigation, so it is not clear whether the similarities exist.

This paper reports that the flow and heat transfer characteristics are investigated experimentally for the case when an approximately uniform air flow is injected through jet holes or slots in a wall issuing into a rectangular or concentric-annular channel.


[1]Department of Aeronautical Engineering, The National Defense Academy, 1-10-20 Hashirimizu, Yokosuka 239, Japan.

[2]Assoc. Mem. ASME.



Contributed by the Heat Transfer Division for publication in the JOURNAL OF HEAT TRANSFER. Manuscript received by the Heat Transfer Division January 16, 1986. Keywords: Forced Convection, Jets.

## Experimental Apparatus

Figure 1 shows schematically the test channels, which have a perforated wall 300 mm in streamwise length. The channel whole length is 370 mm, which is also the length of the heat transfer wall for both the rectangular (corresponding to $R_w \to \infty$) and the concentric-annular channels. The perforated wall used in this experiment was a flat plate 100 mm in span ($l$) for the rectangular channel, and a semi-annular sector for the concentric-annular channel. The heat transfer wall radius for the concentric-annular channel is $r_w = 80$ mm ($R_w = 4$); these configurations and dimensions are listed in Table 1.

The injection flow rate was controlled by changing the plenum chamber pressure. A paper filter with high pressure loss is attached to the back of the perforated wall to maintain an approximately uniform injection velocity. The injection air temperature $T_a$ had negligible variation over the perforated wall so that the arithmetic mean value at upstream, intermediate, and downstream positions in the channel was taken as $T_a$. The upstream end of the channel was closed and, therefore, the injection air flowed downstream. The heat transfer wall was fabricated from 5 mm copper plate (circular cylinder for the concentric-annular channel) with a water-filled backing tank. The surface was kept at a uniform temperature by circulating hot water through a water tank. Copper-constantan thermocouples were mounted at several positions on the heat transfer surface. The wall temperature differences were within 0.2 K of one another; these temperatures were monitored during the experiment.

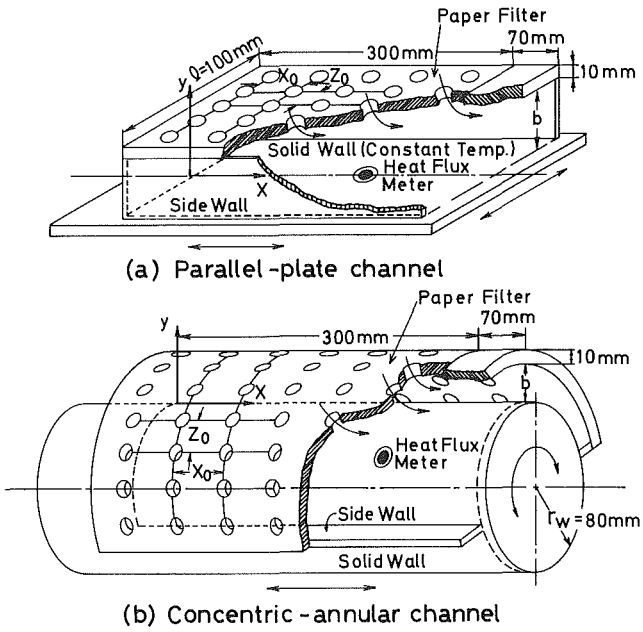


**Fig. 1 Schematic of channel geometries**

The heat flux $\dot{q}_w$ was measured by a Gardon (1960) type heat flux meter (Model GT-1-8-487, Medtherm Corp.), which was 3 mm (1/8 in.) in outside diameter. This meter, mounted on a copper block with 6 mm outside diameter, was screwed into 6.2-mm-dia hole in the heat transfer wall. In addition, a 5-mm-dia hole (not shown) was provided for inserting a hot-wire probe or a thermocouple probe at a position 35 mm downstream of the heat flux meter. O-rings and the Teflon sheets were used to prevent air leakage between the side walls and the heat transfer surface. The heat transfer wall could be easily moved, back and forth or right and left (rotated in concentric-annular channel), so that measurements could be taken at any point.

The ranges of variables in this experiment were: mean injection velocity $v_a = 0.05 \sim 1.5$ m/s ($\mathrm{Re_a} = 40 \sim 2000$); injection air temperature $T_a = 280 \sim 293$ K; and surface temperature $T_w = 329 \sim 350$ K (about 60 K higher than the injection air temperature). The discrepancy for the heat transfer coefficient $h$ was within about 6 percent, including 3 percent in the measurement of heat flux $\dot{q}_w$, and 1.7 K in the measurements of $T_a$ and $T_w$.

## Results and Discussion

Similar results were obtained for the rectangular channel configurations of No. 1 through No. 4 in Table 1. Hereinafter, the experimental results of No. 1 (rectangular channel) and No. 5 (concentric-annular channel) will be shown as the typical examples.

The velocities and temperatures in the spanwise direction for the developed region ($\xi \geq 4$) were almost uniform within the middle 70 percent of span (about 130 deg in sector angle for the concentric-annular channel). On the side-wall boundary layer edge, the velocity observed was about 3 percent higher than the midspan mean velocity. The averaged volumetric flow rate per unit span, obtained by measuring the total volumetric flow rate, was almost (within 3 percent) the same as the volumetric flow rate per unit span based upon measurements in the midspan region obtained by integrating velocity profiles normal to the heat transfer wall. Therefore, the arithmetic mean values of all measurements within the 70 percent midspan region, where the nondimensional velocity and temperature profiles became similar, were used in the experiment.

Figure 2 shows examples of the variation of a nondimensional volumetric flow rate, $Q/Q_{10}$, with downstream distance $\xi$. $Q_{10}$ is the volumetric flow rate per unit span at $\xi = 10$. The mean injection velocity $v_a$ was computed from the slope of the straight line segment of the $Q/Q_{10}$ versus $\xi$ curve. Figure 3 shows examples of $u/u_{\max}$ and nondimensional temperature, $\theta$, profiles across the channel where $u_{\max}$ is the maximum velocity component in the cross section at the chosen $\xi$ station. The reference lines in this figure show the results of Nishioka and Kuroda (1985), which were computed assuming laminar flow. With increasing $\mathrm{Re_a}$, the position of $u_{\max}$ moves close to the heat transfer wall and the near-wall $|d\theta/d\eta|$ increases. On the other hand, for given values of $\mathrm{Re_a}$, the $u/u_{\max}$ and $\theta$ profiles

**Table 1 Configurations and dimensions of channel and perforated wall**

| No. | Configuration | Channel height $b$, mm | Channel span $l$, mm | Hole diameter $d$, mm | Hole distance $x_0$, mm | Hole distance $z_0$, mm | Geometry |
|---|---|---|---|---|---|---|---|
| 1 | Rectangular channel | 21 | 100 | 2 | 3 | 3 | In line |
| 2 | Rectangular channel | 10.5 | 100 | 2 | 3 | 3 | In line |
| 3 | Rectangular channel | 10.5 | 100 | 2 | 2.12 | 2.12 | Staggered |
| 4 | Rectangular channel | 21 | 100 | 1 (width) | 2 | – | Slit |
| 5 | Concentric-annular channel | 20 | 251 ($r_w$=80) | 2 | 3 | 3 | In line |

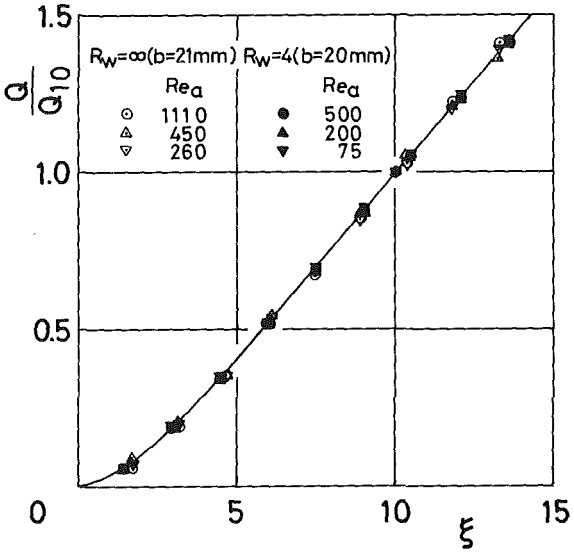


Fig. 2 Volumetric flow rate variation with distance downstream in the channel

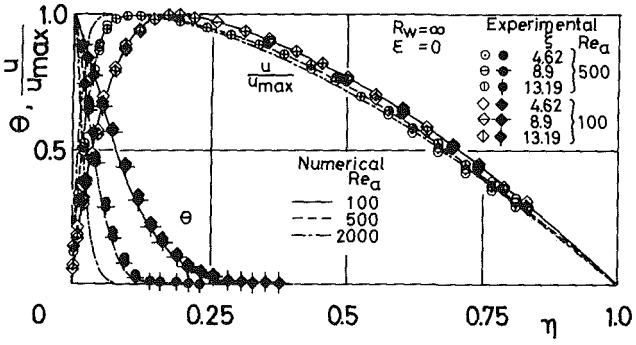


Fig. 3 Velocity and temperature profiles in a parallel-plate channel

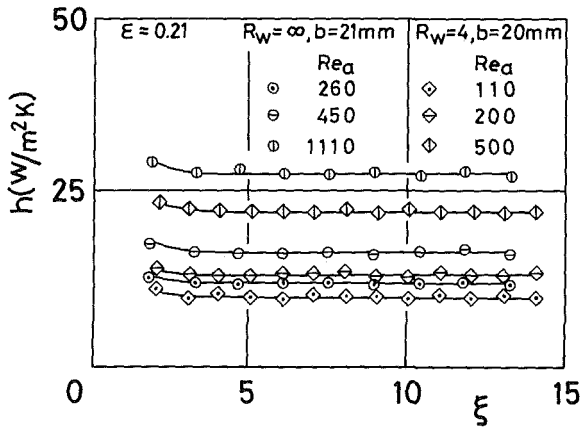


Fig. 4 Heat transfer coefficients for different injection parameters

are unchanged even though a range of $\xi$ from 4.6 to 13.2 is considered. If fully developed flow is defined as one that shows no variation of $u/u_{max}$ in the flow field, then it is shown that $u/u_{max}$ and $\theta$ have similar, developed profiles. For the concentric-annular channel, not shown in the figure, $u/u_{max}$ and $\theta$ profiles were obtained with similar results, except that the slopes near the heat transfer surface are larger than those for the rectangular channel and the position of $u_{max}$ is farther from the heat transfer wall.

The heat transfer coefficient $h$ was calculated using

$$h = \dot{q}_w/(T_w - T_a) \quad (1)$$

Examples of heat transfer coefficient $h$ variations with position

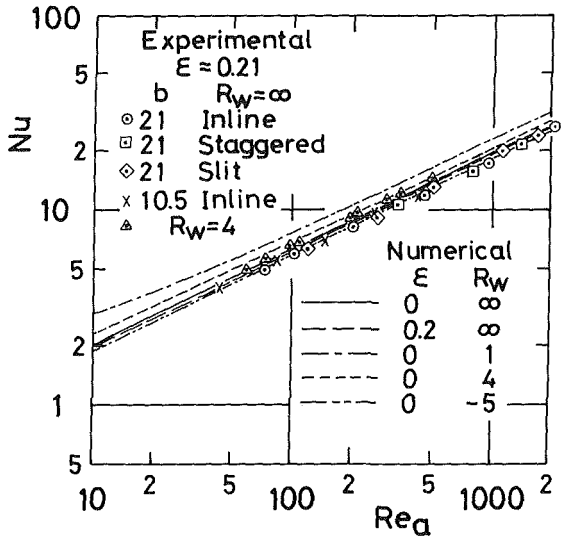


Fig. 5 Comparison of Nusselt numbers for different channel geometries

$\xi$ are illustrated in Fig. 4. The heat transfer coefficients are higher in the upstream region ($\xi \leq 3$) because the thermal boundary layer has not developed and the flow is dominated by impinging jet effects. However, $h$ approaches a uniform value in the region of accelerated flow field ($\xi \geq 4$). It is known that the heat transfer coefficient in accelerated flow (for constant heat flux), without injection, increases in the downstream direction (Tanaka et al., 1977). It has been shown that the heat transfer coefficient in the accelerated flow region for the case of $Re_a = 1110$ is much smaller (about 0.15 times) than that observed with an impinging jet with crossflow (Florschuetz et al., 1980). For channel flow with injection at high values of the injection parameter, it is expected that the heat transfer coefficient is larger than the heat transfer coefficient within injection, because the location of maximum velocity is shifted toward the heat transfer wall (Fig. 3); the heat transfer coefficient at $Re_a = 1110$ in the channel with injection is smaller (about 0.64 times) than the turbulent heat transfer coefficient calculated for the equivalent Reynolds number at $\xi = 14$ in the channel with injection and larger (about 4.4 times) than that for fully developed laminar flow without injection (Keys et al., 1980).

Although the Reynolds number based on mean streamwise velocity and channel height was varied from $1.1 \times 10^3$ ($\xi = 3$) through $1.5 \times 10^4$ ($\xi = 14$) for $Re_a = 1110$, it does not seem that the flow becomes turbulent in that the heat transfer coefficients do not change along the streamwise direction. Furthermore, since the acceleration parameter $K_1$ varies approximately inversely with $Re_a(\xi - 2)^2$ (for $\xi \geq 4$) in this experiment, it takes a minimum value at the exit of the channel. For example, this value was about $K_1 = 5 \times 10^{-6}$ when $Re_a = 1110$ and $\xi = 13$. This value is sufficiently large for "laminarization" in the acceleration flow (Tanaka et al., 1977). Therefore, it seems that the heat transfer coefficient in this experiment is equivalent to that in laminarization flow.

Figure 5 shows the relationship between $Re_a$ and Nusselt number Nu, which can be calculated from the measured mean heat transfer coefficient in the acceleration region ($\xi \geq 4$). Figure 5 includes all the results for the cases listed in Table 1, and the numerical results of Nishioka et al. (1985) (since the transport properties of most fluids vary with temperature through boundary layer, the main effect of temperature-dependent properties is density, and this paper includes the results of temperature-dependent density). The differences in heat transfer coefficients for the several cases with perforated walls in a rectangular channel are small so that the data from one case cannot be distinguished from each other. Nu increases

Table 2 Values of constant $A$ and $B$ in equation (2)

| | $A$ | $B$ | Range of $Re_a$ |
|---|---|---|---|
| Rectangular channel | 0.17 | 0.725 | $40 \le Re_a \le 2000$ |
| Concentric-annular channel | 0.21 | 0.665 | $50 \le Re_a \le 500$ |

approximately proportional to $\sqrt{Re_a}$ for both the rectangular channel and the concentric-annular channel. Thus, the experimental equation for Nusselt number can be expressed as follows (the effect of Prandtl number was computed from Nishioka and Kuroda, 1985):

$$Nu = hb/k = A + B\, Pr_a^{0.388} \sqrt{Re_a} \quad (2)$$

where $A$ and $B$ are constants listed in Table 2. The experimental results are in good agreement with the numerical results.

## Conclusions

To alleviate the thermal stresses and strains due to impingement cooling, it is necessary that the jet array be divided into a number of small jets where approximately uniform injection air from the perforated wall of the channel is approximated. In this case, the nondimensional velocity and temperature profiles are similar, except in the upstream region. The heat transfer coefficient has been measured where the flow has approximately uniform injection, that is, it does not have the characteristics of individual impinging jets. The heat transfer coefficient varies primarily with the injection parameter $Re_a$, and is almost uniform in the streamwise direction for a constant injection parameter. This means that the problem of large local thermal stresses and strains for a jet can be avoided. However, the cooling ability decreases because the flow is highly accelerated and the heat transfer coefficient decreases under the influence of laminarization flow. In the downstream region of the channel with uniform injection, the heat transfer coefficient reduces in value due to laminarization; the heat transfer coefficient reaches a minimum value for a fixed injection rate and channel height in the experiment described in this paper.

## References


Debruge, L. L., and Han, L. S., 1972, "Heat Transfer in a Channel With a Porous Wall for Turbine Cooling Application," ASME JOURNAL OF HEAT TRANSFER, Vol. 94, pp. 385-390.

Florschuetz, L. W., Berry, R. A., and Metzger, D. E., 1980, "Periodic Streamwise Variations of Heat Transfer Coefficients for Inline and Staggered Arrays of Circular Jets With Crossflow of Spent Air," ASME JOURNAL OF HEAT TRANSFER, Vol. 102, pp. 132-137.

Florschuetz, L. W., Metzger, D. E., and Su, C. C., 1984, "Heat Transfer Characteristics for Jet Array Impingement With Initial Crossflow," ASME JOURNAL OF HEAT TRANSFER, Vol. 106, pp. 24-41.

Florschuetz, L. W., Truman, C. R., and Metzger, D. E., 1981, "Streamwise Flow and Heat Transfer Distributions for Jet Array Impingement With Crossflow," ASME JOURNAL OF HEAT TRANSFER, Vol. 103, pp. 337-342.

Gardon, R., 1960, "A Transducer for the Measurement of Heat Rate," ASME JOURNAL OF HEAT TRANSFER, Vol. 82, pp. 396-398.

Gardon, R., and Akfrit, J. C., 1966, "Heat Transfer Characteristics of Impinging Two-Dimensional Air Jets," ASME JOURNAL OF HEAT TRANSFER, Vol. 88, pp. 101-108.

Kays, W. M., and Crawford, M. E., 1980, *Convection Heat and Mass Transfer*, 2nd ed., McGraw-Hill, New York, pp. 117, 255.

Kercher, D. M., and Tabakoff, W., 1970, "Heat Transfer by a Square Array of Round Air Jets Impinging Perpendicular to a Flat Surface Inducing the Effect of Spent Air," ASME *Journal of Engineering for Power*, Vol. 92, pp. 73-82.

Maretti, P. M., and Kays, W. M., 1965, "Heat Transfer to a Turbulent Boundary Layer With Varying Free-Stream Velocity and Varying Surface Temperature—an Experimental Study," *Int. J. Heat Mass Transfer*, Vol. 8, No. 9, pp. 1187-1202.

Metzger, D. E., Florschuetz, L. W., Takeuchi, D. I., Behee, R. D., and Berry, R. A., 1979, "Heat Transfer Characteristics for Inline and Staggered Arrays of Circular Jets With Crossflow of Spent Air," ASME JOURNAL OF HEAT TRANSFER, Vol. 101, pp. 526-531.

Metzger, D. E., and Korstad, R. J., 1972, "Effects of Crossflow on Impingement Heat Transfer," ASME *Journal of Engineering for Power*, Vol. 94, pp. 35-42.

Nishioka, K., and Kuroda, H., 1985-6, "Heat Transfer in the Concentric-Cylinder With a Uniform Injection on a Wall," *Scientific Report of National Defense Academy*, Vol. 23, No. 2, pp. 227-245 [in Japanese].

Perkins, K. R., Schade, K. W., and McEligot, D. M., 1973, "Heated Laminarizing Gas Flow in a Square Duct," *Int. J. Heat Mass Transfer*, Vol. 16, No. 5, pp. 897-915.

Tabakoff, W., and Clevenger, W., 1972, "Gas Turbine Blade Heat Transfer Augumentation by Impingement of Air Jets Having Various Configurations," ASME *Journal of Engineering for Power*, Vol. 94, pp. 51-60.

Tanaka, H., and Shimizu, J., "Laminarization in Low Reynolds Number Turbulent Duct Flows," ASME JOURNAL OF HEAT TRANSFER, Vol. 99, 1977, pp. 682-684.


# The Effect of Heat Generation on Convective Heat Transfer for Laminar Flows in a Multipassage Circular Pipe Subjected to an External Uniform Heat Flux


**M. A. Ebadian,[1] H. C. Topakoglu,[2] and O. A. Arnas[3]**


## Introduction

A literature survey (Shah and London, 1978; Soloukhin and Martynenko, 1983; Eckert et al., 1986; Lundberg et al., 1972; Kays and Crawford, 1980; Eckert and Drake, 1972; Kakac et al., 1987; Gebhart, 1971) indicates that heat transfer studies for laminar flows in multipassage circular pipes based on exact temperature distributions and including the heat generation effects are not available. The existing traditional calculation of convective heat transfer for flows in multipassage conduits are based on lumped parameter analyses (e.g., Shah and London, 1978), which are neither rigorous nor exact. The interest for heat transfer coefficients based on exact temperature distributions is of practical importance in the design of heat exchangers involving flows in separated sections with independent heat generation densities. In this technical note, the results of Ebadian et al (1986) are extended to include the effect of heat generation in the outer and inner flow regions (Fig. 1). The thickness of the separating surface and the heat conductivity of the inner wall, however, are neglected. It was shown by Ebadian et al. (1986) that the Nusselt numbers on the outer and separating surfaces can be defined for all practical purposes in three different ways. Of these three definitions, there are two that are the most suitable for heat exchanger applications. It was also shown that the Nusselt numbers depend on the following dimensionless parameters:

($i$) The ratio of the thermal conductivities of the fluids in the inner and outer passages, $k_k$.

($ii$) The product of $k_k$ and the ratio of the Peclet numbers of the flows between the inner and outer passages, $\eta = k_k k_{Pe}$ (the heat exchange number of the multipassage flow).

($iii$) The dimensionless heat generation numbers $\gamma_i$, $\gamma_o$ of the inner and outer flows, respectively, as defined in Ebadian et al. (1985) as $\gamma = (LH)/[kc(Pe)]$ where $L$ is the radius of the conduit, $H$ is heat generation volume density, $k$ is the thermal conductivity, $C$ is the temperature gradient along the pipe, and Pe is the Peclet number.

Considering the applications involving heat generation, one


[1]Department of Mechanical Engineering, Florida International University, The State University of Florida at Miami, Miami, FL 33199; Mem. ASME.

[2]Department of Mechanical Engineering, Southern University, Baton Rouge, LA 70813; Mem. ASME.

[3]Department of Mechanical Engineering, California State University, Sacramento, CA 95819; Fellow ASME.



Contributed by the Heat Transfer Division and presented at the 4th ATAA/ASME Heat Transfer Conference, Boston, Massachusetts, June 2-4, 1986. Manuscript received by the Heat Transfer Division June 30, 1986. Paper No. 86-HT-4. Keywords: Augmentation and Enhancement, Forced Convection, Heat Exchangers.

Table 2 Values of constant $A$ and $B$ in equation (2)

| | $A$ | $B$ | Range of $Re_a$ |
|---|---|---|---|
| Rectangular channel | 0.17 | 0.725 | $40 \le Re_a \le 2000$ |
| Concentric-annular channel | 0.21 | 0.665 | $50 \le Re_a \le 500$ |

approximately proportional to $\sqrt{Re_a}$ for both the rectangular channel and the concentric-annular channel. Thus, the experimental equation for Nusselt number can be expressed as follows (the effect of Prandtl number was computed from Nishioka and Kuroda, 1985):

$$Nu = hb/k = A + B\, Pr_a^{0.388} \sqrt{Re_a} \quad (2)$$

where $A$ and $B$ are constants listed in Table 2. The experimental results are in good agreement with the numerical results.

## Conclusions

To alleviate the thermal stresses and strains due to impingement cooling, it is necessary that the jet array be divided into a number of small jets where approximately uniform injection air from the perforated wall of the channel is approximated. In this case, the nondimensional velocity and temperature profiles are similar, except in the upstream region. The heat transfer coefficient has been measured where the flow has approximately uniform injection, that is, it does not have the characteristics of individual impinging jets. The heat transfer coefficient varies primarily with the injection parameter $Re_a$, and is almost uniform in the streamwise direction for a constant injection parameter. This means that the problem of large local thermal stresses and strains for a jet can be avoided. However, the cooling ability decreases because the flow is highly accelerated and the heat transfer coefficient decreases under the influence of laminarization flow. In the downstream region of the channel with uniform injection, the heat transfer coefficient reduces in value due to laminarization; the heat transfer coefficient reaches a minimum value for a fixed injection rate and channel height in the experiment described in this paper.

## References


Debruge, L. L., and Han, L. S., 1972, "Heat Transfer in a Channel With a Porous Wall for Turbine Cooling Application," ASME JOURNAL OF HEAT TRANSFER, Vol. 94, pp. 385-390.

Florschuetz, L. W., Berry, R. A., and Metzger, D. E., 1980, "Periodic Streamwise Variations of Heat Transfer Coefficients for Inline and Staggered Arrays of Circular Jets With Crossflow of Spent Air," ASME JOURNAL OF HEAT TRANSFER, Vol. 102, pp. 132-137.

Florschuetz, L. W., Metzger, D. E., and Su, C. C., 1984, "Heat Transfer Characteristics for Jet Array Impingement With Initial Crossflow," ASME JOURNAL OF HEAT TRANSFER, Vol. 106, pp. 24-41.

Florschuetz, L. W., Truman, C. R., and Metzger, D. E., 1981, "Streamwise Flow and Heat Transfer Distributions for Jet Array Impingement With Crossflow," ASME JOURNAL OF HEAT TRANSFER, Vol. 103, pp. 337-342.

Gardon, R., 1960, "A Transducer for the Measurement of Heat Rate," ASME JOURNAL OF HEAT TRANSFER, Vol. 82, pp. 396-398.

Gardon, R., and Akfrit, J. C., 1966, "Heat Transfer Characteristics of Impinging Two-Dimensional Air Jets," ASME JOURNAL OF HEAT TRANSFER, Vol. 88, pp. 101-108.

Kays, W. M., and Crawford, M. E., 1980, *Convection Heat and Mass Transfer*, 2nd ed., McGraw-Hill, New York, pp. 117, 255.

Kercher, D. M., and Tabakoff, W., 1970, "Heat Transfer by a Square Array of Round Air Jets Impinging Perpendicular to a Flat Surface Inducing the Effect of Spent Air," ASME *Journal of Engineering for Power*, Vol. 92, pp. 73-82.

Maretti, P. M., and Kays, W. M., 1965, "Heat Transfer to a Turbulent Boundary Layer With Varying Free-Stream Velocity and Varying Surface Temperature—an Experimental Study," *Int. J. Heat Mass Transfer*, Vol. 8, No. 9, pp. 1187-1202.

Metzger, D. E., Florschuetz, L. W., Takeuchi, D. I., Behee, R. D., and Berry, R. A., 1979, "Heat Transfer Characteristics for Inline and Staggered Arrays of Circular Jets With Crossflow of Spent Air," ASME JOURNAL OF HEAT TRANSFER, Vol. 101, pp. 526-531.

Metzger, D. E., and Korstad, R. J., 1972, "Effects of Crossflow on Impingement Heat Transfer," ASME *Journal of Engineering for Power*, Vol. 94, pp. 35-42.

Nishioka, K., and Kuroda, H., 1985-6, "Heat Transfer in the Concentric-Cylinder With a Uniform Injection on a Wall," *Scientific Report of National Defense Academy*, Vol. 23, No. 2, pp. 227-245 [in Japanese].

Perkins, K. R., Schade, K. W., and McEligot, D. M., 1973, "Heated Laminarizing Gas Flow in a Square Duct," *Int. J. Heat Mass Transfer*, Vol. 16, No. 5, pp. 897-915.

Tabakoff, W., and Clevenger, W., 1972, "Gas Turbine Blade Heat Transfer Augumentation by Impingement of Air Jets Having Various Configurations," ASME *Journal of Engineering for Power*, Vol. 94, pp. 51-60.

Tanaka, H., and Shimizu, J., "Laminarization in Low Reynolds Number Turbulent Duct Flows," ASME JOURNAL OF HEAT TRANSFER, Vol. 99, 1977, pp. 682-684.


# The Effect of Heat Generation on Convective Heat Transfer for Laminar Flows in a Multipassage Circular Pipe Subjected to an External Uniform Heat Flux


**M. A. Ebadian,[1] H. C. Topakoglu,[2] and O. A. Arnas[3]**


## Introduction

A literature survey (Shah and London, 1978; Soloukhin and Martynenko, 1983; Eckert et al., 1986; Lundberg et al., 1972; Kays and Crawford, 1980; Eckert and Drake, 1972; Kakac et al., 1987; Gebhart, 1971) indicates that heat transfer studies for laminar flows in multipassage circular pipes based on exact temperature distributions and including the heat generation effects are not available. The existing traditional calculation of convective heat transfer for flows in multipassage conduits are based on lumped parameter analyses (e.g., Shah and London, 1978), which are neither rigorous nor exact. The interest for heat transfer coefficients based on exact temperature distributions is of practical importance in the design of heat exchangers involving flows in separated sections with independent heat generation densities. In this technical note, the results of Ebadian et al (1986) are extended to include the effect of heat generation in the outer and inner flow regions (Fig. 1). The thickness of the separating surface and the heat conductivity of the inner wall, however, are neglected. It was shown by Ebadian et al. (1986) that the Nusselt numbers on the outer and separating surfaces can be defined for all practical purposes in three different ways. Of these three definitions, there are two that are the most suitable for heat exchanger applications. It was also shown that the Nusselt numbers depend on the following dimensionless parameters:

($i$) The ratio of the thermal conductivities of the fluids in the inner and outer passages, $k_k$.

($ii$) The product of $k_k$ and the ratio of the Peclet numbers of the flows between the inner and outer passages, $\eta = k_k k_{Pe}$ (the heat exchange number of the multipassage flow).

($iii$) The dimensionless heat generation numbers $\gamma_i$, $\gamma_o$ of the inner and outer flows, respectively, as defined in Ebadian et al. (1985) as $\gamma = (LH)/[kc(Pe)]$ where $L$ is the radius of the conduit, $H$ is heat generation volume density, $k$ is the thermal conductivity, $C$ is the temperature gradient along the pipe, and Pe is the Peclet number.

Considering the applications involving heat generation, one


[1]Department of Mechanical Engineering, Florida International University, The State University of Florida at Miami, Miami, FL 33199; Mem. ASME.

[2]Department of Mechanical Engineering, Southern University, Baton Rouge, LA 70813; Mem. ASME.

[3]Department of Mechanical Engineering, California State University, Sacramento, CA 95819; Fellow ASME.



Contributed by the Heat Transfer Division and presented at the 4th ATAA/ASME Heat Transfer Conference, Boston, Massachusetts, June 2-4, 1986. Manuscript received by the Heat Transfer Division June 30, 1986. Paper No. 86-HT-4. Keywords: Augmentation and Enhancement, Forced Convection, Heat Exchangers.

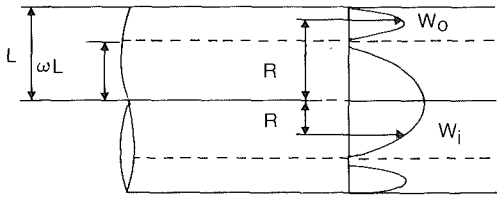


L :Outer radius
ωL :Radius of interface
R :Radial coordinate for a particle Located at the inner or outer region
$W_O$,$W_i$ :Velocities of the outer and inner flows respectively

**Fig. 1 Annular geometry**

of the three previously mentioned definitions for Nusselt numbers (Case I of Ebadian et al., 1986) is used and repeated here for convenience.

**Case I:** The inner and outer wall heat transfer coefficients are defined relative to mixed, combined flow bulk temperature of the inner and outer flows.

In order to present the obtained results graphically, typical values for the ratio of the thermal conductivities of the two fluids and the heat exchange numbers are selected. A heat generation number, $\gamma = 3.01$, a value corresponding to the elements involved in breeder type reactor designs (Duderstadt and Hamilton, 1976), is selected for both fluids.

### Temperature Fields

By neglecting the thermal resistance of the inner separation wall and at sufficient distances downstream from both entrances of the conduit, fully developed thermal conditions are established and the temperature distributions in the outer and inner passages due to convective heat transfer caused by the external uniform heat flux have the following functional forms, as given by Topakoglu and Arnas (1974):

$$T_o = CZ + E_o(X, Y), \quad T_i = CZ + E_{in} + E_i(X, Y) \tag{1}$$

where $C$ is the uniform external temperature gradient along the pipe, $Z$ is the dimensional longitudinal coordinate, $E_o$ and $E_i$ are the excess temperatures of the outer and inner flows, respectively, $E_{in}$ is the interface temperature, and $X$ and $Y$ are transversal rectangular coordinates. It must be noted that the term $CZ$ indicates the wall temperature variation in the longitudinal direction. The boundary conditions of excess temperatures are

$$\begin{aligned} E_o &= 0 \quad \text{on the outer periphery} \\ E_o &= E_{in} \quad \text{on the interface} \\ E_i &= 0 \quad \text{on the interface} \end{aligned} \tag{2}$$

The energy equation to be satisfied by each temperature distribution, including a uniform heat generation density $H$ $(W/m^3)$ is

$$\tilde{V} \cdot \text{grad}\, T = \alpha\left(\nabla^2 T + \frac{H}{k}\right) \tag{3}$$

where $\tilde{V}$ is the velocity vector, $T$ is temperature, and $\alpha$ is thermal diffusivity for the fluids in each passage.

The dimensionless thermal variables are introduced by the following relations:

$$H_o = \frac{F}{L} h_o, \quad C = \frac{F}{k_o} c, \quad E_o = \frac{LF}{k_o} e_o$$

$$H_i = \frac{F}{L} h_i, \quad E_{in} = \frac{LF}{k_o} e_{in}, \quad E_i = \frac{LF}{k_o} e_i \tag{4}$$

where $H_o$, $H_i$ and $h_o$, $h_i$ are dimensional and dimensionless heat generation densities for outer and inner passage flows, respectively. $F$ denotes an arbitrary heat flux. $C$ and $c$ are dimensional and dimensionless temperature gradient along the pipe $E_o$, $E_i$ and $e_o$, $e_i$ are dimensional and dimensionless excess temperatures for outer and inner passage flows, respectively.

The value of the dimensionless interface temperature $e_{in}$ must be determined by the condition of heat flux continuity at the interface as

$$k_o\left(\frac{de_o}{dr}\right)_{r=\omega} = k_i\left(\frac{de_i}{dr}\right)_{r=\omega} \tag{5}$$

Introducing an alternate dimensionless interface temperature $\beta$ as $\beta = e_{in}/G_o$ and substituting $e_o$ and $e_i$ from equations (13) and (15) of Ebadian et al. (1986) into equation (5), one finds

$$\beta = \frac{1}{4}\left[\frac{1}{4}\frac{u}{\omega}(3 - 4u + 7\omega^2) - \omega^3 + \frac{k_i}{k_o}\frac{G_i}{G_o} + \gamma_o\left(2\omega - \frac{u}{\omega}\right) - 2\gamma_i\omega\right]\omega \ln \omega \tag{6}$$

where

$$\gamma_o = h_o/G_o, \quad \gamma_i = h_i/G_o$$

and

$$\begin{aligned} G_o &= c(\text{Pe})_o, \quad (\text{Pe})_o = \text{Peclet number of outer flow} \\ G_i &= c\omega^3(\text{Pe})_i, \quad (\text{Pe})_i = \text{Peclet number of inner flow} \end{aligned} \tag{7}$$

Substitution of $G_o$ and $G_i$ into equation (6) yields

$$\beta = \left[\frac{1}{16}u(3 - 4u + 7\omega^2) - \frac{1}{4}(1 - \eta)\omega^4 + \frac{1}{4}\gamma_o(2\omega^2 - u) - \frac{1}{2}\gamma_i\omega^2\right]\ln \omega \tag{8}$$

where

$$\eta = \frac{k_i}{k_o}\frac{(\text{Pe})_i}{(\text{Pe})_o} = k_k\, k_{\text{Pe}} \tag{9}$$

This factor along with the effect of the heat generation densities determines the heat flow crossing the separating surface; here is called the heat exchanger number of the multipassage flow. Furthermore, the sign of this parameter indicates the relative directions of the flows in the outer and inner regions. That is, when $\eta$ is positive, the flows are unidirectional, parallel-flow combination, and when $\eta$ is negative, the flows are in opposite directions, the counterflow combination.

### Heat Fluxes and Heat Transfer Coefficients

The rates of heat flows per unit length of pipe through the outer and inner surfaces, considered positive when flowing into the outer flow region, are expressed as (Topakoglu and Arnas, 1974)

$$\begin{aligned} U_o &= 2\pi LFG_o\left[\frac{\beta}{\ln \omega} + e'_{oo}(1)\right] \\ U_i &= -2\pi LFG_o\left[\frac{\beta}{\ln \omega} + \omega e'_{oo}(\omega)\right] \end{aligned} \tag{10}$$

where, including the heat generation effect,

$$\begin{aligned} e'_{oo}(1) &= \frac{1}{4}(1 - u) - \frac{3}{16}u(1 + \omega^2) + \frac{1}{4}u^2 + \frac{1}{4}h_o(u - 2) \\ \omega e'_{oo}(\omega) &= e'_{oo}(1) - I_{oo} \\ I_{oo} &= \frac{1}{4}(1 - \omega^2)(1 + \omega^2 - u) \end{aligned} \tag{11}$$

Here, the primes indicate differentiation with respect to $r$.

By substituting $\beta$ from equation (8) and $e'_{oo}(1)$ and $\omega e'_{oo}(\omega)$ from equation (11) into equation (10), the rates of heat flows are simplified as

$$U_o = 2\pi LFG_o \frac{1}{4}[(1-\omega^2)(1+\omega^2-u)+\eta\omega^4 + 2\gamma_o(\omega^2-1)-2\gamma_i\omega^2] \quad (12)$$

$$U_i = -2\pi LFG_o \frac{1}{4}(\eta\omega^2-2\gamma_i)\omega^2$$

The existence of two separate independent flow regions makes it possible for the surface heat transfer coefficients to be defined in various ways (Ebadian et al., 1986).

The mixed mean temperature of the combined flow is

$$T_m = \left(C_{po}\rho_o\int_{A_o} W_oT_odA + C_{pi}\rho_i\int_{A_i} W_iT_idA\right)/(C_{po}Q_o + C_{pi}Q_i) \quad (13)$$

where $\rho_o$, $A_o$, $C_{po}$ and $\rho_i$, $A_i$, $C_{pi}$ are the densities, the cross-sectional areas, and the specific heats for the outer and inner passages, respectively.

Substituting $T_o$ and $T_i$ from equation (1), this reduces to

$$T_m = CZ + (E_{mo} + k_c\lambda E_{in} + k_c\lambda E_{mi})\left(\frac{1}{1+k_c\lambda}\right) \quad (14)$$

where

$$E_{mo} = \frac{\rho_o}{Q_o}\int_{A_o} W_oE_odA, \quad E_{mi} = \frac{\rho_i}{Q_i}\int_{A_i} W_iE_idA \quad (15)$$

and

$$k_c = C_{pi}/C_{po} \quad (16)$$

Substituting the dimensional variables for the dimensionless counterparts, the mixed mean excess temperatures $E_{mo}$ and $E_{mi}$ are expressed as

$$E_{mo} = -\frac{FL}{k_o}\frac{J_o}{I_{oo}}, \quad E_{mi} = -\frac{FL}{k_o}\frac{4}{\omega^4}J_i \quad (17)$$

where

$$J_o = -\frac{1}{(\mathrm{Re})_o}\int_\omega^1 rw_oe_odr, \quad J_i = -\frac{1}{(\mathrm{Re})_i}\frac{v_o}{v_i}\int_0^\omega rw_ie_idr \quad (18)$$

After performing the integrations for $J_o$ and $J_i$, one finds

$$\frac{J_o}{G_o} = \beta Y + J_{00} + J_{02}, \quad Y = -\frac{1}{\ln\omega}I_{01} \quad (19)$$

where $I_{01}$ and $J_{00}$ are given by Ebadian et al. (1986), and

$$J_{02} = \frac{1}{4}h_o\Big[-\frac{1}{2}(1-\omega^2)+\frac{1}{2}(1-\omega^4) - \frac{1}{6}(1-\omega^6)+\frac{3}{8}u + \frac{1}{2}u\omega^2(2-u)\ln\omega+\frac{1}{4}u(u-2)\omega^2 + \frac{1}{8}u\omega^4(1-4\ln\omega)-\frac{1}{4}u^2(1-2\omega^2\ln^2\omega)\Big] \quad (20)$$

$$\frac{J_i}{G_o} = \frac{11}{384}\omega^8\frac{\eta}{k_k} - \frac{1}{24}\frac{1}{k_k}\gamma_i\omega^6 \quad (21)$$

where $k_k = k_i/k_o$.

The individual bulk temperatures of the outer and inner flows are

$$T_{mo} = \frac{\rho_o}{Q_o}\int_{A_o} W_oT_odA, \quad T_{mi} = \frac{\rho_i}{Q_i}\int_{A_i} W_iT_idA \quad (22)$$

Substituting the expressions for $T_o$ and $T_i$ from (1) into (22) gives

$$T_{mo} = CZ + E_{mo}, \quad T_{mi} = CZ + E_{in} + E_{mi} \quad (23)$$

where $E_{mo}$ and $E_{mi}$ are the same expressions as given in equation (15).

If the heat transfer coefficients ($\bar{h}_o$ and $\bar{h}_i$) at the outer and inner surfaces are defined relative to the overall bulk temperature of the entire section, one can write

$$U_o = (CZ - T_m)2\pi L\bar{h}_o, \quad U_i = (CZ + E_{in} - T_m)2\pi\omega L\bar{h}_i \quad (24)$$

Selecting the fluid in the outer passage as the reference fluid, the Nusselt numbers on each surface based on their diameters are

$$(\mathrm{Nu})_o = \frac{2L}{k_o}\bar{h}_o \text{ and } (\mathrm{Nu})_i = \frac{2\omega L}{k_o}\bar{h}_i \quad (25)$$

Equating the heat flows in equations (12) and (24), the result simplifies to give

$$4I_{oo} + \eta\omega^4 + 2\gamma_o(\omega^2-1) - 2\gamma_i\omega^2 = \frac{8}{4I_{oo}+\eta\omega^4}\left[\frac{J_o}{G_o} + \frac{1}{4}\eta\omega^4\left(\frac{4}{\omega^4}\frac{J_i}{G_o} - \beta\right)\right](\mathrm{Nu})_o \quad (26)$$

and

$$\eta\omega^4 - 2\gamma_i\omega^2 = -\frac{8}{4I_{oo}+\eta\omega^4}\left[\frac{J_o}{G_o} + \eta\frac{J_i}{G_o} + \beta I_{oo}\right](\mathrm{Nu})_i \quad (27)$$

It is to be noted that the Nusselt numbers, besides being dependent on the size of the interface, depend only on the following three dimensionless parameters:

(*i*) The ratio of the thermal conductivities of two fluids $k_k$

(*ii*) The heat exchanger number $\eta$

(*iii*) The heat generation number $\gamma_o$ and $\gamma_i$

**Discussion of Numerical Results and Conclusions**

Selecting a heat generation number $\gamma = 3.01$ for both fluids and a numerical value for the ratio of the thermal conductivities of the two fluids as $k_k = 1$, and using four fixed values for heat exchanger number $\eta$ (1, 10, −1, −10), the ratios of $(\mathrm{Nu}_o)_w/(\mathrm{Nu}_o)_{wo}$ and $(\mathrm{Nu}_i)_w/(\mathrm{Nu}_i)_{wo}$ each representing the ratio of Nusselt number with heat generation to without heat generation are given in Figs. 2 and 3, respectively.

**Figure 2.** The ratio of $\mathrm{Nu}_o$ with heat generation to $\mathrm{Nu}_o$ without heat generation is plotted against the dimensionless core size $\omega$. It is observed that for parallel flows with $\eta = 1.0$ and $\eta = 10.0$, the ratio remain about 1.37. But for counterflows with $\eta = -1.0$ and $\eta = -10.0$, the ratio of the Nusselt numbers could reach very high values for particular core size values, $\omega = 0.4100$ and $\omega = 0.5800$, corresponding to each $\eta$ value mentioned above. The reason for this is that for counterflow arrangements with $\eta = -1.0$ and $\eta = -10.0$, the Nusselt number $\mathrm{Nu}_i$ has a zero value at the above-mentioned values of $\omega$ (Ebadian et al., 1986), thus making the ratio of the Nusselt number infinite at these points.

**Figure 3.** The ratio of $\mathrm{Nu}_i$ with heat generation to $\mathrm{Nu}_i$ without heat generation against the dimensionless core size $\omega$ is given. It is seen that, in the limiting case of $\omega = 1$, which is, as noted before, corresponding to a simple pipe, Nusselt number is increasing with the amount of heat generation considered by 37.7 percent (Ebadian et al., 1986). For the parallel flow case of $\eta = 1.0$, the ratio remains positive. Also, except

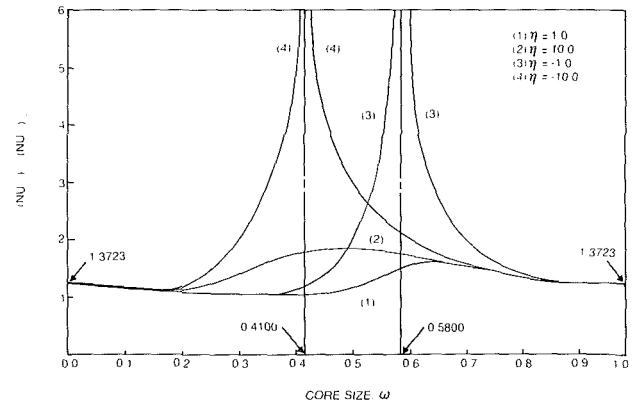


**Fig. 2 Ratio of outer Nusselt number with heat generation to $Nu_o$ without heat generation**

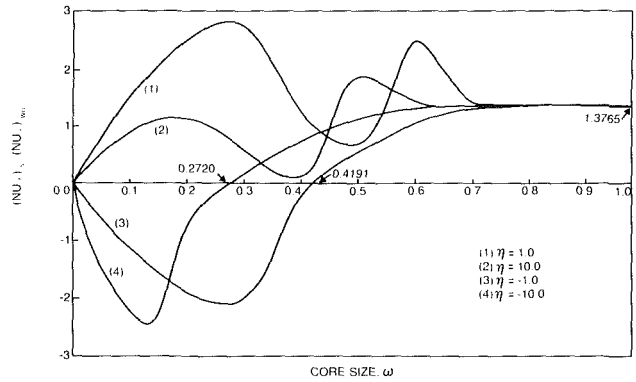


**Fig. 3 Ratio of inner Nusselt number with heat generation to $Nu_i$ without heat generation**

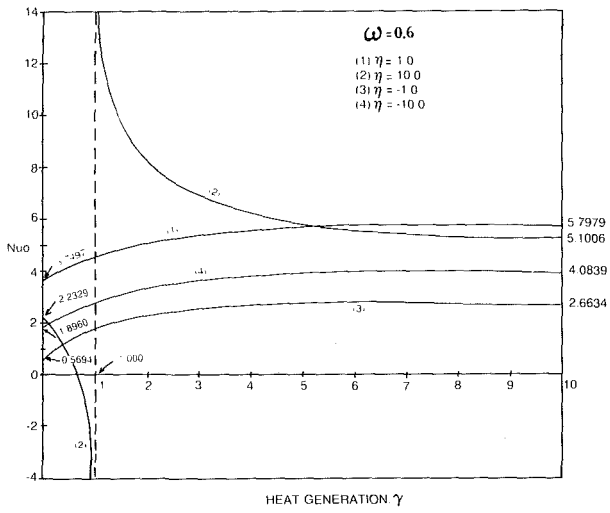


**Fig. 4 Outer Nusselt number versus heat generation number for core size $\omega = 0.6$**

for a small region around $\omega = 0.0$ and $\omega = 0.5$, it is greater than one. This indicates that except for the cases when $\omega$ is close to 0.0 or 0.5, $Nu_i$ with heat generation, becomes larger than $Nu_i$ without heat generation. For $\eta = 10.0$, the ratio remains positive, but becomes less than one for values of $\omega$ around $\omega = 0$ and $\omega = 0.4$. Outside these two regions, $Nu_i$ with heat generation, becomes larger than $Nu_i$ without heat generation. For counterflow arrangements with $\eta = -1.0$ and $\eta = -10.0$, the sign of the ratio changes. Especially at two particular values of (0.2720 and 0.4191), the ratio vanishes. The meaning of this behavior is that by the existence of heat generation when $\omega$ is greater than the values mentioned above, the heat

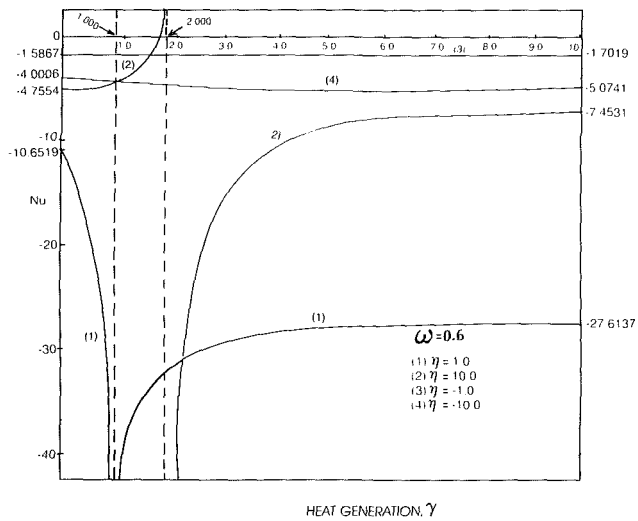


**Fig. 5 Inner Nusselt number versus heat generation number for core size $\omega = 0.6$**

transfer across the inner separation takes place along the radial direction. When $\omega$ is smaller than the values mentioned, heat transfer across the inner separation takes place toward the center. For $\omega$ values equal exactly to these special values, no heat transfer takes place through the inner separation.

**Figure 4.** The curves shown in Fig. 4 depict the variations in the outer wall Nusselt number $Nu_o$, which is defined relative to the combined flow bulk temperature of the inner and outer flows as a function of the dimensionless heat generation number $\gamma$, when the core size of the inner pipe is kept at $\omega = 0.6$. It is observed that at $\gamma_i = \gamma_o = 0$, the curves reduce to the curves in Fig. 2 of Ebadian et al. (1986). The presence of heat generation, therefore, increases the outer Nusselt number. At particular values of $\gamma$, the $Nu_o$ becomes infinite in a parallel flow arrangement of $\eta = 10.0$.

**Figure 5.** The inner Nusselt number is plotted against the dimensionless heat generation number $\gamma$, when the core size of the pipe is kept at $\omega = 0.6$. It is observed that for parallel flow with $\eta = 1.0$ and $\eta = 10.0$, the inner Nusselt number has vertical asymptotes at $\gamma = 1.0$ and $\gamma = 2.0$, respectively. This behavior corresponds to the case for which the fully developed conditions cannot be reached with finite external heat flux. In that case, a uniform temperature prevails everywhere with no external heat flux. In the case of counterflow arrangement $\eta = -1.0$ and $\eta = -10.0$, the increases in heat generation causes a decrease in Nusselt number.

## Acknowledgments

This material is based upon work supported by the National Science Foundation under Grant No. (R11-8305297).

## References

Duderstadt, J. J., and Hamilton, L. J., 1976, *Nuclear Reactor Analysis*, Wiley, New York.

Ebadian, M. A., Topakoglu, H. C., and Arnas, O. A., 1985, "The Effect of Heat Generation on the Convection Heat Transfer With a Tube Having a Constant Wall Temperature and Elliptical Cross Section," ASME Paper No. 85-WA/HT-57.

Ebadian, M. A., Arnas, O. A., and Topakoglu, H. C., 1986, "Convective Heat Transfer for Laminar Flows in a Multi-Passage Circular Pipe Subjected to an External Uniform Heat Flux," *International Journal of Heat and Mass Transfer*, Vol. 29, No. 1, pp. 107-217.

Eckert, E. R. G., and Drake, R. M., Jr., 1972, *Analysis of Heat and Mass Transfer*, McGraw-Hill, New York.

Eckert, E. R. G., Goldstein, R. J., Pfender, E., Ibele, W. E., Patanker, S. W., Ramsey, S. W., Simon, T. W., Deckor, N. A., Kuehn, T. H., Lee, H. O., and Girshick, S. L., 1986, "Heat Transfer—A Review of the 1985 Literature," *International Journal of Heat and Mass Transfer*, Vol. 29, pp. 1767-1842.

Gebhart, B., 1971, *Heat Transfer*, McGraw-Hill, New York.

Kakac, S., Shah, R. K., and Aung, W., 1987, *Handbook of Single-Phase Convective Heat Transfer*, Wiley, New York.

Kays, W. M., and Crawford, M. E., 1980, *Convective Heat and Mass Transfer*, 2nd ed., McGraw-Hill, New York.

Lundberg, R. E., Reynolds, W. C., and Kays, W. M., 1972, "Heat Transfer With Laminar Flow in Concentric Annuli With Constant and Variable Wall Temperature With Heat Flux," NASA TN D-1972.

Shah, R. K., and London, A. L., 1978, *Laminar Flow Forced Convection in Ducts*, Academic Press, New York.

Soloukhin, R. I., and Martynenko, O. G., 1983, "Heat and Mass Transfer Bibliography," *International Journal of Heat and Mass Transfer*, Vol. 26, pp. 1771-1781.

Topakoglu, H. C., and Arnas, O. A., 1974, "Convective Heat Transfer for Steady Laminar Flow Between Two Confocal Elliptic Pipes With Longitudinal Uniform Wall Temperature Gradient," *International Journal of Heat and Mass Transfer*, Vol. 17, pp. 1487-1498.

## Effects of Prandtl Number on Free Convection Heat Transfer From a Vertical Plate to a Non-Newtonian Fluid

**Ming-Jer Huang,[1] Jhy-Shean Huang,[1] You-Li Chou,[1] and Cha'o-Kuang Chen[2]**

### Nomenclature

$f$ = dimensionless stream function
$g$ = gravitational acceleration
$\mathrm{Gr}_x$ = modified Grashof number $= (g\beta\Delta T)^{2-n}x^{n+2}/(K/\rho)^2$
$h$ = local heat transfer coefficient
$\bar{h}$ = average heat transfer coefficient
$k$ = thermal conductivity
$K$ = parameter in the power-law model
$L$ = characteristic length
$n$ = flow index
$\mathrm{Nu}_x$ = local Nusselt number
$\mathrm{Nu}_L$ = average Nusselt number
Pr = modified Prandtl number $= 1/\alpha(K/\rho)^{2/(n+1)}(g\beta\Delta T)^{3(n-1)/2(n+1)}L^{(n-1)/2(n+1)}$
$q$ = heat flux
$T$ = temperature
$u, v$ = velocity components in the $x$ and $y$ directions, respectively
$x, y$ = coordinates along the plate and normal to the plate, respectively
$\alpha$ = thermal diffusivity
$\beta$ = thermal expansion coefficient
$\eta$ = pseudo-similarity variable
$\theta$ = dimensionless temperature
$\xi$ = normalized streamwise coordinate
$\rho$ = density
$\tau$ = shear stress
$\psi$ = stream function

### Subscripts

$x$ = the local value at the wall
$w$ = condition at the wall
$\infty$ = in the ambient fluid

### Introduction

Because of rapid growth in applications of rheology, complex fluid problems of free convective flow in non-Newtonian fluids have attracted the interest of many researchers since Acrivos (1960). He was the first to present the concept of an asymptotic boundary layer for power law fluids with large Prandtl numbers. Emery et al. (1970) investigated the free convection across two-dimensional vertical layers of power law fluids by experiment and used a composite model of the fluid to obtain numerical solutions. Shulman et al. (1976) solved the problem by the method of matched asymptotic expansions. Kawase and Ulbrecht (1984), based on the partial similarity between the velocity profiles for forced and free convection, obtained solutions by an integral method.

Moreover, Reilly et al. (1965), Lee and Ames (1966), Na and Hansen (1966), Dale and Emery (1972), and Som and Chen (1984) reported solutions for free convection in non-Newtonian fluids, but they were all based on an assumption of high Prandtl number. In fact, the Prandtl number of non-Newtonian fluids is not an infinite value, it is finite. For example, 0.5 percent carboxymethylcellulose (CMC) water solution has Pr = 85-500; 0.05 percent carbopol solution 934 has Pr = 65-90.

### Analysis

Consider a vertical flat plate with uniform surface temperature. The heat transfer between the plate and the non-Newtonian fluid is by the free convective flow. The physical properties are assumed to be constant except for the fluid density, which is described by the Boussinesq approximation. The conservation equations of the laminar boundary layer can be written as

$$\frac{\partial u}{\partial x}+\frac{\partial v}{\partial y}=0 \tag{1}$$

$$u\frac{\partial u}{\partial x}+v\frac{\partial u}{\partial y}=g\beta(T-T_\infty)+\frac{K}{\rho}\left|\frac{\partial u}{\partial y}\right|^{n-1}\frac{\partial u}{\partial y} \tag{2}$$

$$u\frac{\partial T}{\partial x}+v\frac{\partial T}{\partial y}=\alpha\frac{\partial^2 T}{\partial y^2} \tag{3}$$

$$u=v=0,\quad T=T_w \qquad \text{at } y=0$$
$$u\to 0,\quad T\to T_\infty \qquad \text{as } y\to\infty \tag{4}$$

Due to the nature of non-Newtonian fluids, similarity solutions only exist at infinite Prandtl number, i.e., when the inertia terms in equation (2) can be neglected. However, when the inertia force becomes of the same order of magnitude as the viscous force, similarity solutions do not exist. Thus, using dimensional analysis, one can obtain the following transformation, which can be used to transform the equations (1)-(3) and (4) to the nonsimilar equations. Let

$$\xi=x/L,\quad \eta=\frac{y}{x}\left(\rho(xg\beta\Delta T)^{\frac{2-n}{2}}x^n/K\right)^{\frac{1}{n+1}} \tag{5}$$

along with the dimensionless stream function $f(\xi,\eta)$ and the dimensionless temperature $\theta(\xi,\eta)$ defined, respectively, by

$$f(\xi,\eta)=\psi(x,y)\Big/\left[\frac{K}{\rho}x(xg\beta\Delta T)^{\frac{2n-1}{2}}\right]^{\frac{1}{n+1}} \tag{6}$$

$$\theta(\xi,\eta)=(T(x,y)-T_\infty)/\Delta T \tag{7}$$

where $\Delta T=T_w-T_\infty$.

Substituting equations (5)-(7) into equations (2)-(4), one obtains

$$\frac{\partial}{\partial\eta}\left[|f''|^{n-1}f''\right]+\frac{2n+1}{2(n+1)}ff''-\frac{1}{2}f'^2+\theta=\xi\left(f'\frac{\partial f'}{\partial\xi}-f''\frac{\partial f}{\partial\xi}\right) \tag{8}$$

[1]Department of Engineering Science, National Cheng Kung University, Tainan, Taiwan.
[2]Department of Mechanical Engineering, National Cheng Kung University, Tainan, Taiwan.

Contributed by the Heat Transfer Division for publication in the JOURNAL OF HEAT TRANSFER. Manuscript received by the Heat Transfer Division September 21, 1985. Keywords: Natural Convection, Non-Newtonian Flows and Systems, Numerical Methods.

Kays, W. M., and Crawford, M. E., 1980, *Convective Heat and Mass Transfer*, 2nd ed., McGraw-Hill, New York.

Lundberg, R. E., Reynolds, W. C., and Kays, W. M., 1972, "Heat Transfer With Laminar Flow in Concentric Annuli With Constant and Variable Wall Temperature With Heat Flux," NASA TN D-1972.

Shah, R. K., and London, A. L., 1978, *Laminar Flow Forced Convection in Ducts*, Academic Press, New York.

Soloukhin, R. I., and Martynenko, O. G., 1983, "Heat and Mass Transfer Bibliography," *International Journal of Heat and Mass Transfer*, Vol. 26, pp. 1771-1781.

Topakoglu, H. C., and Arnas, O. A., 1974, "Convective Heat Transfer for Steady Laminar Flow Between Two Confocal Elliptic Pipes With Longitudinal Uniform Wall Temperature Gradient," *International Journal of Heat and Mass Transfer*, Vol. 17, pp. 1487-1498.

## Effects of Prandtl Number on Free Convection Heat Transfer From a Vertical Plate to a Non-Newtonian Fluid

**Ming-Jer Huang,[1] Jhy-Shean Huang,[1] You-Li Chou,[1] and Cha'o-Kuang Chen[2]**

### Nomenclature

$f$ = dimensionless stream function
$g$ = gravitational acceleration
$\mathrm{Gr}_x$ = modified Grashof number $= (g\beta\Delta T)^{2-n}x^{n+2}/(K/\rho)^2$
$h$ = local heat transfer coefficient
$\bar{h}$ = average heat transfer coefficient
$k$ = thermal conductivity
$K$ = parameter in the power-law model
$L$ = characteristic length
$n$ = flow index
$\mathrm{Nu}_x$ = local Nusselt number
$\mathrm{Nu}_L$ = average Nusselt number
Pr = modified Prandtl number $= 1/\alpha(K/\rho)^{2/(n+1)}(g\beta\Delta T)^{3(n-1)/2(n+1)}L^{(n-1)/2(n+1)}$
$q$ = heat flux
$T$ = temperature
$u, v$ = velocity components in the $x$ and $y$ directions, respectively
$x, y$ = coordinates along the plate and normal to the plate, respectively
$\alpha$ = thermal diffusivity
$\beta$ = thermal expansion coefficient
$\eta$ = pseudo-similarity variable
$\theta$ = dimensionless temperature
$\xi$ = normalized streamwise coordinate
$\rho$ = density
$\tau$ = shear stress
$\psi$ = stream function

### Subscripts

$x$ = the local value at the wall
$w$ = condition at the wall
$\infty$ = in the ambient fluid

### Introduction

Because of rapid growth in applications of rheology, complex fluid problems of free convective flow in non-Newtonian fluids have attracted the interest of many researchers since Acrivos (1960). He was the first to present the concept of an asymptotic boundary layer for power law fluids with large Prandtl numbers. Emery et al. (1970) investigated the free convection across two-dimensional vertical layers of power law fluids by experiment and used a composite model of the fluid to obtain numerical solutions. Shulman et al. (1976) solved the problem by the method of matched asymptotic expansions. Kawase and Ulbrecht (1984), based on the partial similarity between the velocity profiles for forced and free convection, obtained solutions by an integral method.

Moreover, Reilly et al. (1965), Lee and Ames (1966), Na and Hansen (1966), Dale and Emery (1972), and Som and Chen (1984) reported solutions for free convection in non-Newtonian fluids, but they were all based on an assumption of high Prandtl number. In fact, the Prandtl number of non-Newtonian fluids is not an infinite value, it is finite. For example, 0.5 percent carboxymethylcellulose (CMC) water solution has Pr = 85-500; 0.05 percent carbopol solution 934 has Pr = 65-90.

### Analysis

Consider a vertical flat plate with uniform surface temperature. The heat transfer between the plate and the non-Newtonian fluid is by the free convective flow. The physical properties are assumed to be constant except for the fluid density, which is described by the Boussinesq approximation. The conservation equations of the laminar boundary layer can be written as

$$\frac{\partial u}{\partial x}+\frac{\partial v}{\partial y}=0 \tag{1}$$

$$u\frac{\partial u}{\partial x}+v\frac{\partial u}{\partial y}=g\beta(T-T_\infty)+\frac{K}{\rho}\left|\frac{\partial u}{\partial y}\right|^{n-1}\frac{\partial u}{\partial y} \tag{2}$$

$$u\frac{\partial T}{\partial x}+v\frac{\partial T}{\partial y}=\alpha\frac{\partial^2 T}{\partial y^2} \tag{3}$$

$$u=v=0, \quad T=T_w \qquad \text{at } y=0$$
$$u\to 0, \quad T\to T_\infty \qquad \text{as } y\to\infty \tag{4}$$

Due to the nature of non-Newtonian fluids, similarity solutions only exist at infinite Prandtl number, i.e., when the inertia terms in equation (2) can be neglected. However, when the inertia force becomes of the same order of magnitude as the viscous force, similarity solutions do not exist. Thus, using dimensional analysis, one can obtain the following transformation, which can be used to transform the equations (1)-(3) and (4) to the nonsimilar equations. Let

$$\xi=x/L, \quad \eta=\frac{y}{x}\left(\rho(xg\beta\Delta T)^{\frac{2-n}{2}}x^n/K\right)^{\frac{1}{n+1}} \tag{5}$$

along with the dimensionless stream function $f(\xi,\eta)$ and the dimensionless temperature $\theta(\xi,\eta)$ defined, respectively, by

$$f(\xi,\eta)=\psi(x,y)\Big/\left[\frac{K}{\rho}x(xg\beta\Delta T)^{\frac{2n-1}{2}}\right]^{\frac{1}{n+1}} \tag{6}$$

$$\theta(\xi,\eta)=(T(x,y)-T_\infty)/\Delta T \tag{7}$$

where $\Delta T=T_w-T_\infty$.

Substituting equations (5)-(7) into equations (2)-(4), one obtains

$$\frac{\partial}{\partial\eta}\left[|f''|^{n-1}f''\right]+\frac{2n+1}{2(n+1)}ff''-\frac{1}{2}f'^2+\theta=\xi\left(f'\frac{\partial f'}{\partial\xi}-f''\frac{\partial f}{\partial\xi}\right) \tag{8}$$

[1]Department of Engineering Science, National Cheng Kung University, Tainan, Taiwan.
[2]Department of Mechanical Engineering, National Cheng Kung University, Tainan, Taiwan.

Contributed by the Heat Transfer Division for publication in the JOURNAL OF HEAT TRANSFER. Manuscript received by the Heat Transfer Division September 21, 1985. Keywords: Natural Convection, Non-Newtonian Flows and Systems, Numerical Methods.

$$\mathrm{Pr}^{-1}\xi^{\frac{1-n}{2(n+1)}}\theta'' + \frac{2n+1}{2(n+1)} f\theta' = \xi\left(f'\frac{\partial\theta}{\partial\xi} - \theta'\frac{\partial f}{\partial\xi}\right) \quad (9)$$

$$f'(\xi,0) = f(\xi,0) = 0, \quad \theta(\xi,0) = 1; \quad f'(\xi,\infty) = \theta(\xi,\infty) = 0 \quad (10)$$

where Pr is the Prandtl number, defined as

$$\mathrm{Pr} = \frac{1}{\alpha}\left(\frac{K}{\rho}\right)^{\frac{2}{n+1}} (g\beta\Delta T)^{\frac{3(n-1)}{2(n+1)}} L^{\frac{n-1}{2(n+1)}} \quad (11)$$

The interest of the present work is in the heat transfer coefficient. From the definition $h = q/(T_w - T_\infty)$, and using equations (5)-(7), the local Nusselt number can be shown to be

$$\mathrm{Nu}_x \mathrm{Gr}_x^{-\frac{1}{2(n+1)}} = -\theta(\xi, 0) \quad (12)$$

where $\mathrm{Gr}_x$ is the Grashof number, defined as

$$\mathrm{Gr}_x = (g\beta\Delta T)^{2-n} x^{n+2} / \left(\frac{K}{\rho}\right)^2 \quad (13)$$

### Numerical Results and Discussion

The two systems of partial differential equations (8)-(10) are coupled and nonlinear. In the present study, these equations were solved by an implicit finite difference technique devised by Cebeci and Bradshaw (1977). Due to the high degree of nonlinearity, the finite difference of the first term in the momentum equation can be expressed as follows:

$$\frac{\partial}{\partial\eta}\{\,|f''|^{n-1}f''\,\} = \{\,|p_j|^{n-1}p_j - |p_{j-1}|^{n-1}p_{j-1}\,\}/\Delta\eta \quad (14)$$

where $p = f''$. Substituting the following interative forms:

$$p_j^{(i+1)} = p_j^{(i)} + \delta p_j^{(i)} \text{ and } p_{j-1}^{(i+1)} = p_{j-1}^{(i)} + \delta p_{j-1}^{(i)} \quad (15)$$

where $(i)$ is the number of the iteration, into equation (8), expanding and neglecting the nonlinear terms, the final difference form is

$$\Big\{\Big\{|p_j^{(i)}|^{n-1}p_j^{(i)} + \Big[|p_j^{(i)}|^{n-1} + (n-1)|p_j^{(i)}|^{n-2}p_j^{(i)}\Big]\delta p_j^{(i)}\Big\} - \Big\{|p_{j-1}^{(i)}|^{n-1}p_{j-1}^{(i)} + \Big[|p_{j-1}^{(i)}|^{n-1} + (n-1)|p_{j-1}^{(i)}|^{n-2}p_{j-1}^{(i)}\Big]\delta p_{j-1}^{(i)}\Big\}\Big\}/\Delta\eta \quad (16)$$

Since a singular point ($\xi = 0$) exists in equation (9), we begin with $\xi = 10^{-10}$. Moreover, in order to ensure high accuracy, nonuniform grid points were used. For small $\xi$, a smaller $\xi$ subdivision was needed for the boundary layer solutions.

To confirm the accuracy of the present numerical method, the comparisons in Nusselt number, $\mathrm{Nu}_x/\mathrm{Gr}_x^{1/4}$, have been shown in Table 1 with different values of Prandtl number. When $n = 1$ (Newtonian fluid), the problem can be reduced to that of Ede (1967), which was used as a check on our calculations. Table 1 shows that Acrivos' solution (1960) and Kawase and Ulbrecht's solution (1984) are only appropriate for high Prandtl numbers. The results of the present work are found to be in agreement with Ede's exact solution (1967) for any Prandtl number.

Representative results for the local heat transfer rate at $\xi = 1$ are depicted in Table 2 with flow index values, $n = 0.6$, 0.8, 1.0, 1.2, and 1.5 and Prandtl numbers, Pr = 10, 100, and 1000. It can be found that with an increase of the Prandtl number, the difference between heat transfer computed by the present work and others decreases for all flow index values $n$. When Pr = 1000, it becomes less than 3 percent. Hence, it is obvious that results of Acrivos (1960) and Kawase and Ulbrecht (1984) are only correct for large Prandtl number, while our work can be used for all Prandtl numbers.

**Table 1 Comparisons of local Nusselt number, $\mathrm{Nu}_x/\mathrm{Gr}_x^{1/4}$, for $n = 1$**

| Pr | Acrivos (1960) | Kawase and Ulbrecht (1984) | Ede (1967) | Present work |
|---|---|---|---|---|
| 10 | 0.8943 | 0.8936 | 0.8269 | 0.8268 |
| 100 | 1.5903 | 1.5891 | 1.5506 | 1.5486 |
| 1000 | 2.8285 | 2.8264 | 2.8047 | 2.8084 |

**Table 2 Comparisons of local Nusselt number, $\mathrm{Nu}_x/\mathrm{Gr}_x^{1/2(n+1)}$, for $\xi = 1$**

| Pr | $n$ | Acrivos (1960) | Kawase and Ulbrecht (1984) | Present work |
|---|---|---|---|---|
| | 0.6 | 0.8166 | 0.8210 | 0.7384 |
| | 0.8 | 0.8602 | 0.8619 | 0.7902 |
| 10 | 1.0 | 0.8943 | 0.8936 | 0.8268 |
| | 1.2 | 0.9285 | 0.9189 | 0.8546 |
| | 1.5 | 0.9706 | 0.9486 | 0.8860 |
| | 0.6 | 1.3375 | 1.3447 | 1.2754 |
| | 0.8 | 1.4788 | 1.4818 | 1.4334 |
| 100 | 1.0 | 1.5903 | 1.5891 | 1.5486 |
| | 1.2 | 1.6930 | 1.6755 | 1.6408 |
| | 1.5 | 1.8188 | 1.7775 | 1.7470 |
| | 0.6 | 2.1907 | 2.2025 | 2.1292 |
| | 0.8 | 2.5421 | 2.5472 | 2.5116 |
| 1000 | 1.0 | 2.8280 | 2.8259 | 2.8084 |
| | 1.2 | 3.0868 | 3.0551 | 3.0479 |
| | 1.5 | 3.4081 | 3.3306 | 3.3345 |

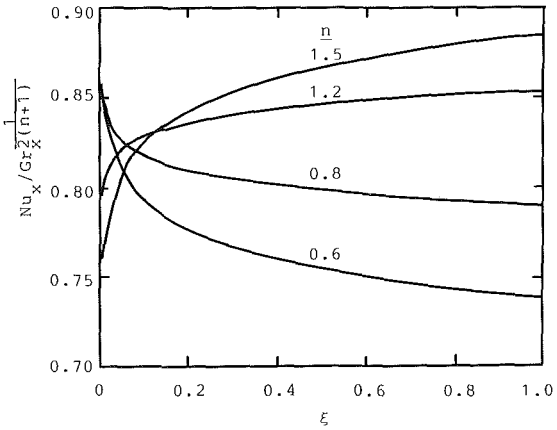


**Fig. 1 Local Nusselt number for Pr = 10**

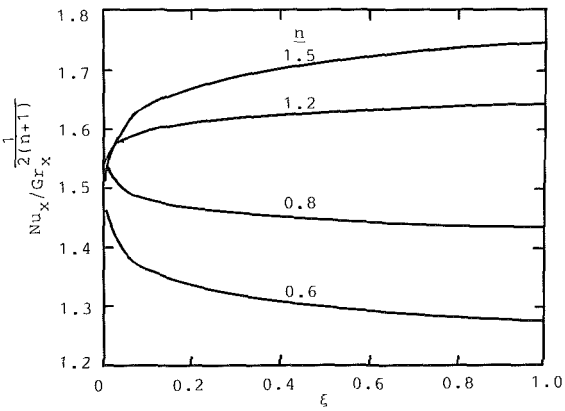


**Fig. 2 Local Nusselt number for Pr = 100**

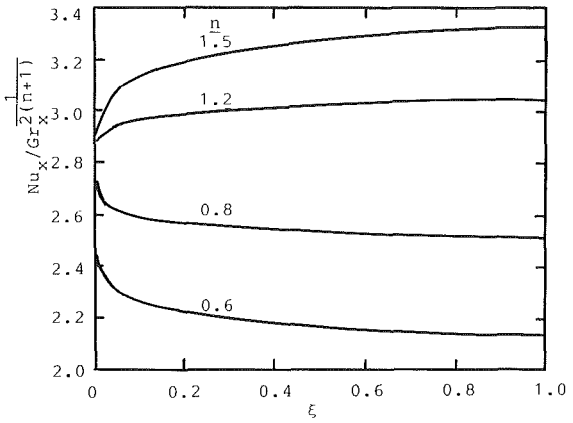


Fig. 3 Local Nusselt number for Pr = 1000

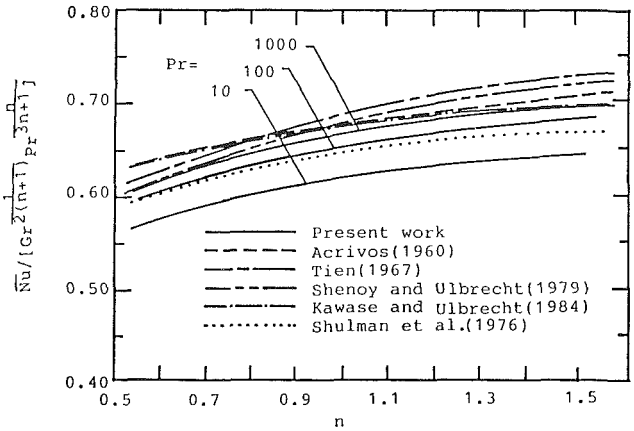


Fig. 4 Comparisons of average Nusselt numbers

Distributions of the dimensionless local Nusselt number are illustrated in Figs. 1-3, respectively, for Pr = 10, 100, and 1000. From the figures, it can be seen that along the surface the heat transfer rate increases for dilatant fluids ($n > 1$) and decreases for pseudoplastic fluids ($n < 1$). Except in the neighborhood of the leading edge, the greater the Prandtl number, the less the variations of the Nusselt number for each value of $n$. Accordingly, it can be concluded that at high Prandtl number there exists a similarity solution that had been proposed by Acrivos (1960). Furthermore, the figures reveal that the higher the Prandtl number the greater the Nusselt number for all values of the flow index $n$.

The average Nusselt number, $\overline{Nu}_L = \bar{h}L/K$, where $L$ is the characteristic length and $\bar{h}$ is the average heat transfer coefficient, can be expressed as

$$\overline{Nu}_L Gr_L^{-\frac{1}{2(n+1)}} = -\int_0^1 \theta'(\xi, 0)\xi^{-\frac{n}{2(n+1)}} d\xi \qquad (17)$$

Comparisons of the average Nusselt numbers are plotted in Fig. 4. It can be seen from the figure that at lower Prandtl number (Pr = 10), the average Nusselt numbers from the work of others are higher than that of present work. With an increase in the Prandtl number, the deviation between the results of others and present work gradually decreases. This can be explained by the fact that their works are only correct for high Prandtl number.

## Conclusions

A study has been conducted to analyze the heat transfer characteristics of non-Newtonian power law fluids on the free convective flow over a vertical flat plate. The analysis includes the inertia force in the momentum equation with a finite Prandtl number. In general, it has been found that the average heat transfer increases with increasing Prandtl number.

## References


Acrivos, A., 1960, "A Theoretical Analysis of Laminar Natural Convection Heat Transfer to Non-Newtonian Fluids," *AIChE J.*, Vol. 16, pp. 584-590.

Cebeci, T., and Bradshaw, P., 1977, *Momentum Transfer in Boundary Layers*, Hemisphere, Washington, DC.

Dale, J. D., and Emery, A. F., 1972, "The Free Convection of Heat From a Vertical Plate to Several Non-Newtonian Pseudoplastic Fluids," ASME JOURNAL OF HEAT TRANSFER, Vol. 94, pp. 64-72.

Ede, A. J., 1967, "Advances in Free Convection," *Adv. Heat Transfer*, Vol. 4, pp. 1-64.

Emery, A. F., Chi, H. S., and Dale, J. D., 1970, "Free Convection Through Vertical Plane Layers of Non-Newtonian Power Law Fluids," ASME JOURNAL OF HEAT TRANSFER, Vol. 93, pp. 164-171.

Kawase, K., and Ulbrecht, J., 1984, "Approximate Solution to the Natural Convection Heat Transfer From a Vertical Plate," *Int. Comm. Heat Transfer*, Vol. 11, pp. 143-155.

Lee, S. Y., and Ames, W. F., 1966, "Similarity Solutions for Non-Newtonian Fluids," *AIChE J.*, Vol. 22, pp. 700-708.

Na, T. Y., and Hansen, A. G., 1966, "Possible Similarity Solutions of the Laminar Natural Convection Flow of Non-Newtonian Fluids," *Int. J. Heat Mass Transfer*, Vol. 9, pp. 261-262.

Reilly, I. G., Tien, C., and Adelman, M., 1965, "Experimental Study of Natural Convection Heat Transfer From a Vertical Plate in a Non-Newtonian Fluids," *Can. J. Chem. Eng.*, Vol. 43, pp. 157-160.

Shulman, Z. P., Baikov, V. I., and Zaltsgendler, E. A., 1976, "An Approach to Prediction of Free Convection in Non-Newtonian Fluids," *Int. J. Heat Mass Transfer*, Vol. 19, pp. 1003-1006.

Som, A., and Chen, J. L. S., 1984, "Free Convection of Non-Newtonian Fluids Over Non-isothermal Two-Dimensional Bodies," *Int. J. Heat Mass Transfer*, Vol. 27, pp. 791-794.


# Ice Formation Over an Isothermally Cooled Vertical Circular Cylinder in Natural Convection


**K. C. Cheng[1] and P. Sabhapathy[1]**


## Nomenclature

- Bi = Biot number = $h_c r_o/k_s$
- $c$ = specific heat
- $g$ = acceleration due to gravity
- $h$ = heat transfer coefficient
- $\bar{h}$ = average heat transfer coefficient
- $H$ = convection parameter at the interface = $h_f r_o/(k_s\theta_c)$
- $k$ = thermal conductivity
- $L$ = latent heat of freezing
- $Nu_x$ = local Nusselt number = $h_f x/k_l$
- Nu = average Nusselt number = $h_f x/k_l$
- Pr = Prandtl number
- $r_o$ = radius of the cylinder
- $r_f$ = interface position
- $Ra_x$ = Rayleigh number = $g\beta_l(t_\infty - t_f)x^3/(\alpha_l\nu_l)$
- $S$ = dimensionless interface position = $r_f/r_o$
- $t$ = temperature
- $x$ = distance from the start of cooling along axial direction
- $\alpha$ = thermal diffusivity
- $\beta$ = coefficient of thermal expansion


[1]Department of Mechanical Engineering, University of Alberta, Edmonton, Alberta, Canada T6G 2G8.



Contributed by the Heat Transfer Division and presented at the National Heat Transfer Conference, Denver, Colorado, August 4-7, 1985. Manuscript received by the Heat Transfer Division May 30, 1986. Keywords: Materials Processing and Manufacturing Processes, Moving Boundaries, Phase-Change Phenomena.

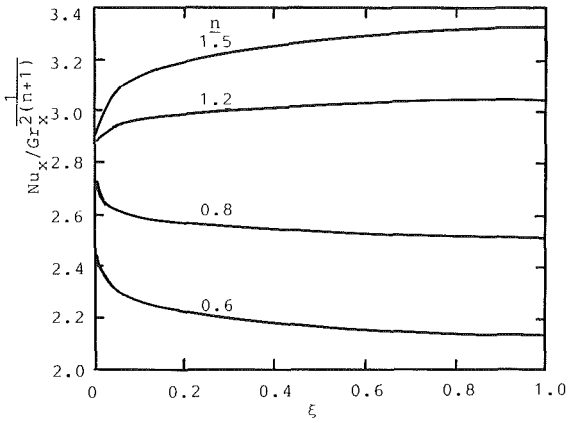


Fig. 3 Local Nusselt number for Pr = 1000

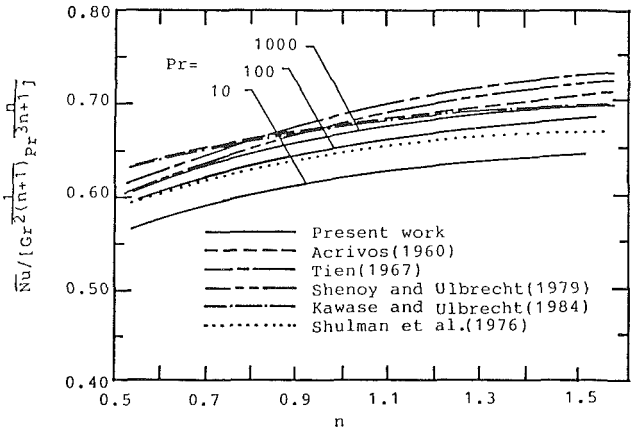


Fig. 4 Comparisons of average Nusselt numbers

Distributions of the dimensionless local Nusselt number are illustrated in Figs. 1-3, respectively, for Pr = 10, 100, and 1000. From the figures, it can be seen that along the surface the heat transfer rate increases for dilatant fluids ($n > 1$) and decreases for pseudoplastic fluids ($n < 1$). Except in the neighborhood of the leading edge, the greater the Prandtl number, the less the variations of the Nusselt number for each value of $n$. Accordingly, it can be concluded that at high Prandtl number there exists a similarity solution that had been proposed by Acrivos (1960). Furthermore, the figures reveal that the higher the Prandtl number the greater the Nusselt number for all values of the flow index $n$.

The average Nusselt number, $\overline{Nu}_L = \bar{h}L/K$, where $L$ is the characteristic length and $\bar{h}$ is the average heat transfer coefficient, can be expressed as

$$\overline{Nu}_L Gr_L^{-\frac{1}{2(n+1)}} = -\int_0^1 \theta'(\xi, 0)\xi^{-\frac{n}{2(n+1)}} d\xi \qquad (17)$$

Comparisons of the average Nusselt numbers are plotted in Fig. 4. It can be seen from the figure that at lower Prandtl number (Pr = 10), the average Nusselt numbers from the work of others are higher than that of present work. With an increase in the Prandtl number, the deviation between the results of others and present work gradually decreases. This can be explained by the fact that their works are only correct for high Prandtl number.

## Conclusions

A study has been conducted to analyze the heat transfer characteristics of non-Newtonian power law fluids on the free convective flow over a vertical flat plate. The analysis includes the inertia force in the momentum equation with a finite Prandtl number. In general, it has been found that the average heat transfer increases with increasing Prandtl number.

## References


Acrivos, A., 1960, "A Theoretical Analysis of Laminar Natural Convection Heat Transfer to Non-Newtonian Fluids," *AIChE J.*, Vol. 16, pp. 584-590.

Cebeci, T., and Bradshaw, P., 1977, *Momentum Transfer in Boundary Layers*, Hemisphere, Washington, DC.

Dale, J. D., and Emery, A. F., 1972, "The Free Convection of Heat From a Vertical Plate to Several Non-Newtonian Pseudoplastic Fluids," ASME JOURNAL OF HEAT TRANSFER, Vol. 94, pp. 64-72.

Ede, A. J., 1967, "Advances in Free Convection," *Adv. Heat Transfer*, Vol. 4, pp. 1-64.

Emery, A. F., Chi, H. S., and Dale, J. D., 1970, "Free Convection Through Vertical Plane Layers of Non-Newtonian Power Law Fluids," ASME JOURNAL OF HEAT TRANSFER, Vol. 93, pp. 164-171.

Kawase, K., and Ulbrecht, J., 1984, "Approximate Solution to the Natural Convection Heat Transfer From a Vertical Plate," *Int. Comm. Heat Transfer*, Vol. 11, pp. 143-155.

Lee, S. Y., and Ames, W. F., 1966, "Similarity Solutions for Non-Newtonian Fluids," *AIChE J.*, Vol. 22, pp. 700-708.

Na, T. Y., and Hansen, A. G., 1966, "Possible Similarity Solutions of the Laminar Natural Convection Flow of Non-Newtonian Fluids," *Int. J. Heat Mass Transfer*, Vol. 9, pp. 261-262.

Reilly, I. G., Tien, C., and Adelman, M., 1965, "Experimental Study of Natural Convection Heat Transfer From a Vertical Plate in a Non-Newtonian Fluids," *Can. J. Chem. Eng.*, Vol. 43, pp. 157-160.

Shulman, Z. P., Baikov, V. I., and Zaltsgendler, E. A., 1976, "An Approach to Prediction of Free Convection in Non-Newtonian Fluids," *Int. J. Heat Mass Transfer*, Vol. 19, pp. 1003-1006.

Som, A., and Chen, J. L. S., 1984, "Free Convection of Non-Newtonian Fluids Over Non-isothermal Two-Dimensional Bodies," *Int. J. Heat Mass Transfer*, Vol. 27, pp. 791-794.


# Ice Formation Over an Isothermally Cooled Vertical Circular Cylinder in Natural Convection


**K. C. Cheng[1] and P. Sabhapathy[1]**


## Nomenclature

- Bi = Biot number = $h_c r_o/k_s$
- $c$ = specific heat
- $g$ = acceleration due to gravity
- $h$ = heat transfer coefficient
- $\bar{h}$ = average heat transfer coefficient
- $H$ = convection parameter at the interface = $h_f r_o/(k_s\theta_c)$
- $k$ = thermal conductivity
- $L$ = latent heat of freezing
- $Nu_x$ = local Nusselt number = $h_f x/k_l$
- Nu = average Nusselt number = $h_f x/k_l$
- Pr = Prandtl number
- $r_o$ = radius of the cylinder
- $r_f$ = interface position
- $Ra_x$ = Rayleigh number = $g\beta_l(t_\infty - t_f)x^3/(\alpha_l\nu_l)$
- $S$ = dimensionless interface position = $r_f/r_o$
- $t$ = temperature
- $x$ = distance from the start of cooling along axial direction
- $\alpha$ = thermal diffusivity
- $\beta$ = coefficient of thermal expansion


[1]Department of Mechanical Engineering, University of Alberta, Edmonton, Alberta, Canada T6G 2G8.



Contributed by the Heat Transfer Division and presented at the National Heat Transfer Conference, Denver, Colorado, August 4-7, 1985. Manuscript received by the Heat Transfer Division May 30, 1986. Keywords: Materials Processing and Manufacturing Processes, Moving Boundaries, Phase-Change Phenomena.

$\delta$ = ice layer thickness
$\epsilon$ = perturbation parameter = $c_s(t_f - t_c)/L$
$\theta_c$ = cooling temperature ratio = $(t_f - t_c)/(t_\infty - t_f)$
$\bar{\tau}$ = time
$\tau$ = dimensionless time = $(\bar{\tau}\epsilon\alpha_s)/r_o^2$

**Subscripts**

$c$ = coolant
$f$ = freezing front
$l$ = liquid
$s$ = solid
$w$ = surface
$x$ = distance $x$ from the leading edge
$\infty$ = ambient medium

## 1 Introduction

Freezing and melting problems occur in many industrial and engineering applications such as energy storage, metal casting, and food processing. Recent experiments on both freezing and melting problems show that the natural convection in the liquid has a considerable influence on the shape of the solid–liquid interface. Recent literature on the subject can be found in Viskanta (1983). One notes that recent investigations were mainly concerned with laminar natural convective flow adjacent to the interface. If the superheating in the liquid or the dimension of the cooling system is large, transition and turbulent flow regimes will also occur in the natural convective flow adjacent to the interface. It is noted that when water freezes over a cooled planar plate or inside a tube under the condition of forced convection cooling, transition and turbulent flows may have dramatic effects (such as ice band phenomena) on the shape of the ice layer profile (Hirata et al., 1979; Gilpin, 1981).

Chao and Schoenhals (1981) carried out an experimental study of ice formation around an evaporator section of a closed two-phase thermosyphon. In their experiments, the initial water temperature was around 0.2°C, in contrast to $t_\infty$ = 8 to 17.5°C used in this study. Furthermore, the cooled cylinder wall temperature was not uniform in their experiments.

The purpose of this note is to report the results of experimental investigations on the effects of natural convection on the ice formation over an isothermally cooled vertical circular cylinder involving laminar, transitional, and turbulent flow regimes. Further details and one-dimensional analysis of the transient development of the interface for the present study can be found in Cheng and Sabhapathy (1985).

## 2 Experimental Apparatus and Procedure

The experimental apparatus consists mainly of a water tank, a test section, a coolant circulating system, and a traversing mechanism. The detailed description of the apparatus and procedure can be found in Sabhapathy and Cheng (1986). The water tank is 0.6 m long, 0.6 m wide, and 1.6 m high, and was fabricated from galvanized mild steel plates (4 mm thickness). The tank has 19-mm-thick plexiglass windows on all four sides. The sides of the tank were insulated with fiberglass leaving small portions for flow visualization. The temperature of water was measured by a copper-constantan thermocouple.

The test section consists of a 1-m-long copper pipe with an outside diameter of 41.3 mm and wall thickness of 3 mm. It is connected to two concentric PVC pipes at both ends. The whole arrangement was held vertically in the center of the water tank. The coolant, a mixture of 60 percent (by volume) ethylene glycol, 10 percent methanol, and 30 percent water, was circulated at a high flow rate ($4 \sim 6 \times 10^{-3}$ m$^3$/s) by a centrifugal pump through the copper pipe. The temperature of the coolant can be maintained at any desired temperature in a large constant-temperature bath. The coolant temperatures near the inlet and outlet of the test section were measured by iron-constantan sheath thermocouples with an accuracy of 0.1°C. The ice layer thickness was measured by a special probe mounted on a traversing mechanism.

The steel tank was filled with deaerated (~27.5 in Hg vacuum) tap water at a desired temperature and was allowed to reach a steady state for about 1 to 2 h. The coolant at a set temperature was kept circulating in the bypass loop. The coolant was then allowed to circulate through the test section.

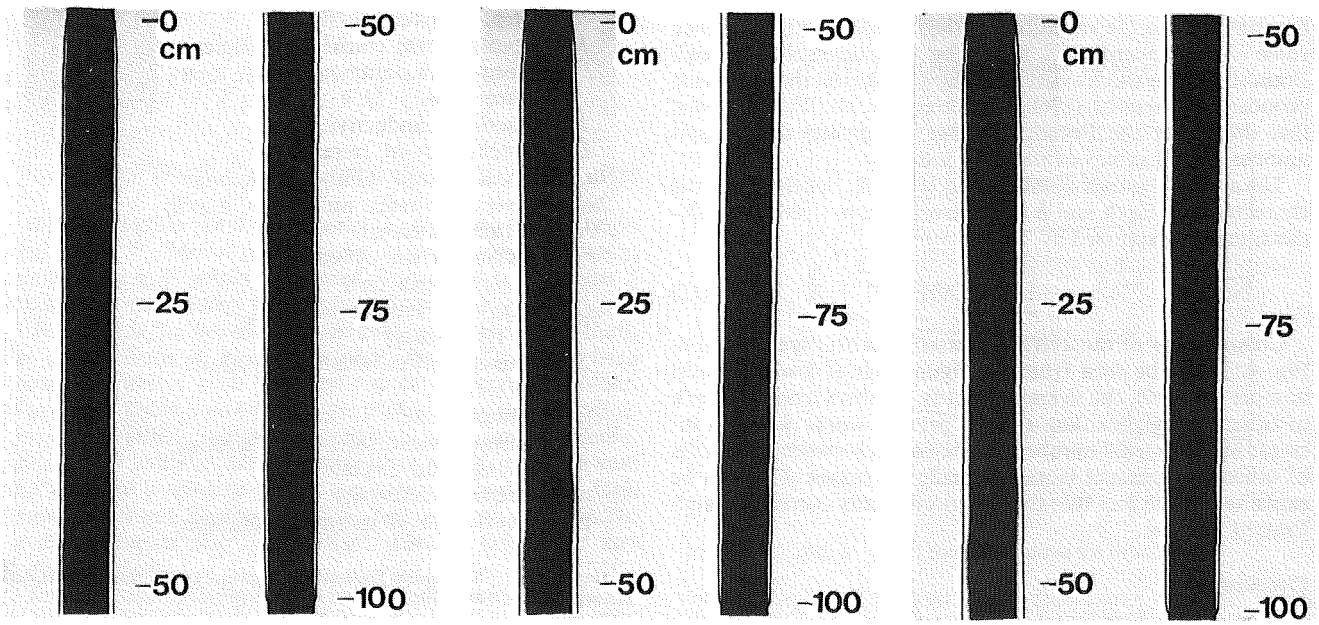


Fig. 1(a) $\bar{\tau}$ = 5 min  Fig. 1(b) $\bar{\tau}$ = 15 min  Fig. 1(c) $\bar{\tau}$ = 45 min

Fig. 1 Photographs of the ice layer at various times for $t_\infty$ = 17.5°C and $t_c$ = −15.0°C

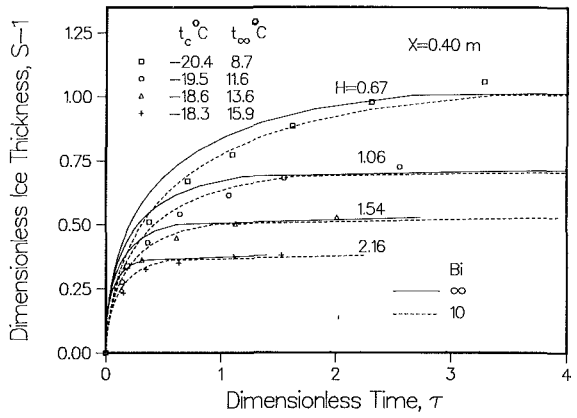


**Fig. 2 Comparison of experimentally obtained dimensionless transient ice layer thickness with that of a one-dimensional analysis (Cheng and Sabhapathy, 1985)**

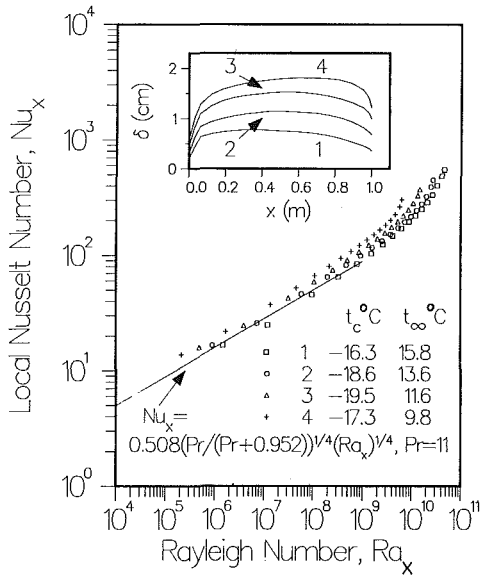


**Fig. 3 Variation of local Nusselt number $Nu_x$ with Rayleigh number $Ra_x$ at the interface**

The ice profiles were photographed at different times. At selected locations, the ice thickness was also measured with the probe. The natural convective flow was visualized by the shadowgraph technique.

## 3 Results and Discussion

**3.1 Transient Development of the Interface.** Experiments were performed for various coolant temperatures in the range $-10$ to $-20$°C and ambient water temperatures in the range 8 to 17.5°C. An estimate of the convective heat transfer coefficient at the coolant side shows that the Biot number is in the range 10 to 30.

Figures 1(*a*) to 1(*c*) show typical photographs of the transient ice layer growth for $t_\infty = 17.5$°C and $t_c = -15$°C. The flow visualization by shadowgraph method reveals that the natural convective flow is laminar up to about $x = 25$ cm. Small disturbances on the laminar flow are observed in the region $x = 25$ cm to $x = 40$ cm. As the disturbances move downward, they amplify and become vortices. The large disturbances on the laminar flow are present in the region $x = 40$ cm to $x = 75$ cm. In the region $x = 75$ cm to $x = 90$ cm, the vortices are observed to break down intermittently into turbulence. This region is considered to be the transition regime. The flow is fully turbulent below 90 cm from the leading edge.

In the laminar regime, the thickness of the ice layer changes rapidly with distance near the leading edge and continues to increase slowly away from it. This is due to the decrease in heat transfer coefficient with distance $x$ in the laminar regime of the natural convective flow. The thickness is nearly uniform when the disturbances on the laminar flow are of large amplitude and also in the transition regime as can be seen from the photographs. The ice thickness slowly decreases with downstream distance in the turbulent regime. This is due to the increasing heat transfer coefficient with distance in the turbulent flow regime. The change in the ice layer thickness is not as sharp as that observed by Hirata et al. (1979) for ice formation along a cooled flat plate in forced flow.

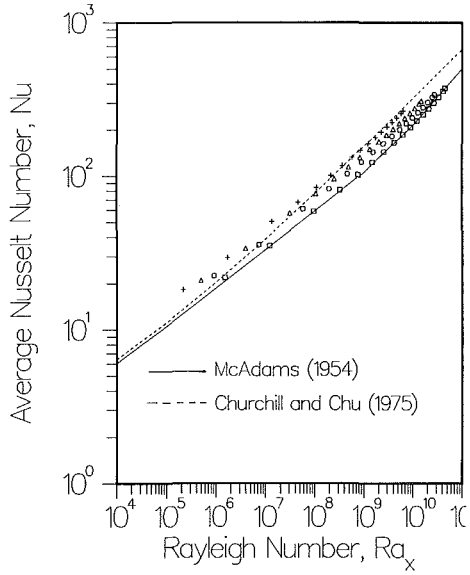


**Fig. 4 Variation of average Nusselt number Nu with Rayleigh number, $Ra_x$ at the interface**

In all three regimes of the natural convective flow in water adjacent to the ice-water interface, the ice layer continues to grow until the conduction heat transfer through the ice layer is balanced exactly by the natural convection heat transfer in water at the interface. As expected, the ice layer growth slows down as time progresses. The lower the ambient water temperature, the longer is the time required for the steady-state condition to be reached for a given wall temperature. Figure 2 compares the theoretically predicted transient dimensionless ice layer thicknesses (Cheng and Sabhapathy, 1985) with those obtained experimentally for typical coolant and ambient temperatures at $x = 40$ cm. The details of the theoretical analysis can be found in Cheng and Sabhapathy (1985). The numerically predicted values are in fair agreement with the experimental values.

**3.2 Local and Average Heat Transfer Coefficients at the Interface.** At steady state, the heat transfer by natural convection in water at the interface is exactly balanced by the heat transfer by conduction through the ice layer. The local heat transfer coefficient at the ice-water interface was evaluated from one-dimensional conduction analysis of the ice layer. Figures 3 and 4 show the variations of the local and the average Nusselt numbers, respectively, at the interface with Rayleigh number for some typical combinations of ambient and coolant temperatures. The variations of the local and the average Nusselt numbers with Rayleigh number from the literature (McAdams, 1954; Churchill and Chu, 1975) for the natural convective flow along an isothermal flat plate are also shown for comparison. It is seen that the experimentally obtained Nusselt numbers agree well with the values from the literature.

## 4 Conclusions

The effects of natural convection flow on ice formation over a cooled vertical cylinder were studied experimentally. In the laminar regime, the thickness of the ice layer increases with the axial distance from the start of cooling. In the transition regime, the ice layer has a nearly uniform thickness. In the turbulent regime, the ice layer thickness decreases slowly with distance. The three regimes were confirmed by flow visualization experiment. The local and average heat transfer coefficients at the interface obtained by the heat conduction analysis of the ice layer agree fairly well with the values for the natural convective flow along an isothermal vertical flat plate reported in the literature. Within the scope of this investigation, the wavy interface phenomenon was not observed.


### Acknowledgments

This work was supported by the Natural Sciences and Engineering Research Council of Canada through an operating grant.


### References


Chao, S. L., and Schoenhals, R. J., 1981, "An Experimental Study of a Closed Two-Phase Thermosyphon for Ice Production," ASME Paper No. 81-HT-16.

Cheng, K. C., and Sabhapathy, P., 1985, "An Experimental Investigation of Ice Formation Over an Isothermally Cooled Vertical Circular Cylinder in Natural Convection," ASME Paper No. 85-HT-1.

Churchill, S. W., and Chu, H. H. S., 1975, "Correlating Equations for Laminar and Turbulent Free Convection From a Vertical Plate," *Int. J. Heat Mass Transfer*, Vol. 18, pp. 1323–1329.

Gilpin, R. R., 1981, "Ice Formation in a Pipe Containing Flows in the Transition and Turbulent Regimes," ASME JOURNAL OF HEAT TRANSFER, Vol. 103, pp. 363–368.

Hirata, T., Gilpin, R. R., and Cheng, K. C., 1979, "The Steady State Ice Layer Profile on a Constant Temperature Plate in Forced Convection Flow. II. The Transition and Turbulent Regimes," *Int. J. Heat Mass Transfer*, Vol. 22, pp. 1438–1443.

McAdams, W. H., 1954, *Heat Transmission*, 3rd ed., McGraw-Hill, New York.

Sabhapathy, P., and Cheng, K. C., 1986, "The Effects of Temperature-Dependent Viscosity and Coefficient of Thermal Expansion on the Stability of Laminar, Natural Convective Flow Along an Isothermal, Vertical Surface," *Int. J. Heat Mass Transfer*, Vol. 29, pp. 1521–1529.

Viskanta, R., 1983, "Phase-Change Heat Transfer, Solar Heat Storage: Latent Heat Materials," Vol. 1, G. A. Lane, ed., Uniscience Edition, CRC Press, Boca Raton.


# Solution of the Conduction/Radiation Problem With Linear-Anisotropic Scattering in an Annular Medium by the Spherical Harmonics Method


**J. A. Harris**[1]


### Nomenclature

$E_b$ = black body emissive power $= \bar{\sigma} T^4$

$f$ = parameter in the linear-anisotropic scattering phase function

Ho = Hottel number $= k/4\bar{\sigma} T_{w1}^3 (r_2 - r_1) = \mathrm{Sk}/OT$

$I$ = radiation intensity

$I_b$ = blackbody radiation intensity $= \bar{\sigma} T^4/\pi$

$I_0$ = zeroth moment of intensity $\int_{\omega=4\pi} I \, d\omega$

$I_2$ = first moment of intensity in radial direction $= \int_{\omega=4\pi} I \sin\theta \cos\phi \, d\omega$

$k$ = thermal conductivity

$L$ = length of cylinder

$OT$ = optical thickness $= \beta(r_2 - r_1)$

$Q^*$ = dimensionless heat transfer between cylinders $= q/(Lr_1 \bar{\sigma} T_{w1}^4)$

$q$ = rate of heat transfer

$r$ = radial coordinate of position in bed

$s$ = distance along direction of radiation intensity

Sk = Stark number $= k\beta/(4\bar{\sigma} T_{w1}^3)$

$T$ = temperature

$\beta$ = extinction coefficient $= \kappa + \sigma$

$\epsilon$ = emissivity

$\theta$ = one angular coordinate defining direction of radiation intensity

$\Theta$ = dimensionless temperature $= T/T_1$

$\kappa$ = medium absorption coefficient

$\rho$ = surface reflectivity

$\sigma$ = medium scattering coefficient

$\bar{\sigma}$ = Stefan–Boltzmann constant

$\tau$ = dimensionless radial coordinate $= r\beta$

$\phi$ = one angular coordinate defining direction of radiation intensity

$\Phi$ = phase function for scattering

$\Omega$ = scattering albedo $\sigma/\beta$

$\omega$ = solid angle

#### Superscripts

$'$ = denotes order of differentiation with respect to $\tau$

#### Subscripts

1 = inner surface of annulus

2 = outer surface of annulus

### Introduction

Solution of the heat transfer equations in a conducting and radiatively participating medium presents a difficult mathematical challenge. The radiation transfer equation in a gray medium may be written for the general case as

$$\frac{dI}{ds} = -\beta I + \kappa I_b + \frac{\sigma}{4\pi} \int_{\omega_i = 4\pi} I(\omega_i) \Phi(\omega, \omega_i) d\omega_i$$

This is coupled with the energy conservation equation for the medium

$$-k \nabla^2 T + \kappa \left[ 4\pi I_b - \int_{\omega} I \, d\omega \right] = 0$$

which is valid for a medium with no volumetric energy source.

Numerous methods for obtaining an approximate solution to the pure radiation problem ($k = 0$) have been proposed. Pertinent to the methodology presented herein is the method of spherical harmonics originally proposed by Jeans (1971) and


[1]Assistant Professor, Mechanical Engineering Department, The Wichita State University, Wichita, KS 67208.



Contributed by the Heat Transfer Division for publication in the JOURANL OF HEAT TRANSFER. Manuscript received by the Heat Transfer Division January 23, 1987. Keywords: Packed and Fluidized Beds, Radiation, Radiation Interactions.

## 4 Conclusions

The effects of natural convection flow on ice formation over a cooled vertical cylinder were studied experimentally. In the laminar regime, the thickness of the ice layer increases with the axial distance from the start of cooling. In the transition regime, the ice layer has a nearly uniform thickness. In the turbulent regime, the ice layer thickness decreases slowly with distance. The three regimes were confirmed by flow visualization experiment. The local and average heat transfer coefficients at the interface obtained by the heat conduction analysis of the ice layer agree fairly well with the values for the natural convective flow along an isothermal vertical flat plate reported in the literature. Within the scope of this investigation, the wavy interface phenomenon was not observed.


### Acknowledgments

This work was supported by the Natural Sciences and Engineering Research Council of Canada through an operating grant.


### References


Chao, S. L., and Schoenhals, R. J., 1981, "An Experimental Study of a Closed Two-Phase Thermosyphon for Ice Production," ASME Paper No. 81-HT-16.

Cheng, K. C., and Sabhapathy, P., 1985, "An Experimental Investigation of Ice Formation Over an Isothermally Cooled Vertical Circular Cylinder in Natural Convection," ASME Paper No. 85-HT-1.

Churchill, S. W., and Chu, H. H. S., 1975, "Correlating Equations for Laminar and Turbulent Free Convection From a Vertical Plate," *Int. J. Heat Mass Transfer*, Vol. 18, pp. 1323–1329.

Gilpin, R. R., 1981, "Ice Formation in a Pipe Containing Flows in the Transition and Turbulent Regimes," ASME JOURNAL OF HEAT TRANSFER, Vol. 103, pp. 363–368.

Hirata, T., Gilpin, R. R., and Cheng, K. C., 1979, "The Steady State Ice Layer Profile on a Constant Temperature Plate in Forced Convection Flow. II. The Transition and Turbulent Regimes," *Int. J. Heat Mass Transfer*, Vol. 22, pp. 1438–1443.

McAdams, W. H., 1954, *Heat Transmission*, 3rd ed., McGraw-Hill, New York.

Sabhapathy, P., and Cheng, K. C., 1986, "The Effects of Temperature-Dependent Viscosity and Coefficient of Thermal Expansion on the Stability of Laminar, Natural Convective Flow Along an Isothermal, Vertical Surface," *Int. J. Heat Mass Transfer*, Vol. 29, pp. 1521–1529.

Viskanta, R., 1983, "Phase-Change Heat Transfer, Solar Heat Storage: Latent Heat Materials," Vol. 1, G. A. Lane, ed., Uniscience Edition, CRC Press, Boca Raton.


# Solution of the Conduction/Radiation Problem With Linear-Anisotropic Scattering in an Annular Medium by the Spherical Harmonics Method


**J. A. Harris**[1]


### Nomenclature

$E_b$ = black body emissive power $= \bar{\sigma} T^4$

$f$ = parameter in the linear-anisotropic scattering phase function

Ho = Hottel number $= k/4\bar{\sigma} T_{w1}^3 (r_2 - r_1) = \mathrm{Sk}/OT$

$I$ = radiation intensity

$I_b$ = blackbody radiation intensity $= \bar{\sigma} T^4/\pi$

$I_0$ = zeroth moment of intensity $\int_{\omega=4\pi} I \, d\omega$

$I_2$ = first moment of intensity in radial direction $= \int_{\omega=4\pi} I \sin\theta \cos\phi \, d\omega$

$k$ = thermal conductivity

$L$ = length of cylinder

$OT$ = optical thickness $= \beta(r_2 - r_1)$

$Q^*$ = dimensionless heat transfer between cylinders $= q/(Lr_1 \bar{\sigma} T_{w1}^4)$

$q$ = rate of heat transfer

$r$ = radial coordinate of position in bed

$s$ = distance along direction of radiation intensity

Sk = Stark number $= k\beta/(4\bar{\sigma} T_{w1}^3)$

$T$ = temperature

$\beta$ = extinction coefficient $= \kappa + \sigma$

$\epsilon$ = emissivity

$\theta$ = one angular coordinate defining direction of radiation intensity

$\Theta$ = dimensionless temperature $= T/T_1$

$\kappa$ = medium absorption coefficient

$\rho$ = surface reflectivity

$\sigma$ = medium scattering coefficient

$\bar{\sigma}$ = Stefan–Boltzmann constant

$\tau$ = dimensionless radial coordinate $= r\beta$

$\phi$ = one angular coordinate defining direction of radiation intensity

$\Phi$ = phase function for scattering

$\Omega$ = scattering albedo $\sigma/\beta$

$\omega$ = solid angle

#### Superscripts

$'$ = denotes order of differentiation with respect to $\tau$

#### Subscripts

1 = inner surface of annulus

2 = outer surface of annulus

### Introduction

Solution of the heat transfer equations in a conducting and radiatively participating medium presents a difficult mathematical challenge. The radiation transfer equation in a gray medium may be written for the general case as

$$\frac{dI}{ds} = -\beta I + \kappa I_b + \frac{\sigma}{4\pi} \int_{\omega_i = 4\pi} I(\omega_i) \Phi(\omega, \omega_i) d\omega_i$$

This is coupled with the energy conservation equation for the medium

$$-k \nabla^2 T + \kappa \left[ 4\pi I_b - \int_{\omega} I \, d\omega \right] = 0$$

which is valid for a medium with no volumetric energy source.

Numerous methods for obtaining an approximate solution to the pure radiation problem ($k = 0$) have been proposed. Pertinent to the methodology presented herein is the method of spherical harmonics originally proposed by Jeans (1971) and


[1]Assistant Professor, Mechanical Engineering Department, The Wichita State University, Wichita, KS 67208.



Contributed by the Heat Transfer Division for publication in the JOURANL OF HEAT TRANSFER. Manuscript received by the Heat Transfer Division January 23, 1987. Keywords: Packed and Fluidized Beds, Radiation, Radiation Interactions.

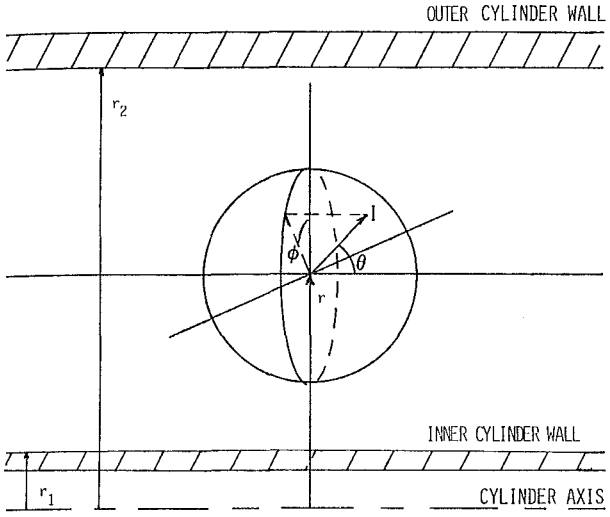


**Fig. 1 Geometric variables in cylindrical geometry; local spherical coordinate system at location defined by $r$ in the annulus**

developed for the cylindrical geometry by Bayazitoglu and Higenyi (1979).

Consideration of the conduction/radiation problem ($k \neq 0$) has been largely limited to the plane parallel geometry, in which the medium separates infinite parallel planes. Viskanta (1965), Crosbie and Viskanta (1971), and Yuen and Wong (1980) present exact solutions (arrived at numerically), and Amlin and Korpela (1979) and Ratzel and Howell (1981) have applied the spherical harmonics method to arrive at approximate solutions. Ratzel reports excellent agreement between the heat transfer estimates of the $P_1$ and $P_3$ spherical harmonics approximations and the exact results of Crosbie.

Fernandes and Francis (1982) have solved the conduction/radiation problem for concentric cylinders using a Galerkin finite element method. Their methodology may be applied to a gray absorbing, emitting, and isotropically scattering medium contained between gray concentric isothermal cylinders.

In this paper, the conduction/radiation problem in a gray cylindrical medium is considered. The medium absorbs, emits, and scatters radiation. A linear-anisotropic scattering phase function is assumed. This allows for the consideration of strong forward and backward scattering, as well as isotropic scattering. The $P_1$ and $P_3$ approximations have been developed and applied to the case where the medium is contained between infinite concentric cylinders that are gray and axially isothermal.

One area of application for this methodology as it continues to evolve is in the design and analysis of packed or fluidized bed reactors. Such reactors are characterized by

(A) cylindrical geometry, in many cases;

(B) conduction, convection, and radiation heat transfer in a radiatively participating medium that absorbs, emits, and scatters radiation;

(C) anisotropic scattering (e.g., strong back-scattering in a packed bed of spheres);

(D) a volumetric energy source term;

(E) prescribed boundary temperatures, with the medium temperature profile and rate of heat transfer to be found.

To address this problem fully, subsequent work will have to include an energy source term and a convection term in the energy equation.

## Formulation

Details of the $P_1$ and $P_3$ methodology as applied to the annular geometry can be found in Bayazitoglu and Higenyi (1979), who solve the pure radiation problem. Details of the methodology applied to the conduction/radiation problem in the annular geometry with isotropic scattering can be found in Harris (1984).

The geometric variables used throughout are pictured in Fig. 1. The dimensionless transfer and energy equations in cylindrical geometry with no volumetric energy source term are

$$\sin\theta\left[\cos\phi\,\frac{\partial i(\tau,\theta,\phi)}{\partial\tau}-\frac{\sin\phi}{\tau}\,\frac{\partial i(\tau,\theta,\phi)}{\partial\phi}\right]+i(\tau,\theta,\phi)$$

$$=\frac{\kappa}{\beta}\,i_b(\tau)+\frac{\sigma}{\beta}\,\frac{1}{4\pi}\,[i_0(\tau)+fi_2(\tau)\sin\theta\cos\theta]$$

$$\frac{-k\beta}{\bar{\sigma}T_1^3}\left[\frac{d^2\Theta(\tau)}{d\tau^2}+\frac{1}{\tau}\,\frac{d\Theta(\tau)}{d\tau}\right]-\frac{\kappa}{\beta}\,[4e_b(\tau)-i_0(\tau)]=0$$

where

$$i\equiv\frac{I}{\bar{\sigma}T_1^4},\quad i_b\equiv\frac{I_b}{\bar{\sigma}T_1^4},\quad i_0\equiv\frac{I_0}{\bar{\sigma}T_1^4},\quad i_2\equiv\frac{I_2}{\bar{\sigma}T_1^4},$$

$$e_b\equiv\frac{E_b}{\bar{\sigma}T_1^4},\quad \Theta=\frac{T}{T_1},\quad \tau=\beta r$$

In this analysis, a linear-anisotropic phase function is assumed (see Ozisik, 1973, p. 261). This phase function has the form

$$\Phi(\alpha)=1+f\cos\alpha$$

where $\alpha$ is the angle between the incident radiation and the scattered radiation. The parameter $f$ can range from $-1$ to $+1$. Results for three values of $f$ are presented in this work:

| | |
|---|---|
| $f=0$ | isotropic scattering |
| $f=-1$ | strong back scattering |
| $f=+1$ | strong forward scattering |

The resulting $P_1$ approximation can be expressed as a nonlinear fourth-order ODE in $\Theta(\tau)$:

$$\Theta^{IV}+\frac{2}{\tau}\,\Theta'''+\left[\frac{-1}{\tau^2}-(3-f\,\Omega)(1-\Omega)\right]\Theta''$$

$$+\left[\frac{-1}{\tau^3}-\frac{1}{\tau}\,(3-f\,\Omega)(1-\Omega)\right]\Theta'$$

$$+\left[\frac{-(1-\Omega)}{\mathrm{Ho}\;OT}\right]e_b''+\left[\frac{-(1-\Omega)}{\tau\;\mathrm{Ho}\;OT}\right]e_b'=0$$

Two of the BCs are the imposed wall temperatures, to wit

$$\Theta=1 \text{ at } \tau=\tau_1$$
$$\Theta=\Theta_2 \text{ at } \tau=\tau_2$$

The other two BCs can be formulated using Marshak's technique (see Ozisik, 1973, p. 34), resulting in

$$2(1+\rho_1)i_2+\epsilon_1 i_0-4\epsilon_1 e_{b1}=0 \text{ at } \tau=\tau_1$$
$$-2(1+\rho_2)i_2+\epsilon_2 i_0-4\epsilon_2 e_{b1}=0 \text{ at } \tau=\tau_2$$

The $P_3$ approximation can be arranged as a sixth-order nonlinear ODE in $\Theta(\tau)$, having the two temperatures BCs and four Marshak BCs (see Harris, 1984).

The dimensionless rate of heat transfer between the inner and outer cylinders is

$$Q^*=\frac{q/L}{r_1\bar{\sigma}T_1^4}$$

A physical interpretation of the Hottel number may be obtained by considering pure conduction heat transfer between concentric cylinders, where

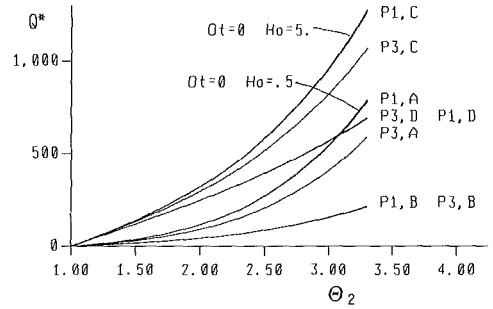


Fig. 2 Predicted heat transfer for $r_2/r_1 = 3.0$, $\epsilon = 1.0$, $\Omega = 0.7$, $f = 0$; A: Ho = 0.5, $OT = 1.0$; B: Ho = 0.5, $OT = 10.0$; C: Ho = 5.0, $OT = 1.0$; D: Ho = 5.0, $OT = 10.0$

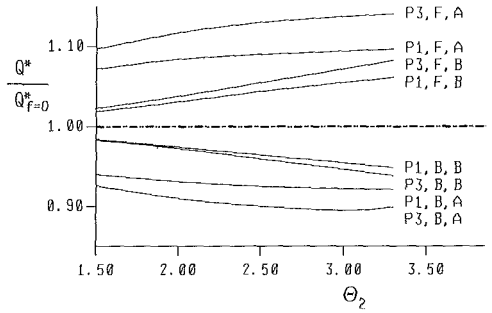


Fig. 3 Effect of forward and backward scattering on predicted heat transfer; $r_2/r_1 = 3.0$, $\epsilon = 1.0$, $\Omega = 0.7$, $OT = 1.0$, F: forward scattering; B: backward scattering; A: Ho = 0.5; B: Ho = 5.0

$$Q^* = \frac{k}{4\bar{\sigma}T_1^3(r_2 - r_1)} \frac{8\pi(r_2 - r_1)}{\ln(r_2/r_1)r_1} (\Theta_2 - 1)$$

$$= \mathrm{Ho}(\Theta_2 - 1) \frac{8\pi(r_2/r_1 - 1)}{\ln(r_2/r_1)}$$

The Hottel number is dimensionless thermal conductivity.

### Solution Technique

The higher order nonlinear ODEs of the $P_1$ and $P_3$ models were solved numerically. The annular region is divided into nodes equally spaced in the radial direction. At a given node, finite difference expressions for derivatives of $\Theta$ with respect to $\tau$ can be written and then substituted into the ODE. The boundary nodes are treated similarly; the result is a set of nonlinear equations in the unknown nodal temperatures. The set of equations is solved via a multidimensional Newton method. More detail on the solution methodology can be found in Harris (1984).

The models have been run on two different mainframe computers: a CDC Cyber 171 and an IBM 3081D. In general, the $P_1$ algorithm requires less than 1 CPU min, $P_3$ requires up to 2 CPU min.

### Results

With seven parameters in each model, it is difficult to assess fully the performance of the models over the full range of the parameters. In Fig. 2, dimensionless heat transfer for isotropic scattering is plotted against the temperature ratio of the outer to inner cylinder for a radius ratio of 3.0. $Q^*$ was found for $\Theta_2 = 1.5$, 2.0, 2.5, 3.0, and 3.3, and a spline fitting routine was used to draw a curve through the points. The solution algorithm for each model computes the total radial heat transfer at each nodal point in the annulus; for each case shown, the computed radial heat transfer varies less than 3 percent among all annular nodes, which is an indication of the level of precision of the numerical solution.

A low value for the Stark number (Hottel number times optical thickness) indicates that radiation predominates over conduction, and the curves exhibit the high degree of nonlinearity characteristic of radiation heat transfer. As $\mathrm{Sk} \to \infty$, the curves become linear, with a slope proportional to the dimensionless conductivity Ho. It is possible to group curves having the same radius ratio and Hottel number. All curves in a family have the same slope at $\Theta_2 = 1.0$, and range from a straight line at $\mathrm{Sk} \to \infty$ to the highly curved line at $\mathrm{Sk} = 0$.

As expected, the predictions of $P_1$ approach those of $P_3$ as the optical thickness increases. As indicated in Fig. 2, at $OT = 10.0$, the heat transfer and temperature predictions of $P_1$ and $P_3$ become nearly identical. At low optical thickness, $P_1$ overestimates heat transfer.

The $P_1$ and $P_3$ solution algorithms were tested over a range

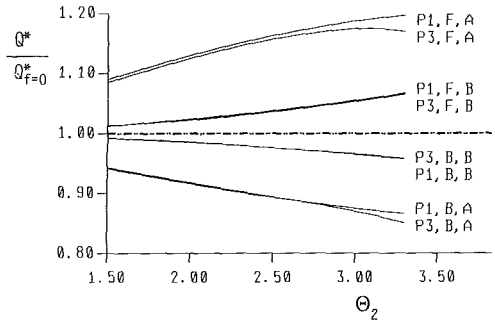


Fig. 4 Effect of forward and backward scattering on predicted heat transfer; $r_2/r_1 = 3.0$, $\epsilon = 1.0$, $\Omega = 0.7$, $OT = 10.0$; F: forward scattering; B: backward scattering; A: Ho = 0.5; B: Ho = 5.0

of parameters to test the robustness of the methods. The parameter values that were fixed in this series of runs were: $r_2/r_1 = 3.0$, $\Theta_2 = 2.0$, and $f = 0$. In testing for the success of the algorithm, successful convergence was declared if computed radial heat transfer varied less than 3 percent among all annular nodes. Convergence problems occur at very low optical thickness and extremes in albedo. Both $P_1$ and $P_3$ were found to converge successfully for $OT > 0.2$ and $0.01 > \Omega > 0.90$.

All results shown in this paper are for scattering albedo equal to 0.7. It has been found that, for isotropic scattering, variation in this parameter does not have a great deal of effect on the predictions of the $P_1$ and $P_3$ models. For black surfaces, variation of $\Omega$ from 0.01 to 0.90 affects the heat transfer predictions of $P_3$ by 2–3 percent, except for $OT < 1.0$. As tube wall emissivity decreases, variation in $\Omega$ has a greater effect on heat transfer predictions; at $\epsilon = 0.3$, the $P_3$ model predictions for heat transfer were found to vary through a range of 30 percent at most as $\Omega$ was varied from 0.01 to 0.90.

The effects of strong forward and backward scattering vis-à-vis isotropic scattering are shown in Figs. 3 and 4. For albedo equal to 0.7, forward or backward scattering results in a variation of $Q^*$ of less than 20 percent in relation to the corresponding result for isotropic scattering for all parameters tested. It is important to note that these results are all for a scattering albedo of 0.7. For higher values of scattering albedo, greater variation in heat transfer predictions is to be expected as the scattering phase function changes. A limited number of runs were made for the $P_1$ model at a scattering albedo of 0.95, and the results showed a variation in heat transfer predictions roughly 30 percent higher than the corresponding variation for $\Omega = 0.7$. The conclusion is that a strong forward or backward scattering phase function can have a fairly significant effect on heat transfer predictions vis-à-vis isotropic scattering.

### Conclusion

The $P_1$ and $P_3$ models have been formulated for the con-

duction/radiation problem in a cylindrical medium. A Newton method numerical algorithm was employed to solve the resulting nonlinear ordinary differential equation associated with each model for a representative group of parameters. The $P_1$ model gives predictions that approach those of the $P_3$ model as optical thickness increases, and its computation time is one-half to one-third that of $P_3$. For lower optical thicknesses where accuracy is required, the $P_3$ model is recommended.

A linear-anisotropic scattering phase function was incorporated into the models. It was found that strong forward and backward scattering has a modest effect on the model predictions in comparison to results for isotropic scattering.


### Acknowledgments

This work was supported in part by a Summer Faculty Research Grant from The Wichita State University.


### References


Amlin, D. W., and Korpela, S. A., 1979, "Influence of Thermal Radiation on the Temperature Distribution in a Semi-transparent Solid," ASME JOURNAL OF HEAT TRANSFER, Vol. 101, pp. 76–80.

Bayazitoglu, Y., and Higenyi, J., 1979, "Higher-Order Differential Equations of Radiative Transfer: $P_3$ Approximation," *AIAA J.*, Vol. 17, No. 4, pp. 424–431.

Crosbie, A. L., and Viskanta, R., 1971, "Interaction of Heat Transfer by Conduction and Radiation in a Non-gray Planar Medium," *Warme- und Stoffubertragung*, Vol. 4, pp. 205–212.

Fernandes, R., and Francis, J., 1982, "Combined Conductive and Radiative Heat Transfer in an Absorbing, Emitting, and Scattering Cylindrical Medium," ASME JOURNAL OF HEAT TRANSFER, Vol. 104, pp. 594–601.

Harris, J. A., 1984, "Heat Transfer in High Temperature Packed Beds," Ph.D. Thesis, Colorado State University.

Jeans, J. H., 1917, "The Equations of Radiative Transfer of Energy," *Monthly Notices Roy. Astron. Soc.*, Vol. 78, pp. 28–36.

Ozisik, M. N., 1973, *Radiative Transfer*, Wiley, New York.

Ratzel, A. C., and Howell, J. R., 1981, "Heat Transfer by Conduction and Radiation in One-Dimensional Planar Medium Using the Differential Approximation," ASME Paper No. 81-HT-72.

Viskanta, R., 1965, "Heat Transfer by Conduction and Radiation in Absorbing and Scattering Materials," ASME JOURNAL OF HEAT TRANSFER, Vol. 87, pp. 143–150.

Yuen, W. W., and Wong, L. W., 1980, "Heat Transfer by Conduction and Radiation in a One-Dimensional Absorbing, Emitting, and Anisotropically-Scattering Medium," ASME JOURNAL OF HEAT TRANSFER, Vol. 102, pp. 303–307.


## Natural Convection and Radiation Heat Transfer From an Array of Inclined Pin Fins


**M. E. Alessio[1] and D. A. Kaminski[2]**


### Nomenclature

- $a$ = center-to-center fin spacing in a horizontal pin fin array
- $c_p$ = specific heat at constant pressure of air
- $d$ = length defined by equation (2)
- $D$ = diameter of pin fin
- $g$ = acceleration of gravity
- $h_A$ = heat transfer coefficient based on actual fin area
- $h_s$ = heat transfer coefficient based on baseplate area
- $k$ = thermal conductivity of air
- $L$ = length of pin fin
- $\mathrm{Nu}_d$ = Nusselt number based on center-to-center fin spacing
- $\mathrm{Nu}_s$ = Nusselt number based on baseplate height
- $Q$ = total power input at baseplate
- $Q_R$ = power lost to radiation
- $\mathrm{Ra}_d$ = Rayleigh number based on center-to-center fin spacing
- $\mathrm{Ra}_s$ = Rayleigh number based on baseplate height
- $S$ = length of a side of the square base plate
- $T_b$ = temperature of baseplate
- $T_f$ = temperature of ambient air
- $\beta$ = volume expansivity of air
- $\theta$ = angle of inclination from the horizontal
- $\mu$ = dynamic viscosity of air
- $\rho$ = density of air

Natural convection and radiation from an air-cooled, highly populated pin-fin array were studied experimentally. The effects of pin density, pin length, and the angle of the pin to the horizontal were measured. Previous work by Sparrow and Vemuri (1985) treated the case of a vertical base plate with horizontal fins. Recently, Sparrow and Vemuri (1986) extended their study to include results for vertical fins wth a horizontal down-facing base plate, as well as vertical fins with a horizontal up-facing base plate. In this study, the base plate is maintained in a vertical position and the angle of the pins is varied from the horizontal.

There are several papers available on the effect of inclination on heat transfer from a single cylinder. Three early works, conducted by Farber and Rennar (1957), Oosthuizen (1976), and Al-Arabi and Salman (1979), showed that free convection from a horizontal cylinder was greater than that from an inclined cylinder. Later, Al-Arabi and Khamis (1982) published results that showed that, in the case of short cylinders, an inclined cylinder could display better heat transfer than a horizontal cylinder.

The pin fins examined in this study consisted of solid, right circular cylinders of exposed length $L$ and diameter $D$. The pin fins were press fit into holes in a square base plate to form a staggered array on equilateral triangular centers, as illustrated in Figs. 1 and 2, respectively. Eighteen arrays were assembled, with dimensions listed in Table 1.

The pin fins, which were 0.635 cm in diameter, and the base plate, which was 7.62 cm square by 1.27 cm thick, were machined from aluminum stock. The assembled arrays were black anodized to obtain a consistent, high-emissivity, smooth surface. Four fine-gage thermocouples were located in small holes drilled into the center of each side of the base plate. Pin tip temperatures were measured by six thermocouples dispersed around the array.

Heat was applied to the bases with Minco thermofoil heaters. The entire pin fin array-heater-thermocouple assembly was inset into a 27.94-cm-square, 10.16-cm-thick block of styrofoam. To obtain a hydrodynamically smooth surface, the styrofoam was covered with contact paper. The styrofoam block with inset pin fin array was suspended using nylon wire in the center of a Ransco temperature chamber, which provided protection of the array from air drafts. The chamber was large enough so that the proximity of the walls, top, or bottom did not influence experimental results.


[1]Product Design Engineer, Tactical Systems Department, General Electric Co., Pittsfield, MA 01201.

[2]Assistant Professor, Department of Mechanical Engineering, Rensselaer Polytechnic Institute, Troy, NY 12180-3590; Assoc. Mem. ASME.



Contributed by the Heat Transfer Division for publication in the JOURNAL OF HEAT TRANSFER. Manuscript received by the Heat Transfer Division October 26, 1987. Keywords: Natural Convection, Radiation, Radiation Interactions.

duction/radiation problem in a cylindrical medium. A Newton method numerical algorithm was employed to solve the resulting nonlinear ordinary differential equation associated with each model for a representative group of parameters. The $P_1$ model gives predictions that approach those of the $P_3$ model as optical thickness increases, and its computation time is one-half to one-third that of $P_3$. For lower optical thicknesses where accuracy is required, the $P_3$ model is recommended.

A linear-anisotropic scattering phase function was incorporated into the models. It was found that strong forward and backward scattering has a modest effect on the model predictions in comparison to results for isotropic scattering.


### Acknowledgments

This work was supported in part by a Summer Faculty Research Grant from The Wichita State University.


### References


Amlin, D. W., and Korpela, S. A., 1979, "Influence of Thermal Radiation on the Temperature Distribution in a Semi-transparent Solid," ASME JOURNAL OF HEAT TRANSFER, Vol. 101, pp. 76–80.

Bayazitoglu, Y., and Higenyi, J., 1979, "Higher-Order Differential Equations of Radiative Transfer: $P_3$ Approximation," *AIAA J.*, Vol. 17, No. 4, pp. 424–431.

Crosbie, A. L., and Viskanta, R., 1971, "Interaction of Heat Transfer by Conduction and Radiation in a Non-gray Planar Medium," *Warme- und Stoffubertragung*, Vol. 4, pp. 205–212.

Fernandes, R., and Francis, J., 1982, "Combined Conductive and Radiative Heat Transfer in an Absorbing, Emitting, and Scattering Cylindrical Medium," ASME JOURNAL OF HEAT TRANSFER, Vol. 104, pp. 594–601.

Harris, J. A., 1984, "Heat Transfer in High Temperature Packed Beds," Ph.D. Thesis, Colorado State University.

Jeans, J. H., 1917, "The Equations of Radiative Transfer of Energy," *Monthly Notices Roy. Astron. Soc.*, Vol. 78, pp. 28–36.

Ozisik, M. N., 1973, *Radiative Transfer*, Wiley, New York.

Ratzel, A. C., and Howell, J. R., 1981, "Heat Transfer by Conduction and Radiation in One-Dimensional Planar Medium Using the Differential Approximation," ASME Paper No. 81-HT-72.

Viskanta, R., 1965, "Heat Transfer by Conduction and Radiation in Absorbing and Scattering Materials," ASME JOURNAL OF HEAT TRANSFER, Vol. 87, pp. 143–150.

Yuen, W. W., and Wong, L. W., 1980, "Heat Transfer by Conduction and Radiation in a One-Dimensional Absorbing, Emitting, and Anisotropically-Scattering Medium," ASME JOURNAL OF HEAT TRANSFER, Vol. 102, pp. 303–307.


## Natural Convection and Radiation Heat Transfer From an Array of Inclined Pin Fins


**M. E. Alessio[1] and D. A. Kaminski[2]**


### Nomenclature

- $a$ = center-to-center fin spacing in a horizontal pin fin array
- $c_p$ = specific heat at constant pressure of air
- $d$ = length defined by equation (2)
- $D$ = diameter of pin fin
- $g$ = acceleration of gravity
- $h_A$ = heat transfer coefficient based on actual fin area
- $h_s$ = heat transfer coefficient based on baseplate area
- $k$ = thermal conductivity of air
- $L$ = length of pin fin
- $\mathrm{Nu}_d$ = Nusselt number based on center-to-center fin spacing
- $\mathrm{Nu}_s$ = Nusselt number based on baseplate height
- $Q$ = total power input at baseplate
- $Q_R$ = power lost to radiation
- $\mathrm{Ra}_d$ = Rayleigh number based on center-to-center fin spacing
- $\mathrm{Ra}_s$ = Rayleigh number based on baseplate height
- $S$ = length of a side of the square base plate
- $T_b$ = temperature of baseplate
- $T_f$ = temperature of ambient air
- $\beta$ = volume expansivity of air
- $\theta$ = angle of inclination from the horizontal
- $\mu$ = dynamic viscosity of air
- $\rho$ = density of air

Natural convection and radiation from an air-cooled, highly populated pin-fin array were studied experimentally. The effects of pin density, pin length, and the angle of the pin to the horizontal were measured. Previous work by Sparrow and Vemuri (1985) treated the case of a vertical base plate with horizontal fins. Recently, Sparrow and Vemuri (1986) extended their study to include results for vertical fins wth a horizontal down-facing base plate, as well as vertical fins with a horizontal up-facing base plate. In this study, the base plate is maintained in a vertical position and the angle of the pins is varied from the horizontal.

There are several papers available on the effect of inclination on heat transfer from a single cylinder. Three early works, conducted by Farber and Rennar (1957), Oosthuizen (1976), and Al-Arabi and Salman (1979), showed that free convection from a horizontal cylinder was greater than that from an inclined cylinder. Later, Al-Arabi and Khamis (1982) published results that showed that, in the case of short cylinders, an inclined cylinder could display better heat transfer than a horizontal cylinder.

The pin fins examined in this study consisted of solid, right circular cylinders of exposed length $L$ and diameter $D$. The pin fins were press fit into holes in a square base plate to form a staggered array on equilateral triangular centers, as illustrated in Figs. 1 and 2, respectively. Eighteen arrays were assembled, with dimensions listed in Table 1.

The pin fins, which were 0.635 cm in diameter, and the base plate, which was 7.62 cm square by 1.27 cm thick, were machined from aluminum stock. The assembled arrays were black anodized to obtain a consistent, high-emissivity, smooth surface. Four fine-gage thermocouples were located in small holes drilled into the center of each side of the base plate. Pin tip temperatures were measured by six thermocouples dispersed around the array.

Heat was applied to the bases with Minco thermofoil heaters. The entire pin fin array-heater-thermocouple assembly was inset into a 27.94-cm-square, 10.16-cm-thick block of styrofoam. To obtain a hydrodynamically smooth surface, the styrofoam was covered with contact paper. The styrofoam block with inset pin fin array was suspended using nylon wire in the center of a Ransco temperature chamber, which provided protection of the array from air drafts. The chamber was large enough so that the proximity of the walls, top, or bottom did not influence experimental results.


[1]Product Design Engineer, Tactical Systems Department, General Electric Co., Pittsfield, MA 01201.

[2]Assistant Professor, Department of Mechanical Engineering, Rensselaer Polytechnic Institute, Troy, NY 12180-3590; Assoc. Mem. ASME.



Contributed by the Heat Transfer Division for publication in the JOURNAL OF HEAT TRANSFER. Manuscript received by the Heat Transfer Division October 26, 1987. Keywords: Natural Convection, Radiation, Radiation Interactions.

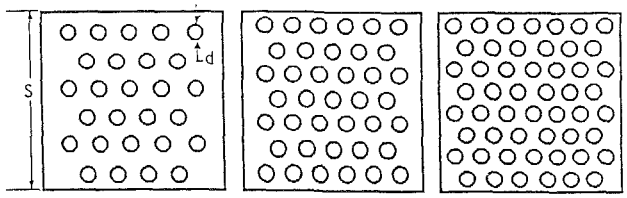


Fig. 1 Front view of pin fin arrays

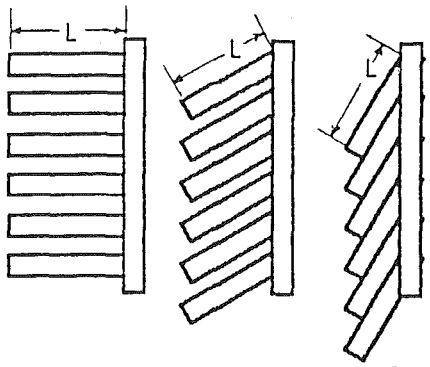


a. 0° · b. 30° down c. 60° down

Fig. 2 Side view of pin fin arrays

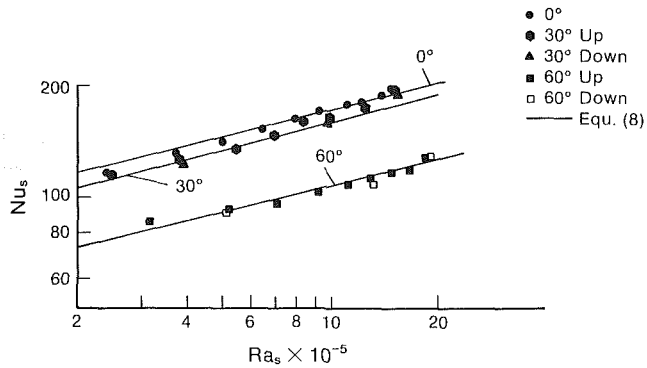


Fig. 3 Heat transfer results for 39-pin array, *L/D* = 8

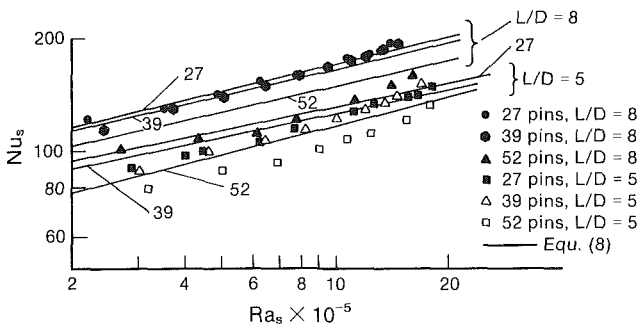


Fig. 4 Heat transfer results for horizontal arrays with *L/D* = 5, 8

From initial testing, it was determined that a dwell time of 6–8 h per power setting was necessary to achieve steady state. At steady state, the chamber temperature drifted by no more than 1°C per hour and the difference between pin tip temperature and chamber temperature was repeatable to within 0.25°C. Arrays were subjected to ten power settings ranging from 1.275 W to 20.4 W. Temperature levels varied from 10 to 50°C above ambient.

In the present study, two different Nusselt numbers were found to be useful in presenting results. One Nusselt number, based on the center-to-center pin fin spacing, was defined as

Table 1 Pin fin array configurations

| Diameter | No. of fins | Angle to Horizontal | *L/D* |
|---|---|---|---|
| 0.635 cm | 27 | 60°up 30°up 0° 30° down 60°down | 5 8 |
| | 39 | 60°up 30°up 0° 30° down 60°down | 5 8 |
| | 52 | 60°up 30°up 0° 30° down 60°down | 5 8 |

$$\mathrm{Nu}_d = \frac{h_A d}{k} \tag{1}$$

where

$$d = a \cos\theta \tag{2}$$

and

$$h_A = \frac{Q}{A(T_b - T_f)} \tag{3}$$

In these equations, $a$ is the center-to-center fin spacing, and $A$ is the surface area of the array, including the sides of the pins, the tips of the pins, and the exposed area of the baseplate. The Nusselt number $\mathrm{Nu}_d$ was found to give the best correlation of the test data. An alternate Nusselt number $\mathrm{Nu}_s$, which was based on the height of the pin fin bank, was defined as

$$\mathrm{Nu}_s = \frac{h_s S}{k} \tag{4}$$

where

$$h_s = \frac{Q}{S^2(T_b - T_f)} \tag{5}$$

Since the pin bank height $S$ was not varied in this study, $\mathrm{Nu}_s$ reflects only the changes in $Q/(T_b - T_f)$. Note that $h_s$ is based on the surface area of the baseplate, which is the actual area that requires cooling. This Nusselt number was used in all the plots of data that follow. It has the advantages of being easy to interpret physically and allowing direct comparison of the cooling performance of the different arrays tested. It does not, however, allow very good correlation of the test data. Not surprisingly, $\mathrm{Nu}_d$, which is based on more physically meaningful length and area scales, gave better correlation than $\mathrm{Nu}_s$.

Two different Rayleigh numbers, corresponding to the two different Nusselt numbers, were defined for use in this study. They are

$$\mathrm{Ra}_d = \frac{g\beta\rho^2 c_p (T_b - T_f) d^3}{\mu k} \tag{6}$$

and

$$\mathrm{Ra}_s = \frac{g\beta\rho^2 c_p (T_b - T_f) S^3}{\mu k} \tag{7}$$

As one might expect, $\mathrm{Ra}_d$ was used together with $\mathrm{Nu}_d$ in the correlation of the test data, and $\mathrm{Ra}_s$ was used together with $\mathrm{Nu}_s$ in the graphic presentation of results.

The primary purpose of this study was to observe the effect of pin inclination on overall heat transfer rates. This effect is illustrated in Fig. 3, which represents all the data taken for the 39-pin array with an $L/D$ ratio of 8. The arrays that were angled 30 deg from the horizontal exhibited about a 10 percent lower heat transfer rate than their horizontal counterparts. The performance of the 60 deg arrays was still worse, being about 20 to 40 percent lower than the horizontal array. Note that it makes little difference whether the array is angled up or down.

The density of the finned arrays influenced heat transfer rates as shown in Fig. 4. There is very little difference between the behavior of the 27-pin array and the 39-pin array. Although the 39-pin array has much more fin surface area than the 27-pin array, the increased crowding of the pins lowered the heat transfer coefficient so that the product of area and heat transfer coefficient remained about the same. The 52-pin array produced substantially less overall heat

Table 2 Radiative heat transfer compared to total heat transfer

| Pins | $L/D$ | Inclination | $Ra_S \times 10^{-5}$ | $Q_R/Q$ |
|---|---|---|---|---|
| 39 | 5 | 0° | 3.0 | .44 |
| 39 | 5 | 0° | 6.5 | .38 |
| 39 | 5 | 0° | 12.1 | .34 |
| 39 | 5 | 0° | 17.2 | .33 |
| 39 | 8 | 0° | 2.4 | .49 |
| 39 | 8 | 0° | 6.4 | .39 |
| 39 | 8 | 0° | 12.1 | .36 |
| 39 | 8 | 0° | 14.4 | .34 |
| 27 | 5 | 0° | 11.2 | .35 |
| 52 | 5 | 0° | 11.1 | .39 |
| 39 | 5 | 30° | 12.1 | .35 |
| 39 | 5 | 60° | 15.2 | .48 |

transfer than the less densely populated arrays. For all arrays shown in Fig. 4, increasing the $L/D$ ratio from 5 to 8 dramatically improved the heat transfer. This is an expected result since the fin efficiency for the pins is high. These results agree well with the previous work of Sparrow and Vemuri (1985).

It was possible to represent all of the data with a single correlation. The correlation is

$$\mathrm{Nu}_d = 1.035\mathrm{Ra}_d^{0.24}\left(\frac{a-D}{D}\cos\theta\right)^{1.3}\left(\frac{L\cos\theta}{D}\right)^{-0.37} \quad (8)$$

Note that the Nusselt and Grashof numbers used in this correlation are different from those used previously in the figures. The correlation was obtained by a linear, least-square, multiple regression analysis. The multiple correlation coefficient $r$ was found to be 0.993, and $r^2$, which is an indication of the goodness of fit of the data, was 0.987. The correlation was based on 174 data points.

The Nusselt numbers predicted by the correlation are plotted on Figs. 3 and 4. The correlation predicts excellently for all of the data on Fig. 3. In Fig. 4, the correlation predict very well for the 27 and 39-pin $L/D = 8$ cases, but is about 10 percent high for other cases.

A significant portion of the total heat transfer from the array escapes by radiation. To investigate the size of the radiative contribution, a simple model was generated. It was assumed that the finned array acts very much like a cavity. Any radiation entering between the outermost layer of pins is likely to be absorbed somewhere within the finned array and is unlikely to be reflected back out of the array. Therefore, equivalent black surfaces were placed between the pins in the outermost layer of pins all around the periphery of the array. Each black surface was flat and in the same plane as the axes of the two pins connected to that black surface. The outermost pins were considered to be gray and diffuse with an emissivity $\epsilon$ of 0.82.

Interactions between pins were neglected since configurations factors between the pins were very small. The ends of the pins were modeled as gray and diffuse with $\epsilon = 0.82$. The space between the ends of the pins was replaced by an equivalent black surface. The exposed base-plate area, i.e., that part outside the outermost layer of pins, was also assumed to be black.

With these assumptions, the radiative exchange of the array with the surroundings was estimated based on the measured temperatures of the array and the enclosure. Results are given in Table 2. In all cases studied, the radiative contribution was substantial. Radiation was more important at lower Grashof numbers, longer pin lengths, and large inclination angles. These results agree well with the computations of Sparrow and Vemuri (1985).

The main intent of this study was to compare the performance of inclined pin fins with straight pin fins. In all cases studied, the straight, horizontal fins were superior to the inclined fins. It was possible to obtain a single general correlation of the test data. While this correlation is recommended within the range of parameters that were tested here, one significant parameter, the size of the base plate, was not varied.

The base plate used here was a 7.62-cm-square block. The two fin lengths, which were 3.175 cm and 5.08 cm, were of the same order of magnitude as the side of the base plate. This means that the arrays, in some cases, appeared almost cubic. With an array of these proportions, the fins on the edge of the array dissipate a significant proportion of the total heat dissipated. These edge fins have higher heat transfer rates than the fins near the center of the array, both because of enhanced radiation (edge fins have a better view of the surroundings than center fins), and enhanced free convection (edge fins are less crowded than center fins). The measured tip temperatures confirm these ideas. The tip temperatures of fins near the edge were significantly lower than the tip temperature of fins in the center of the array.

Because the edge fins have high heat transfer rates and because they comprise a significant proportion of the total number of fins, increasing the size of the base plate is likely to degrade the overall heat transfer. Caution should be exercised in using the results described here for large arrays. Conversely, smaller arrays should perform better, and the results here would be conservative.

## References


Al-Arabi, M., and Khamis, M., 1982, "Natural Convection Heat Transfer From Inclined Cylinders," *Int. J. Heat Mass Transfer*, Vol. 25, pp. 3–15.

Al-Arabi, M., and Salman, Y. K., 1980, "Laminar Natural Convection Heat Transfer From an Inclined Cylinder," *Int. J. Heat Mass Transfer*, Vol. 23, pp. 45–51.

Farber, E. A., and Rennat, H. O., 1957, "Variation of Heat Transfer Coefficient With Length Inclined Tubes in Still Air," *Ind. Eng. Chem.*, Vol. 49, pp. 437–440.

Farouk, B., and Guceri, S. I., 1983, "Natural Convection From Horizontal Cylinders in Interacting Flow Fields," *Int. J. Heat Mass Transfer*, Vol. 26, pp. 231–243.

Kaminski, D. A., Roecker, R. H., Fitzroy, N. D., Buckland, F. F., and Norris, R. H., eds., 1987, *Heat Transfer and Fluid Flow Design Data Book*, Genium Publishing Co., Schenectady.

Oosthuizen, P. H., 1976, "Experimental Study of Free Convective Heat Transfer From Inclined Cylinders," ASME JOURNAL OF HEAT TRANSFER, Vol. 98, pp. 672–674.

Sparrow, E. M., and Vemuri, S. B., "Natural Convection/Radiation Heat Transfer From Highly Populated Pin Fin Arrays," ASME JOURNAL OF HEAT TRANSFER, Vol. 107, pp. 190–197.

Sparrow, E. M., and Vemuri, S. B., 1986, "Orientation Effects on Natural Convection/Radiation Heat Transfer From Pin-Fin Arrays," *Int. J. Heat Mass Transfer*, Vol. 29, pp. 359–368.


# Transient Radiative Cooling of an Absorbing and Scattering Cylinder


**R. Siegel**[1]


## Nomenclature

$a$ = absorption coefficient of absorbing-scattering region
$c_p$ = specific heat of radiating region
$c_{p,d}$ = specific heat of droplet or particle material


[1]Research Scientist, Office of the Chief Scientist, NASA Lewis Research Center, Cleveland, OH 44135; Fellow ASME.



Contributed by the Heat Transfer Division for publication in the JOURNAL OF HEAT TRANSFER. Manuscript received by the Heat Transfer Division July 31, 1987. Keywords: Radiation, Radiation Interactions, Transient and Unsteady Heat Transfer.

Table 2 Radiative heat transfer compared to total heat transfer

| Pins | $L/D$ | Inclination | $Ra_S \times 10^{-5}$ | $Q_R/Q$ |
|---|---|---|---|---|
| 39 | 5 | 0° | 3.0 | .44 |
| 39 | 5 | 0° | 6.5 | .38 |
| 39 | 5 | 0° | 12.1 | .34 |
| 39 | 5 | 0° | 17.2 | .33 |
| 39 | 8 | 0° | 2.4 | .49 |
| 39 | 8 | 0° | 6.4 | .39 |
| 39 | 8 | 0° | 12.1 | .36 |
| 39 | 8 | 0° | 14.4 | .34 |
| 27 | 5 | 0° | 11.2 | .35 |
| 52 | 5 | 0° | 11.1 | .39 |
| 39 | 5 | 30° | 12.1 | .35 |
| 39 | 5 | 60° | 15.2 | .48 |

transfer than the less densely populated arrays. For all arrays shown in Fig. 4, increasing the $L/D$ ratio from 5 to 8 dramatically improved the heat transfer. This is an expected result since the fin efficiency for the pins is high. These results agree well with the previous work of Sparrow and Vemuri (1985).

It was possible to represent all of the data with a single correlation. The correlation is

$$\mathrm{Nu}_d = 1.035\mathrm{Ra}_d^{0.24}\left(\frac{a-D}{D}\cos\theta\right)^{1.3}\left(\frac{L\cos\theta}{D}\right)^{-0.37} \quad (8)$$

Note that the Nusselt and Grashof numbers used in this correlation are different from those used previously in the figures. The correlation was obtained by a linear, least-square, multiple regression analysis. The multiple correlation coefficient $r$ was found to be 0.993, and $r^2$, which is an indication of the goodness of fit of the data, was 0.987. The correlation was based on 174 data points.

The Nusselt numbers predicted by the correlation are plotted on Figs. 3 and 4. The correlation predicts excellently for all of the data on Fig. 3. In Fig. 4, the correlation predict very well for the 27 and 39-pin $L/D = 8$ cases, but is about 10 percent high for other cases.

A significant portion of the total heat transfer from the array escapes by radiation. To investigate the size of the radiative contribution, a simple model was generated. It was assumed that the finned array acts very much like a cavity. Any radiation entering between the outermost layer of pins is likely to be absorbed somewhere within the finned array and is unlikely to be reflected back out of the array. Therefore, equivalent black surfaces were placed between the pins in the outermost layer of pins all around the periphery of the array. Each black surface was flat and in the same plane as the axes of the two pins connected to that black surface. The outermost pins were considered to be gray and diffuse with an emissivity $\epsilon$ of 0.82.

Interactions between pins were neglected since configurations factors between the pins were very small. The ends of the pins were modeled as gray and diffuse with $\epsilon = 0.82$. The space between the ends of the pins was replaced by an equivalent black surface. The exposed base-plate area, i.e., that part outside the outermost layer of pins, was also assumed to be black.

With these assumptions, the radiative exchange of the array with the surroundings was estimated based on the measured temperatures of the array and the enclosure. Results are given in Table 2. In all cases studied, the radiative contribution was substantial. Radiation was more important at lower Grashof numbers, longer pin lengths, and large inclination angles. These results agree well with the computations of Sparrow and Vemuri (1985).

The main intent of this study was to compare the performance of inclined pin fins with straight pin fins. In all cases studied, the straight, horizontal fins were superior to the inclined fins. It was possible to obtain a single general correlation of the test data. While this correlation is recommended within the range of parameters that were tested here, one significant parameter, the size of the base plate, was not varied.

The base plate used here was a 7.62-cm-square block. The two fin lengths, which were 3.175 cm and 5.08 cm, were of the same order of magnitude as the side of the base plate. This means that the arrays, in some cases, appeared almost cubic. With an array of these proportions, the fins on the edge of the array dissipate a significant proportion of the total heat dissipated. These edge fins have higher heat transfer rates than the fins near the center of the array, both because of enhanced radiation (edge fins have a better view of the surroundings than center fins), and enhanced free convection (edge fins are less crowded than center fins). The measured tip temperatures confirm these ideas. The tip temperatures of fins near the edge were significantly lower than the tip temperature of fins in the center of the array.

Because the edge fins have high heat transfer rates and because they comprise a significant proportion of the total number of fins, increasing the size of the base plate is likely to degrade the overall heat transfer. Caution should be exercised in using the results described here for large arrays. Conversely, smaller arrays should perform better, and the results here would be conservative.

## References


Al-Arabi, M., and Khamis, M., 1982, "Natural Convection Heat Transfer From Inclined Cylinders," *Int. J. Heat Mass Transfer*, Vol. 25, pp. 3–15.

Al-Arabi, M., and Salman, Y. K., 1980, "Laminar Natural Convection Heat Transfer From an Inclined Cylinder," *Int. J. Heat Mass Transfer*, Vol. 23, pp. 45–51.

Farber, E. A., and Rennat, H. O., 1957, "Variation of Heat Transfer Coefficient With Length Inclined Tubes in Still Air," *Ind. Eng. Chem.*, Vol. 49, pp. 437–440.

Farouk, B., and Guceri, S. I., 1983, "Natural Convection From Horizontal Cylinders in Interacting Flow Fields," *Int. J. Heat Mass Transfer*, Vol. 26, pp. 231–243.

Kaminski, D. A., Roecker, R. H., Fitzroy, N. D., Buckland, F. F., and Norris, R. H., eds., 1987, *Heat Transfer and Fluid Flow Design Data Book*, Genium Publishing Co., Schenectady.

Oosthuizen, P. H., 1976, "Experimental Study of Free Convective Heat Transfer From Inclined Cylinders," ASME JOURNAL OF HEAT TRANSFER, Vol. 98, pp. 672–674.

Sparrow, E. M., and Vemuri, S. B., "Natural Convection/Radiation Heat Transfer From Highly Populated Pin Fin Arrays," ASME JOURNAL OF HEAT TRANSFER, Vol. 107, pp. 190–197.

Sparrow, E. M., and Vemuri, S. B., 1986, "Orientation Effects on Natural Convection/Radiation Heat Transfer From Pin-Fin Arrays," *Int. J. Heat Mass Transfer*, Vol. 29, pp. 359–368.


## Transient Radiative Cooling of an Absorbing and Scattering Cylinder


**R. Siegel**[1]


### Nomenclature

$a$ = absorption coefficient of absorbing-scattering region
$c_p$ = specific heat of radiating region
$c_{p,d}$ = specific heat of droplet or particle material


[1]Research Scientist, Office of the Chief Scientist, NASA Lewis Research Center, Cleveland, OH 44135; Fellow ASME.



Contributed by the Heat Transfer Division for publication in the JOURNAL OF HEAT TRANSFER. Manuscript received by the Heat Transfer Division July 31, 1987. Keywords: Radiation, Radiation Interactions, Transient and Unsteady Heat Transfer.

$D_n(x)$ = the function $\int_0^{\pi/2} (\cos\alpha)^{n-1} e^{-x/\cos\alpha} d\alpha = \int_0^1 \frac{\mu^{n-1} e^{-x/\mu}}{(1-\mu^2)^{1/2}} d\mu$

$E_a$, $E_s$ = efficiency factors for absorption and scattering by a drop or particle

$I$ = source function in absorbing-scattering region; $\tilde{I} = \pi I/\sigma T_i^4$

$i$ = radiation intensity

$N$ = number of drops or particles per unit volume of region

$q_r$ = radial radiative heat flow per unit area and time

$R$ = radial coordinate in cylinder; $R_o$ = outer radius

$R_d$ = radius of spherical drop or particle

$r$ = optical radial coordinate $= (a+\sigma_s)R$; $r_o = (a+\sigma_s)R_o$

$r'$ = dummy variable for optical radial coordinate

$T$ = absolute temperature; $\tilde{T} = T/T_i$

$T_i$ = initial temperature at $Z=0$

$\tilde{T}_o$ = value of $\tilde{T}$ at $r=r_o$

$T_m$ = integrated bulk mean temperature at $Z$, equation (6); $\tilde{T}_m = T_m/T_i$

$\bar{u}$ = velocity through space of cylindrical region

$Z$ = axial coordinate along length of cylinder

$z$ = dimensionless length $= \sigma T_i^3 (E_a+E_s)Z/R_d\rho_d c_{p,d}\,\bar{u} = 4\sigma T_i^3(a+\sigma_s)Z/3\bar{u}\rho c_p$

$\epsilon$ = local emittance of cylinder based on local value of $T_m^4$

$\epsilon_{ul}$ = emittance of a cylinder that has a uniform temperature

$\kappa_D$ = optical thickness of entire plane layer thickness

$\rho$ = density of cylindrical region

$\rho_d$ = density of droplet or particle material

$\sigma$ = Stefan–Boltzmann constant

$\sigma_s$ = scattering coefficient in absorbing-scattering region

$\Omega$ = albedo for scattering $= \sigma_s/(a+\sigma_s)$

## Introduction

This is a companion paper to the plane layer analysis of Siegel (1987), and is a continuation of the analysis for a cylinder (Siegel, 1988). The transient cooling is studied for a cylindrical stream of radiating medium in very cold surroundings. The study by Siegel (1987) of a plane layer filled with many small drops was motivated by the need for dissipation of waste heat from power plants operating in outer space. A potentially lightweight and easily deployable system is the liquid drop radiator (Mattick and Hertzberg, 1981; Presler et al., 1986; White, 1987). Hot liquid drops in the form of many parallel directed streams would be passed directly through space. After losing a portion of its energy by radiative cooling, the fluid is collected for reuse.

While studying the radiative behavior of a plane layer, it was found that for cooling in an environment at a low enough temperature so that reradiation from the surroundings could be neglected, a "fully developed" condition was reached wherein the transient emittance arrived at a constant value lower than that for a layer at uniform temperature (Siegel, 1987). If the layer begins with a uniform temperature distribution across its thickness, then the initial and fully developed emittances provide upper and lower bounds for the emittance values during cooling. The emittance for a cylinder in the fully developed transient cooling region was obtained by use of a similarity solution by Siegel (1988). The entire transient cooling behavior will be studied here by forward integration of the energy transfer equations.

The cylinder was chosen as a basic nonplanar shape that occurs in radiative heat transfer applications such as tubular combustors and flames. The cylindrical shape may have application to some types of liquid drop or particle radiators, and some of the current laboratory heat transfer tests for the liquid drop radiator utilize a cylindrical geometry as a convenient shape (White, 1987). The radiative flux relations for a cylinder were given by Heaslet and Warming (1966) and Kesten (1968), and some steady-state calculations were carried out. The present analysis will provide cooling curves for a cylindrical region, initially at uniform temperature and then suddenly exposed to a much cooler environment. Results are obtained for several optical radii and a few values of the scattering albedo.

## Analysis

The cylindrical region containing a radiating medium is shown in Fig. 1. With regard to applications for radiative heat dissipation in space, the region could be filled with streams of liquid drops or particles. The region is traveling through space with uniform velocity $\bar{u}$, so that the cooling will be formulated as a function of axial distance $Z$. By use of the transformation in terms of transit time, $\tau = Z/\bar{u}$, the solution also applies for transient radiative cooling of a stationary cylinder. It is assumed that the outer space environment is at a much lower temperature than the radiating cylinder. The radiative properties are assumed gray; for the considered working fluids in a liquid drop radiator, this can be a reasonable approximation in the infrared region of interest (Presler et al., 1986). The scattering is isotropic; this is expected to yield reasonable results, as multiple reflections within the region cause the effects of anisotropy mostly to cancel out, yielding a behavior that is reasonably isotropic. Some results for anisotropic scattering in a plane layer are in Fig. 11 of White (1987); these show only a modest effect. Heat conduction can be neglected for a droplet- or particle-filled region in the vacuum of outer space.

**Equations for Radiative Cooling.** Since the analysis here is for the same geometry as in Siegel (1988) it is not necessary to repeat the derivation. The energy and radiative source function equations for an absorbing and scattering region can be derived from relations in Chap. 14 of Siegel and Howell (1981) as

$$\bar{u}\rho c_p \frac{\partial T}{\partial Z} = -\frac{4\pi a}{\Omega}\left(\frac{\sigma T^4}{\pi} - I\right) \tag{1}$$

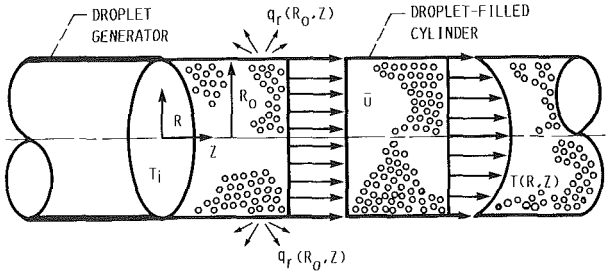


**Fig. 1 Geometry of radiating cylindrical region filled with hot droplets (or particles)**

$$I=\frac{\sigma T^4}{\pi}-\frac{\Omega}{1-\Omega}\frac{1}{4\pi}\frac{1}{r}\frac{\partial}{\partial r}\left[rq_r(r, Z)\right] \quad (2)$$

where $T$ and $I$ are functions of $r$ and $Z$. The radiative flux in the $Z$ direction is neglected; the $\bar{u}$ would need to be large enough so that the cooling distances in the axial direction are much larger than the cylinder radius. The velocity required can be obtained from the cooling curves given later. The $q_r$ depends on both $r$ and $Z$ because $T$ is a function of these variables.

The radial radiative flux $q_r$ for a cylinder was derived by Kesten (1968), and it involves a double integration over radius and angle in the cylindrical geometry. As shown in Siegel (1988) the flux relation can be somewhat simplified for uniform properties along the radiation paths within the volume, and then the order of the integrations is changed to provide a more convenient form. The quantity $rq_r(r)$ is then differentiated with respect to $r$ and substituted into equation (2). Equations (1) and (2) are then put into dimensionless form to yield

$$\frac{\partial \tilde{T}}{\partial z}=-3\frac{1-\Omega}{\Omega}(\tilde{T}^4-\tilde{I}) \quad (3)$$

$$\tilde{I}=(1-\Omega)\tilde{T}^4+\Omega\left[\int_0^r \tilde{I}(r')K_1(r', r)dr' + \int_r^{r_o}\tilde{I}(r')K_2(r', r)dr'\right] \quad (4)$$

The $\tilde{T}$ and $\tilde{I}$ are functions of $r$ and $z$, but the notation is abbreviated here. The $K_1$ and $K_2$ functions are given in Siegel (1988) and the dimensionless variables are defined in the Nomenclature. The $z$ is given in two equivalent forms, one being based on the overall properties of the radiating medium. The other, $z=\sigma T_i^3(E_a+E_s)Z/R_d\rho_d c_{p,d}\,\bar{u}$, was chosen particularly to examine the cooling of a region filled with drops or particles. This form contains the properties of the drops but not the cylinder radius or the drop number density. These quantities appear only in the optical radius $r_o=(a+\sigma_S)R_o=\pi R_d^2 N(E_a+E_s)R_o$, which is therefore an independent parameter showing the influence of $NR_o$ when the drop radius $R_d$ and efficiency factors $E_a$ and $E_s$ are fixed. Note that $\rho c_p=\rho_d c_{p,d}(4/3)\pi R_d^3 N$.

Equations (3) and (4) will be solved numerically for $\tilde{T}(r, z)$ and $\tilde{I}(r,z)$. When the drops or particles are highly absorbing, $\Omega \to 0$, the equations are combined to yield

$$\frac{\partial \tilde{T}}{\partial z}=-3\left\{\tilde{T}^4-\left[\int_0^r \tilde{T}^4(r')K_1(r', r)dr' + \int_r^{r_o}\tilde{T}^4(r')K_2(r', r)dr'\right]\right\} \quad (5)$$

**Relations for Local Energy and Emittance.** The energy remaining in the cylindrical stream at $z$ is given by

$$\frac{\text{Energy }(z)}{\text{Energy }(z=0)}=\frac{1}{\pi R_o^2 T_i}\int_0^{R_o}2\pi T(R, Z)R\,dR = \frac{2}{r_o^2}\int_0^{r_o}\tilde{T}(r, z)r\,dr=\tilde{T}_m(z) \quad (6)$$

The local heat flux radiated from the cylinder, and the local emittance along the cylinder, can be obtained from the following heat balances in dimensionless form:

$$\epsilon(z)=\frac{q_r(r_o, z)}{\sigma T_i^4}\frac{1}{\tilde{T}_m^4}=-\frac{2r_o}{3}\frac{1}{\tilde{T}_m^4}\frac{d\tilde{T}_m}{dz}=-\frac{4}{3r_o\tilde{T}_m^4}\int_0^{r_o}\frac{\partial \tilde{T}}{\partial z}r\,dr \quad (7)$$

Hence $\epsilon(z)$ and $q_r(r_o, z)/\sigma T_i^4$ can be readily calculated after $\tilde{T}_m(z)$ or $\partial\tilde{T}(r, z)/\partial z$ is obtained.

Another relation for $\epsilon(z)$ was used as a check on the numerical calculations. The radiative heat flux leaving the cylinder was found from the $q_r$ relation used in equation (2) evaluated at $r=r_o$; the $q_r(r, z)$ is from Siegel (1988). This yields

$$\epsilon(z)=\frac{q_r(r_o, z)}{\sigma T_m^4(z)}=\frac{4}{\pi}\frac{1}{\tilde{T}_m^4(z)}\int_0^{r_o}\tilde{I}(r', z)K_3(r', r_o)dr' \quad (8)$$

where $K_3(r', r_o)$ is from Siegel (1988).

A special case for comparison purposes is a cylinder with a uniform radial temperature distribution with absorption only ($\Omega=0$). In this instance, $\tilde{I}=\tilde{T}^4=1$, and equation (8) can be integrated to obtain the emittance

$$\epsilon_{ut}=1-\frac{4}{\pi}\int_0^{\pi/2}D_3(2r_o\cos\beta)\cos\beta\,d\beta \quad (9)$$

The behavior of the $D_n$ functions is given by Yuen and Wong (1983). For an optically thin cylinder, this reduces to $\epsilon_{ut}=2r_o$.

When a cylinder has a uniform radial temperature distribution, the cooling equation (7) can be easily integrated since $\epsilon=\epsilon_{ut}$ is not a function of $z$

$$\tilde{T}_m(z)=\left(1+\frac{9}{2}\frac{\epsilon_{ut}}{r_o}z\right)^{-1/3} \quad (10)$$

In the optically thin limit for $\Omega=0$, $\epsilon_{ut}=2r_o$ and this becomes

$$\tilde{T}_m(z)=(1+9z)^{-1/3} \quad (11)$$

**Numerical Solution.** By using the integration subroutines described by Siegel (1988), equations (3) and (4) were solved numerically for $\tilde{T}(r, z)$ and $\tilde{I}(r, z)$. Starting with the initial condition $\tilde{T}(r, 0)=1$, equation (4) was solved for $\tilde{I}(r, 0)$ by using $\tilde{I}(r, 0)=1$ as an initial guess on the right-hand side. At each $r$, the difference between the right-hand side and the trial $\tilde{I}$ was multiplied by an acceleration factor of 1.4 and the result added to the trial $\tilde{I}$ to obtain a new $\tilde{I}$ for use in the next iteration. The iteration at each $z$ was continued until the relative change in $\tilde{I}$ at all $r$ converged within at least four decimal places; eight or fewer iterations were required. The $\tilde{I}(r, z)$ and $\tilde{T}(r, z)$ were inserted into equation (3), and the $\partial\tilde{T}/\partial z$ was used to extrapolate forward to obtain $\tilde{T}(r, z+\Delta z)$. The numerical results were checked by reducing the size of the $\Delta r$ and $\Delta z$ increments. Usually 10 or 20 radial increments were required with the integration methods used. The $\Delta z$ increments were varied in size, starting with a very small $\Delta z$ and then letting $\Delta z$ become larger as the cooling rate decreased.

When $\Omega=0$, equation (5) was solved starting with $\tilde{T}(r, 0)=1$ on the right-hand side and integrating forward in $z$. An iteration loop was not required; the calculation of cooling from $\tilde{T}_m=1$ to 0.5 required about 10 min. on an IBM 370 computer. Each case with scattering required about 25 min.

To carry out the integrations, radial spline fits were made of the $\tilde{I}$ and $\tilde{T}^4$ values at the grid points. The spline coefficients were used to interpolate values between the grid points for use

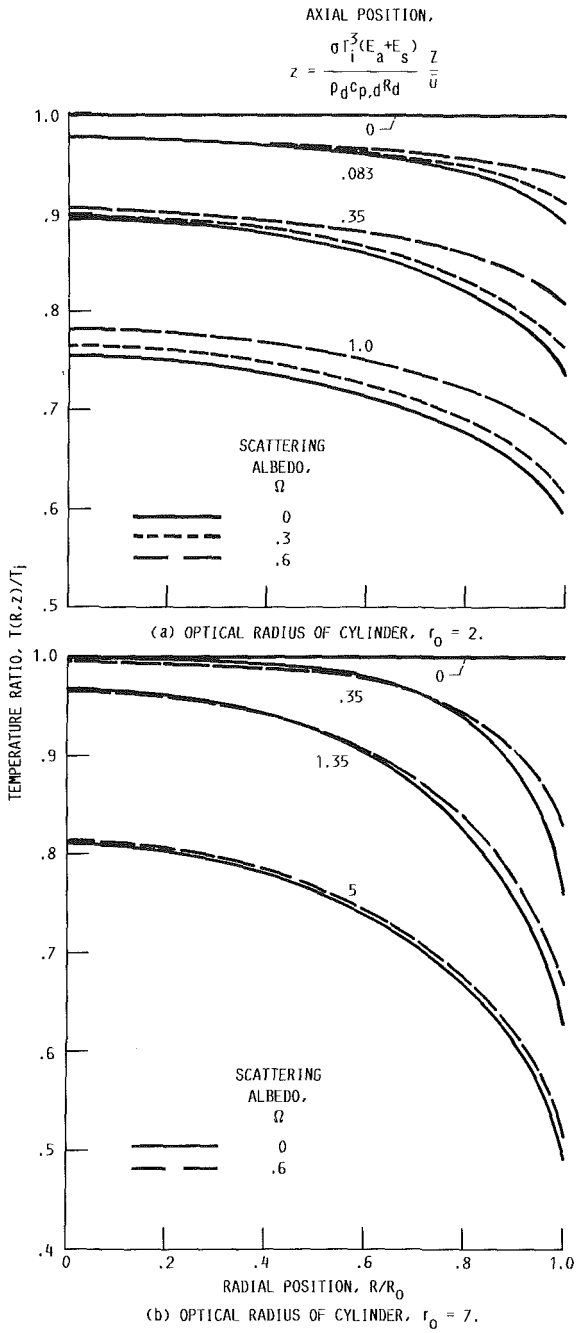


Fig. 2 Temperature distributions during transient cooling

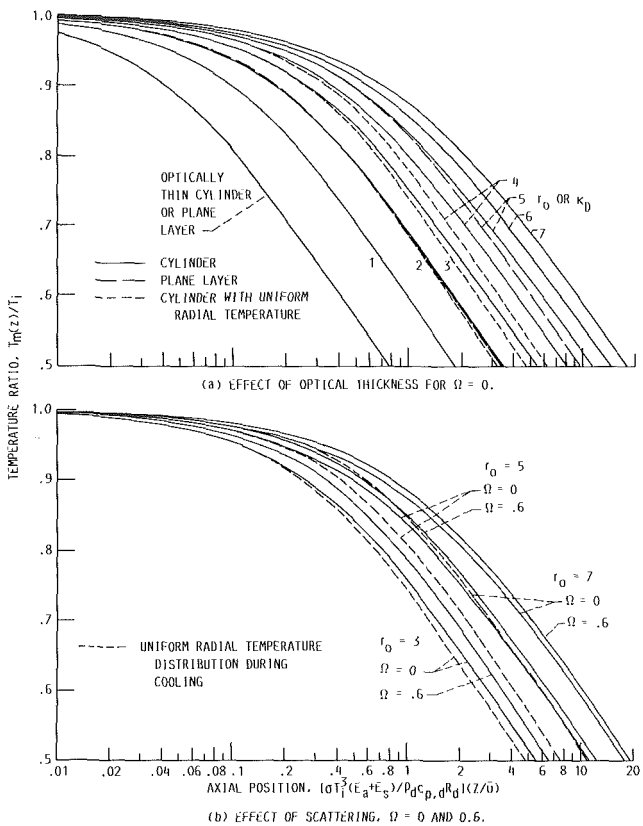


Fig. 3 Cooling curves for a radiating cylinder

in a Gaussian integration subroutine. The number of integration points was usually ten to twenty times the number of grid points. The solution of equations (4) and (5) requires evaluating the integration kernels $K_1(r', r)$ and $K_2(r', r)$ as described in Siegel (1988). With the exception of $K_2(0, 0) = \pi/2$, the $K$ values become infinite as $r' \rightarrow r$. The method of dealing with this by analytically integrating the kernels for a small region adjacent to the singularity is also from Siegel (1988).

## Results and Discussion

As shown by Fig. 1, the radiating cylindrical stream originates at uniform temperature $T_i$. Typical temperature distributions during cooling are in Fig. 2, where parts (*a*) and (*b*) contrast the behavior of a cylinder of moderate optical radius, $r_o = 2$, with a thick cylinder, $r_o = 7$. The temperature ratio at $z = 0$ is a horizontal line $T/T_i = 1.0$, so initially $T_m/T_i = 1.0$. The three axial locations show profiles where $T_m/T_i$ is approximately 0.95, 0.85, and 0.70 for the cases when $\Omega = 0$. For $r_o = 2$ the profiles in Fig. 2(*a*) are only moderately curved. Energy can be radiated away fairly well from the interior of the cylinder, and the entire cross section tends to cool somewhat uniformly. As the scattering is increased, the ability of the medium to emit is decreased. Hence, for a given axial location, the temperatures for $\Omega > 0$ are higher than those for $\Omega = 0$. Increased scattering provides increased energy reflection within the cylinder so the temperature profiles become more uniform. Scattering has less effect as $r_o$ is increased, since it becomes more difficult to redistribute the energy across a thick cylinder. When the axial variable in Fig. 2(*b*) is increased to 5, the temperature profiles for $\Omega = 0$ and 0.6 are practically the same.

For dissipation of waste heat by radiative cooling in outer space, the results in Fig. 3 are quite useful, as they show the axial decrease in bulk mean temperature. The results in Fig. 3(*a*) are for absorbing-emitting cylinders without scattering. The most rapid cooling with axial distance is for an optically thin cylinder as the outer portions do not offer interference for radiation leaving from the inner regions. The cooling relation is given by equation (11), which is also valid for a plane layer. As the optical radius is increased, the cylinder cools more slowly as each portion of the cross section can no longer radiate away energy independently as in the optically thin limit. For comparison, a few curves are included for a plane layer where $\kappa_D$ is the optical dimension of the entire layer thickness (not the half-thickness). For fairly small $r_o$ and $\kappa_D$, such as $r_o = \kappa_D = 2$, the cylinder and plane layer cooling curves are practically the same. As the optical thickness is increased, the cylinder cools somewhat more slowly than the

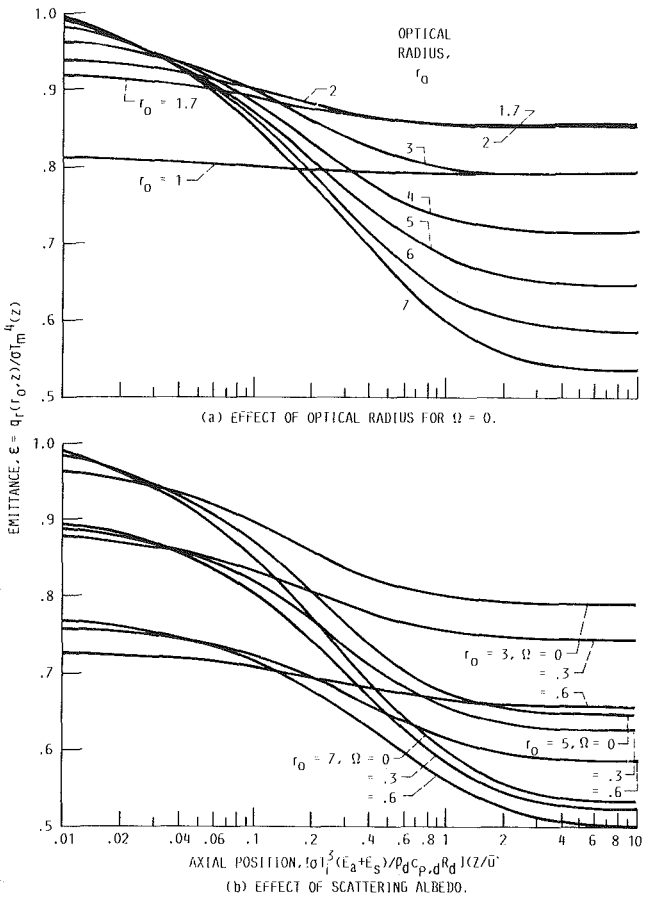


**Fig. 4 Local emittance values based on local heat loss and local mean temperature**

plane layer, as shown by the results for $r_o = \kappa_D = 5$ on Fig. 3(*a*).

Some additional effects are examined in Fig. 3(*b*); the solid lines for $\Omega = 0$ and $r_o = 3$, 5, and 7 are the same as in Fig. 3(*a*). The other three solid lines are for a scattering medium with $\Omega = 0.6$. For $r_o = 3$ the scattering increases the distance for cooling by about 20 percent. As $r_o$ is increased to 7, the scattering has less effect; the cooling distances for $\Omega = 0.6$ are about 8 percent larger than for $\Omega = 0$. The dashed lines on Fig. 3(*b*) are for a cylinder without scattering that has a uniform radial temperature distribution at all $Z$ throughout the cooling process. In this instance the emittance remains constant, and a very simple cooling solution is obtained. However, the resulting axial cooling distances can be considerably in error. For $r_o = 3$, the distances are about 15 percent too small; for $r_o = 5$ and 7, the error becomes much larger. For a cylinder with a uniform radial temperature and with $\Omega = 0$, the emittances vary from 0.977 to 0.995 for $r_o$ from 3 to 7 (Siegel, 1988), so these cylinders radiate essentially like a blackbody. In an actual cooling process the outer portion of a cylinder cools more rapidly than the central region, which reduces the cylinder emittance.

The local emittance is defined as the local heat flux radiated away, divided by the local blackbody emissive power based on the local bulk mean temperature. Figure 4(*a*) shows the emittance for several values of the optical radius from $r_o = 1$ to 7 for a cylinder with no scattering. At $z = 0$ the emittance is that for a cylinder at uniform temperature as obtained from equation (9). As cooling progresses, the temperature distribution develops a similarity behavior (Siegel, 1988) such that the ratio $q_r(r_o)/T_m^4$ becomes constant even though $q_r(r_o)$ and $T_m$ are both decreasing. As a result, the emittance reaches a constant value for each optical radius $r_o$. The decrease of emittance with $z$ is accentuated as $r_o$ increases. For a cylinder that is optically rather thin, $r_o = 1$, the radial temperature distribution remains almost uniform throughout the cooling process, and the emittance decreases only a little from its value at $z = 0$. Results for $r_o = 1.7$ are given, as this $r_o$ yields the largest value of $\epsilon$ in the fully developed region after the temperature profile has reached its similarity behavior. For a smaller $r_o$ the cylinder is too thin to be as good a radiator, and for $r_o > 1.7$ the outer layers of the cylinder begin to cool more significantly.

The results in Fig. 4(*a*) are for absorption and emission only ($\Omega = 0$); the effect of finite scattering is in Fig. 4(*b*). For a fixed $r_o$, an increase in $\Omega$ lowers the emittance since the medium is more reflective. Increased scattering also tends to make the temperature profiles more uniform throughout the cooling process. This reduces the amount that the emittance decreases when going from the initial value for a cylinder at uniform temperature to the fully developed value at larger axial positions. For larger scattering with $\Omega$ up to 0.98, results for the initial and fully developed emittances are in Siegel (1988). This range would be of interest if liquid metals were used for the droplet fluid.

## Conclusions

An analysis was carried out for the radiative cooling of an absorbing, emitting, and scattering cylinder initially at uniform temperature. As cooling proceeds, the outer regions of the cylinder become cooler than the interior, and the cylinder emittance decreases. The temperature profile reaches a similarity condition for which the emittance, based on the local bulk mean temperature, has a constant value lower than that for the cylinder at uniform temperature. For an optically thin region, the cooling of a cylinder is the same as for a plane layer having total thickness equal to the cylinder radius. For a cylinder without scattering, this similarity to plane-layer cooling is still approximately valid for an optical radius up to about 2. For an optical radius of 2, and for no scattering, the cooling of a cylinder to a given temperature level requires about 7 percent greater axial distance than for a cylinder with a uniform radial temperature distribution, except for small axial distances where the agreement is much closer since the cylinder starts at uniform temperature. As $r_o$ increases, the cooling distances become increasingly longer than for a cylinder with a uniform radial distribution. Scattering has a significant effect in increasing the cooling distances.

## References


Heaslet, M. A., and Warming, R. F., 1966, "Theoretical Predictions of Radiative Transfer in a Homogeneous Cylindrical Medium," *Journal of Quantitative Spectroscopy and Radiative Transfer*, Vol. 6, No. 6, pp. 751–774.

Kesten, A. S., 1968, "Radiant Heat Flux Distribution in a Cylindrically-Symmetric Nonisothermal Gas With Temperature-Dependent Absorption Coefficient," *Journal of Quantitative Spectroscopy and Radiative Transfer*, Vol. 8, No. 1, pp. 419–434.

Mattick, A. T., and Hertzberg, A., 1981, "Liquid Droplet Radiators for Heat Rejection in Space ," *Journal of Energy*, Vol. 5, No. 6, pp. 387–393.

Presler, A. F., Coles, C. E., Diem-Kirsop, P. S., and White, K. A., III, 1986, "Liquid Droplet Radiator Program at the NASA Lewis Research Center," ASME Paper No. 86-HT-15.

Siegel, R., 1987, "Transient Radiative Cooling of a Droplet-Filled Layer," ASME JOURNAL OF HEAT TRANSFER, Vol. 109, No. 1, pp. 159–164.

Siegel, R., 1988, "Transient Radiative Cooling of an Absorbing and Scattering Cylinder – A Separable Solution," AIAA *Journal of Thermophysics and Heat Transfer*, Vol. 2, No. 2, pp. 110–117.

Siegel, R., and Howell, J. R., 1981, *Thermal Radiation Heat Transfer*, 2nd ed., Hemisphere Publishing Co., Washington, DC.

White, K. A., 1987, "Liquid Droplet Radiator Development Status," AIAA Paper No. 87-1537.

Yuen, W. W., and Wong, L. W., 1983, "Numerical Computation of an Important Integral Function in Two-Dimensional Radiative Transfer," *Journal of Quantitative Spectroscopy and Radiative Transfer*, Vol. 29, No. 2, pp. 145–149.

# Correlation of Pool Boiling Curves for the Homologous Group: Freons

J. W. Westwater,[1] J. C. Zinn,[2] and K. J. Brodbeck[3]

## Nomenclature

$C_L$ = specific heat of liquid
$g$ = gravitational acceleration
$h_{fg}$ = latent heat of evaporation
$k_L$ = thermal conductivity of liquid
$P_C$ = thermodynamic critical pressure
$q$, $q_{max}$, $q_{min}$ = heat flux, maximum flux, minimum flux
$T_{BP}$, $T_C$ = atmospheric boiling temperature, thermodynamic critical temperature
$\Delta T$, $\Delta T_{max}$, $\Delta T_{min}$ = temperature difference between solid surface and boiling liquid at heat flux $q$, $q_{max}$, $q_{min}$
$\rho_L$, $\rho_V$ = density of liquid, vapor
$\sigma$ = surface tension

## Introduction

A knowledge of the complete boiling curve $q$ versus $\Delta T$ for a liquid, including the regimes of nucleate boiling, transition boiling, and film boiling, and the peak and minimum crisis points is needed for the design and operation of various types of heat transfer equipment. No general method exists for predicting the complete curve. Most difficult is the prediction of the nucleate boiling curve, the transition curve, and the temperature that separates the two. If the curve for every liquid at every pressure must be determined experimentally, we are faced with a formidable task. This paper shows that some simplification is possible for members of a homologous group.

## Experimental

A homologous group consists of a series of compounds that are closely related chemically. For the present study, a series of six freons manufactured by the DuPont Co. was selected. The pool-boiling curve for each was determined in our laboratories at atmospheric pressure on pure copper having a mirror polish. The solid copper pieces were large enough to be representative of commercial heat transfer surfaces. They are not representative of small wires. For R-113 ($CClF_2$–$CCl_2F$) a horizontal, steam-heated tube of 7.94 mm o.d. in a large liquid pool was used (Broussard and Westwater, 1985). For this freon only, the tests were at steady state. For R-116 ($CF_3$–$CF_3$) a face-up, horizontal plate of 6.35 cm thickness and 5 cm diameter, connected to a vessel of the same diameter, was quenched from room temperature (Zinn, 1984). The temperature versus time data were received at high speed in a digital computer and were reduced to the boiling curve by means of an inverse-conduction mathematical technique (Westwater et al., 1986; Peyayopanakul and Westwater, 1978). This method does not assume uniform temperature throughout the solid as does the older lumped-parameter technique. For R-22 ($CHClF_2$), R-12 ($CCl_2F_2$), R-114 ($CClF_2$–$CClF_2$), and R-11 ($CCl_3F$), a solid sphere of 5 cm diameter was heated in an oven and then quenched in a liquid pool in a vessel of 9.53 cm diameter (Brodbeck, 1987). The high-speed temperature versus time data were reduced to boiling curves by use of a two-dimensional, inverse-conduction mathematical technique (Irving and Westwater, 1986; Westwater et al., 1986). This method allows the temperature to vary with azimuthal angle and radial distance at any instant.

Four other liquids not part of the freon family were considered also. Three were tested in our laboratories at atmospheric pressure on mirror-smooth copper. Ethane ($C_2H_6$) was used with the quenching technique on a 5 cm diameter plate, 6.35 cm thick (Zinn, 1984). Helium was used (Zinn, 1984) with the quenching technique on a 6.35 mm diameter sphere in a 0.35 liter Dewar vessel. For this small sphere only, the simple lumped-parameter data reduction method was justified and was used. Nitrogen was used with the quenching technique on a 5 cm diameter sphere (Irving and Westwater, 1986) and also on horizontal plates, including effectively infinite diameter and effectively infinite thickness (Peyayopanakul and Westwater, 1978; Lin and Westwater, 1982; Zinn, 1984; Egan and Westwater, 1985). The boiling curves for nitrogen in Figs. 1 and 2, and the nitrogen heat transfer data in Table 1, are for the 5 cm sphere. Data for nitrogen in Fig. 3 include the effectively infinite flat plate, as well as the sphere, for comparison purposes.

The tenth liquid, water, was not tested in our laboratories. The boiling curve shown is that of Braunlich reported by McAdams (1954). The minimum in film boiling was not obtained. The minimum tabulated in this paper is from Nishio (1987).

Table 1 shows physical properties plus the measured crisis points during boiling for the six freons and four comparison liquids, all boiling at atmospheric pressure. The physical properties for the freons are from the manufacturer (DuPont Co., 1969). In cases where the surface tension was not given at the atmospheric boiling point, the value was estimated herein by linear interpolation, assuming the value to be zero at the thermodynamic critical temperature. The physical properties in Table 1 cover a great range: For example the surface tension varies from 0.12 to 58.9 dynes/cm, and the latent heat of evaporation varies from 21 to 2253 kJ/kg.

## Results

The ten boiling curves are shown in Fig. 1. The apparent symbols on the freon curves are used to separate the lines; they are not discrete data points. Continuous smooth lines result from the quenching technique coupled to computer data acquisition and automatic graphing. For every case, from three to five replicate runs were made. The average curve for each liquid is shown herein, and the amount of data scatter is illustrated for R-113 and nitrogen only by the vertical bars in Fig. 1.

The curves for the freons are similar in that the nucleate boiling branches of the curves (positive slope region on the left) have nearly the same slope. The transition boiling branches of the curves (negative slope) also have nearly a common slope. The four nonfreons are different. The similarity of

[1]Department of Chemical Engineering, University of Illinois, Urbana, IL 61801; Mem. ASME.
[2]Monsanto Co., St. Louis, MO 63167.
[3]Clorox Corp., Pleasanton, CA 94566.

Contributed by the Heat Transfer Division for publication in the JOURNAL OF HEAT TRANSFER. Manuscript received by the Heat Transfer Division December 10, 1987. Keywords: Boiling, Modeling and Scaling.

**Table 1 Physical properties and heat transfer data for ten liquids boiling at atmospheric pressure**

| | R-116 | R-22 | R-12 | R-114 | R-11 | R-113 | Helium | Nitrogen | Ethane | Water |
|---|---|---|---|---|---|---|---|---|---|---|
| $T_c$, K | 293 | 369 | 385 | 419 | 471 | 487 | 5.2 | 151 | 306 | 647 |
| $P_c$, atm | 29 | 49 | 41 | 32 | 44 | 34 | 2.3 | 33 | 49 | 218 |
| $T_{BP}$, K | 195 | 232 | 243 | 277 | 297 | 321 | 4.22 | 77 | 185 | 373 |
| $k_L$, W/m•K × $10^{-3}$ | 80 | 138 | 98 | 65 | 86 | 60 | 27 | 156 | 187 | 678 |
| $C_L$, J/kg•K | 967 | 1054 | 887 | 962 | 870 | 933 | 4561 | 1987 | 2435 | 4210 |
| $\rho_L$, kg/m$^3$ | 1587 | 1194 | 1311 | 1456 | 1476 | 1565 | 125 | 810 | 543 | 958 |
| $\rho_v$, kg/m$^3$ | 9.00 | 4.73 | 6.33 | 7.83 | 5.88 | 7.33 | 16.69 | 4.61 | 2.06 | 0.598 |
| $h_{fg}$, kJ/kg | 117 | 233 | 165 | 136 | 180 | 147 | 21 | 199 | 489 | 2253 |
| $\sigma$, N/cm × $10^{-5}$ | 16.8 | 15.4 | 14.7 | 14.1 | 17.8 | 15.2 | 0.12 | 8.85 | 16.31 | 58.9 |
| $q_{max}$, kW/m$^2$ | 186 | 237 | 197 | 205 | 106 | 190 | 6.5 | 142 | 338 | 1200 |
| $q_{min}$, kW/m$^2$ | 18 | 4.0 | 3.7 | 3.8 | 3.4 | 23 | 1.4 | 5.4 | 22 | 25 |
| $\Delta T_{max}$, K | 26 | 26 | 25 | 22 | 28 | 35 | 14.5 | 9.3 | 26 | 22 |
| $\Delta T_{min}$, K | 40 | 66 | 63 | 58 | 66 | 88 | 16 | 22 | 48 | 105 |

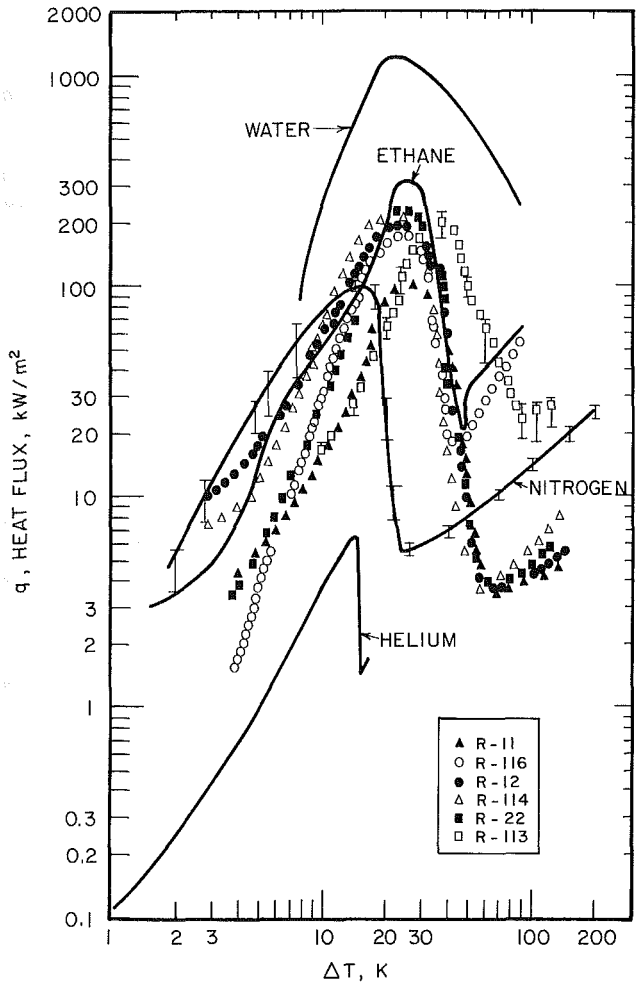


**Fig. 1 Pool boiling curves for ten liquids at atmospheric pressure on mirror-smooth copper; vertical bars illustrate the data scatter for R-113 (three runs) and nitrogen (five runs)**

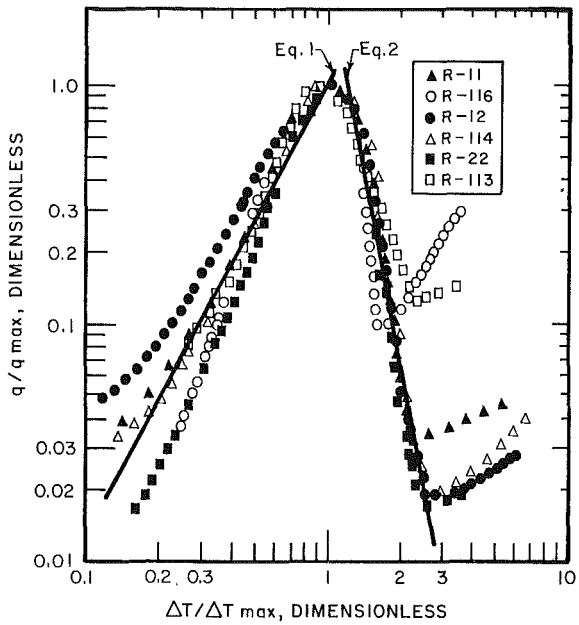


**Fig. 2 Normalized pool boiling curves for freons at atmospheric pressure on mirror-smooth copper**

the freons is not surprising, because the physical properties of the freons are similar even though their atmospheric boiling points range from 195 to 321 K. The surface tensions of the freons vary from 14.1 to 17.8 dyne/cm, and the latent heat is from 117 to 233 kJ/kg.

The freon boiling curves may be normalized. Each heat flux is divided by the maximum heat flux for that liquid, and the corresponding $\Delta T$ is divided by the $\Delta T$ at the maximum heat flux. This was done in Fig. 2. The peak flux crisis has coordinates of unity on both axes. The six curves coincide to a significant degree for the ascending left branch (nucleate boiling) and the descending right branch (transition boiling), but not for film boiling.

For the nucleate boiling regime, a fit for all the freons is equation (1). It is graphed in Fig. 2.

$$q/q_{max} = (\Delta T/\Delta T_{max})^{1.89} \quad (1)$$

(nucleate boiling freons on smooth copper)

The equation is good from about $0.3 < (\Delta T/\Delta T_{max}) < 1.0$. At an abscissa value of 0.3, the mean deviation for the ordinate is 22 percent. The deviation decreases to zero as the normalized $\Delta T$ approaches unity. As the normalized $\Delta T$ decreases below 0.3 the equation is poor. At low $\Delta T$, free convection becomes dominant, and the exponent on $\Delta T$ should be 1.25 to 1.33.

The peak heat flux in Fig. 2 is not a sharp spike. Rather $q_{max}$ is more or less constant for $\Delta T/\Delta T_{max}$ from 1.0 to about 1.2. If electric heat is used, physical burnout does occur at the crisis, and a sharp endpoint is observed. With steam heat, or if the quenching technique is used, a gradual roundoff occurs. The shape of the curve at the peak is dependent also on the thermal mass of the heater. A "large" thermal mass was used herein for the freons.

For the transition boiling regime, a fit for all the freons is equation (2). It is graphed in Fig. 2.

$$q/q_{max} = 2.60(\Delta T/\Delta T_{max})^{-5.31} \quad (2)$$

(transition boiling freons on smooth copper)

The equation is excellent for abscissa values from 1.2 to the onset of film boiling. For example at an abscissa value of 2, four freons are still in the transition boiling regime, and the

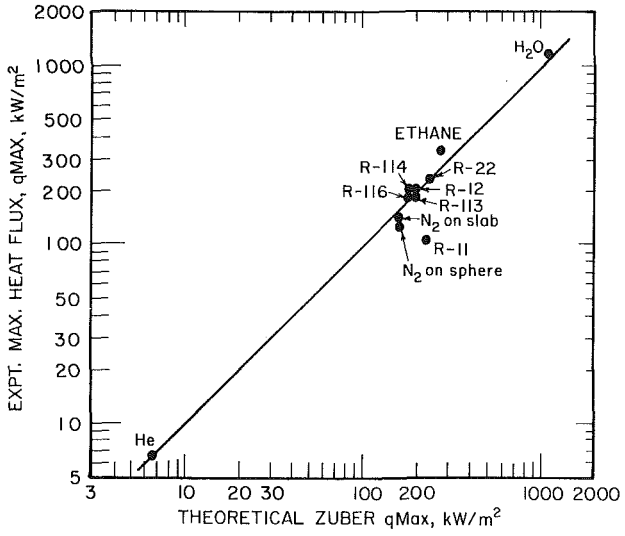


**Fig. 3 Comparison of the Zuber prediction of the maximum pool-boiling heat flux with the measured values for ten liquids at atmospheric pressure on mirror-smooth copper**

mean deviation of the ordinate from the normalized curve is only 6 percent. The usable range of equation (2) is: $1.2\ \Delta T_{max} < \Delta T < \Delta T_{min}$. At high $\Delta T$ values, film boiling occurs, and the exponent on $\Delta T$ is usually about 0.75.

Film boiling curves are seen as ascending lines on the far right side of Fig. 2. They are not coincident when this style of normalized graphing is used. Fortunately, prior equations exist that give good values for $q$ versus $\Delta T$ in film boiling (Bromley, 1950; Breen and Westwater, 1962; Sakurai et al., 1984).

Figure 2 does not show normalized curves for the four non-freons. Water, helium, and nitrogen give poor fits to the "universal" curves for freons. Ethane comes closer, but we do not recommend that it be considered as equivalent.

## Use of the Homologous Group Correlation

If one intends to use a different member of the homologous series, that is a freon which has not been tested, how may one proceed? If the intended use is on smooth copper, the general correlation of Fig. 2 should apply. It is necessary to locate a specific point on the graph. The obvious choice is the peak heat flux and its driving force, that is, $q_{max}$ and $\Delta T_{max}$. The value of the peak flux poses no problem, because it may be predicted from the theoretical equation (3) by Zuber (1958)

$$q_{max} = (\pi/24) h_{fg} \rho_v^{0.5} [g\sigma(\rho_L - \rho_v)]^{0.25} \quad (3)$$

or from some recent modifications of the same, for example Lienhard and Dhir (1973).

The line in Fig. 3 shows that equation (3) gives good agreement with the observed peak heat flux for nine of the ten liquids. Only freon-11 has unsatisfactory agreement. The mean of the absolute values of the deviation between the observed values and the theoretical values in Fig. 3 is 9.0 percent excluding freon-11, or 18.8 percent including freon-11. According to Zuber, equation (3) has an inherent uncertainty of ±12 percent. We conclude that the Zuber equation is reasonable for an estimate of $q_{max}$.

Prediction of the critical driving force $\Delta T_{max}$ is unreliable at present. For decades it has been known that $\Delta T_{max}$ is a strong function of the surface texture. In addition, it depends on the metal used (Lin and Westwater, 1982). At present its value is best determined experimentally.

There exists a real need for an improved method for predicting $\Delta T_{max}$. This requires the prediction of the number of nucleation sites for bubble formation not only as a function of the $\Delta T$ but also as a function of the metal used and its surface preparation (machining, polishing, fouling, corrosion).

Once the peak point is fixed for the new freon, the normalized boiling curves for nucleate boiling and transition boiling in Fig. 2 are assumed to apply. Equation (1) holds from about $0.3\ \Delta T_{max}$ to $\Delta T_{max}$; $q_{max}$ persists from $\Delta T_{max}$ to about $1.2\ \Delta T_{max}$; and equation (2) applies from $1.2\ \Delta T_{max}$ to $\Delta T_{min}$ or from $q_{max}$ down to $q_{min}$. The minimum flux may be predicted by one of various relationships, such as those of Zuber (1958), Berenson (1961), or Lienhard and Dhir (1980). The corresponding $\Delta T_{min}$ may also be predicted, but with less reliability, from published relationships such as those of Berenson (1961), Lienhard and Wong (1964), or Nishio (1987). For film boiling one of the various prior equations should be used.

An alternate way of predicting the boiling curve for a new freon is to work backward from the film boiling crisis that occurs at $q_{min}$, $\Delta T_{min}$. One would select published equations such as mentioned above to predict $q_{min}$, $\Delta T_{min}$, and $q_{max}$. The ratio of $q_{min}/q_{max}$ will lie on the normalized transition-boiling line in Fig. 2. The abscissa value read from the graph is the ratio $\Delta T_{min}/\Delta T_{max}$. From that, $\Delta T_{max}$ is found, and we can proceed to calculate the peak flux crisis point and the rest of the complete boiling curve. The reliability of this procedure remains to be tested.

## Conclusions

It is interesting to speculate further. For every homologous group, for example the simple alcohols, the straight chain hydrocarbons, or the aromatics (benzene, toluene, xylenes), we expect that a general normalized boiling curve exists. The relationship will not be identical with Fig. 2, unless the physical properties fall within the range of the freon properties in Table 1. The surface texture of the heater will be an important variable, because it affects nucleate boiling and the value of $\Delta T_{max}$. The choice of metal can become a significant parameter, particularly if the solid has a poor conductivity.

We conclude that it is not necessary for anyone to produce a reference book with thousands of experimental boiling curves, one for each known liquid. Instead, the profession can manage with appropriate curves for homologous groups. This paper demonstrates that conclusion for freons.

## Acknowledgments

Financial assistance was provided by the National Science Foundation. Graduate fellowships were furnished by E. I. DuPont Co. and General Electric Co.

## References

Berenson, P. J., 1961, "Film Boiling Heat Transfer From a Horizontal Surface," ASME JOURNAL OF HEAT TRANSFER, Vol. 83, pp. 351–362.

Breen, B. P., and Westwater, J. W., 1962, "Effect of Diameter of Horizontal Tubes on Film Boiling Heat Transfer," *Chem. Eng. Progress*, Vol. 58, No. 7, pp. 67–72.

Brodbeck, K. J., 1987, "Effects of Thermophysical Properties on the Boiling Curves of Five Freons," M.S. Thesis, Chemical Engineering Department, University of Illinois, Urbana, IL.

Bromley, L. A., 1950, "Heat Transfer in Stable Film Boiling," *Chem. Eng. Progress*, Vol. 46, pp. 221–227.

Broussard, R. A., and Westwater, J. W., 1985, "Diameter and Velocity Effects for Cross-Flow Boiling," *AIAA Journal*, Vol. 23, No. 10, pp. 1615–1620.

DuPont Co., 1969, *Freon Product Information B-2*, E. I. duPont de Nemours and Co., Wilmington, Del., 10 pages; also see Bulletin T-113B, *Properties of Freon-113*, no date, Bulletin T-11-B, *Thermodynamic Properties of Freon-11*, 1938, and Bulletin D-27A, *Surface Tension of Freon-12 and Freon-22*, 1960.

Egan, J. P., and Westwater, J. W., 1985, "Effect of Horizontal Plate Diameter on Boiling Heat Transfer From Copper to Nitrogen," *J. Thermal Engineering*, Vol. 4, No. 1, pp. 1–12.

Irving, M. E., and Westwater, J. W., 1986, "Limitations for Obtaining Boiling Curves by the Quenching Method With Spheres," *Proceedings, 8th Interna-*

*tional Heat Transfer Conference*, C. L. Tien et al., eds., Hemisphere, Washington, DC, Vol. 4, pp. 2061–2066.

Lienhard, J. H., and Dhir, V. K., 1973, "Hydrodynamic Prediction of Peak Pool Boiling Heat Fluxes From Finite Bodies," ASME JOURNAL OF HEAT TRANSFER, Vol. 95, pp. 152–158.

Lienhard, J. H., and Dhir, V. K., 1980, "On the Prediction of the Minimum Pool Boiling Heat Flux," ASME JOURNAL OF HEAT TRANSFER, Vol. 102, pp. 457–460.

Lienhard, J. H., and Wong, P. T. Y., 1964, "The Dominant Unstable Wavelength and Minimum Heat Flux During Film Boiling on a Horizontal Cylinder," ASME JOURNAL OF HEAT TRANSFER, Vol. 86, pp. 220–226.

Lin, D. Y. T., and Westwater, J. W., 1982, "Effect of Metal Thermal Properties on Boiling Curves Obtained by the Quenching Method," *Proceedings, 7th International Heat Transfer Conference*, V. Grigull et al., eds., Hemisphere, Washington, DC, Vol. 4, pp. 155–160.

McAdams, W. H., 1954, *Heat Transmission*, 3rd ed., McGraw-Hill, New York, p. 380.

Nishio, S., 1987, "Prediction Technique for Minimum Heat Flux (MHF) Point Condition of Saturated Pool Boiling," *Int. J. Heat Mass Transfer*, Vol. 30, pp. 2045–2057.

Peyayopanakul, W., and Westwater, J. W., 1978, "Evaluation of the Unsteady State Quenching Method for Determining Boiling Curves," *Int. J. Heat Mass Transfer*, Vol. 21, pp. 1437–1445.

Sakurai, A., Shiotsu, M., and Hata, K., 1984, "Film Boiling Heat Transfer on Horizontal Cylinder (II)," *Proc. 21st National Heat Transfer Symp. Japan*, pp. 466–468.

Westwater, J. W., Hwalek, J. J., and Irving, M. E., 1986, "Suggested Standard Method for Obtaining Boiling Curves by Quenching," *I and EC Fundamentals*, Vol. 25, No. 4, pp. 685–692.

Zinn, J. C., 1984, "Determining Boiling Curves of Different Liquids by the Quenching Method," M.S. Thesis, Chemical Engineering Department, University of Illinois, Urbana, IL.

Zuber, N., 1958, "On the Stability of Boiling Heat Transfer," *Trans. ASME*, Vol. 80, pp. 711–720.

## Water-Injection Effect on Boiling Heat Transfer in a Water-Saturated Porous Bed

**S. Fukusako[1] and N. Hotta[2]**

### Nomenclature

$A$ = area of heating surface
$C$ = specific heat
$d_p$ = diameter of beads
$g$ = gravitational acceleration
$H$ = height of water-saturated porous bed
$L$ = latent heat of evaporation
$M$ = water-injection rate
$m$ = mass flux of water injection $= M/A$
Nu = Nusselt number $= qd_p/(\Delta T_s \lambda_{ml})$
Pr = Prandtl number
$q$ = heat flux
$\mathrm{Re}_m$ = modified Reynolds number $= d_p m(\mu_l \epsilon)$
$T_s$ = temperature of saturated water
$T_w$ = temperature of heating surface
$\Delta T_s$ = temperature difference between heating surface and saturated water $= T_w - T_s$
$\epsilon$ = void fraction
$\lambda$ = thermal conductivity
$\mu$ = viscosity
$\rho$ = density
$\sigma$ = surface tension

#### Subscripts

$l$ = liquid
$m$ = equivalent
$p$ = bead particles
$v$ = vapor

### Introduction

A number of experimental studies of boiling heat transfer in liquid-saturated porous media have been motivated by such diverse technological problems as high-flux heat transfer porous surface, geothermal energy extraction, and heat-transport characteristics in heat pipes (e.g., Costello and Redeker, 1963; Cornwell et al., 1976; Sugawara et al., 1978; Nakayama et al., 1980; Sommerton et al., 1981; Bergles and Chyu, 1982; Itoh et al., 1982; Bau and Torrance, 1982). Most of the previous studies of boiling heat transfer in liquid-saturated porous layers have been carried out for the purpose of finding methods to augment nucleate pool boiling.

Recently, Fukusako et al. (1986) conducted an experimental sutdy of the boiling heat transfer characteristics of a liquid-saturated porous bed. They focused their attention in particular on the effect of diameter of the beads on boiling behavior in both transition boiling and film boiling regions, and found that for small bead diameters, the heat flux $q$ rose both continuously and monotonically with temperature difference $\Delta T_s$ from nucleate boiling to film boiling without going through a peak heat flux.

From the literature survey, it is apparent that very little is known about the boiling heat transfer behavior in a saturated porous bed with liquid injection to the heating surface, which appears to provide the fundamental data for the geothermal energy-extraction technology.

The objective of this technical note is to report the results of an experimental study of the effect of saturated-water injection on boiling heat transfer in a water-saturated porous bed.

### Experimental Apparatus and Procedure

The schematic diagram of the experimental setup is shown in Fig. 1. The apparatus consists of an inner Pyrex tube 60 mm in diameter and 80 mm in height and an outer Pyrex tube 220 mm in diameter and 150 mm in height. The inner tube was filled with a water-saturated porous bed, while the other annulus was used as both an insulating thermal guard and a saturation-water storage. In order to maintain the saturation temperature within the inner tube, four guard heaters were inserted in the annulus.

The inner tube and the outer annulus were filled to the same height with saturated water and a constant water level was held above the heating surface. To prevent fluidization of the porous bed, a screen plate (12 or 18 mesh, depending on bead diameter) was attached to the top of the inner tube. All of the data reported here were obtained at atmospheric pressure. As is shown in Fig. 1, a water make-up tank, condensate collection equipment, and a reservoir tank for maintaining system pressure and water level were used. Water injection was accomplished using three stainless tubes 3 mm in diameter, which were arranged in a triangular array (distance between tubes is 25 mm) at a distance of about 2 mm from the heating

[1]Professor, Department of Mechanical Engineering, Hokkaido University, Sapporo 060, Japan.

[2]Graduate Student, Department of Mechanical Engineering, Hokkaido University, Sapporo 060, Japan.

Contributed by the Heat Transfer Division for publication in the JOURNAL OF HEAT TRANSFER. Manuscript received by the Heat Transfer Division October 27, 1986. Keywords: Boiling, Porous Media.

*tional Heat Transfer Conference*, C. L. Tien et al., eds., Hemisphere, Washington, DC, Vol. 4, pp. 2061–2066.

Lienhard, J. H., and Dhir, V. K., 1973, "Hydrodynamic Prediction of Peak Pool Boiling Heat Fluxes From Finite Bodies," ASME JOURNAL OF HEAT TRANSFER, Vol. 95, pp. 152–158.

Lienhard, J. H., and Dhir, V. K., 1980, "On the Prediction of the Minimum Pool Boiling Heat Flux," ASME JOURNAL OF HEAT TRANSFER, Vol. 102, pp. 457–460.

Lienhard, J. H., and Wong, P. T. Y., 1964, "The Dominant Unstable Wavelength and Minimum Heat Flux During Film Boiling on a Horizontal Cylinder," ASME JOURNAL OF HEAT TRANSFER, Vol. 86, pp. 220–226.

Lin, D. Y. T., and Westwater, J. W., 1982, "Effect of Metal Thermal Properties on Boiling Curves Obtained by the Quenching Method," *Proceedings, 7th International Heat Transfer Conference*, V. Grigull et al., eds., Hemisphere, Washington, DC, Vol. 4, pp. 155–160.

McAdams, W. H., 1954, *Heat Transmission*, 3rd ed., McGraw-Hill, New York, p. 380.

Nishio, S., 1987, "Prediction Technique for Minimum Heat Flux (MHF) Point Condition of Saturated Pool Boiling," *Int. J. Heat Mass Transfer*, Vol. 30, pp. 2045–2057.

Peyayopanakul, W., and Westwater, J. W., 1978, "Evaluation of the Unsteady State Quenching Method for Determining Boiling Curves," *Int. J. Heat Mass Transfer*, Vol. 21, pp. 1437–1445.

Sakurai, A., Shiotsu, M., and Hata, K., 1984, "Film Boiling Heat Transfer on Horizontal Cylinder (II)," *Proc. 21st National Heat Transfer Symp. Japan*, pp. 466–468.

Westwater, J. W., Hwalek, J. J., and Irving, M. E., 1986, "Suggested Standard Method for Obtaining Boiling Curves by Quenching," *I and EC Fundamentals*, Vol. 25, No. 4, pp. 685–692.

Zinn, J. C., 1984, "Determining Boiling Curves of Different Liquids by the Quenching Method," M.S. Thesis, Chemical Engineering Department, University of Illinois, Urbana, IL.

Zuber, N., 1958, "On the Stability of Boiling Heat Transfer," *Trans. ASME*, Vol. 80, pp. 711–720.

# Water-Injection Effect on Boiling Heat Transfer in a Water-Saturated Porous Bed

**S. Fukusako[1] and N. Hotta[2]**

## Nomenclature

$A$ = area of heating surface
$C$ = specific heat
$d_p$ = diameter of beads
$g$ = gravitational acceleration
$H$ = height of water-saturated porous bed
$L$ = latent heat of evaporation
$M$ = water-injection rate
$m$ = mass flux of water injection $= M/A$
Nu = Nusselt number $= qd_p/(\Delta T_s \lambda_{ml})$
Pr = Prandtl number
$q$ = heat flux
$\mathrm{Re}_m$ = modified Reynolds number $= d_p m(\mu_l \epsilon)$
$T_s$ = temperature of saturated water
$T_w$ = temperature of heating surface
$\Delta T_s$ = temperature difference between heating surface and saturated water $= T_w - T_s$
$\epsilon$ = void fraction
$\lambda$ = thermal conductivity
$\mu$ = viscosity
$\rho$ = density
$\sigma$ = surface tension

### Subscripts

$l$ = liquid
$m$ = equivalent
$p$ = bead particles
$v$ = vapor

## Introduction

A number of experimental studies of boiling heat transfer in liquid-saturated porous media have been motivated by such diverse technological problems as high-flux heat transfer porous surface, geothermal energy extraction, and heat-transport characteristics in heat pipes (e.g., Costello and Redeker, 1963; Cornwell et al., 1976; Sugawara et al., 1978; Nakayama et al., 1980; Sommerton et al., 1981; Bergles and Chyu, 1982; Itoh et al., 1982; Bau and Torrance, 1982). Most of the previous studies of boiling heat transfer in liquid-saturated porous layers have been carried out for the purpose of finding methods to augment nucleate pool boiling.

Recently, Fukusako et al. (1986) conducted an experimental sutdy of the boiling heat transfer characteristics of a liquid-saturated porous bed. They focused their attention in particular on the effect of diameter of the beads on boiling behavior in both transition boiling and film boiling regions, and found that for small bead diameters, the heat flux $q$ rose both continuously and monotonically with temperature difference $\Delta T_s$ from nucleate boiling to film boiling without going through a peak heat flux.

From the literature survey, it is apparent that very little is known about the boiling heat transfer behavior in a saturated porous bed with liquid injection to the heating surface, which appears to provide the fundamental data for the geothermal energy-extraction technology.

The objective of this technical note is to report the results of an experimental study of the effect of saturated-water injection on boiling heat transfer in a water-saturated porous bed.

## Experimental Apparatus and Procedure

The schematic diagram of the experimental setup is shown in Fig. 1. The apparatus consists of an inner Pyrex tube 60 mm in diameter and 80 mm in height and an outer Pyrex tube 220 mm in diameter and 150 mm in height. The inner tube was filled with a water-saturated porous bed, while the other annulus was used as both an insulating thermal guard and a saturation-water storage. In order to maintain the saturation temperature within the inner tube, four guard heaters were inserted in the annulus.

The inner tube and the outer annulus were filled to the same height with saturated water and a constant water level was held above the heating surface. To prevent fluidization of the porous bed, a screen plate (12 or 18 mesh, depending on bead diameter) was attached to the top of the inner tube. All of the data reported here were obtained at atmospheric pressure. As is shown in Fig. 1, a water make-up tank, condensate collection equipment, and a reservoir tank for maintaining system pressure and water level were used. Water injection was accomplished using three stainless tubes 3 mm in diameter, which were arranged in a triangular array (distance between tubes is 25 mm) at a distance of about 2 mm from the heating

[1]Professor, Department of Mechanical Engineering, Hokkaido University, Sapporo 060, Japan.

[2]Graduate Student, Department of Mechanical Engineering, Hokkaido University, Sapporo 060, Japan.

Contributed by the Heat Transfer Division for publication in the JOURNAL OF HEAT TRANSFER. Manuscript received by the Heat Transfer Division October 27, 1986. Keywords: Boiling, Porous Media.

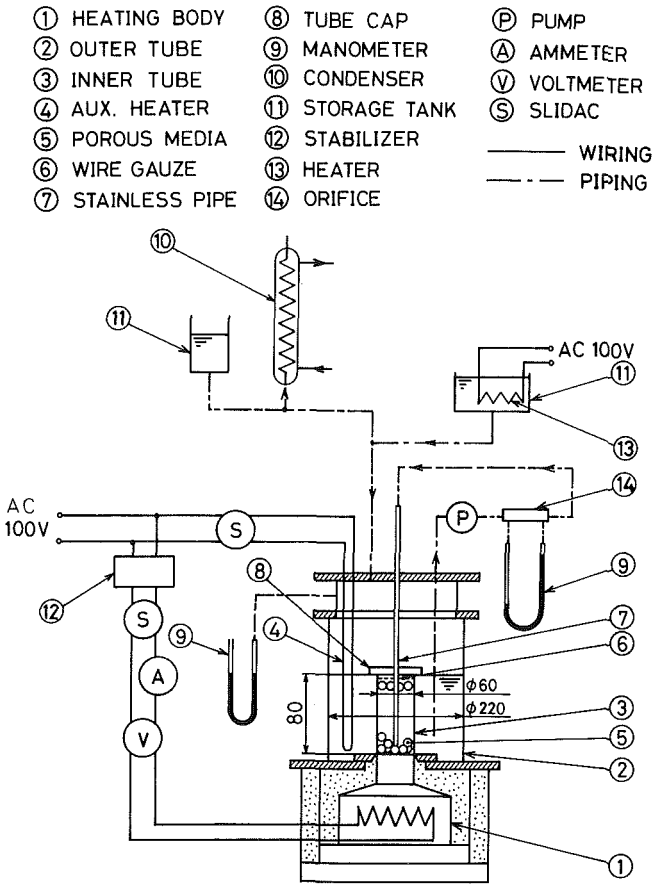


Fig. 1 Schematic diagram of experimental setup

Table 1 Dimensions of beads

| MATERIAL | $d_p$ mm | $\lambda_p$ W/m·K | ε |
|---|---|---|---|
| ALUMINA | 1.9 | 1.59 | 0.40 |
| | 5.2 | | 0.41 |
| | 10.0 | | 0.44 |
| GLASS | 5.3 | 0.74 | 0.42 |
| STEEL | 4.0 | 40.2 | 0.42 |

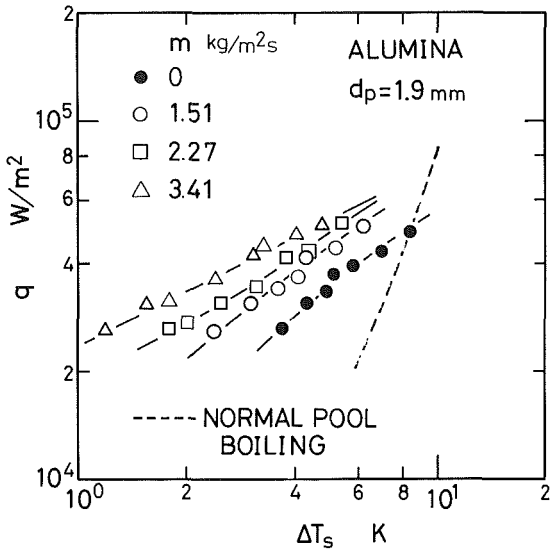


Fig. 2 Effect of water injection on boiling heat transfer

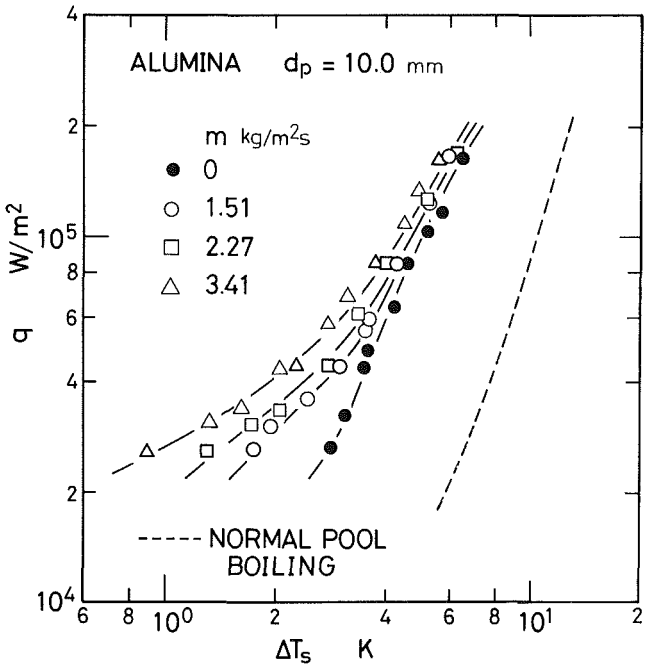


Fig. 3 Effect of water injection on boiling heat transfer

surface. Saturated water from the annulus was supplied to the tubes by a gear pump. The injection rate was accurately measured using a calibrated orifice meter. The water-injection rate was varied from 0.98 to 3.41 kg/m²s, which corresponds to a water velocity of 0.16 to 0.35 m/s at the tube nozzle.

The heater assembly included a cylindrical copper block 80 mm in diameter and 172 mm in height on top, and the main mica heaters, inserted into the copper fins below. Nine copper-constantan thermocouples positioned radially at three levels in the upper heater block were arranged axially. The surface temperature was estimated by extrapolating the temperature distributions obtained by the thermocouples. The heat flux was assessed by measuring the temperature gradient along the central axis.

Commercially available spherical materials were utilized for the porous bed. They included three kinds of spherical beads with diameters ranging from 1.9 to 10.0 mm, as listed in Table 1. Prior to the experiments, the spherical beads and the tubes were thoroughly washed with acetone and water. The depth of the porous bed overlying the heating surface was 80 mm. Experiments were carried out by starting from a quiescent initial state where the porous bed was in the saturation condition. It took about 1 to 3 h to reach steady state.

## Results and Discussion

Measurements were performed as the temperature differences between the heating surface and the saturated water varied from 0.9 to 15.5 K. An error in temperature measurement by the thermocouples was 0.2 K; thus the relative error was ±0.8 percent for most runs. The water-injection rate was measured with an orifice meter; the experimental error for the injection was predicted to be on the order of ±2.1 percent.

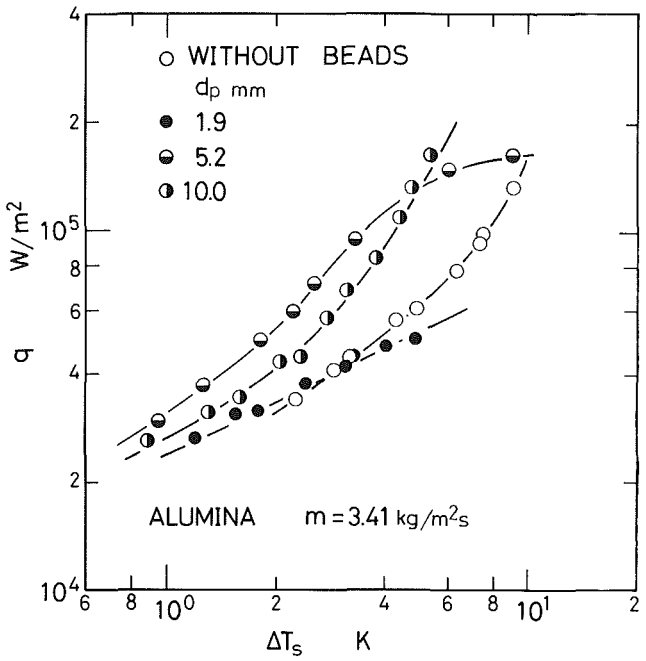


Fig. 4 Effect of bead diameter on boiling heat transfer

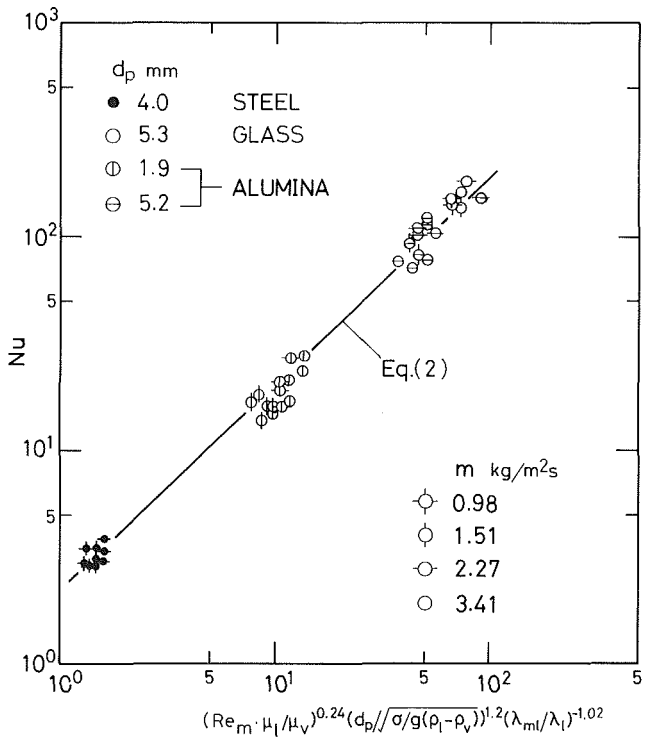


Fig. 5 Correlation of boiling heat transfer with water injection

The error in thermal conductivity of the copper block for the temperature range covered was estimated to be within ±0.6 percent. The area $A$ was measured within an error of ±0.4 percent. Consequently, the maximum indeterminant error for the boiling curve may amount to ±4.8 percent. Complete documentation of the data is given by Hotta (1984).

**Effect of Water Injection on Boiling Heat Transfer.** The experimental data of boiling heat transfer with water injection for alumina beads are presented in Figs. 2 and 3. In each figure, the ordinate is the heat flux $q$ at the heating surface, while the abscissa is the temperature difference $\Delta T_s$ between the heating surface and the saturated water. In the figures, the data for pool boiling with and without a porous bed are presented for comparison. There are, moreover, three groupings of data, which correspond to water-injection rates of 1.51, 2.27, and 3.41 kg/(m²s). With respect to the effects of water injection, the following three factors are to be considered: (1) The liquid may be both successfully and directly supplied to the heating surface. (2) The liquid flow caused by the water injection may help the bubbles depart easily from the heating surface. (3) Water injection may promote mixing between the superheated-liquid layer just adjacent to the heating surface and the surrounding saturated liquid.

Inspection of the figures reveals that for smaller $\Delta T_s$ the heat fluxes with water injection increase appreciably in comparison with those for porous bed without water injection. It is also observed in the figures that the effect of water injection of the boiling heat transfer decreases with an increase in $\Delta T_s$. This appears to indicate that when the heating surface becomes densely populated with bubbles the effect of water jet and water supply based on the water injection is unexpectedly small.

**Effect of Bead Diameter on Boiling Heat Transfer.** Figure 4 shows the effect of bead diameter on boiling heat transfer for $m = 3.41$ kg/(m²s). The figure also includes data for pool boiling (without porous bed) with water injection for comparison. As shown in the figure, for the lower $\Delta T_s$, the $q$ values for $d_p = 5.2$ mm are the greatest, while for the higher $\Delta T_s$, the heat fluxes for $d_p = 10.0$ mm are the greatest. It is also observed that the boiling curve tends to level off at smaller $\Delta T_s$ with decreasing bead diameter. These characteristics were also observed for boiling heat transfer in a porous bed without liquid injection (Fukusako et al., 1986).

For the boiling within a water-saturated porous bed, there might be in general three main factors affecting the boiling performance, based on the particles being in contact with the heating surface, as pointed out by both Bergles and Chyu (1982) and Fukusako et al. (1986). The first of the factors is that additional nucleation sites may be available due to cavities being formed between the beads and the heating surface. The second one is the fin-like character of the beads being directly in contact with the heating surface. The third one is that the beads may disturb both the growth of the steam bubbles and the smooth departure of the bubbles from the heating surface. In addition to the effects mentioned above, the existence of the beads may cause an increase in hydrodynamic resistance for both the liquid and steam bubbles to pass through the small passages of the porous structure. It appears that the former two factors may enhance boiling heat transfer, while the latter two factors may inhibit it.

As $\Delta T_s$ increases, the nuclei of the steam bubble increase gradually, which tends to result in a dense bubble cover over the heating surface. For smaller bead diameters, the void spaces among the beads are quite small, interfering with bubble growth and interrupting bubble departure from the heating surface. Furthermore, the liquid supply to the heating surface through the small passages composed of small beads may be obstructed. Thus, in the relationship $q \sim \Delta T_s^n$, the value of $n$ for the boiling curve with a porous bed tends to be quite a bit less than that for normal pool boiling. On the other hand, for larger bead diameters, the growth of the bubbles, departure of the bubbles from the heating surface, and liquid supply to the heating surface may occur more easily because of the larger passages through the large beads. It seems that the $q$ value at even larger $\Delta T_s$ may not decrease. Thus, it might be concluded that the effect of bead diameter on boiling heat transfer with water injection is fundamentally similar to that without water injection.

**Correlation Equation.** Attention will now be turned to the correlation of the resulting heat-flux data with water injection. It was found that the heat transfer coefficient, defined in terms of the difference between the heating surface and saturation water temperatures, might be expressed by the following functional relation among dimensionless groups:

$$\mathrm{Nu} = f[\mathrm{Re}_m,\ d_p/\sqrt{\sigma/g(\rho_l-\rho_v)},\ \mathrm{Pr}_l,\ \lambda_{ml}/\lambda_l,\ \mu_l/\mu_v] \quad (1)$$

where $\lambda_{ml}$ is the equivalent thermal conductivity, defined as $\lambda_{ml} = \epsilon\lambda_l + (1-\epsilon)\lambda_p$ where $\epsilon$ is the void fraction of the porous bed.

The data, except those for $d_p = 10.0$ mm, for $0.9 \le \Delta T_s \le 6.5$ K are plotted in terms of dimensionless groups in Fig. 5. A best fit through these points yields the final correlation equation in the form

$$\mathrm{Nu} = 2.23(\mathrm{Re}_m \cdot \mu_l/\mu_v)^{0.24}[d_p/\sqrt{\sigma/g(\rho_l-\rho_v)}]^{1.20}(\lambda_{ml}/\lambda_l)^{-1.02} \quad (2)$$

## Conclusions

An experimental study of boiling heat transfer in a water-saturated porous bed with water injection was carried out. Pure water was used as a testing liquid. The following conclusions may be drawn within the parameters covered in the present experiments:

1 For small $\Delta T_s$ the boiling heat flux with water injection increases appreciably in comparison with that without water injection, while for large $\Delta T_s$ the effect of water injection on boiling heat transfer tends to fall off.

2 The heat transfer coefficients in boiling heat transfer with water injection in the range $0.9 \le \Delta T_s \le 6.5$ K might be reasonably correlated by equation (2).


## Acknowledgments

The authors are indebted to Professor Emeritus N. Seki, the president of Hokkaido Polytechnical College, for his advice in preparing the manuscript.


## References


Bau, H. H., and Torrance, K. E., 1982, "Boiling in Low-Permeability Porous Materials," *Int. J. Heat Mass Transfer*, Vol. 25, pp. 45–55.

Bergles, A. E., and Chyu, M. C., 1982, "Characteristics of Nucleate Pool Boiling From Porous Metallic Coatings," ASME JOURNAL OF HEAT TRANSFER, Vol. 104, pp. 279–285.

Cornwell, K., Nair, B. G., and Pattern, T. D., 1976, "Observation of Boiling in Porous Media," *Int. J. Heat Mass Transfer*, Vol. 19, pp. 236–238.

Costello, C. P., and Redeker, E. R., 1963, "Boiling Heat Transfer and Maximum Heat Flux for a Surface With Coolant Supplied by Capillary Wicking," *Chem. Eng. Progr. Symposium Ser.*, No. 41, Vol. 59, pp. 104–113.

Fukusako, S., Komoriya, T., and Seki, N., 1986, "An Experimental Study of Transition and Film Boiling Heat Transfer in Liquid-Saturated Porous Bed," ASME JOURNAL OF HEAT TRANSFER, Vol. 108, pp. 117–124.

Hotta, N., 1984, "Boiling Heat-Transfer Characteristics in a Liquid-Saturated Porous Bed," M.E. Thesis, Department of Mechanical Engineering, Hokkaido University, Japan.

Itoh, T., Nishikawa, K., and Tanaka, K., 1982, "Enhanced Heat Transfer by Nucleate Boiling at Sintered Metal Layer; Discussion on Sintered Layer and Experiments by Piled Layer and Form Layer," *Refrigeration*, Vol. 57, pp. 77–81.

Nakayama, W., Daikoku, T., Kuwahara, H., and Nakajima, T., 1980, "Dynamic Model of Enhanced Boiling Heat Transfer on Porous Surfaces. Part I; Experimental Investigation," ASME JOURNAL OF HEAT TRANSFER, Vol. 102, pp. 445–450.

Sommerton, C., Catton, I., and Thompson, L., 1981, "An Experimental Investigation Into Dryout in Deep Debris Bed," ASME Paper No. 81-WA/HT-17.

Sugawara, A., Takahashi, I., Ohba, S., and Sugawara, S., 1978, "Pool Boiling From Surface With Particulated Bed," *15th National Heat Transfer Symposium of Japan*, pp. 169–171.


# Evaporation of a Water Droplet Deposited on a Hot High Thermal Conductivity Surface


**M. di Marzo[1] and D. D. Evans[2]**


## Nomenclature

- $c$ = specific heat
- $D$ = mass diffusivity
- $h$ = overall heat transfer coefficient
- $h_c$ = convective heat transfer coefficient
- $h_m$ = mass transfer coefficient
- $k$ = thermal conductivity
- $M$ = molecular weight
- $q$ = heat flux
- $r$ = radial coordinate tangent to the solid surface orginating at the center of the wetted area
- $R$ = radius of the wetted area
- $s$ = nondimensional thickness of the droplet $= y_i/R$
- $t$ = time
- $T$ = temperature
- $V$ = droplet volume
- $W$ = vapor molar flux
- $x$ = vapor molar fraction
- $y$ = coordinate normal to the solid surface originating at the center of the wetted area
- $z$ = nondimensional radius $= r/R$
- $\alpha$ = thermal diffusivity
- $\beta$ = wetting parameter
- $\gamma$ = shape parameter $= s$ (at $r = 0$)
- $\Lambda$ = latent heat of vaporization
- $\rho$ = density

### Subscripts

- $a$ = air
- $i$ = interface
- $o$ = initial value (at $t = 0$)
- $s$ = solid or solid surface
- $w$ = water

## Introduction

Many studies have been performed to quantify the vaporization process for both single droplets and multiple-droplet arrays impacting on hot surfaces. For the studies found in the published literature, the full span of the droplet vaporization processes is usually reported. These would include evaporation, nucleate boiling, film boiling, and Leidenfrost transition. The present investigation is limited in the span of vaporization processes studied, being only concerned with the evaporation of a droplet on a hot surface. The study does report very detailed results for spatial and temporal variation of the heat flux at the exposed surface of the droplet, and for temporal variation of the droplet volume. Limiting the study to evaporation implies that conditions are maintained under which nucleate boiling is fully suppressed.


[1]Mechanical Engineering Department, University of Maryland, College Park, MD 20742.

[2]Center for Fire Research, National Bureau of Standards, Gaithersburg, MD 20899.



Contributed by the Heat Transfer Division for publication in the JOURNAL OF HEAT TRANSFER. Manuscript received by the Heat Transfer Division November 18, 1986. Keywords: Evaporation, Sprays/Droplets, Transient and Unsteady Heat Transfer.

**Correlation Equation.** Attention will now be turned to the correlation of the resulting heat-flux data with water injection. It was found that the heat transfer coefficient, defined in terms of the difference between the heating surface and saturation water temperatures, might be expressed by the following functional relation among dimensionless groups:

$$\mathrm{Nu} = f[\mathrm{Re}_m,\ d_p/\sqrt{\sigma/g(\rho_l-\rho_v)},\ \mathrm{Pr}_l,\ \lambda_{ml}/\lambda_l,\ \mu_l/\mu_v] \quad (1)$$

where $\lambda_{ml}$ is the equivalent thermal conductivity, defined as $\lambda_{ml} = \epsilon\lambda_l + (1-\epsilon)\lambda_p$ where $\epsilon$ is the void fraction of the porous bed.

The data, except those for $d_p = 10.0$ mm, for $0.9 \le \Delta T_s \le 6.5$ K are plotted in terms of dimensionless groups in Fig. 5. A best fit through these points yields the final correlation equation in the form

$$\mathrm{Nu} = 2.23(\mathrm{Re}_m \cdot \mu_l/\mu_v)^{0.24}[d_p/\sqrt{\sigma/g(\rho_l-\rho_v)}]^{1.20}(\lambda_{ml}/\lambda_l)^{-1.02} \quad (2)$$

## Conclusions

An experimental study of boiling heat transfer in a water-saturated porous bed with water injection was carried out. Pure water was used as a testing liquid. The following conclusions may be drawn within the parameters covered in the present experiments:

1 For small $\Delta T_s$ the boiling heat flux with water injection increases appreciably in comparison with that without water injection, while for large $\Delta T_s$ the effect of water injection on boiling heat transfer tends to fall off.

2 The heat transfer coefficients in boiling heat transfer with water injection in the range $0.9 \le \Delta T_s \le 6.5$ K might be reasonably correlated by equation (2).


## Acknowledgments

The authors are indebted to Professor Emeritus N. Seki, the president of Hokkaido Polytechnical College, for his advice in preparing the manuscript.


## References


Bau, H. H., and Torrance, K. E., 1982, "Boiling in Low-Permeability Porous Materials," *Int. J. Heat Mass Transfer*, Vol. 25, pp. 45–55.

Bergles, A. E., and Chyu, M. C., 1982, "Characteristics of Nucleate Pool Boiling From Porous Metallic Coatings," ASME JOURNAL OF HEAT TRANSFER, Vol. 104, pp. 279–285.

Cornwell, K., Nair, B. G., and Pattern, T. D., 1976, "Observation of Boiling in Porous Media," *Int. J. Heat Mass Transfer*, Vol. 19, pp. 236–238.

Costello, C. P., and Redeker, E. R., 1963, "Boiling Heat Transfer and Maximum Heat Flux for a Surface With Coolant Supplied by Capillary Wicking," *Chem. Eng. Progr. Symposium Ser.*, No. 41, Vol. 59, pp. 104–113.

Fukusako, S., Komoriya, T., and Seki, N., 1986, "An Experimental Study of Transition and Film Boiling Heat Transfer in Liquid-Saturated Porous Bed," ASME JOURNAL OF HEAT TRANSFER, Vol. 108, pp. 117–124.

Hotta, N., 1984, "Boiling Heat-Transfer Characteristics in a Liquid-Saturated Porous Bed," M.E. Thesis, Department of Mechanical Engineering, Hokkaido University, Japan.

Itoh, T., Nishikawa, K., and Tanaka, K., 1982, "Enhanced Heat Transfer by Nucleate Boiling at Sintered Metal Layer; Discussion on Sintered Layer and Experiments by Piled Layer and Form Layer," *Refrigeration*, Vol. 57, pp. 77–81.

Nakayama, W., Daikoku, T., Kuwahara, H., and Nakajima, T., 1980, "Dynamic Model of Enhanced Boiling Heat Transfer on Porous Surfaces. Part I; Experimental Investigation," ASME JOURNAL OF HEAT TRANSFER, Vol. 102, pp. 445–450.

Sommerton, C., Catton, I., and Thompson, L., 1981, "An Experimental Investigation Into Dryout in Deep Debris Bed," ASME Paper No. 81-WA/HT-17.

Sugawara, A., Takahashi, I., Ohba, S., and Sugawara, S., 1978, "Pool Boiling From Surface With Particulated Bed," *15th National Heat Transfer Symposium of Japan*, pp. 169–171.


# Evaporation of a Water Droplet Deposited on a Hot High Thermal Conductivity Surface


**M. di Marzo[1] and D. D. Evans[2]**


## Nomenclature

- $c$ = specific heat
- $D$ = mass diffusivity
- $h$ = overall heat transfer coefficient
- $h_c$ = convective heat transfer coefficient
- $h_m$ = mass transfer coefficient
- $k$ = thermal conductivity
- $M$ = molecular weight
- $q$ = heat flux
- $r$ = radial coordinate tangent to the solid surface orginating at the center of the wetted area
- $R$ = radius of the wetted area
- $s$ = nondimensional thickness of the droplet $= y_i/R$
- $t$ = time
- $T$ = temperature
- $V$ = droplet volume
- $W$ = vapor molar flux
- $x$ = vapor molar fraction
- $y$ = coordinate normal to the solid surface originating at the center of the wetted area
- $z$ = nondimensional radius $= r/R$
- $\alpha$ = thermal diffusivity
- $\beta$ = wetting parameter
- $\gamma$ = shape parameter $= s$ (at $r = 0$)
- $\Lambda$ = latent heat of vaporization
- $\rho$ = density

### Subscripts

- $a$ = air
- $i$ = interface
- $o$ = initial value (at $t = 0$)
- $s$ = solid or solid surface
- $w$ = water

## Introduction

Many studies have been performed to quantify the vaporization process for both single droplets and multiple-droplet arrays impacting on hot surfaces. For the studies found in the published literature, the full span of the droplet vaporization processes is usually reported. These would include evaporation, nucleate boiling, film boiling, and Leidenfrost transition. The present investigation is limited in the span of vaporization processes studied, being only concerned with the evaporation of a droplet on a hot surface. The study does report very detailed results for spatial and temporal variation of the heat flux at the exposed surface of the droplet, and for temporal variation of the droplet volume. Limiting the study to evaporation implies that conditions are maintained under which nucleate boiling is fully suppressed.


[1]Mechanical Engineering Department, University of Maryland, College Park, MD 20742.

[2]Center for Fire Research, National Bureau of Standards, Gaithersburg, MD 20899.



Contributed by the Heat Transfer Division for publication in the JOURNAL OF HEAT TRANSFER. Manuscript received by the Heat Transfer Division November 18, 1986. Keywords: Evaporation, Sprays/Droplets, Transient and Unsteady Heat Transfer.

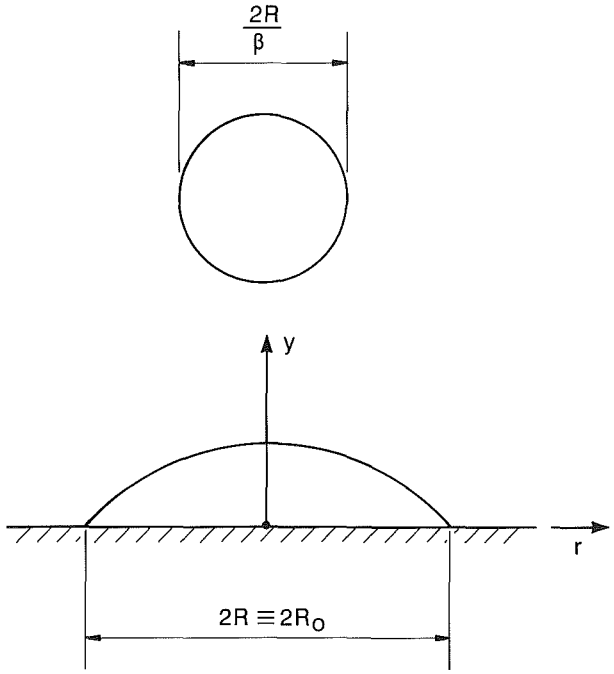


**Fig. 1 Parameter $\beta$ and coordinate system**

## Phenomenology

A spherical droplet impacting on a solid surface spreads on it. The final configuration of the liquid varies a great deal and depends on a multitude of parameters. For the case of water impinging on a surface at near-saturation temperature, the shape can be regarded as a segment of a sphere (Zhang and Yang, 1982). Note that, in this study, the droplet is considered to be homogeneous in the liquid phase at all times, and *evaporation* at the liquid-vapor interface is the only mean of generating the vapor phase.

The radius of the wetted area is a very important parameter, as recognized by Bonacina et al. (1979) and other investigators. In the literature, the radius of the wetted area is nondimensionalized with the radius of the sphere with equivalent initial liquid volume. This ratio is the parameter $\beta_o$. For droplets "softly" deposited on the surface (droplet released from height less than 1 cm), a value of $\beta_o$ in the range 1.2 to 1.5 is observed. However, for sprayed water, several investigators have reported values of $\beta_o$ up to 4.5 (Bonacina et al., 1979; Rizza, 1981). In this study the emphasis is on "softly" deposited droplets. It is crucial to note that these values of $\beta_o$ are referred to the initial condition at deposition before evaporation begins ($t=0$). Values for the more general parameter $\beta$ based on the liquid volume at any time during the evaporation process can be calculated using as a reference the radius of the wetted area and normalizing it with the radius of the spherical droplet having volume equal to the instantaneous volume of the water present. *Note that the radius of the wetted area is constant throughout most (90 to 95 percent) of the total evaporation time* as illustrated in Fig. 1. Wayner (1973) proposed a model to evaluate the liquid-solid contact angle during the evaporative process of a droplet wetting surface of constant radius.

The importance of the parameter $\beta$ is that it accounts for the effects of a number of variables that characterize the surface conditions (wettability, roughness, etc.), the fluid (surface tension, wetting ability, etc.), and the droplet deposition process. All the present experimental data were obtained for pure, degassed and de-ionized water droplets deposited on an aluminum block that was coated with a very thin ($\simeq 0.06$ $\mu$m) chromium layer. The chromium was vapor deposited on the aluminum to obtain a polished, smooth (roughness of 0.1–0.15 $\mu$m), and scratch-resistant surface. Prior to each droplet deposition, the surface was cleaned with ethyl alcohol to remove particles and grease. In spite of this careful procedure, some scatter in the experimental data was observed. This scatter is due mainly to the deposition technique, in which there was some uncertainty in positioning the hypodermic needle used to dispense the water above the surface. For each temperature considered (seven values between 75 and 100°C) and for each volume considered (five between 10 and $50\times10^{-9}$ m$^3$) ten values of $\beta_o$ were measured for a total of 350 data points. No systematic variation with volume was found because, in the limited range of droplet volume of interest, the values of $\beta_o$ obtained for the various volumes were not clearly distinguishable. The temperature dependence of $\beta_o$ was more evident; most of the data especially in the low-temperature range lie in the 5 percent band about the linear regression of the average values, which is given by

$$\beta_o = 0.009\, T_{so} + 0.6 \tag{1}$$

An analytical formulation defining the surface of a spherical segment representing the droplet on the surface in cylindrical coordinates is given by equating the volume of the spherical segment to the volume of the spherical droplet (and by assuming that at the droplet outer edge its thickness is zero). By introducing nondimensional coordinates, the equation for the droplet shape can be written as

$$s = \left[\frac{(1/\gamma+\gamma)^2}{4} - z^2\right]^{1/2} - \frac{(1/\gamma-\gamma)}{2} \tag{2}$$

where $s$ is $y/R$, $z$ is $r/R$, and $\gamma$ is found to be

$$\gamma = [4/\beta^3 + (1+16/\beta^6)^{1/2}]^{1/3} + [4/\beta^3 - (1+16/\beta^6)^{1/2}]^{1/3} \tag{3}$$

## Theoretical Evaporation Time

The high thermal conductivity of the metal solid suggests that the temperature of the solid surface under the droplet can be assumed constant during the evaporative process. This assumption implicitly uncouples the solid substrate properties from the evaporation process. For the case of a low-conductivity material it is anticipated that such uncoupling will not be possible.

In order to evaluate the liquid-vapor interfacial molar fraction, mass transfer as well as heat transfer must be considered. The heat balance at the interface can be written as

$$q = W\Lambda M_w + h(T_i - T_a) \tag{4}$$

where $W$ is the molar flux of the vapor at the water-air interface. The temperature profile in the liquid can be assumed to be linear (Bonacina et al., 1979), and the heat transfer contribution by convection and radiation can be neglected; this yields

$$\frac{k_w(T_s - T_i)}{Rs} = \left[\frac{x_i - x_a}{1-x_i}\right]\rho_a h_m \Lambda \left[\frac{M_w}{M_a}\right] \tag{5}$$

where $T_s$ is the surface temperature defined by Seki et al. (1978). By noting that the water-air molecular weight ratio is 0.624 and referring to Chilton and Colburn (1934), one obtains

$$\frac{k_w}{Rh_c s}(T_s - T_i) = 0.624\left[\frac{D}{\alpha_a}\right]^{2/3}\left[\frac{\Lambda}{c_a}\right]\left[\frac{x_i - x_a}{1-x_i}\right] \tag{6}$$

Note that the only unknown $x_i$ is a single-valued function of $T_s$. The left-hand side of this equation is finite at $r=R$ if the temperature at the droplet exposed surface coincides with the solid surface temperature. This condition seems reasonable

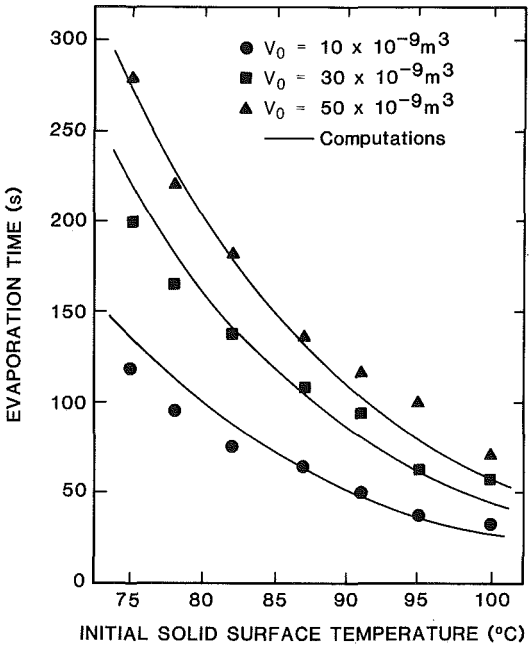


Fig. 2 Evaporation time as a function of initial solid surface temperature for various droplet volumes

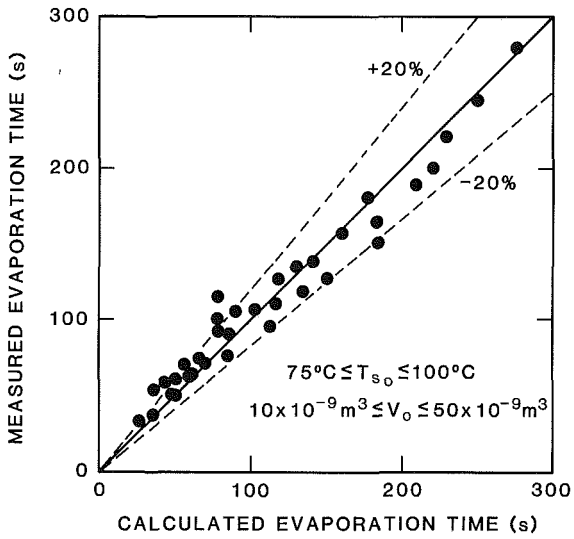


Fig. 3 Evaporation time: theory versus experiments

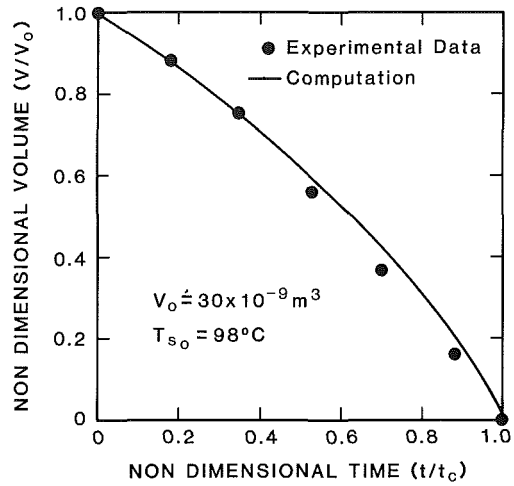


Fig. 4 Liquid water inventory versus time

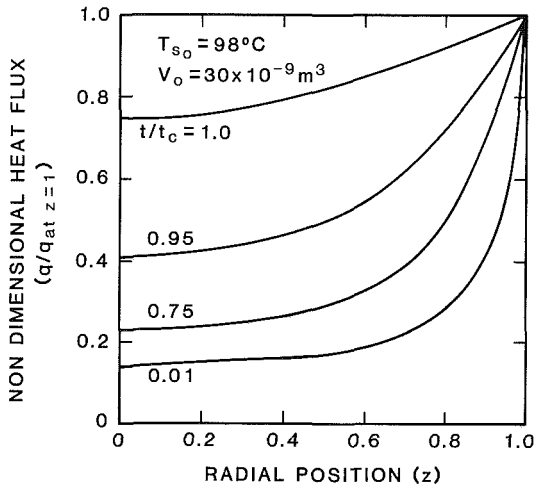


Fig. 5 Temporal and spatial heat flux behavior

and it is used to determine the vapor molar fraction in the air at the outer edge of the droplet.

By considering the energy balance on the liquid droplet, the instantaneous rate of evaporation is then deduced as

$$-\frac{dV}{dt}=\frac{2\pi R^2(0.624)h_c}{\rho_w c_a}\left[\frac{D}{\alpha_a}\right]^{2/3}\int_0^1\left[\frac{x_i-x_a}{1-x_i}\right]z\,dz \qquad (7)$$

and the local heat flux at the liquid–vapor interface is given by

$$q=0.624h_c\left[\frac{\Lambda}{c_a}\right]\left[\frac{D}{\alpha_a}\right]^{2/3}\left[\frac{x_i-x_a}{1-x_i}\right] \qquad (8)$$

When the initial volume is known, a numerical technique allows one to determine the total evaporation time from equation (7). Note that at each time step the evaporative mass flux is obtained by computing the integral in the right-hand side of the equation.

## Model Validation

The details of the experimental setup and a complete description of the data acquistion, in particular concerning the overall and convective heat transfer coefficients, are given by diMarzo and Trehan (1986). Figure 2 illustrates the comparison of results between the computations of the model developed in this study and experiments. Good agreement is observed. Figure 3 shows a comparison of the total evaporation time measured and calculated for a large number of experiments conducted in this study. In all these experiments, the droplet volume ranges between 10 and $50\times10^{-9}$ ms, and the initial surface temperature is in the range of 75 to 100°C. To validate the model further, the normalized liquid volume is plotted versus the time, nondimensionalized with respect to the total evaporation time, in Fig. 4. Very good agreement is found for the data, which were obtained from measurements of the volumes observed in photographic sequences of the droplet evaporation.

It is interesting to deduce information concerning the temporal and spatial distribution of the heat flux on the droplet-to-air interface from the model calculations. Figure 5 shows model predictions of the spatial heat flux distribution. The high heat flux at the droplet outer edge is evident. This finding is in agreement with the trends illustrated by the computations of Cook et al. (1981) based on measured local liquid mass flow rates at the liquid–solid contact line. Note that for three quarters of the total evaporation time the central portion of the droplet liquid–vapor interface does not contribute much to the process; in the last quarter, the dramatic flux increase is produced by the contribution of most of the droplet surface

because the reduced thickness of the droplet enhances the heat transfer across the liquid layer.

Michiyoshi and Makino (1978) observed that the temperatures at the solid surface and at a fixed point above it (in the liquid) are constant during the evaporation process. This fact implies that the heat flux is also constant. The results just shown confirm that during most of the evaporation process, in the region close to the droplet symmetry axis, the heat flux does not vary significantly.

These results show that the heat flux at the droplet edge can be as high as three times the spatial average heat flux at the beginning of the evaporation process. As the phenomenom progresses, the spatial average heat flux increases but the flux distribution in the radial direction becomes more uniform. Note that the droplet under consideration has a radius of about $3 \times 10^{-3}$ m and that a gradient of 1°C across that distance produces a heat flux of more than 40,000 $W/m^{-2}$ in the aluminum. It follows that the hypothesis of uniform temperature distribution under the droplet seems reasonable since the temporal and spatial average heat flux for this case is about 50,000 $W/m^{-2}$. The application of this simple boundary condition to the case of low thermal conductivity solid materials is not possible and a significant temperature distribution in the radial direction under the droplet is expected. To solve this problem, the droplet energy equation must be coupled with the solid energy equation at the liquid-solid interface in order to obtain a solution that accounts for the temperature distribution under the droplet.

## Conclusions

A model based on the assumption of uniform solid surface temperature is formulated for applications to droplets deposited on solids with large thermal conductivity. The droplet shape is successfully characterized using a spherical segment. The energy equation written for the droplet and at the liquid-vapor interface allows the determination of the evaporation time in reasonable agreement with experimental data. Further validation of the model is presented to describe the spatial and temporal behavior of the evaporative heat flux.


## Acknowledgments

This research was supported by a grant of the Center for Fire Research of the National Bureau of Standards. The authors are deeply indebted to Professor Michiyoshi for his prompt and courteous comments on the experimental data reported in his paper. The Computer Science Center of the University of Maryland provided funding for the numerical computation.


## References


Bonacina, C., Del Giudice, S., and Comini, G., 1979, "Dropwise Evaporation," ASME JOURNAL OF HEAT TRANSFER, Vol. 101, pp. 441-446.

Chilton, T. H., and Colburn, A. P., 1934, "Mass Transfer (Absorption) Coefficients—Prediction Data on Heat Transfer Fluid Motion," *Industrial Engineering Chemistry*, Vol. 26, pp. 1183-1187.

Cook, R., Tung, C. Y., and Wayner, P. C., 1981, "Use of Scanning Microphotometer to Determine the Evaporative Heat Transfer Characteristics of the Contact Line Region," ASME JOURNAL OF HEAT TRANSFER, Vol. 103, pp. 325-330.

diMarzo, M., and Trehan, A. K., 1986, "Transient Cooling of a Hot Surface by Droplets Evaporation," Technical Report, NBS-GCR-86-516, National Bureau of Standards, Gaithersburg, MD.

Michiyoshi, I., and Makino, K., 1978, "Heat Transfer Characteristics of Evaporation of a Liquid Droplet on Heated Surfaces," *International Journal of Heat and Mass Transfer*, Vol. 21, pp. 605-613.

Rizza, J. J., 1981, "A Numerical Solution to Dropwise Evaporation," ASME JOURNAL OF HEAT TRANSFER, Vol. 103, pp. 501-507.

Seki, M., Kawamura, H., and Sanokawa, K., 1978, "Transient Temperature Profile of a Hot Wall Due to an Impinging Liquid Droplet," ASME JOURNAL OF HEAT TRANSFER, Vol. 100, pp. 167-169.

Wayner, P. C., 1973, "Fluid Flow in the Interline Region of an Evaporating Non-zero Contact Angle Meniscus," *International Journal of Heat and Mass Transfer*, Vol. 16, pp. 1777-1783.

Zhang, N., and Yang, W. J., 1982, "Natural Convection in Evaporating Minute Drops," ASME JOURNAL OF HEAT TRANSFER, Vol. 104, pp. 656-662.